

https://dspace.org/

The role of sulphur in siderophile and chalcophile element enrichment of the lithospheric mantle: constraints from Kaapvaal mantle xenoliths and high-pressure partial melting experiments of S±C-bearing eclogite

Burness, Sara

2019

https://hdl.handle.net/10539/30460

Burness, Sara (2019) The role of sulphur in siderophile and chalcophile element enrichment of the lithospheric mantle: constraints from Kaapvaal mantle xenoliths and high-pressure partial melting experiments of S±C-bearing eclogite, University of the Witwatersrand, Johannesburg, <http://hdl.handle.net/10539/30460>

Downloaded from a DSpace repository. https://dspace.org/

UNIVERSITY OF THE WITWATERSRAND

JOHANNESBURG



FACULTY OF SCIENCE

SCHOOL OF GEOSCIENCES

THE ROLE OF SULPHUR IN SIDEROPHILE AND CHALCOPHILE ELEMENT ENRICHMENT OF THE LITHOSPHERIC MANTLE: CONSTRAINTS FROM KAAPVAAL MANTLE XENOLITHS AND HIGH-PRESSURE PARTIAL MELTING EXPERIMENTS OF S±C-BEARING ECLOGITE

By

Sara Burness

A thesis submitted to the Faculty of Science, University of the Witwatersrand, Johannesburg, in fulfilment of the requirements for the degree of

Doctor of Philosophy

Supervisors:

Dr. Katie A. Smart

Prof. Gary Stevens

25 September 2019

DECLARATION

By submitting this thesis, I declare that the work is my own, original work. It is being submitted for the degree of Doctor of Philosophy at the University of the Witwatersrand, Johannesburg. I have not previously in its entirety or in part submitted this work for examination at any other University. All aspects of this thesis including; sample preparation, experimental technique, data acquisition and manuscript preparation (save to the extent explicitly otherwise stated), were conducted independently under the supervisory guidance of Dr. Katie A. Smart and Prof. Gary Stevens (Stellenbosch University).

S. Burness

…….

(Signature of candidate)

Signed on the 25th of September 2019 at the University of the Witwatersrand

PREAMBLE

This PhD thesis embodies the results of my research conducted at the University of the Witwatersrand and Stellenbosch University between 2015 and 2019. The thesis is divided into six main chapters as described below.

CHAPTER 1: Introduction

CHAPTER 2: The Kaapvaal Craton

CHAPTER 3: Presentation of the research paper entitled, "Sulphur-rich mantle metasomatism of Kaapvaal craton eclogites and its role in redox-controlled platinum group element mobility".

CHAPTER 4: Presentation of the research paper entitled, "Pervasive Fe- and S-rich metasomatism of the cratonic lithospheric mantle below Premier kimberlite, South Africa".

CHAPTER 5: Presentation of the research paper entitled, "The mobility of sulphur in the upper mantle: constraints from S±C-bearing eclogite experiments".

CHAPTER 6: Summary style conclusions and implications of this research.

ABSTRACT

Sulphur- and carbon-bearing melts play an important role as metasomatic agents within the cratonic mantle lithosphere. While carbon-bearing melt metasomatism has been linked to various lithosphere enrichment processes including, diamond formation and kimberlite magmatism as part of the deep carbon cycle, information about the behaviour of sulphur during metasomatism and partial melting is less well constrained. Sulphide minerals predominantly host the mantle platinum group element (PGE), siderophile and chalcophile element budgets, and their behaviour during melting controls the movement of these economically important metals. Here I present a case study of eclogite and peridotite metasomatism by sulphur±carbon-bearing fluids/melts by comparing new experimental work with geochemical, stable isotopic and petrologic investigations of sulphide-bearing eclogite and peridotite xenoliths from several key kimberlite occurrences on the Kaapvaal craton, South Africa. The experiments conducted from 2 to 3.5 GPa and 1050 to 1300 ºC on sulphur±carbon-bearing eclogite compositions demonstrate that the critical factors concerning the mobility of sulphur in upper mantle eclogite are the degree of partial melting and the compositions of the resulting melts. Pure sulphide melt is shown to be largely immobile within the MORB-like eclogite system unless aided by more fluid-mobile carbonate±silicate melts at these upper mantle conditions. Sulphur is effectively mobilised as immiscible sulphide liquid melt pools within CO_2-free basaltic-andesite melts and as dissolved elemental sulphur within intermediate carbonate-silicate melts at >15 % partial melting of the mixed volatile-bearing eclogite compositions. Comparative investigations of eclogite and peridotite xenoliths show that the metasomatic precipitation of secondary sulphide is intimately linked to metasomatism of the host silicate assemblage. The sulphide minerals are exceptionally redox sensitive and contain variable PGE contents with characteristic I-PGE/P-PGE fractionations, which are controlled by the compositional character of the metasomatic melt/fluid. Specifically, the xenoliths investigated here show evidence for several contrasting depth-dependent, and sometimes location-specific, metasomatic events which may have affected both the Kaapvaal cratonic lithosphere as well as the craton above. Moreover, this study demonstrates that metasomatic enrichment of the cratonic lithosphere by sulphur±carbon-bearing fluids/melts has resulted in isotopic heterogeneities and the addition of new minerals such as sulphide and potentially also diamond since the Archean.

KEYWORDS: base metal sulphide; lithospheric mantle; mantle redox; metasomatism; oxygen isotopes; peridotite; platinum group elements; sulphur isotopes

ACKNOWLEDGEMENTS

I am greatly indebted to several people and institutions who have provided guidance as well as technical and financial support during my PhD research. The following deserve special acknowledgements:

First, a heartfelt thank-you to my supervisor Katie Smart who has put in countless hours assisting me with my scientific research and writing skills. For sharing new scientific techniques and affording me the opportunity to present at international conferences, where you happily introduced me to fellow academics within our unique 'mantle land' field. Your ambition, dedication and pure talent inspires me to become a better researcher.

Gary Stevens, for your supervisory guidance and financial support over the years. Thank-you for introducing me to the field of experimental petrology and for imparting your expert skills in the experimental lab.

Sebastian Tappe, for sourcing samples from Helam and Cullinan Diamond Mines. In addition, thank-you for all your helpful advice during all stages of the project and for including me in discussions at the Deep & Early Earth Processes (DEEP) Research Group meetings. This participation has added great value to my academic development and has improved my understanding of mantle petrogenetic processes.

Alan Woodland, for garnet Fe^{3+} compositions determined by Mössbauer spectroscopy at Goethe Universität Frankfurt, Germany. This data is key to understanding mantle redox compositions.

Emilie Thomassot, for the invitation to CNRS-CRPG facility in Nancy, France, where I learned about multiple sulphur-isotope analysis on the SIMS.

Riana Russouw, is thanked for enabling both silicate and sulphide trace element analysis using the LA-ICP-MS system at the University of Stellenbosch.

Phillip Janney, for access to the "John J. Gurney Upper Mantle Research Collection" at the University of Cape Town.

James Brenan, for provision of the NiS5b (MB2014) sulphide standard, which proved instrumental to this study.

I would like to recognise the Freestanding, Innovation and Scarce Skills Doctoral Scholarship (ref no: 111369) that I received from the National Research Foundation (NRF) in 2016 and 2017, as well as the extension support (ref no: 102211) received in 2018. Additionally, I would like to thank the Centre of Excellence for Integrated Mineral & Energy Resource Analysis (CIMERA) for providing further financial support.

My colleagues and friends at the geoscience department of Stellenbosch, who have assisted with a variety of tasks (including keeping me sane!): Simon Couzinié, Andrew Watson, Matthew Mayne, Kelley Swana, Nonkuselo Madlakana, and Elrika Harmzen-Pretorius.

To my wonderful family, Mom, Dad, Amy and Darren, without your endless support and care none of this would have been possible!

Finally, to Alexander Reichle, thank-you for being my best friend, confidant and pillar of strength. The world is our oyster.

TABLE OF CONTENTS

CHAPTER 1: 1

1. INTRODUCTION 1

CHAPTER 2: 17

2. THE KAAPVAAL CRATON 17

2.1. KAAPVAAL CRATON GEOLOGY AND EVOLUTION 17
2.2. CRATONIC LITHOSPHERIC MANTLE PETROLOGY 18
CHAPTER 2: FIGURES 28

CHAPTER 3: 29

3. PRESENTATION OF THE RESEARCH PAPER:

"SULPHUR-RICH MANTLE METASOMATISM OF KAAPVAAL CRATON ECLOGITES AND ITS ROLE IN REDOX CONTROLLED PLATINUM GROUP ELEMENT MOBILITY" 29

ABSTRACT 30
3.1. INTRODUCTION 31
3.2. GEOLOGICAL SETTING 32
3.3. SAMPLES AND PETROGRAPHY 34
3.4. ANALYTICAL METHODS 35
3.4.1. Major and minor element compositions 35
3.4.2. Trace element compositions 35
3.4.3. Oxygen isotope analysis of garnet 36
3.4.4. Garnet $Fe^{3+}/\Sigma Fe$ contents 37
3.5. RESULTS 37
3.5.1. Major element compositions of garnet and clinopyroxene 37
3.5.2. Trace element compositions of garnet and clinopyroxene 38
3.5.3. Calculated bulk eclogite compositions 39
3.5.3.1. Metasomatism 39
3.5.3.2. Major element compositions 40
3.5.3.3. Trace element compositions and eclogie groups 40
3.5.4. Thermobarometry 41
3.5.5. Garnet $Fe^{3+}/\Sigma Fe$ and eclogite oxybarometry 41
3.5.6. Garnet oxygen isotope compositions 42

3.5.7. Base metal sulphide petrography 42
3.5.7.1. Modal abundance and distribution 42
3.5.7.2. Habits and textural relationships 42
3.5.7.3. Low-temperature sulphide major element compositions 44
3.5.7.4. BMS major element reconstructions 45
3.5.7.5. BMS trace element compositions 46
3.6. DISCUSSION 47
3.6.1. Petrogenesis of Kaapvaal craton eclogite xenoliths 47
3.6.2. Evaluating the effects of sulphur-bearing metasomatism on cratonic mantle lithosphere 48
3.6.2.1. Mantle eclogites residing within the lower lithosphere 48
3.6.2.2. Mantle eclogites residing at mid-lithospheric levels 50
3.7. SUMMARY AND CONCLUSIONS 52
CHAPTER 3: TABLES 71
CHAPTER 3: FIGURES 83

CHAPTER 4: 94

4. PRESENTATION OF THE RESEARCH PAPER:

"PERVASIVE FE- AND S-RICH METASOMATISM OF THE CRATONIC LITHOSPHERIC MANTLE BELOW PREMIER KIMBERLITE, SOUTH AFRICA" ... 97

ABSTRACT 98
4.1. INTRODUCTION 99
4.2. GEOLOGICAL SETTING AND PREVIOUS INVESTIGATION OF PREMIER LITHOSPHERIC MANTLE 101
4.3. SAMPLES AND PETROGRAPHY 103
4.4. ANALYTICAL METHODS 104
4.4.1. Scanning electron microscopy 104
4.4.2. Laser Ablation Inductively Coupled Plasma Mass Spectrometry 104
4.4.3. Secondary-ion mass spectrometry 105
4.5. RESULTS 106
4.5.1. Peridotite mineral compositions 106
4.5.1.1. Major element composition 106
4.5.1.2. Trace element composition 107
4.5.2. Geothermobarometry 108
4.5.3. Base metal sulphides 109
4.5.3.1. Modal abundance and distribution 109

4.5.3.2. Habits and textural relationships *109*
4.5.3.3. BMS major element chemistry *111*
4.5.3.4. BMS trace element chemistry *112*
4.5.3.5. Sulphur isotopic compositions *113*
4.6. DISCUSSION: FE- AND S-RICH METASOMATISM OF THE PREMIER GARNET-BEARING LHERZOLITES 114
4.6.1. Evidence for metasomatism of the silicate mineral phases *114*
4.6.2. A metasomatic origin for base metal sulphide in Premier garnet-bearing lherzolites *116*
4.6.3. Evidence from multiple sulphur isotopes *118*
4.7. POSSIBLE IMPLICATIONS 120
4.8. CONCLUSIONS 121
CHAPTER 4: TABLES 136
CHAPTER 4: FIGURES 143

CHAPTER 5: 155

5. PRESENTATION OF THE RESEARCH PAPER:

"THE MOBILITY OF SULPHUR IN THE UPPER MANTLE: CONSTRAINTS FROM S±C-BEARING ECLOGITE EXPERIMENTS" 155

ABSTRACT 156
5.1. INTRODUCTION 157
5.2. PREVIOUS WORK 159
5.3. EXPERIMENTAL APPROACH 161
5.3.1. Starting materials 161
5.3.2. Experimental methods 162
5.4. ANALYTICAL TECHNIQUES 163
5.4.1. Scanning electron microscopy 163
5.5. EXPERIMENTAL RESULTS 164
5.5.1. Approach to equilibrium 164
5.5.2. Oxygen fugacity and sulphur speciation 165
5.5.3. Phase assemblages, textural relationships, and modal proportions 166
5.5.3.1. SKG–1 (SKG glass + 5 wt. % Pn) *166*
5.5.3.2. SKG–2 (SKG glass + 5 wt. % Pn + 4.7 % CO_2) *166*
5.5.3.3. SKG–3 (SKG glass + 5 wt. % Pn + 11.8 % CO_2) *167*
5.5.4. Solidus location and phase chemistry 167
5.5.4.1. Silicate mineral assemblage *168*
5.5.4.2. Quenched melt products *170*

5.5.4.3. Sulphur-rich phases *171*
5.6. DISCUSSION 173
5.6.1. The role of sulphur in the melting of (CO_2-bearing) eclogite at the upper mantle conditions 173
5.6.1.1. Sulphide anatexis in the silicate eclogite system *173*
5.6.1.2. Sulphide anatexis in the CO_2-bearing eclogite system *174*
5.6.1.3. Anatexis in the CO_2-bearing eclogite system with implications for the mobility of sulphur *175*
5.6.2. Sulphur transport within the eclogite-derived melts in the upper mantle 177
5.6.2.1. Creation of fertile sulphide-bearing mantle lithologies *178*
5.6.2.2. Base metal sulphides mobility in the upper mantle *179*
5.6.2.3. Implications for diamond formation and mantle magmatism *179*
5.7. CONCLUSIONS 181
CHAPTER 5: TABLES 200
CHAPTER 5: FIGURES 205

CHAPTER 6: 213

6. THE KAAPVAAL CRATON 213

6.1. MAJOR FINDINGS 213
6.1.1. Kaapvaal cratonic mantle eclogite petrogenesis with emphasis on the effects of S-bearing metasomatism 214
6.1.2. Premier peridotite petrogenesis with emphasis on the effects of S-bearing metasomatism 215
6.1.3. Sulphur±carbon-bearing eclogite experiments with emphasis on the mobility of sulphur/sulphide in the upper mantle 217
6.2. SUMMARY AND FUTURE DIRECTIONS 218

APPENDICES I

ADDITIONAL DATA: MULTIPLE SULPHUR ISOTOPES I

CHAPTER 3: APPENDICES VII

APPENDIX A VII
APPENDIX B VIII
APPENDIX C IX
APPENDIX D X
APPENDIX D.1 XVI

APPENDIX E XVII

CHAPTER 4: APPENDICES XVIII

APPENDIX A XVIII
APPENDIX B XX
APPENDIX C XXIII

CHAPTER 5: APPENDICES XXIV

APPENDIX A XXIV
APPENDIX B XXV
APPENDIX B.2 XXIX
APPENDIX B.3 XXX
APPENDIX B.4 XXXI
APPENDIX C XXXII
APPENDIX D XXXIII
APPENDIX E XXXIV
APPENDIX F XXXV

LIST OF TABLES

CHAPTER 3: TABLES 71

Table 3.1. Major and minor element compositions of garnet and clinopyroxene from the Kaapvaal eclogite xenoliths 71

Table 3.2. Representative major element compositions of low-temperature sulphides from the Kaapvaal eclogite xenoliths 73

Table 3.3. Sulphide occurrence and bulk-sulphide compositions from Kaapvaal eclogite xenoliths 74

Table 3.4. Trace element compositions of garnet and clinopyroxene from Kaapvaal eclogite xenoliths 75

Table 3.5. Trace element compositions of sulphides from Kaapvaal eclogite xenoliths 79

Table 3.6. Thermobarometry, oxybarometry and garnet oxygen isotope compositions for the Kaapvaal eclogite xenoliths 80

Table 3.7. Calculated whole-rock major and trace element compositions for Kaapvaal eclogite xenoliths 81

CHAPTER 4: TABLES 136

Table 4.1. Major element composition of minerals from Premier garnet-bearing lherzolite xenoliths 136

Table 4.2. Representative major element analyses of base metal sulphides and associated magnetite from Premier garnet-bearing lherzolite xenoliths 137

Table 4.3. Select garnet and clinopyroxene trace element compositions from Premier garnet-bearing lherzolite xenoliths 138

Table 4.4. Select olivine and orthopyroxene trace element compositions from Premier garnet-bearing lherzolite xenoliths 139

Table 4.5. Select sulphide trace element compositions from Premier garnet-bearing lherzolite xenoliths 140

Table 4.6. Sulphur isotope measurements of xenolith-derived sulphides from Premier kimberlite 141

Table 4.7. Pressure - Temperature estimates of last equilibration of the Premier garnet-bearing lherzolites 142

CHAPTER 5: TABLES 200

Table 5.1. Model mafic starting compositions used in previous experimental studies on mantle melting of eclogite or pyroxenite 200

Table 5.2. Composition of the "SKG" starting materials 201

Table 5.3. Partial melting experiments of "SKG" starting compositions 202

Table 5.4. Experimental run-product mineral and quenched liquid compositions 203

Table 5.5. Experimental run-product sulphide melt (LS) and mono-sulphide solid solution (MSS) compositions 204

LIST OF FIGURES

CHAPTER 2: FIGURES 28

Figure 2.1 Schematic of the Kaapvaal craton modified after Friese et al. (2003)..... 28

CHAPTER 3: FIGURES 83

Figure 3.1 Schematic of the Kaapvaal craton modified after Friese et al. (2003)..... 83

Figure 3.2 Select Kaapvaal Craton mantle eclogite xenoliths. 84

Figure 3.3 (a) Ternary Ca-Mg-Fe compositions of the Kaapvaal eclogite garnets. **(b)** Na_2O vs. MgO (wt. %) contents of clinopyroxene. 85

Figure 3.4 Chondrite-normalised REE patterns for garnet **(a - c)** and clinopyroxene **(d - f)** from the Kaapvaal eclogite xenoliths. 86

Figure 3.5 Multi-element variation diagrams showing the calculated bulk-rock compositions of the Kaapvaal eclogites. **(a)** MgO vs. Al_2O_3; **(b)** vs. SiO_2; **(c)** vs. CaO; **(d)** vs. Na_2O; **(e)** vs. FeO; **(f)** vs. TiO_2. 87

Figure 3.6 Calculated whole-rock REE patterns of the Kaapvaal eclogite xenoliths. 88

Figure 3.7 Calculated whole-rock trace-element patterns of the Kaapvaal craton eclogite xenoliths. **(a)** average pattern for each trace element group, **(b)** "HREE-enriched", **(c)** "LREE-depleted", **(d)** "LREE-enriched" 89

Figure 3.8 Estimated pressure-temperature conditions for the Kaapvaal xenoliths... 90

Figure 3.9 Oxybarometry of the Kaapvaal eclogite xenoliths. **(a)** $\Delta \mathrm{Log}fO_2$ values (relative to the FMQ buffer). **(b)** T_{EG79} and $\Delta \log fO_2$ (FMQ). 91

Figure 3.10 (a) Oxygen isotope compositions of garnet from Kaapvaal eclogite xenoliths... 92

Figure 3.11 Select BSE images of sulphide grains from the Kaapvaal eclogites. 93

Figure 3.12 Kaapvaal eclogite low-temperature sulphide compositions in the Cu-Fe-Ni-S system at 300ºC..... 94

Figure 3.13 Ni/(Ni+Fe) at. % vs. Metal/Sulphur at. % of low-temperature sulphide phases..... 95

Figure 3.14 In-situ chondrite normalised HSE patterns for (a) Group 1 and (b) Group 2 base metal sulphides. (c) Chondrite normalised calculated whole-rock HSE patterns for the Kaapvaal eclogites. 96

CHAPTER 4: FIGURES 143

Figure 4.1 Schematic of the Kaapvaal craton modified after Friese et al. (2003)..... 143

Figure 4.2 Select garnet-bearing lherzolite xenoliths from Premier kimberlite. **(a – c)** Coarse garnet-bearing lherzolites, **(d – f)** deformed garnet-bearing lherzolites..... 144

Figure 4.3 Primitive-mantle normalised REE and trace element patterns for garnet **(a - b**) and clinopyroxene **(c – d)** from the Premier garnet-bearing lherzolite xenoliths. 145

Figure 4.4 Premier garnet-bearing lherzolite P-T conditions calculated iteratively using the four-phase geothermobarometer of Brey and Köhler (1990). 146

Figure 4.5 Select back-scattered electron images of BMS grains of different perographic types and assemblages from Premier garnet-bearing lherzolites. 147

Figure 4.6 Detailed back-scattered electron images of BMS grains of different perographic types and compositions from the Premier garnet-lherzolite lherzolite xenoliths. 148

Figure 4.7 Premier BMS major element compositions in the Cu-Fe-Ni-S system at 300 ºC. 149

Figure 4.8 Premier sulphide major element compositions, including oxidised/altered sulphide mineral phases. **(a)** Fe/metals (Fe+Ni+Cu+Co±Zn) ratio vs. metals/sulphur ratio. **(b)** Ni/metals ratio vs. metals/sulphur ratio..... 150

Figure 4.9 Binary variation plots of highly siderophile and chalcophile element concentrations and their inter-elemental ratios. **(a)** Ir vs. Pt. **(b)** Pt vs. Pd. **(c)** Pd_N/Pt_N vs. Pd_N/Ir_N. **(d)** Pt_N/Ir_N vs. Pd. **(e)** Te vs. Se. **(f)** Pd_N/Ir_N vs. Se/Te. 151

Figure 4.10 (a – b) In-situ chondrite-normalised HSE patterns for pentlandite and pyrite from Premier coarse-lherzolite xenoliths CIM15-006 and -004. 152

Figure 4.11 Plot of $\delta^{34}S$ (relative to CDT) vs $\Delta^{33}S$ for sulphides (Pn) from coarse lherzolite CIM15-006. **(a)** Individual measurements on each perdotite-derived sulphide grain (S1 to S4).**(b)** Average $\delta^{34}S$ vs. $\Delta^{33}S$ for each sulphide grain. 153

Figure 4.12 (a) Garnet Ca-intercept vs. total FeO (wt. %). **(b)** Zr and Y of garnet. **(c)** Garnet Y vs. chondrite-normalised Lu/Yb ratio. **(d)** Clinopyroxene Mg# vs. Cr_2O_3 contents. **(e)** Clinopyroxene Ca# vs. molar Na content. **(f)** Clinopyroxene chondrite-normalised Sm/Hf vs. La/Nb. 154

CHAPTER 5: FIGURES 205

Figure 5.1 (a) A summary of published sulphide, CO_2-bearing eclogite and peridotite melting curves. (**b)** P-T diagram showing the experimental phase assemblages of the different SKG bulk compositons. 205

Figure 5.2 BSE images of select experimental runs. **(a)** SKG-1.2; 2.0 GPa and 1200 ºC. **(b)** SKG-2.1; 2.0 GPa and 1200 ºC. **(c)** SKG-2.3; 3.5 GPa and 1150 ºC. **(d)** SKG-3.1; 2.5 GPa and 1050 ºC. **(e)** SKG-3.4; 2.5 GPa and 1150 ºC. **(f)** Phase assemblages of selected experiments. 206

Figure 5.3 (a) Molar Mg-Ca-Fe diagram depicting the compositions of the experimental garnets. **(b)** Na_2O vs. MgO (wt. %) contents of clinopyroxene. 207

Figure 5.4 Multi-element variation diagrams showing the liquid silicate-dominated melt compositions produced by the SKG-1 and SKG-2 experiments. (**a)** SiO_2 vs. Na_2O+K_2O. **(b)** MgO vs. CaO. **(c)** MgO vs. FeO. (**d)** MgO vs. Al_2O_3. 208

Figure 5.5 (a) Temperature (ºC) vs. **(a)** SiO_2 (wt. %) and **(b)** CO_2 (wt. %) of the SKG experimental melts. **(c)** Pressure (GPa) vs. molar Ca /(Ca + Mg) of the SKG experimental melts. **(d)** MgO (wt. %) vs. CaO (wt.%) of the SKG experimental clinopyroxenes. 209

Figure 5.6 Ternary diagrams diagrams (a) and (b) showing the SKG experimental melt compositions in wt.%. 210

Figure 5.7 (a) Fe-Ni-S (wt. %) ternary diagram showing the experimentally produced sulphide melt compositions at 2.0 GPa and 1200 ºC. **(b)** Experimentally produced MSS Fe (wt. %) composition vs. experimental pressure (GPa). **(c)** Metals (Fe+Ni+Cu+Co)/Sulphur (at. %) vs. Cu/Metals (at. %) of experimentally produced MSS 211

Figure 5.8 (a–b) Backscattered electron microprobe images of globular sulphides along spongy clinopyroxene grain boundaries around a diamond inclusion within eclogitic garnet. 212

ABBREVIATIONS, NOMECLATURE, SYMBOLS

GEOLOGIC TIME SCALES

Archean	Geologic eon from 3.8 to 2.5 Ga
Paleoarchean	Geologic era within the Archean from 3.6 to 3.2 Ga
Mesoarchean	Geologic era within the Archean from 3.2 to 2.8 Ga
Proterozoic	Gologic eon from 2500 to 542 Ma
Paleoproterozoic	Geologic era within the Proterozoic from 2.5 to 1.6 Ga
Mesozoic	Geologic era from 252 to 66 Ma
Ga	Billions of years ago
Ma	Millions of years ago

UNITS OF MEASURE

%	Parts per hundred (per cent)
‰	Parts per thousand (per mil)
cm	Centimetre
ºC	Degrees celcius
GPa	Gigapascal
kV	Kilovolt
log unit	Quantity on a logarithmic scale
nm	Nanometre
nA	Nanoampere
ppm	Parts per million
s	Second
µm	Micrometre
µg/g	Microgram per gram
wt. %	Weight percent, concentration
W	Watt

σ	One standard deviation from the mean
Σr^2	Sum of squared residuals
Ca-intercept	A measure of how far a garnet is removed from the G10/G9 division
Ca#	Molar ratio of Ca/(Ca+Mg+Fe)
Mg-number/Mg#	Molar ratio of Mg/(Mg+Fe)

ELEMENT CLASSIFICATIONS

CSE	Chalcophile (sulphur-loving) and siderophile (metal-loving) elements
HFSE	High Field Strength Element
HREE	Heavy Rare Earth Element
HSE	Highly Siderophile Element
LILE	Large Ion Lithophile Element
LREE	Light Rare Earth Element
MREE	Middle rare earth element
PGE	Platinum Group Element
REE	Rare earth element
$_N$	Subscript to indicate normalised values

ANALYTICAL METHODS

LA-ICP-MS	Laser Ablation Inductively Coupled Mass Spectrometry
SEM	scanning electron microscopy
SIMS	Secondary-ion mass spectrometry

ISOTOPE NOMECLATURE

α	Isotopic fractionation factor
Δ	"Uppercase delta" approximation of ln α
$\delta^{18}O$	Oxygen isotope relative to a standard
$\delta^{33}S$	Sulphur isotope relative to a standard
SMOW	Standard Mean Ocean Water oxygen isotope standard

S-MIF	Sulphur-mass independent fractionation
V–CDT	Vienna-Canon Diablo Troilite

OXYGEN AND SULPHUR FUGACITY NOMECLATURE

$\boldsymbol{fO_2}$	Oxygen fugacity
$\mathbf{Fe^{3+}}$	Ferric/oxidised iron
$\mathbf{S^{2-}}$	Sulphide
$\mathbf{SO_4^{2-}}$	Sulphate
QFM	Quartz-fayalite-magnetite oxygen
IW	Iron-wüstite buffer

ABBREVIATIONS

ca.	Circa
c.f.	Confer with
e.g.	For example
i.e.	That is
CLM	Cratonic lithospheric mantle
PUM	Primitive upper mantle
BMS	Base metal sulphide
MSS	Mono-sulphide solid solution
Pn	Pentlandite
Py	Pyrite
Po	Pyrrhotite
Cp	Chalcopyrite
Hz	Heazlewoodite

INSTITUTIONS/ LABORATORIES

CAF	Central Analytical Facility, Stellenbosch University, South Africa
CRPG-CNRS	Centre de Recherche Pétrographiques et Géochimiques, France

CHAPTER 1

1. INTRODUCTION

Sulphur is an abundant element that occurs in a variety of valence states ranging from reduced S^{2-} (sulphide and reduced organic sulphur) to oxidised S^{6+} (sulphate; e.g. Hagström et al., 1964). While sulphur is an essential element for life, it only comprises ~1% of Earth's living organisms (Beinert, 2000). The majority of sulphur in the Earth's crust occurs in metal-sulphide ore deposits (Canfield, 2004) and sulphate-bearing evaporite reservoirs (Barton and Johnson, 1996; Spencer, 2000). The cycling of sulphur between the interior of the Earth and the surface governs the mobility of other chalcophile elements and makes the mantle an important reservoir of sulphur as well (Mandeville, 2010). The most important hosts of sulphur in the Earth's upper mantle are redox-sensitive base metal sulphides (BMS; Chaussidon et al., 1989; Alard et al., 2000; Luguet et al., 2003, 2007; Lorand et al., 2013; Mungall and Brenan, 2014; Wainwright et al., 2015; Kiseeva et al., 2017; Luguet and Pearson, 2019) as well as a lower abundance of platinum group alloy minerals (PGM; Brenan and Andrews, 2001; Luguet et al., 2007). The chief base metal sulphide phases observed in upper mantle lithologies, namely peridotite and eclogite, are pentlandite (Pn) and chalcopyrite (Cp) as well as lesser pyrrhotite (Po). These phases are interpreted as residual sub-solidus products of a single high-temperature sulphide melt/liquid that occurred within the upper mantle (e.g. Fleet and Pan, 1994; Guo et al., 1999; Lorand and Gregoire, 2006; Lorand et al., 2013; Wainwright et al., 2015), and which subsequently quenched as a result of xenolith or rock exhumation to the surface.

It is well established that base metal sulphides predominantly host the chalcophile and highly siderophile element (HSE, including platinum group elements) budgets of the upper mantle (e.g. Luguet et al., 2007; Liu et al., 2009), and that sulphur governs the petrogenetic processes surrounding the transportation and concentration of these economically important metals within upper mantle lithologies as either metasomatic sulphide nuggets (e.g. Alard et al., 2000) or diamond mineral inclusions (e.g. Westerlund et al., 2004). The mobility of sulphur and associated trace elements within the upper mantle requires that sulphide minerals break down in melt- or fluid-forming reactions that release sulphur into a mobile phase. For example, experiments show that base metal sulphides melt incongruently to form mono-sulphide solid solution (MSS) that preferentially concentrates I-PGE and relatively mobile Cu-Ni-Fe-rich sulphide melt that that preferentially concentrates P-PGE at upper mantle pressures and temperatures (c.f. Peach et al., 1990; Li et al., 1996; Peregoedova et al., 2004; Bockrath et al., 2004; Mungall et al., 2005; Ballhaus et al., 2006; Fonseca et al., 2011; Mungall and Brenan, 2014). This evidence suggests that melting of BMS within the upper mantle could potentially fractionate both mantle and mantle-derived melt PGE abundances (e.g. Luguet et al., 2007).

Experiments conducted in the sulphide-silicate (MORB) system show that sulphur solubility within silicate-dominated melts is a complex function of both temperature and pressure (e.g. Mavrogenes and O'Neill, 1999), oxygen fugacity and sulphur speciation (Scaillet and Pichavant, 2005; Jugo, 2009; Li and Ripley, 2009), as well as both the silicate melt composition (specifically the FeO content; Holzheid and Grove, 2002; Liu et al., 2007) and the composition of the sulphide component (e.g. Smythe et al., 2017). However, it is generally suggested that during partial melting, I-PGE enriched MSS most probably remains refractory within mantle peridotite residues during the extraction of low melt fractions of 10 – 15% (Jégo and Dasgupta, 2013; Ding and Dasgupta, 2017, 2018), unless the partial melting event is particularly oxidising (e.g. FMQ = >1) then sulphides will be efficiently removed (Jugo et al., 2005; Jugo, 2009). Comparatively, at high degrees of mantle melting (> 15%), MSS may be completely consumed within the melt component and thus I-PGE concentrations in mantle residues could decrease to below detection (c.f. Lorand et al., 2013).

Like other trace elements within the mantle, the movement and sequestration of the HSEs can be used to trace fluid-mantle reactions during melt depletion, re-fertilisation and metasomatism of upper mantle lithologies (Barnes et al., 1988; Luguet et al., 2007; Lorand et al., 2013; Wainwright et al., 2015; Lorand and Luguet, 2016; Luguet and Pearson, 2019). Incompatible (e.g. the light rare earth elements, La, Ce, Sm, etc.) and fluid-mobile (e.g. the large ion lithophile elements, Ba, Rb, etc.) lithophile elements involved in metasomatism that predominantly affect the silicate mantle, are well known to produce marked incompatible element enrichment, for example, in mantle peridotite garnet and clinopyroxene phases (e.g. Grégoire et al., 2003; O'Reilly and Griffin, 2013). These mobile elements may also be linked to the growth of new minerals (such as diamond and pyroxene; e.g. Stachel and Harris, 2008) or even the creation of long-term isotopically enriched mantle reservoirs (e.g. Pearson et al., 1995). The chalcophile nature of the HSEs means their movement and storage are instead intimately linked to deep sulphur cycles (De Hoog et al., 2001; Tsuno and Dasgupta, 2015; Ding and Dasgupta, 2017) and movement of volatile-bearing melts (e.g. Ding and Dasgupta, 2018). Many depleted (e.g. I-PGE or P-PGE poor) or enriched (e.g. I-PGE/P-PGE enriched) HSE signatures described in mantle peridotite and eclogite xenoliths as well as crustal mantle-derived enclaves may be explained by reaction with infiltrating, frequently volatile-rich, fluids or additionally a combination of partial melting and secondary overprinting events, which can result in contrasting behaviour of base metal sulphides and characteristically different HSE fractionations. For example, melt-rock interaction with large quantities of "silicate melt" (i.e. andesitic or basaltic in composition) will result in residual sulphide PGE contents that largely represent that of the metasomatic fluid(s) (e.g. Lorand et al., 2013). Comparatively, interaction with melts produced during low degrees of melting (e.g. melts that are geochemically enriched in incompatible elements and likely have higher volatile contents) may result in the precipitation of P-PGE enriched BMS with prominent suprachondritic P-PGE/I-PGE ratios (e.g. Luguet et al., 2007, 2015; Reisberg et al., 2004; Lorand et al., 2010, 2013; Delpech et al., 2012;

Bragagni et al., 2017). These small volume melts may also cause fractionation of sulphur relative to other chalcogen elements (Group 16 of the peridodic table, e.g. Se and Te; Lorand et al., 2013) due to the comparatively oxidising nature of these melts compared to the largely volatile-depleted nature of melts (e.g. MORB) produced during large degrees of mantle melting (e.g. Saal et al., 2002). Therefore, by noting the relative fractionations of HSE and specifically PGE in the sulphides one may be able to trace potential source reservoirs for the metasomatic melts/fluids (i.e. primitive mantle (PM) vs. cratonic mantle (CLM) vs. depleted MORB mantle (DMM) vs. recycled sediments).

Estimates for the sulphur content of the primitive upper mantle are low and range between 200 and 300 ppm (McDonough and Sun, 1995; Rehkaemper et al., 1999; Palme and O'Neill, 2003). However, the incompatible behaviour of sulphur during the melting of mafic silicates and preference of chalcophile and highly siderophile elements for a sulphide phase (D sulphide phase/silicate phase >>100; Fleet et al., 1996; Li and Audétat, 2015; Kiseeva and Wood, 2013) ensures that, during partial melting of the mantle, sulphides plus some economic elements are efficiently liberated from mantle residues and may move out of the mantle during oceanic crust formation (Wallace and Carmichael, 1992; Rehkaemper et al., 1999; Wallace and Edmonds, 2011), arc volcanism (e.g. Richards, 2015), and other deep melt related magmatism (e.g. kimberlites/carbonatites; Kitayama et al., 2017; Maier et al., 2017). This is supported by mafic arc magmas which contain relatively high sulphur contents (800 – 2400 ppm S; Perfit et al., 1983; Wallace and Carmichael, 1992; le Roux et al., 2006) and thus require sulphur concentrations in the mantle source to be significantly enriched (~250 – 500 ppm S; Métrich et al., 1999; De Hoog et al., 2001) compared to that of the depleted MORB-source mantle (~70 – 200 ppm S; Saal et al., 2002; Lorand et al., 2003; Ding and Dasgupta, 2017).

Evaluation of the effectiveness of the mantle melting process in creating melts that play a role in the formation of crustal PGE deposits associated with mafic and ultramafic intrusions has been strongly influenced by the assumptions that the crustal magmatic ore systems begin with a mantle-derived silicate magma within which sulphur and PGE are dissolved (e.g. Cawthorn, 1999). More recently, however, it has been suggested that transport of highly siderophile and chalcophile elements within separate (immiscible) sulphide melts together with silicate melts may instead provide an essential mechanism for later concentration of ore minerals in the crust (Arndt et al., 2005). To date, most investigations of sulphur in mantle magmatic systems have been centred around the partitioning of highly siderophile elements (HSE) between silicate and sulphide melts for application to magma ocean processes in the deep primordial mantle (e.g. Peach et al., 1990; Alard et al., 2000; Fonseca et al., 2011; Mungall and Brenan, 2014) and sulphur-silicate miscibility and ore petrogenesis at crustal levels (e.g. Holzheid and Grove, 2002; Bockrath et al., 2004; Mungall et al., 2005; Liu et al., 2007; Li and Ripley, 2009; Li and Audétat, 2012, 2013; Zajacz et al., 2013; Kiseeva and Wood, 2015; Liu and Brenan, 2015; Brenan et al., 2016). Few studies have placed emphasis on the formation and characteristics of sulphide-bearing melts within the upper mantle that may be related to crustal ore body magma sources, diamond-

forming melt/fluid generation, or on the importance of sulphur activity in petrogenetic processes that invoke volatile-driven mantle magmatism (e.g. Kullerud, 1963; Palyanov et al., 2007; Jégo and Dasgupta, 2014; Kiseeva et al., 2017b). In other words, what are the systematics of sulphide-melt formation in the upper mantle and how do sulphur-rich melts interact with, or metasomatise, peridotitic and eclogitic mantle in terms of geochemical enrichment of chalcophile elements and the growth of new minerals?

Several studies have linked the reservoirs of HSE and especially PGE from the mantle lithosphere to the crust. For example, the metal endowment in magmatic ore complexes hosted in mafic to ultramafic rocks near the Earth's surface may have been ultimately sourced from sulphide-bearing peridotitic (Griffin et al., 2004) or eclogitic lithospheric mantle domains (Aulbach et al., 2012). Additionally, sulphides in the Earth's mantle, and by proxy, metasomatic S-bearing melts or fluids are suggested to be intimately linked to diamond formation (Sato and Katsura, 2001; Palyanov et al., 2007, 2009). This is supported by a significant proportion of sulphide inclusions compared to silicate inclusions in diamond (Pearson et al., 1998; Griffin et al., 2003a; Stachel and Harris, 2008; Cartigny et al., 2009; Taylor and Liu, 2009; Thomassot et al., 2009) and suggests that sulphur may be catalytic during diamond formation (Gunn and Luth, 2006; Palyanov et al., 2007). Low-degree melting of volatile-bearing (e.g. CO_2 and/or H_2O) peridotite and eclogite produces (potentially metasomatising) melts such as alkali basalts, basanites, carbonatites and kimberlites (Dasgupta et al., 2004; Yaxley and Brey, 2004), that have moderate (~45 wt.% SiO_2) to low (<15 wt.% SiO_2) silica contents (Dasgupta et al., 2005b; Kiseeva et al., 2012). These volatile-bearing, often silica-undersaturated melts are often implicated in diamond genesis based on the presence of fluid/melt inclusions in diamonds with very similar Si, Ca, Mg, and CO_2 contents (e.g. Schrauder and Navon, 1994; Weiss et al., 2009), and additionally from trends in the stable isotope compositions of diamonds that suggest redox-controlled diamond formation processes involving volatile-rich fluids/melts (e.g. Thomassot et al., 2007; Smart et al., 2011). The incompatible nature of sulphur and sulphides during mantle melting implies that metasomatic agents linked to diamond formation may also contain a significant sulphur component that could promote diamond formation (e.g. Palyanov et al., 2007) and additionally lead to secondary sulphide (plus associated chalcophile and siderophile element) enrichment of the mantle, highlighting the importance of sulphur within deep volatile cycles (e.g. Jugo, 2009; Ding and Dasgupta, 2017, 2018).

This study investigates the behavior of sulphur as well as highly siderophile and chalcophile elements in mantle petrogenetic processes. Specifically, the goal of this study is to report the results of petrographic, geochemical and stable isotopic investigations of sulphide-bearing cratonic mantle eclogite and peridotite xenoliths, to enable the sources and systematics of sulphur-bearing melt formation in the upper mantle, as well as the manner in which these melts interact with, or metasomatise, peridotitic and eclogitic lithologies in terms of geochemical enrichment and the growth of new minerals (e.g. sulphide) can be understood. Additionally, the petrogenesis of the xenoliths will be assessed to

provide a holistic picture of the evolution of the cratonic mantle as well as the secondary processes that affected it. To complement the mantle xenolith-focussed research, novel high-pressure and temperature experiments were conducted on C±S-bearing eclogite compositions. Of particular interest is the relationship of sulphide melt formation relative to carbonate±silicate melt formation (e.g. in terms of determination of the different solidi, and the solubility of sulphide within the carbonatite±silicate melt), the composition of such sulphide melts, and the partitioning of various elements between the silicate residuum and the melt(s) produced. Emphasis is also placed on defining the behaviour of the C±S-bearing eclogite system close to the silicate, sulphide and carbonate solidi, between 1050 and 1300 ºC and 2.0 and 3.5 GPa. The results of these investigations will be applied to several important and broad-reaching research questions including the role that sulphur – and sulphide – bearing melts play in mantle metasomatic processes, which may include diamond growth, sulphide/sulphur enrichment or depletion of the CLM, and the cratonic mantle as a source of HSE involved in crustal ortho-magmatic processes.

The results of this research project take the form of three separate chapters presented in Chapters 3 through 5. These chapters were prepared as manuscripts to be submitted to scientific journals. A content description of each manuscript, its status in terms of journal submission, as well as details of author contributions are presented on the first page of each of these chapters. Methodology and analytical routine specifics are also outlined within each stand-alone chapter. In general, the high pressure and temperature experiments were performed on a piston-cylinder apparatus in the Centre for Crustal Petrology (C.C.P) experimental laboratory at the University of Stellenbosch, South Africa. Experiments were run at 2 to 3.5 GPa and a range of temperatures relevant to conditions in the upper mantle to ensure generation of S±C-bearing melts in equilibrium with appropriate residuum. The work focusses on relatively "fertile" synthetic bulk compositions that are applicable to natural systems and to ensure sufficient production of S±C-bearing melts and residual minerals. The resulting experimental charges were examined by scanning-electron microscopy (SEM) in order to characterise the product assemblages, including quenched melt(s) phases, and attain major and minor element compositions of these assemblages.

Both peridotite and eclogite xenoliths selected for study came from five key Kaapvaal craton kimberlite locations, namely; the Kamfersdam, Roberts Victor, Jagersfontein, Swartruggens and Premier kimberlites. These specific kimberlites were chosen because they span a wide range of ages, locations and tectonic settings (some of which are associated with crustally hosted magmatic ore complexes) in the context of the geological history of the Kaapvaal craton. The eclogite and peridotite xenoliths were chosen based on the presence of base metal sulphides and other secondary minerals (e.g. clinopyroxene and phlogopite). Xenoliths were assessed petrographically (i.e. for the presence of sulphide minerals), geochemically (in situ LA-ICPMS trace element analyses) and isotopically (garnet $\delta^{18}O$ by laser fluorination methods and multiple sulphur isotopes by secondary-ion mass spectroscopy). Analyses of the natural samples is critical for comparison and evaluation of the experimental results

and to independently evaluate the role of the cratonic mantle as an ore source. Assessment and interpretation of the resulting experimental, petrographic and geochemical data is presented in Chapter 6. As an adjunct to the data presented in the thesis, multiple sulphur isotope data for sulphides from select eclogite xenoliths described in Chapter 3 are presented in the Appendices (i.e. Additional data: multiple sulphur isotopes).

REFERENCES

Alard, O., Griffin, W.L., Lorand, J.P., Jackson, S.E. and O'reilly, S.Y. (2000). Non-chondritic distribution of the highly siderophile elements in mantle sulphides. Nature **407**, 891

Alard, O., Luguet, A., Pearson, N.J., Griffin, W.L., Lorand, J.-P., Gannoun, A., Burton, K.W. and O'reilly, S.Y. (2005) In situ Os isotopes in abyssal peridotites bridge the isotopic gap between MORBs and their source mantle. Nature **436**, 1005

Arndt, N., Lesher, C.M. and Czamanske, G.K. (2005). Mantle-derived magmas and magmatic Ni-Cu-(PGE) deposits, 5-24

Aulbach, S., Mungall, J.E. and Pearson, D.G. (2016). Distribution and processing of highly siderophile elements in cratonic mantle lithosphere. Reviews in Mineralogy and Geochemistry **81**, 239–304

Aulbach, S., Stachel, T., Seitz, H. M. and Brey, G. P. (2012). Chalcophile and siderophile elements in sulphide inclusions in eclogitic diamonds and metal cycling in a Paleoproterozoic subduction zone. Geochimica et Cosmochimica Acta **93**, 278-299.

Ballhaus, C., Bockrath, C., Wohlgemuth-Ueberwasser, C., Laurenz, V. and Berndt, J. (2006). Fractionation of the noble metals by physical processes. Contributions to Mineralogy and Petrology **152**, 667–684

Barnes, S.-J., Boyd, R., Korneliussen, A., Nilsson, L.P., Often, M., Pedersen, R.B. and Robins, B. (1988). The use of mantle normalization and metal ratios in discriminating between the effects of partial melting, crystal fractionation and sulphide segregation on platinum-group elements, gold, nickel and copper: examples from Norway. In: Geo-platinum **87**, 113–143

Barnes, S.-J., Makovicky, E., Makovicky, M., Rose-Hansen, J. and Karup-Moller, S. (1997). Partition coefficients for Ni, Cu, Pd, Pt, Rh, and Ir between monosulfide solid solution and sulfide liquid and the formation of compositionally zoned Ni--Cu sulfide bodies by fractional crystallization of sulfide liquid. Canadian Journal of Earth Sciences **34**, 366–374

Barton, M.D. and Johnson, D.A. (1996). Evaporitic-source model for igneous-related Fe oxide-(REE-Cu-Au-U) mineralization. Geology **24**, 259–262

Beinert, H. (2000). A tribute to sulfur. European Journal of Biochemistry **267**, 5657–5664

Bockrath, C., Ballhaus, C. and Holzheid, A. (2004). Fractionation of the platinum-group elements during mantle melting. Science **305**, 1951–1953

Bragagni, A., Luguet, A., Fonseca, R.O.C., Pearson, D.G., Lorand, J.-P., Nowell, G.M. and Kjarsgaard, B.A. (2017). The geological record of base metal sulfides in the cratonic mantle: A

microscale 187Os/188Os study of peridotite xenoliths from Somerset Island, Rae Craton (Canada). Geochimica et Cosmochimica Acta **216**, 264–285

Brenan, J.M. and Andrews, D. (2001) High-temperature stability of laurite and Ru-Os-Ir alloy and their role in PGE fractionation in mafic magmas. The Canadian Mineralogist **39**, 341–360

Brenan, J.M., Bennett, N.R. and Zajacz, Z. (2016) Experimental results on fractionation of the highly siderophile elements (HSE) at variable pressures and temperatures during planetary and magmatic differentiation. Reviews in Mineralogy and Geochemistry **81**, 1–87

Brey, G.P., Bulatov, V.K., Girnis, A. V. and Lahaye, Y. (2008). Experimental melting of carbonated peridotite at 6-10 GPa. Journal of Petrology **49**, 797–821

Canfield, D. E. (2004). The evolution of the Earth surface sulfur reservoir. American Journal of Science **304**, 839–861

Cartigny, P., Farquhar, J., Thomassot, E., Harris, J.W., Wing, B., Masterson, A., McKeegan, K. and Stachel, T. (2009). A mantle origin for Paleoarchean peridotitic diamonds from the Panda kimberlite, Slave Craton: evidence from ^{13}C-, ^{15}N-and $^{33, 34}S$-stable isotope systematics. Lithos **112**, 852-864.

Cawthorn, R. G. (1999). Platinum-group element mineralization in the Bushveld Complex-a critical reassessment of geochemical models. South African Journal of Geology **102**, 268-281.

Chaussidon, M., Albarède, F. and Sheppard, S. M. (1989). Sulphur isotope variations in the mantle from ion microprobe analyses of micro-sulphide inclusions. Earth and Planetary Science Letters **92**, 144-156.

Dasgupta, R., Hirschmann, M. M. and Stalker, K. (2005). Immiscible transition from carbonate-rich to silicate-rich melts in the 3 GPa melting interval of eclogite+ CO_2 and genesis of silica-undersaturated ocean island lavas. Journal of Petrology **47**, 647-671.

Dasgupta, R., Hirschmann, M. M. and Withers, A. C. (2004). Deep global cycling of carbon constrained by the solidus of anhydrous, carbonated eclogite under upper mantle conditions. Earth and Planetary Science Letters **227**, 73-85.

Dawson, J. B. (1984). Contrasting types of upper-mantle metasomatism?. In developments in petrology (Vol. 11, No. 2, pp. 289-294). Elsevier.

De Hoog, J. C. M., Taylor, B. E. and Van Bergen, M. J. (2001). Sulfur isotope systematics of basaltic lavas from Indonesia: implications for the sulfur cycle in subduction zones. Earth and Planetary Science Letters **189**, 237-252.

Delpech, G., Lorand, J. P., Grégoire, M., Cottin, J. Y. and O'Reilly, S. Y. (2012). In-situ geochemistry

of sulfides in highly metasomatized mantle xenoliths from Kerguelen, southern Indian Ocean. Lithos **154**, 296-314.

Ding, S. and Dasgupta, R. (2017). The fate of sulfide during decompression melting of peridotite–implications for sulfur inventory of the MORB-source depleted upper mantle. Earth and Planetary Science Letters **459**, 183-195.

Ding, S. and Dasgupta, R. (2018). Sulfur inventory of ocean island basalt source regions constrained by modeling the fate of sulfide during decompression melting of a heterogeneous mantle. Journal of Petrology **59**, 1281-1308.

Fleet, M. E., Crocket, J. H. and Stone, W. E. (1996). Partitioning of platinum-group elements (Os, Ir, Ru, Pt, Pd) and gold between sulfide liquid and basalt melt. Geochimica et Cosmochimica Acta **60**, 2397-2412.

Fleet, M. E. and Pan, Y. (1994). Fractional crystallization of anhydrous sulfide liquid in the system Fe-Ni-Cu-S, with application to magmatic sulfide deposits. Geochimica et Cosmochimica Acta **58**, 3369-3377.

Fonseca, R. O., Mallmann, G., O'Neill, H. S. C., Campbell, I. H. and Laurenz, V. (2011). Solubility of Os and Ir in sulfide melt: Implications for Re/Os fractionation during mantle melting. Earth and Planetary Science Letters **311**, 339-350.

Friese, A. E., Reimold, W. U. and Layer, P. W. (2003). ^{40}Ar-^{39}Ar dating of and structural information on tectonite-bearing faults in the Witwatersrand Basin: Evidence for multi-stage, tectono-thermal activity in the central Kaapvaal Craton. South African Journal of Geology **106**, 41-70.

Gréau, Y., Huang, J. X., Griffin, W. L., Renac, C., Alard, O. and O'Reilly, S. Y. (2011). Type I eclogites from Roberts Victor kimberlites: products of extensive mantle metasomatism. Geochimica et Cosmochimica Acta **75**, 6927-6954.

Grégoire, M., Bell, D. R. and Le Roex, A. P. (2003). Garnet lherzolites from the Kaapvaal Craton (South Africa): trace element evidence for a metasomatic history. Journal of Petrology **44**, 629-657.

Griffin, W. L., Graham, S., O'Reilly, S. Y. and Pearson, N. J. (2004). Lithosphere evolution beneath the Kaapvaal Craton: Re–Os systematics of sulfides in mantle-derived peridotites. Chemical Geology **208**, 89-118.

Griffin, W.L., O'Reilly, S.Y., Abe, N., Aulbach, S., Davies, R.M., Pearson, N.J., Doyle, B.J. and Kivi, K.. (2003). The origin and evolution of Archean lithospheric mantle. Precambrian Research **127**, 19-41.

Gunn, S. C. and Luth, R. W. (2006). Carbonate reduction by Fe-SO melts at high pressure and high temperature. American Mineralogist **91**, 1110-1116.

Guo, J., Griffin, W. L. and O'Reilly, S. Y. (1999). Geochemistry and origin of sulphide minerals in mantle xenoliths: Qilin, Southeastern China. Journal of Petrology **40**, 1125-1149.

Hagström, S., Nordling, C. and Siegbahn, K. (1964). Electron spectroscopic determination of the chemical valence state. Zeitschrift für Physik **178**, 439-444.

Holzheid, A. and Grove, T. L. (2002). Sulfur saturation limits in silicate melts and their implications for core formation scenarios for terrestrial planets. American Mineralogist **87,** 227-237.

Jégo, S. and Dasgupta, R. (2014). The fate of sulfur during fluid-present melting of subducting basaltic crust at variable oxygen fugacity. Journal of Petrology **55**, 1019-1050.

Jugo, P. J. (2009). Sulfur content at sulfide saturation in oxidized magmas. Geology **37**(5), 415-418.

Kiseeva, E. S., Fonseca, R. O. and Smythe, D. J. (2017). Chalcophile elements and sulfides in the upper mantle. Elements **13**(2), 111-116.

Kiseeva, E. S., Kamenetsky, V. S., Yaxley, G. M. and Shee, S. R. (2017b). Mantle melting versus mantle metasomatism–"The chicken or the egg" dilemma. Chemical Geology **455**, 120-130.

Kiseeva, E. S. and Wood, B. J. (2013). A simple model for chalcophile element partitioning between sulphide and silicate liquids with geochemical applications. Earth and Planetary Science Letters **383**, 68-81.

Kiseeva, E. S. and Wood, B. J. (2015). The effects of composition and temperature on chalcophile and lithophile element partitioning into magmatic sulphides. Earth and Planetary Science Letters **424**, 280-294.

Kiseeva, E. S., Yaxley, G. M., Hermann, J., Litasov, K. D., Rosenthal, A. and Kamenetsky, V. S. (2012). An experimental study of carbonated eclogite at 3.5–5.5 GPa: implications for silicate and carbonate metasomatism in the cratonic mantle. Journal of Petrology **53**(4), 727-759.

Kitayama, Y., Thomassot, E., Galy, A., Golovin, A., Korsakov, A., d'Eyrames, E., Assayag, N., Bouden, N. and Ionov, D. (2017). Co-magmatic sulfides and sulfates in the Udachnaya-East pipe (Siberia): A record of the redox state and isotopic composition of sulfur in kimberlites and their mantle sources. Chemical Geology **455,** 315-330.

Kullerud, G. (1963). The Fe-Ni-S system. Carnegie Institution Washington Year Book **62**, 175-189.

le Roux, P. J., Shirey, S. B., Hauri, E. H., Perfit, M. R. and Bender, J. F. (2006). The effects of variable sources, processes and contaminants on the composition of northern EPR MORB (8–10

N and 12–14 N): Evidence from volatiles (H_2O, CO_2, S) and halogens (F, Cl). Earth and Planetary Science Letters **251**(3-4), 209-231.

Li, C., Barnes, S. J., Makovicky, E., Rose-Hansen, J. and Makovicky, M. (1996). Partitioning of nickel, copper, iridium, rhenium, platinum, and palladium between monosulfide solid solution and sulfide liquid: effects of composition and temperature. Geochimica et Cosmochimica Acta **60**(7), 1231-1238.

Li, C. and Ripley, E. M. (2009). Sulfur contents at sulfide-liquid or anhydrite saturation in silicate melts: empirical equations and example applications. Economic Geology **104**(3), 405-412.

Li, Y. and Audétat, A. (2015). Effects of temperature, silicate melt composition, and oxygen fugacity on the partitioning of V, Mn, Co, Ni, Cu, Zn, As, Mo, Ag, Sn, Sb, W, Au, Pb, and Bi between sulfide phases and silicate melt. Geochimica et Cosmochimica Acta **162**, 25-45.

Li, Y. and Audétat, A. (2012). Partitioning of V, Mn, Co, Ni, Cu, Zn, As, Mo, Ag, Sn, Sb, W, Au, Pb, and Bi between sulfide phases and hydrous basanite melt at upper mantle conditions. Earth and Planetary Science Letters **355**, 327-340.

Li, Y. and Audétat, A. (2013). Gold solubility and partitioning between sulfide liquid, monosulfide solid solution and hydrous mantle melts: Implications for the formation of Au-rich magmas and crust–mantle differentiation. Geochimica et Cosmochimica Acta **118**, 247-262.

Liu, C. Z., Snow, J. E., Brügmann, G., Hellebrand, E. and Hofmann, A. W. (2009). Non-chondritic HSE budget in Earth's upper mantle evidenced by abyssal peridotites from Gakkel ridge (Arctic Ocean). Earth and Planetary Science Letters **283**(1-4), 122-132.

Liu, Y. and Brenan, J. (2015). Partitioning of platinum-group elements (PGE) and chalcogens (Se, Te, As, Sb, Bi) between monosulfide-solid solution (MSS), intermediate solid solution (ISS) and sulfide liquid at controlled fO_2–fS_2 conditions. Geochimica et Cosmochimica Acta **159**, 139-161.

Liu, Y., Samaha, N. T. and Baker, D. R. (2007). Sulfur concentration at sulfide saturation (SCSS) in magmatic silicate melts. Geochimica et Cosmochimica Acta **71**(7), 1783-1799.

Lorand, J. P., Alard, O. and Luguet, A. (2010). Platinum-group element micronuggets and refertilization process in Lherz orogenic peridotite (northeastern Pyrenees, France). Earth and Planetary Science Letters **289**(1-2), 298-310.

Lorand, J. P., Alard, O., Luguet, A. and Keays, R. R. (2003). Sulfur and selenium systematics of the subcontinental lithospheric mantle: inferences from the Massif Central xenolith suite (France). Geochimica et Cosmochimica Acta **67**(21), 4137-4151.

Lorand, J. P. and Gregoire, M. (2006). Petrogenesis of base metal sulphide assemblages of some peridotites from the Kaapvaal craton (South Africa). Contributions to Mineralogy and Petrology **151**(5), 521.

Lorand, J. P. and Luguet, A. (2016). Chalcophile and siderophile elements in mantle rocks: Trace elements controlled by trace minerals. Reviews in Mineralogy and Geochemistry **81**(1), 441-488.

Lorand, J. P., Luguet, A. and Alard, O. (2013). Platinum-group element systematics and petrogenetic processing of the continental upper mantle: A review. Lithos **164**, 2-21.

Luguet, A., Behrens, M., Pearson, D. G., König, S. and Herwartz, D. (2015). Significance of the whole rock Re–Os ages in cryptically and modally metasomatised cratonic peridotites: Constraints from HSE–Se–Te systematics. Geochimica et Cosmochimica Acta **164**, 441-463.

Luguet, A., Lorand, J. P. and Seyler, M. (2003). Sulfide petrology and highly siderophile element geochemistry of abyssal peridotites: A coupled study of samples from the Kane Fracture Zone (45 W 23 20N, MARK area, Atlantic Ocean). Geochimica et Cosmochimica Acta **67**(8), 1553-1570.

Luguet, A. and Pearson, G. (2019). Dating mantle peridotites using Re-Os isotopes: The complex message from whole rocks, base metal sulfides, and platinum group minerals. American Mineralogist **104**(2), 165-189.

Luguet, A., Shirey, S. B., Lorand, J. P., Horan, M. F. and Carlson, R. W. (2007). Residual platinum-group minerals from highly depleted harzburgites of the Lherz massif (France) and their role in HSE fractionation of the mantle. Geochimica et Cosmochimica Acta **71**(12), 3082-3097.

Maier, W. D., O'Brien, H., Peltonen, P. and Barnes, S. J. (2017). Platinum-group element contents of Karelian kimberlites: Implications for the PGE budget of the sub-continental lithospheric mantle. Geochimica et Cosmochimica Acta **216**, 358-371.

Mandeville, C. W. (2010). Sulfur: A ubiquitous and useful tracer in Earth and planetary sciences. Elements **6**(2), 75-80.

Marchesi, C., Dale, C.W., Garrido, C.J., Pearson, D.G., Bosch, D., Bodinier, J.L., Gervilla, F. and Hidas, K. (2014). Fractionation of highly siderophile elements in refertilized mantle: Implications for the Os isotope composition of basalts. Earth and Planetary Science Letters **400**, 33-44.

Mavrogenes, J. A. and O'Neill, H. S. C. (1999). The relative effects of pressure, temperature and oxygen fugacity on the solubility of sulfide in mafic magmas. Geochimica et Cosmochimica

Acta **63**(7-8), 1173-1180.

McDonough, W. F. and Sun, S. S. (1995). The composition of the Earth. Chemical geology **120**(3-4), 223-253.

Métrich, N., Schiano, P., Clocchiatti, R. and Maury, R. C. (1999). Transfer of sulfur in subduction settings: an example from Batan Island (Luzon volcanic arc, Philippines). Earth and Planetary Science Letters **167**(1-2), 1-14.

Mitchell, R. H. and Keays, R. R. (1981). Abundance and distribution of gold, palladium and iridium in some spinel and garnet lherzolites: implications for the nature and origin of precious metal-rich intergranular components in the upper mantle. Geochimica et Cosmochimica Acta **45**(12), 2425-2442.

Morgan, J. W., Walker, R. J., Brandon, A. D. and Horan, M. F. (2001). Siderophile elements in Earth's upper mantle and lunar breccias: data synthesis suggests manifestations of the same late influx. Meteoritics & Planetary Science **36**(9), 1257-1275.

Mungall, J. E., Andrews, D. R., Cabri, L. J., Sylvester, P. J. and Tubrett, M. (2005). Partitioning of Cu, Ni, Au, and platinum-group elements between monosulfide solid solution and sulfide melt under controlled oxygen and sulfur fugacities. Geochimica et Cosmochimica Acta **69**(17), 4349-4360.

Mungall, J. E. and Brenan, J. M. (2014). Partitioning of platinum-group elements and Au between sulfide liquid and basalt and the origins of mantle-crust fractionation of the chalcophile elements. Geochimica et Cosmochimica Acta **125**, 265-289.

O'Reilly, S. Y. and Griffin, W. L. (2013). Mantle metasomatism. In: Metasomatism and the Chemical Transformation of Rock, Springer, Berlin, 471-533

Palme, H. and O'Neill, H. S. C. (2003). Cosmochemical estimates of mantle composition. Treatise on Geochemistry **2**, 1-38.

Palyanov, Y. N., Borzdov, Y. M., Bataleva, Y. V., Sokol, A. G., Palyanova, G. A. and Kupriyanov, I. N. (2007). Reducing role of sulfides and diamond formation in the Earth's mantle. Earth and Planetary Science Letters **260**(1-2), 242-256.

Palyanov, Y. N., Kupriyanov, I. N., Borzdov, Y. M., Sokol, A. G. and Khokhryakov, A. F. (2009). Diamond crystallization from a sulfur− carbon system at HPHT conditions. Crystal Growth and Design **9**(6), 2922-2926.

Peach, C. L., Mathez, E. A. and Keays, R. R. (1990). Sulfide melt-silicate melt distribution coefficients for noble metals and other chalcophile elements as deduced from MORB:

Implications for partial melting. Geochimica et Cosmochimica Acta **54**(12), 3379-3389.

Pearson, D. G., Shirey, S. B., Carlson, R. W., Boyd, F. R., Pokhilenko, N. P. and Shimizu, N. (1995). Re-Os, Sm-Nd, and Rb-Sr isotope evidence for thick Archaean lithospheric mantle beneath the Siberian craton modified by multistage metasomatism. Geochimica et Cosmochimica Acta **59**(5), 959-977.

Pearson, D. G., Shirey, S. B., Harris, J. W. and Carlson, R. W. (1998). Sulphide inclusions in diamonds from the Koffiefontein kimberlite, S Africa: constraints on diamond ages and mantle Re–Os systematics. Earth and Planetary Science Letters **160**(3-4), 311-326.

Peregoedova, A., Barnes, S. J. and Baker, D. R. (2004). The formation of Pt–Ir alloys and Cu–Pd-rich sulfide melts by partial desulfurization of Fe–Ni–Cu sulfides: results of experiments and implications for natural systems. Chemical Geology **208**(1-4), 247-264.

Perfit, M. R., Fornari, D. J., Malahoff, A. and Embley, R. W. (1983). Geochemical studies of abyssal lavas recovered by DSRV Alvin from Eastern Galapagos Rift, Inca Transform, and Ecuador Rift: 3. Trace element abundances and petrogenesis. Journal of Geophysical Research: Solid Earth **88**(B12), 10551-10572.

Rehkaemper, M., Halliday, A. N., Fitton, J. G., Lee, D. C., Wieneke, M. and Arndt, N. T. (1999). Ir, Ru, Pt, and Pd in basalts and komatiites: new constraints for the geochemical behavior of the platinum-group elements in the mantle. Geochimica et Cosmochimica Acta **63**(22), 3915-3934.

Reisberg, L., Lorand, J. P. and Bedini, R. M. (2004). Reliability of Os model ages in pervasively metasomatized continental mantle lithosphere: a case study of Sidamo spinel peridotite xenoliths (East African Rift, Ethiopia). Chemical Geology **208**(1-4), 119-140.

Richards, J. P. (2015). The oxidation state, and sulfur and Cu contents of arc magmas: implications for metallogeny. Lithos **233**, 27-45.

Saal, A. E., Hauri, E. H., Langmuir, C. H. and Perfit, M. R. (2002). Vapour undersaturation in primitive mid-ocean-ridge basalt and the volatile content of Earth's upper mantle. Nature **419**(6906), 451.

Sato, K. and Katsura, T. (2001). Sulfur: a new solvent-catalyst for diamond synthesis under high-pressure and high-temperature conditions. Journal of Crystal Growth **223**(1-2), 189-194.

Scaillet, B. and Pichavant, M. (2005). A model of sulphur solubility for hydrous mafic melts: application to the determination of magmatic fluid compositions of Italian volcanoes. Annals of Geophysics.

Schrauder, M. and Navon, O. (1994). Hydrous and carbonatitic mantle fluids in fibrous diamonds

from Jwaneng, Botswana. Geochimica et Cosmochimica Acta **58**(2), 761-771.

Smart, K. A., Chacko, T., Stachel, T., Muehlenbachs, K., Stern, R. A. and Heaman, L. M. (2011). Diamond growth from oxidized carbon sources beneath the Northern Slave Craton, Canada: a $\delta^{13}C$–N study of eclogite-hosted diamonds from the Jericho kimberlite. Geochimica et Cosmochimica Acta **75**(20), 6027-6047.

Smythe, D. J., Wood, B. J. and Kiseeva, E. S. (2017). The S content of silicate melts at sulfide saturation: new experiments and a model incorporating the effects of sulfide composition. American Mineralogist **102**(4), 795-803.

Spencer, R. J. (2000). Sulfate minerals in evaporite deposits. Reviews in Mineralogy and Geochemistry **40**(1), 173-192.

Stachel, T. and Harris, J. W. (2008). The origin of cratonic diamonds: constraints from mineral inclusions. Ore Geology Reviews **34**(1-2), 5-32.

Taylor, L. A. and Liu, Y. (2009). Sulfide inclusions in diamonds: not monosulfide solid solution. Russian Geology and Geophysics **50**(12), 1201-1211.

Thomassot, E., Cartigny, P., Harris, J. W., Lorand, J. P., Rollion-Bard, C. and Chaussidon, M. (2009). Metasomatic diamond growth: A multi-isotope study (^{13}C, ^{15}N, ^{33}S, ^{34}S) of sulphide inclusions and their host diamonds from Jwaneng (Botswana). Earth and Planetary Science Letters **282**(1-4), 79-90.

Thomassot, E., Cartigny, P., Harris, J. W. and Viljoen, K. F. (2007). Methane-related diamond crystallization in the Earth's mantle: stable isotope evidences from a single diamond-bearing xenolith. Earth and Planetary Science Letters **257**(3-4), 362-371.

Tsuno, K. and Dasgupta, R. (2015). Fe–Ni–Cu–C–S phase relations at high pressures and temperatures–The role of sulfur in carbon storage and diamond stability at mid-to deep-upper mantle. Earth and Planetary Science Letters **412**, 132-142.

Wainwright, A. N., Luguet, A., Fonseca, R. O. C. and Pearson, D. G. (2015). Investigating metasomatic effects on the ^{187}Os isotopic signature: a case study on micrometric base metal sulphides in metasomatised peridotite from the Letlhakane kimberlite (Botswana). Lithos **232**, 35-48.

Wallace, P. and Carmichael, I. S. (1992). Sulfur in basaltic magmas. Geochimica et Cosmochimica Acta **56**(5), 1863-1874.

Wallace, P. J. and Edmonds, M. (2011). The sulfur budget in magmas: evidence from melt inclusions, submarine glasses, and volcanic gas emissions. Reviews in Mineralogy and Geochemistry **73**(1),

215-246.

Weiss, Y., Kessel, R., Griffin, W.L., Kiflawi, I., Klein-BenDavid, O., Bell, D.R., Harris, J.W. and Navon, O. (2009). A new model for the evolution of diamond-forming fluids: Evidence from microinclusion-bearing diamonds from Kankan, Guinea. Lithos **112**, 660-674.

Westerlund, K. J., Gurney, J. J., Carlson, R. W., Shirey, S. B., Hauri, E. H. and Richardson, S. H. (2004). A metasomatic origin for late Archean eclogitic diamonds: Implications from internal morphology of diamonds and Re-Os and S isotope characteristics of their sulfide inclusions from the late Jurassic Klipspringer kimberlites. South African Journal of Geology **107**(1-2), 119-130.

Yaxley, G. M. and Brey, G. P. (2004). Phase relations of carbonate-bearing eclogite assemblages from 2.5 to 5.5 GPa: implications for petrogenesis of carbonatites. Contributions to Mineralogy and Petrology **146**(5), 606-619.

Zajacz, Z., Candela, P. A., Piccoli, P. M., Sanchez-Valle, C. and Wälle, M. (2013). Solubility and partitioning behavior of Au, Cu, Ag and reduced S in magmas. Geochimica et Cosmochimica Acta **112**, 288-304.

CHAPTER 2

2. THE KAAPVAAL CRATON

2.1. KAAPVAAL CRATON GEOLOGY AND EVOLUTION

The Archean Kaapvaal craton of central South Africa covers an area of 1.2×10^6 km^2 (**Fig. 2.1**). It is bound in the north to the Zimbabwe craton by the 2.8 – 2.5 Ga Limpopo granulite terrane (Barton and Van Reenen, 1992) and together the Kaapvaal and Zimbabwe cratons form the continental heart of Southern Africa. The Kaapvaal craton is flanked by Proterozoic orogenic belts to the west (2.0–1.7 Ga Kheis overthrust belt; de Wit et al., 1992) and south (1.04 – 1.2 Ga the Namaqua-Natal mobile belt; Eglington, 2006), and to the east by Jurassic to Cretaceous age volcanic magmas (i.e. the Karoo-age Lebombo monocline) that are associated with the break-up of Gondwana (Cox, 1992; Watkeys and Sokoutis, 1998; Hawkesworth et al., 1999). The oldest portions (basement rocks) of the Archean granitoid-greenstone shield of the Kaapvaal craton resulted from ~500 Ma of intra-oceanic tectonics between 3.7 and 3.2 Ga (de Wit et al., 1992) that caused collision of juvenile oceanic lithospheric plates and subsequent tonalite-trondhjemite magmatism to produce the Meso- to Paleoachrean Barberton greenstone belt and Ancient Gneiss terranes (Kröner et al., 1989; Armstrong et al,. 1991; Poujol et al., 2003). Various stages of deformational collision and episodic extensional tectonics as well as magmatism further shaped the craton (Armstrong et al., 1991; De Wit et al., 1992).

The Kaapvaal craton itself is divided into two major Archean granite-greenstone terranes, an older eastern terrane (~3.7 to 2.7 Ga; Witwatersrand block; Kröner et al., 1989; Armstrong et al., 1991) and younger western terrane (~3.3 to 2.9 Ga; Kimberley block; Schmitz et al., 2004) that assembled along the Colesberg magnetic lineament between 2.93 and 2.88 Ga (Schmitz et al., 2004) via subduction-collision events (Shirey et al., 2001). Following central craton stabilisation around 3.1 Ga (de Wit et al., 1992) and ceasing of continental margin tectonics around ~2.65 Ga (Barton and Van Reenen, 1992), the craton was disrupted by various intra-cratonic magmatic intrusions. The most important of which is the ~2.056 Ga (Zeh et al., 2015) Bushveld Igneous Complex which intruded the north-central part of the Kaapvaal craton, producing the world's largest platinum group metal (PGM) deposit (e.g. Von Gruenewaldt et al., 1985; Cawthorn, 2010). Other significant magmatic events include, the 2.7 Ga (Armstrong et al., 1991) Ventersdorp and 1.1 Ga (Hanson et al., 1998) Umkondo large igneous provinces (LIP) as well as the Karoo LIP (~182 Ma; Riley et al., 2005), which extruded in the south-central part of the Kaapvaal craton.

The Kaapvaal craton has also been affected by numerous kimberlite eruptions. Kimberlite magmatic activity occurred on and around the Kaapvaal craton between 1.8 Ga and 60 Ma (Skinner and Truswell, 2006; Tappe et al., 2018a), with the majority intruding during the Mesozoic era (Jelsma et al., 2009). Increased kimberlite magmatic activity across southern Africa between 140-120 and 100-80 Ma was

recently linked to the pronounced acceleration of the African tectonic plate during Pangea supercontinent break-up (Tappe et al., 2018a), which facilitated deep-sourced kimberlitic melt drainage propagated through areas of intense stress that contain fractures and faults (i.e. terrane boundaries, incipient continental rifts or major dyke swarms; Jelsma et al., 2009). This hypothesis, however, is quite controversial and seismic evidence for such large melt reservoirs at the lithosphere-asthenosphere boundary today is largely lacking (e.g. James et al., 2001; Snyder et al., 2004). Older episodic kimberlite eruptions have been further associated with mantle thermal perturbations, for example, the ~1.6 Ga Kuruman kimberlite has been linked to a localised transient magmatic occurrence (Griffin et al., 2014). Mantle xenolith samples used for this study were collected from five separate kimberlite localities found across the Kaapvaal craton, namely the Kamfersdam, Roberts Victor, Jagersfontein, Swartruggens and Premier kimberlites. Kamfersdam (part of the Kimberley cluster of kimberlites), Roberts Victor and Jagersfontein kimberlites are geographically closely associated and are situated on the southern edge of the Kaapvaal craton near the town of Kimberley. Both Kamfersdam and Jagersfontein have Group I petrographic and isotopic affinity and Cretaceous ages of 84±3 Ma (Allsopp and Barrett, 1975) and 85.6±1.0 Ma (Smith et al., 1985), respectively. Roberts Victor has Group II affinity with Mesozoic age of 128±15 Ma (Smith et al., 1985). The Premier and Swartruggens kimberlites are in the north-central part of the craton near the the Bushveld Igneous Complex and the city of Pretoria (**Fig. 2.1**). The 1153.3±5.3 Ma (Wu et al., 2013; Tappe et al., 2018b) Premier kimberlite is of Group I affinity and Swartruggens is of Group II affinity with a Mesozoic age of 156±13 Ma (Smith et al., 1985).

2.2. CRATONIC LITHOSPHERIC MANTLE PETROLOGY

The cratonic lithospheric mantle (CLM) is the rigid uppermost portion part of the Earth's mantle that is welded to the base of cratons and extends from the Moho (Mohorovičić discontinuity) to depths of ~250 km. The CLM forms a mechanical, thermal and chemical boundary layer between the crust and the asthenospheric mantle, where heat transfer occurs by thermal conduction unlike the convective "adiabatic" heat flow of the more ductile asthenosphere (e.g. Lee et al., 2011). The largely chemically depleted CLM is both ancient and chemically overprinted and is sampled in the form of rock fragments (xenoliths) and single mantle minerals (xenocrysts, e.g. garnet, clinopyroxene, ilmenite, olivine, diamond) by various forms of silica-undersaturated alkaline magmatism (e.g. kimberlites, lamproites, lamprophyres, carbonatites etc…). The chemically depleted nature of the dominantly peridotite CLM is suggested to be the result of significant partial melt extraction, where certain elements such as Ca and Al are preferentially partitioned into the melt while elements such as Mg selectively remain within the melt-depleted residues (i.e. Harzburgites; Carlson et al., 2005). Both Kaapvaal mantle-derived xenoliths (Pearson et al., 1995a; Carlson et al., 1999) and diamond inclusions (Richardson et al., 2001a; Shirey et al., 2002) suggest establishment of the Kaapvaal mantle lithosphere in the Paleo-archean (i.e. ~3.5 to 2.7 Ga). Moreover, subsequent metasomatic overprinting resulted in CLM lithologies with younger Re-

Os model ages (e.g. Richardson et al., 2001b; Shirey et al., 2004; Richardson and Shirey, 2008) and this is further discussed below.

The estimated thickness of the Kaapvaal CLM calculated by mantle xenolith thermobarometry is 175 – 215 km, depending on the kimberlite xenolith suite (Boyd and Gurney, 1986; Griffin et al., 2003; Eaton et al., 2009). This depth range agrees with both electrical conductivity and seismic studies that show comparable depth estimates of the Kaapvaal lithosphere (James et al., 2001, 2003; Evans et al., 2011). Peridotite is the most prominent Kaapvaal CLM lithology in the suites of xenoliths brought to surface by kimberlite magmatism, while mafic rocks (i.e. eclogite) form a much smaller component (i.e. peridotite = 85 – 97 % vs. eclogite = 3 – 15 %; Schulze 1989; Carlson et al. 2005). Locally, however, eclogite xenoliths are more dominant from certain kimberlites (e.g. Roberts Victor; Gurney et al., 1984). The Kaapvaal CLM is dominated by orthopyroxene-rich harzburgite xenoliths (e.g. garnet ± spinel, olivine and orthopyroxene; Boyd et al., 1998; Lee, 2006; Simon et al., 2007; Arndt et al., 2009) with fewer lherzolites (garnet ± spinel, olivine, orthopyroxene and clinopyroxene) and scarce dunite samples (~90 % olivine; Rehfeldt et al., 2008). This suggests that subsequent to the Archean cratonic lithosphere formation there were a series of complex cratonic root modification and re-working events that transformed depleted harzburgite and dunite assemblages into more fertile, pyroxene and hydrous mineral-bearing assemblages (e.g. Hawkesworth et al., 1990; van Achterbergh et al., 2001; Grégoire et al., 2003). Moreover, common ca. 2.1–2.9, ca. 1.8–2.0 Ga and ca. ~1 Ga ages displayed by both peridotite and eclogite xenoliths as well as diamond inclusions, suggest post-Archean cratonic root modification and diamond genesis that may relate significantly to large igneous events (e.g. Bushveld LIP) or mobile belt activity (e.g. Keis belt and Namaqua-Natal belt) associated with Kaapvaal craton evolution (e.g. Pearson et al., 1998; Richardson et al., 2001, 2004; Westerlund et al., 2004; Richardson and Shirey, 2008; Aulbach et al., 2009).

The Kaapvaal CLM is shown to be both vertically and horizontally stratified with respect to its chemical composition (e.g. Jacob et al., 2009; Viljoen et al., 2009). Specifically, the CLM-derived peridotite xenoliths can be subdivided into two main groups. The first group includes, high-temperature deformed/sheared peridotites, which may represent localised shearing at the base of the lithosphere. These high-temperature deformed/sheared peridotites generally have more fertile compositions (i.e. geochemically enriched in basaltic components Fe, Ca, and Al, and incompatible elements), and have probably interacted metasomatically with high-temperature asthenosphere-derived melts, which could have enabled the localised shearing, prior to kimberlite eruption (O'Reilly and Griffin, 2010). These sheared/deformed peridotites may represent zones f localised shearing enabled by the presence of kimberlite melt and may not be representative of everywhere on the lithosphere boundary.

The second group includes, low-temperature coarse-grained peridotites located at shallow to mid-lithospheric depths, which have largely depleted compositions (i.e. high Mg/Fe, and relative depletions

in Ca and Al; Simon et al., 2003; Grégoire et al., 2005), and are considered to represent refractory lithospheric mantle residues. These low-temperature coarse peridotite residues primarily formed from past partial melting events probably connected to large volumes (> 40%) of komatiitic/basaltic-type melt extracted from the mantle during craton formation (Walter, 1998; Wilson et al., 2003; Carlson et al., 2005; Lee, 2006). It is notable also that the coarse-lherzolites often display re-enrichment signatures (e.g. re-enrichments in LREE and other incompatible elements as well as the addition of secondary "metasomatic" minerals; Grégoire et al., 2003; Jacob et al., 2009; Viljoen et al., 2009) that could be linked to several Kaapvaal mantle-derived magmatic episodes (e.g. the Bushveld Igneous complex or the Karoo LIP) or even to kimberlite magmatism (Simon et al., 2007).

Lateral seismic anomalies indicate that the Kaapvaal-Zimbabwe craton is split into two distinct areas of fast P-wave velocity mantle divided by a WNW trending corridor of slower P-wave velocity mantle (James et al., 2001; Shirey et al., 2002; Fouch et al., 2004), where the the Bushveld complex is located. The fast P-wave regions are considered representative of "normal" relatively depleted CLM, while the slower P-wave sliver has been linked to anomalous Fe-rich metasomatism of the cratonic mantle root near the Bushveld Igneous Complex (Danchin, 1979; Shirey et al., 2002; Richardson and Shirey, 2008). Several complex metasomatic signatures observed in xenoliths sampled from both areas suggest metasomatism from a range of compositionally diverse metasomatic melts/fluids. For example, many low-temperature coarse peridotite xenoliths sampled from Group I kimberlites on the Kaapvaal craton (e.g. Kimberley and Jagersfontein) show evidence for Si-rich melt metasomatism from the crystallisation of large proportions of orthopyroxene (e.g. Boyd and Mertzman, 1987). These orthopyroxene-enriched xenoliths are suggested to not be representative of primary "depleted" cratonic mantle (e.g. Boyd et al., 1997), and instead may have interacted with silica-rich fluids related to melts or fluids derived from late or post-Archean subduction at the margins of the Kaapvaal craton (Bell et al., 2005; Simon et al., 2007; Baptiste et al., 2012). Besides the apparent Si-rich metasomatism of the Kaapvaal CLM, crystallisation of secondary MARID- or PIC-type minerals (e.g. diopsidic clinopyroxene, mica, ilmenite and rutile) in predominantly peridotite (e.g. Dawson, 1984; Sweeney et al., 1993; Konzett et al., 1998; Grégoire et al., 2002; Rehfeldt et al., 2008; Aulbach et al., 2011; Fitzpayne et al., 2018) but also eclogite xenoliths (e.g. Jacob et al., 2009) suggests that potassic, volatile-rich (kimberlite-related) metasomatism also affected the Kaapvaal lithospheric mantle around Kimberley. In contrast, peridotite and eclogite xenoliths sampled from the seismically-slow WNW band in the center of the craton (e.g. from the Premier kimberlite) show evidence for re-fertilisation by melts/fluids that added basaltic components (e.g. Ca, Fe and Al) to a previously depleted protolith (e.g. Danchin, 1979; Viljoen et al. 2009). This "basaltic" metasomatism may be related to magmatism associated with the ca. 2 Ga Bushveld or 180 Ma Karoo large igneous provinces (e.g. Danchin, 1979; Boyd et al., 1998; Hoal, 2003; Gregoire et al., 2003, 2005; Dludla et al., 2006; Viljoen et al., 2009).

REFERENCES

Allsopp, H. L. and Barrett, D. R. (1975). Rb–Sr age determinations on South African kimberlite pipes. In Physics and Chemistry of the Earth (pp. 605-617). Pergamon.

Armstrong, R. A., Compston, W., Retief, E. A., Williams, I. T. and Welke, H. J. (1991). Zircon ion microprobe studies bearing on the age and evolution of the Witwatersrand triad. Precambrian Research **53**(3-4), 243-266.

Arndt, N. T., Coltice, N., Helmstaedt, H. and Gregoire, M. (2009). Origin of Archean subcontinental lithospheric mantle: Some petrological constraints. Lithos **109**(1-2), 61-71.

Aulbach, S., O'Reilly, S. Y. and Pearson, N. J. (2011). Constraints from eclogite and MARID xenoliths on origins of mantle Zr/Hf–Nb/Ta variability. Contributions to Mineralogy and Petrology **162**(5), 1047.

Aulbach, S., Shirey, S. B., Stachel, T., Creighton, S., Muehlenbachs, K. and Harris, J. W. (2009). Diamond formation episodes at the southern margin of the Kaapvaal Craton: Re–Os systematics of sulfide inclusions from the Jagersfontein Mine. Contributions to Mineralogy and Petrology **157**(4), 525-540.

Baptiste, V., Tommasi, A. and Demouchy, S. (2012). Deformation and hydration of the lithospheric mantle beneath the Kaapvaal craton, South Africa. Lithos **149**, 31-50.

Barton Jr, J. M. and Van Reenen, D. D. (1992). When was the Limpopo orogeny?. Precambrian Research **55**(1-4), 7-16.

Bell, D. R., Gregoire, M., Grove, T. L., Chatterjee, N., Carlson, R. W. and Buseck, P. R. (2005). Silica and volatile-element metasomatism of Archean mantle: a xenolith-scale example from the Kaapvaal Craton. Contributions to Mineralogy and Petrology **150**(3), 251.

Boyd, F. R. and Gurney, J. J. (1986). Diamonds and the African lithosphere. Science **232**(4749), 472-477.

Boyd, F. R. and Mertzman, S. A. (1987). Composition and structure of the Kaapvaal lithosphere, southern Africa. Magmatic processes: physicochemical principles **1**, 3-12.

Boyd, F. R., Pearson, D. G. and Mertzman, S. A. (1998). Spinel-facies peridotites from the Kaapvaal root. In International Kimberlite Conference: Extended Abstracts (Vol. 7, No. 1, pp. 100-102).

Boyd, F. R., Pokhilenko, N. P., Pearson, D. G., Mertzman, S. A., Sobolev, N. V. and Finger, L. W. (1997). Composition of the Siberian cratonic mantle: evidence from Udachnaya peridotite xenoliths. Contributions to Mineralogy and Petrology **128**(2-3), 228-246.

Carlson, R. W., Pearson, D. G., Boyd, F. R., Shirey, S. B., Irvine, G., Menzies, A. H. and Gurney, J. J. (1999). Re–Os systematics of lithospheric peridotites: implications for lithosphere formation and preservation. In: Proceedings of the 7th International Kimberlite Conference, Gurney, J. J. (Ed.), Red Roof Design, Cape Town, 99-108.

Carlson, R. W., Pearson, D. G. and James, D. E. (2005). Physical, chemical, and chronological characteristics of continental mantle. Reviews of Geophysics **43**(1).

Cawthorn, R. G. (2010). The platinum group element deposits of the Bushveld Complex in South Africa. Platinum Metals Review **54**(4), 205-215.

Cox, K. G. (1992). Karoo igneous activity, and the early stages of the break-up of Gondwanaland. Geological Society, London, Special Publications **68**(1), 137-148.

Danchin, R. V. (1979). Mineral and bulk chemistry of garnet lherzolite and garnet harzburgite xenoliths from the Premier Mine, South Africa. In: The Mantle Sample: Inclusion in Kimberlites and Other Volcanics, Proceedings of the Second International Kimberlite Conference, Boyd, F.R. and Meyer, H.O.A. (Ed.), American Geophysical Union, Washington, D.C., 104-126.

Dawson, J.B., 1984. Contrasting types of upper-mantle metasomatism. In: Kimberlites: II. The Mantle and Crust–mantle Relationships, Kornprobst, J. (Ed.), Elsevier, Amsterdam, 289 – 294.

de Wit, M.J., de Ronde, C.E., Tredoux, M., Roering, C., Hart, R.J., Armstrong, R.A., Green, R.W., Peberdy, E. and Hart, R.A. (1992). Formation of an Archaean continent. Nature **357**(6379), p.553.

Dludla, S., Le Roex, A. P. and Gurney, J. J. (2006). Eclogite xenoliths from the Premier kimberlite, South Africa: geochemical evidence for a subduction origin. South African Journal of Geology **109**(3), 353-368.

Eaton, D. W., Darbyshire, F., Evans, R. L., Grütter, H., Jones, A. G. and Yuan, X. (2009). The elusive lithosphere–asthenosphere boundary (LAB) beneath cratons. Lithos **109**(1-2), 1-22.

Eglington, B. M. (2006). Evolution of the Namaqua-Natal Belt, southern Africa–A geochronological and isotope geochemical review. Journal of African Earth Sciences **46**(1-2), 93-111.

Evans, R.L., Jones, A.G., Garcia, X., Muller, M., Hamilton, M., Evans, S., Fourie, C.J.S., Spratt, J., Webb, S., Jelsma, H. and Hutchins, D. (2011). Electrical lithosphere beneath the Kaapvaal craton, southern Africa. Journal of Geophysical Research: Solid Earth, **116**(B4).

Fitzpayne, A., Giuliani, A., Phillips, D., Hergt, J., Woodhead, J.D., Farquhar, J., Fiorentini, M.L., Drysdale, R.N. and Wu, N. (2018). Kimberlite-related metasomatism recorded in MARID and PIC mantle xenoliths. Mineralogy and Petrology **112**(1), pp.71-84.

Fouch, M. J., James, D. E., VanDecar, J. C., Van der Lee, S. and Kaapvaal Seismic Group. (2004).

Mantle seismic structure beneath the Kaapvaal and Zimbabwe Cratons. South African Journal of Geology **107**(1-2), 33-44.

Friese, A. E., Reimold, W. U. and Layer, P. W. (2003). ^{40}Ar-^{39}Ar dating of and structural information on tectonite-bearing faults in the Witwatersrand Basin: Evidence for multi-stage, tectono-thermal activity in the central Kaapvaal Craton. South African Journal of Geology **106**(1), 41-70.

Grégoire, M., Bell, D. and Le Roex, A. (2002). Trace element geochemistry of phlogopite-rich mafic mantle xenoliths: their classification and their relationship to phlogopite-bearing peridotites and kimberlites revisited. Contributions to Mineralogy and Petrology **142**(5), 603-625.

Grégoire, M., Bell, D. R. and Le Roex, A. P. (2003). Garnet lherzolites from the Kaapvaal Craton (South Africa): trace element evidence for a metasomatic history. Journal of Petrology **44**(4), 629-657.

Grégoire, M., Tinguely, C., Bell, D. R. and Le Roex, A. P. (2005). Spinel lherzolite xenoliths from the Premier kimberlite (Kaapvaal craton, South Africa): nature and evolution of the shallow upper mantle beneath the Bushveld complex. Lithos **84**(3-4), 185-205.

Griffin, W. L., Batumike, J. M., Greau, Y., Pearson, N. J., Shee, S. R. and O'Reilly, S. Y. (2014). Emplacement ages and sources of kimberlites and related rocks in southern Africa: U–Pb ages and Sr–Nd isotopes of groundmass perovskite. Contributions to Mineralogy and Petrology **168**(1), 1032.

Griffin, W. L., O'Reilly, S. Y., Natapov, L. M. and Ryan, C. G. (2003). The evolution of lithospheric mantle beneath the Kalahari Craton and its margins. Lithos **71**(2-4), 215-241.

Gurney, J. J., Harris, J. W. and Rickard, R. S. (1984). Minerals associated with diamonds from the Roberts Victor Mine. In: Kimberlites: II. The Mantle and Crust–mantle Relationships, Kornprobst, J. (Ed.), Proceedings of the Third International Kimberlite Conference. Elsevier, Amsterdam, 25 – 32.

Hanson, R. E., Martin, M. W., Bowring, S. A. and Munyanyiwa, H. (1998). U-Pb zircon age for the Umkondo dolerites, eastern Zimbabwe: 1.1 Ga large igneous province in southern Africa–East Antarctica and possible Rodinia correlations. Geology **26**(12), 1143-1146.

Hawkesworth, C., Kelley, S., Turner, S., Le Roex, A. and Storey, B. (1999). Mantle processes during Gondwana break-up and dispersal. Journal of African Earth Sciences **28**(1), 239-261.

Hawkesworth, C. J., Erlank, A. J., Kempton, P. D., & Waters, F. G. (1990). Mantle metasomatism: isotope and trace-element trends in xenoliths from Kimberley, South Africa. Chemical Geology **85**(1-2), 19-34.

Hoal, K. O. (2003). Samples of Proterozoic iron-enriched mantle from the Premier kimberlite. Lithos

71(2-4), 259-272.

Jacob, D. E., Viljoen, K. S. and Grassineau, N. V. (2009). Eclogite xenoliths from Kimberley, South Africa—a case study of mantle metasomatism in eclogites. Lithos **112**, 1002-1013.

James, D. E., Fouch, M. J., VanDecar, J. C., Van Der Lee, S. and Kaapvaal Seismic Group. (2001). Tectospheric structure beneath southern Africa. Geophysical Research Letters **28**(13), 2485-2488.

James, D. E., Niu, F. and Rokosky, J. (2003). Crustal structure of the Kaapvaal craton and its significance for early crustal evolution. Lithos **71**(2-4), 413-429.

Jelsma, H., Barnett, W., Richards, S. and Lister, G. (2009). Tectonic setting of kimberlites. Lithos **112**, 155-165.

Konzett, J., Armstrong, R. A., Sweeney, R. J. and Compston, W. (1998). The timing of MARID metasomatism in the Kaapvaal mantle: an ion probe study of zircons from MARID xenoliths. Earth and Planetary Science Letters **160**(1-2), 133-145.

Kröner, A., Compston, W. and Williams, I. S. (1989). Growth of early Archaean crust in the Ancient Gneiss Complex of Swaziland as revealed by single zircon dating. Tectonophysics **161**(3-4), 271-298.

Lee, C. T. A., Luffi, P. and Chin, E. J. (2011). Building and destroying continental mantle. Annual Review of Earth and Planetary Sciences **39**, 59-90.

Lee, C. T. A. (2006). Geochemical/petrologic constraints on the origin of cratonic mantle. Geophysical monograph **164**, 89-114.

O'Reilly, S. Y. and Griffin, W. L. (2010). The continental lithosphere–asthenosphere boundary: can we sample it?. Lithos **120**(1-2), 1-13.

Pearson, D. G., Carlson, R. W., Shirey, S. B., Boyd, F. R. and Nixon, P. H. (1995). Stabilisation of Archaean lithospheric mantle: A ReOs isotope study of peridotite xenoliths from the Kaapvaal craton. Earth and Planetary Science Letters **134**(3-4), 341-357.

Pearson, D. G., Shirey, S. B., Harris, J. W., & Carlson, R. W. (1998). Sulphide inclusions in diamonds from the Koffiefontein kimberlite, S Africa: constraints on diamond ages and mantle Re–Os systematics. Earth and Planetary Science Letters **160**(3-4), 311-326.

Poujol, M., Robb, L. J., Anhaeusser, C. R. and Gericke, B. (2003). A review of the geochronological constraints on the evolution of the Kaapvaal Craton, South Africa. Precambrian Research **127**(1-3), 181-213.

Rehfeldt, T., Foley, S. F., Jacob, D. E., Carlson, R. W. and Lowry, D. (2008). Contrasting types of

metasomatism in dunite, wehrlite and websterite xenoliths from Kimberley, South Africa. Geochimica et Cosmochimica Acta **72**(23), 5722-5756.

Richardson, S. H. and Shirey, S. B. (2008). Continental mantle signature of Bushveld magmas and coeval diamonds. Nature **453**(7197), 910.

Richardson, S. H., Shirey, S. B., & Harris, J. W. (2004). Episodic diamond genesis at Jwaneng, Botswana, and implications for Kaapvaal craton evolution. Lithos 77(1-4), 143-154.

Richardson, S. H., Shirey, S. B., Harris, J. W. and Carlson, R. W. (2001). Archean subduction recorded by Re–Os isotopes in eclogitic sulfide inclusions in Kimberley diamonds. Earth and Planetary Science Letters **191**(3-4), 257-266.

Richardson, S. H., Shirey, S. B., Harris, J. W. and Carlson, R. W. (2001). Episodic diamond formation in the Kaapvaal Craton keel. In AGU Spring Meeting Abstracts (Abstract id. V52A-07 INVITED).

Riley, T. R., Curtis, M. L., Leat, P. T., Watkeys, M. K., Duncan, R. A., Millar, I. L. and Owens, W. H. (2005). Overlap of Karoo and Ferrar magma types in KwaZulu-Natal, South Africa. Journal of Petrology **47**(3), 541-566.

Schmitz, M. D., Bowring, S. A., de Wit, M. J. and Gartz, V. (2004). Subduction and terrane collision stabilize the western Kaapvaal craton tectosphere 2.9 billion years ago. Earth and Planetary Science Letters **222**(2), 363-376.

Schulze, D. J. (1989). Constraints on the abundance of eclogite in the upper mantle. Journal of Geophysical Research **94**(B4), 4205-4212.

Shirey, S.B., Carlson, R.W., Richardson, S.H., Menzies, A., Gurney, J.J., Pearson, D.G., Harris, J.W. and Wiechert, U. (2001). Archean emplacement of eclogitic components into the lithospheric mantle during formation of the Kaapvaal Craton. Geophysical Research Letters **28**(13), 2509-2512.

Shirey, S.B., Harris, J.W., Richardson, S.H., Fouch, M.J., James, D.E., Cartigny, P., Deines, P. and Viljoen, F. (2002). Diamond genesis, seismic structure, and evolution of the Kaapvaal-Zimbabwe craton. Science **297**(5587), 1683-1686.

Shirey, S. B., Richardson, S. H. and Harris, J. W. (2004). Integrated models of diamond formation and craton evolution. Lithos **77**(1-4), 923-944.

Simon, N. S., Carlson, R. W., Pearson, D. G. and Davies, G. R. (2007). The origin and evolution of the Kaapvaal cratonic lithospheric mantle. Journal of Petrology **48**(3), 589-625.

Simon, N. S., Irvine, G. J., Davies, G. R., Pearson, D. G. and Carlson, R. W. (2003). The origin of garnet and clinopyroxene in “depleted” Kaapvaal peridotites. Lithos **71**(2-4), 289-322.

Skinner, E.M.W. and Truswell, J.F. (2006). Kimberlites. In: The geology of South Africa. Johnson, M.R., Anheausser, C.R. and Thomas, R.J. (Ed.), Geological Society of South Africa, Johannesburg, Council of Geoscience, Pretoria, 651–659.

Smith, C. B., Allsop, H. L., Kramers, J. D., Hutchinson, G. and Roddick, J. C. (1985). Emplacement ages of Jurassic-Cretaceous South African kimberlites by the Rb-Sr method on phlogopite and whole-rock samples. Transactions of the Geological Society of South Africa **88**(2), 249-266.

Snyder, D. B., Rondenay, S., Bostock, M. G. and Lockhart, G. D. (2004). Mapping the mantle lithosphere for diamond potential using teleseismic methods. Lithos **77**(1-4), 859-872.

Sweeney, R. J., Thompson, A. B. and Ulmer, P. (1993). Phase relations of a natural MARID composition and implications for MARID genesis, lithospheric melting and mantle metasomatism. Contributions to Mineralogy and Petrology **115**(2), 225-241.

Tappe, S., Smart, K., Torsvik, T., Massuyeau, M. and de Wit, M. (2018a). Geodynamics of kimberlites on a cooling Earth: Clues to plate tectonic evolution and deep volatile cycles. Earth and Planetary Science Letters **484,** 1-14.

Tappe, S., Dongre, A., Liu, C. Z. and Wu, F. Y. (2018b). 'Premier'evidence for prolonged kimberlite pipe formation and its influence on diamond transport from deep Earth. Geology **46**(10), 843-846.

van Achterbergh, E., Griffin, W. L. and Stiefenhofer, J. (2001). Metasomatism in mantle xenoliths from the Letlhakane kimberlites: estimation of element fluxes. Contributions to Mineralogy and Petrology **141**(4), 397-414.

Viljoen, F., Dobbe, R. and Smit, B. (2009). Geochemical processes in peridotite xenoliths from the Premier diamond mine, South Africa: evidence for the depletion and refertilisation of subcratonic lithosphere. Lithos **112**, 1133-1142.

Von Gruenewaldt, G., Sharpe, M. R. and Hatton, C. J. (1985). The Bushveld Complex; introduction and review. Economic Geology **80**(4), 803-812.

Walter, M. J. (1998). Melting of garnet peridotite and the origin of komatiite and depleted lithosphere. Journal of Petrology **39**(1), 29-60.

Watkeys, M.K. and Sokoutis, D. (1998). Transtension in southeastern Africa associated with the Gondwana break-up, In: Continental Transpressional and Transtensional Tectonics, Holdsworth, R.E., Strachan, R.A., Dewey, J.F. (Eds.), Geological Society of London Special Publication, vol. 135, 203–214.

Westerlund, K. J., Gurney, J. J., Carlson, R. W., Shirey, S. B., Hauri, E. H. and Richardson, S. H. (2004). A metasomatic origin for late Archean eclogitic diamonds: Implications from internal morphology

of diamonds and Re-Os and S isotope characteristics of their sulfide inclusions from the late Jurassic Klipspringer kimberlites. South African Journal of Geology **107**(1-2), 119-130.

Wilson, A. H., Shirey, S. B. and Carlson, R. W. (2003). Archaean ultra-depleted komatiites formed by hydrous melting of cratonic mantle. Nature **423**(6942), 858.

Wu, F. Y., Mitchell, R. H., Li, Q. L., Sun, J., Liu, C. Z. and Yang, Y. H. (2013). In situ UPb age determination and SrNd isotopic analysis of perovskite from the Premier (Cullinan) kimberlite, South Africa. Chemical Geology **353**, 83-95.

Zeh, A., Ovtcharova, M., Wilson, A. H. and Schaltegger, U. (2015). The Bushveld Complex was emplaced and cooled in less than one million years–results of zirconology, and geotectonic implications. Earth and Planetary Science Letters **418**, 103-114.

CHAPTER 2: FIGURES

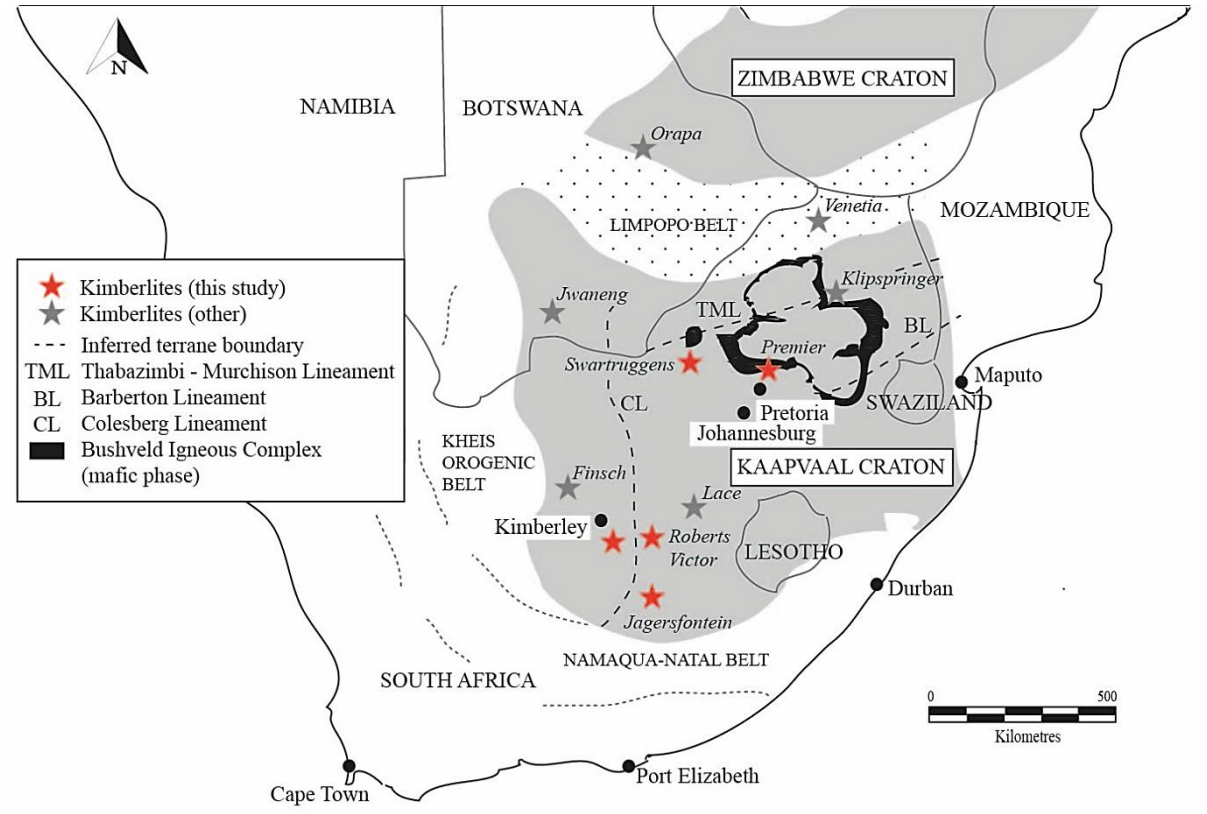

Fig. 2.1 *Schematic of the Kaapvaal craton modified after Friese et al. (2003). The Kaapvaal craton is subdivided into the Kimberley (western) and Witwatersrand (eastern) blocks along the Colesberg Lineament. Xenoliths are sampled from five kimberlite localities; Kimberley (Kamfersdam), Roberts Victor and Jagersfontein are situated close to the southern edge of the craton near the town of Kimberley, and Premier and Swartruggens are located in the north-central part of the craton near the western limb of the Bushveld Igneous Complex.*

CHAPTER 3

3. PRESENTATION OF THE RESEARCH PAPER

"SULPHUR-RICH MANTLE METASOMATISM OF KAAPVAAL CRATON ECLOGITES AND ITS ROLE IN REDOX CONTROLLED PLATINUM GROUP ELEMENT MOBILITY"

This research paper has been submitted to Chemical Geology by the authors:

S. Burness, University of the Witwatersrand (primary author, conducted the research)
K.A. Smart, University of the Witwatersrand (supervisor, reviewed the manuscript)
S. Tappe, University of Johannesburg (provided certain samples, reviewed the manuscript)
G. Stevens, University of Stellenbosch (supervisor, access to analytical equipment and funding)
A.B. Woodland, Institut für Geowissenschaften, Universität Frankfurt (Mössbauer spectroscopy)
E. Cano, University of New Mexico, U.S.A. (assisted with laser fluorination oxygen isotope analysis)

A detailed study was conducted of 19 sulphide-bearing eclogite and pyroxenite xenoliths from five kimberlites on the Kaapvaal craton, with the main purpose to investigate the occurrence of sulphide phases within the eclogitic portions of the lithospheric mantle. In addition to eclogite major, trace and stable oxygen isotope compositions, we report major, chalcophile and siderophile element compositions of the eclogite-hosted sulphides. These data are complemented by eclogite redox compositions calculated from Mossbauer spectroscopy-determined garnet Fe^{3+} contents. This new data demonstrates that the distribution of sulphides and their economically important trace metal contents within the eclogitic portion of the Kaapvaal lithospheric mantle is linked to both eclogite equilibration depth and redox composition. In turn, we develop a holistic model that links sulphide petrogenesis and the evolution of the Kaapvaal craton. This study has implications for the sulphur budget of the lithospheric mantle, and for models that aim to constrain the source regions of crustally-hosted economically important magmatic ore deposits.

This manuscript contains new, original work that has not been previously published or submitted elsewhere. All aspects of the sample preparation, data acquisitions and calculations were conducted by me under the supervision of Katie Smart. I wrote the manuscript and created all the diagrams. K. A. Smart conceptualised the research idea and participated in the writing as a typical second author. S. Tappe provided research samples from Helam and the Cullinan diamond mine. G. Stevens made available analytical equipment and funding. A.B. Woodland analysed the eclogitic garnets for Fe^{3+} using Mössbauer spectroscopy. E. Cano assisted with the garnet oxygen isotope analysis using laser fluorination techniques. All co-authors have actively contributed to the paper and agree to its use within this PhD thesis.

Chemical Geology, Impact factor: 3.57

ABSTRACT

Eclogite and garnet pyroxenite mantle xenoliths from various kimberlite occurrences on the Kaapvaal craton show evidence for depth- and redox-dependent metasomatic events that led to variable sulphide and HSE and incompatible element enrichments. Xenoliths from Roberts Victor, Jagersfontein, Kimberley (Kamfersdam), Premier and Swartruggens kimberlites were investigated for their silicate and sulphide geochemistry, stable isotope compositions and oxybarometry. The variably metasomatised eclogites contain sulphide ± kyanite ± phlogopite ± coesite ± carbonate and display a wide range of bulk compositions, with 6 to 18 wt.% MgO and 13 to 20 wt.% Al_2O_3. The xenoliths also fall into distinctive trace element groups that feature relative LREE enrichments and depletions, variable Eu and Sr anomalies, and present some fractionated HREEs. Additionally, the eclogite and pyroxenite xenoliths have garnet $\delta^{18}O$ values that range from 3.3 to 10.4 ‰, which, when coupled with the trace element characteristics, particularly Eu and Sr anomalies and Cs contents, indicate oceanic lithosphere protoliths that had undergone variable degrees of seawater alteration. The deepest equilibrated eclogites (175 – 220 km depth) from near the base of the Kaapvaal craton lithosphere are the most refractory and feature significant LREE depletions. They show the most oxidized redox compositions with $\Delta\log fO_2$ values of FMQ-3.9 to FMQ-1.5. Subtle metasomatic overprinting of these eclogites resulted in base metal sulphides with relatively depleted and highly fractionated HSE compositions. These deepest eclogites and their included base metal sulphides support interaction with relatively oxidised melts or fluids, which, based on their HSE characteristics, could be related to precursor kimberlite metasomatism that was widespread within the Kaapvaal craton lithosphere. In contrast, eclogites that reside at shallower, "mid-lithospheric" depths (140 – 180 km) have been enriched in LREE and secondary diopside/phlogopite. Importantly, they host abundant metasomatic base metal sulphides, which have higher HSE contents than the deeper eclogites residing at the lithosphere base. The "mid-lithospheric" eclogites have more reducing redox compositions ($\Delta\log fO_2$ = FMQ-5.3 – FMQ-3.3) than the eclogites from the lower Kaapvaal lithosphere. The compositional overprint of the shallower eclogites resembles basaltic rather than kimberlitic/carbonatitic metasomatism, which is also supported by their relatively reducing redox state. Base metal sulphides from the "mid-lithospheric" eclogites have HSE abundances and distributions that are similar to Karoo basalts from southern Africa, suggesting a link between the identified shallow metasomatism of the Kaapvaal cratonic lithosphere and the Karoo large igneous event during the Mesozoic. The sulphide platinum group element abundances of the "mid-lithospheric" eclogites are higher compared with their analogues from the deeper lithospheric eclogites, which in combination with their contrasting oxidation state, may imply redox-controlled PGE mobility during sulphur-rich metasomatism of continental lithosphere.

KEYWORDS: mantle redox; oxygen isotopes; highly siderophile elements; sulphides; lithospheric mantle; eclogite xenoliths

3.1. INTRODUCTION

The most important hosts of sulphur in the Earth's upper mantle are sulphide minerals and melts (Chaussidon et al., 1989; Shirey and Richardson, 2011), which provide important information for understanding the origin and evolution of the cratonic lithospheric mantle, including recurrent volatile-rich metasomatic processes (Lorand ,1989; Guo et al., 1999; Lee et al., 2011; Gréau et al., 2013; Aulbach et al., 2016). Sulphide minerals largely control the chalcophile and highly siderophile element (HSE), including platinum group element (PGE), budgets of the lithospheric mantle (e.g. Alard et al., 2000; Luguet et al., 2007; Liu et al., 2009; König et al., 2014). In addition, the behaviour of sulphide minerals during mantle melting buffers the sulphur content of silicate melts (e.g. Fleet et al., 1996; Ding and Dasgupta, 2017), and determines the mobility of these economically important elements (c.f. Barnes et al., 1997, 2015; Alard et al., 2000; Luguet et al., 2003, 2007; Bockrath et al., 2004; Peregoedova et al., 2004; Mungall et al., 2005; Mungall and Brenan, 2014; Jenner, 2017). Several studies have linked the reservoirs of economically important metals (i.e. HSE elements) from the mantle lithosphere to the crust. For example, the PGE metal endowment in magmatic ore complexes hosted in mafic to ultramafic rocks near the Earth's surface may have been ultimately sourced from sulphide-bearing peridotitic (Griffin et al., 2004) or eclogitic lithospheric mantle domains (Aulbach et al., 2012). Sulphides in the Earth's mantle, and by proxy, metasomatic S-bearing melts or fluids are intimately linked to diamond formation. This is supported by the abundance of sulphide inclusions in diamond (Griffin et al., 2003; Cartigny et al., 2009; Thomassot et al., 2009; Smart et al., 2017a) and suggests that sulphur may be catalytic to diamond formation (Palyanov et al., 2007), highlighting the importance of sulphur within deep volatile cycles.

Base metal sulphides (BMS), found as inclusions or interstitial grains within mantle-derived peridotite and eclogite xenoliths, are largely composed of monosulphide solid solution (MSS), intermediate solid solution (ISS), or low-temperature sulphide phases derived from these solid solutions (e.g. Craig, 1973; Fleet and Pan, 1994; Bockrath et al., 2004; Peregoedova et al., 2004; Li and Audétat, 2012; Lorand et al., 2013; Marchesi et al., 2014). It is suggested that these re-equilibrated sulphides are formed from a single high-temperature sulphide melt/liquid at upper mantle pressure and temperature conditions (e.g. Fleet and Pan, 1994; Lorand and Gregoire, 2006; Lorand et al., 2013; Wainwright et al., 2015a). The HSE content of BMS grains is often highly fractionated due to interaction with percolating metasomatic fluids/melts during mantle residence and further during re-equilibration reactions throughout the cooling history of the base metal sulphides (e.g. Ballhaus et al., 2006; Lorand and Gregoire, 2006; Luguet et al., 2007, 2015; Aulbach et al., 2009a; Alard et al., 2011; Delpech et al., 2012; Gréau et al., 2013; Wainwright et al., 2015a; Bragagni et al., 2017). In contrast, sulphides encapsulated in diamonds are frequently protected from subsequent metasomatism and are thus critical for placing age constraints on cratonic lithospheric mantle (CLM) evolution (Pearson et al., 1998; Richardson et al., 2001a; Shirey et al., 2004; Aulbach et al., 2009b).

The origin of cratonic lithospheric mantle-derived eclogite is debated (see Jacob, 2004 vs. Griffin and O'Reilly, 2007), but there is convincing evidence that many eclogite xenolith suites represent ancient oceanic crust emplaced tectonically into the cratonic mantle during subduction processes (MacGregor and Manton, 1986; Jacob and Foley, 1999; Shirey et al., 2001; Smart et al., 2014; Dongre et al., 2015; Aulbach and Jacob, 2016; Tappe et al. 2018a). Many studies demonstrate that sulphur and other HSE are volatile and may not survive slab dehydration and partial melting processes during prograde subduction-zone metamorphism (e.g. Alt et al., 1993; Dale et al., 2009; Jégo and Dasgupta, 2013; Patten et al., 2013; Evans et al., 2014; Mungall and Brenan, 2014). However, experiments indicate that sulphides can remain stable/unaffected during low-degree partial melting of basalt (i.e. 10 – 15 %, Jégo and Dasgupta, 2013; Ding and Dasgupta, 2017), unless melting occurred under particularly oxidising conditions, in which case sulphide crystals will be effectively removed by dissolution in the melt (Jugo et al., 2005; Jugo, 2009). Therefore, relatively 'dry' basaltic rocks that experience minimal partial melting during subduction processes may retain some crustal sulphur and this could explain – to some extent – the high abundances of sulphides observed in eclogites compared to other mantle lithologies (e.g. Pearson et al., 1998; De Hoog et al., 2004; Evans et al., 2014; Giuliani et al., 2016).

In this study we report new major and trace element data for silicate and sulphide minerals from a suite of nineteen mantle-derived eclogite and pyroxenite xenoliths from five kimberlite occurrences on the Kaapvaal craton (**Fig. 3.1**). This dataset is complemented by the Mössbauer spectroscopic determination of Fe^{3+} in garnet and laser fluorination oxygen isotope ratio measurements, which in concert with standard petrologic methods, enables us to address the distinctive depth- and redox-related base metal sulphide distribution in eclogites, with important implications for sulphur and PGE remobilisation within the crust-mantle system.

3.2. GEOLOGICAL SETTING

The Kaapvaal craton, located in southern Africa (**Fig. 3.1**), is made up of two major Archean terranes: the Witwatersrand block (3.7 to 2.7 Ga; Kröner and Compston, 1988; Armstrong et al., 1991) and the Kimberley block (3.3 to 2.9 Ga; Schmitz et al., 2004), which were assembled along the Colesberg magnetic lineament between 2.93 and 2.88 Ga (Schmitz et al., 2004) via subduction collision (Shirey et al., 2001). The northern margin of the Kaapvaal craton is sutured to the Zimbabwe craton by the 2.8 – 2.5 Ga Limpopo orogenic belt (Barton and Van Reenen, 1992). To the east, the Kaapvaal craton is flanked by the ~200 Ma Lebombo monocline, and to the west by the Kheis orogenic belt (2.0–1.7 Ga). At ca. 1.04 – 1.2 Ga, the Namaqua-Natal mobile belt formed along the southern margin of the Kaapvaal craton due to continental collision and accretion (Eglington, 2006). The Bushveld Igneous Complex intruded the craton at 2056 Ma (Zeh et al., 2015), and at ca. 180 Ma, the entire Kaapvaal craton and surrounding mobile belts were affected by basaltic magmatism of the Karoo large igneous province (Jourdan et al., 2004).

Kimberlite magmatic activity occurred on and around the Kaapvaal craton between 1.8 Ga and 60 Ma (Skinner and Truswell, 2006; Tappe et al., 2018a), with Mesozoic pulses being predominant (Jelsma et al., 2009). Increased kimberlite magmatic activity across southern Africa between 140-120 and 100-80 Ma was recently linked to the pronounced acceleration of the African tectonic plate during Pangea supercontinent breakup, which facilitated drainage of deep-sourced low-volume melts (Tappe et al., 2018a).

The Kaapvaal craton crust has been supported by a thick mantle lithosphere since ca. 3.3–3.5 Ga (Richardson et al., 2001a; Smart et al., 2016), which has been episodically sampled by kimberlite and related magmatism since 1.8 Ga. Some of the oldest dated Kaapvaal xenoliths and diamond inclusions suggest ages between 3.5 and 2.7 Ga for the formation of the lithospheric keel, including peridotitic diamonds which yield ages between 3.5 to 3.1 Ga (Richardson et al., 1984; Shirey et al., 2013). Placer diamonds of eclogitic/pyroxenitic derivation from the ca. 2.8 – 3 Ga Witwatersrand Supergroup attest to diamond formation during Early Archean craton amalgamation (Smart et al., 2016). Archean ages of ca. 3.1 – 2.9 Ga were also determined for eclogitic diamonds from Jwaneng, Orapa and Koffiefontein (Richardson et al., 2001a, 2004; Shirey et al., 2002), as well as for eclogite-hosted (Shirey et al., 2001; Menzies et al., 2003) and peridotite-hosted base metal sulphides in mantle-derived xenoliths from Finsch, Jagersfontein and Kimberley (Griffin et al., 2004). Together, these age constraints support the establishment of the Kaapvaal mantle lithosphere in the Paleo- to Mesoarchean, followed by subsequent craton growth processes (e.g. Richardson et al., 2004; Shirey et al., 2004). Post-Archean cratonic root modification is demonstrated by ca. 2 Ga mantle xenolith and diamond inclusions ages found for Jagersfontein, Premier, Venetia and Jwaneng. These ages either relate to large igneous events (e.g., Bushveld Large Igneous Province) or mobile belt activity (e.g., Kheis belt) that triggered concomitant diamond formation (e.g. Richardson and Shirey, 2008). Finally, ca. 1 Ga diamond growth events at Jagersfontein, Koffiefontein and Orapa could be possibly linked to the ca. 1.2 –1.0 Ga Namaqua-Natal metamorphic belt. However, some of these Proterozoic ages (e.g. Hopp et al., 2008) may be linked to younger metasomatic events, or may have no geologic meaning if the dated base metal sulphides formed during mantle hybridization events (Pearson et al., 1998; Shirey et al., 2004; Aulbach et al., 2009b).

The eclogite xenoliths of this study were sampled from kimberlites at Roberts Victor, Jagersfontein, Kimberley (specifically the Kamfersdam pipe), Swartruggens and Premier (**Fig. 3.1)**. Roberts Victor, Jagersfontein and Kamfersdam are located in the southern portion of the Kaapvaal craton close to the Colesberg lineament and the town of Kimberley. The Swartruggens (Helam mine) and Premier (Cullinan mine) kimberlites are located west and east of Pretoria respectively, near the margins of the Bushveld Complex (**Fig. 3.1**). The Kimberley (Kamfersdam), Jagersfontein and Premier kimberlites are of Group I affinity, with ages that range from the Cretaceous for Kimberley (84±3 Ma; Clement, 1982) and Jagersfontein (85.6±1.0 Ma; Smith et al., 1985) to the Proterozoic for Premier (1153±5.3 Ma; Tappe et al., 2018b). Roberts Victor and Swartruggens are Group II kimberlites, with ages of

128±15 Ma (Smith et al., 1985) and 156±13 Ma (Smith et al., 1985), respectively. Cratonic mantle eclogites from the Roberts Victor and Jagersfontein kimberlites on the southern Kaapvaal craton have been extensively studied (see review in Jacob, 2004), and isotopic investigations of these and other Kaapvaal eclogite xenoliths and diamonds have consistently revealed maximum protolith formation ages of ca. 3 Ga (Richardson et al., 2001a; Menzies et al., 2003). Based on $\delta^{18}O$ isotope systematics and trace element evidence (MacGregor and Manton, 1986; Taylor and Neal, 1989; Schulze et al., 2000; Jacob et al., 2003; Gonzaga et al., 2010; Riches et al., 2016), these eclogite suites have been interpreted as evidence for recycled Archean oceanic crust components in the Kaapvaal CLM. However, relatively little is known about the petrology and geochemistry of Kaapvaal craton eclogite suites from Kimberley, Swartruggens, and Premier; consequently, mantle xenoliths from these kimberlites are the focus of this contribution.

3.3. SAMPLES AND PETROGRAPHY

Eighteen eclogite xenoliths and one pyroxenite xenolith were selected for study based on the presence of visible sulphides from the five Kaapvaal kimberlite occurrences described in **Section 3.2** (**Fig. 3.1**; **Table 3.1)**. The petrography and modal abundance of the eclogite silicate minerals are presented here and information specific to the base metal sulphides is presented in **Section 3.4.** The garnet-pyroxenite xenolith (Swartruggens) was distinguished from the eclogite xenoliths due to modally abundant clinopyroxene (>80 vol. %) with low Na_2O contents (< 1.5 wt.%). Most eclogites are composed of roughly equal proportions of bright orange to light-pink garnet and light apple- to- dark green clinopyroxene (**Fig. 3.2**), with minor amounts of coesite, phlogopite, rutile, ilmenite, kyanite, calcite, barite and base metal sulphide. The Kaapvaal eclogites in general have medium- to coarse-grained (1–5 mm) equiangular textures and are variably metasomatised, with most samples displaying alteration along mineral rims or cleavage planes in addition to some micro-veining (e.g. **Figs 3.2a – f**). If kyanite or phlogopite constitute a significant portion of the rock (e.g. > 5 – 8 %), the terms 'kyanite eclogite' (e.g. ROVIC-MBK, JJG-4492, and HRV-172B) and 'phlogopite eclogite' (e.g. HRV-161A and B) are used. Eclogites in general were texturally and chemically classified into Type I (A/B) and Type II (A/B) according to MacGregor and Carter (1970) and McCandless and Gurney (1989; **Table 3.1)**, but difficulty with classification due to alteration modifying Na_2O in garnet and K_2O in clinopyroxene (due to secondary processes; e.g. Mysen, 1973; Pearson et al. 1995) required an additional geochemical classification (see **Sections 3.5.3.2 and 3.5.3.3**). The eclogite xenoliths HRV-161A and B, HRV-172A, HRV-174B and MBK from Roberts Victor, CIM15-102 from Kamfersdam, and JJG-2914, JJG-2919, and JJG-2920 from Jagersfontein show a greater degree of modal metasomatism, with 5–10 modal % of secondary cloudy and 'spongy' clinopyroxene, in addition to the variable occurrence of phlogopite, ilmenite, base metal sulphide and nepheline. Eclogite xenoliths MBK, HRV-161A and B from Roberts Victor contain significant coarse-grained phlogopite and large discrete base metal sulphides. Kyanite-bearing samples JJG-4492 and HRV-172B from Roberts Victor

show a breakdown of clinopyroxene to a white matrix of presumably augite and albite (Gréau et al., 2013) or analcime-like zeolite (Chinner and Cornell, 1974). Sample JJG-2920 from Jagersfontein contains 1 modal % calcite.

3.4. ANALYTICAL METHODS

3.4.1. Major and minor element compositions

Mineral major and minor element compositions were determined using a Zeiss EVO MA15VP Scanning Electron Microscope (SEM) equipped with an Oxford X-Max energy dispersive spectrometer (EDS) silicon drift detector (SDD), coupled to a Link ISIS energy dispersive spectrometry system at the Central Analytical Facility at Stellenbosch University (South Africa). Quantitative analysis on garnet and clinopyroxene (**Table 3.1**) (± phlogopite, rutile, ilmenite, kyanite, calcite and nepheline) was performed using an accelerating voltage of 20 kV, a 10-s counting time (5 s background) and a beam current range of 19 to 21.5 nA. The beam current was controlled by adjusting the spot size and the focussed beam was set at a working distance of 8.5 mm. The operating conditions for sulphide mineral analyses include an accelerating voltage of 20 kV, beam current of 19 to 21.5 nA, beam size of <3 µm and 20 s on peak (10 s background) counting times. Individual low-temperature sulphide phases (e.g. pyrite, chalcopyrite, pentlandite etc…) were analysed and reassembled into bulk sulphide compositions using modal abundances. BSE image point counting methods or X-ray element distribution maps, integrated through image analysis software (JMicroVision v1.27; **Appendix A**), were used to calculate these modes. Where exsolved phases were not distinguishable, a compositional traverse was taken across the sulphide to yield an average composition. All spectra were processed by ZAF corrections and quantified using natural mineral standards (**Table 3.2 – 3.3**). Oxygen and sulphur were measured for the sulphide phases and oxygen was calculated by stoichiometry for the silicates. Minimum detection limits and reproducibility for the elements of interest are provided in **Appendix B**.

3.4.2. Trace element compositions

Only clear and inclusion-free portions of garnet and clinopyroxene were identified for in-situ trace element analysis. Between 6 and 10 grains of garnet and clinopyroxene from each xenolith were analysed by LA-ICP-MS at Stellenbosch University. The LA-ICP-MS system includes a 193-nm excimer laser system coupled to an Agilent 7500ce quadrupole ICP-MS. Internal standardisation used ^{29}Si (based on prior quantitative SEM measurements of the silicates), and external calibration was set on the NIST SRM 610 standard reference glass. A typical run used a beam diameter of 100 µm, laser fluence of 2.5 J/cm^2 and a 20s gas blank measurement followed by 30 s of ablation time. With every 15 unknowns, measurements of NIST SRM 612, BCR-2G and BHVO-2G standard reference glasses were performed. The Iolite©2017 software package was used to reduce the time resolved data and calculate the trace element concentrations. The results of the standards are within 2σ of the average concentrations reported by Jochum et al. (2005), with standard errors of 2 to 7 % (**Appendix C**).

Secondary alteration products were identified using Ba as an alteration monitor with unaltered garnets containing less than ~0.5 ppm Ba. Minimum detection limits (generally < 0.1 ppm) and 1-sigma uncertainties are found in **Appendix D**.

Sulphides were analysed with a laser repetition rate of 4 Hz, 20 s of background acquisition followed by ablation for 60 s, 100 µm and 45 µm spot size (dependent on sulphide size), with the analysis area rastered over the entire sulphide grain during ablation. The largest possible spot size was chosen for each sulphide grain to attain a representative trace element analysis. When possible, between 3 to 6 analyses were conducted on a grain. Analyses of unknowns were interspersed with the "NiS5b" (MB2014) sulphide standard (provided by J Brenan; Mungall and Brenan, 2014; Brenan, 2015), as well as BCR-2G and NIST 610. Importantly, analyses of the unknown sulphides were bracketed by analysis of the calibration standard "NiS5b" (MB2014) at the same spot size to minimise apparent fractionation effects. Various HSE were quantified using the NiS5b (MB2014) sulphide standard, which contains 51.8 µg/g As, 101.1 µg/g Se, 2.2 µg/g Ag, 109.4 µg/g Te, 8.4 µg/g Au, 62.1 µg/g Pb, 97.7 µg/g Bi, 81.2 µg/g Os, 80.4 µg/g Ir, 151.9 µg/g Ru, 151.9 µg/g Rh, 93.5 µg/g Pt, 152.8 µg/g Pd, and 35.4 µg/g Re. Helium was used as a carrier gas, which was merged with Ar prior to entering the ablation cell. Some $^{65}Cu\,^{40}Ar$ and $^{63}Cu\,^{40}Ar$ interference is observed on ^{103}Rh and ^{105}Pd leading to weak correlations between these respective concentrations, and as such ^{103}Rh and ^{105}Pd is not reported. Concentrations for Pd were based on ^{106}Pd, which give comparable values to ^{108}Pd but consistently lower values than ^{105}Pd. Ru is not reported due to $^{63}Cu\,^{40}Ar$, $^{61}Ni^{40}Ar$ and $^{59}Co^{40}Ar$ interferences. Where calculated concentrations of an element (using more than one isotope) differed by more than 10 µg g^{-1}, the concentrations obtained for that element were rejected. Trace element compositions are reported in **Table 3.4** and **3.5**, with NiS5b, NIST-612, BCR-2G and BVHO-2G glass SRM data and minimum detection limits for elements (mostly <0.1ppm) reported in **Appendix C**.

3.4.3. Oxygen isotope analysis of garnet

Oxygen isotope compositions were determined by conventional laser fluorination methods and gas-source dual-inlet mass spectrometer at the University of New Mexico, USA. Following the procedure of Sharp (1990), between 1 and 2 mg of inclusion and crack-free garnet were loaded into a nickel block, placed into the sample chamber of the Thermo Scientific MAT 253 mass spectrometer and heated under vacuum overnight to remove contaminants. After a pre-fluorination BrF_5 cleaning step, samples were further reacted with BrF5 and heated with a Merchantek 25 W CO_2 laser. Oxygen gas was measured with the dual-inlet Thermo Scientific MAT 253 mass spectrometer after passing through three cryogenic (liquid nitrogen) traps for purification and over scientific grade NaCl, mainly to convert HF to HCl and NaF. San Carlos olivine was repeatedly measured during each analytical session. The average San Carlos $\delta^{18}O$ value for the analytical session was 5.54 ± 0.1 ‰, in comparison to the "accepted" value of 5.35 ± 0.2 ‰ (1σ; Eiler et al. 1996). The Gee Whiz quartz laboratory standard (12.5

± 0.1‰, Larson and Sharp, 2003) was used as a secondary standard, and duplicates yielded $\delta^{18}O$ values of 12.4 ± 0.1 ‰ (1σ). The oxygen isotope results are reported in **Table 3.6**.

3.4.4. Garnet $Fe^{3+}/\Sigma Fe$ contents

The Fe^{3+} contents, reported in **Table 3.1** as $Fe^{3+}/\Sigma Fe$, were determined by Mössbauer spectroscopy at Goethe Universität Frankfurt, Germany. Spectra were obtained from hand-picked, optically clean garnet separates from selected xenoliths. Powdered samples were mixed with a small quantity of sugar prior to being placed into a Pb sample holder as this helps to prevent the ferrous iron from being oxidised. The amount of garnet (generally ~2–4 mg) and sample diameter were adjusted to produce samples of <5 mg cm^{-2} to minimize saturation effects. Measurements were made at constant acceleration with a velocity ramp of ±5 mm s^{-1} and a ~ 50 mCi ^{57}Co in Rh source. Mirror-image spectra, calibrated with α-Fe metal foil, were collected over 512 channels (wavelengths) until ~2×10^6 counts per channel were reached. Fitting the garnet spectra followed the approach described by Woodland and Koch (2003), including a correction to account for different recoil free fractions of Fe^{3+} and Fe^{2+} in garnet (Woodland and Ross, 1994). The Fe^{3+} peak width was constrained to 0.4 mm s^{-1} in all but one case in order to obtain physically reasonable hyperfine parameters for this doublet. Corrected $Fe^{3+}/\Sigma Fe$ values reported in **Table 3.1** have absolute uncertainties of ±0.01.

3.5. RESULTS

3.5.1. Major element compositions of garnet and clinopyroxene

Major and minor element compositions of garnet and clinopyroxene are presented in **Table 3.1**. Garnet compositions are plotted in terms of pyrope, almandine and grossular endmembers in **Figure 3.3a**, where they are also classified as Group A, B or C according to Coleman et al. (1965). The majority of the Kaapvaal eclogitic garnets are Group B, with 8.8 to 15.4 wt.% MgO, 12.7 to 19.1 wt.% FeO, 4.2 to 11.1 wt.% CaO contents, and low Cr_2O_3 (maximum 0.1 wt.%) and TiO_2 (maximum 0.4 wt.%) contents. High-MgO (Mg# = 68 – 79) pyropic garnets plot in Group A and have elevated Cr_2O_3 (0.05 to 0.37 wt.%) contents, along with relatively lower CaO (2.9 and 4.1 wt.%), and TiO_2 (maximum 0.08 wt.%) contents. Two Roberts Victor samples, JJG-4492 and HRV-172B, have Group C garnet compositions, with 7.6 and 7.0 wt.% MgO, 18.5 and 15.9 wt.% CaO, 0.15 and 0.34 wt.% TiO_2, and 22.4 and 22.6 wt.% Al_2O_3, respectively. These samples are termed ‘grospydites’ (grossular-pyroxene-kyanite rocks; Sobolev et al., 1968), with grossular contents of 43 and 48 mol.%, respectively. In comparison, garnet from the Swartruggens pyroxenite (Mg# = 69) classifies as Group B.

Clinopyroxene from the Kaapvaal eclogites are diopside-hedenbergite-jadeite solid solutions that have a wide compositional range, and classify as Group A, B or C using the MgO vs. Na_2O scheme of Taylor and Neal (1989) (**Table 3.1; Fig. 3.3b**). Primary Group B clinopyroxenes are found at all localities and have intermediate compositions (e.g. jadeite contents of 18 – 45 mol.%; 2.7 – 5.9 wt.%

Na_2O, 13.0 – 17.1 wt.% CaO, 7.2 – 9.9 wt.% Al_2O_3) compared with jadeite-rich (vs. 53 – 58 mol.%) Group C clinopyroxene (7.3 – 8.4 wt.% Na_2O, 9.9 – 11.6 wt.% CaO, 13.4 – 17.3 wt.% Al_2O_3; **Fig. 3.3b**) that are only found at Roberts Victor. Primary Group A clinopyroxenes, found in two samples from Roberts Victor (MBK) and Kimberley (CIM15-102), are diopside-rich with the lowest jadeite contents (12.2 – 12.8 mol.%), having low Na_2O (2.9 and 2.1 wt.%) and Al_2O_3 (3.4 and 3.2 wt.%) but high MgO (15.3 and 15.4 wt.%) and CaO (19.3 and 20.6 wt.%) contents, respectively. The discrimination ratio of Tschermak's to jadeite components in clinopyroxene expressed as $^{[6]}Al$ /$^{[4]}Al$ (Aoki and Shiba, 1973) was used to distinguish eclogitic ($^{[6]}Al$ /$^{[4]}Al$ ratios > 2) from pyroxenitic Group A clinopyroxene (e.g. Jacob, 2004). Diopsidic clinopyroxene from pyroxenite ST16-H-04 (X_{di} = 81.9; **Fig. 3.3b**) has 3.1 wt.% Al_2O_3, 2.3 wt.% Na_2O, 19.2 wt.% CaO, 0.3 wt.% TiO_2 and 15.6 wt.% MgO contents. Widespread spongy-textured secondary diopsidic clinopyroxene was analysed for a selection of the Kaapvaal samples (**Appendix E**), and the majority plot in the Group A field (0.7 – 3.1 wt.% Na_2O).

3.5.2. Trace element compositions of garnet and clinopyroxene

The trace element contents of eclogite garnet and clinopyroxene are presented in **Table 3.4** and **Figure 3.6**. The eclogitic garnets from all localities have variable trace element concentrations; 33 – 211 ppm V, 21 – 83 ppm Sc, 4.9 – 54 ppm Y and 2.1 – 73 ppm Zr. Ni contents range between 12 and 45 ppm, excluding Roberts Victor samples ROVIC-MBK, HRV-172A, EJB-86 that have elevated Ni contents of 104, 123 and 78 ppm, respectively. Most garnets have low Ba contents (below detection limit to 0.9 ppm), but elevated Ba (e.g. 65 ppm in altered sample JJG-2717) is associated with variable enrichment in LREE and other incompatible elements (**Table 3.4**). In general, eclogitic garnet from Roberts Victor, Jagersfontein and Kimberley (n = 17) display two distinctive chondrite-normalised REE patterns (denoted by subscript "N"; McDonough and Sun, 1995). The garnet displays either LREE-depleted (i.e., Ce_N <1), variably fractionated HREE patterns (i.e., Lu_N/Gd_N = 0.4 – 4.1; Lu_N = 5 to 55) with weak to absent Eu anomalies (i.e., $Eu^* = 2*Eu_N/[Sm_N+Gd_N]$) = 0.9 – 1.1), or has prominent Eu anomalies (i.e., $Eu^* = 2*Eu_N/[Sm_N+Gd_N]$) = 1.1 – 1.7) with a range of HREE patterns (Lu_N/Gd_N = 0.2 – 2.1; Lu_N = 2.8 – 29.2; **Figs 3.4a – c**). Garnet from Premier eclogite JJG-2717 has a sinusoidal chondrite-normalised REE pattern (**Fig. 3.4c**), with decreasing HREE from Gd to Lu (Lu_N/Gd_N = 0.2), enriched MREEs (Sm_N= 30.6, Eu_N= 38.3; Eu*=1.1, Gd_N= 42.1), and a steep increase in LREE from La to Sm (La_N/Sm_N = 0.02). The Swartruggens pyroxenitic garnet (**Fig. 3.4c**) is LREE-depleted (La_N = 0.7) with no Eu anomaly and displays fractionated HREEs (Lu_N/Gd_N = 2.8).

The majority of primary clinopyroxene from Roberts Victor, Jagersfontein and Kimberley (n = 15) display typical convex-upward chondrite-normalized REE patterns (**Figs 3.4d – f**), with moderate (i.e., La_N/Sm_N = 0.5 – 5.6, Ce_N = 1.2 – 9.6; n = 6) to extreme (i.e., La_N/Sm_N = 0.5 to 3.3, Ce_N = 11.4 to 91.7; n = 9) LREE enrichments relative to HREE (i.e., Lu_N/Gd_N = 0.02 – 1). Most of these clinopyroxenes also exhibit positive Eu (Eu* = 1 – 7.9; n = 12) and Sr (Sr* = 1.1 – 20.5; n = 13) anomalies. Two

samples from Roberts Victor (HRV-174B) and Jagersfontein (JJG-2919) display extreme LREE depletion (i.e., $La_N/Sm_N = 0.02$; $Ce_N = 0.1$) and no distinct Eu* but small Sr* of 3.8 and 3.7, respectively. Highly altered clinopyroxene from the Premier eclogite (JJG-2717) displays a "sinusoidal" LREE pattern (**Fig. 3.4f**), with a weak positive Eu (Eu* = 1.2) and a more pronounced Sr (Sr* = 6.5) anomaly. The small size constraints limited trace element analyses of the secondary "spongy" diopsidic clinopyroxene, but several analyses from the Roberts Victor, Jagersfontein and Kimberley eclogites are depicted in **Figure 3.4e**. The pyroxenitic clinopyroxene also displays a convex-upward, chondrite-normalised REE pattern (**Fig. 3.4f**), with moderately enriched LREE contents ($Ce_N = 25.7$; $La_N/Sm_N = 0.9$), a progressive depletion in HREE from Gd to Lu ($Lu_N/Gd_N = 0.1$) and weak Eu (0.9) and Sr (1.6) anomalies.

3.5.3. Calculated bulk eclogite compositions

3.5.3.1. Metasomatism

Mantle eclogites are commonly affected by metasomatism that can cause new mineral growth, geochemical and isotopic overprinting (e.g. Taylor and Neal, 1989; Harte et al., 1993; Schmidberger et al., 2005; Jacob et al., 2009; Liu et al., 2009; Smart et al., 2009, 2012; Tappe et al., 2011; Huang et al., 2012; Gréau et al., 2013). Fresh, unaltered xenoliths are necessary for unravelling the age and petrogenetic history of mantle eclogites, but those that display evidence of metasomatism also provide insights into lithospheric mantle evolution and modification (e.g. Jacob et al., 2009; Ongley et al., 1987; Shirey et al., 2004). The aim of this study was to investigate eclogite-hosted sulphides, which often occur in variably metasomatised xenoliths. Therefore, bulk eclogite compositions were calculated from mineral mode estimations and measured mineral compositions (e.g. Barth et al., 2001; Jacob, 2004) to avoid kimberlite contamination (c.f. Schmidberger et al., 2001). The coarse grain size (maximum 0.5 cm) and small size (2 – 7 cm) of the eclogite xenoliths hampered accurate modal estimations, and thus an overall mode of 50% garnet and 50% clinopyroxene was chosen (which excludes the heterogeneous occurrence of phlogopite±kyanite±rutile in some eclogites). This modal proportion is within petrologically reasonable limits of results from eclogite experimental petrology and previous studies (c.f. Aulbach and Jacob, 2016; Smart et al., 2017b). Small variations (10%) in mineral mode is illustrated in **Figure 3.5** for HRV-172B. A bulk composition for pyroxenite ST16-H-04 was calculated using the estimated modes of 20% garnet and 80% clinopyroxene. Log-normalised trace element patterns are only little affected by differences in mineral modes (Jerde et al., 1993). Highly incompatible elements (e.g. Ba, Sr, Nb, Ta, LREE) may be more susceptible to metasomatic modification, but the HREE are less influenced by metasomatic events and should represent original eclogite compositions (e.g. Barth et al., 2001, 2002; Jacob, 2004). Reconstructed bulk xenolith major and trace element compositions can be found in **Table 3.7**.

3.5.3.2. Major element compositions

The calculated whole-rock compositions are plotted in **Figures 3.5a – f**. The eclogites contain 46.5 – 49 wt.% SiO_2, 13.1 – 19.9 wt.% Al_2O_3, 6.2 – 12 wt.% FeO, 6.4 – 17.7 wt.% MgO, and 5.5 – 15 wt.% CaO and have Mg-numbers between 43 and 74 (**Table 3.7**). Samples MBK, HRV-174A, HRV-161A, HRV-161B from Roberts Victor, JJG-2914 and JJG-2920 from Jagersfontein, and CIM15-102 from Kimberley, have calculated bulk MgO contents of between 12 and 18 wt.%, SiO_2 between 37 and 52 wt.% and Na_2O+K_2O of <3 wt.% (**Figs 3.5a, b** and **d**), and are picritic in composition (Le Bas, 2000). Samples HRV-174B, HRV-172A from Roberts Victor, JJG-2919 from Jagersfontein, have basaltic compositions, and HRV-162A, HRV-162B, ROVIC MBK, JJG-4492, EJB-86 and HRV-172B from Roberts Victor, JJG-2717 from Premier and CIM15-101 from Kimberley, show some MgO, Al_2O_3, CaO and Na_2O compositional affinities for gabbroic rocks, some of which contain kyanite. The Swartruggens pyroxenite (ST16-H-04) has distinctly lower Al_2O_3 (7 wt.%) and higher CaO (16.7 wt.%) and SiO_2 (52.8 wt.%) contents compared to the eclogites (**Figs 3.5a – c**) but has partially overlapping MgO (15.5 wt.%) and Na_2O (1.9 wt.%). The Roberts Victor eclogite xenoliths are compositionally similar to those previously described (e.g. Jacob, 2004, 2005; Gréau et al., 2011), with MgO displaying negative correlations with both Al_2O_3 and Na_2O (**Figs 3.5a, d**). The Swartruggens pyroxenite shows compositional similarities to pyroxenites found in ophiolites (e.g. Monnier et al., 2003; de Wit, 2004; Smart et al., 2017b; **Fig. 3.5**).

3.5.3.3. Trace element compositions and eclogite groups

The calculated whole-rock trace element compositions are listed in **Table 3.7** and the eclogites have been divided into three REE pattern groups depicted in **Figures 3.6** and **3.7**. "LREE-enriched" eclogites (**Fig. 3.6a**) have strong enrichments in LREE (Pr_N = 6 – 54), weak to slightly negative Eu* (0.8 – 1.1; except JJG-2920 = 1.5), and variably fractionated HREE (Lu_N/Gd_N = 0.3-1.3). Roberts Victor samples MBK, HRV-161A, HRV-161B and HRV-172A, Kimberley samples CIM15-101 and CIM15-102 and Jagersfontein samples JJG-2914 and JJG-2920 fall within this group. "LREE-depleted" eclogites (**Fig. 3.6a**) are characterised by positively sloping LREE (La_N/Sm_N= 0.1 – 0.6), predominantly negatively sloped HREE (Lu_N/Gd_N = 0.2-0.8; except HRV-174A = 1.6) and distinct positive Eu* anomalies (1.1 – 1.9). Seven samples from Roberts Victor (ROVIC MBK, JJG-4492, HRV-174A, HRV-162A and B, HRV-172B, EJB-86) and one from Premier (JJG-2717) fall into this group (noting that this last sample exhibits La enrichment and also abnormally enriched MREE). The final two eclogites (HRV-174B; JJG-2919) are characterised as "HREE-enriched" and show both enriched and fractionated HREE patterns (Lu_N/Gd_N = 3.5 and 3.7; Lu_N = 26 and 28; **Fig. 3.6b**), with no distinct Eu* anomalies (0.9) and extremely depleted LREE (below detection; **Fig. 3.6b**). Note that very few primary clinopyroxene grains were found in JJG-2919 due to extensive metasomatic overprinting and therefore, the "whole-rock" trace element composition is calculated with both primary and secondary clinopyroxene

compositions as shown in **Fig. 3.6b**. The Swartruggens pyroxenite ST16-H-04 displays a similar REE pattern to the "HREE-enriched" eclogite REE pattern (**Fig. 3.6b**), with Pr_N = 27.5, a slightly negative Eu anomaly (Eu* = 0.9) and relatively enriched HREE (Lu_N/Gd_N = 0.2) and is thus grouped with the "HREE-enriched" eclogites for discussion purposes.

The three groups are also distinguished in primitive-mantle normalised multi-element plots (**Figs 3.7a – d**). "LREE-enriched" eclogites (**Fig. 3.7d**) have variably enriched LILEs, excluding samples HRV-161A and HRV-161B (Roberts Victor) and CIM15-101 (Kimberley) that display depletions of Ce, Rb and Ba. High field strength elements (e.g. Th, U, Nb, Ta, Zr and Hf) vary in abundance within this group. For example; samples MBK and HRV-172A (Roberts Victor), JJG-2920 (Jagersfontein), and CIM15-102 (Kimberley) are enriched in HSFE. In contrast, HSFE depletions are seen in samples HRV-161A, HRV-161B (Roberts Victor) and CIM15-101 (Kimberley). The "HREE-enriched" eclogites (**Fig. 3.7b**) are generally similar to the HFSE-enriched "LREE-enriched" eclogites (**Fig. 3.7d**), with more highly fractionated HREE and lesser enrichment in the LILE. "LREE-depleted" eclogites have the smallest negative Ti anomalies, but do not exhibit significant depletion in Zr – Hf and are enriched in Ba and Rb (**Fig. 3.7c**). All groups are Ti depleted, probably resulting from omission of rutile from the bulk calculations (e.g. Xiong et al., 2005).

3.5.4. Thermobarometry

Eclogite equilibrium pressure and temperature conditions were calculated iteratively using two methods (**Table 3.6; Fig. 3.8**). The first method estimates temperature and pressure using iterative calculations of the Ellis and Green (1979) Fe-Mg exchange thermometer (T_{EG79}) and the Beyer et al. (2015) Grt-Cpx barometer (P_{B15}), with an initial pressure estimate of 5 GPa. P_{B15} requires clinopyroxene with [Si] > 1.995 a.p.f.u. and thus for those samples where P_{B15} could not be used, eclogite PT conditions were calculated iteratively using T_{EG79} and pressures determined from peridotite-defined geotherms ($P_{Geotherm}$) specific to each locality (O'Reilly and Griffin, 1995; Pearson et al., 1995; Viljoen et al., 2009; Grütter, 2009; Katayama et al., 2009). The final eclogite T_{EG-79} – $P_{Geotherm}$ calculations yielded equilibration conditions of 985 – 1250 ºC and 3.7 – 6.7 GPa, compared to the T_{EG-79} – P_{B15} conditions of 1019 – 1107 ºC and 3.4 – 6.6 GPa. The Swartruggens pyroxenite has a T_{EG79} – P_{B15} equilibrium temperature of 1078 ºC and pressure of 5.5 GPa. The iteratively calculated T_{EG79} – $P_{Geotherm}$ estimates for the eclogites are plotted in **Figure 3.8** and used for the oxybarometry calculations.

3.5.5. Garnet $Fe^{3+}/\Sigma Fe$ and eclogite oxybarometry

Measured $Fe^{3+}/\Sigma Fe$ contents in garnet from selected samples range from 0.010 to 0.041 (±0.01; n = 16; **Table 3.1**). The garnets of this study have a somewhat smaller $Fe^{3+}/\Sigma Fe$ range compared to eclogitic garnets from the Lace kimberlite, central Kaapvaal craton (0.009 – 0.063, n=16; Aulbach et al., 2017). There does not appear to be a relationship between eclogite type and garnet ferric iron content. Oxygen fugacities calculated for the Kaapvaal eclogites using the oxybarometer of Stagno et al. (2015) with

$T_{EG\text{-}79} - P_{Geotherm}$ values are at $\Delta \log fO_2$ between FMQ-1.5 and FMQ-5.3, with an uncertainty of ±0.5 log units (**Table 3.6; Figs 3.9a, b**).

3.5.6. Garnet oxygen isotope compositions

Eclogitic garnets display $\delta^{18}O$ values between 3.3 and 7.9 ‰ (±0.1 ‰; **Table 3.6**), comparable to garnet oxygen isotope compositions reported previously for Kaapvaal eclogites (~2 – 8.2 ‰; see **Fig. 3.10** and references therein). In this study, garnets from Roberts Victor eclogites have $\delta^{18}O$ values between 3.3 and 7.9 ‰ (n = 12), Jagersfontein garnets have values between 6.3 and 6.6 ‰ (n = 3), Kimberley garnets have $\delta^{18}O$ values of 5.9 and 7.6 ‰, and the Premier eclogitic garnet has a value of 6.1 ‰. Garnet from the Swartruggens pyroxenite has a $\delta^{18}O$ value of 10.4 ‰.

3.5.7. Base metal sulphide petrography

3.5.7.1. Modal abundance and distribution

Most of the eclogite samples studied here were chosen based on the occurrence of visible sulphide phases, however during sample petrography, it was found that samples HRV-174B from Roberts Victor and JJG-2914 from Jagersfontein did not contain base metal sulphides (**Table 3.1**). The other eclogites contain between <1 – 2 modal % base metal sulphides (BMS), and there is a general decrease in eclogite BMS modal abundances in the following order of kimberlite localities: Roberts Victor, Jagersfontein, Kimberley and Premier. Base metal sulphides can occur as rounded inclusions towards the edges of primary silicate mineral grains (**Fig. 3.11a**), within secondary 'spongy' clinopyroxene (**Fig. 3.11b**), as rounded to elongate interstitial grains, or less commonly, within micro-veinlets associated with kimberlite fluid infiltration (**Fig. 3.11c**). Eclogites HRV-161A and B, HRV-162A, HRV-162B, and MBK from Roberts Victor and JJG-2919 and JJG-2920 from Jagersfontein contain the most abundant BMS, where on average more than five grains of >50 μm were observed per thin section, excluding small (<30 μm) interstitial BMS grains that are often disseminated throughout the predominantly clinopyroxene and garnet eclogitic matrix.

3.5.7.2. Habits and textural relationships

The base metal sulphides are divided into two main groups; **BMS inclusions** and **interstitial BMS**, which are then further divided into four sub-groups based on texture, size and location. The individual BMS groupings follow a similar approach to previous research conducted on BMS in CLM-derived eclogite and peridotite xenoliths (e.g. Szabó and Bodnar, 1995; Alard et al., 2005, 2011; Lorand and Gregoire, 2006; Aulbach et al., 2009a; Greau et al., 2013; Wainwright et al., 2015; Bragagni et al., 2017; Luguet and Pearson, 2019).

BMS inclusions

Small "semi-isolated" BMS inclusions occur as rounded to sub-angular blebs with a diameter of <45 µm mostly within clinopyroxene (**Fig. 3.11a**) and garnet (**Fig. 3.11d**), and to a lesser extent within phlogopite. Some of these BMS inclusions are completely enclosed within the host silicate phases, but the majority are associated with crystal rims and fractures (**Fig. 3.11e**). The "freshest" small BMS inclusions consist either of fine veins of pentlandite (Pn) within a "fish-net"-like pyrrhotite (Po) matrix with coronas or patches of chalcopyrite (Cp; **Fig. 3.11d**.1), or of exsolved patches ("mottled texture") of pentlandite and chalcopyrite or pentlandite and pyrrhotite. These textural relationships indicate sub-solidus exsolution from a previous mono-sulphide solid solution phase (MSS). These small "semi-isolated" BMS inclusions that are associated with silicate crystal rims and fractures **(Fig. 3.11e)** often display finely inter-fingered pyrite/Ni-Py as well as smythite/violarite mineral phases, indicating a degree of alteration. In contrast, the completely enclosed "isolated" grains are least affected by alteration processes as shown by their low oxygen contents (**Table 3.2; Section 3.5.7.3**), lack of pyrite (Py), Ni-rich pyrite (Ni-Py) and altered sulphide (i.e. smythite and violarite) mineral phases.

Large "semi-isolated" BMS inclusions are located within individual silicate grains, but are either associated with large cracks **(Fig. 3.11f)** that may form pathways for metasomatic fluids, or are situated on crystal rims where a portion of the inclusion in contact with the eclogite matrix **(Fig. 3.11g**); either situation may potentially facilitate alteration of these partially-enclosed sulphides. The occurrence of large BMS inclusions at silicate grain boundaries suggests that sulphide melt was probably entrapped during metasomatic recrystallisation of the host eclogite. The large "semi-isolated" BMS inclusions are globular in shape, have a diameter of 50 to 150 µm and consist of mixtures of pentlandite ± chalcopyrite ± pyrrhotite ± pyrite/Ni-Py ± "altered sulphide" (e.g. smythite and violarite) and occasionally even magnetite or iron-(oxy)hydroxide phases (**Fig. 3.11f.1)**. The large "semi-isolated" BMS inclusions display both "fish-net"-like and patchy textures (**Table 3.4; Figs. 3.11f.1**) and often exhibit sulphide strings which radiate out from the main BMS inclusion into stress fractures present in the host silicate (**Fig. 3.11f**), probably having resulted from BMS partial melting and volume expansion during ascent to the surface. The sulphide strings are largely (>50 %) replaced by iron-(oxy)hydroxide.

Interstitial BMS

Small interstitial BMS occur at grain boundaries between individual silicate minerals or are disseminated within micro-veinlets associated with fluid infiltration (**e.g. Fig. 3.11b, c**). These small (10 to 30 µm in size) BMS interstitials are rounded to elongate in shape and are either randomly dispersed throughout the eclogite matrix (**Figs 3.11b**) or have a close spatial relationship with secondary phlogopite (**Figs 3.11c**) and oxide minerals such as ilmenite and rutile. The small interstitial grains consist of patchy-textured combinations of pentlandite ± chalcopyrite ± pyrite/Ni-Py as well as the "altered sulphide" phases (**Fig. 3.11h, h.1**). Most small interstitial BMS are largely (>60 %) replaced

by magnetite or iron(oxy)hydroxide mineral phases. A few small interstitial BMS identified in two Kimberley samples (CIM15-101 and 102) and three samples from Roberts Victor (e.g. EJB-86, HRV-174A, HRV-161B) were associated with barite in thin veins that crosscut the eclogite matrix. These grains were identified as low Ni-pyrite (<1 wt.% Ni) that probably formed during kimberlite melt infiltration and are therefore not considered further.

Large interstitial BMS are located at grain boundaries (**Fig. 3.11i**) between garnet and clinopyroxene (± kyanite ± phlogopite) and are also disseminated within secondary spongy clinopyroxene (**Fig. 3.11j**). These large interstitial BMS grains are usually rounded (**Fig. 3.11j**) but also exhibit irregular shapes, have a diameter of 50 to 150 µm and principally consist of patchy and "fish-net"-like textured blends of pentlandite ± chalcopyrite ± pyrite/Ni-Py and sometimes smythite and violarite mineral phases (**Fig. 3.11j.1**). Trails of minute interstitial sulphides, often altered to iron(oxy)hydroxide phases, radiate out from many of the large interstitial BMS grains, which indicates decrepitation of the original sulphide (**Fig. 3.11g**). The Kimberley eclogites contain large interstitial BMS (less than three grains per sample), which are highly altered and texturally unique, as they consist of a rounded outer corona (60 to 90 µm diameter) of chalcopyrite, pyrrhotite and iron-(oxy)hydroxide phases as well as small traces of patchy pentlandite (**Fig. 3.11k**). In addition, various eclogites from Roberts Victor, Kimberley and Premier contain large individual pyrite grains which are often associated with phlogopite and spongy clinopyroxene (**Fig. 3.11**).

3.5.7.3. Low-temperature sulphide major element compositions

The textural observations demonstrate that most of the **BMS inclusions** and the **interstitial BMS** consist of mixed multi-phase assemblages (***Section 3.5.7.2***). Like previous authors (e.g. Kullerud et al., 1969; Craig and Kullerud, 1973; Fleet and Pan, 1994; Aulbach et al., 2004, 2016b; Wainwright et al., 2015; Luguet et al., 2015), we interpret these mixed sulphide assemblages as low-temperature recrystallisation products that have stabilised upon cooling from a single high-temperature sulphide melt or solid solution phase. There is no distinguishable chemical difference between the individual low-temperature sulphide mineral phases (i.e. Pn, Po, Py, Cp) of the **interstitial BMS** and the **BMS inclusions**. Therefore, a representative composition for each mineral is presented in **Table 3.2** and described below.

Pyrrhotite (n = 17) on average has a metal/sulphur [M/S = (Fe+Cu+Ni+Co)/S] atomic ratio of 0.9 and contains 39.8 wt.% S and 57.8 wt. % Fe as well as 0.3 wt.% Ni (**Table 3.2; Fig. 3.12**). Pyrrhotite is not common in the Roberts Victor eclogites, only comprising ~49 modal % of a single ***large "isolated" BMS inclusion*** in sample HRV-172B and does not comprise any Roberts Victor **interstitial BMS** (**Table 3.2**). Pyrrhotite is more prevalent in the Jagersfontein eclogites and can contribute up to 79 modal % of both ***small*** *and* ***large BMS inclusion*** grains. Pyrrhotite was not identified in any of the Kimberley or Premier eclogites. Two types of **pentlandite** were observed in the eclogites studied here,

pentlandite (Pn) and **cobalt-rich pentlandite (Co-Pn)**. **Pentlandite** (n = 15) on average has a high M/S ratio of 1.1 and contains 33.5 wt.% S, 38.6 wt. % Fe, 25.3 wt.% Ni, 1.8 wt.% Co, and 1.0 wt.% Cu (**Table 3.2; Fig. 12**). **Cobalt-rich pentlandite** (n = 10) also has an average M/S ratio of 1.1, but contains 32.6 wt.% S, 31.1 wt. % Fe, 30.7 wt.% Ni, 3.9 wt.% Co, and 0.3 wt.% Cu. Pentlandite is only found in four Roberts Victor samples (MBK, JJG-4492, HRV-161B and HRV-162B) where is comprises <5 modal % of both ***small*** *and* ***large "isolated" BMS inclusions*** and is not observed as interstitial grains. Pentlandite is most prevalent in the Jagersfontein eclogites where it comprises up to 25 modal % of ***small*** *and* ***large "isolated" BMS inclusions*** only. Co-rich pentlandite only exists as part the low-temperature assemblages of some ***small*** *and* ***large "isolated" BMS inclusions*** of the Jagersfontein (JJG-2920) and Kimberley (CIM15-101) eclogites (**Table 3.2; Fig. 3.12**). **Chalcopyrite** (n= 65) on average has a M/S value of 1 and contains 34.1 wt. % S, 31.6 wt. % Fe, 33.6 wt. % Cu, 0.3 wt. % Ni and a range of Co contents from 0.06 to 0.15 wt. %. Chalcopyrite can comprise up to 30 modal % of both **interstitial BMS** and **BMS inclusions** and is present in samples from all localities except Premier (**Table 3.2; Fig. 3.12**). **Pyrite** (n = 30) and **Ni-rich pyrite** (n = 20) have a low average M/S ratio of 0.5 which indicates sulphur deficiency and Fe-Ni substitution (e.g. Gréau et al., 2013). Pyrite (n = 30) has an average Ni content of 0.6 wt. %, whereas the Ni-rich pyrite (n = 20) has an average Ni content of 3.1 wt.%, with a maximum Ni content of ~12 wt. %. Pyrite and Ni-rich pyrite often occur in **interstitial BMS** and **BMS inclusions** located towards silicate crystal rims, where both types can exist within the same BMS grain (**Table 3.2; Fig. 3.12**). Individual large interstitial pyrite grains occur in samples from Roberts Victor, Kimberley and Premier.

Generally, BMS alteration is characterised by substantial oxygen contents (~0.5 – 5 wt.%) but may also be correlated with a decrease in sulphur content and early conversion into iron(oxy)hydroxide mineral phases (see oxidation trend in **Fig. 3.13**). In addition, **interstitial BMS** grains from Roberts Victor often contain altered Ni-rich sulphide phases which are difficult to categorise into distinct mineral species. However, using M/S ratios and atomic proportions of S, Fe, and Ni we can distinguish between two main altered sulphide groups; **Smythite** and **Violarite** (**Table 3.2; Fig. 3.12**). Smythite (n = 15) has an average M/S ratio of 0.6, ~61.1 at. % S, 23.4 at. % Fe and 14.8 at. % Ni. Violarite (n = 17) has an average M/S ratio of 0.8, ~57 at. % S, 16.4 at. % Fe and 26.1 at. % Ni. These phases and others for which mineral species determination is compromised by alteration are collectively termed "altered sulphide".

3.5.7.4. BMS major element reconstructions

In order to estimate the original mantle sulphide compositions, we reconstruct the bulk composition of each sulphide grain using the compositions of the individual low-temperature phases weighted by their modal abundances as imaged on multi-element distribution maps or by point counting methods (**Section 3.4.1**). The reconstructed bulk sulphide compositions can be divided into three distinct groups

(Table 3.3). **Group 1 BMS** contain the relatively un-oxidised sulphides that are generally enclosed within predominantly clinopyroxene grains (e.g. ***small and large isolated BMS inclusions***). These calculated bulk sulphide compositions fall within a Ni-poor MSS group **(Table 3.3; Fig. 3.12),** and specifically have high proportions of pyrrhotite ± chalcopyrite ± pentlandite, or less common Ni-pyrite ± chalcopyrite ± smythite/violarite assemblages. In general, the clinopyroxene-enclosed sulphides have Ni contents that range from 2.5 to 6.5 wt.%, with a mean of 4.9 wt.%. **Group 2 BMS** contain the majority of BMS, which can be highly altered, and occur as ***interstitial BMS or as "semi-isolated" BMS inclusions*** at silicate mineral boundaries. This group is compositionally diverse and tends to have higher abundances of sulphur and nickel-rich phases such as "smythite/violarite" and (Ni)-rich pyrite. The sulphides in this group have a large compositional range between a less altered "pyrite" end-member and a more highly altered "Smy/Vi" end-member (**Fig. 3.12**). Ni contents for the interstitial sulphides (i.e. "Smy/Vi" end-member) range from 0.5 to 30 wt.% (mean of 14.7 wt.%). Nickel contents for the "semi-isolated" sulphides range from 0.5 to 15 wt.% (mean of 10.3 wt.%; **Table 3.3**) and are often more representative of the "pyrite" end-member. **Group 3 BMS** contain both ***interstitial*** and ***"semi-isolated" inclusions*** of pyrite that have nickel contents up to 3.1 wt. % (**Fig. 3.12**). It should be noted that the large compositional variation in Group 1 and Group 2 may potentially result from sectioning effects during sample preparation, limitations of the SEM image processing technique, and/or heterogeneous alteration of the sulphide phases. Therefore, the bulk sulphide compositions should be considered estimations.

3.5.7.5. BMS trace element compositions

Due to the small grain sizes and variable alteration of the BMS, in-situ LA-ICP-MS trace element analyses were only obtained for BMS from Roberts Victor and Jagersfontein eclogites. The low-temperature sulphide assemblages that comprise the BMS grains were probably initially derived upon cooling from a high temperature (~1200 ºC) Ni-poor MSS/melt (Bockrath et al., 2004; Lorand and Luguet, 2016; Bragagni et al., 2017), and subsequently re-equilibrated through complex sub-solidus reactions between ~900 and 300 ºC (**Fig. 3.12**; Yund and Kullerud, 1966; Craig, 1969). The intricate re-equilibration reactions that occur upon cooling are expected to fractionate highly siderophile elements, and especially PGE, between the different low-temperature assemblages that comprise BMS grains (Lorand and Gregoire, 2006; Luguet et al., 2007, 2015; Delpech et al., 2012; Bragagni et al., 2017). Therefore, for this study, the largest possible spot size (45–100 µm) was used during LA-ICP-MS analysis to account for these HSE fractionations (**Section 3.5.7.4**). Group 1 and 2 BMS (see **Section 3.5.7.4**) show distinctive trace element compositional variability (**Table 3.5)**, and Group 3 pyrites have HSE contents below detection limits and are therefore not reported.

In general, BMS from the Roberts Victor eclogites contain low Os (bdl to 0.35 µg/g), Ir (<0.01 to 0.36 µg/g), Pt (bdl to 4.9 µg/g) and Pd (bdl to 6.1 µg/g) contents, with the exception of sample MBK,

which contains significant Os (0.18 µg/g), Ir (0.59 µg/g), Pt (32.7 µg/g) and Pd (108 µg/g) contents. Rhenium contents range from 0.05 to 0.9 µg/g, selenium from 68 to 315 µg/g, tellurium from 68 to 315 µg/g and gold from bdl to 0.64 µg/g (**Table 3.5**). In addition, all Roberts Victor BMS have suprachondritic Se/Te values that range from 4 to 42. Group 1 BMS are only found at Roberts Victor and generally display relatively I-PGE poor and P-PGE (excluding Pt) enriched, positively sloping chondrite-normalised HSE patterns (**Fig. 3.14a**), with Pt depletions (often below detection) and systematic enrichment in Os over other I-PGE (Os_N/Ir_N = >1; **Table 3.5**). The Roberts Victor Group 1 BMS highly fractionated Re_N/Os_N values that range from 18 to 299 (n=7). In contrast, Roberts Victor Group 2 BMS display less fractionated, "flatter" chondrite-normalised HSE patterns (**Fig. 3.14b**), with Re_N/Os_N values that range from 3 to 53 (n=6). The Roberts Victor Group 2 BMS are comparatively more enriched in PGE than the Group 1 BMS (**Fig, 3.14a,b**) and often display minor Pd-enrichments (e.g. Pd_N/Pt_N = 2 to 5 and Pd_N/Ir_N = 5 to 92 (**Table 3.5**), excluding the Ni-rich sulphide "BMK" from Roberts Victor which displays extreme Pd-enrichment with Pd_N/Pt_N = 6 and Pd_N/Ir_N = 185.

Group 1 BMS from the Jagersfontein eclogites were too small and friable to analyse reliably for trace elements. Group 2 BMS from Jagersfontein contain low Os (0.01 to 0.26 µg/g), Ir (0.05 to 0.6 µg/g), Pt (0.4 to 0.8 µg/g) and Pd (0.5 to 3.9 µg/g) contents. They also display Pd-enriched (Pd_N/Pt_N = 2 to 19 and Pd_N/Ir_N = 5 to 81; **Table 3.5),** positively sloping chondrite-normalised HSE patterns (Re_N/Os_N values that range from 27 to 202; n=4), similar to those described for the Roberts Victor Group 2 BMS (**Fig. 3.14b**). The Jagersfontein sulphides have highly variable Se (bdl to 588 µg/g) and Te (4 to 46 µg/g) contents, with Se/Te ratios that range from 12 to 13 (n=3).

3.6. DISCUSSION

3.6.1. Petrogenesis of Kaapvaal craton eclogite xenoliths

Previously investigated Kaapvaal craton eclogite xenoliths and eclogitic diamond inclusions, specifically from the Roberts Victor (Ongley et al., 1987; Schulze et al., 2000; Jacob, 2004; Riches et al., 2016), Jagersfontein (Tappert et al., 2005; Aulbach et al., 2009b), Kimberley (Jacob et al., 2009), Premier (Viljoen et al., 2010) and Lace kimberlites (Aulbach and Viljoen, 2015; Aulbach et al., 2017) are consistent with an oceanic crustal origin. The petrogenesis of eclogite xenoliths from cratons worldwide has been much debated (see Jacob, 2004 vs. Griffin and O'Reilly, 2007), but due to the presence of kyanite or coesite/quartz (MacGregor and Manton, 1986; Schulze and Helmstaedt, 1988; Schulze et al., 2000; Jacob et al., 2003), positive Eu and Sr anomalies plus relatively flat normalized HREE patterns (Snyder et al., 1997; Jacob, 2004; Smart et al., 2014, 2017; Aulbach and Jacob, 2016), and non-mantle like oxygen isotope compositions (MacGregor and Manton, 1986; Ongley et al., 1987; Tappe et al., 2011; Pernet-Fisher et al., 2014; Riches et al., 2016), it is evident that many (but perhaps not all, cf. Smyth et al., 1989; Taylor and Neal, 1989; Caporuscio and Smyth, 1990; Huang et al., 2012) eclogite xenoliths from kimberlites have protoliths that formed as crustal oceanic basalts and gabbros,

with variable amounts of plagioclase accumulation and seawater alteration. Likewise, it is argued that the Kaapvaal eclogites studied here also have crustal protoliths based upon key geochemical and isotopic signatures that point to oceanic crustal origins. For example, the $\delta^{18}O$ values of garnet from the Kaapvaal eclogite and garnet pyroxenite xenoliths are both significantly higher (up to +10.4 ‰; **Table 3.6, Fig. 3.10**) and lower (down to +3.4 ‰; **Table 3.6, Fig. 3.10**) than the accepted mantle composition of +5.5 ± 0.4 ‰ (Mattey et al., 1994; Regier et al., 2018). This wide range of $\delta^{18}O$ values observed for the xenoliths probably results from oceanic lithosphere (e.g. ophiolites; see **Fig. 3.10** and references therein) that underwent seawater alteration at different depth levels and, thus, variable temperature conditions (Muehlenbachs, 1998; Alt et al., 2012). Eclogites that show unequivocal geochemical features of crustal protoliths include the "LREE-depleted" eclogites (**Figs. 3.6 - 3.7**), which may contain kyanite ± coesite (**Table 3.1**), have strongly positive Eu and Sr anomalies (**Table 3.1**), and exhibit relatively flat HREE patterns (i.e. "ghost-plagioclase" signatures from seawater-altered, oceanic gabbroic cumulates; Sobolev et al., 2000). In contrast, eclogites that do not contain kyanite ± coesite, and display "LREE-enriched" or relatively HREE-enriched patterns with weakly positive Eu anomalies (**Figs. 3.6 - 3.7**) are in better agreement with low-temperature seawater-altered basaltic oceanic crust (Schmickler et al., 2004; Dongre et al., 2015). In summary, the eclogite xenoliths studied here likely had seawater-altered oceanic lithosphere protoliths that were emplaced into the Kaapvaal CLM, probably during the Late Archean (Shirey et al., 2001), although later addition to the cratonic root is also a possibility (e.g. Proterozoic eclogitic diamond inclusion ages; Richardson et al., 2001, 2004; Shirey et al., 2002; Timmerman et al., 2017).

3.6.2. Evaluating the effects of sulphur-bearing metasomatism on cratonic mantle lithosphere

3.6.2.1. Mantle eclogites residing within the lower lithosphere

The Kaapvaal eclogites investigated here have been divided into two distinct classes based on incompatible element content, equilibration pressure, redox composition and base metal sulphide geochemistry. The first class appears to be present only at Roberts Victor, and is characterised by depleted LREE (and incompatible element) compositions, with pronounced Eu anomalies (**Fig 3.6a**). These "depleted" eclogites have oceanic gabbroic-like protoliths and last equilibrated at pressures >4.9 GPa, equivalent to depths greater than ~175 km within the lower cratonic mantle lithosphere (**Fig. 3.8**). Additionally, the redox state of the deep and depleted eclogites ($\Delta\log fO_2$ values from FMQ-3.9 to FMQ-1.5) extend to relatively oxidised conditions when compared to those of Kaapvaal peridotite xenoliths at equivalent depths (e.g. Woodland and Koch, 2003; **Fig. 3.9a, b**). This first eclogite class does not contain abundant secondary clinopyroxene or phlogopite, but we suggest that these eclogites have been partially overprinted based on the textural and HSE systematics of "semi-isolated" BMS inclusions **(Section 3.5.7.2)** that occur at (sometimes spongy) clinopyroxene crystal rims (**Fig. 3.11a,e)**. These

BMS inclusions may have been entrapped during partial melting and recrystallisation of the host eclogite (e.g. Aulbach et al., 2009a; Gréau et al., 2013). They are **Group 1** (Ni-poor MSS to Cu-bearing assemblages; **Section 3.5.7.4**) and generally have low PGE contents **(Table 3.5)**, displaying positively sloped chondrite-normalised HSE patterns (**Fig. 3.14a**), large Pt depletions and systematic enrichment in Os over other I-PGE (Os_N/Ir_N >1). The supra-chondritic Os_N/Ir_N >1 and extreme sub-chondritic Pd_N/Ir_N and Pt_N/Ir_N <<1 of some Group 1 BMS (**Table 3.3**) are typical of mantle residues after high degrees of partial melting (Luguet et al., 2015). However, in combination with relative enrichments in Re, Pd and Au plus non-systematic correlations between "semi-metal" (i.e., Se/Te) and P-PGE contents (**Table 3.3**), a secondary metasomatic overprint may better explain the Group 1 BMS compositions. Similar chondrite-normalised HSE patterns have been described for BMS within mantle-derived peridotites that have been metasomatised by an oxidising agent (e.g. CO_2-bearing) at low melt to rock ratios (Alard et al., 2011; Delpech et al., 2012; Lorand et al., 2013; Hughes et al., 2017; Luguet and Pearson, 2019). This is significant as the Roberts Victor "LREE-depleted" refractory eclogites that host the Group 1 BMS extend to the most oxidising compositions of the Kaapvaal eclogite sample suite (**Fig. 3.9a, b**). Moreover, the Group 1 BMS have HSE contents comparable to those reported for sulphide inclusions within eclogitic diamonds (**Fig. 3.14a**; Aulbach et al., 2012), suggesting that the sulphide included diamonds may also have formed from a sulphur-bearing oxidising melt/fluid (e.g. Palyanov et al., 2007).

In order to evaluate potential metasomatic agents, representative "whole-rock" HSE contents of the Kaapvaal eclogites (**Fig. 3.14c**) were calculated using BMS modes (1% for the deep, depleted eclogites), assuming that the HSE are hosted entirely within the BMS. The estimated "whole-rock" HSE compositions of the deep eclogites roughly mimic kimberlite magmas, which in general are more HSE-depleted than the cratonic mantle lithosphere (**Fig. 3.14c;** Maier et al., 2017a; Tappe et al., 2017). During formation of an oxidising metasomatic agent (e.g. kimberlite melt), the low-degree partial melting process may effectively produce relatively P-PGE enriched and I-PGE depleted melts, potentially leaving behind residues containing I-PGE-bearing MSS or Pt-telluride, Pt-Fe, Ir-Pt-Os and other PGE alloys (e.g. Luguet et al., 2007; Alard et al., 2011; Luguet and Pearson, 2019). Interaction with such an oxidising kimberlitic metasomatic agent would thus explain not only the relatively more oxidised eclogite compositions, but also the presence of highly fractionated and I-PGE poor BMS of Group 1 affinity as found in these eclogites.

There is ample evidence of interaction between kimberlitic (oxidising) melts and the deep Kaapvaal cratonic mantle. For example, Pearson et al. (1998) show overlap of P-type diamond sulphide inclusion ages of 69±30 Ma with emplacement of the host Koffiefontein kimberlite at ca. 90 Ma (Pearson et al., 1998). Potassic silicate- and carbonate-bearing diamond fluid inclusion compositions suggest that lithospheric diamond formation may have involved proto-kimberlitic fluids in the diamond stability field (e.g. Schrauder and Navon, 1994; Klein-BenDavid et al., 2009; Palyanov and Sokol, 2009; Weiss

et al., 2009). Studies of MARID xenoliths from the Kimberley area show significant trace element compositional overlap as well as isotopic and age data that could be related to Mesozoic kimberlite magmatism on the Kaapvaal craton (Kramers et al., 1983; Konzett et al., 1998; Grégoire et al., 2002; Fitzpayne et al., 2018). In addition, evidence of kimberlite-related fluid metasomatism of deep-seated (i.e. PT estimates below the graphite-diamond phase boundary in the Kaapvaal lithosphere) peridotite (e.g. Giuliani et al., 2016b) and eclogite (e.g. Jacob et al., 2009; Gréau et al., 2013; Huang et al., 2014) xenoliths has been reported based on significant incompatible element overprinting and stable isotope (specifically sulphur; Giuliani et al., 2014a) compositions that overlap with those of some regional Kaapvaal kimberlites.

3.6.2.2. Mantle eclogites residing at mid-lithospheric levels

The second class of Kaapvaal eclogites, present at both Roberts Victor and Jagersfontein, is characterised by more enriched LREE compositions, without Eu anomalies (**Fig. 3.6a, b**). In comparison to the depleted, relatively deep first class, these more enriched eclogites record last equilibration pressures from 3.7 to 5.1 GPa, corresponding to "mid-lithospheric" depths (~140 – 180 km; **Fig 3.8**). They also record relatively more reduced redox states ($\Delta\log fO_2$ values of FMQ-5.3 to FMQ-3.3; **Fig. 3.9a, b**). The redox conditions of these mid-lithospheric eclogites overlap with Kaapvaal craton peridotites from the same depth interval (e.g. Woodland and Koch, 2003), excluding two eclogite xenoliths that are even more reduced (**Fig. 3.9a**). Significantly, these shallower, more enriched eclogites contain abundant secondary clinopyroxene, phlogopite and "semi-isolated" BMS inclusions plus interstitial BMS grains (**Fig. 3.11**; **Section 3.5.7.2)**. All the BMS are of **Group 2** affinity (**Section 3.5.7.4)** and tend to be more enriched in HSE (specifically Os, Ir, Pt and Re) than the Group 1 BMS from Roberts Victor. The Group 2 BMS have positively sloped chondrite-normalised HSE patterns and notably no Pt depletions (**Fig. 3.14b**), little variation in P-PGE concentrations but significant variation in P-PGE/I-PGE ratios (**Section 3.5.7.5**). The Se/Te ratios range from 4 to 13 (excluding xenolith MBK with Se/Te = 17) and tend to cluster near the chondritic value of ~9 (Brenan, 2015; Luguet et al., 2015). Textural evidence (**Section 3.5.7.2)** suggests that a metasomatic agent introduced both secondary clinopyroxene and phlogopite together with abundant Group 2 BMS to the matrix of the "mid-lithospheric", LREE-enriched eclogites.

The presence of both modal (BMS + secondary clinopyroxene and phlogopite) and cryptic (LREE and incompatible element enrichment) metasomatism of the mid-lithospheric eclogites probably resulted from interaction with a metasomatic agent at high melt to rock ratios (Lorand et al., 2013). Whole-rock HSE compositions of the shallower eclogites were estimated using a higher BMS mode of 2% compared to 1% for the deeper eclogites. Both the reconstructed HSE contents and chondrite-normalised HSE patterns of the mid-lithospheric eclogites overlap with those of the ca. 180 Ma Karoo large igneous province basalts (see **Fig. 3.14c**; Maier et al., 2003; Zhang et al., 2008). The Karoo basalts

have higher HSE contents and less fractionated P-PGE/I-PGE patterns when compared to kimberlites. High degrees of mantle melting of up to 35% were suggested for the petrogenesis of the Karoo large igneous province basalts (Campbell and Griffiths, 1990; Jourdan et al., 2007), which would enable complete PGE mobilisation from their mantle sources (Lorand et al., 2013) and imply that the redox state of the resulting large-volume melts should be comparable to their mantle source regions (e.g. Ballhaus et al., 1991; Carmichael, 1991; Frost and McCammon, 2008; Cottrell and Kelley, 2011). Thus, metasomatism of the mid-lithospheric eclogites by Karoo-related mafic silicate melts can result in the formation of secondary silicates and BMS with relatively enriched HSE signatures without significantly affecting the eclogite redox states.

Modification of the Kaapvaal lithospheric mantle by Karoo-age basaltic magmatism has been previously proposed based on the occurrence of comparatively Fe-rich dunite xenoliths in kimberlites from Kimberley (Rehfeldt et al., 2007). These dunites have more radiogenic Os isotopic compositions than Archean cratonic mantle peridotites, which suggests that they are post-Archean in age. Rehfeldt et al. (2007) proposed that the Fe-rich dunites represent cumulates related to flood basalt magmatism of the Karoo large igneous province. Additionally, incompatible element overprinting of the Kaapvaal mantle lithosphere was linked to the ca. 180 Ma Karoo magmatic activity based on the occurrence of titanite and zircon in heavily metasomatised relatively shallow (800 850 ºC; 3.0 3.7 GPa) peridotite xenoliths from Kimberley, which yielded U-Pb ages of ca. 180 – 190 Ma (Giuliani et al., 2014b).

In summary, the Kaapvaal eclogites of this study were variably affected by sulphur-bearing metasomatic events that produced base metal sulphides with different HSE contents and diverse silicate geochemical signatures. These discrete metasomatic events appear to have affected eclogites at different depth horizons within the Kaapvaal CLM, and they may be linked to known magmatic events that affected the Kaapvaal craton during the Phanerozoic, such as widespread episodic kimberlite magmatism (e.g. Griffin et al., 2014; Tappe et al., 2018a) and the Karoo large igneous event (Jourdan et al., 2004). The variable sulphur and HSE endowment of these discrete metasomatic events, as expressed by the shallow vs. deep Kaapvaal eclogites, may be linked to the inherently different nature of these two events. The low-volume and relatively oxidising kimberlite-related event identified in the deepest eclogites may have been sulphur- and HSE poorer, whereas the large-volume basaltic event identified in the shallower mid-lithospheric eclogites may have been more strongly sulphur- and HSE enriched due to higher degrees of mantle melting and enhanced volatile solubility of the resultant melts (Jugo et al., 2005; Ding and Dasgupta, 2017; Woodland et al., 2019).

3.7. SUMMARY AND CONCLUSIONS

- Eclogite xenoliths from Kaapvaal craton kimberlites studied here exhibit a wide range of equilibrium pressure (3.7 to 6.7 GPa) and temperature (985 to 1250 °C) conditions. They also have large ranges in calculated whole-rock MgO and Al_2O_3 contents, plus trace element features that correspond to basaltic, picritic and gabbroic protoliths compositions. Eclogite garnets have $\delta^{18}O$ values between +3.3 and +7.9 ‰, with most samples exhibiting $\delta^{18}O$ values higher than the mantle average. Combined with positive Eu and Sr anomalies and the occurrence of coesite±kyanite, we interpret most of the studied eclogites to have had seawater-altered basaltic/gabbroic protoliths.
- Metasomatic base metal sulphides hosted by the Kaapvaal eclogites fall within two distinct groups based on texture, as well as major and trace element compositions. Group 1 contains Ni-poor MSS with I-PGE poor, highly fractionated HSE patterns. Group 2 contains variably Ni- and Cu-rich sulphides with comparably PGE-enriched but less fractionated HSE patterns. Eclogites with relatively deeper equilibration depths (~175 – 220 km) and LREE-depleted trace element compositions contain fewer base metal sulphide grains, which are of Group 1 affinity. In contrast, eclogites derived from mid-lithospheric depths (~140 – 180 km) have LREE-enriched compositions and contain more abundant base metal sulphide grains of Group 2 affinity.
- The Kaapvaal eclogite xenoliths record a large range of oxygen fugacities of over 4 log units fO_2, and there is a correlation between eclogite redox state and BMS composition. The mid-lithospheric, LREE- and relatively PGE-enriched (Group 2 BMS) eclogites have similar redox states to the ambient mantle, whereas the deeper and LREE- and I-PGE-poor (Group 1 BMS) eclogites from the lower cratonic lithosphere are relatively oxidised.
- Overprinting of the Kaapvaal eclogites involves separate pulses of sulphur-bearing metasomatism. The deepest metasomatism involved an oxidising agent, possibly kimberlite-related, which introduced Group 1 BMS to the eclogites without producing incompatible element enrichment or significant modal addition of clinopyroxene±phlogopite. The shallower metasomatism reveals similar redox compositions to Kaapvaal peridotitic mantle, with base metal sulphide (Group 2) HSE affinities to Karoo basaltic magmatism.
- Although the PGE budget of the cratonic lithospheric mantle, including eclogitic components, is relatively low, the importance of redox-controlled melting processes in this setting could enable highly efficient scavenging of PGEs and other metals from CLM-hosted sulphides. Further upgrading of such CLM-derived metal budgets within sizeable crustal magma chambers provides the basis for the superlative PGE deposits that are associated mainly with Precambrian shield lithosphere.

REFERENCES

Alard, O., Griffin, W.L., Lorand, J.P., Jackson, S.E. and O'reilly, S.Y. (2000). Non-chondritic distribution of the highly siderophile elements in mantle sulphides. Nature **407**, 891.

Alard, O., Lorand, J.-P., Reisberg, L., Bodinier, J.-L., Dautria, J.-M. and O'Reilly, S.Y. (2011) Volatile-rich Metasomatism in Montferrier Xenoliths (Southern France): Implications for the Abundances of Chalcophile and Highly Siderophile Elements in the Subcontinental Mantle. Journal of Petrology **52**, 2009-2045.

Alard, O., Luguet, A., Pearson, N.J., Griffin, W.L., Lorand, J.P., Gannoun, A., Burton, K.W. and O'Reilly, S.Y. (2005). In situ Os isotopes in abyssal peridotites bridge the isotopic gap between MORBs and their source mantle. Nature **436**(7053), 1005.

Alt, J.C., Garrido, C.J., Shanks III, W.C., Turchyn, A., Padrón-Navarta, J.A., Sánchez-Vizcaíno, V.L., Pugnaire, M.T.G. and Marchesi, C. (2012). Recycling of water, carbon, and sulfur during subduction of serpentinites: A stable isotope study of Cerro del Almirez, Spain. Earth and Planetary Science Letters **327**, 50-60.

Alt, J.C., Shanks III, W.C. and Jackson, M.C. (1993) Cycling of sulfur in subduction zones: The geochemistry of sulfur in the Mariana Island Arc and back-arc trough. Earth and Planetary Science Letters **119**, 477-494.

Aoki, K.-I. and Shiba, I. (1973) Pyroxenes from lherzolite inclusions of Itinome-gata, Japan. Lithos **6**, 41-51.

Appleyard, C., Bell, D. and Le Roex, A. (2007) Petrology and geochemistry of eclogite xenoliths from the Rietfontein kimberlite, Northern Cape, South Africa. Contributions to Mineralogy and Petrology **154**, 309-333.

Armstrong, R.A., Compston, W., Retief, E.A., Williams, I.S. and Welke, H.J. (1991) Zircon ion microprobe studies bearing on the age and evolution of the Witwatersrand triad. Precambrian Research **53**, 243-266.

Aulbach, S., Creaser, R.A., Pearson, N.J., Simonetti, S.S., Heaman, L.M., Griffin, W.L. and Stachel, T. (2009a) Sulfide and whole rock Re–Os systematics of eclogite and pyroxenite xenoliths from the Slave Craton, Canada. Earth and Planetary Science Letters **283**, 48-58.

Aulbach, S. and Jacob, D.E. (2016a) Major-and trace-elements in cratonic mantle eclogites and pyroxenites reveal heterogeneous sources and metamorphic processing of low-pressure protoliths. Lithos **262**, 586-605.

Aulbach, S., Mungall, J.E. and Pearson, D.G. (2016b) Distribution and processing of highly siderophile elements in cratonic mantle lithosphere. Reviews in Mineralogy and Geochemistry **81**, 239-304.

Aulbach, S., Shirey, S.B., Stachel, T., Creighton, S., Muehlenbachs, K. and Harris, J.W. (2009b) Diamond formation episodes at the southern margin of the Kaapvaal Craton: Re–Os systematics of sulfide inclusions from the Jagersfontein Mine. Contributions to Mineralogy and Petrology **157**, 525-540.

Aulbach, S., Stachel, T., Seitz, H.-M. and Brey, G.P. (2012) Chalcophile and siderophile elements in sulphide inclusions in eclogitic diamonds and metal cycling in a Paleoproterozoic subduction zone. Geochimica et Cosmochimica Acta **93**, 278-299.

Aulbach, S. and Viljoen, K. (2015) Eclogite xenoliths from the Lace kimberlite, Kaapvaal craton: From convecting mantle source to palaeo-ocean floor and back. Earth and Planetary Science Letters **431**, 274-286.

Aulbach, S., Woodland, A., Vasilyev, P., Galvez, M. and Viljoen, K. (2017) Effects of low-pressure igneous processes and subduction on Fe3+/ΣFe and redox state of mantle eclogites from Lace (Kaapvaal craton). Earth and Planetary Science Letters **474**, 283-295.

Ballhaus, C., Berry, R.F. and Green, D.H. (1991). High pressure experimental calibration of the olivine-orthopyroxene-spinel oxygen geobarometer: implications for the oxidation state of the upper mantle. Contributions to Mineralogy and Petrology **107**(1), pp.27-40.

Ballhaus, C., Bockrath, C., Wohlgemuth-Ueberwasser, C., Laurenz, V. and Berndt, J. (2006). Fractionation of the noble metals by physical processes. Contributions to Mineralogy and Petrology **152**(6), 667-684.

Barnes, S. J., Makovicky, E., Makovicky, M., Rose-Hansen, J. and Karup-Moller, S. (1997). Partition coefficients for Ni, Cu, Pd, Pt, Rh, and Ir between monosulfide solid solution and sulfide liquid and the formation of compositionally zoned Ni–Cu sulfide bodies by fractional crystallization of sulfide liquid. Canadian Journal of Earth Sciences **34**(4), 366-374.

Barnes, S.J., Mungall, J.E. and Maier, W.D. (2015) Platinum group elements in mantle melts and mantle samples. Lithos **232**, 395-417.

Barth, M.G., Foley, S.F. and Horn, I. (2002) Partial melting in Archean subduction zones: constraints from experimentally determined trace element partition coefficients between eclogitic minerals and tonalitic melts under upper mantle conditions. Precambrian Research **113**, 323-340.

Barth, M.G., Rudnick, R.L., Horn, I., McDonough, W.F., Spicuzza, M.J., Valley, J.W. and Haggerty, S.E. (2001) Geochemistry of xenolithic eclogites from West Africa, Part I: a link between low MgO eclogites and Archean crust formation. Geochimica et Cosmochimica Acta **65**, 1499-1527.

Barton, J.M. and van Reenen, D.D. (1992) When was the Limpopo Orogeny? Precambrian Research **55**, 7-16.

Beyer, C., Frost, D. and Miyajima, N. (2015) Experimental calibration of a garnet–clinopyroxene geobarometer for mantle eclogites. Contributions to Mineralogy and Petrology **169**, 18.

Bézos, A., Lorand, J. P., Humler, E. and Gros, M. (2005). Platinum-group element systematics in Mid-Oceanic Ridge basaltic glasses from the Pacific, Atlantic, and Indian Oceans. Geochimica et Cosmochimica Acta **69**(10), 2613-2627.

Bockrath, C., Ballhaus, C. and Holzheid, A. (2004). Fractionation of the platinum-group elements during mantle melting. Science **305**(5692), 1951-1953.

Bodinier, J., Guiraud, M., Fabries, J., Dostal, J. and Dupuy, C. (1987) Petrogenesis of layered pyroxenites from the Lherz, Freychinede and Prades ultramafic bodies (Ariege, French Pyrenees). Geochimica et Cosmochimica Acta **51**, 279-290.

Bragagni, A., Luguet, A., Fonseca, R. O. C., Pearson, D. G., Lorand, J. P., Nowell, G. M. and Kjarsgaard, B. A. (2017). The geological record of base metal sulfides in the cratonic mantle: A microscale 187Os/188Os study of peridotite xenoliths from Somerset Island, Rae Craton (Canada). Geochimica et Cosmochimica Acta **216**, 264-285.

Brenan, J.M. (2015) Se–Te fractionation by sulfide–silicate melt partitioning: Implications for the composition of mantle-derived magmas and their melting residues. Earth and Planetary Science Letters **422**, 45-57.

Campbell, I.H. and Griffiths, R.W. (1990). Implications of mantle plume structure for the evolution of flood basalts. Earth and Planetary Science Letters **99**(1-2), 79-93.

Caporuscio, F.A. and Smyth, J.R. (1990) Trace element crystal chemistry of mantle eclogites. Contributions to Mineralogy and Petrology **105**, 550-561.

Carmichael, I. S. (1991) The redox states of basic and silicic magmas: a reflection of their source regions?. Contributions to Mineralogy and Petrology **106**(2), 129-141.

Carswell, D., Dawson, J. and Gibb, F. (1981) Equilibration conditions of upper-mantle eclogites: implications for kyanite-bearing and diamondiferous varieties. Mineralogical magazine **44**, 79-89.

Cartigny, P., Farquhar, J., Thomassot, E., Harris, J.W., Wing, B., Masterson, A., McKeegan, K. and Stachel, T. (2009) A mantle origin for Paleoarchean peridotitic diamonds from the Panda kimberlite, Slave Craton: evidence from 13C-, 15N-and 33, 34S-stable isotope systematics. Lithos **112**, 852-864.

Chaussidon, M., Albarède, F. and Sheppard, S.M. (1989) Sulphur isotope variations in the mantle from ion microprobe analyses of micro-sulphide inclusions. Earth and Planetary Science Letters **92**, 144-156.

Chinner, G. and Cornell, D. (1974) Evidence of kimberlite-grospydite reaction. Contributions to Mineralogy and Petrology **45**, 153-160.

Clement, C.R., Skinner, E.M., Hawthorne, J.B., Kleinjan, L. and Allsopp, H.L. (1979) Precambrian ultramafic dykes with kimberlite affinities in the Kimberley area. Kimberlites, Diatremes, and Diamonds: Their Geology, Petrology, and Geochemistry, 101-110.

Coleman, R., Lee, D., Beatty, L. and Brannock, W.W. (1965) Eclogites and eclogites: their differences and similarities. Geological Society of America Bulletin **76**, 483-508.

Cottrell, E., and Kelley, K. A. (2011). The oxidation state of Fe in MORB glasses and the oxygen fugacity of the upper mantle. Earth and Planetary Science Letters **305**(3), 270-282.

Craig, J. R. (1969). Phase relations in the Cu-Fe-Ni-S system and their application to magmatic ore deposits. Economic Geology Monograph **4**, 344-358.

Craig, J. and Kullerud, G. (1973) The Cu-Zn-S system. Mineralium Deposita **8**, 81-91.

Creighton, S., Stachel, T., Matveev, S., Höfer, H., McCammon, C. and Luth, R.W. (2009) Oxidation of the Kaapvaal lithospheric mantle driven by metasomatism. Contributions to Mineralogy and Petrology **157**, 491.

Dale, C., Burton, K., Pearson, D., Gannoun, A., Alard, O., Argles, T. and Parkinson, I. (2009) Highly siderophile element behaviour accompanying subduction of oceanic crust: whole rock and mineral-scale insights from a high-pressure terrain. Geochimica et Cosmochimica Acta **73**, 1394-1416.

Day, J. M. (2013). Hotspot volcanism and highly siderophile elements. Chemical Geology **341**, 50-74.

Delpech, G., Lorand, J. P., Grégoire, M., Cottin, J. Y. and O'Reilly, S. Y. (2012). In-situ geochemistry of sulfides in highly metasomatized mantle xenoliths from Kerguelen, southern Indian Ocean. Lithos **154**, 296-314.

de Wit, M.J. (2004) Archean greenstone belts do contain fragments of ophiolites. Developments in Precambrian Geology **13**, 599-614.

Ding, S. and Dasgupta, R. (2017) The fate of sulfide during decompression melting of peridotite–implications for sulfur inventory of the MORB-source depleted upper mantle. Earth and Planetary Science Letters **459**, 183-195.

Dludla, S., Le Roex, A. P., and Gurney, J. J. (2006) Eclogite xenoliths from the Premier kimberlite, South Africa: geochemical evidence for a subduction origin. South African Journal of Geology **109**(3), 353-368.

Dongré, A., Jacob, D. and Stern, R. (2015) Subduction-related origin of eclogite xenoliths from the Wajrakarur kimberlite field, Eastern Dharwar craton, Southern India: Constraints from petrology and geochemistry. Geochimica et Cosmochimica Acta **166**, 165-188.

Eglington, B. (2006) Evolution of the Namaqua-Natal Belt, southern Africa–A geochronological and isotope geochemical review. Journal of African Earth Sciences **46**, 93-111.

Eiler, J.M., Farley, K.A., Valley, J.W., Hofmann, A.W. and Stolper, E.M. (1996) Oxygen isotope constraints on the sources of Hawaiian volcanism. Earth and Planetary Science Letters **144**, 453-467.

Eiler, J.M., Schiano, P., Kitchen, N. and Stolper, E.M. (2000) Oxygen-isotope evidence for recycled crust in the sources of mid-ocean-ridge basalts. Nature **403**, 530.

Ellis, D. and Green, D. (1979) An experimental study of the effect of Ca upon garnet-clinopyroxene Fe-Mg exchange equilibria. Contributions to Mineralogy and Petrology **71**, 13-22.

Evans, K., Tomkins, A., Cliff, J. and Fiorentini, M. (2014) Insights into subduction zone sulfur recycling from isotopic analysis of eclogite-hosted sulfides. Chemical Geology **365**, 1-19.

Fischer-Gödde M, Becker H, Wombacher F (2010) Rhodium, gold and other highly siderophile element abundances in chondritic meteorites. Geochim Cosmochim Acta 74:356–379

Fitzpayne, A., Giuliani, A., Phillips, D., Hergt, J., Woodhead, J.D., Farquhar, J., Fiorentini, M.L., Drysdale, R.N. and Wu, N. (2018). Kimberlite-related metasomatism recorded in MARID and PIC mantle xenoliths. Mineralogy and Petrology **112**(1), pp.71-84.

Fleet, M.E., Crocket, J.H. and Stone, W.E. (1996) Partitioning of platinum-group elements (Os, Ir, Ru, Pt, Pd) and gold between sulfide liquid and basalt melt. Geochimica et Cosmochimica Acta **60**, 2397-2412.

Fleet, M. E. and Pan, Y. (1994). Fractional crystallization of anhydrous sulfide liquid in the system Fe-Ni-Cu-S, with application to magmatic sulfide deposits. Geochimica et Cosmochimica Acta **58**(16), 3369-3377.

Friese, A.E., Reimold, W.U. and Layer, P.W. (2003) 40Ar-39Ar dating of and structural information on tectonite-bearing faults in the Witwatersrand Basin: Evidence for multi-stage, tectono-thermal activity in the central Kaapvaal Craton. South African Journal of Geology **106**, 41-70.

Frost, D.J. and McCammon, C.A. (2008) The redox state of Earth's mantle. Annu. Rev. Earth Planet. Sci. **36**, 389-420.

Giuliani, A., Fiorentini, M.L., Martin, L.A., Farquhar, J., Phillips, D., Griffin, W.L. and LaFlamme, C. (2016) Sulfur isotope composition of metasomatised mantle xenoliths from the Bultfontein kimberlite (Kimberley, South Africa): Contribution from subducted sediments and the effect of sulfide alteration on S isotope systematics. Earth and Planetary Science Letters **445**, 114-124.

Giuliani, A., Fiorentini, M. L., Martin, L. A., Farquhar, J., Phillips, D., Griffin, W. L. and LaFlamme, C. (2016a). Sulfur isotope composition of metasomatised mantle xenoliths from the Bultfontein kimberlite (Kimberley, South Africa): Contribution from subducted sediments and the effect of sulfide alteration on S isotope systematics. Earth and Planetary Science Letters **445**, 114-124.

Giuliani, A., Phillips, D., Kamenetsky, V. S., Fiorentini, M. L., Farquhar, J. and Kendrick, M. A. (2014a). Stable isotope (C, O, S) compositions of volatile-rich minerals in kimberlites: a review. Chemical Geology, **374**, 61-83.

Giuliani, A., Phillips, D., Kamenetsky, V. S. and Goemann, K. (2016b). Constraints on kimberlite ascent mechanisms revealed by phlogopite compositions in kimberlites and mantle xenoliths. Lithos **240**, 189-201.

Giuliani, A., Kamenetsky, V.S., Kendrick, M.A., Phillips, D. and Goemann, K. (2013) Nickel-rich metasomatism of the lithospheric mantle by pre-kimberlitic alkali-S–Cl-rich C–O–H fluids. Contributions to Mineralogy and Petrology **165**, 155-171.

Giuliani, A., Phillips, D., Maas, R., Woodhead, J.D., Kendrick, M.A., Greig, A., Armstrong, R.A., Chew, D., Kamenetsky, V.S. and Fiorentini, M.L. (2014b) LIMA U–Pb ages link lithospheric mantle metasomatism to Karoo magmatism beneath the Kimberley region, South Africa. Earth and Planetary Science Letters **401**, pp.132-147.

Gonzaga, R., Lowry, D., Jacob, D., LeRoex, A., Schulze, D. and Menzies, M. (2010) Eclogites and garnet pyroxenites: similarities and differences. Journal of Volcanology and Geothermal Research **190**, 235-247.

Gréau, Y., Alard, O., Griffin, W.L., Huang, J.-X. and O'Reilly, S.Y. (2013) Sulfides and chalcophile elements in Roberts Victor eclogites: unravelling a sulfide-rich metasomatic event. Chemical Geology **354**, 73-92.

Gréau, Y., Huang, J.-X., Griffin, W.L., Renac, C., Alard, O. and O'Reilly, S.Y. (2011) Type I eclogites from Roberts Victor kimberlites: products of extensive mantle metasomatism. Geochimica et Cosmochimica Acta **75**, 6927-6954.

Gregoire, M., Bell, D. and Le Roex, A. (2002) Trace element geochemistry of glimmerite and MARID mantle xenoliths: their relationship to kimberlite and to phlogopite-bearing peridotite revisited. Contributions to Mineralogy and Petrology **142**, 603-625.

Griffin, W. L., Batumike, J. M., Greau, Y., Pearson, N. J., Shee, S. R. and O'Reilly, S. Y. (2014). Emplacement ages and sources of kimberlites and related rocks in southern Africa: U–Pb ages and Sr–Nd isotopes of groundmass perovskite. Contributions to Mineralogy and Petrology **168**(1), 1032.

Griffin, W., Graham, S., O'Reilly, S.Y. and Pearson, N. (2004) Lithosphere evolution beneath the Kaapvaal Craton: Re–Os systematics of sulfides in mantle-derived peridotites. Chemical Geology **208**, 89-118.

Griffin, W., O'Reilly, S., Abe, N., Aulbach, S., Davies, R., Pearson, N., Doyle, B. and Kivi, K. (2003) The origin and evolution of Archean lithospheric mantle. Precambrian Research **127**, 19-41.

Griffin, W. and Ryan, C. (1995) Trace elements in indicator minerals: area selection and target evaluation in diamond exploration. Journal of geochemical Exploration **53**, 311-337.

Griffin, W.L. and O'Reilly, S.Y. (2007) Cratonic lithospheric mantle: is anything subducted? Episodes **30** (1), 43-53.

Grütter, H.S. (2009) Pyroxene xenocryst geotherms: Techniques and application. Lithos **112**, 1167-1178.

Guo, J., Griffin, W.L. and O'Reilly, S.Y. (1999) Geochemistry and origin of sulphide minerals in mantle xenoliths: Qilin, Southeastern China. Journal of Petrology **40**, 1125-1149.

Harte, B., Hunter, R. and Kinny, P. (1993) Melt geometry, movement and crystallization, in relation to mantle dykes, veins and metasomatism. Phil. Trans. R. Soc. Lond. A 342, 1-21.

Harte, B. and Kirkley, M.B. (1997) Partitioning of trace elements between clinopyroxene and garnet: data from mantle eclogites. Chemical Geology **136**, 1-24.

Hopp, J., Trieloff, M., Brey, G.P., Woodland, A.B., Simon, N.S.C., Wijbrans, J.R., Siebel, W. and Reitter, E. (2008) 40 Ar/39 Ar-ages of phlogopite in mantle xenoliths from South African kimberlites: evidence for metasomatic mantle impregnation during the Kibaran orogenic cycle. Lithos **106**(3), pp.351-364.

Huang, J.-X., Gréau, Y., Griffin, W.L., O'Reilly, S.Y. and Pearson, N.J. (2012) Multi-stage origin of Roberts Victor eclogites: progressive metasomatism and its isotopic effects. Lithos **142**, 161-181.

Huang, J. X., Griffin, W. L., Gréau, Y., Pearson, N. J., O'Reilly, S. Y., Cliff, J. and Martin, L. (2014). Unmasking xenolithic eclogites: progressive metasomatism of a key Roberts Victor sample. Chemical Geology **364**, 56-65.

Hughes, H. S., McDonald, I., Loocke, M., Butler, I. B., Upton, B. G. and Faithfull, J. W. (2017). Paradoxical co-existing base metal sulphides in the mantle: the multi-event record preserved in Loch Roag peridotite xenoliths, North Atlantic Craton. Lithos **276**, 103-121.

Jacob, D. (2004) Nature and origin of eclogite xenoliths from kimberlites. Lithos **77**, 295-316.

Jacob, D., Bizimis, M. and Salters, V. (2005) Lu–Hf and geochemical systematics of recycled ancient oceanic crust: evidence from Roberts Victor eclogites. Contributions to Mineralogy and Petrology **148**, 707-720.

Jacob, D., Jagoutz, E., Lowry, D., Mattey, D. and Kudrjavtseva, G. (1994) Diamondiferous eclogites from Siberia: Remnants of Archean oceanic crust. Geochimica et Cosmochimica Acta **58**, 5191-5207.

Jacob, D., Schmickler, B. and Schulze, D. (2003) Trace element geochemistry of coesite-bearing eclogites from the Roberts Victor kimberlite, Kaapvaal craton. Lithos **71**, 337-351.

Jacob, D., Viljoen, K. and Grassineau, N. (2009) Eclogite xenoliths from Kimberley, South Africa—a case study of mantle metasomatism in eclogites. Lithos **112**, 1002-1013.

Jacob, D.E. and Foley, S.F. (1999) Evidence for Archean ocean crust with low high field strength element signature from diamondiferous eclogite xenoliths. Lithos **48**, 317-336.

Jégo, S. and Dasgupta, R. (2013) Fluid-present melting of sulfide-bearing ocean-crust: Experimental constraints on the transport of sulfur from subducting slab to mantle wedge. Geochimica et Cosmochimica Acta **110**, 106-134.

Jelsma, H., Barnett, W., Richards, S. and Lister, G. (2009) Tectonic setting of kimberlites. Lithos **112**, 155-165.

Jenner, F.E. (2017) Cumulate causes for the low contents of sulfide-loving elements in the continental crust. Nature Geoscience **10**, 524.

Jenner, F. E., and O'Neill, H. S. C. (2012) Analysis of 60 elements in 616 ocean floor basaltic glasses. Geochemistry, Geophysics, Geosystems, **13**(2).

Jerde, E.A., Taylor, L.A., Crozaz, G., Sobolev, N.V. and Sobolev, V.N. (1993) Diamondiferous eclogites from Yakutia, Siberia: evidence for a diversity of protoliths. Contributions to Mineralogy and Petrology **114**, 189-202.

Jochum, K. P., Nohl, U., Herwig, K., Lammel, E., Stoll, B. and Hofmann, A. W. (2005). GeoReM: a new geochemical database for reference materials and isotopic standards. Geostandards and Geoanalytical Research **29**(3), 333-338.

Jourdan, F., Féraud, G., Bertrand, H., Kampunzu, A.B., Tshoso, G., Le Gall, B., Tiercelin, J.J. and Capiez, P. (2004). The Karoo triple junction questioned: evidence from Jurassic and Proterozoic 40Ar/39Ar ages and geochemistry of the giant Okavango dyke swarm (Botswana). Earth and Planetary Science Letters **222**(3-4), 989-1006.

Jourdan, F., Féraud, G., Bertrand, H. and Watkeys, M.K. (2007). From flood basalts to the inception of oceanization: Example from the 40Ar/39Ar high-resolution picture of the Karoo large igneous province. Geochemistry, Geophysics, Geosystems, **8**(2).

Jugo, P.J. (2009) Sulfur content at sulfide saturation in oxidized magmas. Geology **37**, 415-418.

Jugo, P.J., Luth, R.W. and Richards, J.P. (2005) An experimental study of the sulfur content in basaltic melts saturated with immiscible sulfide or sulfate liquids at 1300° C and 1· 0 GPa. Journal of Petrology **46**, 783-798.

Katayama, I., Suyama, Y., Ando, J.-i. and Komiya, T. (2009) Mineral chemistry and P–T condition of granular and sheared peridotite xenoliths from Kimberley, South Africa: origin of the textural variation in the cratonic mantle. Lithos **109**, 333-340.

Kennedy, C.S. and Kennedy, G.C. (1976) The equilibrium boundary between graphite and diamond. Journal of Geophysical Research **81**, 2467-2470.

Klein-BenDavid, O., Logvinova, A.M., Schrauder, M., Spetius, Z.V., Weiss, Y., Hauri, E.H., Kaminsky, F.V., Sobolev, N.V. and Navon, O. (2009). High-Mg carbonatitic microinclusions in some Yakutian diamonds—a new type of diamond-forming fluid. Lithos **112**, pp.648-659.

Konzett, J., Armstrong, R. A., Sweeney, R. J. and Compston, W. (1998). The timing of MARID metasomatism in the Kaapvaal mantle: an ion probe study of zircons from MARID xenoliths. Earth and Planetary Science Letters **160**(1-2), 133-145.

Kramers, J. D., Roddick, J. C. M. and Dawson, J. B. (1983). Trace element and isotope studies on veined, metasomatic and "MARID" xenoliths from Bultfontein, South Africa. Earth and Planetary Science Letters **65**(1), 90-106.

Kröner, A. and Compston, W. (1988) Ion microprobe ages of zircons from early Archaean granite pebbles and greywacke, Barberton greenstone belt, southern Africa. Precambrian Research **38**, 367-380.

Kullerud, G., Yund, R.A., and Moh, G.H. (1969). Phase relations in the CuFe-S, Cu-Ni-S, and Fe-Ni-S systems. Economic Geology Monograph 4, 323–343.

Larson, T. and Sharp, Z. (2003) Stable isotope constraints on the Al2SiO5 ‘triple-point’rocks from the Proterozoic Priest pluton contact aureole, New Mexico, USA. Journal of Metamorphic Geology **21**, 785-798.

Le Bas, M. (2000) IUGS reclassification of the high-Mg and picritic volcanic rocks. Journal of Petrology **41**, 1467-1470.

Lee, C.-T.A., Luffi, P. and Chin, E.J. (2011) Building and destroying continental mantle. Annual Review of Earth and Planetary Sciences **39**, 59-90.

Li, Y. and Audétat, A. (2012). Partitioning of V, Mn, Co, Ni, Cu, Zn, As, Mo, Ag, Sn, Sb, W, Au, Pb, and Bi between sulfide phases and hydrous basanite melt at upper mantle conditions. Earth and Planetary Science Letters 355, 327-340.

Liu, Y., Taylor, L.A., Sarbadhikari, A.B., Valley, J.W., Ushikubo, T., Spicuzza, M.J., Kita, N., Ketcham, R.A., Carlson, W. and Shatsky, V. (2009) Metasomatic origin of diamonds in the world's largest diamondiferous eclogite. Lithos **112**, 1014-1024.

Lorand, J.P. (1989) Mineralogy and chemistry of Cu-Fe-Ni sulfides in orogenic-type spinel peridotite bodies from Ariege (Northeastern Pyrenees, France). Contributions to Mineralogy and Petrology **103**, 335-345.

Lorand, J. P. and Gregoire, M. (2006). Petrogenesis of base metal sulphide assemblages of some peridotites from the Kaapvaal craton (South Africa). Contributions to Mineralogy and Petrology **151**(5), 521.

Lorand, J. P. and Luguet, A. (2016). Chalcophile and siderophile elements in mantle rocks: Trace elements controlled by trace minerals. Reviews in Mineralogy and Geochemistry **81**(1), 441-488.

Lorand, J. P., Luguet, A. and Alard, O. (2013). Platinum-group element systematics and petrogenetic processing of the continental upper mantle: A review. Lithos **164**, 2-21.

Luguet, A., Behrens, M., Pearson, D. G., König, S. andHerwartz, D. (2015). Significance of the whole rock Re–Os ages in cryptically and modally metasomatised cratonic peridotites: Constraints from HSE–Se–Te systematics. Geochimica et Cosmochimica Acta **164,** 441-463.

Luguet, A. and Pearson, G. (2019). Dating mantle peridotites using Re-Os isotopes: The complex message from whole rocks, base metal sulfides, and platinum group minerals. American Mineralogist: Journal of Earth and Planetary Materials **104**(2), 165-189.

Luguet, A., Lorand, J. P. and Seyler, M. (2003). Sulfide petrology and highly siderophile element geochemistry of abyssal peridotites: A coupled study of samples from the Kane Fracture Zone (45 W 23 20N, MARK area, Atlantic Ocean). Geochimica et Cosmochimica Acta **67**(8), 1553-1570.

Luguet, A., Shirey, S. B., Lorand, J. P., Horan, M. F. and Carlson, R. W. (2007). Residual platinum-group minerals from highly depleted harzburgites of the Lherz massif (France) and their role in HSE fractionation of the mantle. Geochimica et Cosmochimica Acta **71**(12), 3082-3097.

Luth, R. W., and Stachel, T. (2014) The buffering capacity of lithospheric mantle: implications for diamond formation. Contributions to Mineralogy and Petrology **168**(5), 1083.

MacGregor, I.D. and Carter, J. (1970) The chemistry of clinopyroxenes and garnets of eclogite and peridotite xenoliths from the Roberts Victor Mine, South Africa. Physics of the Earth and Planetary Interiors **3**, 391-397.

MacGregor, I.D. and Manton, W.I. (1986) Roberts Victor eclogites: ancient oceanic crust. Journal of Geophysical Research: Solid Earth **91**, 14063-14079.

Maier, W. D., Barnes, S. J., and Marsh, J. S. (2003) The concentrations of the noble metals in Southern African flood-type basalts and MORB: implications for petrogenesis and magmatic sulphide exploration. Contributions to Mineralogy and Petrology **146**, 44-61.

Maier, W.D., O'Brien, H., Peltonen, P. and Barnes, S.-J. (2017) Platinum-group element contents of Karelian kimberlites: Implications for the PGE budget of the sub-continental lithospheric mantle. Geochimica et Cosmochimica Acta **216**, 358-371.

Marchesi, C., Dale, C.W., Garrido, C.J., Pearson, D.G., Bosch, D., Bodinier, J.L., Gervilla, F. and Hidas, K. (2014). Fractionation of highly siderophile elements in refertilized mantle: Implications for the Os isotope composition of basalts. Earth and Planetary Science Letters **400**, 33-44.

Mattey, D., Lowry, D. and Macpherson, C. (1994) Oxygen isotope composition of mantle peridotite. Earth and Planetary Science Letters **128**, 231-241.

McCandless, T. and Gurney, J. (1989) Sodium in garnet and potassium in clinopyroxene: criteria for classifying mantle eclogites. GROUP 2, 30.

McDonough, W.F. and Sun, S.-S. (1995) The composition of the Earth. Chemical Geology **120**, 223-253.

McKenzie, D. (1989) Some remarks on the movement of small melt fractions in the mantle. Earth and Planetary Science Letters **95**, 53-72.

Menzies, A.H., Carlson, R.W., Shirey, S.B. and Gurney, J.J. (2003) Re–Os systematics of diamond-bearing eclogites from the Newlands kimberlite. Lithos **71**, 323-336.

Monnier, C., Girardeau, J., Permana, H., Rehault, J.-P., Bellon, H. and Cotten, J. (2003) Dynamics and age of formation of the Seram-Ambon ophiolites (Central Indonesia). Bulletin de la Société géologique de France **174**, 529-543.

Muehlenbachs, K. and Clayton, R.N. (1972) Oxygen isotope studies of fresh and weathered submarine basalts. Canadian Journal of Earth Sciences **9**, 172-184.

Mungall, J. E., Andrews, D. R., Cabri, L. J., Sylvester, P. J. and Tubrett, M. (2005). Partitioning of Cu, Ni, Au, and platinum-group elements between monosulfide solid solution and sulfide melt under controlled oxygen and sulfur fugacities. Geochimica et Cosmochimica Acta **69**(17), 4349-4360.

Mungall, J.E. and Brenan, J.M. (2014) Partitioning of platinum-group elements and Au between sulfide liquid and basalt and the origins of mantle-crust fractionation of the chalcophile elements. Geochimica et Cosmochimica Acta **125**, 265-289.

Mungall, J.E., Hanley, J.J., Arndt, N.T. and Debecdelievre, A. (2006) Evidence from meimechites and other low-degree mantle melts for redox controls on mantle-crust fractionation of platinum-group elements. Proceedings of the National Academy of Sciences 103, 12695-12700.

Mysen, B. (1973) Pyroxene stoichiometry and the breakdown of omphacite. American Mineralogist **58**, 60-63.

Neal, C. R., Taylor, L. A., Davidson, J. P., Holden, P., Halliday, A. N., Nixon, P. H. and Mayeda, T. K. (1990) Eclogites with oceanic crustal and mantle signatures from the Bellsbank kimberlite, South Africa, part 2: Sr, Nd, and O isotope geochemistry. Earth and Planetary Science Letters **99**(4), 362-379.

O'Reilly, S.Y. and Griffin, W. (1995) Trace-element partitioning between garnet and clinopyroxene in mantle-derived pyroxenites and eclogites: PTX controls. Chemical Geology **121**, 105-130.

Ongley, J.S., Basu, A.R. and Kyser, T.K. (1987) Oxygen isotopes in coexisting garnets, clinopyroxenes and phlogopites of Roberts Victor eclogites: implications for petrogenesis and mantle metasomatism. Earth and Planetary Science Letters **83**, 80-84.

Palyanov, Y.N., Borzdov, Y.M., Bataleva, Y.V., Sokol, A., Palyanova, G. and Kupriyanov, I. (2007) Reducing role of sulfides and diamond formation in the Earth's mantle. Earth and Planetary Science Letters **260**, 242-256.

Palyanov, Y. N. and Sokol, A. G. (2009). The effect of composition of mantle fluids/melts on diamond formation processes. Lithos **112**, 690-700.

Patten, C., Barnes, S.-J., Mathez, E.A. and Jenner, F.E. (2013) Partition coefficients of chalcophile elements between sulfide and silicate melts and the early crystallization history of sulfide liquid: LA-ICP-MS analysis of MORB sulfide droplets. Chemical Geology **358**, 170-188.

Pearson, D., Carlson, R., Shirey, S., Boyd, F. and Nixon, P. (1995) Stabilisation of Archaean lithospheric mantle: A ReOs isotope study of peridotite xenoliths from the Kaapvaal craton. Earth and Planetary Science Letters **134**, 341-357.

Pearson, D., Shirey, S., Harris, J. and Carlson, R. (1998) Sulphide inclusions in diamonds from the Koffiefontein kimberlite, S Africa: constraints on diamond ages and mantle Re–Os systematics. Earth and Planetary Science Letters **160**, 311-326.

Pearson, N.J., Alard, O., Griffin, W.L., Jackson, S.E. and O'Reilly, S.Y. (2002) In situ measurement of Re-Os isotopes in mantle sulfides by laser ablation multicollector-inductively coupled plasma mass spectrometry: analytical methods and preliminary results. Geochimica et Cosmochimica Acta **66**, 1037-1050.

Peregoedova, A., Barnes, S. J. and Baker, D. R. (2004). The formation of Pt–Ir alloys and Cu–Pd-rich sulfide melts by partial desulfurization of Fe–Ni–Cu sulfides: results of experiments and implications for natural systems. Chemical Geology **208**(1-4), 247-264.

Pernet-Fisher, J.F., Howarth, G.H., Liu, Y., Barry, P.H., Carmody, L., Valley, J.W., Bodnar, R.J., Spetsius, Z.V. and Taylor, L.A. (2014) Komsomolskaya diamondiferous eclogites: evidence for oceanic crustal protoliths. Contributions to Mineralogy and Petrology **167**, 981.

Pollack, H.N. and Chapman, D.S. (1977) On the regional variation of heat flow, geotherms, and lithospheric thickness. Tectonophysics **38**, 279-296.

Pyle, J.M. and Haggerty, S.E. (1998) Eclogites and the metasomatism of eclogites from the Jagersfontein Kimberlite: Punctuated transport and implications for alkali magmatism. Geochimica et Cosmochimica Acta **62**, 1207-1231.

Regier, M. E., Miskovic, A., Ickert, R. B., Pearson, D. G., Stachel, T., Stern, R. A. and Kopylova, M. (2018). An oxygen isotope test for the origin of Archean mantle roots. Geochem. Perspect. Lett. **9**, 453-10.

Rehfeldt, T., Jacob, D. E., Carlson, R. W. and Foley, S. F. (2007). Fe-rich dunite xenoliths from South African kimberlites: cumulates from Karoo flood basalts. Journal of Petrology **48**(7), 1387-1409.

Richardson, S., Gurney, J., Erlank, A. and Harris, J. (1984) Origin of diamonds in old enriched mantle. Nature **310**, 198.

Richardson, S., Shirey, S. and Harris, J. (2004) Episodic diamond genesis at Jwaneng, Botswana, and implications for Kaapvaal craton evolution. Lithos **77**, 143-154.

Richardson, S., Shirey, S., Harris, J. and Carlson, R. (2001) Archean subduction recorded by Re–Os isotopes in eclogitic sulfide inclusions in Kimberley diamonds. Earth and Planetary Science Letters **191**, 257-266.

Richardson, S.H. and Shirey, S.B. (2008) Continental mantle signature of Bushveld magmas and coeval diamonds. Nature **453**, 910.

Riches, A., Ickert, R., Pearson, D., Stern, R., Jackson, S., Ishikawa, A., Kjarsgaard, B. and Gurney, J. (2016) In situ oxygen-isotope, major-, and trace-element constraints on the metasomatic modification and crustal origin of a diamondiferous eclogite from Roberts Victor, Kaapvaal Craton. Geochimica et Cosmochimica Acta **174**, 345-359.

Schmickler, B., Jacob, D. and Foley, S. (2004) Eclogite xenoliths from the Kuruman kimberlites, South Africa: geochemical fingerprinting of deep subduction and cumulate processes. Lithos **75**, 173-207.

Schmidberger, S., Simonetti, A. and Francis, D. (2001) Sr-Nd-Pb isotope systematics of mantle xenoliths from Somerset Island kimberlites: Evidence for lithosphere stratification beneath Arctic Canada. Geochimica et Cosmochimica Acta **65**, 4243-4255.

Schmidberger, S.S., Heaman, L.M., Simonetti, A., Creaser, R.A. and Cookenboo, H.O. (2005) Formation of Paleoproterozoic eclogitic mantle, Slave Province (Canada): insights from in-situ Hf and U–Pb isotopic analyses of mantle zircons. Earth and Planetary Science Letters **240**, 621-633.

Schmitz, M.D., Bowring, S.A., de Wit, M.J. and Gartz, V. (2004) Subduction and terrane collision stabilize the western Kaapvaal craton tectosphere 2.9 billion years ago. Earth and Planetary Science Letters **222**, 363-376.

Schrauder, M. and Navon, O. (1994). Hydrous and carbonatitic mantle fluids in fibrous diamonds from Jwaneng, Botswana. Geochimica et Cosmochimica Acta **58**(2), 761-771.

Schulze, D.J. and Helmstaedt, H. (1988) Coesite-sanidine eclogites from kimberlite: products of mantle fractionation or subduction? Journal of Geology **96**, 435-443.

Schulze, D.J., Valley, J.W. and Spicuzza, M.J. (2000) Coesite eclogites from the Roberts Victor kimberlite, South Africa. Lithos **54**, 23-32.

Schulze, D.J., Valley, J.W., Viljoen, K.F. and Spicuzza, M.J. (2003) Oxygen isotope composition of mantle eclogites, 8th International Kimberlite Conference Long Abstract, pp. 1-2.

Sharp, Z.D. (1990) A laser-based microanalytical method for the in situ determination of oxygen isotope ratios of silicates and oxides. Geochimica et Cosmochimica Acta **54**, 1353-1357.

Shirey, S.B., Carlson, R.W., Richardson, S.H., Menzies, A., Gurney, J.J., Pearson, D.G., Harris, J.W. and Wiechert, U. (2001) Archean emplacement of eclogitic components into the lithospheric mantle during formation of the Kaapvaal Craton. Geophysical Research Letters **28**, 2509-2512.

Shirey, S.B., Cartigny, P., Frost, D.J., Keshav, S., Nestola, F., Nimis, P., Pearson, D.G., Sobolev, N.V. and Walter, M.J. (2013) Diamonds and the geology of mantle carbon. Reviews in Mineralogy and Geochemistry **75**, 355-421.

Shirey, S.B., Harris, J.W., Richardson, S.H., Fouch, M.J., James, D.E., Cartigny, P., Deines, P. and Viljoen, F. (2002) Diamond genesis, seismic structure, and evolution of the Kaapvaal-Zimbabwe craton. Science **297**, 1683-1686.

Shirey, S.B. and Richardson, S.H. (2011) Start of the Wilson cycle at 3 Ga shown by diamonds from subcontinental mantle. Science **333**, 434-436.

Shirey, S.B., Richardson, S.H. and Harris, J.W. (2004) Integrated models of diamond formation and craton evolution. Lithos **77**, 923-944.

Skinner, E. and Truswell, J. (2006) Kimberlites. The geology of South Africa, 651-659.

Smart, K., Cartigny, P., Tappe, S., O'Brien, H. and Klemme, S. (2017a) Lithospheric diamond formation as a consequence of methane-rich volatile flooding: An example from diamondiferous eclogite xenoliths of the Karelian craton (Finland). Geochimica et Cosmochimica Acta **206**, 312-342.

Smart, K., Tappe, S., Simonetti, A., Simonetti, S., Woodland, A. and Harris, C. (2017b) Tectonic significance and redox state of Paleoproterozoic eclogite and pyroxenite components in the Slave cratonic mantle lithosphere, Voyageur kimberlite, Arctic Canada. Chemical Geology **455**, 98-119.

Smart, K.A., Chacko, T., Simonetti, A., Sharp, Z.D. and Heaman, L.M. (2014) A record of Paleoproterozoic subduction preserved in the Northern Slave cratonic mantle: Sr–Pb–O isotope and trace-element investigations of eclogite xenoliths from the Jericho and Muskox kimberlites. Journal of Petrology **55**, 549-583.

Smart, K.A., Chacko, T., Stachel, T., Tappe, S., Stern, R.A. and Ickert, R.B. (2012) Eclogite formation beneath the northern Slave craton constrained by diamond inclusions: Oceanic lithosphere origin without a crustal signature. Earth and Planetary Science Letters **319**, 165-177.

Smart, K.A., Heaman, L.M., Chacko, T., Simonetti, A., Kopylova, M., Mah, D. and Daniels, D. (2009) The origin of high-MgO diamond eclogites from the Jericho Kimberlite, Canada. Earth and Planetary Science Letters **284**, 527-537.

Smart, K.A., Tappe, S., Stern, R.A., Webb, S.J. and Ashwal, L.D. (2016) Early Archaean tectonics and mantle redox recorded in Witwatersrand diamonds. Nature Geoscience **9**, 255.

Smith, C.B., Allsop, H., Kramers, J., Hutchinson, G. and Roddick, J. (1985) Emplacement ages of Jurassic-Cretaceous South African kimberlites by the Rb-Sr method on phlogopite and whole-rock samples. Transactions of the Geological Society of South Africa **88**, 249-266.

Smyth, J.R., Caporuscio, F.A. and McCormick, T.C. (1989) Mantle eclogites: evidence of igneous fractionation in the mantle. Earth and Planetary Science Letters **93**, 133-141.

Snyder, G.A., Taylor, L.A., Crozaz, G., Halliday, A.N., Beard, B.L., Sobolev, V.N. and Sobolev, N.V. (1997) The origins of Yakutian eclogite xenoliths. Journal of Petrology **38**, 85-113.

Sobolev, A.V., Hofmann, A.W. and Nikogosian, I.K. (2000) Recycled oceanic crust observed in 'ghost plagioclase'within the source of Mauna Loa lavas. Nature **404**, 986.

Sobolev Jr, N., Kuznetsova, I. and Zyuzin, N. (1968) The petrology of grospydite xenoliths from the Zagadochnaya kimberlite pipe in Yakutia. Journal of Petrology **9**, 253-280.

Stagno, V., Frost, D., McCammon, C., Mohseni, H. and Fei, Y. (2015) The oxygen fugacity at which graphite or diamond forms from carbonate-bearing melts in eclogitic rocks. Contributions to Mineralogy and Petrology **169**, 16.

Szabó, C. and Bodnar, R. J. (1995). Chemistry and origin of mantle sulfides in spinel peridotite xenoliths from alkaline basaltic lavas, Nógraád-Gömör Volcanic Field, northern Hungary and southern Slovakia. Geochimica et Cosmochimica Acta **59**(19), 3917-3927.

Tappe, S., Brand, N.B., Stracke, A., van Acken, D., Liu, C.-Z., Strauss, H., Wu, F.-Y., Luguet, A. and Mitchell, R.H. (2017a) Plates or plumes in the origin of kimberlites: U/Pb perovskite and Sr-Nd-Hf-Os-CO isotope constraints from the Superior craton (Canada). Chemical Geology **455**, 57-83.

Tappe, S., Romer, R.L., Stracke, A., Steenfelt, A., Smart, K.A., Muehlenbachs, K. and Torsvik, T.H. (2017b) Sources and mobility of carbonate melts beneath cratons, with implications for deep carbon cycling, metasomatism and rift initiation. Earth and Planetary Science Letters **466**, 152-167.

Tappe, S., Smart, K., Torsvik, T., Massuyeau, M. and de Wit, M. (2018a). Geodynamics of kimberlites on a cooling Earth: Clues to plate tectonic evolution and deep volatile cycles. Earth and Planetary Science Letters **484**, 1-14.

Tappe, S., Dongre, A., Liu, C. Z. and Wu, F. Y. (2018b). 'Premier'evidence for prolonged kimberlite pipe formation and its influence on diamond transport from deep Earth. Geology **46**(10), 843-846.

Tappe, S., Smart, K.A., Pearson, D.G., Steenfelt, A. and Simonetti, A. (2011) Craton formation in Late Archean subduction zones revealed by first Greenland eclogites. Geology **39**, 1103-1106.

Tappert, R., Stachel, T., Harris, J.W., Muehlenbachs, K., Ludwig, T. and Brey, G.P. (2005) Diamonds from Jagersfontein (South Africa): messengers from the sublithospheric mantle. Contributions to Mineralogy and Petrology **150**, 505-522.

Taylor, L.A. and Neal, C.R. (1989) Eclogites with oceanic crustal and mantle signatures from the Bellsbank kimberlite, South Africa, Part I: mineralogy, petrography, and whole rock chemistry. The Journal of Geology **97**, 551-567.

Thomassot, E., Cartigny, P., Harris, J., Lorand, J., Rollion-Bard, C. and Chaussidon, M. (2009) Metasomatic diamond growth: A multi-isotope study (^{13}C, ^{15}N, ^{33}S, ^{34}S) of sulphide inclusions and their host diamonds from Jwaneng (Botswana). Earth and Planetary Science Letters **282**, 79-90.

Timmerman, S., Koornneef, J. M., Chinn, I. L. and Davies, G. R. (2017). Dated eclogitic diamond growth zones reveal variable recycling of crustal carbon through time. Earth and Planetary Science Letters **463**, 178-188.

Viljoen, F., Dobbe, R., Harris, J. and Smit, B. (2010) Trace element chemistry of mineral inclusions in eclogitic diamonds from the Premier (Cullinan) and Finsch kimberlites, South Africa: implications for the evolution of their mantle source. Lithos **118**, 156-168.

Viljoen, F., Dobbe, R. and Smit, B. (2009) Geochemical processes in peridotite xenoliths from the Premier diamond mine, South Africa: evidence for the depletion and refertilisation of subcratonic lithosphere. Lithos **112**, 1133-1142.

Viljoen, K., Smith, C.B. and Sharp, Z. (1996) Stable and radiogenic isotope study of eclogite xenoliths from the Orapa kimberlite, Botswana. Chemical Geology **131**, 235-255.

Wainwright, A. N., Luguet, A., Fonseca, R. O. C. and Pearson, D. G. (2015). Investigating metasomatic effects on the 187Os isotopic signature: a case study on micrometric base metal sulphides in metasomatised peridotite from the Letlhakane kimberlite (Botswana). Lithos **232**, 35-48.

Weiss, Y., Kessel, R., Griffin, W.L., Kiflawi, I., Klein-BenDavid, O., Bell, D.R., Harris, J.W. and Navon, O. (2009). A new model for the evolution of diamond-forming fluids: Evidence from microinclusion-bearing diamonds from Kankan, Guinea. Lithos **112**, 660-674.

Woodland, A. B., Girnis, A. V., Bulatov, V. K., Brey, G. P. and Höfer, H. E. (2019). Experimental study of sulfur solubility in silicate–carbonate melts at 5–10.5 GPa. Chemical Geology 505, 12-22.

Woodland, A. and Koch, M. (2003) Variation in oxygen fugacity with depth in the upper mantle beneath the Kaapvaal craton, Southern Africa. Earth and Planetary Science Letters **214**, 295-310.

Woodland, A.B. and Ross, C.R. (1994) A crystallographic and Mössbauer spectroscopy study of $Fe_3^{2+}Al_2Si_3O_{12}$-$Fe_3^{2+}Fe_2^{3+}Si_3O_{12}$,(almandine-"skiagite") and $Ca_3Fe_2^{3+}Si_3O_{12}$-$Fe_3^{2+}Fe_2^{3+}Si_3O_{12}$ (andradite-"skiagite") garnet solid solutions. Physics and Chemistry of Minerals **21**, 117-132.

Xiong, X., Adam, J. and Green, T. (2005) Rutile stability and rutile/melt HFSE partitioning during partial melting of hydrous basalt: implications for TTG genesis. Chemical Geology **218**, 339-359.

Yund, R. A. and Kullerud, G. (1966). Thermal stability of assemblages in the Cu—Fe—S system. Journal of Petrology **7**(3), 454-488.

Zeh, A., Ovtcharova, M., Wilson, A.H. and Schaltegger, U. (2015) The Bushveld Complex was emplaced and cooled in less than one million years – results of zirconology, and geotectonic implications. Earth and Planetary Science Letters **418**, 103-114.

Zhang, M., O'Reilly, S.Y., Wang, K.-L., Hronsky, J. and Griffin, W.L. (2008) Flood basalts and metallogeny: the lithospheric mantle connection. Earth-Science Reviews **86**, 145-174.

Table 3.1. Major and minor element compositions of garnet and clinopyroxene from the Kaapvaal eclogite xenoliths

Sample	ROVIC-MBK	MBK	JJG-4492	HRV-174A	HRV-174B	HRV-162A	HRV-162B	HRV-161A	HRV-161B
Location	Roberts Victor	Roberts Victor	Roberts Victor	Roberts Victor	Roberts Victor	Roberts Victor	Roberts Victor	Roberts Victor	Roberts Victor
Mineralogy	Grt + Cpx	Grt + Cpx	Grt + Cpx	Grt + Cpx	Grt + Cpx	Grt + Cpx	Grt + Cpx	Grt + Cpx	Grt + Cpx
Minor phases	Phl, Ky	Phl, Rt, BMS	Ky, Ap, BMS	Phl, BMS	Phl, Ilm	Phl, Ilm, BMS	Ilm, BMS, Phl	BMS, Phl, Rt	BMS, Phl, Rt
Trace phases	BMS	Ne	Ne, Coe	Coe, Ne	-	-	Ne, Phl, Coe	Ne	Ne
Description	inf.	inf.	mass.	mass.	alt.	inf.	inf.	fol.	inf.
Textures	Type I	Type I	Type I	Type I	Type II	Type I	Type I	Type I	Type I
ME Group	Ky-gabbroic	Picritic	Ky-grospydite	Picritic	Basaltic	Gabbroic	Gabbroic	Picritic/ Phl-ecl.	Picritic/ Phl-ecl.
TE Group	LREE-depleted	LREE-enriched	LREE-depleted	LREE-depleted	HREE-enriched	LREE-depleted	LREE-depleted	LREE-enriched	LREE-enriched
mineral:	*Grt*	*Grt*	*Grt*	*Grt*	*Grt*	*Grt*	*Grt*	*Grt*	*Grt*
SiO_2	41.7	41.5	40.4	40.7	39.7	40.8	40.8	41.4	41.6
TiO_2	0.2	0.1	0.2	0.3	0.04	0.3	0.2	0.05	bdl
Al_2O_3	23.2	22.9	22.4	22.7	22.0	22.9	23.1	23.5	23.7
Cr_2O_3	0.10	0.37	0.03	0.13	0.03	0.03	0.03	0.13	0.13
FeO	12.7	11.6	11.0	15.0	18.5	15.3	15.6	11.9	12.1
MnO	0.4	0.5	0.3	0.6	0.5	0.4	0.3	0.3	bdl
MgO	14.3	18.8	7.6	15.2	8.8	15.4	13.6	19.0	19.4
CaO	8.0	3.8	18.5	4.7	10.7	5.2	7.2	2.9	3.1
Na_2O	0.12	0.05	0.07	0.13	0.07	0.11	0.14	0.03	0.03
K_2O	0.01	0.01	bdl	bdl	0.01	0.02	0.01	bdl	0.01
Total (wt. %)	100.7	99.6	100.5	99.3	100.2	100.4	100.9	99.1	100.0
Mg#	67	74	55	64	46	64	61	74	74
$Fe^{3+}/\sum Fe$*	0.027	0.041	0.025	0.031	0.036	0.025	0.013	0.020	0.019
Gt Class	B	A	C	B	B	B	B	A	A
mineral:	*Cpx*	*Cpx*	*Cpx*	*Cpx*	*Cpx*	*Cpx*	*Cpx*	*Cpx*	*Cpx*
SiO_2	56.3	55.5	56.1	56.0	54.8	56.0	56.3	55.7	55.5
TiO_2	0.33	0.09	0.04	0.34	0.22	0.39	0.37	0.07	0.20
Al_2O_3	13.4	3.4	16.9	7.9	9.5	14.9	14.6	7.3	7.2
Cr_2O_3	0.18	0.42	bdl	0.14	bdl	bdl	bdl	0.31	0.32
FeO	2.6	3.9	1.7	4.7	5.4	2.9	3.0	3.2	3.1
MnO	bdl	0.07	0.02	0.08	0.10	0.03	0.03	0.04	0.04
MgO	8.3	15.3	6.2	11.7	9.1	6.9	7.3	12.7	12.6
CaO	11.5	19.3	11.4	13.9	15.4	9.9	10.2	15.1	15.3
Na_2O	7.30	2.87	7.91	5.10	5.09	8.43	8.44	4.71	4.73
K_2O	0.41	bdl	0.21	0.07	0.02	0.08	0.03	0.06	0.06
Total (wt. %)	100.0	100.8	100.5	100.0	99.7	99.5	100.3	99.2	99.0
Mg#	85	88	87	82	75	81	83	88	88
Cpx Class	C	A	C	B	B	C	C	B	B

Ten analyses were conducted on each phase. A maximum standard deviation of 0.05 was observed for the minor elements (Cr, Mn and K).
Mg# = (Mg)/(Mg+Fe); bdl = below detection limit (0.01 w.%); *determined by Mössbauer spectroscopy.
Gt = garnet; cpx = clinopyroxene; coe = coesite; ky= kyanite; rt = rutile; ilm = ilmenite; phl = phogopite; ne = nepheline; ap = apatite.
Garnet class after Coleman, 1965; Clinopyroxene class after Taylor and Neal, 1989
ME group = whole-rock major element classification discribed in **Section 3.5.3.2**
TE group = whole-rock REE trace element classification described in **Section 3.5.3.3** and shown on **Fig. 3.6** and **3.7**.
alt. = altered; inf. = kimberlite infiltrated; mass. = massive; fol. = foliated; Type I, II textures from Macgregor and Carter (1970) and McCandless & Gurney (1989).

Table 3.1. Major and minor element compositions of garnet and clinopyroxene from the Kaapvaal eclogite xenoliths (continued)

Sample	HRV-172A	HRV-172B	EJB-86	JJG-2914	JJG-2919	JJG-2920	CIM15-101	CIM15-102	ST16-H-04	JJG-2717
Location	Roberts Victor	Roberts Victor	Roberts Victor	Jagersfontein	Jagersfontein	Jagersfontein	Kamfersdam	Kamfersdam	Swartruggens	Premier
Mineralogy	Grt + Cpx	Grt + Cpx	Grt + Cpx	Grt + Cpx	Grt + Cpx	Grt + Cpx	Grt + Cpx	Grt + Cpx	Grt + Cpx	Grt + Cpx
Minor phases	BMS, Rt	Ky, BMS, Ilm	Phl, BMS	Ilm	Ilm, BMS	Cal, BMS	Rt, BMS	Rt, BMS, Phl	BMS, Ilm, phl	Ilm, SMS
Trace phases	-	-	-	-	-	-	Phl	-	Coe, Ap	-
Description	alt.	inf.	mass.	alt.	alt.	alt.	mass.	inf.	inf.	inf.
Textures	Type I	Type I	Type I	Type I	Type I	Type I	Type I	Type I	Pyrox.	Type I
ME Group	Basaltic	Ky-grospydite	Gabbroic	Picritic	Basaltic	Picritic	Gab/bas	Picritic	Pyroxenite	Basaltic
TE Group	LREE-enriched	LREE-depleted	LREE-depleted	LREE-enriched	HREE-enriched	LREE-enriched	LREE-enriched	LREE-enriched	HREE-enriched	LREE-depleted
mineral:	*Grt*	*Grt*	*Grt*	*Grt*	*Grt*	*Grt*	*Grt*	*Grt*	*Grt*	*Grt*
SiO_2	41.2	40.0	40.0	41.2	41.0	40.2	40.3	42.3	41.5	39.8
TiO_2	0.3	0.3	0.3	0.0	0.1	0.1	0.0	0.0	0.3	0.4
Al_2O_3	23.4	22.6	22.6	23.4	23.3	22.9	22.8	23.8	22.4	22.8
Cr_2O_3	0.05	0.02	0.07	0.05	0.03	0.07	0.04	0.08	0.06	0.01
FeO	13.3	13.2	15.0	13.9	16.1	16.1	19.1	9.4	12.1	14.2
MnO	0.3	0.4	0.3	0.6	0.6	0.4	0.5	0.5	0.6	0.3
MgO	14.3	7.0	10.6	16.8	15.4	12.9	12.9	20.0	15.1	11.5
CaO	7.3	15.9	11.1	4.0	4.2	6.6	4.2	4.1	6.9	10.1
Na_2O	0.08	0.21	0.14	0.05	0.04	0.05	0.05	0.04	0.07	0.09
K_2O	bdl	0.02	bdl	bdl	bdl	bdl	bdl	bdl	0.01	bdl
Total (wt. %)	100.1	99.8	100.1	99.9	100.8	99.5	99.8	100.1	99.1	99.2
Mg#	65	49	56	68	63	59	55	79	69	59
$Fe^{3+}/\sum Fe$*	0.021	n/a	0.010	0.027	0.020	0.019	0.018	0.034	n/a	n/a
Gt Class	B	C	B	A	B	B	B	A	B	B
mineral:	*Cpx*	*Cpx*	*Cpx*	*Cpx*	*Cpx*	*Cpx*	*Cpx*	*Cpx*	*Cpx*	*Cpx*
SiO_2	55.8	55.7	56.1	55.3	56.0	53.1	56.1	54.8	55.7	53.3
TiO_2	0.33	0.41	0.37	0.24	0.27	0.70	0.29	bdl	0.31	0.93
Al_2O_3	9.1	17.2	14.5	8.3	9.2	8.6	9.9	3.2	3.1	7.6
Cr_2O_3	bdl	bdl	0.06	bdl	bdl	bdl	bdl	0.36	bdl	bdl
FeO	3.3	2.6	2.6	4.7	4.2	4.6	4.8	3.0	4.0	5.1
MnO	0.05	0.03	0.02	0.06	0.03	0.15	0.05	0.06	0.12	0.24
MgO	11.1	5.8	7.3	11.3	10.6	13.3	9.9	15.4	15.6	13.9
CaO	15.2	10.7	11.6	14.3	13.6	16.2	13.0	20.6	19.2	17.1
Na_2O	5.01	7.99	7.68	5.41	5.85	3.46	5.95	2.09	2.34	2.69
K_2O	0.16	0.21	0.39	bdl	bdl	0.52	0.01	bdl	0.03	0.38
Total (wt. %)	100.0	100.7	100.7	99.7	99.8	100.7	100.1	99.4	100.4	101.3
Mg#	86	80	84	81	82	84	78	91	87	73
Cpx Class	B	C	C	B	B	B	B	A	A	B

Ten analyses were conducted on each phase. A maximum standard deviation of 0.05 was observed in the minor elements (Cr, Mn and K).
Mg# = (Mg)/(Mg+Fe); bdl = below detection limit (0.01 w.%); *determined by Mössbauer spectroscopy.
Gt = garnet; cpx = clinopyroxene; coe = coesite; ky= kyanite; rt = rutile; ilm = ilmenite; phl = phogopite; ne = nepheline; ap = apatite.
Garnet class after Coleman, 1965; Clinopyroxene class after Taylor and Neal, 1989
ME group = whole-rock major element classification discribed in **Section 3.5.3.2**
TE group = whole-rock REE trace element classification described in **Section 3.5.3.3** and shown on **Fig. 3.6** and **3.7**.
alt. = altered; inf. = kimberlite infiltrated; mass. = massive; fol. = foliated; Type I, II textures from Macgregor and Carter (1970) and McCandless & Gurney (1989).

Table 3.2. Representative major element compositions of low-temperature sulphides from the Kaapvaal eclogite xenoliths

Sulphide phase:	Po	Pn	Co-Pn	Cp	Py	Ni-Py	Smy	Vi
BMS incl. (modal %)	0 - 79	0 - 58	0 - 58	0 - 30	0 - 100	0 - 70	0 - 70	0 - 70
BMS int. (modal %)	< 5	0 - 25	0 - 67	0 - 33	0 - 100	0 - 80	0 - 80	0 - 80
Locality	RV, J	RV, J, K	RV, J, K	RV, J, K	RV, J, K, P	RV	RV, J, K	RV, J. K
n =	17	25	10	65	30	20	15	17
O	0.2	0.5	0.9	0.2	0.2	0.6	0.5	0.2
S	39.8	33.5	32.6	34.1	52.1	51.9	46.5	42.4
Fe	57.8	38.6	31.1	31.6	46.4	44.5	31.0	21.2
Cu	0.1	1.0	0.3	33.6	0.5	0.2	0.1	0.1
Co	0.3	1.8	3.9	0.06 (0.15)	0.4	0.3	0.9	0.7
Ni	2.0	25.3	30.7	0.3	0.6	3.1	20.7	35.6
Total (wt. %)	100.0	100.1	99.5	99.6	100.0	100.1	99.2	100.0
O	0.4	1.3	2.5	0.7	0.4	1.5	1.2	0.6
S	53.6	47.3	45.7	49.1	65.5	65.4	61.1	57.0
Fe	44.7	31.2	25.0	26.2	33.5	32.1	23.4	16.4
Cu	0.0	0.7	0.2	24.4	0.3	0.2	0.1	0.1
Co	0.2	1.4	3.0	0.0	0.3	0.2	0.6	0.5
Ni	1.5	19.4	23.5	0.3	0.4	2.2	14.8	26.1
Total (at. %)	100.4	101.3	99.9	100.7	100.4	101.4	101.2	100.6
M/S (at. %)	0.9	1.1	1.1	1.0	0.5	0.5	0.6	0.8

BMS incl. = base metal sulphide inclusions; BMS int. = interstitial base metal suphides. Po = pyrrhotite; Pn = pentlandite; Co-Pn = cobalt-rich pentlandite;
Cp = chalcopyrite, (Co) = average cobalt-rich chalcopyrite; Py = pyrite; Ni-Py = Ni-rich pyrite; Smy = Smythite; Vi = Violarite.
RV = Roberts Victor, J = Jagersfontein, K = Kimberley (Kamfersdam); P = Premier.
n = total number of sulphides analysed; a maximum standard deviation of 0.2 was observed in the minor elements Cu, Ni and Co.
M/S = metal/ sulphur ratio, where M = Fe + Cu + Co + Ni.

Table 3.3. Base metal sulphide occurrence and and reconstructed bulk base metal sulphide compositions from the Kaapvaal eclogite xenoliths

Sample	TE group	low-T assemblage (%)	Host mineral	BMS grouping	Reconstructed bulk sulphide (wt.%)						at%		
					O	S	Fe	Cu	Co	Ni	M/S	Cu/ metals	(Ni+Co)/Fe
Roberts Victor													
ROVIC MBK	LREE-depleted	100 Py	int. cpx	Group 3	2.8	53.2	44.8	bdl	bdl	bdl	0.5	-	-
MBK	LREE-enriched	100 Py	int. cpx/phl	Group 3	2.6	53.4	46.3	bdl	bdl	bdl	0.5	-	-
		100 Py	encl. cpx	Group 3	bdl	52.2	47.6	bdl	bdl	bdl	0.5	-	-
		4 Py 36 Ni-Py 47 Smy/Vi 13 Cp	encl. cpx[b]	Group 2	0.6	40.6	37.3	4.5	0.6	15.0	0.8	0.1	0.4
JJG-4492	LREE-depleted	50 Ni-Py 30 Smy/Vi 20 Cp	encl. cpx[a]	Group 2	3.6	41.2	33.4	6.0	6.3	8.8	0.7	0.1	0.4
		20 Cp 10 high-Co Cp 70 Ni-Py	encl. cpx[a]	Group 1	3.2	43.4	34.1	9.3	5.3	3.7	0.7	0.2	0.3
		3 Py 49 Cp 58 high-Co Pn	encl. cpx[b]	Group 2	4.9	43.7	37.6	5.9	6.8	6.7	0.7	0.1	0.3
HRV-174A	LREE-depleted	80 Ni-Py 20 Cp	int. grt/cpx[a]	Group 1	3.1	48.4	40.0	6.5	0.1	0.5	0.5	0.1	-
		46 Py 21 Ni-Py 14 Mss 19 Cp	encl. cpx[b]	Group 1	3.4	48.1	39.5	6.8	0.1	0.6	0.6	0.1	-
HRV-162A	LREE-depleted	36 Ni-Py 57 Smy/Vi 7 Cp	int. cpx [b]	Group 2	0.5	48.0	36.0	2.5	0.7	9.3	0.6	-	0.3
		60 Ni-Py 35 Smy/Vi 6 Cp	int. cpx [b]	Group 2	0.7	48.6	34.3	2.0	0.7	13.3	0.6	-	0.4
		70 Smy/Vi 30 Cp	encl. cpx[b]	Group 2	0.5	41.0	25.5	10.4	0.9	18.6	0.8	0.2	0.7
		70 Smy/Vi 30 Cp	encl. grt[b]	Group 2	0.4	41.9	25.1	10.1	0.9	20.3	0.7	0.2	0.7
HRV-162B	LREE-depleted	39 Ni-Py 40 Smy/Vi 21 Cp	int. cpx [b]	Group 2	0.9	46.0	33.2	7.2	0.5	11.8	0.6	0.1	0.4
		80 Smy/Vi 20 Cp	int. cpx/neph[b]	Group 2	0.9	44.7	29.6	7.1	1.0	12.1	0.6	0.1	0.4
HRV-161A	LREE-enriched	59 Ni-Py 33 Smy/Vi 7 Cp	encl. cpx[b]	Group 1	0.4	48.1	36.4	2.4	0.5	6.4	0.6	-	0.2
		17 Py 83 Ni-Py	encl. cpx[b]	Group 1	0.8	51.1	43.8	bdl	1.0	bdl	0.5	-	-
HRV-161B	LREE-enriched	50 Ni-Py 35 Smy/Vi 15 Cp	encl. cpx[b]	Group 2	0.3	44.1	34.6	7.4	0.7	13.6	0.7	0.1	0.4
		46 Ni-Py 41 Smy/Vi 15 Cp	encl. cpx[b]	Group 2	0.2	47.9	36.0	5.1	0.5	12.4	0.6	0.1	0.3
HRV-172B	LREE-depleted	9 Ni-Py 49 Po 25 Smy/Vi 17 Cp	encl. cpx[a]	Group 1	0.3	39.6	46.7	5.8	0.1	6.9	0.8	0.1	0.1
		100 Py	int. cpx	Group 1	1.2	52.4	47.6	bdl	bdl	bdl	0.5	-	-
EJB-86	LREE-depleted	100 Mss	encl. cpx[a]	Group 1	0.2	49.5	34.7	bdl	0.4	10.7	0.5	-	0.2
		Py Ni-Py		Group 3	bdl	52.1	41.9	bdl	bdl	3.1	0.5	-	0.1
Jagersfontein													
JJG-2919	HREE-enriched	72 Po 17 Smy/Vi 11 Cp	int. cpx[b]	Group 1	1.3	34.7	53.4	4.9	0.6	3.8	1.0	0.1	0.1
		74 Po 16 Pn 10 Cp	encl. cpx[b]	Group 1	0.3	37.7	52.5	3.6	0.1	5.4	0.9	0.1	0.1
JJG-2920	LREE-enriched	65 Po 25 Pn 11 Cp	encl. cpx[b]	Group 1	0.4	35.0	54.2	3.8	0.4	6.1	1.0	0.1	0.1
		79 Po 16 Pn 5 Cp	encl. cpx[b]	Group 1	1.3	37.4	52.0	2.6	0.4	6.4	0.9	-	0.1
		100 Mss	encl. cpx[b]	Group 2	bdl	33.4	34.3	13.8	1.3	17.0	1.1	0.2	0.5
Kimberley (Kamfersdam)													
CIM15-101	LREE-enriched	67 high-Co Pn 33 Cp	int. cpx[a]	Group 2	0.9	32.2	26.0	10.9	2.5	25.7	1.1	0.2	1.0
		alt. Pn	int. cpx[a]	Group 2	4.4	29.5	24.0	6.2	1.3	30.3	1.2	0.1	1.3
CIM15-102	LREE-enriched	100 Py	int. phl	Group 3	0.3	49.3	46.5	bdl	bdl	bdl	0.9	-	-
		100 Py	int. cpx	Group 3	0.4	53.0	47.9	bdl	bdl	bdl	0.9	-	-
Premier													
JJG-2717	LREE-depleted	100 Py	int. cpx	Group 3	bdl	52.9	46.0	bdl	bdl	bdl	0.5	-	-

Mss = monosulphide solid solution; Py = pyrite; Pn = pentlandite; Cp = chalcopyrite; Po = pyrrhotite; Smy/Vi = smythite/violarite

alt. = altered; int. = interstitial; encl. = enclosed; M/S = (Fe + Cu + Co + Ni)/S; Cu/Metals = Cu/(Fe + Cu + Co + Ni); [a]fish-net-altered, [b]mottled texture.

Oxygen contents above 0.6 wt.% sugget the presence of an oxide phase (i.e. iron(oxy)hydroxide or magnetite).

Group 1, 2 and 3 defined using BMS major and trace element reconstructions, see **Sections 3.5.7.4** and **3.5.7.5** for details.

Table 3.4. Trace element compositions of garnet and clinopyroxene from Kaapvaal eclogite xenoliths

Sample	ROVIC-MBK	MBK	JJG-4492	HRV-174A	HRV-174B	HRV-162A	HRV-162B	HRV-161A	HRV-161B
ME Group	Ky-gabbroic	Picritic	Ky-grospydite	Picritic	Basaltic	Gabbroic	Gabbroic	Picritic/ Phl-ecl.	Picritic/ Phl-ecl.
TE Group	LREE-depleted	LREE-enriched	LREE-depleted	LREE-depleted	HREE-enriched	LREE-depleted	LREE-depleted	LREE-enriched	LREE-enriched
mineral:	*Grt*	*Grt*	*Grt*	*Grt*	*Grt*	*Grt*	*Grt*	*Grt*	*Grt*
Sc	42	83	21	54	80	35	35	28	29
V	111	99	33	63	211	45	42	38	39
Co	88	55	44	59	71	68	68	48	47
Ni	104	31	30	14.8	20.7	43.2	44.6	16.2	16.4
Cu	1.4	0.3	0.6	0.1	3.2	0.7	0.7	0.1	0.1
Zn	108	14	93	29	85	131	131	56	54
Rb	0.58	0.09	0.03	0.01	0.2	0.8	0.6	0.1	0.2
Sr	3.4	0.8	7.5	0.7	0.5	2.0	3.8	0.7	0.7
Y	18	23	5	30	53	11	11	10	10
Zr	33	58	28	35	3	17	17	6	6
Nb	0.14	0.18	0.08	0.16	0.00	0.03	0.06	0.02	0.01
Cs	0.02	0.06	bdl	bdl	bdl	bdl	1.5	bdl	0.02
Ba	8.9	5.8	bdl	0.5	0.6	4.5	1.2	bdl	7.0
La	0.3	0.5	0.1	0.05	bdl	0.1	0.3	0.03	0.1
Ce	0.9	0.3	1.1	0.3	bdl	0.3	0.8	0.3	0.3
Pr	0.2	0.1	0.4	0.1	bdl	0.1	0.2	0.1	0.1
Nd	1.9	0.8	2.9	1.4	0.3	1.4	1.5	1.2	1.2
Sm	1.4	1.1	1.9	1.6	0.6	1.2	1.1	0.9	0.9
Eu	0.7	0.6	1.1	0.8	0.4	0.8	0.8	0.5	0.4
Gd	2.5	3.0	1.9	2.8	2.6	1.7	1.7	1.7	1.7
Tb	0.5	0.6	0.2	0.6	0.7	0.3	0.3	0.3	0.3
Dy	3.3	4.2	1.0	4.5	7.3	1.8	1.9	1.9	1.8
Ho	0.7	0.8	0.2	1.1	1.9	0.4	0.4	0.4	0.3
Er	1.9	2.4	0.4	3.9	6.9	1.2	1.3	0.9	0.9
Tm	0.26	0.34	0.05	0.6	1.1	0.2	0.2	0.1	0.1
Yb	1.6	2.5	0.5	4.56	8.31	1.40	1.37	0.82	0.84
Lu	0.24	0.40	0.07	0.7	1.4	0.2	0.2	0.1	0.1
Hf	0.7	0.5	0.4	0.30	0.11	0.29	0.29	0.07	0.06
Ta	0.01	0.02	0.01	0.01	bdl	bdl	0.01	bdl	bdl
Pb	0.1	0.3	bdl	0.02	0.5	0.03	0.07	bdl	bdl
Th	0.04	0.13	bdl	0.02	bdl	0.03	0.05	0.01	0.02
U	0.01	0.01	bdl	bdl	bdl	bdl	bdl	bdl	bdl
Eu*	1.1	1.0	1.7	1.1	0.9	1.8	1.7	1.1	1.1
Lu/Gd	0.8	1.1	0.3	2.1	4.1	1.0	1.0	0.6	0.6

bdl = below detection imit; 2σ standard errors are found in Appendices C and D

Eu*, Lu/Gd, La/Sm are calculated using Chondrite C1 normalized values from McDonough and Sun (1995).

Sr* is calculated using primitive mantle 'pyrolite' normalized values from McDonough and Sun (1995).

Trace element concentrations in ppm; secondary clinopyroxene values in **Appendix E.**

ME Group = major element classification; see **Section 3.5.3.2**; TE Group = trace element classification; see **Section 3.5.3.3**.

Table 3.4. Trace element compositions of garnet and clinopyroxene from Kaapvaal eclogite xenoliths (continued)

Sample	HRV-172A	HRV-172B	EJB-86	JJG-2914	JJG-2919	JJG-2920	CIM15-101	CIM15-102	ST16-H-04	JJG-2717
ME Group	Basaltic	Ky-grospydite	Gabbroic	Picritic	Basaltic	Picritic	Gab/bas	Picritic	Pyroxenite	Basaltic
TE Group	LREE-enriched	LREE-depleted	LREE-depleted	LREE-enriched	HREE-enriched	LREE-enriched	LREE-enriched	LREE-enriched	HREE-enriched	LREE-depleted
mineral:	*Grt*	*Grt*	*Grt*	*Grt*	*Grt*	*Grt*	*Grt*	*Grt*	*Grt*	*Grt*
Sc	21	25	33	52	68	46	44	55	60	47
V	61	51	122	60	208	74	71	102	158	88
Co	79	46	59	58	76	54	63	39	46	75
Ni	122.5	33.7	78.3	12.9	22.1	12.1	17.7	12.8	20.7	45.1
Cu	1.6	0.6	1.0	0.0	2.9	bdl	0.1	0.1	0.3	1.0
Zn	129	139	114	29	87	159	111	10	47	54
Rb	0.1	1.0	bdl	bdl	0.02	bdl	bdl	0.1	0.1	38.6
Sr	0.9	38.4	3.5	0.3	0.1	1.0	0.9	3.0	2.7	11.6
Y	22	16	20	27	54	24	20	31	45	26
Zr	44	51	73	35	2	8	6	20	66	71
Nb	0.02	0.11	bdl	0.08	bdl	bdl	0.05	0.13	0.28	0.54
Cs	0.05	0.8	bdl	bdl	bdl	bdl	bdl	0.6	0.3	0.5
Ba	0.3	7.0	bdl	bdl	bdl	bdl	bdl	2.2	13.3	64.6
La	0.1	0.3	0.1	bdl	bdl	bdl	0.01	0.3	0.2	0.2
Ce	0.3	1.5	0.8	0.2	bdl	0.3	0.3	0.8	0.7	0.6
Pr	0.1	0.5	0.3	0.1	bdl	0.1	0.2	0.1	0.2	0.2
Nd	2.1	4.3	3.2	0.8	0.3	1.6	2.1	1.4	2.2	2.9
Sm	2.3	2.4	2.7	1.1	0.7	1.1	2.1	0.8	1.4	4.5
Eu	1.1	1.2	1.2	0.8	0.5	1.0	1.0	0.4	0.6	2.2
Gd	4.3	3.2	3.7	2.6	2.7	2.8	3.4	1.5	2.8	8.4
Tb	0.7	0.5	0.6	0.6	0.8	0.5	0.6	0.4	0.7	1.2
Dy	4.5	3.1	3.9	3.7	7.3	3.7	3.8	4.0	6.4	6.2
Ho	0.8	0.6	0.8	1.0	2.0	0.9	0.8	1.1	1.7	1.0
Er	2.0	1.7	2.1	3.4	6.9	2.7	2.2	3.9	5.6	2.2
Tm	0.2	0.2	0.3	0.5	1.1	0.4	0.3	0.6	0.8	0.2
Yb	1.57	1.69	2.14	4.29	8.50	3.04	2.29	4.45	6.12	1.48
Lu	0.2	0.3	0.3	0.5	1.3	0.5	0.3	0.7	1.0	0.2
Hf	0.66	0.99	1.22	0.25	0.08	0.10	0.06	0.20	1.37	0.81
Ta	bdl	bdl	bdl	bdl	bdl	bdl	bdl	bdl	bdl	bdl
Pb	0.09	0.08	bdl	bdl	0.01	bdl	0.01	0.09	0.02	0.07
Th	0.01	0.02	bdl	bdl	bdl	bdl	bdl	0.05	0.02	0.02
U	bdl	bdl	bdl	bdl	bdl	bdl	bdl	bdl	bdl	bdl
Eu*	1.0	1.3	1.1	1.3	0.9	1.6	1.2	1.0	1.0	1.1
Lu/Gd	0.4	0.7	0.7	1.5	3.9	1.3	0.8	3.8	2.8	0.2

bdl = below detection imit; 2σ standard errors are found in Appendices C and D

Eu*, Lu/Gd, La/Sm are calculated using Chondrite C1 normalized values from McDonough and Sun (1995).

Sr* is calculated using primitive mantle 'pyrolite' normalized values from McDonough and Sun (1995).

Trace element concentrations in ppm; secondary clinopyroxene values in **Appendix E.**

ME Group = major element classification; see **Section 3.5.3.2**; TE Group = trace element classification; see **Section 3.5.3.3**.

Table 3.4. Trace element compositions of garnet and clinopyroxene from Kaapvaal eclogite (continued)

Samp.	ROVIC-MBK	MBK	JJG-4492	HRV-174A	HRV-174B	HRV-162A	HRV-162B	HRV-161A	HRV-161B
mineral:	Cpx	Cpx	Cpx	Cpx	Cpx	Cpx	Cpx	Cpx	Cpx
Sc	5	36	6	19	25	9	8	9	10
V	1	329	57	417	513	179	128	167	168
Co	0.2	24	17	30	38	21	19	18	18
Ni	1	282	158	277	300	234	200	170	165
Cu	2	1	6	9	7	8	12	2	2
Zn	5	13	51	56	77	69	67	45	43
Rb	32	bdl	1.97	0.03	0.22	1.3	0.01	0.1	0.06
Sr	27	304	170	282	18	179	132	828	843
Y	1.0	4.1	0.04	2.0	1.2	0.6	0.4	1.5	1.6
Zr	74	91	9	27	4	12	9	14	13
Nb	0.88	1.07	0.06	0.03	bdl	0.06	0.01	0.02	0.02
Cs	0.81	bdl	0.26	0.60	0.18	12	bdl	0.01	0.06
Ba	591	0.3	2712	1	1	197	48	2	2
La	1.3	6.7	0.3	1.3	bdl	0.7	0.3	12.3	12.8
Ce	2	25	1	6	0.1	3	2	39	40
Pr	0.2	4.3	0.1	1.1	0.04	0.5	0.3	5.9	6.0
Nd	1.0	23.6	0.5	5.9	0.4	2.5	1.8	26.2	26.9
Sm	0.1	6.4	0.1	1.3	0.3	0.6	0.4	4.0	4.1
Eu	0.1	1.8	0.2	0.4	0.1	0.2	0.2	0.9	0.9
Gd	0.1	4.4	0.1	0.9	0.4	0.4	0.3	2.0	2.0
Tb	0.02	0.4	bdl	0.1	0.1	0.04	0.03	0.2	0.2
Dy	0.1	1.5	bdl	0.5	0.3	0.2	0.1	0.6	0.6
Ho	0.03	0.18	bdl	0.09	0.05	0.02	0.02	0.07	0.07
Er	0.1	0.3	bdl	0.2	0.1	0.05	0.03	0.1	0.1
Tm	0.01	0.03	bdl	0.02	0.01	0.004	0.003	0.01	0.01
Yb	0.1	0.1	bdl	0.1	0.1	0.02	0.02	0.04	0.04
Lu	0.02	0.01	bdl	0.01	0.01	0.004	0.002	0.004	0.004
Hf	1.8	2.3	0.4	1.7	0.4	0.6	0.4	0.3	0.3
Ta	0.06	0.14	0.03	0.003	bdl	0.004	0.002	0.004	0.003
Pb	4.0	0.5	0.3	0.6	0.1	0.3	0.2	7.5	7.5
Th	0.30	0.14	0.01	0.004	bdl	0.03	bdl	0.33	0.31
U	0.19	0.03	0.01	bdl	bdl	bdl	bdl	0.03	0.03
Eu*	2.5	1.0	7.9	1.0	1.0	1.4	1.5	0.9	0.9
La/Sm	5.6	0.7	2.3	0.7	0.02	0.8	0.5	1.9	2.0
Sr*	1.6	0.8	20.5	3.1	3.8	4.7	5.0	1.9	1.9

bdl = below detection imit; 2σ standard errors are found in Appendices C and D

Eu*, Lu/Gd, La/Sm are calculated using Chondrite C1 normalized values from McDonough and Sun (1995).

Sr* is calculated using primitive mantle 'pyrolite' normalized values from McDonough and Sun (1995).

Trace element concentrations in ppm; secondary clinopyroxene values in **Appendix E.**

ME Group = major element classification; see **Section 3.5.3.2**; TE Group = trace element classification; see **Section 3.5.3.3**.

Table 3.4. Trace element compositions of garnet and clinopyroxene from Kaapvaal eclogite (continued)

Samp.	HRV-172A	HRV-172B	EJB-86	JJG-2914	JJG-2919	JJG-2920	CIM15-101	CIM15-102	ST16-H-04	JJG-2717
mineral:	Cpx	Cpx	Cpx	Cpx	Cpx	Cpx	Cpx	Cpx	Cpx	Cpx
Sc	11	5	8	22	25	18	19	29	23	55
V	206	127	339	368	515	770	368	459	240	191
Co	37	15	23	21	38	22	25	16	29	84
Ni	744	198	470	114	302	152	168	176	202	175
Cu	12	3	9	1	7	5	2	0.2	2	7
Zn	78	64	68	21	76	62	86	9	57	81
Rb	5.26	5.01	5.52	0.02	bdl	35	bdl	0.13	0.01	667
Sr	244	215	269	294	17	1460	514	806	391	469
Y	3.3	0.2	0.5	3.2	1.2	4.3	1.6	5.7	3.6	30.2
Zr	64	15	44	79	4	47	15	66	24	87
Nb	3.86	0.19	0.16	0.80	bdl	1.46	0.29	1.12	0.18	10
Cs	117	17	6	bdl	bdl	1	bdl	0.21	bdl	9
Ba	380	1053	532	0.2	bdl	159	0.1	15	1	308
La	14.5	0.6	1.1	3.1	bdl	2.8	3.1	12.6	3.1	6.9
Ce	30	2	4	14	0.09	7	14	56	16	9
Pr	3.6	0.3	0.6	3.0	0.03	1.0	2.8	9.8	3.1	1.0
Nd	14.8	1.5	3.1	17.4	0.4	4.6	15.7	45.9	14.6	4.4
Sm	2.7	0.2	0.7	3.9	0.3	0.9	3.3	6.2	2.1	2.7
Eu	0.8	0.1	0.2	1.0	0.1	0.3	0.9	1.3	0.5	1.8
Gd	1.9	0.1	0.4	2.5	0.3	0.9	1.8	3.0	1.5	6.9
Tb	0.2	0.01	0.04	0.2	0.1	0.1	0.1	0.3	0.2	1.2
Dy	0.9	0.1	0.2	1.0	0.3	0.8	0.5	1.6	0.9	6.8
Ho	0.13	0.01	0.02	0.13	0.05	0.15	0.06	0.24	0.15	1.1
Er	0.3	0.02	0.04	0.3	0.1	0.4	0.1	0.5	0.3	2.7
Tm	0.03	0.002	0.005	0.03	0.01	0.06	0.01	0.05	0.03	0.31
Yb	0.2	bdl	0.02	0.2	0.1	0.4	0.1	0.3	0.2	1.9
Lu	0.02	bdl	0.003	0.02	0.01	0.06	0.01	0.03	0.02	0.25
Hf	2.6	1.0	2.2	2.3	0.3	1.3	0.5	2.8	1.4	1.3
Ta	0.20	0.01	0.01	0.17	bdl	0.09	0.02	0.04	0.02	0.38
Pb	1.1	0.2	1.1	0.4	bdl	3.1	0.3	2.7	1.0	1.1
Th	1.33	0.04	0.02	0.03	bdl	0.37	0.02	0.85	0.02	0.30
U	0.35	0.01	0.01	0.02	bdl	0.27	0.01	0.05	0.01	0.12
Eu*	1.0	1.7	1.1	1.0	1.0	1.1	1.0	0.8	0.9	1.2
La/Sm	3.3	1.7	1.0	0.5	0.02	2.0	0.6	1.3	0.9	1.6
Sr*	0.9	8.6	5.7	1.2	3.7	19.1	2.2	1.1	1.6	6.5

bdl = below detection imit; 2σ standard errors are found in Appendices C and D

Eu*, Lu/Gd, La/Sm are calculated using Chondrite C1 normalized values from McDonough and Sun (1995).

Sr* is calculated using primitive mantle 'pyrolite' normalized values from McDonough and Sun (1995).

Trace element concentrations in ppm; secondary clinopyroxene values in **Appendix E.**

ME Group = major element classification; see **Section 3.5.3.2**; TE Group = trace element classification; see **Section 3.5.3.3**.

Table 3.5. Trace-element compositions of select base metal sulphides from the Kaapvaal eclogite xenoliths

Sample	TE group	n.	BMS grouping	Fe	Ni	Cu	Co	As	Se	Pd	Ag	Te	Re	Os	Ir	Pt	Au	Pb	Bi	Pd_N/Pt_N	Pt_N/Ir_N	Pd_N/Ir_N	Os_N/Ir_N	Re_N/Os_N	Re_N/Pd_N	Se/Te
Roberts Victor																										
HRV-174A	LREE-depleted	8	Group 1	52	3.4	0.1	0.1	1570	120	bdl	1.8	21.6	0.57	0.02	0.02	bdl	0.14	7	0.1	-	-	-	1.27	299	-	6
		3	Group 1	49.5	3.6	0.1	0.1	2710	134	0.01	9.2	19.9	0.5	0.12	0.13	bdl	0.03	13	0.2	-	-	0.06	0.89	50	693	7
		5	Group 1	51.3	6.2	0.1	0.2	700	158	bdl	4.7	19.7	0.44	0.07	0.06	bdl	0.02	11	0.1	-	-	-	1.10	71	-	8
EJB-86	LREE-depleted	10	Group 1	39.1	14.8	1.5	0.1	726	239	0.77	10.4	5.6	0.06	0.04	0.01	bdl	0.08	16	0.9	-	-	65	3.28	18	1	42
		4	Group 1	43.1	9.4	3.2	0.2	755	213	0.35	8.1	5.6	0.06	bdl	0.01	bdl	0.05	12	0.8	-	-	60	-	-	2.04	38
HRV-162A	LREE-depleted	6	alt. Group 1	37.2	15	12	0.6	2411	315	0.89	8.9	24.7	0.53	bdl	0.02	0.2	0.64	68	0.4	11	4.4	47	-	-	6.58	13
		4	alt. Group 1	38.4	20	6	0.5	4510	244	0.03	0.02	21.8	0.89	0.02	0.02	0.1	0.06	211	0.2	0.49	2.9	1.4	0.93	483	318	11
HRV-162B	LREE-depleted	5	alt. Group 1	32.3	16.7	9.4	1.5	778	182	3.05	9.0	12.2	0.6	0.03	0.01	bdl	0.23	98	0.9	-	-	289	2.19	290	2	15
		7	alt. Group 1	34.4	22.9	2.4	1.6	933	200	2.61	23.8	15.7	0.8	0.07	0.05	bdl	0.13	156	0.3	-	-	53	1.26	144	3	13
HRV-161A	LREE-enriched	7	Group 2	36.6	3.4	14.2	0.3	3020	105	6.10	11.3	15.0	0.3	0.12	0.09	4.9	0.10	122	1.0	2.51	29.1	73	1.28	31	0.55	7
		20	Group 2	28	17.6	2.3	1.6	350	145	1.48	26.2	21.5	0.44	0.35	0.29	1.4	0.05	61	2.8	2.18	2.37	5	1.14	15	3	7
MBK	LREE-enriched	10	Group 2	14.7	42.6	5.9	8.4	67	198	108	102.6	11.7	0.05	0.18	0.59	32.7	0.15	2410	6.4	7	28	185	0.29	3	-	17
HRV-161B	LREE-enriched	9	Group 2	38.5	12.3	1.6	0.3	51.3	68	4.61	4.5	15.2	0.19	0.14	0.05	1.8	bdl	26	0.7	5.19	17.7	92	2.52	16	0.45	4
		7	Group 2	43	9.1	2.3	1.0	120	69	4.48	5.3	14.2	0.39	0.09	0.14	2.5	bdl	37	0.4	3.62	9.1	33	0.61	53	1	5
		5	Group 2	38.5	17.4	0.3	0.7	3520	119	0.10	35.5	24.1	0.47	0.40	0.36	1.3	0.11	66	1.3	0.15	1.9	0.29	1.05	14	51	5
Jagersfontein																										
JJG-2919	HREE-enriched	5	Group 2	15.4	22.4	0.3	0.8	18.5	588	3.36	45.6	43.8	3.02	0.26	0.6	0.6	0.56	34	2.7	11	0.5	6	0.40	143	10	13
		6	Group 2	18.3	18.8	0.1	1.2	59	567	2.84	25.0	46.0	2.60	0.19	0.56	0.8	1.63	45	1.3	7	0.7	5	0.32	165	10.2	12
JJG-2920	LREE-enriched	4	alt. Group 2	42	2.2	2.1	0.3	bdl	49	0.45	5.6	4.0	0.15	0.01	0.05	0.4	bdl	2	0.2	2	4.2	9	0.17	202	3.7	12
		5	Group 2	53.5	17.6	4.5	1.6	2.95	bdl	3.89	49.7	6.4	0.27	0.12	0.05	0.4	bdl	2	0.2	19	4.2	81	2.24	27	0.76	-
Sulphide standard data																										
Standard		n.	S	Fe	Ni	Cu	Co	As	Se	Pd	Ag	Te	Re	Os	Ir	Pt	Au	Pb	Bi	-		-	-	-		-
iS5b (referenc	MB 2014	20	27.87	3.26	67.37	1.18	-	51.8	101.1	152.8	2.2	109.4	35.4	81.3	80.4	93.5	8.4	62.1	97.7	-		-	-	-		-
1σ Glitter	-	-	0.37	0.8	1.78	0.24	-		39.8	5.9	0.2	33.9	2.7	5.9	5	5.3	2.6	3.3	4.3	-		-	-	-		-
iS5b (measure	this study	5	27.15	3.16	68.28	0.98	-	52.3	101.1	155.2	2.2	109.7	35.5	81.4	80.1	93.3	8.4	62.2	97.8	-		-	-	-		-
2σ Iolite	-	-	0.27	0.82	1.42	0.25	-	5.3	18.4	14.3	0.3	12.2	3.1	7.5	8.2	10.4	0.8	6.1	7.3	-		-	-	-		-
mdl	-	-	-	-	-	-	-	1.5	1.1	0.005	0.05	0.1	0.07	0.013	0.005	0.07	0.01	0.1	0.09	-		-	-	-		-
'arience (NiS5	%diff	-	-	-	-	-	-	0.8	-	1.6	-	0.3	0.4	0.2	0.3	0.2	-	0.1	0.1	-		-	-	-		-

Fe, Ni, Cu and Co are reported in wt.% and measured by SEM. Trace elements are reported in µg/g and measured by LA-ICP-MS. Normalisation values from Fischer-Gödde et al. (2010).

BMS grouping: Group 1 = Ni- and I-PGE poor sulphide compositions; Group 2 = relatively Ni- and PGE-enriched sulphide compositions; see **Sections 3.5.7.4 and 3.5.7.5** for detail.

NiS5b (reference) from Mungall and Brenan (2014) and Brenan (2015)

Isotopes used to measure each element = ^{75}As, ^{77}Se ^{106}Pd, ^{107}Ag, ^{125}Te, ^{185}Re, ^{189}Os, ^{193}Ir, ^{195}Pt, ^{197}Au, ^{208}Pb, ^{209}Bi.

Table 3.6. Thermobarometry, oxybarometry and garnet oxygen isotope compositions for the Kaapvaal eclogite xenoliths

Sample	Location	ME Group	TE Group	T_{EG79} (°C)	P_{B15} (GPa)	$T_{EG79\ (Geotherm)}$ (°C)	$P_{Geotherm}$ (GPa)	Δlog fO_2 (FMQ)	Grt $\delta^{18}O$ (‰)
ROVIC-MBK	Roberts Victor	Ky-gabbroic	LREE-depleted	-	-	1203	5.9	-2.8	6.6
MBK	Roberts Victor	Picritic	LREE-enriched	-	-	1050	4.1	-3.3	5.6
JJG-4492	Roberts Victor	Ky-grospydite	LREE-depleted	-	-	1176	5.7	-1.5	7.1
HRV-174A	Roberts Victor	Picritic	LREE-depleted	-	-	1164	5.6	-3.8	6.3
HRV-174B	Roberts Victor	Basaltic	HREE-enriched	-	-	1155	5.6	-2.3	3.4
HRV-162A	Roberts Victor	Gabbroic	LREE-depleted	-	-	1063	4.9	-3.8	6.1
HRV-162B	Roberts Victor	Gabbroic	LREE-depleted	-	-	1113	5.3	-3.9	6.5
HRV-161A	Roberts Victor	Picritic/ Phl-ecl.	LREE-enriched	1055	4.4	1063	4.6	-5.2	6.6
HRV-161B	Roberts Victor	Picritic/ Phl-ecl.	LREE-enriched	1019	3.4	1031	3.7	-4.7	6.6
HRV-172A	Roberts Victor	Basaltic	LREE-enriched	1085	4.8	1094	5.1	-4.1	6.1
HRV-172B	Roberts Victor	Ky-grospydite	LREE-depleted	-	-	1250	6.3	n/a	7.9
EJB-86	Roberts Victor	Gabbroic	LREE-depleted	-	-	1092	5.1	-3.6	6.2
JJG-2914	Jagersfontein	Picritic	LREE-enriched	-	-	1217	4.9	-4.2	6.5
JJG-2919	Jagersfontein	Basaltic	HREE-enriched	1107	5.3	1105	5.2	-4.6	6.4
JJG-2920	Jagersfontein	Picritic	LREE-enriched	-	-	985	3.8	-3.4	6.7
CIM15-101	Kamfersdam	Gab/bas	LREE-enriched	1089	6.6	1089	6.7	-5.3	7.6
CIM15-102	Kamfersdam	Picritic	LREE-enriched	-	-	1089	4.5	-3.7	5.9
ST16-H-04	Swartruggens	Pyroxenite	HREE-enriched	1078	5.5	-	-	n/a	10.4
JJG-2717	Premier	Basaltic	LREE-depleted	-	-	1128	4.5	n/a	6.1

P_{B15} calculated according to Beyer et al. (2015); T_{EG79} calculated using Ellis and Green (1979).

$P_{Geotherm}$ calculated iteratively from each localities peridotite defined geotherm (Grütter, 2009), see text for details.

Oxygen fugacity for all Kaapvaal xenoliths calculated after Stagno et al. (2015) with T_{EG79} and $P_{Geotherm}$; n/a = values not collected.

Oxygen isotope values are relative to VSMOW; 2σ for all analyses is ±0.1‰.

Table 3.7. Calculated whole-rock major and trace element compositions from Kaapvaal eclogite xenoliths

Sample	ROVIC-MBK	MBK	JJG-4492	HRV-174A	HRV-174B	HRV-162A	HRV-162B	HRV-161A	HRV-161B
ME group	Ky-gabbroic	Picritic	Ky-grospydite	Picritic	Basaltic	Gabbroic	Gabbroic	Picritic/ Phl-ecl.	Picritic/ Phl-ecl.
TE group	LREE-depleted	LREE-enriched	LREE-depleted	LREE-depleted	Sinusoidal	LREE-depleted	LREE-depleted	LREE-enriched	LREE-enriched
SiO_2	49.0	48.5	48.3	48.4	47.2	48.4	48.6	48.5	48.5
TiO_2	0.3	0.1	0.1	0.3	0.1	0.4	0.3	0.1	0.1
Al_2O_3	18.3	13.1	19.7	15.3	15.8	18.9	18.9	15.4	15.5
Cr_2O_3	0.1	0.4	0.01	0.1	0.02	0.02	0.02	0.2	0.2
FeO_t	7.6	7.7	6.4	9.8	11.9	9.1	9.3	7.5	7.6
MnO	0.2	0.3	0.1	0.3	0.3	0.2	0.2	0.1	0.02
MgO	11.3	17.0	6.9	13.4	8.9	11.2	10.4	15.9	16.0
CaO	9.7	11.5	15.0	9.3	13.0	7.5	8.7	9.0	9.2
Na_2O	3.7	1.5	4.0	2.6	2.6	4.3	4.3	2.4	2.4
K_2O	0.21	bdl	0.10	0.04	0.02	0.05	0.02	0.03	0.03
Total	100.5	100.2	100.5	99.7	99.9	100.0	100.6	99.2	99.5
Mg#	60	69	52	58	43	55	53	68	68
Sc	24	59	14	37	52	22	21	19	19
V	56	214	45	240	362	112	85	102	103
Co	44	39	31	44	54	45	44	33	33
Ni	52	156	94	146	160	138	122	93	91
Cu	1.6	0.5	3.4	4.3	4.8	4.2	6.2	1.3	1.0
Zn	57	14	72	42	81	100	99	50	49
Rb	16	0.05	1	0.02	0.2	1	0.3	0.1	0.1
Sr	15	152	89	141	9	91	68	414	422
Y	9.5	13.6	2.5	16.1	27.1	5.6	5.7	5.6	5.6
Zr	53	75	18	31	3	14	13	10	9
Nb	0.5	0.6	0.07	0.09	bdl	0.05	0.04	0.02	0.02
Cs	0.41	0.03	0.13	0.30	0.11	5.83	0.73	0.01	0.04
Ba	300	3	1356	1	1	101	25	1	4
La	0.8	3.6	0.2	0.7	0.01	0.4	0.3	6.2	6.4
Ce	1.5	12.8	0.9	3.1	0.04	1.5	1.2	19.6	20.2
Pr	0.2	2.2	0.2	0.6	0.03	0.3	0.2	3.0	3.0
Nd	1.4	12.2	1.7	3.6	0.3	1.9	1.6	13.7	14.1
Sm	0.8	3.7	1.0	1.4	0.4	0.9	0.8	2.4	2.5
Eu	0.4	1.2	0.6	0.6	0.3	0.5	0.5	0.7	0.7
Gd	1	4	1	2	1	1	1	2	2
Tb	0.3	0.5	0.1	0.3	0.4	0.2	0.2	0.2	0.2
Dy	1.7	2.8	0.5	2.5	3.8	1.0	1.0	1.2	1.2
Ho	0.4	0.5	0.1	0.6	1.0	0.2	0.2	0.2	0.2
Er	1.0	1.3	0.2	2.0	3.5	0.6	0.7	0.5	0.5
Tm	0.14	0.18	0.03	0.32	0.58	0.10	0.09	0.07	0.07
Yb	0.9	1.3	0.2	2.3	4.2	0.7	0.7	0.4	0.4
Lu	0.13	0.21	0.03	0.37	0.68	0.11	0.11	0.06	0.06
Hf	1.2	1.4	0.4	1	0.2	0.5	0.4	0.2	0.2
Ta	0.03	0.08	0.02	0.01	bdl	0.003	0.004	0.002	0.002
Pb	2.0	0.4	0.2	0.3	0.3	0.2	0.1	3.8	3.8
Th	0.17	0.13	0.004	0.01	0.002	0.03	0.02	0.17	0.16
U	0.10	0.02	0.01	0.005	bdl	0.004	0.004	0.02	0.02
Sm/Nd	0.56	0.31	0.57	0.39	1.33	0.46	0.46	0.18	0.18
Eu*	1.2	1.0	1.9	1.1	0.9	1.7	1.7	1.0	0.9
Sr*	0.7	0.8	4.0	2.7	2.4	3.4	3.0	1.8	1.8

Major element concentrations in wt. %; Trace element concentrations in ppm; bdl = below detection limit

Eu* is calculated using Chondrite C1 normalized values from McDonough and Sun (1995); Sr* is calculated using primitive mantle 'pyrolite' normalized values from McDonough and Sun (1995).

ME group = Major element group; Ky-gabbroic, Phl-eclogite, Basaltic, Gabbroic, Picritic; TE group = trace element classification; LREE-depleted, LREE-enriched, HREE-enriched

Major element concentrations in wt. %; Trace element concentrations in ppm; bdl = below detection limit

Mineral proportions; eclogites = 50% Grt + 50% Cpx, pyroxenite = 20% Grt + 80% Cpx.

Table 3.7. Calculated whole-rock major and trace element compositions from Kaapvaal eclogite xenoliths (continued)

Sample	HRV-172A	HRV-172B	EJB-86	JJG-2914	JJG-2919	JJG-2920	CIM15-101	CIM15-102	ST16-H-04	JJG-2717
ME group	Basaltic	Ky-grospydite	Gabbroic	Picritic	Basaltic	Picritic	Gab/bas	Picritic	Pyroxenite	Basaltic
TE group	LREE-enriched	LREE-depleted	LREE-depleted	Sinusoidal	Sinusoidal	LREE-enriched	LREE-enriched	LREE-enriched	Sinusoidal	LREE-depleted
SiO_2	48.5	47.9	48.1	48.3	48.5	46.7	48.2	48.5	52.8	46.5
TiO_2	0.3	0.4	0.3	0.1	0.2	0.4	0.1	0.0	0.3	0.7
Al_2O_3	16.3	19.9	18.6	15.9	16.3	15.8	16.4	13.5	7.0	15.2
Cr_2O_3	0.03	0.01	0.1	0.03	0.02	0.03	0.02	0.2	0.01	bdl
FeO_t	8.3	7.9	8.8	9.3	10.2	10.4	12.0	6.2	5.6	9.6
MnO	0.2	0.2	0.1	0.3	0.3	0.3	0.3	0.3	0.2	0.3
MgO	12.7	6.4	8.9	14.1	13.0	13.1	11.4	17.7	15.5	12.7
CaO	11.2	13.3	11.4	9.2	8.9	11.4	8.6	12.4	16.7	13.6
Na_2O	2.5	4.1	3.9	2.7	2.9	1.8	3.0	1.1	1.9	1.4
K_2O	0.08	0.12	0.19	bdl	bdl	0.26	bdl	bdl	0.03	0.19
Total	100.1	100.3	100.4	99.8	100.3	100.1	100.0	99.8	100.1	100.3
Mg#	60	45	50	60	56	56	49	74	73	57
Sc	16	15	20	37	46	32	31	42	30	51
V	134	89	230	214	361	422	219	281	223	140
Co	58	31	41	40	57	38	44	28	32	80
Ni	433	116	274	63	162	82	93	94	166	110
Cu	6.9	1.5	5.0	0.7	4.7	2.3	1.2	0.2	1.4	4.2
Zn	104	102	91	25	81	111	98	10	55	67
Rb	3	3	3	0.01	0.01	18	bdl	0.11	0.03	353
Sr	123	127	136	147	8	731	257	405	313	240
Y	12.6	8.0	10.4	15.1	27.8	14.1	11.0	18.2	11.9	28.1
Zr	54	33	58	57	3	28	10	43	32	79
Nb	1.94	0.15	0.08	0.44	bdl	0.7	0.2	0.6	0.2	5
Cs	59	9	3.13	bdl	bdl	0.50	bdl	0.38	0.06	5
Ba	190	530	266	bdl	bdl	79	0	9	3	1687
La	7.3	0.5	0.6	1.5	bdl	1.4	1.5	6.4	2.5	4
Ce	15.2	1.8	2.2	7.3	0.05	3.6	7.3	28.5	12.8	5
Pr	1.9	0.4	0.4	1.5	0.02	0.6	1.5	5.0	2.6	0.6
Nd	8.5	2.9	3.2	9.1	0.3	3.1	8.9	23.6	12.1	3.7
Sm	2.5	1.3	1.7	2.5	0.5	1.0	2.7	3.5	2.0	3.6
Eu	0.9	0.6	0.7	0.9	0.3	0.7	1.0	0.8	0.6	2.0
Gd	3	2	2	3	2	2	3	2	2	8
Tb	0.5	0.3	0.3	0.4	0.4	0.3	0.4	0.4	0.3	1.2
Dy	2.7	1.6	2.0	2.3	3.8	2.3	2.2	2.8	2.0	6.5
Ho	0.5	0.3	0.4	0.5	1.0	0.5	0.4	0.7	0.5	1.1
Er	1.1	0.8	1.1	1.8	3.5	1.6	1.2	2.2	1.4	2.4
Tm	0.14	0.12	0.15	0.26	0.57	0.25	0.18	0.34	0.20	0.28
Yb	0.9	0.8	1.1	2.2	4.3	1.7	1.2	2.4	1.4	1.7
Lu	0.12	0.13	0.16	0.25	0.65	0.26	0.18	0.37	0.21	0.22
Hf	1.6	1.0	1.7	1.3	0.2	0.7	0.3	1.5	1.4	1.1
Ta	0.10	0.01	0.01	0.09	bdl	0.05	0.01	0.02	0.02	0.21
Pb	0.6	0.1	0.6	0.2	0.01	1.5	0.2	1.4	0.8	0.6
Th	0.67	0.03	0.01	0.02	bdl	0.19	0.01	0.45	0.02	0.16
U	0.18	0.01	0.01	0.01	bdl	0.14	0.01	0.03	0.01	0.07
Sm/Nd	0.30	0.45	0.53	0.27	1.40	0.33	0.30	0.15	0.16	0.99
Eu*	1.0	1.3	1.1	1.1	0.9	1.5	1.1	0.9	0.9	1.1
Sr*	0.9	3.2	3.2	1.1	2.4	15.5	2.0	1.1	1.6	4.6

Major element concentrations in wt. %; Trace element concentrations in ppm; bdl = below detection limit

Eu* is calculated using Chondrite C1 normalized values from McDonough and Sun (1995); Sr* is calculated using primitive mantle 'pyrolite' normalized values from McDonough and Sun (1995).

ME group = Major element group; Ky-gabbroic, Phl-eclogite, Basaltic, Gabbroic, Picritic; TE group = trace element classification; LREE-depleted, LREE-enriched, HREE-enriched

Major element concentrations in wt. %; Trace element concentrations in ppm; bdl = below detection limit

Mineral proportions; eclogites = 50% Grt + 50% Cpx, pyroxenite = 20% Grt + 80% Cpx.

CHAPTER 3: FIGURES

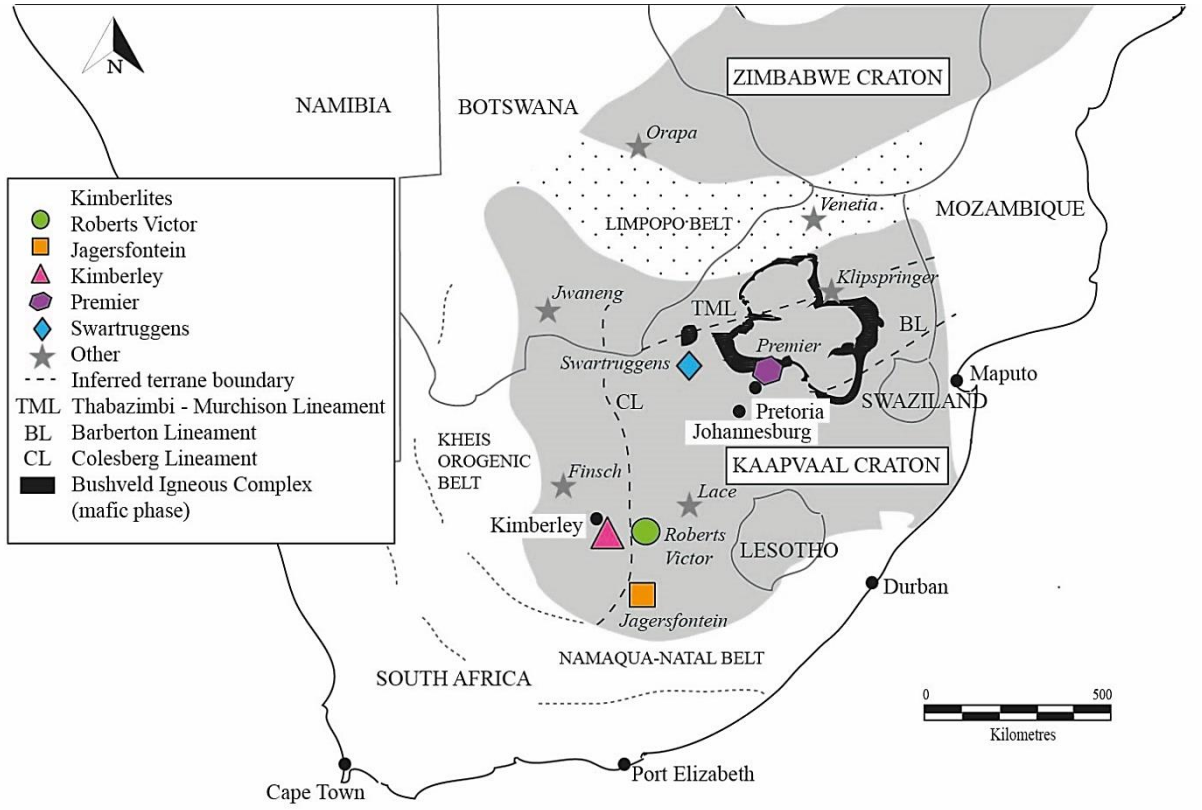

Fig. 3.1 *Schematic of the Kaapvaal craton modified after Friese et al. (2003). The Kaapvaal craton is subdivided into the Kimberley (western) and Witwatersrand (eastern) blocks along the Colesberg Lineament. Eclogite xenoliths are sampled from five kimberlite localities; Kimberley (Kamfersdam), Roberts Victor and Jagersfontein are situated close to the southern edge of the craton near the town of Kimberley, and Premier and Swartruggens are located in the north-central part of the craton near the western limb of the Bushveld complex.*

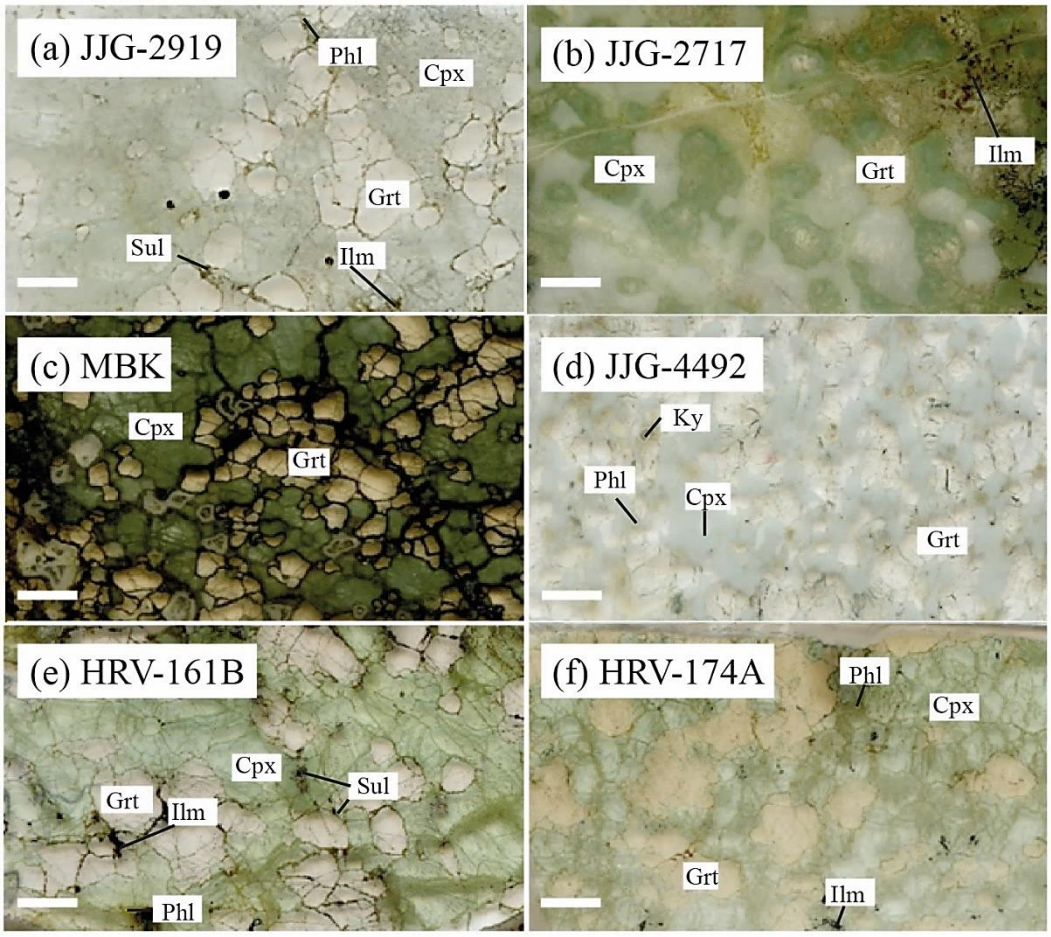

Fig. 3.2 *Select Kaapvaal Craton mantle eclogite xenoliths:* ***(a)*** *Jagersfontein,* ***(b)*** *Premier,* ***(c)****,* ***(d)****,* ***(e)*** *and* ***(f)*** *Roberts Victor. Scale bar = 5mm. Grt = garnet, Cpx = clinopyroxene, Phl = phlogopite, Ilm = ilmenite, Sul = sulphide, Ky = kyanite.*

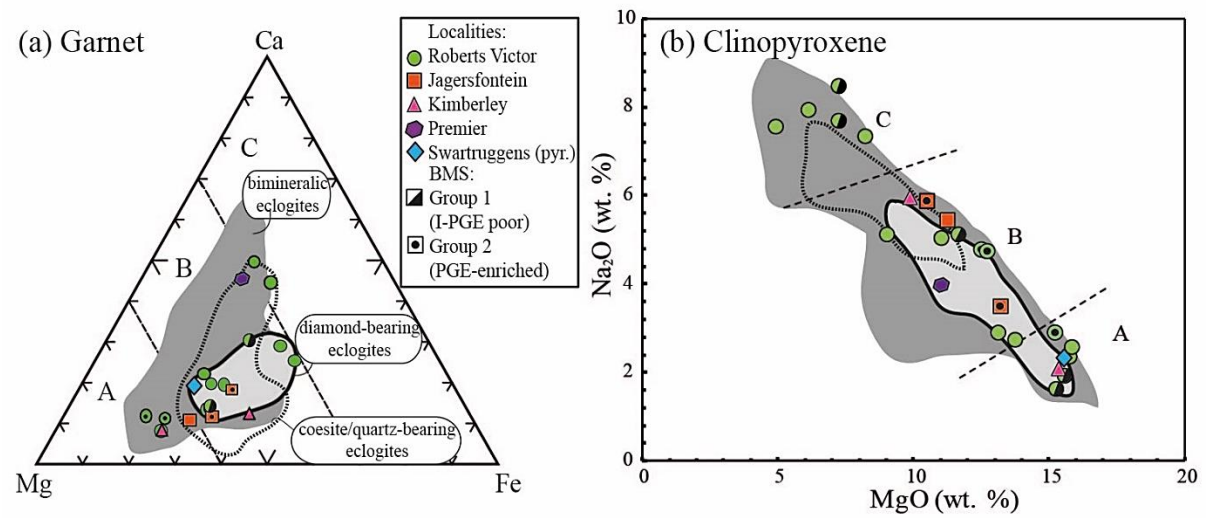

Fig. 3.3 (a) *Ternary Ca-Mg-Fe compositions of the Kaapvaal eclogite garnets. A-B-C classification scheme from Coleman et al. (1965). Swartruggens (pyr.) = pyroxenite. Dark-grey field: bimineralic eclogites from Roberts Victor kimberlite (Harte and Kirkley, 1997; Schulze et al., 2000; Jacob, 2004), Jagersfontein (Pyle and Haggerty 1998; Jacob 2004). Light grey field: diamond-bearing eclogites from Roberts victor (MacGregor and Manton, 1986; McCandless and Gurney, 1989; Jacob, 2004; Gréau et al., 2011; Riches et al., 2016). Dashed field: coesite/quartz-bearing eclogites from Roberts Victor (Schulze et al., 2000; Jacob et al., 2003, 2005).* ***(b)*** *Na_2O vs. MgO (wt. %) contents of clinopyroxene. A-B-C classification from Taylor and Neal (1989) and shading as described in (a). Reconstructed sulphide HSE trace element groupings (marked in symbols) are described in the text (see* ***Section 3.5.7.4****) and depicted in* ***Fig. 3.14****. Symbols without any shading represent samples that either do not contain sulphides or contain sulphides that are not classified.*

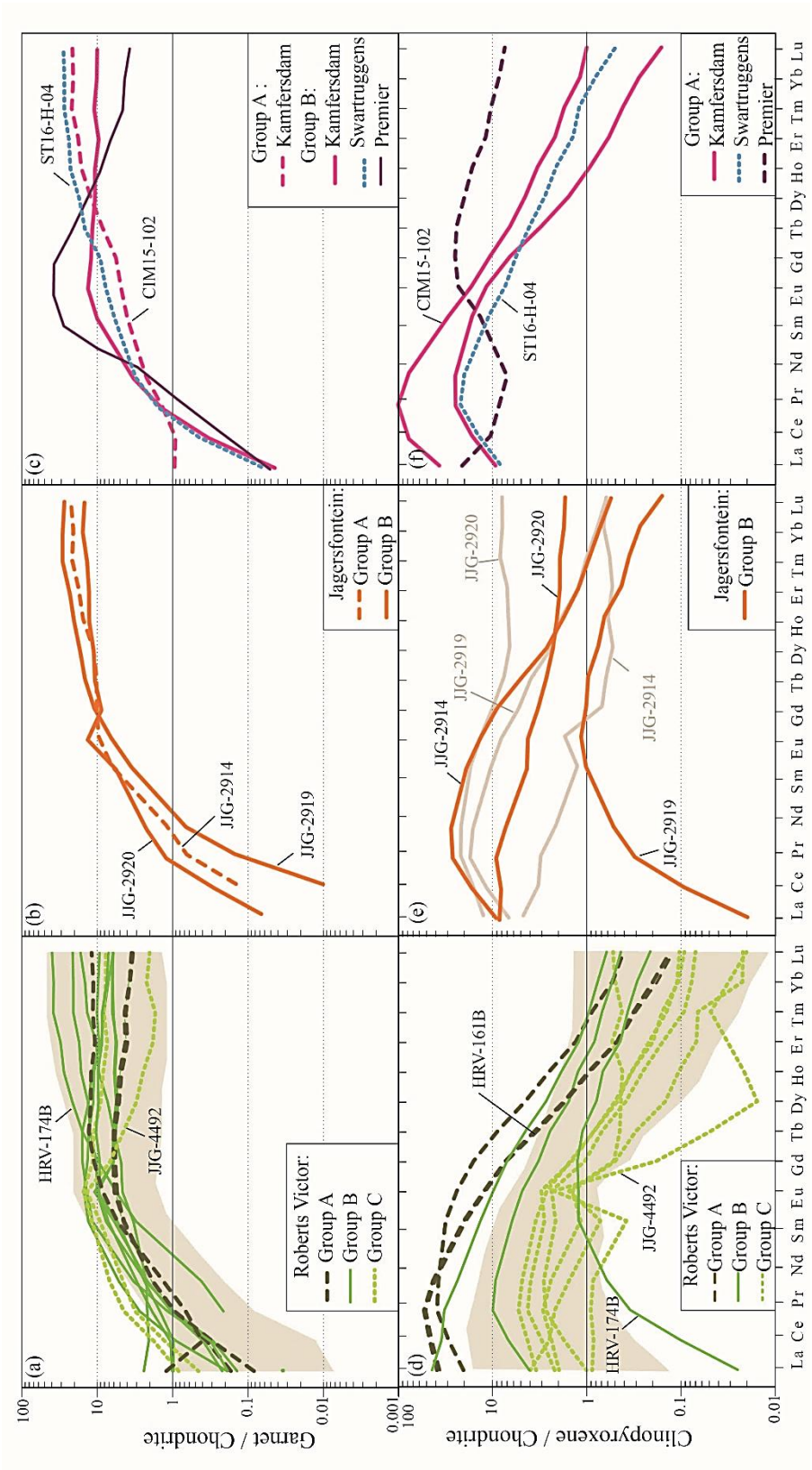

Fig. 3.4 *Chondrite normalised REE patterns for garnet (**a - c**) and clinopyroxene (**d - f**) from the Kaapvaal eclogite xenoliths. Garnets are split into the A-B-C classification scheme of (Coleman et al., 1965) and clinopyroxene after Taylor and Neal (1989). Normalising values are from McDonough and Sun (1995). Typical worldwide eclogitic garnet and clinopyroxene compositions are depicted by the grey field (Jacob, 2004). Select Jagersfontein secondary clinopyroxene REE patterns are depicted as grey lines in panel **(e)**.*

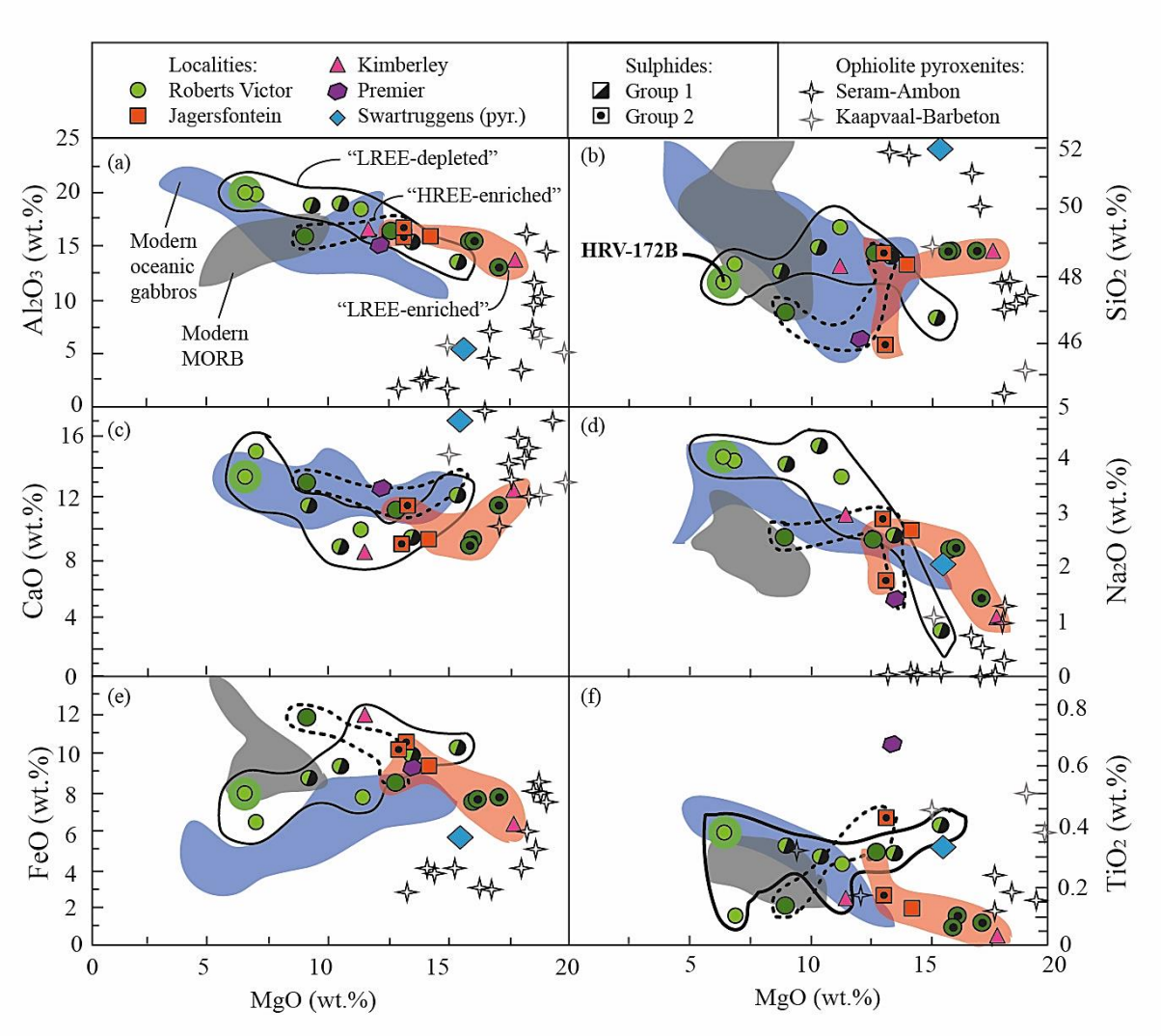

Fig. 3.5 *Multi-element variation diagrams showing the calculated bulk-rock compositions of the Kaapvaal eclogites.* ***(a)*** *MgO vs. Al_2O_3;* ***(b)*** *vs. SiO_2;* ***(c)*** *vs. CaO;* ***(d)*** *vs. Na_2O;* ***(e)*** *vs. FeO;* ***(f)*** *vs. TiO_2. Trace element classes indicated in panel* ***(a)****. The green shading on HRV-172B (indicated in panel b) shows the variation in modal mineral abundances by 10%. Shown for comparison is a field of modern oceanic gabbros from Bach et al. (2001), modern MORB from Jenner and O'Neill, (2012), and pyroxenites from ophiolites (de Wit et al., 2004; Monnier et al., 2003).*

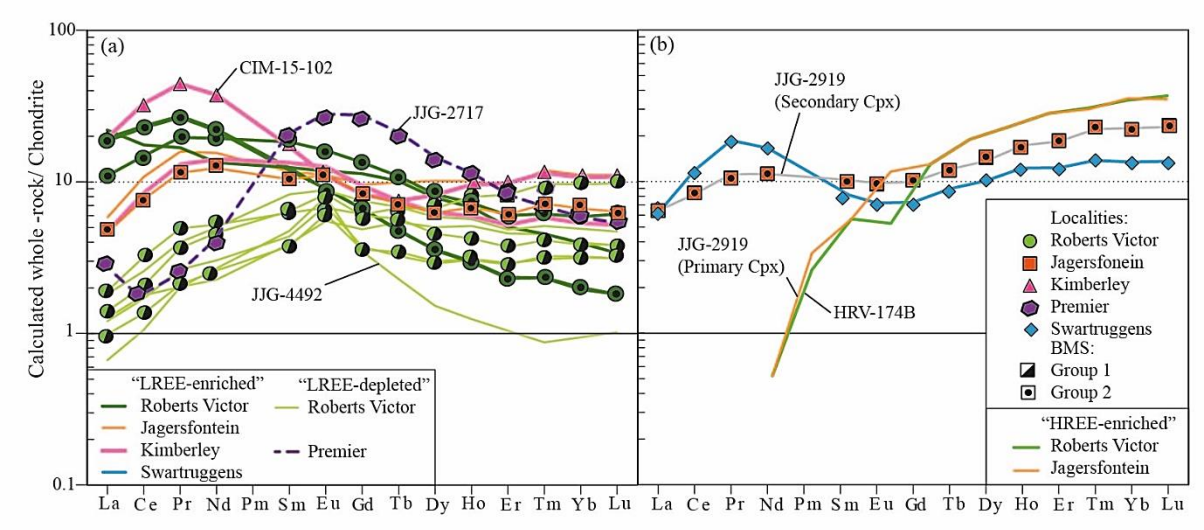

Fig. 3.6 *Calculated whole-rock REE patterns of the Kaapvaal eclogite xenoliths. The Kaapvaal xenoliths are grouped according to bulk-rock REE patterns; (a) "LREE-enriched", "LREE-depleted" and (b) "HREE-enriched" (see text for details). The whole-rock REE pattern for JJG-2919 from Jagersfontein has been calculated using secondary clinopyroxene, see* ***Section 3.5.3.2*** *for details. Chondrite normalising values are from McDonough and Sun (1995).*

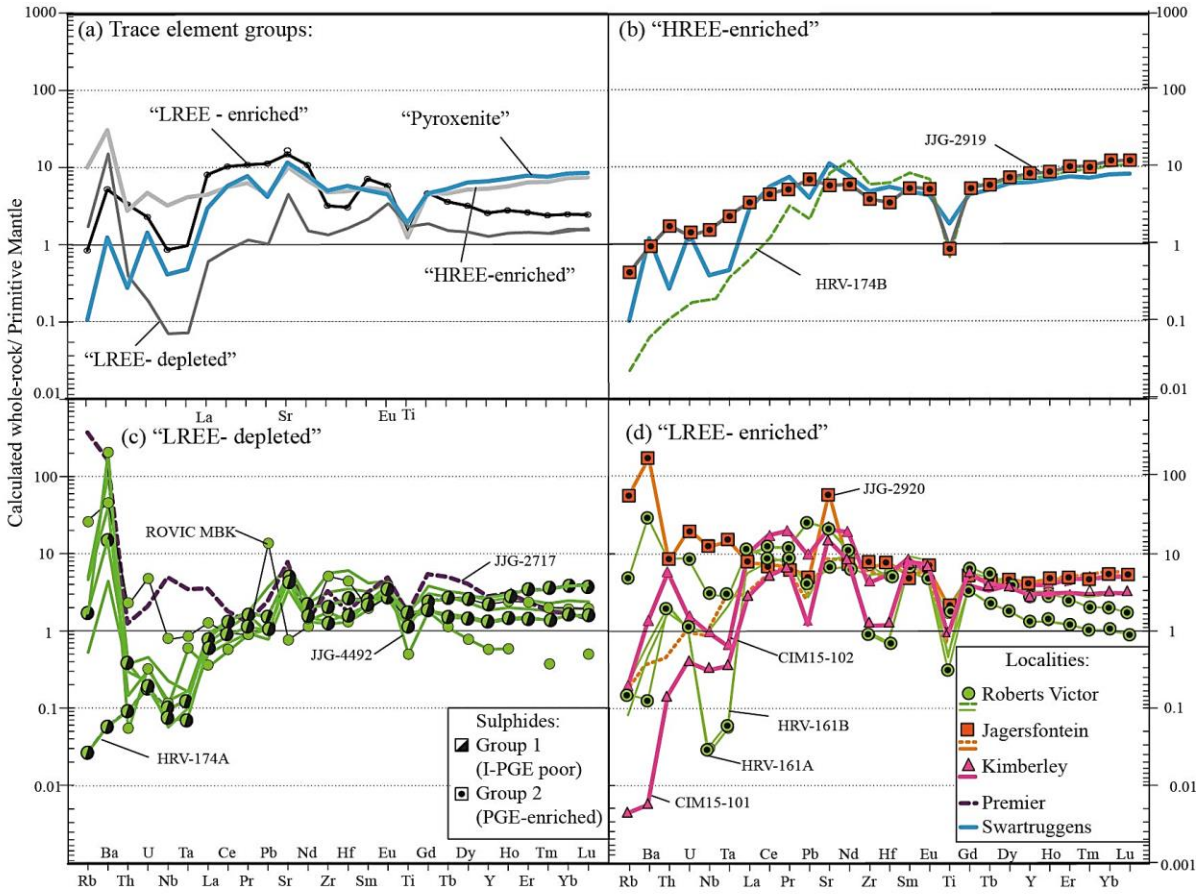

Fig. 3.7 *Calculated whole-rock trace-element patterns of the Kaapvaal craton eclogite xenoliths. The three trace element groupings are from* ***Fig. 6****;* ***(a)*** *average pattern for each trace element group,* ***(b)*** *"HREE-enriched",* ***(c)*** *"LREE-depleted",* ***(d)*** *"LREE-enriched". Primitive mantle normalizing values from McDonough and Sun (1995). Sulphide groups are described in the text and shown on* ***Fig. 3.14****.*

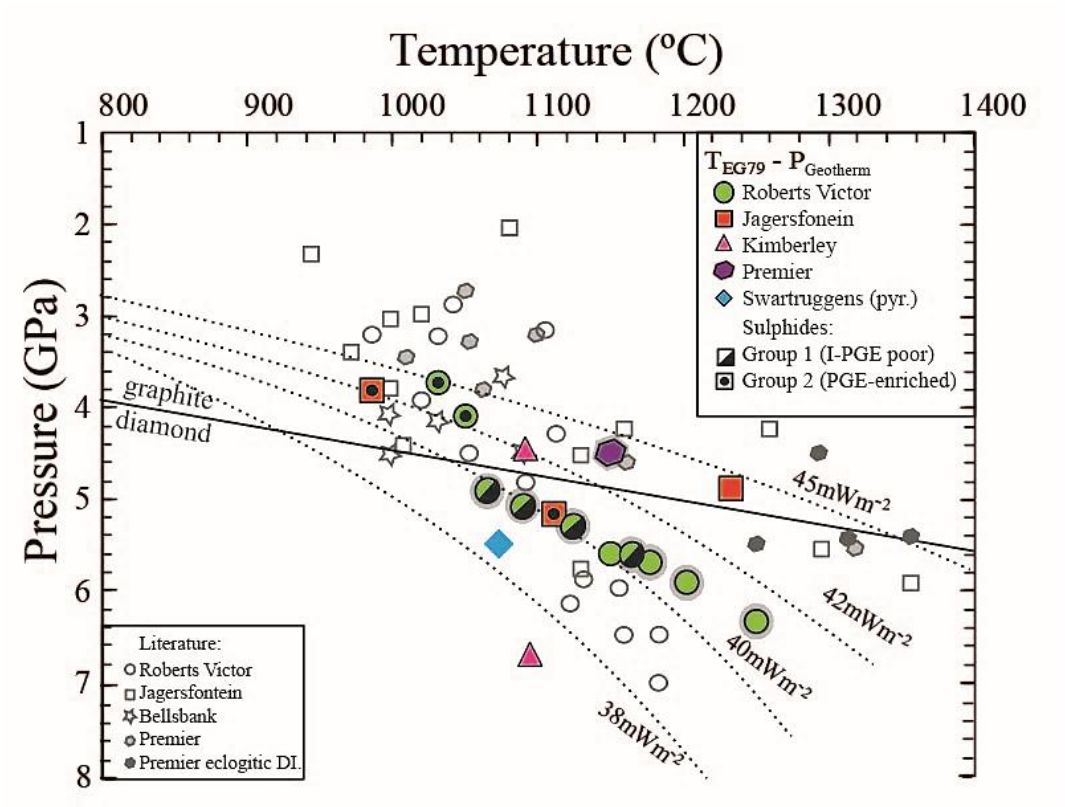

Fig. 3.8 *Estimated pressure-temperature conditions for the Kaapvaal xenoliths. The depicted eclogite P-T array, uses iterative calculations of T_{EG79} and locality-specific peridotite-defined geotherms ($P_{Geotherm}$) of Pearson et al. (1995), Grütter, 2009, Katayama et al. (2009) and Viljoen et al. (2009), see text for details. The temperature and pressure estimate of the Swartruggens pyroxenite was iteratively calculated using $T_{EG79} – P_{B15}$ because there is no geotherm available. Shown for comparison are calculated $P_{B15} – T_{EG79}$ estimates of eclogites; Roberts Victor (Carswell et al., 1981; O'Reilly and Griffin, 1995; Schulze et al., 2000; Jacob 2005), Jagersfontein (Pyle and Haggerty, 1998; Jacob, 2004), Bellsbank (Carswell et al., 1981) and Premier (Dludla et al., 2006), eclogite diamond inclusions from Premier (Viljoen et al., 2010). The graphite-diamond transition is from (Kennedy and Kennedy, 1976). Model conductive geotherms from Pollack and Chapman (1977).*

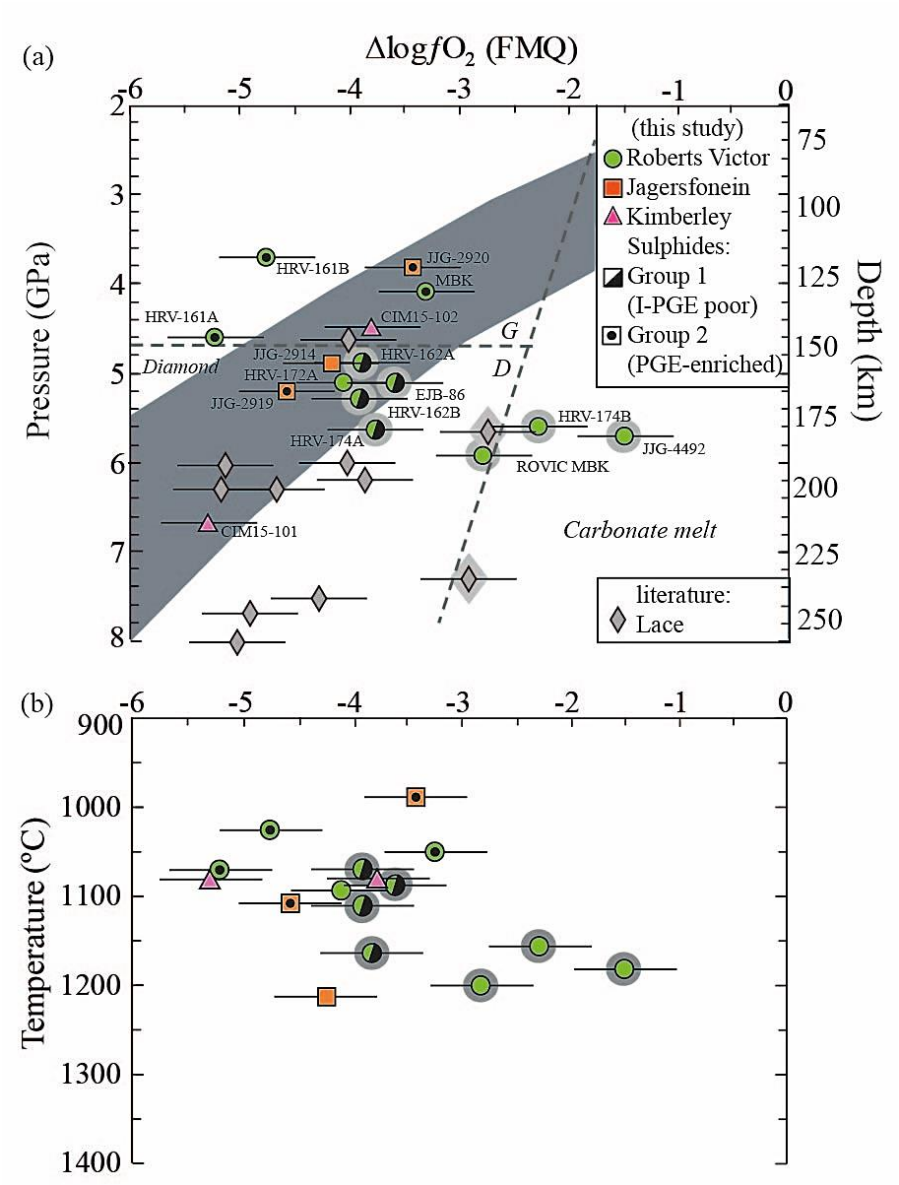

Fig. 3.9 *Oxybarometry of the Kaapvaal eclogite xenoliths.* ***(a)*** *$\Delta Log fO_2$ values (relative to the FMQ buffer) calculated after Stagno et al. (2015) using the $P_{Geotherm}$ values in* ***Table 3.6****. Dark grey field indicates the $log fO_2$ values from Kaapvaal peridotites (Woodland and Koch, 2003; Creighton et al., 2009). Light-grey halos indicate LREE-depleted samples. The carbonate melt, diamond (D) and graphite (G) fields are from Stagno et al. (2015).* ***(b)*** *T_{EG79} and $\Delta log fO_2$ (FMQ). For comparison, Lace eclogite redox data calculated after Stagno et al. (2015) from Aulbach et al. (2017b).*

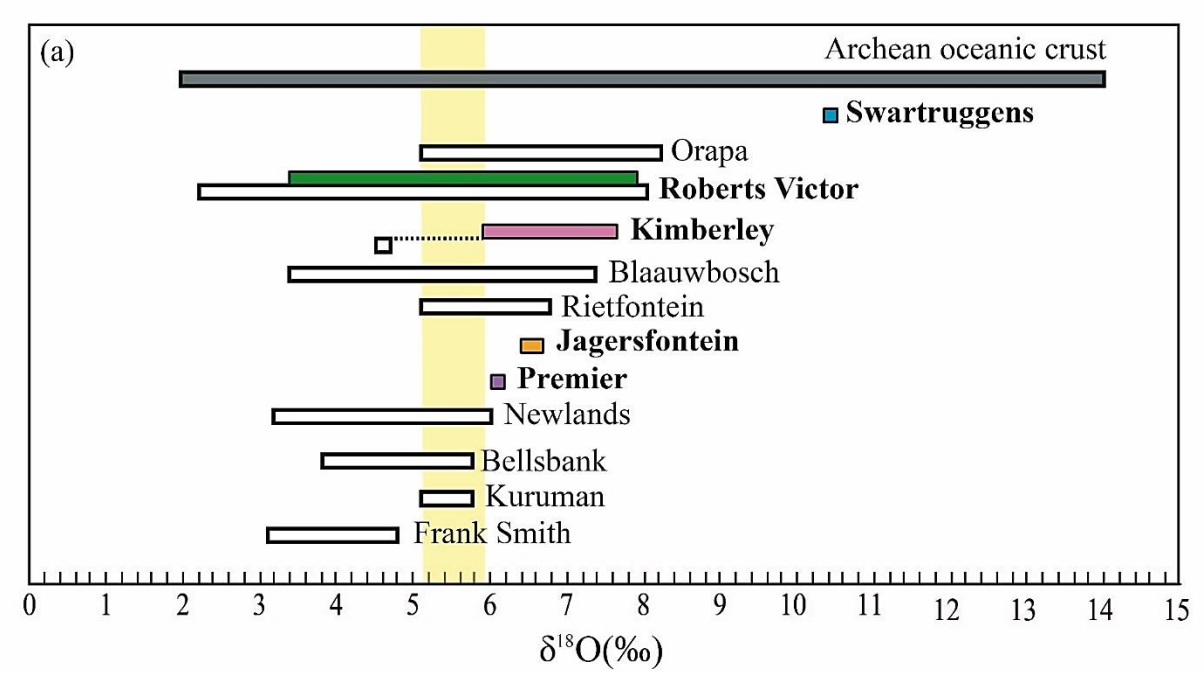

Fig. 3.10 (a) *Oxygen isotope compositions of garnet from Kaapvaal eclogite xenoliths. Archean oceanic crust values taken from >3 Ga mafic rocks from Kaapvaal greenstone belts (Gregory and Taylor 1981; de Wit et al. 2004). Average mantle $\delta^{18}O$ composition of 5.5‰ $\pm$0.4 from Mattey et al. (1994). Coloured bars indicate garnet oxygen isotope compositions measured in this study, and "open" bars indicate values from previous studies of Roberts Victor (MacGregor and Manton, 1986; Schulze et al., 2000; Jacob et al., 2004); Kimberley (Jacob et al., 2009); Bellsbank (Neal et al., 1990); Blaauwbosch (Schulze et al., 2003); Newlands (Schulze et al., 2003); Kuruman (Schmickler et al,. 2004); Rietfontein (Appleyard, 2003); Orapa (Viljoen et al., 1996); and Frank Smith (Schulze et al., 2003) eclogites.*

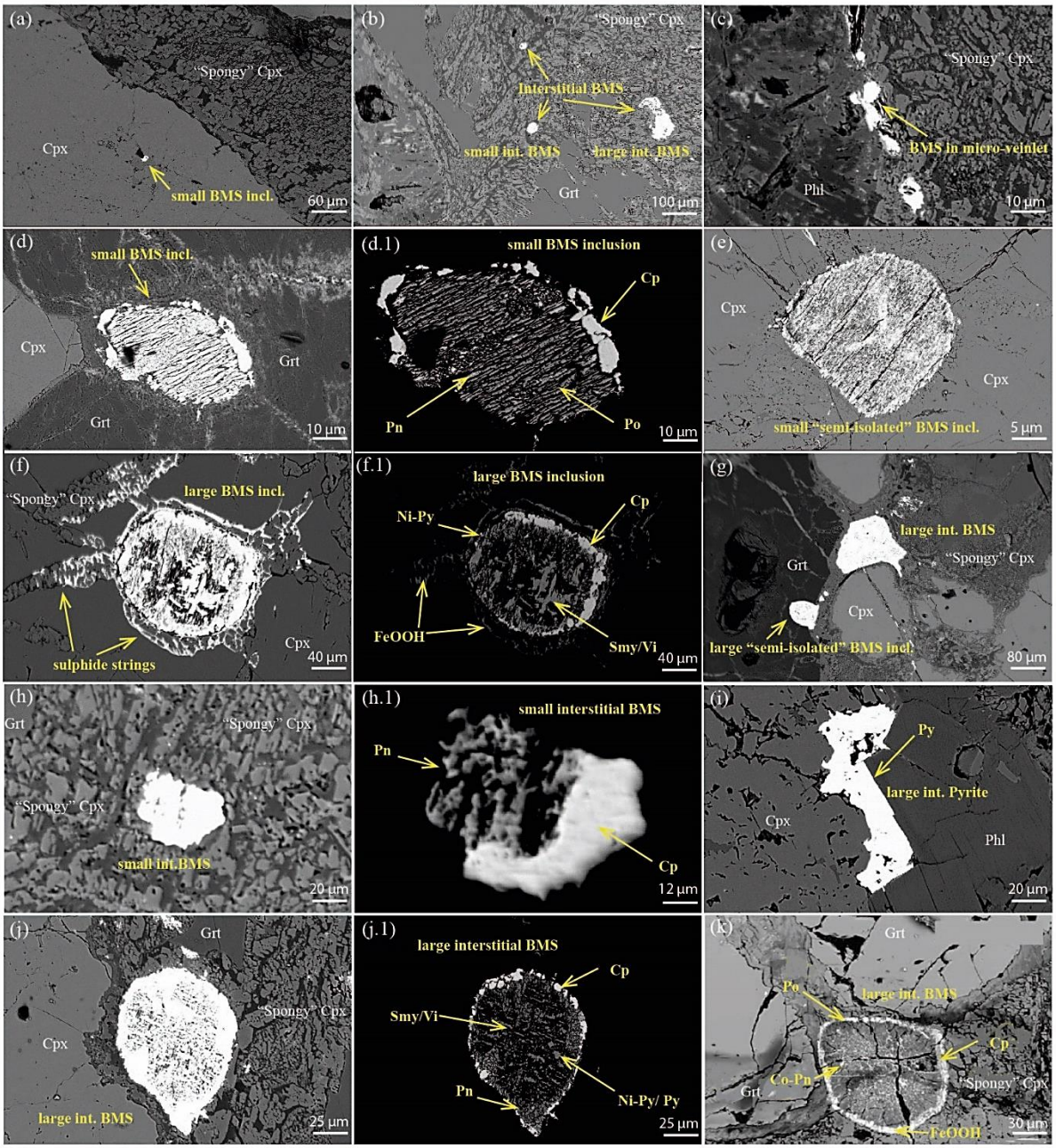

Fig. 3.11 *Select back-scattered electron images of base metal sulphides from the Kaapvaal eclogites. The BMS grains are sub-divided into both small and large "semi-isolated" inclusion grains as well as small and large interstitial grains (**a, b, c**), **see Section 3.5.7.2** for details. The BMS display both patchy (**d, f, h**) and fish-net-like (**e, g, j, k**) exsolution textures, which comprise various re-equilibrated low-temperature sulphide phases including chalcopyrite (Cp), pentlandite (Pn/ Co-Pn), pyrrhotite (Po), pyrite (Py/ Ni-Py), as well as 'altered' sulphide phases smythite and violarite. The interstitial BMS contain higher proportions of 'altered sulphide' and are commonly replaced by iron-(oxy)hydroxide (f, k) and magnetite phases.*

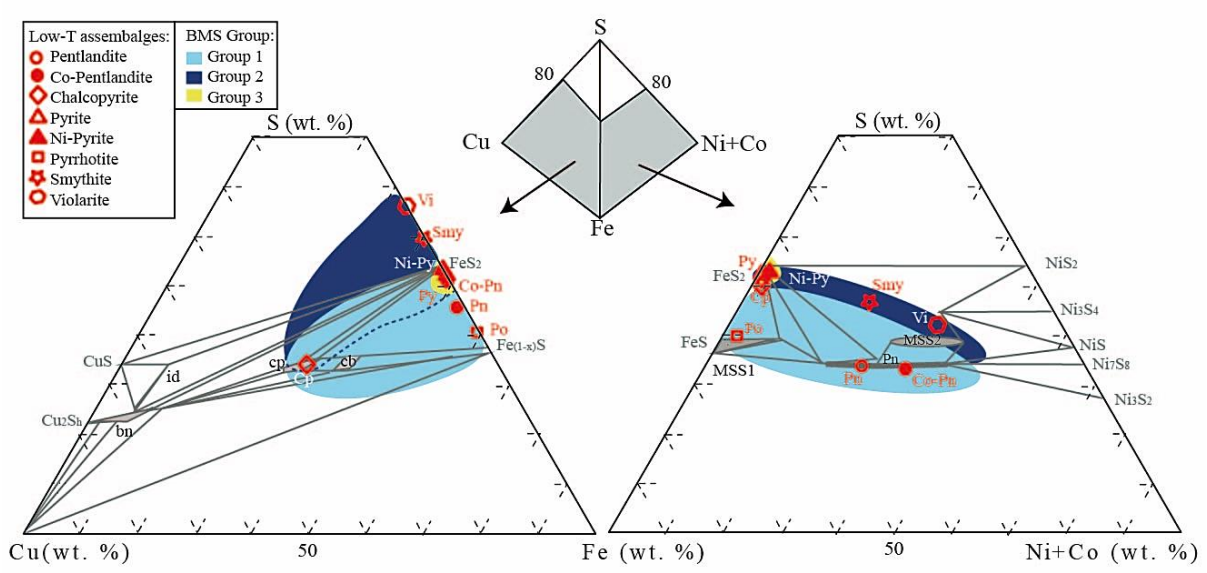

Fig. 3.12 *Kaapvaal eclogite low-temperature sulphide compositions in the Cu-Fe-Ni-S system at 300 ºC after Yund and Kullerud (1966) and Craig (1973). Representative low-temperature sulphide major element compositions from* ***Table 3.2*** *are plotted on the ternary diagrams including the "altered sulphide" phases smythite and violarite (see* ***Section 3.5.7.3****). BMS compositional Groups 1, 2, and 3 are defined in* ***Section 3.5.7.3****. The low-temperature "altered sulphide" phases are more prevalent in Group 2 base metal sulphides (dark-blue field) than in Group 1 (light-blue field; see* ***Section 3.5.7.4*** *for details). Group 3 BMS comprises large interstitial pyrite grains (see* ***Section 3.5.7.4****).*

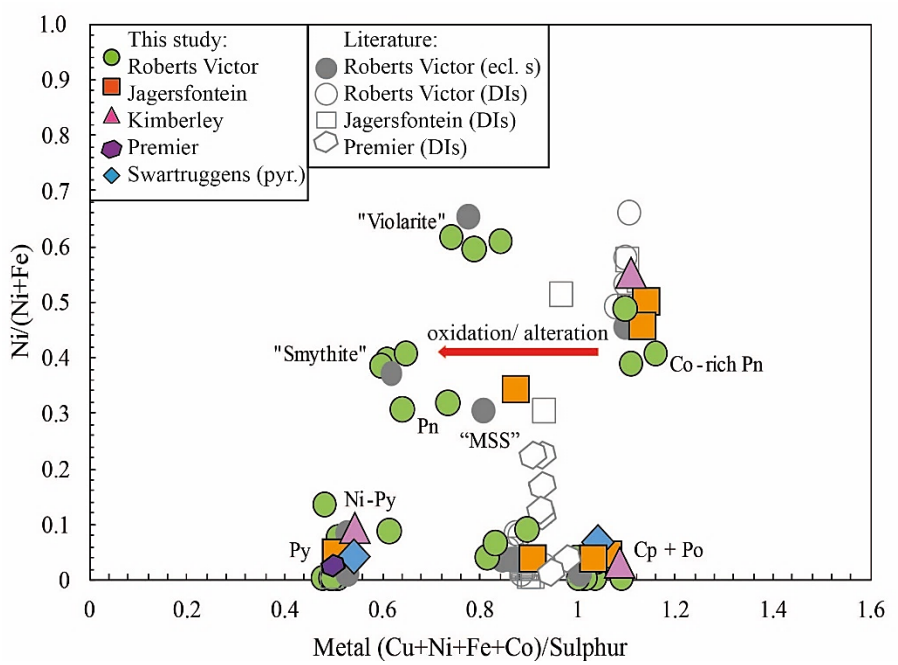

Fig. 3.13 *Ni/(Ni+Fe) at. % vs. Metal/Sulphur at. % of low-temperature sulphide phases. Pyrrhotite (Fe_7S_8), pentlandite ($(Fe, Ni)_9S_8$), chalcopyrite ($CuFeS_2$), pyrite ($(Fe,Ni)S_2$), and 'altered sulphide' (e.g. smythite/violarite). Shown for comparison are sulphides previously described for Roberts Victor eclogitic xenoliths (Gréau et al., 2013), and Roberts Victor, Jagersfontein and Premier diamond-included (DIs) sulphides (e.g. Deines and Harris, 1995)*

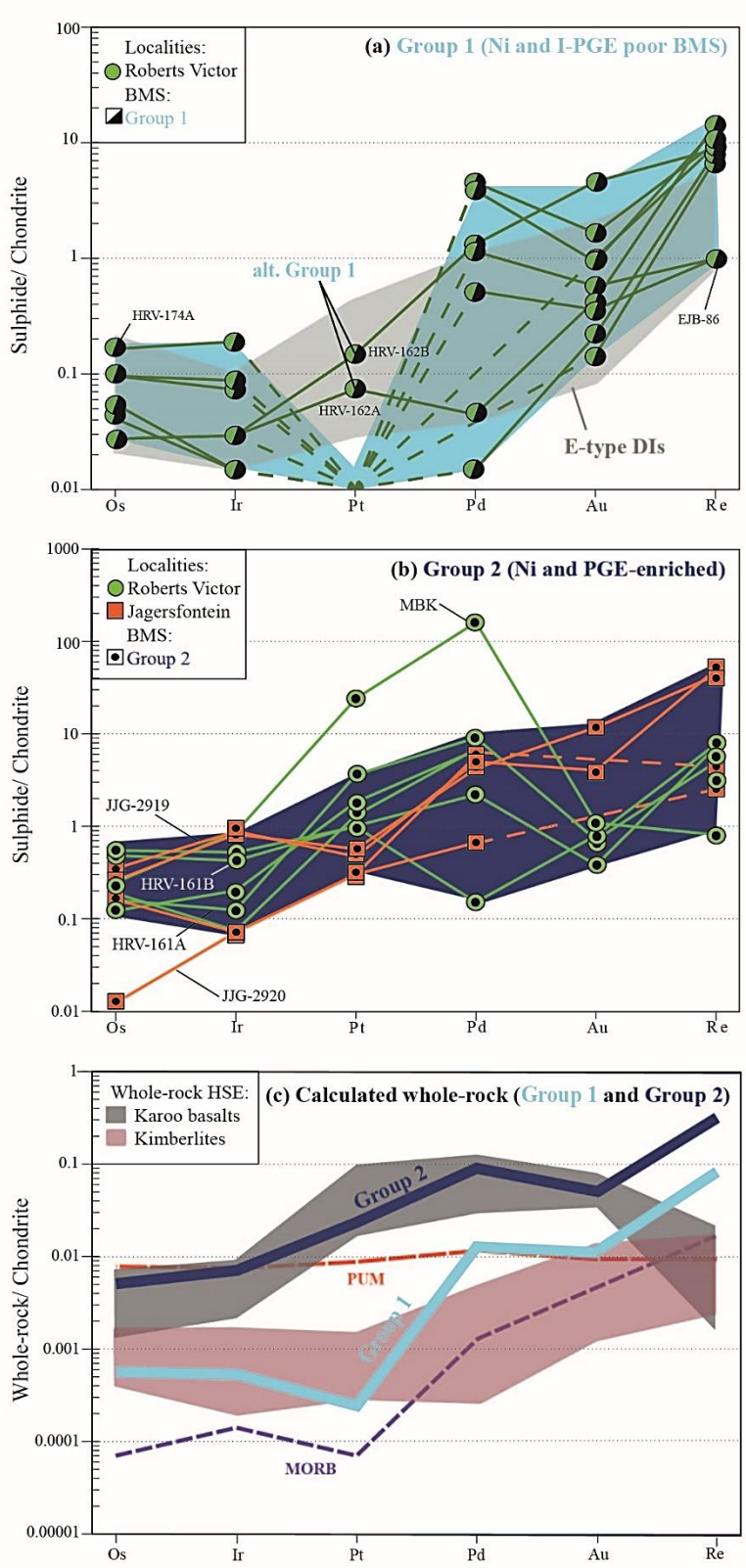

Fig. 3.14 *In-situ chondrite normalised (Fischer-Gödde et al., 2010) HSE patterns for (a) Group 1 and (b) Group 2 base metal sulphides derived from the Kaapvaal eclogites (see* ***Section 3.5.7.4****;* ***Fig. 3.12****). Shown for comparison in* ***(a)*** *are sulphide inclusions from E-type diamonds (grey field; Aulbach et al., 2012).* ***(c)*** *Chondrite normalised calculated whole-rock HSE patterns for the Kaapvaal eclogites (see* ***Section 3.6.2*** *for detail), grouped according to average sulphide HSE contents for Group 1 and Group 2 BMS (see* ***Section 3.5.7****). Shown for comparison are whole-rock HSE contents of Karoo basalts (Maier et al., 2003; Zhang et al., 2008) and global kimberlites (Maier et al., 2017; Tappe et al., 2017), as well as the primitive upper mantle (PUM = Red dashed line; Becker et al., 2006) and MORB (Purple dashed line; Bézos et al., 2005; Day, 2013).*

CHAPTER 4

4. PRESENTATION OF THE RESEARCH PAPER

"PERVASIVE FE- AND S-RICH METASOMATISM OF THE CRATONIC LITHOSPHERIC MANTLE BELOW PREMIER KIMBERLITE, SOUTH AFRICA"

This research paper is prepared for publication in Chemical Geology by the authors:

S. Burness, University of the Witwatersrand (primary author, conducted the research)

K.A. Smart, University of the Witwatersrand (supervisor, reviewed the manuscript)

S. Tappe, University of Johannesburg (provided certain samples, reviewed the manuscript)

E. Thomassot, University of Laurraine (SIMS analysis)

G. Stevens, University of Stellenbosch (supervisor, funding)

A detailed study was conducted of 11 peridoite xenoliths from the Premier kimberlite located on the western limb of the Bushveld Igneous Complex, South Africa, with the main purpose to investigate the occurrence of sulphide phases within the peridotitic portions of the lithospheric mantle. We report detailed textural, mineralogical and chemical (major and minor element) investigations of both the silicate mineral assemblage and base metal sulphides of four coarse-lherzolites and seven deformed-lherzolites. These data are complemented by multiple sulphur isotope compositions (specifically $\delta^{34}S$ and $\Delta^{33}S$) calculated from measurements attained through secondary-ion mass spectrometry. This new data demonstrates that the distribution of sulphides and their economically important trace metal contents within the peridotitic portion of the lithospheric mantle below Premier is linked to partial melting and importantly metasomatic overprinting by Fe-rich basaltic-type fluids possibly related to BIC magmas. This study has implications for the sulphur budget of the lithospheric mantle, and for studies that aim to constrain the source regions of crustally-hosted orthomagmatic ore deposits like the Bushveld Igneous Complex.

This manuscript contains new, original work that has not been previously published or submitted elsewhere. All aspects of the sample preparation, data acquisitions and calculations were conducted by me under the supervision of Katie Smart. I wrote the manuscript and created all the diagrams. K. A. participated in the writing as a second author. S. Tappe provided research samples from the Cullinan diamond mine. E. Thomassot analysed the base metal sulphides for multiple sulphur isotopes using secondary-ion mass spectrometry. G. Stevens made available analytical equipment and funding.

Chemical Geology, Impact factor: 3.57

ABSTRACT

Highly metasomatised garnet-bearing lherzolite xenoliths were recovered from the Premier kimberlite located on the western limb of the Bushveld complex, South Africa. We report detailed textural, mineralogical and chemical investigations of both the silicate mineral assemblage and base metal sulphides of four coarse lherzolites and seven deformed lherzolites. The xenoliths were selected based on the presence of modal metasomatic features such as the presence of secondary clinopyroxene and base metal sulphides. Specifically, cryptic metasomatism resulted in the enrichment of incompatible elements (notably LILE, REE and metals) to Fe-rich garnet, clinopyroxene, orthopyroxene and olivine mineral phases. Whereas, modal metasomatism resulted in the addition of secondary clinopyroxene and significant sulphide and associated magnetite alteration products. Base metal sulphides display large compositional heterogeneity and either occur as inclusions in silicate mineral phases or as interstitial grains. Very few sulphide phases likely represent residual primary sulphide melts (i.e. pentlandite ± pyrrhotite ± mono-sulphide solid solution), and the majority of BMS is considered either metasomatically altered or purely metasomatic in origin. Highly siderophile element (HSE) and Se–Te (telluride) systematics of select coarse-lherzolite sulphides allow us to make inferences about the metasomatic history of these rocks. Specifically, the highly suprachondritic fractionations (i.e. Pt/Ir, Pd/Ir, and Re/Pd ratios) defined by the Premier coarse-lherzolite sulphides cannot be interpreted purely in terms of partial melting models, and this evidence is the "smoking gun" for a strongly metasomatic origin of the Premier xenolith BMS. The sulphide HSE systematics are complemented by multiple sulphur isotope compositions, specifically $\delta^{34}S$ and $\Delta^{33}S$, which enables us to trace the presence of recycled sedimentary material and further address a possible genetic link between the Premier coarse-lherzolite sulphides studied here and sulphides present in ultramafic lithologies of the Bushveld Igneous Complex (BIC). Significantly, this genetic relationship may relate back to subduction-accretion Kaapvaal craton formation processes at 2.9 Ga, where significant crustal components were introduced into the CLM.

KEYWORDS: Bushveld Igneous Complex; chalcophile elements; deep volatile cycles; highly siderophile elements; cratonic mantle lithosphere; ore deposits

4.1. INTRODUCTION

Cratonic mantle-derived peridotite xenoliths brought to the surface by kimberlites provide unique opportunities to study the composition of the upper mantle but also to track the evolution of the cratonic mantle via metasomatic processes since its formation in the Archean (e.g. Pearson et al., 1995; Griffin et al., 2003a). Due to the ubiquitous melt-depleted character of the cratonic lithospheric mantle (Carlson et al., 2005), metasomatism in mantle-derived peridotites is commonly recognised by the addition of secondary volatile-rich phases (e.g. modal metasomatic addition of amphibole and phlogopite; Wallace and Green, 1991; Sweeney et al., 1993; Sen and Dunn, 1995; Konzett et al., 2000; Bell et al., 2005) or by minerals with isotopic and fluid-mobile incompatible element enrichments (i.e. cryptic metasomatism; Dawson, 1984) Commonly, enrichments of lithophile trace elements such as the relatively mobile and incompatible large ion lithophile (LILE) or light rare earth (LREE) elements provide information on secondary processes that have affected the cratonic lithospheric mantle (e.g. Stachel et al., 1998; Grégoire et al., 2003; Bell et al., 2005). Metasomatic enrichment of previously depleted peridotitic cratonic mantle have been linked to post-Archean subduction-related melt re-fertilization (e.g. Prouteau et al., 2001; Arndt et al., 2009), large igneous province-related basaltic metasomatism (e.g. Carlson et al., 1999; Maier et al., 2005) and potentially much younger diamond formation (Richardson and Shirey, 2008). An additional avenue to trace the metasomatic overprinting of Archean cratonic mantle involves examination of highly siderophile elements (HSE), including platinum group elements (PGE), which predominantly reside within base metal sulphides (BMS). The HSE can also be powerful geochemical tracers of fluid-mantle reactions during re-fertilisation and metasomatism through liquid percolation (Morgan et al., 2001; Luguet et al., 2007, 2015) and importantly, in contrast to the lithophile elements involved in silicate-dominated metasomatism, HSE are intimately linked to deep sulphur cycles.

Pentlandite, chalcopyrite and pyrrhotite are the most common BMS phases observed in mantle-derived peridotites. The BMS can occur as a single sulphide phase or as multiple phase assemblages, which are often interpreted as quenched derivatives of a high-temperature melt that was once present within the upper mantle (e.g. Kullerud, 1969; Fleet and Pan, 1994; Guo et al., 1999; Lorand and Gregoire, 2006; Lorand et al., 2013; Luguet et al., 2015; Wainwright et al., 2015). Partial melting experiments show that BMS can melt incongruently to form both mono-sulphide solid solution (MSS) and Cu-Ni-rich sulphide phases and potentially also metal alloys (Bockrath et al., 2004; Peregoedova et al., 2004). Moreover, mono-sulphide solid solution is shown to preferentially sequester I-PGE elements while the Cu-Ni-rich phases strongly sequester the P-PGE (e.g. Peach et al., 1990; Barnes et al., 1997; Alard et al., 2000; Luguet et al., 2003, 2007; Mungall et al., 2005; Ballhaus et al., 2006; Fonseca et al., 2011; Li and Audétat, 2012; Liu and Brenan, 2015).

Previous studies of mantle-derived peridotites show that they either display relatively enriched or depleted HSE signatures (e.g. Luguet et al., 2015; Alard et al., 2005; Lorand et al., 2010; Delpech et al., 2012; Marchesi et al., 2014; Aulbach et al., 2016; Bragagni et al., 2017). These signatures can be explained by reaction with infiltrating fluids, which can result in contrasting behaviour of BMS and typically different HSE fractionations (specifically between I-PGE and P-PGE) depending on the compositional character of the melt. For example, melt-rock interactions with a low-degree, silica-undersaturated melt is likely to precipitate P-PGE enriched BMS with potentially suprachondritic Pd/Ir, Pt/Ir and Rh/Ir ratios (e.g. Luguet et al., 2003, 2007, 2015). Whereas, exceptionally oxidising, volatile-rich melts/fluids may fractionate Os compared to Ir and S compared to Se as well (e.g. Delpech et al., 2012; Marchesi et al., 2014; Brenan, 2015; Aulbach et al., 2016; Bragagni et al., 2017).

In addition to the HSE content of peridotite-hosted sulphides, the sulphur isotope composition of BMS are also effective as geochemical tracers of mantle metasomatic processes, due to minimal isotope fractionation during high-temperature reactions including partial melting or sulphide crystallisation from sulphide or silicate melts (Ohmoto, 1979; Marini et al., 2011; Giuliani et al., 2016). The combination of measured $\delta^{32}S$, $\delta^{33}S$, $\delta^{34}S$ and $\delta^{36}S$ can be used to trace sulphur from different reservoirs, such as mantle or recycled crustal/sedimentary, which have significantly different sulphur isotope compositions (Farquhar et al., 2002; Cartigny et al., 2009; Thomassot et al., 2009). Furthermore, some mantle-derived materials (e.g. diamonds) are thought to contain Archean recycled sedimentary sulphur due to measured mass-independent sulphur isotope fractionation (S-MIF), which is indicated by $\Delta^{33}S$ ($= \delta^{33}S - 1000 * [(1 + \delta^{34}S /1000)^{0.515} - 1$; Farquhar et al., 2001) values that do not follow the mass-dependent trend (i.e. samples that do not display the expected mass dependent fractionation relationship between ^{33}S and ^{32}S and $^{34,33,32}S$ ratios, see Farquhar et al. (2002) and Thomassot et al. (2009) for details). The mass-independent fractionation of sulphur isotopes occured in surficial material during the Archean in response to the activity of UV radiation in the absence of a modern atmosphere (Thomassot et al., 2015). Therefore, any significant non-zero deviation of $\delta^{34}S$ or $\Delta^{33}S$ in mantle rocks is generally interpreted to reflect contributions from recycled (and potentially ancient) crustal components (e.g. Chaussidon et al., 1987; Eldridge et al., 1991; Ionov et al., 1992; Wilson et al., 1996; De Hoog et al., 2001; Thomassot et al., 2009; Labidi et al., 2012, 2014, 2015).

This study focusses on the occurrence and composition of sulphides hosted in peridotite xenoliths from the 1.2 Ga Premier kimberlite of the Kaapvaal craton (South Africa). Previous research conducted on the silicate minerals present in Premier peridotites suggest metasomatic alteration from a Fe-rich basanite-like metasomatic fluid (Danchin, 1979; Griffin et al., 2003b; Hoal, 2003), which is unlike the characteristic potassium-rich metasomatism often described for CLM-derived peridotite xenoliths from central Kaapvaal craton kimberlites (e.g. Kimberley kimberlite; Konzett et al., 2000; Grégoire et al., 2002; Fitzpayne et al., 2018). Additionally, the occurrence of voluminous visible sulphide minerals within the Premier peridotite samples suggests that at least a portion of the BMS grains are secondary

and probably precipitated from interaction with a S- and HSE-enriched metasomatic fluid, which percolated into the otherwise largely melt and BMS depleted Kaapvaal CLM. Therefore, by integrating petrological and chemical features of both the peridotite silicate and sulphide assemblages, a more holistic view of secondary overprinting of the CLM can be constructed.

Here we present detailed textural, mineralogical and chemical investigations of both the silicate assemblage and base metal sulphides of eleven garnet-bearing lherzolite xenoliths from the Premier kimberlite. The sample suite consists of four coarse lherzolites and seven deformed lherzolites (e.g. "sheared" peridotites; Boyd and Nixon, 1975; Kennedy et al., 2002; O'Reilly and Griffin, 2010). By integrating new silicate geochemistry and textural information with sulphide HSE–Se–Te systematics as well as sulphur isotopes, we are able to determine a metasomatic origin for the Premier peridotite sulphides, which may have a genetic link to sulphides present in ultra-mafic magmas of the Bushveld Igneous Complex (BIC).

4.2. GEOLOGICAL SETTING AND PREVIOUS INVESTIGATION OF PREMIER LITHOSPHERIC MANTLE

The Premier kimberlite pipe is situated in the central Kaapvaal craton of South Africa, located near the town of Cullinan northeast of Pretoria, South Africa (**Fig. 4.1**). The Premier kimberlite has Group I petrographic and isotopic affinity and a Proterozoic eruption age of 1152.3±5.3 Ma (Wu et al., 2013; Tappe et al., 2018a). Premier's extensive diatreme (±32 ha) is the largest on the Kaapvaal craton and was shaped from multiple magmatic pulses over a minimum of ~3 Ma (Tappe et al., 2018a). The Premier kimberlite also hosts the Cullinan diamond mine and is famous for producing some the world's largest gem quality diamonds (e.g. the Cullinan diamond of 3106 carats). Importantly, the Premier kimberlite is located at the southern margin of the Bushveld Igneous Complex, the 2.06 Ga large igneous province that may have formed during massive mantle plume upwelling (Olsson et al., 2011; Zeh et al., 2015). The origin of the Buschveld Igneous Complex is however highly controversial and numerous alternate formation models have also been proposed (e.g. Eales and Cawthorn, 1996; Mondal and Mathez, 2006; Hutchinson et al., 2015; Latypov et al., 2017). In contrast to the rest of the Kaapvaal cratonic mantle that is seismically fast, the lithospheric mantle below Premier and the BIC shows slow seismic velocities (e.g. James et al., 2001; Shirey et al., 2003; Fouch et al., 2004), and this slower P- and S-wave velocity area of the Kaapvaal CLM may have resulted from chemical re-fertilisation during magmatic events associated with emplacement of Paleoproterozoic Bushveld Igneous Complex.

Cratonic mantle material derived from the Premier kimberlite provides some key evidence for potential Bushveld-related overprinting. The Premier kimberlite sampled depleted harzburgite as well as a notable abundance of sheared lherzolites with warm (1200 – 1400 °C) equilibration temperatures (e.g. Danchin, 1979; Luth, 1999; Grégoire et al., 2003, 2005; Viljoen et al., 2009). These sheared peridotite xenoliths have relatively enriched Ca, Ti, Fe, and Al contents compared to the shallower

(~900 – 1100 °C), coarser harzburgite and lherzolite varieties. This is shown by olivine and orthopyroxene with lower Mg# of 0.91 vs 0.92–0.94 and 0.90 vs. 0.94, respectively, garnet with higher TiO_2 (avg. 1.15 wt. %), CaO (>5.0 wt.%) and FeO (>7 wt.%) contents and sometimes also larger modal abundances of clinopyroxene. Additionally, the rare earth element (REE) patterns of the Premier peridotitic garnets define a trend of increasing cryptic metasomatism, from depleted 'sinusoidal' and 'humped' shaped curves displayed by the harzburgite garnets to more enriched 'normal' garnet REE patterns comprising a steep positive slope in the LREE and MREE, with relatively flat HREE in the sheared lherzolites (c.f. Viljoen et al., 2009). Key accessory minerals including Fe- and Ti-rich micas, aluminous amphibole, and Fe-rich clinopyroxene (Hoal, 2003), further indicate modal metasomatism from an Fe-rich basanite-like metasomatic fluid (Danchin, 1979; Griffin et al., 2003b) perhaps related to the the basaltic/komatiitic magmas of the BIC (Boyd and Nixon, 1975; Maier et al., 2005), rather than the potassic, kimberlite-like (MARID) metasomatism common in other parts of the Kaapvaal mantle lithosphere (Konzett et al., 2000; Grégoire et al., 2002; Fitzpayne et al., 2018).

There exist more diamonds with lherzolitic (40 %) and eclogitic (60 %) paragenesis at Premier (Gurney et al. 1985; Viljoen et al. 2004) than is normal for diamond populations worldwide (i.e. world-wide diamonds of peridotitic paragenesis = 65 %, with 77 % harzburgite affinity and 23 % lherzolite affinity; eclogitic populations = 33 %, and websteritic populations = 2 %; Stachel and Harris, 2008). In addition, the atypical diamond suites from Premier have differing age constraints. For example, first generation harzburgitic diamond inclusions have Archean ages (3.2 Ga; Richardson et al., 1993), lherzolitic silicate diamond inclusions have Paleoproterozoic Sm-Nd model ages (1930±40 Ma; Richardson et al., 1993) which overlap with the basic rocks of the BIC (2.06 Ga; Zeh et al., 2015), and third generation eclogitic diamond inclusions have ages of 1150 Ma, which suggests that they formed directly before kimberlite emplacement (1152.3±5.3 Ma; Wu et al., 2013; Tappe et al., 2018). Moreover, of the studied Premier diamonds a large proportion (54 % of eclogitic and 41 % of peridotitic paragenesis) contain silicate inclusions that equilibrated at temperatures that exceed the mantle ambient adiabat of 1327 ºC, recording perhaps transient thermal perturbations associated with the plume-related formation of the BIC (e.g. Korolev et al., 2018).

The previous research conducted on the chemical and isotopic compositions of Premier diamond included sulphides (e.g. Chaussidon et al., 1987; Eldridge et al., 1991; Deines and Harris, 1995; Richardson and Shirey, 2008) may further support Bushveld magma-related overprinting of the lithospheric mantle. Specifically, the Premier diamond sulphide inclusions display both Archean and Paleoproterozoic (~2.0 Ga) Re-Os model ages (Carlson et al., 1999; Irvine et al., 2001; Richardson and Shirey, 2008), suggesting younger modification/metasomatism of the CLM below premier (Shirey et al., 2003) that coincides with the emplacement age of the BIC (2.06 Ga; Zeh et al., 2015). Rare Premier peridotite whole-rock PGE studies (c.f. Maier et al., 2005, 2012) further show notable P-PGE (Pt and Pd) enrichments (much higher than other Kaapvaal peridotite xenolith suites; Pearson et al., 1995, 2002)

which overlap with the P-PGE enriched nature of sulphides present in the ultramafic-mafic layers of the BIC (e.g. Hutchinson and McDonald, 2008). Therefore, Maier et al. (2012) suggests that the CLM below Premier may have been significantly affected by melts related to the Bushveld Igneous Complex.

4.3. SAMPLES AND PETROGRAPHY

Eleven Premier peridotite xenoliths were chosen for this study based on the presence of visible sulphides. The petrography and modal abundance (determined by point counting) of the peridotite minerals is presented here while information specific to the sulphide minerals (and associated magnetite) is presented in **Section 4.5.3**. Most peridotite xenoliths investigated here are less than 2cm in diameter, except for 2 xenoliths that are ~15 cm. The peridotites are grouped into coarse garnet lherzolites and deformed garnet lherzolites after Danchin (1979) and other researchers (e.g. Boyd et al., 1998; Grégoire et al., 2003, 2005; Hoal, 2003; Viljoen et al., 2004, 2009; Maier et al., 2005; **Table 4.1, Fig. 4.2**). Coarse lherzolites display typical proto-intergranular textures with interlocking olivine and orthopyroxene minerals (<0.5 mm) between larger orthopyroxene and garnet porphyroblasts. Whereas, deformed lherzolites have characteristic mosaic-porphyroclastic textures with fluidal-mosaic domains around garnet and orthopyroxene porphyroclasts. Both xenolith groups are altered with some serpentinization of the silicate mineral phases, especially olivine and clinopyroxene. The four **coarse garnet lherzolites** (CIM15-002, -004, -006, and -013) are composed of olivine (60 – 70 %) and lesser amounts of orthopyroxene (10 – 20 %), clinopyroxene (5 – 15 %) and garnet (3 – 5 %) as well as trace spinel (CIM15-002, -013) and calcite (CIM15-004). The modal proportions are based on visual point counting methods. Olivine and orthopyroxene minerals occur as irregular crystals with rounded edges and range in size from 1 to 10 mm. Garnet typically occurs as irregular to rounded grains (1 to 2 mm in size), with kelyphitic alteration along fractures and mineral rims. Clinopyroxene in the coarse garnet lherzolite samples occurs as small grains (< 2 mm) that are associated with fractures (**Fig. 4.2a–c**) and often exhibit “spongy” secondary textures.

The seven **deformed garnet lherzolites** (CIM15-001, -003, -015, -016, -0.17, -021, and -035) are composed of olivine (50 – 80 %), lesser amounts of orthopyroxene (7 – 30 %), clinopyroxene (3 – 10 %, excluding CIM15-015, 016 and 035 that contain upward of 15 %) and garnet (7 – 10 %), as well as trace amounts of calcite, spinel and phlogopite (CIM15-003, -0.17). The deformed garnet lherzolites have a mosaic-porphyroclastic texture (Harte 1977; Gregoire et al. 2003), with fluidalmosaic domains (<200 μm polygonal-shaped olivine grains) around some more resistant and irregularly shaped (2 – 10 mm) garnet and orthopyroxene porphyroclasts (**Fig. 4.2d–f**). Clinopyroxene largely occurs as discrete irregularly shaped crystals that range from 1 to 5mm and are commonly adjacent to garnet. Garnet occurs as rounded crystals that have extensive semi-opaque kelyphitic alteration along fractures and mineral rims. Fine-grained (<10 μm) spinel (magnesium chromite), magnetite and sulphide mineral

phases can be distinguished as comprising part of the garnet alteration rims. Sometimes secondary "spongy" clinopyroxene is also associated with these alteration zones.

4.4. ANALYTICAL METHODS

4.4.1. Scanning electron microscopy

Mineral major and minor element compositions were determined using a Zeiss EVO MA15VP Scanning Electron Microscope (SEM) equipped with a link ISIS energy dispersive spectrometry (EDS) system containing an Oxford X-max silicon drift detector at the Central Analytical Facility (CAF) at Stellenbosch University, South Africa. Quantitative analysis on the silicate mineral assemblages (**Table 4.1**) was performed using an accelerating voltage of 20 kV, a beam current range of 19 to 21.5 nA, and a 10 s counting time (5 s of background). The focussed beam was set at an optimum working distance of 8.5 mm. All mineral spectra were processed using ZAF corrections and calibration was performed with natural mineral standards (**Appendix A**). Oxygen was calculated by stoichiometry for the silicates. For the sulphide analyses (**Table 4.2**), a beam size of 10 µm was used with a 20 s on peak and 10 s background counting time. Sulphide mineral spectra were processed by ZAF corrections and quantified using natural sulphide mineral and pure metal standards (see **Table 4.2**). Additionally, magnetite that occurred together with altered sulphide grains was quantified using a natural magnetite standard (**Appendix A**). A back-scattered electron image point counting method was used to calculate sulphide and magnetite mineral modes (**Table 4.2**). Minimum detection limits and standards for the elements of interest are provided in **Appendix A**.

4.4.2. Laser Ablation Inductively Coupled Plasma Mass Spectrometry

Olivine, pyroxene and garnet grains free from obvious alteration were chosen for in-situ trace element analysis (**Table 4.3, 4.4**). An average of 5 grains of each mineral from the xenoliths were analysed by LA-ICP-MS at CAF. The LA-ICP-MS system includes a 193-nm excimer laser system (Resonetics Resolution S155) coupled to an Agilent 7500ce quadrupole ICP-MS. The carrier gas was a mixture of argon and nitrogen (1L/min Ar + 0.003L/min N) that was subsequently merged with helium (0.3 L/min) prior to entering the ablation cell. Individual silicate mineral analyses consisted of 100 µm spot size, a laser repetition rate of 10 Hz, 10 s of background acquisition followed by ablation for 40 s, and the analysis area moved back and forth during ablation. Internal standardisation used ^{29}Si of each mineral, and external primary calibration was set on the NIST SRM 610 standard reference glass. In addition, the NIST SRM 612, BCR-2G and BHVO-2G standard reference glasses were analysed after every 15 unknowns to ensure analytical accuracy (see average obtained standard values in **Appendix B**). The resultant time-resolved data was processed through Iolite ©2017 software to yield trace element concentrations in µg/g. The element concentrations of the standard glasses are within 2σ of the average concentrations reported by Jochum et al. (2005). Secondary alteration was monitored by the identification of significantly high concentrations of traditionally incompatible elements likely

introduced through metasomatism or interaction with the host kimberlite (e.g. Ba, Cs, La, U, Th). Minimum detection limits are generally < 0.1 ppm and 2-σ uncertainties are found in **Appendix C**.

For the sulphide analyses, two spot sizes (50 µm and 20 µm) were employed depending on the size of the individual sulphide grain. A laser repetition rate of 4 Hz together with a prolonged ablation cycle of 60 s (20 s of background) was used. Helium was used as a carrier gas, which was merged with Ar prior to entering the ablation cell. Between 1 and 4 analyses were conducted on each sulphide grain and the "NiS5b" sulphide standard (provided by J Brenan; Mungall and Brenan, 2014) was analysed after every 10 unknowns. Highly siderophile and chalcophile elements were quantified using the NiS5b sulphide standard, which contains 81.2 µg/g Os, 80.4 µg/g Ir, 151.9 µg/g Ru, 151.9 µg/g Rh, 93.5 µg/g Pt, 152.8 µg/g Pd, 35.4 µg/g Re, 51.8 µg/g As, 101.1 µg/g Se, 2.2 µg/g Ag, 109.4 µg/g Te, 8.4 µg/g Au, µg/g 62.1 Pb, and 97.7 µg/g Bi. Rh is not reported due to $^{65}Cu\,^{40}Ar$ and $^{63}Cu\,^{40}Ar$ interferences. Ru is not reported due to $^{60,61}Ni^{40}Ar$ interferences on the ^{100}Ru and ^{101}Ru isotopes and $^{59}Co^{40}Ar$ interferences on the ^{99}Ru isotope in samples that contain appreciable Co. Overall, no more than a 10 µg/g difference between isotopes of the same element were accepted. Trace element compositions, NiS5b standard data and minimum detection limits are reported in **Table 4.5**.

4.4.3. Secondary-ion mass spectrometry

Multiple sulphur isotopes (^{32}S, ^{33}S, and ^{34}S) of four pentlandite grains from sample CIM15-006 were analysed on the CAMECA IMS-1280 secondary-ion microprobe at Centre de Recherche Pétrographiques et Géochimiques (CRPG-CNRS) SIMS facility in Nancy (France) following the procedure of Thomassot et al. (2009), Kitayama et al. (2012, 2017) and Delavault et al. (2016) described below. The sulphides were polished and placed into indium mounts and coated with gold. Prior to the quantitative analytical cycle, the sample was pre-sputtered with a 1.5 nA Cs^+ beam and a spot size of ~10 µm. The secondary ions produced were accelerated at 10 kV and filtered in energy and mass, and simultaneously the isotope abundances were quantified in multicollection mode using three off-axis Faraday cups (L'2 for ^{32}S-, C for ^{33}S-, H1 for ^{34}S-). This pre-sputtering stage allows the user to calibrate the position of the ion beam source as well as the Faraday cups for the best possible yield. Each quantitative measurement cycle consisted of 120 s of pre-sputtering (when background counts are automatically measured) followed by 40 measurement cycles of 6 s each. The analytical protocol included the analysis of well characterised (c.f. Thomassot et al., 2009) reference sulphides including; pyrrhotite (Enon), pentlandite (ka8), chalcopyrite (Mont roc) as well as highly fractionated pyrite (Galice), galena (PbS), and Ni-sulphide (Legros) and pyrrhotite (MIF-Po) that has a distinct S-MIF anomaly, before and after the analysis of a series of unknowns. Analysis of these sulphide standards is essential to quantify the mass-independent fractionation (MIF) line. Additionally, following the method outlined by Delavault et al. (2016), a correction was applied to the 'unknown' sulphide measurements according to their individual sulphide compositions as previously determined by SEM analysis, because

different sulphide minerals are associated with specific instrumental mass fractionation (MIF). Sulphur isotope measurements are reported in the δ notation with respect to V–CDT (Vienna-Canon Diablo Troilite) defined as $\delta^{34}S$ (‰) = 1000 ∗ [($^{34}S/^{32}S$) sample − ($^{34}S/^{32}S$) V–CDT]/($^{34}S/^{32}S$) V – CDT. Mass-independent fractionation ($\Delta^{33}S$) of the sulphides was calculated following the method outlined by Delavault et al. (2016), see **Table 4.6**.

4.5. RESULTS

4.5.1. Peridotite mineral compositions

The major and trace element chemistry of garnet peridotite xenoliths from Premier has been described in detail by various authors (e.g. Danchin, 1979; Boyd et al., 1998; Grégoire et al., 2003, 2005; Hoal, 2003; Viljoen et al., 2004, 2009). Therefore, only a short summary of the most important chemical features of each silicate mineral of the garnet-bearing lherzolites is presented here (**Table 4.1, 4.3** and **4.4**).

4.5.1.1. Major element composition

Garnet in the peridotite xenoliths is chrome pyrope with molar Mg# [Mg/(Mg+Fe)] ranging from 83 to 86, Cr_2O_3 from 1.6 to 5.5 wt.% and CaO from 4.1 to 5.2 wt.%. The garnets are Ca-saturated G9 lherzolitic garnets (Dawson and Stevens 1975; **Table 4.1**). Garnet TiO_2 and Al_2O_3 contents range from below detection to 1.4 wt. % and 17.9 to 21.7 wt. % respectively. **Clinopyroxene** in the lherzolite xenoliths is Cr-diopside with Mg# of 85 – 92 and CaO from 14.9 to 23.3 wt.%. The clinopyroxene contains 1.1 – 2.5 wt.% Na_2O, 0.6 – 1.8 wt. % Cr_2O_3 and 0.4 – 2.8 wt. % Al_2O_3 (excluding CIM15-003 with 4.1 wt.% Al_2O_3). In general, the clinopyroxene in the coarse lherzolites has lower MgO (16.1 – 18.2 wt. % vs. 18.1 – 20.6 wt. %) contents than in the deformed lherzolites, but higher CaO (18.8 – 23.3 wt. % vs. 14.9 – 20.1 wt. %. **Olivine** in the peridotite suite is magnesian, with Mg# ranging from 90 to 92.6. The deformed lherzolite olivine may contain up to 0.02 wt. % Al_2O_3, 0.05 wt. % Cr_2O_3 and 0.1 wt. % CaO contents. **Orthopyroxene** is enstatite with Mg# ranging between 91 and 92. Orthopyroxene is commonly characterised by low TiO_2 (below detection – 0.3 wt.%) contents and but has variable contents of Cr_2O_3 (0.2 – 0.5 wt.%), CaO (0.4 – 1.4 wt.%), Al_2O_3 (1 – 1.14 wt.%) and Na_2O (0.2 – 0.5 wt.%) contents. Orthopyroxene in the coarse lherzolite samples is generally only slightly depleted in Fe, Al, Ca and Ti compared to that in the deformed lherzolites. Spinel (magnesium chromite) is only found in coarse peridotites CIM15-002 and -013, and deformed peridotites CIM15-003 and -017. **Spinel** in all peridotites has overlapping MgO (14.9 – 16.3 wt. %), Cr_2O_3 (18.2 – 39.2), FeO (12.1 – 18.4 wt. %) and TiO_2 (0.4 – 3.1 wt. %) contents. Primary phlogopite is observed in sample CIM15-003 and contains 38 wt. % SiO_2, 5.8 wt. % TiO_2, 1.8 wt. % Cr_2O_3, 9 wt. % K_2O and 0.5 wt. % Na_2O. Calcite observed in samples CIM15-003 and -004 contains 0.3 to 0.5 wt.% FeO (**Table 4.1**).

4.5.1.2. Trace element composition

Trace element contents of garnet and clinopyroxene, as well as olivine and orthopyroxene, are presented in **Table 4.3** and **4.4**, respectively. No trace element chemistry is presented for sample CIM15-004. **Garnet** from the Premier lherzolites contain 74 – 223 ppm Sc, 221 – 518 ppm V, 7 – 47 ppm Y, 50 – 178 ppm Zr and 117 – 155 ppm Ni (**Table 4.3**). In general, garnet displays three distinctive primitive mantle-normalised (denoted by subscript "N"; McDonough and Sun, 1995) REE patterns (**Fig. 4.3a)** that have previously been described in cratonic mantle peridotites by Stachel et al. (1998) and Viljoen et al. (2009). Garnet found in coarse lherzolites have REE patterns that define a "humped" shaped curve comprising a steep positive slope in LREE and MREE (minor Eu anomalies of Eu* = 0.9 – 1.1; Eu* calculated as primitive mantle normalised 2*Eu/[Sm+Gd]) with generally a slight decrease in HREE from Gd to Lu (Lu_N/Gd_N = 1.3 – 0.8). Garnet in deformed lherzolites typically define "normal" shape curves comprising a steep positive slope in the LREE and MREE (no Eu anomaly; Eu* = 1), with relatively flat HREE (Lu_N/Gd_N = 1). Finally, one deformed lherzolite contains garnet with a "sinusoidal" shaped curve that comprises depleted LREE peaking at Gd with decreasing HREE from Gd to Tm and a small positive slope from Tm to Lu (Lu_N/Tm_N = 1.4). This sinusoidal pattern is only found in the depleted cores (with 0.6 wt. % TiO_2 and 18.6 wt. % Al_2O_3) of extensively altered garnet in deformed lherzolite CIM15-017. In general, the lherzolitic garnets lack significant Ti depletions and garnets from samples CIM-001, -002 and -006 do not display characteristic Sr depletions (**Fig. 4.3b**).

Clinopyroxene contain 28 – 1239 ppm Ni, 1.9 – 74 ppm Sc, 1 – 464 ppm V, and 22 – 588 ppm Sr. All of the deformed lherzolite clinopyroxene displays typical convex-upward REE patterns (e.g. Gregoire et al. 2003; **Fig. 4.3 c, d**), with moderately enriched LREE (La_N/Sm_N = 0.8 – 1.3) relative to HREE (Lu_N/Gd_N = 0.07 – 0.1) and exhibit small positive Sr (Sr* = 1.1 – 1.3, calculated as $2*Sr_N/[Pr_N+Nd_N]$) anomalies. The coarse lherzolites display a range of clinopyroxene REE patterns. For example, clinopyroxene from samples CIM15-006 and CIM15-013 exhibit minor core-to-rim zonation of the trace elements and the large cores display sinusoidal REE curves, with a minimum at Pr (Pr_N = 1.6 and 0.8), maximum at Dy (Dy_N -= 5.5 and 7.4) and relatively flat HREE (Lu_N/Gd_N = 0.9 – 1.0). They also display large positive Sr (Sr* = 8.3 – 16.6) anomalies, no significant Eu (Eu* = 1) anomalies and enrichments in Pb (**Fig. 4.3d**). These core patterns are comparable to those of clinopyroxene found in depleted abyssal peridotites (e.g. Johnson et al., 1990; Rampone et al., 1996; **Fig. 4.3c**). Additionally, clinopyroxene in sample CIM15-002 is highly altered and displays an REE pattern with relative enrichments in LREE (La_N/Sm_N = 5.7), extremely low HREE contents (Lu_N/Gd_N = 1.9) as well as large positive Sr (Sr* = 1.9) and Eu (Eu* = 2.9) anomalies (**Fig. 4.3c, d**).

Olivine from the Premier lherzolites have high concentrations of Cr (61 – 549 ppm), Mn (800 – 1113 ppm), Co (136 –151 ppm), Ni (2683 –3059 ppm), and Zn (58 –79 ppm), while other trace elements occur at levels near to or below detection limits (**Table 4.4**). Similarly, **orthopyroxene** commonly

contains significant amounts of V (45 – 63 ppm), Cr (1154 – 3229 ppm), Mn (867 – 966 ppm), Co (57 – 64 ppm), Ni (797 – 979 ppm), and Zn (34 – 44 ppm), with extremely low/below detection limit concentrations of the other trace elements (**Table 4.4**).

4.5.2. Geothermobarometry

Previous Premier garnet peridotite studies (e.g. Boyd et al.,1998, Gregoire et al., 2003, 2005; Viljoen et al., 2009) show calculated pressure and temperature estimates that lie between the 40 mW/m^{-2} and 45 mW/m^{-2} model conductive geotherms of Pollack and Chapman (1977; **Fig. 4.4**) and a maximum lithospheric thickness of 180 to 210 km. Initially, temperature and pressure conditions for the suite of garnet-bearing lherzolites investigated here were calculated using the four-phase lherzolite geothermobarometer of Brey and Köhler (1990) as well as the Opx-Cpx solvus thermometer of Taylor (1998) and enstatite-in-orthopyroxene barometer of Nickle and Green (1985) (**Table 4.7**). The T_{BKN} – P_{BKN} calculations for the most highly equilibrated garnet-bearing lherzolites (e.g. coarse lherzolites CIM15-002 and -004 as well as deformed lherzolites CIM15-001, -003, -017 and -021) yielded conditions between 1014 and 1410 ºC and 3.4 and 7.4 GPa. The corresponding T_{T98} – P_{NG85} calculations yielded conditions between 1112 and 1426 ºC and 4.1 and 6.9 GPa. These two thermobarometers yielded results within 1 to 98 ºC and 0 to 0.8 GPa of each other. When compared to temperature (1169 1489 ºC) and pressure (4.1 – 6.7 GPa) estimates calculated using the Fe-Mg exchange between olivine and garnet thermometer of O'Neill and Wood (1979) and the enstatite-in-orthopyroxene barometer of Brey et al. (2008), the %-difference between the three PT methods is <15 % for temperature and <18 % for pressure. Therefore, only the results for the T_{BKN} – P_{BKN} calculations have been plotted on **Figure 4.4**, where the coarse lherzolites are defined by the lowest equilibrium pressures (3.4 – 4.4 GPa) and temperatures (1014 – 1221 ºC) and the deformed lherzolites are defined by the highest equilibrium P–T conditions (5.4 – 7.4 GPa and 1370 – 1410 °C), with four derived from inside the diamond stability field (Kennedy and Kennedy, 1976).

Coarse lherzolites CIM15-006 and -013 yielded anomalously low temperature (481 vs. 734 and 1010 vs. 1088 °C) and pressure (0.8 vs. 2.3 and 3.5 vs. 4.2 GPa) conditions calculated using T_{BKN} – P_{BKN} and T_{T98} – P_{NG85}, respectively and both samples show evidence of clinopyroxene disequilibrium (e.g. core-to-rim trace element zonation, **Section 4.5.1.2**). Therefore, these pressures and temperatures should at best be considered rough estimates. The disequilibrium displayed by these samples is possibly due to metasomatism at shallow depths where elemental diffusion is slow resulting in rocks that are not fully equilibrated.

The deformed lherzolites CIM15-015, -016 and -035 show textural evidence for clinopyroxene disequilibrium (e.g. "spongy" secondary textures associated with zones of alteration, **Section 4.5.1.2**) as well as minor Mg-Fe disequilibrium between the clinopyroxene and olivine mineral phases. That is, in a peridotite with minerals in equilibrium, clinopyroxene typically has Mg# 3 – 5% higher than

olivine, orthopyroxene ~1% higher than olivine, whereas garnet is typically 5 – 8% lower than olivine. However, these specific deformed lherzolites have clinopyroxene Mg# of 89 to 91 which overalp with the olivine Mg# (see **Table 4.1**). Thus, although the temperature (1144 – 1459 vs. 1238 – 1391 °C) and pressure (4.6 – 7.5 vs. 5.2 – 6.9 GPa) estimates calculated using T_{BKN} – P_{BKN} and T_{T98} – P_{NG85} seem reasonable, they should also only be considered estimates. All samples that display major and trace element disequilibrium are shown as grey symbols on **Figure 4.4**.

4.5.3. Base metal sulphides

4.5.3.1. Modal abundance and distribution

Base metal sulphides (BMS) are found in all but three (CIM15-015, -016, -035) garnet-lherzolite samples. The BMS are found as inclusions within silicate minerals and as interstitial grains heterogeneously distributed throughout the lherzolite matrix (**Fig. 4.5a–d**). BMS is most abundant in samples CIM15-001, -004, -006, -013 and -021, where on average more than six grains >50 μm were observed per thin section (**Table 4.2**), excluding the small (<30 μm) interstitial BMS grains which are disseminated throughout the serpentinised peridotite matrix. Generally, the coarse lherzolites contain higher modal abundances of BMS than the deformed lherzolite samples, and deformed lherzolite samples CIM15-035, -015 and -016 are base metal sulphide-free. Notably, all the coarse and deformed lherzolites contain interstitial magnetite and an indecipherable proportion of this magnetite may be a residual alteration product from the break-down of BMS.

4.5.3.2. Habits and textural relationships

The base metal sulphides within the garnet-bearing lherzolites occur either as inclusions hosted in silicate minerals or as interstitial grains present in the peridotite matrix. The BMS are divided into four distinct groupings based on texture, size and location. The individual BMS groupings follow a similar approach to previous research conducted on BMS in CLM-derived peridotite xenoliths (c.f. Szabó and Bodnar, 1995; Wainwright et al., 2015; Bragagni et al., 2017).

Small "isolated" BMS inclusions are located within single silicate minerals, mostly within olivine (**Fig. 4.5a**) orthopyroxene (**Fig. 4.5b**) and to a lesser extent within garnet and clinopyroxene. The BMS grains occur as rounded blebs with a diameter of <50 μm. Most of these BMS inclusions are completely enclosed by the host silicate mineral phases (e.g. **Fig. 5b** and **6a**), but some are associated with silicate crystal rims (i.e., a maximum of 300 μm from the edge of the silicate grain) or fractures (e.g. **Fig. 4.5a** and **4.6b**), which potentially links these sulphides to the serpentinised peridotite matrix. The small inclusions predominantly consist of single pentlandite (Pn) and mono-sulphide solid solution (MSS) phases which have been relatively unaffected by oxidation processes as revealed by their low oxygen contents (**see Section 4.5.3.3**). However, within sample CIM15-006 layers of small isolated BMS inclusions, including both pentlandite and monosulphide solid solution phases, are located along healed

growth/fracture zones within a single orthopyroxene crystal (**Fig. 4.5b**), and these small BMS inclusions are increasingly more oxidised than those found in other silicate crystals within the same and other samples (**Table 4.2**). Additionally, some small "isolated" (heazlewoodite and pentlandite) inclusions located towards the rims of the silicate phases have been partially altered to magnetite (**Fig. 4.6a**). Interestingly, a single small isolated BMS inclusion within a clinopyroxene crystal of sample CIM15-013 consists of a complex flame-like intergrowth of both pentlandite and pyrrhotite (**Fig. 4.6b**).

Large "pseudo" BMS inclusions are located within individual silicate grains but may be significantly affected by metasomatic processes because of communication with the peridotite matrix (predominantly serpentinised olivine). For example, the single large (150 µm) pseudo-inclusion identified in this study is located on the metasomatised kelyphitic rim of a single garnet crystal within sample CIM15-001 (**Fig. 4.5c**). This BMS pseudo-inclusion consists of pentlandite and mono-sulphide solid solution (potentially preserved from the initial sulphide composition) and up to 10% magnetite alteration (**Table 4.2**). Additionally, previous mantle-derived peridotite BMS studies show that large BMS pseudo-inclusions may preserve less than 50% of their original sulphide composition when connected to the peridotite matrix by vein networks or an exposed BMS surface (e.g. Wainwright et al., 2015; Bragagni et al., 2017).

Small interstitial BMS occur at grain boundaries between individual silicate minerals or are disseminated within the serpentine veins of the olivine-dominated peridotite matrix (**Fig. 4.5a**). These small (<30 µm in size) BMS interstitials are rounded to elongate in shape and tend to follow the direction of veining (**Fig. 4.6c**), sometimes clustering to form long chains (several tens of µm) within the serpentinised veins (**Fig. 4.6d**). Additionally, the small interstitials are often associated with large interstitial BMS (**Fig. 4.5d**) and to a lesser extent with oxides (e.g. magnesium chromatite and magnetite; **Fig. 4.5c,d**). The small interstitial BMS grains consist mainly of pentlandite but heazlewoodite, pyrite, Co- and Zn-rich sulphide phases also exist (**Table 4.2**). Some grains show no visible alteration, whereas others are replaced by up to 40 % magnetite (**Fig. 4.6c,d**).

Large interstitial BMS are located at grain boundaries between the silicate constituent minerals (olivine, orthopyroxene, garnet and clinopyroxene) and are also disseminated within the serpentine veins of the peridotite matrix (**Fig. 4.5b,d** and **4.6e,f**). These large interstitial BMS grains are irregular in shape, have a diameter of 60 to 200 µm and principally consist of pentlandite with >50 % magnetite alteration (**Fig. 4.6f**). However, altered heazlewoodite (**Fig. 4.6e**) and Zn-rich sulphide phases also exist in some deformed lherzolite samples (**Table 4.2**). Additionally, trails of minute interstitial sulphides radiate out from many of the large interstitial BMS grains and this indicates decrepitation of the original sulphide (**Fig. 4.6f**).

4.5.3.3. BMS major element chemistry

The **small isolated BMS inclusions** generally have low oxygen contents (<1.9 wt.%; **Table 4.2**), but those that are linked to the serpentinised peridotite matrix at silicate mineral rims or by healed growth/fracture zones have higher oxygen contents (2.3 – 21 wt.%). The large proportion of oxygen contained within these "isolated" BMS inclusions is likely a reflection of the open-system evolution and reaction with serpentinising fluids that altered the silicate assemblage (c.f. Fonseca et al., 2008; Wainwright et al., 2015). These oxidised sulphides are not representative of primary isolated BMS compositions and will not be considered for major element chemistry. However, for comparison, the altered/oxidised sulphides are plotted together with the low oxygen assemblages in **Figures 4.7** and **4.8**. **Pentlandite** (n = 7) found as isolated inclusions has a high metal/sulphur [M/S = (Fe+Cu+Ni+Co)/S] atomic ratio of 1.1. The pentlandite Fe contents range from 21.1 to 31.4 wt.%, Ni contents from 30.2 – 37.7 wt.%, and Co contents from 0.2 to 10 wt.%. Pentlandite within the isolated BMS inclusions also contains significant W (0.4 – 0.6 wt.%) and Pt (up to 1.5 wt.%, **Fig. 4.7; Table 4.2**). **Pyrrhotite** (n = 1) has a metal/sulphur ratio of 0.9 and contains 39.7 wt.% S and 59.3 wt. % Fe as well as 0.3 wt.% Ni, Co, and W. **Heazlewoodite** (n =1) has a metal/sulphur ratio of 1.5 and contains 26.2 wt.% S, 67.8 wt. % Ni and 3.6 wt. % Fe as well as 0.6 wt.% W and 1 wt.% Pt. The more oxidised (2.3 wt. % O) Heazlewoodite inclusions can have up to 13 wt.% Fe (**Fig. 4.8**).

Only one single **large "pseudo" BMS inclusion** was found in the peridotites of this study. It is partially altered to magnetite and the preserved primary pentlandite and MSS phase assemblage is slightly oxidised (~2 wt. % O) (**Figs. 4.7, 4.8**). The **pentlandite** (n =1) has a metal/sulphur ratio of 1.1 and contains 33.8 wt.% S, 24.8 wt. % Fe and 38.8 wt. % Ni as well as 0.5 and 0.3 wt.% Co and W contents, respectively. **Mono-sulphide solid solution** (n=1) has a metal/sulphur ratio of 1 and contains 34.4 wt.% S, 26.8 wt. % Fe and 22.4 wt. % Ni (**Fig. 4.8**). The MSS is copper-rich (13.9 wt.%) and poor in both Co (0.3 wt.%) and W (0.5 wt.%).

The **small interstitial BMS** usually consist of single sulphide assemblages but are often partially altered to magnetite (**Table 4.2**). Only sulphide compositions with <2 wt.% oxygen contents are reported here. **Pentlandite** (n=2) has metal/sulphur ratios of 1.0 to 1.1. The pentlandite Fe contents range from 23.9 to 30.6 wt.%, Ni contents from 31.1 to 39.9 wt.%, and Co contents from 0.4 to 4.7 wt.%. Additionally, the pentlandite only contains minor W (up to 0.5 wt.%). **Pyrite** (n=2) has a metal/sulphur ratio of ~0.5 and contains 42.3 to 45.9 wt. % Fe and 54.1 to 57.7 wt. % S. **Co-rich sulphide** (n=1) has a metal/sulphur ratio of 1.1 and contains 33 wt. % S, 7.3 wt.% Fe, 31.5 wt. % Ni, 26.2 wt.% Co and minor Mg (0.3 wt.%) and W (0.6 wt.%) contents. **Heazlewoodite** has an elevated metal/sulphur ratio of 1.5 and contains 26.3 wt. % S, 4.9 wt. % Fe, and 68.2 wt. % Ni, as well as minor W (0.4 wt.%) and As (0.2 wt.%) contents. Altered **Zn-rich sulphide** is also found as small interstitial

inclusions and the oxidised compositions are plotted alongside the other small interstitial BMS compositions on **Figures 7** and **8**.

The **large interstitial BMS** are the most oxidised and are largely altered to magnetite. The preserved **pentlandite** (n=1) is similar in composition to the large "pseudo" BMS inclusion pentlandite, with higher Co (2.1 vs. 0.5 wt.%) contents (**Fig. 4.7, 4.8**). The **heazlewoodite** is similar in composition to the small interstitial BMS heazlewoodite (M/S = 1.5) and can contain up to 1.3 wt.% Pt. Importantly, the compositions of the sulphide phases do not change systematically based on whether they occur as single or multiple phase assemblages (**Table 4.2**).

4.5.3.4. BMS trace element chemistry

Due to the large amounts of alteration and small grain sizes (<50 um) of sulphides from most of the Premier xenoliths, in-situ LAICPMS trace element analyses were only possible on two pentlandite and three pyrite grains from samples CIM15-004 and -006 (**Table 4.5**). Pentlandite was only analysed from CIM15-006 and has very low Os (0.38 and 0.8 µg/g), Ir (0.6 and 0.8 µg/g) and Pt (0.2 and 0.3 µg/g) contents as well as high Pd (4.6 and 5.9 µg/g) contents (**Fig. 4.9a, b**; **Table 4.5**). Rhenium contents are relatively high at ~0.5 µg/g, and mimic Pd concentrations with Re_N/Pd_N = 0.9 and 1.0. Pentlandite Se and Te (**Fig. 4.9e**) contents are 112 and 117 µg/g and 5.2 and 7.6 µg/g, respectively, and Se/Te ratios are 16 and 23 (**Fig. 4.9f**), comparable to those reported for fertile orogenic, and ophiolitic peridotites (Se/Te = ~9 ± 4; König et al., 2012, 2014; Wang et al., 2013) and cratonic peridotites (Se/Te = 8.3 – 59.6; Luguet et al., 2015). The pentlandite grains also contain significant As (2.8 and 2.5 µg/g) and Bi (4.1 to 10.9 µg/g) contents.

The pentlandite displays Pd-enriched chondrite normalised HSE patterns (normalization values from Fischer-Gödde et al., 2010; **Fig. 4.10a**) and are characterised by relatively high (suprachondritic) Pd/Ir (Pd_N/Ir_N = 6.2 and 9.4; **Fig. 4.9c**) and depleted Pt/Ir (Pt_N/Ir_N = 0.11 and 0.17; **Fig. 4.9d**) ratios. Platinum is mildly depleted relative to the I-PGE (e.g. Ir and Os; Os_N/Pt_N = 2.5 and 10.2) and strongly depleted relative to Pd (Pd_N/Pt_N = 32.9 and 72.2; **Fig. 4.9c**). There is only minor fractionation between Os and Ir, with Os_N/Ir_N = 0.5 and 1.2. The pentlandite PGE abundance ratios are fractionated relative to the primitive mantle (Becker et al., 2006) and abyssal peridotites (Liu et al., 2008, 2009; Day et al., 2017; **Fig 4.10b**). The pentlandite HSE pattern observed here has similarities in I-PGE and Pt contents to some previously published Premier peridotite whole-rock HSE patterns (Maier et al., 2005, 2012; **Fig. 4.10b**) noting, however, the relative dilutions in whole-rock HSE concentrations compared to the in-situ sulphide concentrations. Importantly, the Pd-enriched pentlandite HSE pattern also overlaps with "Type 2" HSE patterns described by Luguet and Pearson, (2019) for both BMS inclusions within metasomatic silicates and intergranular BMS blebs found in close association to metasomatic silicates within abyssal peridotites (**Fig. 4.10a**; Alard et al. 2005, 2011; Luguet and Pearson 2019). Moreover, the pentlandite P-PGE ratios (Pd_N/Pt_N = 32.9 and 72.2) are comparable with pentlandite sulphides

derived from Bushveld peridotites (e.g. a relative Pt depletion and Pd enrichment; Pd_N/Pt_N = 12.1 – 9402; **Fig. 4.10a)** (Hutchinson and McDonald, 2008).

Pyrite from samples CIM15-006 and -004 contains relatively low Pd (0.3 – 1.9 µg/g; **Fig. 4.9b**) contents and Os, Re, Ir (bdl – 0.07 µg/g), and Pt (bdl – 0.3 µg/g) are all mostly below detection (**Table 4.5**). The PGE contents of the Premier pyrite is much lower (often below detection) than the pentlandite. However, the telluride (Ag, Au, Se and Te) contents are similar, with Se and Te contents (**Fig. 4.9e**) ranging from 24 to 212 µg/g and 0.9 to 8 µg/g, respectively. Additionally, the Premier pyrite Se/Te ratios have a small range from 27 to 30 (**Fig. 4.9f**). The pyrite has higher As (4.9 – 607 µg/g) and lower Bi (0.5 – 3.7 µg/g) concentrations than the pentlandite. The pyrite has chondrite-normalized HSE patterns reminiscent of the pentlandite patterns discussed above, displaying Pd-enrichments (**Fig. 4.10a**), and are characterised by high Pd/Ir (Pd_N/Ir_N = 16 – 28; **Fig. 4.9c**) and variable Pt/Ir (Pt_N/Ir_N = 0.7 – 2.1; **Fig. 4.9d**) ratios. Both pentlandite and pyrite HSE contents, and specifically their chondrite-normalised HSE patterns, display little evidence for metasomatic interaction with the Premier kimberlitic melt (**Fig. 4.10b**) or even with typical MARID melt metasomatism evident in MARID xenoliths from the central Kaapvaal craton (Kimberley kimberlite; Maier et al., 2012).

4.5.3.5. Sulphur isotopic compositions

Due to the friable nature of most sulphides from the Premier xenoliths, only four pentlandite grains from CIM15-006 were measured for sulphur isotope compositions. The $\delta^{34}S$ values measured for the CIM15-006 sulphides (pentlandite; n=4) display a narrow range from -5.73 to -0.48 ± 0.08 ‰, with a mean value of -3.22 ± 2.06 ‰ ($\delta^{34}S$ median = -4.24 ‰) (**Table 4.6**). These measured $\delta^{34}S$ values partially overlap with rare sulphur isotope data of Premier peridotite-derived sulphides (e.g. -5.19 to +4.35 ‰; Polley, 2011, unpublished thesis data), previously obtained via fluorination and mass spectrometry methods. In addition, the $\delta^{34}S$ values are comparable to sulphides from CLM peridotites in general (e.g. -6 to +11 ‰; Tsai et al., 1979; Chaussidon et al., 1989; Chaussidon and Lorand, 1990), as well as both E- and P-type diamond inclusion sulphides (-11 to +9.5 and -4 to +6 ‰, respectively; **Fig. 4.11**; Chaussidon et al., 1987; Eldridge et al., 1991; Rudnick et al., 1993; Farquhar et al., 2002; Cartigny et al., 2009; Thomassot et al., 2009). The sulphide $\delta^{34}S$ isotope systematics of bulk peridotite from the CLM group toward positive values (see **Fig. 4.11**), and therefore Ionov et al. (1992) suggested that a $\delta^{34}S$ value of +2 ‰ is probably representative of the CLM. In contrast, the $\delta^{34}S$ value suggested for the primitive upper mantle (PUM) is close to zero (~0.5 ‰; Chaussidon et al., 1989) MORB $\delta^{34}S$ compositions range from -2 to +2 ‰ (e.g. Labidi et al., 2012, 2014).

The CIM15-006 sulphides measured here, (four measured pentlandites) have $\Delta^{33}S$ values that range from -0.14 to +0.12 ‰ (**Table 4.6; Fig. 4.11**). For comparison, sulphur isotope compositions were also collected for pyrite from Premier eclogite (JJG-2717; Burness et al., in prep), with $\delta^{34}S$ values from

+0.45 to +3.46‰ (± 0.08‰ 1σ) and average $\Delta^{33}S$ values (per sulphide grain, n=4) between -0.03 and 0.07 ‰. Additionally, both the Premier eclogite and peridotite sulphide $\delta^{34}S$ and $\Delta^{33}S$ values are compared to measured $\delta^{34}S$ (-0.96 to -5.85 ‰) and $\Delta^{33}S$ (-0.15 to 0.17 ‰) values of pentlandite extracted from metasomatised peridotite xenoliths sampled from the Bultfontein kimberlite near Kimberley, South Africa (Giuliani et al., 2016; **Fig. 4.11**). The sulphur isotopic compositions are further discussed in **Section 4.6.3**.

4.6. DISCUSSION: FE- AND S-RICH METASOMATISM OF THE PREMIER GARNET-BEARING LHERZOLITES

4.6.1. Evidence for metasomatism of the silicate mineral phases

Depth-controlled chemical stratification of peridotite xenoliths in the lithospheric mantle below the Premier kimberlite has long been described by various researchers (e.g. Danchin et al., 1979; Griffin et al., 2003a; Hoal ,2003; Viljoen et al., 2009). Previous data shows that many of the low-temperature (900 – 1100 °C; 120 –160 km) coarse peridotites (i.e. harzburgite and lherzolite xenoliths) brought to the surface by the Premier kimberlite have Mg-rich mineral compositions that are relatively depleted in basaltic components (e.g. Ca, Al). This indicates that the coarse peridotites are residues of partial melting events that probably resulted from widespread extraction of basalt and komatiite during craton building in the Archean (e.g. Boyd and Gurney, 1982; de Wit et al., 1992). Consequently, these chemical characteristics overlap with many other low-temperature peridotites from various Kaapvaal localities.

In contrast, prevalent high-temperature equilibrated (~1300 – 1400 °C; 180 – 210 km) deformed peridotites (mostly lherzolites) from Premier display evidence of "Fe-rich" or basaltic melt-metasomatism that likely increased the FeO and TiO_2 content of silicates as well as sometimes adding secondary Fe-rich mica and aluminous amphibole (Danchin et al., 1979; Hoal, 2003; Griffin et al., 2003). This Fe-rich metasomatism is thought to be caused by percolating basaltic melts (Hoal et al., 2003) that may be linked to the intrusion of the Bushveld Igneous Complex (e.g. Maier et al., 2005). The exceptionally high iron contents of these deformed peridotites contrasts with other deep-seated peridotite xenoliths sampled from Kaapvaal kimberlites located away from the Bushveld complex (e.g. Kimberley kimberlite in the central Kaapvaal; Hawkesworth et al., 1990; Jacob et al., 2009). These peridotites instead, typically show hydrous, K-rich metasomatism that caused growth of Mg-phlogopite, K-richterite amphibole, clinopyroxene and Fe-Ti oxides (e.g. the "PIC" or "MARID" xenolith suite; Grégoire et al. 2002) in addition to incompatible element enrichments linked to (proto)kimberlitic magmatism (Dawson, 1984; Grégoire et al., 2002; Fitzpayne et al., 2018).

The garnet-bearing lherzolite xenoliths of this study show extensive evidence for both cryptic (incompatible element enrichments; **Fig. 4.3**) and modal metasomatism (i.e. introduction of secondary clinopyroxene, magnesium chromite, sulphide and magnetite; **Fig. 4.2a–f** and **4.6a–f**). Similar to

previous studies of Premier mantle xenoliths, both the coarse- and deformed-lherzolites studied here do not exhibit typical MARID or PIC-type metasomatism, that is, they do not contain significant secondary (metasomatically grown) phlogopite, ilmenite, rutile or amphibole phases (c.f. Gregoire et al., 2002). Instead, both types of garnet-bearing lherzolites show evidence of Fe-rich or basaltic (**Fig. 4.12a**) melt-related metasomatism (**Fig. 4.12b**). For example, the garnets have elevated TiO_2 (0.68 – 1.43 wt%, excl. coarse lherzolite CIM15-004 where TiO_2 = bdl) and FeO (6.4 – 7.7 wt.%) as well as lower Cr_2O_3 (1.6 – 5.5 wt.%) contents compared to garnet from "normal" depleted cratonic peridotites found at Premier (TiO_2 = <0.4 wt. %, FeO = <6 wt. %, Cr = ~4 – 10 wt. %; Viljoen et al., 2009). But, their major element chemistries (e.g. Ti = >2 wt. %, Fe = >6 wt. %, Cr = >2 wt. %) overlap extremely well with "melt-metasomatised" garnets also described from Premier (Griffin et al., 2003; Viljoen et al., 2009).

Garnet from the majority of the coarse and deformed lherzolites show normal "humped" primitive-mantle normalised REE patterns (**Fig. 4.3a, b**) typical of cratonic lherzolites (Pearson et al., 2003). The difference between the coarse and deformed garnet trace element compositions is minimal and hinges on HREE abundance and fractionation (**Fig. 12c**); coarse lherzolites show mild HREE depletion (Lu_N/Gd_N = 1.3 – 0.8) while deformed garnet show flat HREE (Lu_N/Gd_N = 1). Garnet from deformed lherzolite CIM15-017 is the only exception and displays a sinusoidal REE pattern (**Fig. 4.3a, b**) that is commonly observed in cratonic harzburgites (e.g. Stachel et al., 1998). This atypical garnet REE pattern is not uncommon in Premier garnet-bearing lherzolites. In fact, Viljoen et al. (2009) found garnet harzburgite cores with sinusoidal patterns surrounded by lherzolite rims with "normal" REE patterns in many Premier-derived garnet-lherzolites. This evidence may mark the transition from harzburgitic to lherzolitic assemblages due to Fe-rich basaltic metasomatism. In addition, garnets from some of the low-temperature lherzolites of this study display trace element evidence for a depletion event (minor depletions in Y and HREE; **Fig. 4.12b**) and subsequent re-enrichment (enrichments in Zr and Ti; **Fig. 4.12b**) supporting the major element evidence for a Fe-rich metasomatic overprint of the lithospheric mantle below Premier after primary melt extraction.

The garnet-bearing lherzolites from this study can be split into three distinct groups based on their approach to equilibrium and degree of metasomatism. The first group contains the most highly equilibrated coarse and deformed garnet-lherzolites (e.g. coarse lherzolites CIM15-002 and -004 as well as deformed lherzolites CIM15-001, -003, -017 and -021) that contain up to 10 modal % Fe-rich (up to 3.9 wt.% FeO) clinopyroxene and 1 to 2 modal % BMS. The fertile (or re-fertilised) coarse lherzolites CIM15-002 and -004 have olivine, orthopyroxene, garnet and clinopyroxene Mg# within range of the average Mg# of Premier coarse lherzolites from previous studies (e.g. Danchin et al., 1979; Viljoen et al, 2009). For example, olivine Mg# = 90.2 and 91.4 vs. 92.3±0.5, orthopyroxene Mg# = 92.1 and 92.3 vs. 93.1±0.5, garnet Mg# = 82.8 and 83.3 vs. 84.6±2.0 and clinopyroxene Mg# = 89.2 and 91.7 vs. 93.6±1.5 (1SD)). The deformed lherzolites CIM15-001, -003, -017 and -021 have slightly lower Mg# values than the coarse lherzolites because of increased enrichment in basaltic components (e.g. FeO,

TiO_2 and Al_2O_3; **Fig 12d–f**). Their Mg# are similar to previously studied deformed lherzolites from Danchin et al. (1979) and Viljoen et al. (2009), with olivine Mg# of 90.3 – 91.7 vs. 90.8±0.7, orthopyroxene Mg# of 91.5 – 92.4 vs. 91.8±0.7, garnet Mg# of 84.2 – 85.8 vs. 84.6±1.2 and clinopyroxene Mg# of 89.9 – 91.2 vs. 90.5±1.0, suggesting an excellent approach to equilibrium of these re-fertilised deformed garnet-lherzolites.

The second group consists of deformed garnet-lherzolites CIM15-015, -016 and -035 which contain large modal proportions (up to 15 %) of secondary Fe-rich (up to 4.4 wt.% FeO) clinopyroxene, up to 3 modal % magnetite and no BMS. Although, these rocks display Mg# values akin to previously studied deformed garnet-lherzolites (e.g. avg. ol Mg# = 90.8 vs. 90.8±0.7; avg. opx Mg# = 91.4 vs. 91.8±0.7; avg. grt Mg# = 84.5 vs. 84.6±1.2 and avg. cpx Mg# = 90.3 vs. 90.5±1.0; Danchin et al., 1979; Viljoen et al, 2009), some Fe-Mg disequilibrium exists between the clinopyroxene and olivine mineral phases (see **Section 4.5.2**). As such, it is suggested that the Fe-Mg disequilibrium seen in these rocks may have been caused by interaction with an oxidising Fe-rich melt/fluid which variably enriched the peridotite silicate assemblage in Fe and Ti, and stabilised large modal proportions (~3 modal %) of magnetite and Fe-rich clinopyroxene. The lack of BMS within these samples is not unexpected as sulphide is unstable under relatively oxidising conditions (e.g. Jugo, 2009).

The third group consists of coarse lherzolites CIM15-006 and -013 which contain ~2 modal % BMS as well as 10 and 15 modal % Fe-rich clinopyroxene, respectively. These rocks display significant evidence of both textural and chemical disequilibrium, with olivine, orthopyroxene and clinopyroxene Mg# values much lower than would be expected for four phase peridotites in equilibrium (e.g. olivine Mg# = 90.8 and 90.6 vs. 92.3±0.5, orthopyroxene Mg# = 91.8 and 91.5 vs. 93.1±0.5, garnet Mg# = 84.1 and 84.3 vs. 84.6±2.0 and clinopyroxene Mg# = 91 and 89.7 vs. 93.6±1.5; Danchin et al., 1979; Viljoen et al, 2009). As mentioned previously, the disequilibrium displayed by these samples is possibly due to Fe-rich metasomatism at shallow depths where elemental diffusion is slow resulting in rocks that are not fully equilibrated. The disequilibrium evident in these samples is much greater than has been previously reported for peridotite samples from Premier, but this is a function of sampling bias as the samples for this study were specifically selected based on the presence of metasomatic features and BMS.

Overall, it is suggested that both the shallower coarse lherzolites and deeper deformed lherzolites were affected by a pervasive Fe-rich metasomatic event probably linked to percolating plume-related asthenospheric melts or even the primary mafic-ultramafic melts of the Bushveld complex (e.g. Pearson, 1999; Hoal, 2003; Maier et al., 2005).

4.6.2. A metasomatic origin for base metal sulphide in Premier garnet-bearing lherzolites

The origin of the BMS found in the Premier lherzolites exhibit both textural and chemical evidence for an origin via metasomatism. Small isolated BMS inclusions (**Fig. 4.5a,b** and 4.**6a,b**) that are

completely trapped (e.g. isolated from the serpentinised peridotite matrix) in primary silicate minerals, predominantly orthopyroxene and olivine, are suggested to be the only non-metasomatic sulphide melts in these lherzolites that have re-equilibrated at low temperature (**Fig. 4.7**) into characteristic pentlandite, pyrrhotite and mono-sulphide solid solution phases (i.e. ISS; see Kullerud, 1969; Craig and Kullerud, 1973; Fleet and Pan, 1994). The other **small "isolated" inclusions**, **large "pseudo" inclusion**, as well as the **interstitial sulphides**, all connect texturally to the serpentinised interstitial matrix. Therefore, we considered these three sulphide types either metasomatically altered or purely metasomatic in origin and thus clearly secondary. For example, most **small "isolated" inclusions** are systematically located on silicate mineral rims or near to cracks and fissures, and some **small "isolated" inclusions** are hosted within silicate minerals with clear metasomatic origins (e.g. clinopyroxene; **Fig. 4.3c, d** and **4.6b**). The single **large "pseudo" inclusion** located on a garnet kelyphitic rim (**Fig. 4.6c**) was undoubtedly altered during reaction of the garnet with metasomatic fluids (c.f. Luguet et al., 2015), and it also contains 10% magnetite. Importantly, the **interstitial sulphides** display textures that follow the direction of veining within the coarse-and deformed-lherzolites (**Fig. 4.6c, d**) and this points towards a metasomatic process that involves infiltration of a metasomatic liquid/melt with the concomitant precipitation of base metal sulphides. The metasomatic sulphides are characterised by high M/S ratios (e.g. Alard et al., 2005, 2011; Wainwright et al., 2015; **Fig. 4.8a, b**), a large range of major element compositions (e.g. altered Pn, MSS, Hz, Zn- and Co-rich sulphide phases; **Fig. 4.7**) as well as significant magnetite alteration or addition (**Fig. 4.6c–f; Table 4.2**). Therefore, by combining both the textural characteristics and major element compositions of the multiple BMS phase assemblages found within the Premier peridotite xenoliths, it is suggested that the BMS probably formed from fractional crystallisation of evolved Fe-Ni-Cu-rich sulphide melts and complex sub-solidus re-equilibration.

Sulphide HSE and Se–Te systematics further place important constraints on sulphide paragenesis within the Premier lherzolites and also the extent of sulphide metasomatism that affected the Premier CLM. Relatively unaltered, **interstitial** (see **Section 4.5.3.2**) pentlandite and pyrite extracted from select Premier coarse-lherzolites (CIM15-006 and -004), show distinctive Pd-enriched chondrite-normalised HSE patterns (**Fig. 4.10**), with pyrite containing much lower concentrations of most HSE (e.g. **Fig. 4.9a,b**) due to sulphide host minerals having different partition coefficients for these elements (Luguet et al. 2015). The positively sloped HSE trends of both pentlandite and pyrite from the coarse lherzolites do not resemble the trends of residual sulphides from cratonic peridotitic mantle residues after high degrees of partial melting, as residual sulphides within CLM peridotite concentrate I-PGE and display characteristic depletions in P-PGE (specifically Pd, **Fig. 4.10b**; Pearson et al., 2002b; Day, 2013; Mungall and Brenan, 2014; Luguet and Pearson, 2019). In addition, the pentlandite and pyrite HSE and Se/Te ratios are suprachondritic (**Fig. 4.9a–f**) and therefore cannot be interpreted in terms of partial melting models alone (c.f. Brenan, 2015). For example, pure partial melting of sulphides in mantle residues would produce sub-chondritic Re_N/Pd_N ratios (akin to those seen in the Premier

pentlandite) and further melting would result in large depletions of the most incompatible HSEs (i.e. Te, Pt, Pd, and Re) and Se/Te ratios similar or slightly lower than the canonical chondritic value of ~8 (e.g. Brenan, 2015, Luguet et al., 2015), not the specific Pd, Re and Te enrichments and highly suprachondritic Se/Te ratios (Se/Te = >8; n=4) seen in the pentlandite extracted from CIM15-006.

Instead, the predominantly I-PGE-poor plus suprachondritic HSE systematics of the sulphides studied here are consistent with an origin of metasomatic alteration and/ or addition of BMS (Luguet et al., 2004, 2007, 2015; Delpech et al., 2012; Lorand et al., 2013; Bragagni et al., 2017; McDonald et al., 2017), where melt-rock interactions re-equilibrate sulphide HSE and importantly PGE contents toward that of the percolating fluid (e.g. Luguet et al., 2003, 2007, 2015; Reisberg et al., 2004; Alard et al., 2005; Lorand et al., 2010, 2013; Delpech et al., 2012; Marchesi et al., 2014; Wainwright et al., 2015b; Aulbach et al., 2016; Bragagni et al., 2017; Luguet and Pearson, 2019). Specifically, the suprachondritic Pd/Ir and Pt/Ir ratios observed in both the interstitial pentlandite and pyrite coupled with small fractionations in Os relative to Ir (Os_N/Ir_N = 0.5 and 1.2, for pentlandite) suggest interaction with a percolating fluid (perhaps basaltic in nature) that resulted in the precipitation of P-PGE enriched BMS and concomitant metasomatic enrichment of both the garnet (HREE) and clinopyroxene (LREE) in these rocks (**Fig. 4.3a–d**).

The pentlandite and pyrite studied here bear a partial resemblance to the patterns of bulk-rock Premier lherzolites in terms of Os-Pt, but not in terms of Pd and Au. Although we show that the Premier sulphides of this study have a metasomatic origin, their HSE patterns are not what one would expect for sulphide minerals equilibrated with kimberlitic metasomatic agents (e.g. the host Premier kimberlite and Kaapvaal MARID xenoliths; **Fig 4.10b).** Instead, the distinctive HSE patterns defined by the Premier coarse-lherzolite sulphides bear striking resemblance to metasomatic BMS found within abyssal peridotites (**Fig. 4.10a**), with chondrite-normalised Pd/Ir of 1.8 – 1487, Pd/Pt of 0.1 – 1218 and Re/Os of 1.8 – 603 (Alard et al., 2005, 2011; Luguet et al., 2019), as well as sulphides present in peridotite lithologies from the Bushveld Igneous Complex (**Fig. 4.10a**), with chondrite-normalised Pd/Ir of 1.8 – 948, Pd/Pt of 12.1 – 9402 and Os/Ir of 1.2 – 14.1 (Hutchinson and McDonald, 2008). These similarities allude perhaps to a pervasive sulphur-rich metasomatic event that affected the CLM below the Premier kimberlite and the Bushveld Igneous Complex prior to emplacement. Thus, it appears that a Fe-rich "basaltic" melt was responsible for not only metasomatising the silicate portion of the Premier CLM (e.g. Hoal, 2003; Viljoen et al., 2009) but also facilitating sulphide HSE enrichment (e.g. Maier et al., 2005).

4.6.3. Evidence from multiple sulphur isotopes

The $\delta^{34}S$ values from the four Pn grains of this study show a range from -5.73 to -0.48±0.08 ‰ and $\Delta^{33}S$ from -0.14 to +0.12 (**Table 4.6; Fig. 4.11**). Sulphides analysed from the Premier eclogite have similar $\Delta^{33}S$ values (-0.03±0.1 ‰ and 0.07±0.07 ‰), but in contrast to the peridotite sulphides, have

positive $\delta^{34}S$ of +0.45 to +3.46 ± 0.08 ‰. The $\delta^{34}S$ values of the peridotite and eclogite sulphides at premier vary significantly from the suggested $\delta^{34}S$ values of both the primitive upper mantle (+0.5 ‰; Chaudisson et al., 1989) and the cratonic lithospheric mantle (+2 ‰; Ionov et al., 1992). Therefore, we suggest a recycled sulphur component with negative $\delta^{34}S$ values within the sulphides at Premier, similar to peridotite sulphides from Kimberley with negative $\delta^{34}S$ values of -5.85 ‰ to -0.96 as argued by Giuliani et al. (2016).

Multiple sulphur isotopes are effective tools to trace the presence of recycled sedimentary material in the mantle. In particular, $\Delta^{33}S$ can be used to trace the presence of Archean sedimentary material in mantle-derived materials, due to the mass-independent sulphur isotope fractionation (S-MIF) of surficial material that occurred during the Archean in response to the activity of UV radiation in the absence of a modern atmosphere (Thomassot et al., 2015). Sulphur mass-independent fractionation (S-MIF) is generally defined as $\Delta^{33}S$ values that vary outside of 0 ± 0.12‰ (Farquhar et al., 2002). Additionally, it is important to note that MIF is chemically conservative in the mantle (Thomassot et al., 2009) and cannot be changed through metamorphism or high-temperature metasomatic reactions (Penniston-Dorland et al., 2012). Thus, non-zero $\Delta^{33}S$ values ($\Delta^{33}S$~0 for all mass-dependent S isotope fractionation) can be used to clearly indicate the presence of recycled Archean sedimentary sulphur in the geological rock record.

Although the eclogite and peridotite sulphides show variable $\Delta^{33}S$, the total range is <0.12‰ of the mass-dependent fraction line. However, both positive and negative variation of $\Delta^{33}S$ in the Premier peridotite and eclogite sulphides, suggests there may exist some component of heterogeneous Archean recycled sulphur with a MIF signature (Farquhar et al., 2010, and references therein; Penniston-Dorland et al., 2012). Specifically, crustal components sourced from the local Transvaal Supergroup with $\Delta^{33}S$ values ranging from -0.4 to 5.0 ‰ or even from the neighbouring Griqualand-West sub-basin with $\Delta^{33}S$ values ranging from -2.5 to +9.6 ‰ (Kamber and Whitehouse, 2007; Penniston-Dorland et al., 2008, 2012; Guo et al., 2009; Ono et al., 2009; Magalhães et al., 2018), could account for both the positive and negative heterogeneities seen in the Premier peridotites. It has well been established that recycled crustal material likely was incorporated into the Kaapvaal CLM during amalgamation of the craton during the Neo-Mesoarchean when the Witwatersrand (3.7 to 2.7 Ga; Kröner and Compston, 1988; Armstrong et al., 1991) and Kimberley (3.3 to 2.9 Ga; Schmitz et al., 2004) blocks amalgamated by subduction-accretion and continent-continent collision at 2.9 Ga (Shirey et al., 2001; Schmitz et al., 2004). This amalgamation is widely accepted to have introduced significant crustal components to the CLM, as shown by ca. 2.9 Ga eclogites and diamond inclusions with crustal geochemical and isotopic signatures (c.f. Shirey et al., 2004; Richardson and Shirey, 2008; Thomassot et al., 2009).

Heterogeneity in both $\delta^{34}S$ and $\Delta^{33}S$ between different sulphide grains from the same peridotite sample (CIM15-006; **Fig. 4.11**) could also be explained by localised melt mixing of the original

sulphide isotope characteristics with sulphur carried in by a single or even multiple metasomatic fluids (Luguet et al., 2015). Considering the strongly metasomatic HSE signatures of the peridotite sulphides discussed above, it is suggested that the multiple sulphur isotope compositions probably largely represent that of the percolating metasomatic fluid. However, the sulphur isotope compositions could potentially also represent partial re-equilibration of residual sulphide within the peridotite matrix to that of the percolating fluid.

4.7. POSSIBLE IMPLICATIONS

Previously, we argued that some of the Premier peridotite sulphides have HSE similarities to sulphides found in Bushveld peridotite (see **Fig. 4.10**; **Section 4.5.3.4** and **4.6.2**). At ~2.056 Ga (Zeh et al., 2015), the sulphide and magnetite-rich ultramafic-mafic magmas of the BIC intruded the Kaapvaal craton, coinciding with a pervasive tectonothermal event affecting the local Archean crust. Sulphides recovered from the ultra mafic layered rocks of Bushveld have $\delta^{34}S$ values that range from -1.2 to 5.1 ‰ (Penniston-Dorland et al., 2012; Smith et al., 2016; Magalhães et al., 2018) and non-zero $\Delta^{33}S$ = 0.112 ± 0.024 ‰ (Penniston-Dorland et al., 2008, 2012; Magalhães et al., 2018). The positive $\delta^{34}S$ values overlap with the $\delta^{34}S$ isotope composition of Premier eclogite (JJG-2717). Additionally, some negative $\delta^{34}S$ values and $\Delta^{33}S$ of the Bushveld sulphides partially overlap with the $\delta^{34}S$ and $\Delta^{33}S$ found in the CIM15-006 peridotite sulphides of this study (**Fig 4.11b**). In combination with the similar HSE patterns of the Premier peridotite sulphide and the Bushveld peridotite-hosted sulphide (see **Fig. 4.10a**), there could exist a petrogenetic link between the sulphide mineralization in the Bushveld and its lithospheric mantle. It is also possible however that the BIC sulphur isotope signature indicates a crustal origin. Mass balance calculations by Penniston-Dorland et al. (2012) reveal that only a small portion of Archean crustal material (~0.3 wt. % of the Bushveld magma) with positive $\delta^{34}S$ and non-zero $\Delta^{33}S$ is required to attain the specific sulphur isotope values obtained for the Bushveld sulphides. Based on the relatively homogenous sulphur isotope composition of the Bushveld complex, Penniston-Dorland et al. (2012) suggested that the non-zero $\Delta^{33}S$ and mostly positive $\delta^{34}S$ values observed in the Bushveld sulphides were assimilated into the Bushveld magma prior to crustal emplacement and did not result from post-crystallisation contamination. That is, the ultimate source of the $\Delta^{33}S$ and $\delta^{34}S$ isotope composition of the Bushveld sulphides was inherited from the cratonic mantle, which could be represented by the re-fertilised peridotite- and eclogite-derived sulphides presented here. Admittedly, we are only able to provide sparse data for the sulphur isotope composition of the Premier lithospheric mantle, and further detailed HSE and multiple sulphur isotope studies of CLM-derived samples may help elucidate the origin of sulphur in both the lithospheric mantle below Premier as well as the Bushveld igneous complex.

4.8. CONCLUSIONS

- The metasomatised Premier garnet-bearing lherzolites are split into two distinct groups, coarse and deformed, based on texture as well as mineral major and trace element compositions. Generally, both textural groups are Fe-enriched compared to other Kaapvaal CLM-derived peridotites, but the coarse-lherzolites show slight depletions in Ca, Al, Ti ± Fe compared to the deformed-lherzolites. Garnet in the deformed "sheared" lherzolites display typical "normal" REE patterns with enrichments in LREE and MREE and flat HREE, the equilibrium clinopyroxene display enriched convex-upward REE patterns. Comparatively, the coarse-lherzolite garnet reveal "humped" REE patterns, with steep LREE and MREE and slight depletions in HREE. The analogous clinopyroxene reveal variable REE patterns and Zr, Ti and LREE enrichments in most samples indicate depletion and subsequent re-fertilisation events.
- The equilibrium coarse-lherzolites define the lowest pressures (3.4 – 4.4 GPa) and temperatures (1014 – 1221 ºC), while the deformed lherzolites define the highest equilibrium P–T conditions (between 5.4 – 7.4 GPa and 1370 – 1410 °C). Together with previous research on Premier peridotites and diamond inclusions, the Premier mantle lithosphere is defined by a higher paleogeotherm compared to other kimberlite occurrences on the Kaapvaal craton, potentially recording high-temperature thermal perturbations from the plume-related magmatism of the Bushveld Igneous Complex.
- The Premier garnet-bearing lherzolites experienced distinctive Fe-rich silicate modal metasomatism concomitant with the metasomatic addition of base metal sulphide and magnetite components. The single and multiple assemblage sulphides define various habits and textural relationships to the silicate mineral assemblage, often with close associations to secondary clinopyroxene as well as metasomatic veining. Pentlandite and pyrite from select coarse-lherzolites are characterised by Pd-enriched positively sloping chondrite-normalised HSE patterns. Additionally, fractionated sulphide HSE and Se–Te geochemical systematics, especially suprachondritic Pd/Ir and Se/Te ratios, indicate that these sulphides are distinctly metasomatic and are atypical of PUM-like mantle HSE signatures.
- The Premier peridotite sulphides have $\delta^{34}S$ values that range from -5.7 to -0.5 ‰ and $\Delta^{33}S$ from -0.14 to +0.12 ‰. The eclogite sulphides have $\delta^{34}S$ values that range from +0.5 to +3.5 ‰ and $\Delta^{33}S$ from -0.18 to +0.14 ‰. Both groups of sulphides have either relatively depleted or enriched $\delta^{34}S$ signatures compared to the primitive upper mantle value of close to 0‰. No clear MIF signature is recognized. Therefore, there may exist a recycled crustal sulphur component within these sulphides, mobilised during the Fe- and S-rich metasomatic event that variably enriched the lithospheric mantle below Premier kimberlite.

REFERENCES

Alard, O., Griffin, W. L., Lorand, J. P., Jackson, S. E. and O'Reilly, S. Y. (2000). Non-chondritic distribution of the highly siderophile elements in mantle sulphides. Nature **407**(6806), 891.

Alard, O., Lorand, J. P., Reisberg, L., Bodinier, J. L., Dautria, J. M. and O'reilly, S. Y. (2011). Volatile-rich metasomatism in Montferrier xenoliths (Southern France): Implications for the abundances of chalcophile and highly siderophile elements in the subcontinental mantle. Journal of Petrology **52**(10), 2009-2045.

Alard, O., Luguet, A., Pearson, N.J., Griffin, W.L., Lorand, J.P., Gannoun, A., Burton, K.W. and O'Reilly, S.Y. (2005). In situ Os isotopes in abyssal peridotites bridge the isotopic gap between MORBs and their source mantle. Nature **436**(7053), 1005.

Armstrong, R. A., Compston, W., Retief, E. A., Williams, I. T. and Welke, H. J. (1991). Zircon ion microprobe studies bearing on the age and evolution of the Witwatersrand triad. Precambrian Research **53**(3-4), 243-266.

Arndt, N. T., Coltice, N., Helmstaedt, H. and Gregoire, M. (2009). Origin of Archean subcontinental lithospheric mantle: Some petrological constraints. Lithos **109**(1-2), 61-71.

Aulbach, S., Mungall, J. E. and Pearson, D. G. (2016). Distribution and processing of highly siderophile elements in cratonic mantle lithosphere. Reviews in Mineralogy and Geochemistry **81**(1), 239-304.

Ballhaus, C., Bockrath, C., Wohlgemuth-Ueberwasser, C., Laurenz, V. and Berndt, J. (2006). Fractionation of the noble metals by physical processes. Contributions to Mineralogy and Petrology **152**(6), 667-684.

Barnes, S. J., Makovicky, E., Makovicky, M., Rose-Hansen, J. and Karup-Moller, S. (1997). Partition coefficients for Ni, Cu, Pd, Pt, Rh, and Ir between monosulfide solid solution and sulfide liquid and the formation of compositionally zoned Ni–Cu sulfide bodies by fractional crystallization of sulfide liquid. Canadian Journal of Earth Sciences **34**(4), 366-374.

Becker, H., Horan, M. F., Walker, R. J., Gao, S., Lorand, J. P. and Rudnick, R. L. (2006). Highly siderophile element composition of the Earth's primitive upper mantle: constraints from new data on peridotite massifs and xenoliths. Geochimica et Cosmochimica Acta **70**(17), 4528-4550.

Bell, D. R., Gregoire, M., Grove, T. L., Chatterjee, N., Carlson, R. W. and Buseck, P. R. (2005). Silica and volatile-element metasomatism of Archean mantle: a xenolith-scale example from the Kaapvaal Craton. Contributions to Mineralogy and Petrology **150**(3), 251.

Bockrath, C., Ballhaus, C. and Holzheid, A. (2004). Fractionation of the platinum-group elements

during mantle melting. Science **305**(5692), 1951-1953.

Boyd, F. R. and Gurney, J. J. (1982). Low-calcium garnets: keys to craton structure and diamond crystallization. Carnegie Institution of Washington Yearbook **81**, 261-267.

Boyd, F. R. and Nixon, P. H. (1975). Origins of the ultramafic nodules from some kimberlites of northern Lesotho and the Monastery Mine, South Africa. In: Physics and Chemistry of the Earth **9**, Pergamon, 431-454.

Boyd, F. R., Pearson, D. G. and Mertzman, S. A. (1998). Spinel-facies peridotites from the Kaapvaal root. In: The J.B. Dawson Volume., J.J. Gurney, et al. (Ed.), Proc. 7th Int. Kimberlite Conference **1**, Red Roof Design, Cape Town, 40 – 48.

Bragagni, A., Luguet, A., Fonseca, R. O. C., Pearson, D. G., Lorand, J. P., Nowell, G. M. and Kjarsgaard, B. A. (2017). The geological record of base metal sulfides in the cratonic mantle: A microscale $^{187}Os/^{188}Os$ study of peridotite xenoliths from Somerset Island, Rae Craton (Canada). Geochimica et Cosmochimica Acta **216**, 264-285.

Brenan, J. M. (2015). Se–Te fractionation by sulfide–silicate melt partitioning: Implications for the composition of mantle-derived magmas and their melting residues. Earth and Planetary Science Letters **422**, 45-57.

Brey, G. P. and Köhler, T. (1990). Geothermobarometry in four-phase lherzolites II. New thermobarometers, and practical assessment of existing thermobarometers. Journal of Petrology **31**(6), 1353-1378.

Carlson, R. W., Pearson, D. G., Boyd, F. R., Shirey, S. B., Irvine, G., Menzies, A. H. and Gurney, J. J. (1999). Re–Os systematics of lithospheric peridotites: implications for lithosphere formation and preservation. In: Proceedings of the 7th International Kimberlite Conference, Gurney, J. J. (Ed.), Red Roof Design, Cape Town, 99-108.

Carlson, R. W., Pearson, D. G. and James, D. E. (2005). Physical, chemical, and chronological characteristics of continental mantle. Reviews of Geophysics **43**(1).

Cartigny, P., Farquhar, J., Thomassot, E., Harris, J.W., Wing, B., Masterson, A., McKeegan, K. and Stachel, T. (2009). A mantle origin for Paleoarchean peridotitic diamonds from the Panda kimberlite, Slave Craton: evidence from 13C-, 15N-and 33, 34S-stable isotope systematics. Lithos **112**, 852-864.

Chaussidon, M., Albarede, F. and Sheppard, S. M. F. (1987). Sulphur isotope heterogeneity in the mantle from ion microprobe measurements of sulphide inclusions in diamonds. Nature **330**(6145), 242.

Chaussidon, M., Albarède, F. and Sheppard, S. M. (1989). Sulphur isotope variations in the mantle from ion microprobe analyses of micro-sulphide inclusions. Earth and Planetary Science Letters **92**(2), 144-156.

Chaussidon, M. and Lorand, J. P. (1990). Sulphur isotope composition of orogenic spinel lherzolite massifs from Ariege (North-Eastern Pyrenees, France): An ion microprobe study. Geochimica et Cosmochimica Acta **54**(10), 2835-2846.

Craig, J. R. (1969). Phase relations in the Cu-Fe-Ni-S system and their application to magmatic ore deposits. Economic Geology Monograph **4**, 344-358.

Craig, J. and Kullerud, G. (1973) The Cu-Zn-S system. Mineralium Deposita **8**, 81-91.

Danchin, R. V. (1979). Mineral and bulk chemistry of garnet lherzolite and garnet harzburgite xenoliths from the Premier Mine, South Africa. The Mantle Sample: Inclusion in Kimberlites and Other Volcanics **16**, 104-126.

Dawson, J. B. (1984). Contrasting types of upper-mantle metasomatism. In: Kimberlites: II. The Mantle and Crust–mantle Relationships, Kornprobst, J. (Ed.), Elsevier, Amsterdam, 289 – 294.

Day, J. M. (2013). Hotspot volcanism and highly siderophile elements. Chemical Geology **341**, 50-74.

Day, J. M., Walker, R. J. and Warren, J. M. (2017). 186Os–187Os and highly siderophile element abundance systematics of the mantle revealed by abyssal peridotites and Os-rich alloys. Geochimica et Cosmochimica Acta **200**, 232-254.

De Hoog, J. C. M., Taylor, B. E. and Van Bergen, M. J. (2001). Sulfur isotope systematics of basaltic lavas from Indonesia: implications for the sulfur cycle in subduction zones. Earth and Planetary Science Letters **189**(3-4), 237-252.

de Wit, M.J., de Ronde, C.E., Tredoux, M., Roering, C., Hart, R.J., Armstrong, R.A., Green, R.W., Peberdy, E. and Hart, R.A., 1992.(1992) Formation of an Archaean continent. Nature **357**(6379), 553.

Deines, P. and Harris, J. W. (1995). Sulfide inclusion chemistry and carbon isotopes of African diamonds. Geochimica et Cosmochimica Acta **59**(15), 3173-3188.

Delavault, H., Chauvel, C., Thomassot, E., Devey, C. W. and Dazas, B. (2016). Sulfur and lead isotopic evidence of relic Archean sediments in the Pitcairn mantle plume. Proceedings of the National Academy of Sciences **113**(46), 12952-12956.

Delpech, G., Lorand, J. P., Grégoire, M., Cottin, J. Y. and O'Reilly, S. Y. (2012). In-situ geochemistry of sulfides in highly metasomatized mantle xenoliths from Kerguelen, southern Indian Ocean. Lithos **154**, 296-314.

Eales, H. V. and Cawthorn, R. G. (1996). The Bushveld Complex. In: Developments in Petrology. Cawthorn ,G. (Ed.), Elsevier **15**, 181-229.

Eldridge, C. S., Compston, W., Williams, I. S., Harris, J. W. and Bristow, J. W. (1991). Isotope evidence for the involvement of recycled sediments in diamond formation. Nature **353**(6345), 649.

Farquhar, J., Savarino, J., Airieau, S. and Thiemens, M. H. (2001). Observation of wavelength-sensitive mass-independent sulfur isotope effects during SO_2 photolysis: Implications for the early atmosphere. Journal of Geophysical Research: Planets **106**(E12), 32829-32839.

Farquhar, J., Wing, B. A., McKeegan, K. D., Harris, J. W., Cartigny, P. and Thiemens, M. H. (2002). Mass-independent sulfur of inclusions in diamond and sulfur recycling on early Earth. Science **298**(5602), 2369-2372.

Farquhar, J., Wu, N., Canfield, D. E. and Oduro, H. (2010). Connections between sulfur cycle evolution, sulfur isotopes, sediments, and base metal sulfide deposits. Economic Geology **105**(3), 509-533.

Fischer-Gödde, M., Becker, H. and Wombacher, F. (2010). Rhodium, gold and other highly siderophile element abundances in chondritic meteorites. Geochimica et Cosmochimica Acta **74**(1), 356-379.

Fitzpayne, A., Giuliani, A., Phillips, D., Hergt, J., Woodhead, J.D., Farquhar, J., Fiorentini, M.L., Drysdale, R.N. and Wu, N. (2018). Kimberlite-related metasomatism recorded in MARID and PIC mantle xenoliths. Mineralogy and Petrology **112**(1), pp.71-84.

Fleet, M. E., Crocket, J. H. and Stone, W. E. (1996). Partitioning of platinum-group elements (Os, Ir, Ru, Pt, Pd) and gold between sulfide liquid and basalt melt. Geochimica et Cosmochimica Acta **60**(13), 2397-2412.

Fleet, M. E. and Pan, Y. (1994). Fractional crystallization of anhydrous sulfide liquid in the system Fe-Ni-Cu-S, with application to magmatic sulfide deposits. Geochimica et Cosmochimica Acta **58(**16), 3369-3377.

Fonseca, R. O., Mallmann, G., O'Neill, H. S. C., Campbell, I. H. and Laurenz, V. (2011). Solubility of Os and Ir in sulfide melt: Implications for Re/Os fractionation during mantle melting. Earth and Planetary Science Letters **311**(3-4), 339-350.

Fouch, M. J., James, D. E., VanDecar, J. C., Van der Lee, S. and Kaapvaal Seismic Group. (2004). Mantle seismic structure beneath the Kaapvaal and Zimbabwe Cratons. South African Journal of Geology **107**(1-2), 33-44.

Giuliani, A., Fiorentini, M. L., Martin, L. A., Farquhar, J., Phillips, D., Griffin, W. L. and LaFlamme, C. (2016). Sulfur isotope composition of metasomatised mantle xenoliths from the Bultfontein kimberlite (Kimberley, South Africa): Contribution from subducted sediments and the effect of sulfide alteration on S isotope systematics. Earth and Planetary Science Letters **445**, 114-124.

Gréau, Y., Huang, J. X., Griffin, W. L., Renac, C., Alard, O. and O'Reilly, S. Y. (2011). Type I eclogites from Roberts Victor kimberlites: products of extensive mantle metasomatism. Geochimica et Cosmochimica Acta **75**(22), 6927-6954.

Grégoire, M., Bell, D. and Le Roex, A. (2002). Trace element geochemistry of phlogopite-rich mafic mantle xenoliths: their classification and their relationship to phlogopite-bearing peridotites and kimberlites revisited. Contributions to Mineralogy and Petrology **142**(5), 603-625.

Grégoire, M., Bell, D. R. and Le Roex, A. P. (2003). Garnet lherzolites from the Kaapvaal Craton (South Africa): trace element evidence for a metasomatic history. Journal of Petrology **44**(4), 629-657.

Grégoire, M., Tinguely, C., Bell, D. R. and Le Roex, A. P. (2005). Spinel lherzolite xenoliths from the Premier kimberlite (Kaapvaal craton, South Africa): nature and evolution of the shallow upper mantle beneath the Bushveld complex. Lithos **84**(3-4), 185-205.

Griffin, W.L., O'Reilly, S.Y., Abe, N., Aulbach, S., Davies, R.M., Pearson, N.J., Doyle, B.J. and Kivi, K. (2003). The origin and evolution of Archean lithospheric mantle. Precambrian Research **127**(1-3), 19-41.

Griffin, W. L., O'Reilly, S. Y., Natapov, L. M. and Ryan, C. G. (2003). The evolution of lithospheric mantle beneath the Kalahari Craton and its margins. Lithos **71**(2-4), 215-241.

Guo, J., Griffin, W. L. and O'Reilly, S. Y. (1999). Geochemistry and origin of sulphide minerals in mantle xenoliths: Qilin, Southeastern China. Journal of Petrology **40**(7), 1125-1149.

Guo, Q., Strauss, H., Kaufman, A.J., Schröder, S., Gutzmer, J., Wing, B., Baker, M.A., Bekker, A., Jin, Q., Kim, S.T. and Farquhar, J. (2009). Reconstructing Earth's surface oxidation across the Archean-Proterozoic transition. Geology **37**(5), 399-402.

Gurney, J. J., Harris, J. W., Rickard, R. S. and Moore, R. O. (1985). Inclusions in Premier mine diamonds. Transactions of the geological society of South Africa **88**(2), 301-310.

Hawkesworth, C. J., Erlank, A. J., Kempton, P. D., & Waters, F. G. (1990). Mantle metasomatism: isotope and trace-element trends in xenoliths from Kimberley, South Africa. Chemical Geology **85**(1-2), 19-34.

Hoal, K. O. (2003). Samples of Proterozoic iron-enriched mantle from the Premier kimberlite. Lithos

71(2-4), 259-272.

Hutchinson, D. and McDonald, I. (2008). Laser ablation ICP-MS study of platinum-group elements in sulphides from the Platreef at Turfspruit, northern limb of the Bushveld Complex, South Africa. Mineralium Deposita **43**(6), 695.

Hutchinson, D., Foster, J., Prichard, H. and Gilbert, S. (2015). Concentration of particulate platinum-group minerals during magma emplacement; a case study from the Merensky Reef, Bushveld Complex. Journal of Petrology **56**(1), 113-159.

Ionov, D. A., Hoefs, J., Wedepohl, K. H. and Wiechert, U. (1992). Content and isotopic composition of sulphur in ultramafic xenoliths from central Asia. Earth and Planetary Science Letters **111**(2-4), 269-286.

Irvine, G. J., Pearson, D. G. and Carlson, R. W. (2001). Lithospheric mantle evolution of the Kaapvaal Craton: A Re-Os isotope study of peridotite xenoliths from Lesotho kimberlites. Geophysical Research Letters **28**(13), 2505-2508.

Jacob, D. E., Viljoen, K. S. and Grassineau, N. V. (2009). Eclogite xenoliths from Kimberley, South Africa: a case study of mantle metasomatism in eclogites. Lithos **112**, 1002-1013.

James, D. E., Fouch, M. J., VanDecar, J. C., Van Der Lee, S. and Kaapvaal Seismic Group. (2001). Tectospheric structure beneath southern Africa. Geophysical Research Letters **28**(13), 2485-2488.

Jochum, K. P., Nohl, U., Herwig, K., Lammel, E., Stoll, B. and Hofmann, A. W. (2005). GeoReM: a new geochemical database for reference materials and isotopic standards. Geostandards and Geoanalytical Research **29**(3), 333-338.

Johnson, K. T., Dick, H. J. and Shimizu, N. (1990). Melting in the oceanic upper mantle: an ion microprobe study of diopsides in abyssal peridotites. Journal of Geophysical Research **95**(B3), 2661-2678.

Jugo, P. J. (2009). Sulfur content at sulfide saturation in oxidized magmas. Geology **37**(5), 415-418.

Kamber, B. S. and Whitehouse, M. J. (2007). Micro-scale sulphur isotope evidence for sulphur cycling in the late Archean shallow ocean. Geobiology **5**(1), 5-17.

Kennedy, C. S. and Kennedy, G. C. (1976). The equilibrium boundary between graphite and diamond. Journal of Geophysical Research **81**(14), 2467-2470.

Kennedy, L. A., Russell, J. K. and Kopylova, M. G. (2002). Mantle shear zones revisited: The connection between the cratons and mantle dynamics. Geology **30**(5), 419-422.

Kitayama, Y., Thomassot, E., Galy, A., Golovin, A., Korsakov, A., d'Eyrames, E., Assayag, N., Bouden, N. and Ionov, D. (2017). Co-magmatic sulfides and sulfates in the Udachnaya-East pipe (Siberia): A record of the redox state and isotopic composition of sulfur in kimberlites and their mantle sources. Chemical Geology **455**, 315-330.

Kitayama, Y., Thomassot, E., O'Neil, J. and Wing, B. A. (2012). Sulfur-and oxygen-isotope constraints on the sedimentary history of apparent conglomerates from the Nuvvuagittuq Greenstone Belt (Nunavik, Québec). Earth and Planetary Science Letters **355**, 271-282.

König, S., Lorand, J. P., Luguet, A. and Pearson, D. G. (2014). A non-primitive origin of near-chondritic S–Se–Te ratios in mantle peridotites; implications for the Earth's late accretionary history. Earth and Planetary Science Letters **385**, 110-121.

König, S., Luguet, A., Lorand, J. P., Wombacher, F. and Lissner, M. (2012). Selenium and tellurium systematics of the Earth's mantle from high precision analyses of ultra-depleted orogenic peridotites. Geochimica et Cosmochimica Acta **86**, 354-366.

Konzett, J., Armstrong, R. A. and Günther, D. (2000). Modal metasomatism in the Kaapvaal craton lithosphere: constraints on timing and genesis from U–Pb zircon dating of metasomatized peridotites and MARID-type xenoliths. Contributions to Mineralogy and Petrology **139**(6), 704-719.

Korolev, N. M., Kopylova, M., Bussweiler, Y., Pearson, D. G., Gurney, J. and Davidson, J. (2018). The uniquely high-temperature character of Cullinan diamonds: A signature of the Bushveld mantle plume?. Lithos **304**, 362-373.

Kröner, A. and Compston, W. (1988). Ion microprobe ages of zircons from early Archaean granite pebbles and greywacke, Barberton greenstone belt, southern Africa. Precambrian Research **38**(4), 367-380.

Kullerud, G., Yund, R.A., and Moh, G.H. (1969). Phase relations in the CuFe-S, Cu-Ni-S, and Fe-Ni-S systems. Economic Geology Monograph **4**, 323–343.

Labidi, J., Cartigny, P., Birck, J. L., Assayag, N. and Bourrand, J. J. (2012). Determination of multiple sulfur isotopes in glasses: A reappraisal of the MORB δ34S. Chemical Geology **334**, 189-198.

Labidi, J., Cartigny, P., Hamelin, C., Moreira, M. and Dosso, L. (2014). Sulfur isotope budget (32S, 33S, 34S and 36S) in Pacific–Antarctic ridge basalts: A record of mantle source heterogeneity and hydrothermal sulfide assimilation. Geochimica et Cosmochimica Acta **133**, 47-67.

Labidi, J., Cartigny, P. and Jackson, M. G. (2015). Multiple sulfur isotope composition of oxidized Samoan melts and the implications of a sulfur isotope 'mantle array'in chemical geodynamics.

Earth and Planetary Science Letters **417**, 28-39.

Latypov, R., Chistyakova, S. and Mukherjee, R. (2017). A novel hypothesis for origin of massive chromitites in the Bushveld Igneous Complex. Journal of Petrology **58**(10), 1899-1940.

Li, C., Barnes, S. J., Makovicky, E., Rose-Hansen, J. and Makovicky, M. (1996). Partitioning of nickel, copper, iridium, rhenium, platinum, and palladium between monosulfide solid solution and sulfide liquid: effects of composition and temperature. Geochimica et Cosmochimica Acta **60**(7), 1231-1238.

Li, Y. and Audétat, A. (2012). Partitioning of V, Mn, Co, Ni, Cu, Zn, As, Mo, Ag, Sn, Sb, W, Au, Pb, and Bi between sulfide phases and hydrous basanite melt at upper mantle conditions. Earth and Planetary Science Letters **355**, 327-340.

Liu, Y. and Brenan, J. (2015). Partitioning of platinum-group elements (PGE) and chalcogens (Se, Te, As, Sb, Bi) between monosulfide-solid solution (MSS), intermediate solid solution (ISS) and sulfide liquid at controlled fO_2–fS_2 conditions. Geochimica et Cosmochimica Acta **159**, 139-161.

Liu, C. Z., Snow, J. E., Brügmann, G., Hellebrand, E. and Hofmann, A. W. (2009). Non-chondritic HSE budget in Earth's upper mantle evidenced by abyssal peridotites from Gakkel ridge (Arctic Ocean). Earth and Planetary Science Letters **283**(1-4), 122-132.

Liu, C. Z., Snow, J. E., Hellebrand, E., Brügmann, G., Von Der Handt, A., Büchl, A. and Hofmann, A. W. (2008). Ancient, highly heterogeneous mantle beneath Gakkel ridge, Arctic Ocean. Nature **452**(7185), 311.

Lorand, J. P., Alard, O. and Luguet, A. (2010). Platinum-group element micronuggets and refertilization process in Lherz orogenic peridotite (northeastern Pyrenees, France). Earth and Planetary Science Letters **289**(1-2), 298-310.

Lorand, J. P. and Gregoire, M. (2006). Petrogenesis of base metal sulphide assemblages of some peridotites from the Kaapvaal craton (South Africa). Contributions to Mineralogy and Petrology **151**(5), 521.

Lorand, J. P., Luguet, A. and Alard, O. (2013). Platinum-group element systematics and petrogenetic processing of the continental upper mantle: A review. Lithos **164**, 2-21.

Luguet, A., Behrens, M., Pearson, D. G., König, S. andHerwartz, D. (2015). Significance of the whole rock Re–Os ages in cryptically and modally metasomatised cratonic peridotites: Constraints from HSE–Se–Te systematics. Geochimica et Cosmochimica Acta **164,** 441-463.

Luguet, A., Lorand, J. P., Alard, O. and Cottin, J. Y. (2004). A multi-technique study of platinum

group element systematic in some Ligurian ophiolitic peridotites, Italy. Chemical Geology **208**(1-4), 175-194.

Luguet, A., Lorand, J. P. and Seyler, M. (2003). Sulfide petrology and highly siderophile element geochemistry of abyssal peridotites: A coupled study of samples from the Kane Fracture Zone (45 W 23 20N, MARK area, Atlantic Ocean). Geochimica et Cosmochimica Acta **67**(8), 1553-1570.

Luguet, A. and Pearson, G. (2019). Dating mantle peridotites using Re-Os isotopes: The complex message from whole rocks, base metal sulfides, and platinum group minerals. American Mineralogist: Journal of Earth and Planetary Materials **104**(2), 165-189.

Luguet, A., Shirey, S. B., Lorand, J. P., Horan, M. F. and Carlson, R. W. (2007). Residual platinum-group minerals from highly depleted harzburgites of the Lherz massif (France) and their role in HSE fractionation of the mantle. Geochimica et Cosmochimica Acta **71**(12), 3082-3097.

Luth, R. W. (1999). Carbon and carbonates in the mantle. Mantle Petrology: Field Observations and High Pressure Experimentation: A Tribute to Francis R.(Joe) Boyd **6**, 297-316.

Macgregor, I. D. (1974). The System MgO-Ai2O3-Si02: Solubility of Ai2O3 in Enstatite for Spinel and Garnet Peridotite Compositions. American Mineralogist: Journal of Earth and Planetary Materials **59**(1-2), 110-119.

Magalhães, N., Penniston-Dorland, S., Farquhar, J. and Mathez, E. A. (2018). Variable sulfur isotope composition of sulfides provide evidence for multiple sources of contamination in the Rustenburg Layered Suite, Bushveld Complex. Earth and Planetary Science Letters **492**, 163-173.

Maier, W. D., Peltonen, P., Juvonen, R. and Pienaar, C. (2005). Platinum-group elements in peridotite xenoliths and kimberlite from the Premier kimberlite pipe, South Africa. South African Journal of Geology **108**(3), 413-428.

Maier, W. D., Peltonen, P., McDonald, I., Barnes, S. J., Barnes, S. J., Hatton, C. and Viljoen, F. (2012). The concentration of platinum-group elements and gold in southern African and Karelian kimberlite-hosted mantle xenoliths: implications for the noble metal content of the Earth's mantle. Chemical Geology **302**, 119-135.

Marchesi, C., Dale, C.W., Garrido, C.J., Pearson, D.G., Bosch, D., Bodinier, J.L., Gervilla, F. and Hidas, K. (2014). Fractionation of highly siderophile elements in refertilized mantle: Implications for the Os isotope composition of basalts. Earth and Planetary Science Letters **400**, 33-44.

Marini, L., Moretti, R. and Accornero, M. (2011). Sulfur isotopes in magmatic-hydrothermal systems, melts, and magmas. Reviews in Mineralogy and Geochemistry **73**(1), 423-492.

McDonald, I., Hughes, H. S., Butler, I. B., Harris, J. W. and Muir, D. (2017). Homogenisation of sulphide inclusions within diamonds: A new approach to diamond inclusion geochemistry. Geochimica et Cosmochimica Acta **216**, 335-357.

McDonough, W. F. and Sun, S. S. (1995). The composition of the Earth. Chemical geology **120**(3-4), 223-253.

Mondal, S. K. and Mathez, E. A. (2006). Origin of the UG2 chromitite layer, Bushveld Complex. Journal of Petrology **48**(3), 495-510.

Morgan, J. W., Walker, R. J., Brandon, A. D. and Horan, M. F. (2001). Siderophile elements in Earth's upper mantle and lunar breccias: data synthesis suggests manifestations of the same late influx. Meteoritics & Planetary Science **36**(9), 1257-1275.

Mungall, J. E., Andrews, D. R., Cabri, L. J., Sylvester, P. J. andTubrett, M. (2005). Partitioning of Cu, Ni, Au, and platinum-group elements between monosulfide solid solution and sulfide melt under controlled oxygen and sulfur fugacities. Geochimica et Cosmochimica Acta **69**(17), 4349-4360.

Mungall, J. E. and Brenan, J. M. (2014). Partitioning of platinum-group elements and Au between sulfide liquid and basalt and the origins of mantle-crust fractionation of the chalcophile elements. Geochimica et Cosmochimica Acta **125**, 265-289.

Nickel, K. G. and Green, D. H. (1985). Empirical geothermobarometry for garnet peridotites and implications for the nature of the lithosphere, kimberlites and diamonds. Earth and Planetary Science Letters **73**(1), 158-170.

Nimis, P. and Taylor, W. R. (2000). Single clinopyroxene thermobarometry for garnet peridotites. Part I. Calibration and testing of a Cr-in-Cpx barometer and an enstatite-in-Cpx thermometer. Contributions to Mineralogy and Petrology **139**(5), 541-554.

O'Reilly, S. Y. and Griffin, W. L. (2010). The continental lithosphere–asthenosphere boundary: can we sample it?. Lithos **120**(1-2), 1-13.

Ohmoto, H. (1979). Isotopes of sulfur and carbon. In: Geochemistry of Hydrothermal Ore Deposits. Barnes HL (ed.) J Wiley and Sons, 509-567.

Olsson, J. R., Söderlund, U., Hamilton, M. A., Klausen, M. B. and Helffrich, G. R. (2011). A late Archaean radiating dyke swarm as possible clue to the origin of the Bushveld Complex. Nature Geoscience **4**(12), 865.

Ono, S., Beukes, N. J. and Rumble, D. (2009). Origin of two distinct multiple-sulfur isotope

compositions of pyrite in the 2.5 Ga Klein Naute Formation, Griqualand West Basin, South Africa. Precambrian Research **169**(1-4), 48-57.

Peach, C. L., Mathez, E. A. and Keays, R. R. (1990). Sulfide melt-silicate melt distribution coefficients for noble metals and other chalcophile elements as deduced from MORB: Implications for partial melting. Geochimica et Cosmochimica Acta **54**(12), 3379-3389.

Pearson, D. G. (1999). The age of continental roots. Lithos **48**(1-4), 171-194.

Pearson, D. G., Canil, D. and Shirey, S. B. (2003). Mantle samples included in volcanic rocks: xenoliths and diamonds. Treatise on geochemistry **2**, 568.

Pearson, D. G., Carlson, R. W., Shirey, S. B., Boyd, F. R. and Nixon, P. H. (1995). Stabilisation of Archaean lithospheric mantle: A ReOs isotope study of peridotite xenoliths from the Kaapvaal craton. Earth and Planetary Science Letters **134**(3-4), 341-357.

Pearson, D. G., Irvine, G. J., Carlson, R. W., Kopylova, M. G. and Ionov, D. A. (2002a). The development of lithospheric keels beneath the earliest continents: time constraints using PGE and Re-Os isotope systematics. Geological Society, London, Special Publications **199**(1), 65-90.

Pearson, N. J., Alard, O., Griffin, W. L., Jackson, S. E. and O'Reilly, S. Y. (2002b). In situ measurement of Re-Os isotopes in mantle sulfides by laser ablation multicollector-inductively coupled plasma mass spectrometry: analytical methods and preliminary results. Geochimica et Cosmochimica Acta **66**(6), 1037-1050.

Penniston-Dorland, S. C., Mathez, E. A., Wing, B. A., Farquhar, J. and Kinnaird, J. A. (2012). Multiple sulfur isotope evidence for surface-derived sulfur in the Bushveld Complex. Earth and Planetary Science Letters **337**, 236-242.

Penniston-Dorland, S. C., Wing, B. A., Nex, P. A., Kinnaird, J. A., Farquhar, J., Brown, M. and Sharman, E. R. (2008). Multiple sulfur isotopes reveal a magmatic origin for the Platreef platinum group element deposit, Bushveld Complex, South Africa. Geology **36**(12), 979-982.

Peregoedova, A., Barnes, S. J. and Baker, D. R. (2004). The formation of Pt–Ir alloys and Cu–Pd-rich sulfide melts by partial desulfurization of Fe–Ni–Cu sulfides: results of experiments and implications for natural systems. Chemical Geology **208**(1-4), 247-264.

Pollack, H. N. and Chapman, D. S. (1977). On the regional variation of heat flow, geotherms, and lithospheric thickness. Tectonophysics **38**(3-4), 279-296.

Polley, G. (2011). A Study of the $\Delta^{33}S$ Signature of Xenoliths from the Premier Kimberlite, South Africa. Penniston-Dorland, S. and Farquhar, J. (Ed.), (unpublished thesis data, University of Maryland).

Prouteau, G., Scaillet, B., Pichavant, M. and Maury, R. (2001). Evidence for mantle metasomatism by hydrous silicic melts derived from subducted oceanic crust. Nature **410**(6825), 197.

Rampone, E., Hofmann, A. W., Piccardo, G. B., Vannucci, R., Bottazzi, P. and Ottolini, L. (1996). Trace element and isotope geochemistry of depleted peridotites from an N-MORB type ophiolite (Internal Liguride, N. Italy). Contributions to Mineralogy and Petrology **123**(1), 61-76.

Reisberg, L., Lorand, J. P. and Bedini, R. M. (2004). Reliability of Os model ages in pervasively metasomatized continental mantle lithosphere: a case study of Sidamo spinel peridotite xenoliths (East African Rift, Ethiopia). Chemical Geology **208**(1-4), 119-140.

Richardson, S. H., Harris, J. W. and Gurney, J. J. (1993). Three generations of diamonds from old continental mantle. Nature **366**(6452), 256.

Richardson, S. H. and Shirey, S. B. (2008). Continental mantle signature of Bushveld magmas and coeval diamonds. Nature **453**(7197), 910.

Rudnick, R. L., Eldridge, C. S. and Bulanova, G. P. (1993). Diamond growth history from in situ measurement of Pb and S isotopic compositions of sulfide inclusions. Geology **21**(1), 13-16.

Schmitz, M. D., Bowring, S. A., de Wit, M. J. and Gartz, V. (2004). Subduction and terrane collision stabilize the western Kaapvaal craton tectosphere 2.9 billion years ago. Earth and Planetary Science Letters **222**(2), 363-376.

Sen, C. and Dunn, T. (1995). Experimental modal metasomatism of a spinel lherzolite and the production of amphibole-bearing peridotite. Contributions to Mineralogy and Petrology **119**(4), 422-432.

Shirey, S.B., Carlson, R.W., Richardson, S.H., Menzies, A., Gurney, J.J., Pearson, D.G., Harris, J.W. and Wiechert, U. (2001). Archean emplacement of eclogitic components into the lithospheric mantle during formation of the Kaapvaal Craton. Geophysical Research Letters **28**(13), 2509-2512.

Shirey, S.B., Harris, J.W., Richardson, S.H., Fouch, M., James, D.E., Cartigny, P., Deines, P. and Viljoen, F. (2003). Regional patterns in the paragenesis and age of inclusions in diamond, diamond composition, and the lithospheric seismic structure of Southern Africa. Lithos **71**(2-4), 243-258.

Shirey, S. B., Richardson, S. H. and Harris, J. W. (2004). Integrated models of diamond formation and craton evolution. Lithos **77**(1-4), 923-944.

Smith, J. W., Holwell, D. A., McDonald, I. and Boyce, A. J. (2016). The application of S isotopes and S/Se ratios in determining ore-forming processes of magmatic Ni–Cu–PGE sulfide deposits: a

cautionary case study from the northern Bushveld Complex. Ore Geology Reviews **73**, 148-174.

Stachel, T. and Harris, J. W. (2008). The origin of cratonic diamonds—constraints from mineral inclusions. Ore Geology Reviews **34**(1-2), 5-32.

Stachel, T., Viljoen, K. S., Brey, G. and Harris, J. W. (1998). Metasomatic processes in lherzolitic and harzburgitic domains of diamondiferous lithospheric mantle: REE in garnets from xenoliths and inclusions in diamonds. Earth and Planetary Science Letters **159**(1-2), 1-12.

Sweeney, R. J., Thompson, A. B. and Ulmer, P. (1993). Phase relations of a natural MARID composition and implications for MARID genesis, lithospheric melting and mantle metasomatism. Contributions to Mineralogy and Petrology **115**(2), 225-241.

Szabó, C. and Bodnar, R. J. (1995). Chemistry and origin of mantle sulfides in spinel peridotite xenoliths from alkaline basaltic lavas, Nógraád-Gömör Volcanic Field, northern Hungary and southern Slovakia. Geochimica et Cosmochimica Acta **59**(19), 3917-3927.

Tappe, S., Dongre, A., Liu, C. Z. and Wu, F. Y. (2018). 'Premier'evidence for prolonged kimberlite pipe formation and its influence on diamond transport from deep Earth. Geology **46**(10), 843-846.

Taylor, W. R. (1998). An experimental test of some geothermometer and geobaro-meter formulations for upper mantle peridotites with application to the ther-mobarometry of fertile lherzolite and garnet websterite. Neues Jahrbuch für Mineralogie-Abhandlungen **172**, 381-408.

Thomassot, E., Cartigny, P., Harris, J. W., Lorand, J. P., Rollion-Bard, C. and Chaussidon, M. (2009). Metasomatic diamond growth: A multi-isotope study (^{13}C, ^{15}N, ^{33}S, ^{34}S) of sulphide inclusions and their host diamonds from Jwaneng (Botswana). Earth and Planetary Science Letters **282**(1-4), 79-90.

Thomassot, E., O'Neil, J., Francis, D., Cartigny, P. and Wing, B. A. (2015). Atmospheric record in the Hadean Eon from multiple sulfur isotope measurements in Nuvvuagittuq Greenstone Belt (Nunavik, Quebec). Proceedings of the National Academy of Sciences **112**(3), 707-712.

Tsai, H. M., Shieh, Y. N. and Meyer, H. O. (1979). Mineralogy and $^{34}S/^{32}S$ ratios of sulfides associated with kimberlite, xenoliths, and diamonds. In: The Mantle Sample. Boyd, F. R., and Meyer, H.O.A. (Eds.), American Geophysical Union, Washington, D.C., 87-103.

Viljoen, F., Dobbe, R. and Smit, B. (2009). Geochemical processes in peridotite xenoliths from the Premier diamond mine, South Africa: evidence for the depletion and refertilisation of subcratonic lithosphere. Lithos **112**, 1133-1142.

Viljoen, K. F., Dobbe, R., Smit, B., Thomassot, E. and Cartigny, P. (2004). Petrology and

geochemistry of a diamondiferous lherzolite from the Premier diamond mine, South Africa. Lithos **77**(1-4), 539-552.

Wainwright, A. N., Luguet, A., Fonseca, R. O. C. and Pearson, D. G. (2015). Investigating metasomatic effects on the ^{187}Os isotopic signature: a case study on micrometric base metal sulphides in metasomatised peridotite from the Letlhakane kimberlite (Botswana). Lithos **232**, 35-48.

Wallace, M. and Green, D. H. (1991). The effect of bulk rock composition on the stability of amphibole in the upper mantle: implications for solidus positions and mantle metasomatism. Mineralogy and Petrology **44**(1-2), 1-19.

Wang, Z., Becker, H. and Gawronski, T. (2013). Partial re-equilibration of highly siderophile elements and the chalcogens in the mantle: A case study on the Baldissero and Balmuccia peridotite massifs (Ivrea Zone, Italian Alps). Geochimica et Cosmochimica Acta **108**, 21-44.

Wilson, M. R., Kyser, T. K. and Fagan, R. (1996). Sulfur isotope systematics and platinum group element behavior in REE-enriched metasomatic fluids: A study of mantle xenoliths from Dish Hill, California, USA. Geochimica et cosmochimica acta **60**(11), 1933-1942.

Wu, F. Y., Mitchell, R. H., Li, Q. L., Sun, J., Liu, C. Z. and Yang, Y. H. (2013). In situ UPb age determination and SrNd isotopic analysis of perovskite from the Premier (Cullinan) kimberlite, South Africa. Chemical Geology **353**, 83-95.

Yund, R. A. and Kullerud, G. (1966). Thermal stability of assemblages in the Cu—Fe—S system. Journal of Petrology **7**(3), 454-488.

Zeh, A., Ovtcharova, M., Wilson, A. H. and Schaltegger, U. (2015). The Bushveld Complex was emplaced and cooled in less than one million years–results of zirconology, and geotectonic implications. Earth and Planetary Science Letters **418**, 103-114.

CHAPTER 4: TABLES

Table 4.1. Major element composition of minerals from Premier garnet-bearing lherzolite xenoliths

Sample	Texture	Mineral	SiO_2	TiO_2	Al_2O_3	Cr_2O_3	FeO	MnO	MgO	CaO	Na_2O	K_2O	V_2O_3	NiO	CO_2	Total	Mg#
CIM15-001	DEF LRZ	Olivine	41.2	-	-	0.02	8.9	0.09	50.1	-	0.02	-	-	0.30	-	100.61	0.91
		Orthopyroxene	57.3	0.29	1.12	0.34	4.9	0.09	34.0	1.2	0.45	-	-	0.10	-	99.78	0.92
		Clinopyroxene	55.9	0.56	2.5	0.73	3.4	0.09	19.8	15.0	2.11	-	-	0.06	-	100.05	0.91
		Garnet	42.3	1.32	20.2	1.87	7.2	0.38	21.8	4.7	0.34	-	-	0.01	-	100.14	0.84
CIM15-002	CRS LRZ	Olivine	40.8	-	-	0.04	9.5	0.08	49.4	0.0	0.03	-	-	0.30	-	100.07	0.90
		Orthopyroxene	57.2	0.19	1.04	0.48	5.1	0.09	33.8	1.2	0.42	-	-	0.10	-	99.58	0.92
		Clinopyroxene	53.4	1.32	1.8	0.98	3.9	0.21	18.2	18.8	1.33	-	-	0.10	-	100.05	0.89
		Garnet	41.6	1.40	18.3	3.30	7.7	0.38	20.9	5.2	0.36	-	-	0.01	-	99.19	0.83
		Spinel	-	3.07	23.9	39.2	18.4	-	16.3	-	-	-	-	-	-	100.76	0.61
CIM15-003	DEF LRZ	Olivine	41.4	-	0.02	0.03	8.1	0.08	50.3	0.1	0.02	-	-	0.30	-	100.25	0.92
		Orthopyroxene	57.5	-	1.03	0.44	5.1	0.09	33.1	1.3	0.53	-	-	0.10	-	99.20	0.92
		Clinopyroxene	54.0	1.18	4.1	0.93	3.6	0.08	18.1	16.9	1.86	-	-	0.05	-	100.74	0.90
		Garnet	42.7	0.63	20.5	3.51	6.4	0.26	21.8	4.6	0.00	-	-	0.01	-	100.28	0.86
		Spinel	0.5	2.99	22.9	35.54	18.1	-	14.9	-	-	-	0.49	-	-	95.35	0.60
		Phlogopite	38.0	5.75	14.9	1.81	4.1	-	19.4	0.1	0.46	8.96	-	-	-	93.45	0.90
		Calcite	-	-	-	-	0.5	-	-	53.9	-	-	-	-	45.53	99.99	-
CIM15-004	CRS LRZ	Olivine	41.0	-	-	0.08	8.4	-	50.2	-	0.02	-	-	0.39	-	99.99	0.91
		Orthopyroxene	57.5	0.15	1.13	0.28	5.1	-	34.9	0.4	0.19	-	-	-	-	99.65	0.92
		Clinopyroxene	55.2	0.19	2.8	1.77	2.6	0.19	16.1	19.2	2.50	-	-	-	-	100.55	0.92
		Garnet	42.0	-	21.3	3.39	7.4	0.38	20.9	4.6	-	-	-	0.01	-	100.01	0.83
		Calcite	-	-	-	-	0.3	-	-	55.1	-	-	-		44.56	100.00	-
CIM15-006	CRS LRZ	Olivine	41.2	-	-	0.05	9.0	0.09	49.9		0.03	-	-	0.27	-	100.50	0.91
		Orthopyroxene	57.7	0.26	1.09	0.53	5.3	0.10	33.8	1.3	0.42	-	-	0.08	-	100.59	0.92
		Clinopyroxene	54.5	0.49	0.4	0.62	2.9	0.22	16.5	23.3	1.09	0.05	-	0.06	-	100.16	0.91
		Garnet	41.7	1.43	18.0	5.54	7.1	0.24	21.2	5.1	0.30	-	-	0.01	-	100.57	0.84
CIM15-013	CRS LRZ	Olivine	40.7	-	-	0.05	9.0	0.09	49.2		0.03	-	-	0.31	-	99.40	0.91
		Orthopyroxene	57.6	0.19	1.09	0.48	5.5	0.09	33.9	1.3	0.32	-	-	0.10	-	100.65	0.92
		Clinopyroxene	54.9	1.07	0.8	0.57	3.5	0.09	17.0	21.2	1.47	0.07	-	0.11	-	100.75	0.90
		Garnet	42.2	1.34	18.7	4.81	7.0	0.30	21.4	5.0	0.17	-	-	0.01	-	100.98	0.84
		Spinel	-	0.79	48.2	18.2	12.3	-	19.6	-	0.20	-	-		-	99.26	0.74
CIM15-015	Def LRZ	Olivine	40.9	-	-	0.03	8.6	0.09	49.8	0.0	0.02	-	-	0.28	-	99.69	0.91
		Orthopyroxene	57.5	0.33	1.02	0.31	5.2	0.09	34.0	1.3	0.32	-	-	0.08	-	100.21	0.92
		Clinopyroxene	54.6	0.56	1.0	1.26	3.1	0.09	18.1	20.1	1.21	-	-	0.05	-	100.04	0.91
		Garnet	42.0	1.07	20.2	3.17	6.9	0.26	21.7	4.7	-	-	-		-	99.92	0.85
CIM15-016	DEF LRZ	Olivine	40.4	0.00	0.00	0.03	9.7	0.09	48.5	-	0.03	-	-	0.31	-	99.01	0.90
		Orthopyroxene	57.2	0.27	1.14	0.29	5.9	0.09	33.9	1.3	0.40	-	-	0.10	-	100.61	0.91
		Clinopyroxene	56.1	0.45	1.5	1.36	4.4	0.20	19.5	15.4	1.76	-	-	0.12	-	100.85	0.89
		Garnet	42.0	1.33	20.0	3.01	7.6	0.29	21.7	4.7	0.20	-	-		-	100.84	0.84
CIM15-017	DEF LRZ	Olivine	40.9	-	-	0.05	8.5	0.09	50.1	-	0.02	-	-	0.29	-	99.96	0.91
		Orthopyroxene	57.4	-	1.02	0.45	5.1	0.09	33.9	1.4	0.28	-	-	0.09	-	99.69	0.92
		Clinopyroxene	55.7	-	1.8	1.22	3.6	0.20	20.6	15.7	1.60	0.03	-	0.12	-	100.64	0.91
		Garnet	41.8	0.62	18.6	5.38	6.7	0.30	21.2	5.1	-	-	-		-	99.72	0.85
		Spinel	-	0.39	47.1	20.8	12.1	-	19.4	-	0.10	-	-	0.01	-	99.91	0.74
CIM15-021	DEF LRZ	Olivine	41.2	-	-	0.02	9.4	0.09	49.5	-	0.02	-	-	0.28	-	100.47	0.90
		Orthopyroxene	57.6	0.21	1.05	0.18	5.6	0.09	34.2	1.2	0.29	-	-	0.09	-	100.56	0.92
		Clinopyroxene	55.5	0.35	2.5	0.58	3.8	0.20	19.7	15.4	1.84	0.01	-	0.11	-	100.03	0.90
		Garnet	42.8	0.71	21.7	1.63	6.5	0.26	22.0	4.1	0.18	-	-	0.01	-	99.88	0.86
CIM15-035	DEF LRZ	Olivine	40.8	-	-	0.01	8.4	0.11	50.0	-	0.02	-	-	0.27	-	99.63	0.91
		Orthopyroxene	57.5	0.19	0.96	0.46	5.7	0.09	33.6	0.7	0.17	-	-	0.08	-	99.45	0.91
		Clinopyroxene	55.3	0.46	2.4	0.95	3.4	0.08	19.7	15.6	1.95	-	-	0.04	-	99.80	0.91
		Garnet	42.1	0.96	20.2	3.13	6.6	0.25	21.7	4.6	0.20	-	-	0.02	-	99.80	0.86

All values in wt. %. Def LRZ = Deformed Lherzolite. Crs LRZ = Coarse Lherzolite.

Table 4.2. Representative major element analyses of base metal sulphides and associated magnetite from Premier garnet-bearing lherzolite xenoliths

Sample	Texture	Host phase	Textural relationship	Modal %	Mineral	O	S	Fe	Ni	Cu	Co	Mg	W	Zn	Pt	As	Ba	Total	M/S	Fe/M	Ni/M	Cu/M
CIM15-001	DEF LRZ	Garnet	Large “pseudo” BMS inclusion	70	Pentlandite	2.0	33.8	24.8	38.8	-	0.5	-	0.3	-	-	-	-	100.3	1.1	0.4	0.6	0.0
				20	MSS	2.3	34.4	26.8	22.4	13.9	0.3	-	0.5	-	-	-	-	100.5	1.0	0.4	0.4	0.2
				10	Magnetite	23.6	-	76.4	-	-	-	0.3	-	-	-	-	-	100.2	-	-	-	-
		Serpentine vein	Large interstitial BMS	95	Pentlandite	-	33.9	25.9	38.7	-	2.1	-	-	-	-	-	-	100.6	1.1	0.4	0.6	0.0
				5	Magnetite	28.3	0.2	65.8	-	-	-	-	0.4	-	-	-	-	94.7	-	-	-	-
		Serpentine vein	Small interstitial BMS	-	Pentlandite	-	33.3	30.6	31.1	-	4.7	-		-	-	-	-	99.7	1.1	0.5	0.5	0.0
		Serpentine vein	Small interstitial BMS	-	alt. Zn-sulphide	18.8	18.7	29.4	0.5	-	-	-	-	31.1	-	-	-	98.5	1.7	0.5	0.0	0.0
		Serpentine vein	Elongate interstitial	-	Magnetite	23.6	-	76.4	-	-	-	-	-	-	-	-	-	100.0	-	-	-	-
CIM15-002	CRS LRZ	Olivine	Small "isolated" BMS inclusion	-	Pentlandite	1.7	32.7	31.4	30.2	-	0.5	-	0.4	-	1.4	-	-	98.3	1.1	0.5	0.5	0.0
		Orthopyroxene	Small "isolated" BMS inclusion	-	Pentlandite	1.7	32.5	21.1	37.7	-	3.0	-	-	-	1.4	-	-	97.4	1.1	0.4	0.6	0.0
		Serpentine vein	Small interstitial BMS	75	alt. Pentlandite	5.7	30.6	22.7	36.7	-	2.8	-	1.8	-	-	0.3	-	100.6	1.1	0.4	0.6	0.0
				25	Magnetite	30.5	0.8	61.2	0.7	-	0.3	3.7	2.9	-	-	-	-	100.1	-	-	-	-
CIM15-003	DEF LRZ	Serpentine vein	Small interstitial BMS	70	alt. Pentlandite	10.4	26.3	32.8	26.9	-	2.8	0.3	0.3	-	-	-	-	99.8	1.3	0.5	0.4	0.0
				30	alt. Magnetite	29.3	-	65.3	-	-	0.4	0.1	0.4	-	-	-	-	95.5	-	-	-	-
		Serpentine vein	Small interstitial BMS	85	Pentlandite	1.0	34.3	23.9	39.9	-	0.4	-	0.5	-	-	-	-	100.0	1.0	0.4	0.6	0.0
				15	Magnetite	29.5	0.2	69.4	0.5	-	0.3	-	-	-	-	-	-	99.9	-	-	-	-
CIM15-004	CRS LRZ	Serpentine vein	Small interstitial BMS	80	Heazelwoodite		26.3	4.9	68.2	-	-	-	0.4	-	-	0.2	-	100.0	1.5	0.1	0.9	0.0
				20	Magnetite	30.6		69.2	0.2	-	-	-	-	-	-	-	-	100.0	-	-	-	-
		Olivine	Small "isolated" BMS inclusion	-	Pentlandite	1.4	33.5	27.1	33.7	-	4.4	-	0.4	-	-	-	-	100.5	1.1	0.4	0.5	0.0
		Orthopyroxene	Small "isolated" BMS inclusion	-	Pentlandite	1.5	33.3	21.5	33.9	-	10.0	-	0.5	-	-	-	-	100.8	1.1	0.3	0.5	0.0
		Clinopyroxene (rim)	Small "isolated" BMS inclusion	75	Heazelwoodite	2.3	23.4	13.0	60.9	-		-	0.4	-	-	-	-	100.0	1.7	0.2	0.8	0.0
				25	Magnetite	30.3	-	69.1	0.2	-	-	-	0.2	-	-	0.2	-	100.0	-	-	-	-
		Serpentine vein	Small interstitial BMS	-	Pyrite	-	54.1	45.9	-	-	-	-	-	-	-	-	-	100.0	0.5	1.0	-	-
CIM15-006	CRS LRZ	Olivine (rim)	Small "isolated" BMS inclusion	70	Heazelwoodite	1.7	26.2	3.6	67.8	-	-	-	0.6	-	1.0	-	-	100.9	1.5	0.1	0.9	0.0
				30	Magnetite	31.3	0.9	64.9	1.1	1.0	0.2	-	0.3	-	-	0.3	-	100.0	-	-	-	-
		Olivine	Small "isolated" BMS inclusion	-	Pentlandite	1.9	33.0	29.5	33.5	-	0.2	-	0.5	-	1.5	-	-	100.0	1.1	0.5	0.5	0.0
		Orthopyroxene	Small "isolated" BMS inclusion	-	Pentlandite	2.1	33.7	30.1	30.9	0.5	0.4	-	0.6	-	1.3	0.3	-	100.0	1.0	0.5	0.5	0.0
		Orthopyroxene	Small "isolated" BMS healed growth zone	-	Pentlandite	3.7	32.8	30.1	29.5	0.4	0.6	-	1.1	-	1.3	0.5	-	100.0	1.0	0.5	0.5	0.0
		Orthopyroxene	Small "isolated" BMS healed growth zone	-	MSS	5.8	31.7	30.0	22.8	4.3	0.4	-	1.7	-	1.2	1.2	-	99.1	1.0	0.5	0.4	0.1
		Orthopyroxene	Small "isolated" BMS healed growth zone	-	MSS	20.9	22.3	21.6	18.7	1.4	0.4	-	7.7	-	0.3	6.3	-	99.7	1.1	0.5	0.4	0.0
		btw. Ol and Opx	Large interstitial BMS	55	Heazelwoodite	0.9	27.1	3.3	67.4	-	-	-	-	-	1.3	-	-	100.0	1.4	0.0	1.0	0.0
				45	Magnetite	32.0	0.7	65.3	0.9	0.6	0.3	-	0.5	-	-	0.3	-	100.6	-	-	-	-
		Serpentine vein	Small interstitial BMS	-	Pentlandite	2.0	33.9	30.2	30.8	0.3	0.4	-	0.4	-	1.5	0.3	-	99.8	1.0	0.5	0.5	0.0
		Serpentine vein	Small interstitial BMS	-	Pentlandite	-	33.5	32.3	33.5	-	0.5	-	-	-	-	-	-	99.8	1.1	0.5	0.5	
		Serpentine vein	Small interstitial BMS	-	Pyrite	-	57.7	42.3	-	-	-	-	-	-	-	-	-	100.0	0.4	1.0	-	-
CIM15-013	CRS LRZ	Serpentine vein	Small interstitial BMS	5	Co-rich sulphide	0.7	33.0	7.3	31.5	-	26.2	0.3	0.6	-	-	-	-	99.6	1.1	0.1	0.5	0.0
				95	Heazelwoodite	6.4	30.5	2.6	54.3	0.3	2.6	1.5	1.8	-	-	-	-	100.0	1.1	0.0	0.9	0.0
		Serpentine vein	Elongate interstitial	-	Magnetite	27.3	-	69.7	-	-	-	-	1.6	-	-	1.8	-	100.4	-	-	-	-
		Serpentine vein	Small interstitial	-	Barite	30.7	14.6	-	-	-	-	-	0.9	-	-	-	53.9	100.0	-	-	-	-
		Clinopyroxene	Small "isolated" BMS inclusion	55	Pentlandite	1.0	33.3	28.9	35.9	-	0.9	-	0.6	-	-	-	-	100.6	1.1	0.5	0.5	0.0
				45	Pyrrhotite	-	39.7	59.3	0.3	-	0.3	-	0.3	-	-	-	-	99.9	0.9	1.0	0.0	0.0
CIM15-015	DEF LRZ	Serpentine vein	Elongate interstitial	-	Magnetite	29.7	-	70.2	0.2	-	0.3	-	0.2	-	-	-	-	100.7	-	-	-	-
CIM15-016	DEF LRZ	Serpentine vein	Elongate interstitial	-	Magnetite	34.1		65.9	-	-	-	-	-	-	-	-	-	100.0	-	-	-	-
CIM15-017	DEF LRZ	Serpentine vein	Small interstitial BMS	65	alt. Pentlandite	6.2	30.5	19.8	37.1	-	3.6	-	1.4	-	-	1.4	-	100.0	1.1	0.3	0.6	0.0
				45	Magnetite	29.8	0.0	69.0	-	-	0.3	-	0.4	-	-	0.6	-	100.0	-	-	-	-
		Serpentine vein	Elongate interstitial	-	Magnetite	31.2	-	67.1	-	-	-	-	1.2	-	-	0.9	-	100.4	-	-	-	-
CIM15-021	DEF LRZ	Garnet (rim)	Small "isolated" BMS inclusion	-	Pentlandite	2.4	33.1	26.7	35.5	-	1.2	0.3	0.6	-	-	-	-	99.8	1.1	0.4	0.5	0.0
		Orthopyroxene	Small "isolated" BMS inclusion	-	Pentlandite	1.6	34.2	30.1	33.8	-	0.3	-	0.4	-	-	-	-	100.3	1.1	0.5	0.5	0.0
		Serpentine vein	Large interstitial BMS	80	Pentlandite	2.8	29.5	35.4	30.1	-	1.7	0.0	0.5	-	-	-	-	100.0	1.3	0.5	0.4	0.0
				20	Magnetite	28.7	4.2	62.5	3.6	-	0.5	0.1	0.3	-	-	-	-	100.0	-	-	-	-
				5	alt. Zn-sulphide	10.7	22.5	25.7	1.7	0.3	0.3	-	0.5	38.4	-	-	-	100.0	1.5	0.4	0.0	0.0
		Serpentine vein	Large interstitial BMS	45	alt. Pentlandite	16.8	19.7	43.2	18.3	-	1.2	0.4	0.4	-	-	-	-	100.0	1.8	0.7	0.3	0.0
				50	Magnetite	29.8	-	69.6	-	-	0.3	0.2	-	-	-	-	-	100.0	-	-	-	-
CIM15-035	DEF LRZ	Serpentine vein	Elongate interstitial	-	Magnetite	28.3	1.1	68.8	0.9	-	-	0.2	0.3	-	-	-	-	99.5	-	-	-	-

Element concentrations in wt. %; M/S = metals(Cu,Ni,Fe,Co±Zn)/sulphur ratio; Fe/M = Fe/metals; Ni/M = Ni/metals; Cu/M = Cu/metals. All ratios calculated in at.%.

Table 4.3. Select garnet and clinopyroxene trace element compositions from Premier garnet-bearing lherzolite xenoliths

Sample	CIM15-001	CIM15-002	CIM15-003	CIM15-006	CIM15-013	CIM15-015	CIM15-016	CIM15-017	CIM15-021	CIM15-035
Texture	DEF LRZ	CRS LRZ	DEF LRZ	CRS LRZ	CRS LRZ	DEF LRZ	DEF LRZ	DEF LRZ	DEF LRZ	DEF LRZ
TE class	Normal	Humped	Normal	Humped	Humped	Normal	Normal	Sinusoidal	Normal	Normal
mineral:	*Grt*	*Grt*	*Grt*	*Grt*	*Grt*	*Grt*	*Grt*	*Grt*	*Grt*	*Grt*
Sc	85	103	88	99	95	87	74	109	74	223
V	253	318	245	323	304	221	244	284	235	518
Mn	1933	2038	1858	2157	1924	1932	1863	1924	1876	5664
Co	44	45	43	43	44	43	46	43	45	87
Ni	130	135	117	136	140	122	137	132	120	155
Cu	0.96	0.99	0.36	0.82	0.63	0.61	0.60	0.41	0.50	0.65
Zn	14	15	13	15	16	14	19	15	17	31
Rb	4.7	3.7	0.3	5.0	0.2	bdl	bdl	0.03	bdl	0.01
Sr	12.1	24.6	0.67	32.9	1.1	0.58	0.62	0.80	0.49	0.67
Y	18	21	16	27	23	14	19	7.2	18	47
Zr	75	86	52	95	87	56	66	56	50	178
Nb	0.58	0.42	0.56	0.48	0.45	0.34	0.35	0.75	0.35	0.49
Ba	521	301	5.8	94	9.5	0.1	bdl	bdl	bdl	bdl
La	0.14	0.07	0.05	0.09	0.06	0.04	0.05	0.07	0.03	0.04
Ce	0.54	0.51	0.46	0.65	0.54	0.38	0.42	0.65	0.34	0.40
Pr	0.13	0.16	0.15	0.20	0.17	0.12	0.14	0.20	0.12	0.17
Nd	1.3	1.6	1.5	1.9	1.7	1.3	1.4	1.9	1.2	1.8
Sm	1.1	1.4	1.0	1.5	1.3	1.1	1.2	1.3	0.90	2.01
Eu	0.53	0.64	0.48	0.68	0.67	0.50	0.55	0.57	0.43	1.08
Gd	2.2	2.7	1.9	3.1	2.7	1.9	2.3	2.2	1.9	4.9
Tb	0.47	0.57	0.38	0.66	0.58	0.34	0.45	0.32	0.39	1.10
Dy	3.4	4.1	2.8	5.1	4.5	2.4	3.4	1.8	3.0	8.5
Ho	0.70	0.83	0.62	1.08	0.89	0.52	0.75	0.30	0.70	1.95
Er	1.9	2.2	1.9	3.0	2.5	1.6	2.1	0.74	2.2	5.6
Tm	0.27	0.30	0.30	0.44	0.34	0.24	0.33	0.11	0.34	0.80
Yb	1.9	1.9	2.1	2.7	2.2	1.7	2.3	0.8	2.3	5.5
Lu	0.28	0.27	0.32	0.39	0.29	0.26	0.33	0.15	0.36	0.79
Hf	1.9	2.3	1.3	2.5	2.3	1.1	1.5	1.3	1.3	4.2
Ta	0.05	0.04	0.06	0.05	0.04	0.04	0.03	0.08	0.04	0.04
Pb	0.12	0.08	0.01	0.05	0.02	0.03	bdl	bdl	bdl	0.08
Th	0.02	0.02	0.02	0.02	0.01	0.01	0.02	0.03	0.01	0.01
U	0.02	0.02	0.02	0.02	0.02	0.01	0.01	0.03	0.01	0.02
Eu*	1.0	1.0	1.0	0.9	1.1	1.0	1.0	1.0	1.0	1.0
$(Lu/Gd)_N$	1.0	0.8	1.3	1.0	0.8	1.1	1.2	0.5	1.5	1.3
mineral:	*Cpx*	*Cpx*	*Cpx*	*Cpx*	*Cpx*	*Cpx*	*Cpx*	*Cpx*	*Cpx*	*Cpx*
Sc	19	1.9	14	74	73	18	30	33	34	31.09
V	224	1.1	171	307	295	184	392	464	379	340.6
Mn	898	28	841	1865	2176	901	2159	2015	2029	803.85
Co	32	1.6	31	65	79	32	71	65	64	30.1
Ni	559	28	543	553	1084	538	1239	1194	1140	387.1
Cu	4.44	1.4	2.40	16.90	1.49	3.91	7.28	8.37	8.27	1.73
Zn	16	4.6	15	27	54	18	43	36	33	13.845
Rb	0.2	21.9	3.0	29.6	50.4	1.25725	0.12	0.05	0.22	11.71
Sr	116	22	90	588	166	102	199	208	210	267
Y	4	0.8	2	20	16	3	6	6	5	9
Zr	11	86	5	52	56	11	17	18	22	81
Nb	0.47	0.20	0.86	2.09	1.22	0.39	0.48	0.59	0.59	2.39
Cs	0.01	0.54	0.24	0.27	6.59	0.15	0.00	0.00	0.01	0.20
Ba	12	148	5	303	1633	6	1	1	3	43
La	1.9	0.9	2.0	1.7	0.5	1.9	3.6	4.0	3.8	5.9
Ce	6.5	1.6	6.4	3.0	1.2	6.7	12	13	13	21
Pr	1.1	0.2	1.0	0.4	0.2	1.1	2.0	2.2	2.2	3.8
Nd	6.0	0.6	5.2	2.4	1.5	6.3	11	12	12	20
Sm	1.7	0.09	1.3	1.2	1.0	1.7	3.1	3.2	3.3	5.0
Eu	0.6	0.09	0.4	0.5	0.5	0.5	1.1	1.1	1.1	1.6
Gd	1.61	0.08	1.02	2.30	2.02	1.44	2.90	3.09	2.93	4.05
Tb	0.20	0.01	0.12	0.46	0.42	0.17	0.36	0.36	0.34	0.49
Dy	1.1	0.11	0.59	3.7	3.2	0.8	1.7	1.7	1.6	2.4
Ho	0.17	0.02	0.09	0.80	0.67	0.12	0.26	0.26	0.22	0.38
Er	0.34	0.07	0.19	2.33	1.8	0.23	0.54	0.52	0.41	0.82
Tm	0.03	0.01	0.02	0.31	0.25	0.02	0.06	0.06	0.04	0.09
Yb	0.16	0.10	0.12	2.02	1.53	0.13	0.32	0.30	0.22	0.51
Lu	0.02	0.02	0.02	0.29	0.22	0.02	0.04	0.04	0.03	0.07
Hf	0.69	2.00	0.28	1.46	1.57	0.59	0.99	1.11	1.19	1.44
Ta	0.03	0.02	0.04	0.06	0.08	0.02	0.03	0.03	0.04	0.16
Pb	0.16	4.48	0.17	0.51	0.71	0.18	0.31	0.29	0.47	0.21
Th	0.04	0.23	0.09	0.11	0.13	0.03	0.04	0.04	0.05	0.11
U	0.007	0.15	0.01	0.03	0.02	0.006	0.007	0.006	0.009	0.02
Eu*	1.0	6.8	1.0	1.0	1.1	1.0	1.1	1.0	1.0	1.1
La/Sm	1.3	2.1	1.1	16.6	8.3	1.1	1.2	1.2	1.2	0.9
Sr*	0.7	26.4	1.0	0.9	0.3	0.7	0.7	0.8	0.7	0.7

Element concentrations in ppm. $Eu^* = 2*Eu_N/[Sm_N+Gd_N]$, $Sr^* = 2*Sr_N/[Pr_N+Nd_N]$; Chondrite-normalising values from McDonough and Sun (1995).

Table 4.4. Select olivine and orthopyroxene trace element compositions from Premier garnet-bearing lherzolite xenoliths

Sample	CIM15-001	CIM15-002	CIM15-003	CIM15-006	CIM15-013	CIM15-015	CIM15-016	CIM15-017	CIM15-021	CIM15-035
Texture	DEF LRZ	CRS LRZ	DEF LRZ	CRS LRZ	CRS LRZ	DEF LRZ	DEF LRZ	DEF LRZ	DEF LRZ	DEF LRZ
mineral:	*Ol*	*Ol*	*Ol*	*Ol*	*Ol*	*Ol*	*Ol*	*Ol*	*Ol*	*Ol*
Sc	3.7	3.1	2.6	4.7	4.2	4.8	4.4	5.3	4.8	3.3
V	11.4	11.2	9.4	13.2	12.8	10.2	11.6	10.9	11.0	1.8
Cr	191	448	326	549	480	314	294	513	196	61
Mn	872	819	800	933	882	863	872	888	873	1113
Co	151	138	136	140	146	142	148	139	150	141
Ni	3018	2973	2975	2683	3055	2806	3059	2949	2794	2689
Cu	4.8	6.3	7.0	8.0	5.6	6.4	6.0	5.2	5.0	1.4
Zn	78	58	58	65	67	62	79	61	76	71
Rb	bdl	0.05	0.01	bdl	bdl	0.02	bdl	0.02	0.04	0.08
Sr	0.01	0.48	0.07	0.01	0.02	0.18	0.01	0.01	0.08	0.70
Y	0.02	0.02	0.01	0.02	0.02	0.02	0.02	bdl	0.01	0.03
Zr	0.10	0.72	0.09	0.13	0.11	0.15	0.12	0.06	0.10	0.47
Nb	0.01	0.03	0.02	0.01	0.02	0.07	0.02	0.02	0.01	0.44
Ba	bdl	0.4	0.7	bdl	0.07	0.2	bdl	0.03	0.5	1.5
La	bdl	0.02	bdl	bdl	bdl	0.03	bdl	bdl	bdl	0.06
Ce	bdl	0.02	bdl	bdl	bdl	0.03	bdl	0.01	bdl	0.13
Nd	bdl	0.01	bdl	bdl	bdl	0.02	bdl	0.02	bdl	0.04
Sm	bdl	bdl	bdl	bdl	bdl	0.01	bdl	bdl	bdl	0.03
Eu	bdl	bdl	bdl	bdl	bdl	bdl	bdl	bdl	bdl	bdl
Gd	bdl	0.01	bdl	bdl	bdl	0.01	bdl	0.01	bdl	bdl
Dy	bdl	bdl	bdl	0.01	0.01	bdl	bdl	bdl	bdl	bdl
Er	bdl	bdl	bdl	bdl	bdl	bdl	bdl	bdl	bdl	0.01
Yb	bdl	0.03	bdl	bdl	bdl	bdl	bdl	bdl	0.01	0.01
Hf	bdl	0.12	bdl	bdl	bdl	0.01	bdl	bdl	bdl	0.01
Ta	bdl	bdl	bdl	bdl	bdl	bdl	bdl	bdl	bdl	0.03
Pb	bdl	0.06	0.03	0.01	bdl	0.06	bdl	0.12	0.01	0.13
Th	bdl	bdl	0.01	bdl	bdl	bdl	bdl	bdl	bdl	0.03
mineral:	*Opx*	*Opx*	*Opx*	*Opx*	*Opx*	*Opx*	*Opx*	*Opx*	*Opx*	*Opx*
Sc	5.9	5.8	4.7	7.6	6.9	7.1	6.9	8.1	6.0	5.3
V	58	57	47	63	59	48	54	49	55	45
Cr	2207	2831	2104	3229	2770	1819	1685	2788	1154	1753
Mn	891	924	886	966	911	867	894	918	899	874
Co	59	60	60	59	62	57	63	60	64	59
Ni	972	972	979	843	970	832	966	940	947	797
Cu	4.6	4.0	2.9	4.8	3.5	3.4	3.7	3.0	2.9	1.4
Zn	35	34	35	36	38	34	44	35	44	44
Rb	0.34	1.44	0.88	0.38	0.21	0.06	0.57	0.71	0.48	3.99
Sr	3.40	4.93	3.10	3.21	2.32	1.80	2.21	2.66	1.79	15.03
Y	0.24	0.20	0.13	0.26	0.21	0.17	0.22	0.05	0.19	0.14
Zr	0.94	0.85	0.36	0.63	0.55	0.59	0.56	0.22	0.52	0.93
Nb	0.09	0.12	0.20	0.06	0.06	0.06	0.06	0.08	0.10	0.77
Cs	0.06	0.27	0.12	0.03	0.03	0.01	0.06	0.16	0.11	0.13
Ba	3.5	6.4	6.4	8.4	6.0	1.5	2.9	3.0	1.3	31.0
La	0.03	0.06	0.08	0.02	0.02	0.02	0.02	0.02	0.03	0.36
Ce	0.12	0.14	0.18	0.08	0.08	0.07	0.08	0.07	0.10	0.69
Pr	0.02	0.02	0.02	0.02	0.02	0.01	0.02	0.01	0.02	0.08
Nd	0.10	0.11	0.12	0.10	0.10	0.08	0.10	0.09	0.10	0.30
Sm	0.04	0.04	0.03	0.03	0.05	0.03	0.04	0.03	0.04	0.07
Eu	0.01	0.02	0.01	0.02	0.02	0.01	0.02	0.01	0.02	0.02
Gd	0.05	0.05	0.03	0.05	0.05	0.03	0.05	0.02	0.04	0.04
Tb	0.008	0.007	0.006	0.008	0.007	0.006	0.009	0.003	0.008	0.005
Dy	0.05	0.05	0.03	0.05	0.05	0.04	0.05	0.01	0.04	0.03
Ho	0.009	0.008	0.005	0.009	0.009	0.004	0.008	0.002	0.007	0.005
Er	0.02	0.02	0.01	0.03	0.02	0.02	0.02	bdl	0.02	0.01
Tm	0.004	0.003	0.002	0.003	0.003	0.002	0.002	bdl	0.003	0.002
Yb	0.02	0.01	0.01	0.02	0.01	0.01	0.02	bdl	0.02	0.01
Lu	0.003	0.002	0.001	0.003	0.002	bdl	0.002	0.001	0.003	0.003
Hf	0.04	0.04	0.02	0.03	0.03	0.04	0.03	0.01	0.02	0.02
Ta	0.01	0.01	0.01	bdl	0.01	bdl	0.01	0.01	0.01	0.05
Pb	0.09	0.05	0.06	0.08	0.03	0.01	0.02	0.02	0.01	0.13
Th	0.009	0.007	0.02	0.001	0.001	bdl	0.001	0.001	0.005	0.06
U	0.003	0.008	0.002	bdl	0.001	bdl	bdl	0.001	0.004	0.012

Element concentrations in ppm.

Table 4.5. Select sulphide trace element compositions from Premier garnet-bearing lherzolite xenoliths

Sample	Texture	Composition	Major elements					Trace elements											
			S	Fe	Ni	Cu	Co	As	Se	Pd	Ag	Te	Re	Os	Ir	Pt	Au	Pb	Bi
CIM15-006	CRS LRZ	Pentlandite	33.5	32.3	33.5	-	0.5	2.84	122	4.6	32	7.6	0.4	0.38	0.75	0.28	0.03	bdl	4.1
		Pentlandite	34.5	30.8	34.3	-	-	2.54	117	5.9	24	5.2	0.5	0.82	0.64	0.15	0.08	1620	10.9
		Pyrite	57.7	42.3	-	-	-	9.8	198	1.71	11	6.6	bdl	bdl	bdl	bdl	bdl	bdl	0.5
		Pyrite	60.5	39.5	-	-	-	4.96	212	1.9	45	8	bdl	bdl	0.07	0.29	0.04	bdl	3.7
CIM15-004	CRS LRZ	Pyrite	54.1	45.9	-	-	-	607	23.9	0.25	1.8	0.85	bdl	bdl	0.016	0.021	0.016	617	0.54
NiS5b (MB2014)	-	NiS (n=20)	27.87	3.26	67.37	1.18	-	51.8	101.1	152.8	2.2	109.4	35.4	81.3	80.4	93.5	8.4	62.1	97.7
1σ	-	-	0.37	0.8	1.78	0.24	-		39.8	5.9	0.2	33.9	2.7	5.9	5	5.3	2.6	3.3	4.3
NiS5b (measured)	-	NiS (n=5)	27.15	3.16	68.28	0.98	-	52.25	101.1	155.2	2.2	109.7	35.5	81.4	80.1	93.3	8.4	62.2	97.8
2σ	-	-	0.27	0.82	1.42	0.25	-	5.3	18.4	14.3	0.3	12.2	3.1	7.5	8.2	10.4	0.8	6.1	7.3
mdl	-	-	-	-	-	-	-	1.5	1.1	0.005	0.05	0.1	0.07	0.013	0.005	0.07	0.01	0.1	0.09
Varience (NiS5b)	-	-	-	-	-	-	-	0.05	-	1.44	-	0.02	0.004	0.005	0.02	0.01	-	0.003	0.002

Major elements are in wt. % and measured by SEM. Trace elements are in µg/g and measured by LA ICP MS. NiS5b (MB2014) from Mungall and Brenan (2014). bdl = below detection limit.

Variance in published versus measured NiS5b values calculated as; $\frac{\sum(x - \bar{x})^2}{n}$

Table 4.6. Sulphur isotope measurements of xenolith-derived sulphides from Premier kimberlite

Sample	Paragenesis	Sulphide	Composition	$^{33}S/^{32}S$	$^{34}S/^{32}S$	$\delta^{34}S$ ‰ vs CDT	±1σ	$\Delta^{33}S$ ‰
CIM15-006	CRS LRZ	S1	Pentlandite	7.85E-03	4.39E-02	-4.24	0.08	-0.10
				7.85E-03	4.39E-02	-5.73	0.08	-0.14±0.02
		S2	Pentlandite	7.87E-03	4.41E-02	-0.48	0.08	-0.02
		S3	Pentlandite	7.85E-03	4.39E-02	-4.56	0.08	0.12
		S4	Pentlandite	7.87E-03	4.41E-02	-1.10	0.08	0.09
JJG-2717	Eclogite	S1	Pyrite	7.89E-03	4.44E-02	2.52	0.11	0.11
				7.89E-03	4.44E-02	2.81	0.11	-0.18
		S2	Pyrite	7.89E-03	4.43E-02	1.72	0.11	0.06
				7.89E-03	4.43E-02	1.83	0.11	0.00
				7.89E-03	4.43E-02	1.03	0.11	-0.04
		S3	Pyrite	7.90E-03	4.44E-02	3.46	0.11	0.02
				7.89E-03	4.44E-02	3.17	0.11	-0.05
		S4	Pyrite	7.88E-03	4.43E-02	0.45	0.11	0.00
				7.89E-03	4.43E-02	1.70	0.11	0.14

$\Delta^{33}S = \delta^{33}S$ measured - $\delta^{33}S$ predicted (c.f. Thomassot et al. 2009).

Table 4.7. Pressure - Temperature estimates of last equilibration of the Premier garnet-bearing lherzolites

Sample	Texture	$T_{[BKN90]}$ (°C)	$P_{[BKN90]}$ (GPa)	$T_{[T98]}$ (°C)	$P_{[NG85]}$ (GPa)	$T_{[O'NW79]}$ (°C)	$P_{[BBG08]}$ (GPa)
CIM15-001	Def LRZ	**1401**	**5.7**	1386	5.7	1421	5.6
CIM15-002	Crs LRZ	**1221**	**4.4**	1271	4.8	1299	4.5
CIM15-003	Def LRZ	**1370**	**7.4**	1320	6.9	1373	6.7
CIM15-004	Crs LRZ	**1014**	**3.4**	1112	4.1	1169	4.1
CIM15-006	Crs LRZ	481	0.8	734	2.3	-	-
CIM15-013	Crs LRZ	**1010**	**3.5**	1088	4.2	-	-
CIM15-015	Def LRZ	**1144**	**4.6**	1238	5.2	-	-
CIM15-016	Def LRZ	**1459**	**7.5**	1385	6.9	-	-
CIM15-017	Def LRZ	**1376**	**5.4**	1375	6.2	1489	6.6
CIM15-021	Def LRZ	**1410**	**6.6**	1426	5.8	1440	6.6
CIM15-035	Def LRZ	**1367**	**6.2**	1391	6.5	-	-

BKN90 = Brey and Koehler (1990); T98 = Taylor (1998); NG85 = Nickel and Green (1985); O'NW79 = O'Neill and Wood (1979); BBG08 = Brey et al. (2008).

Values in bold are used in **Section 4.5.2** and in **Figure 4.4**. Values in grey represent samples with varying degrees of Fe-Mg disequilibrium.

CHAPTER 4: FIGURES

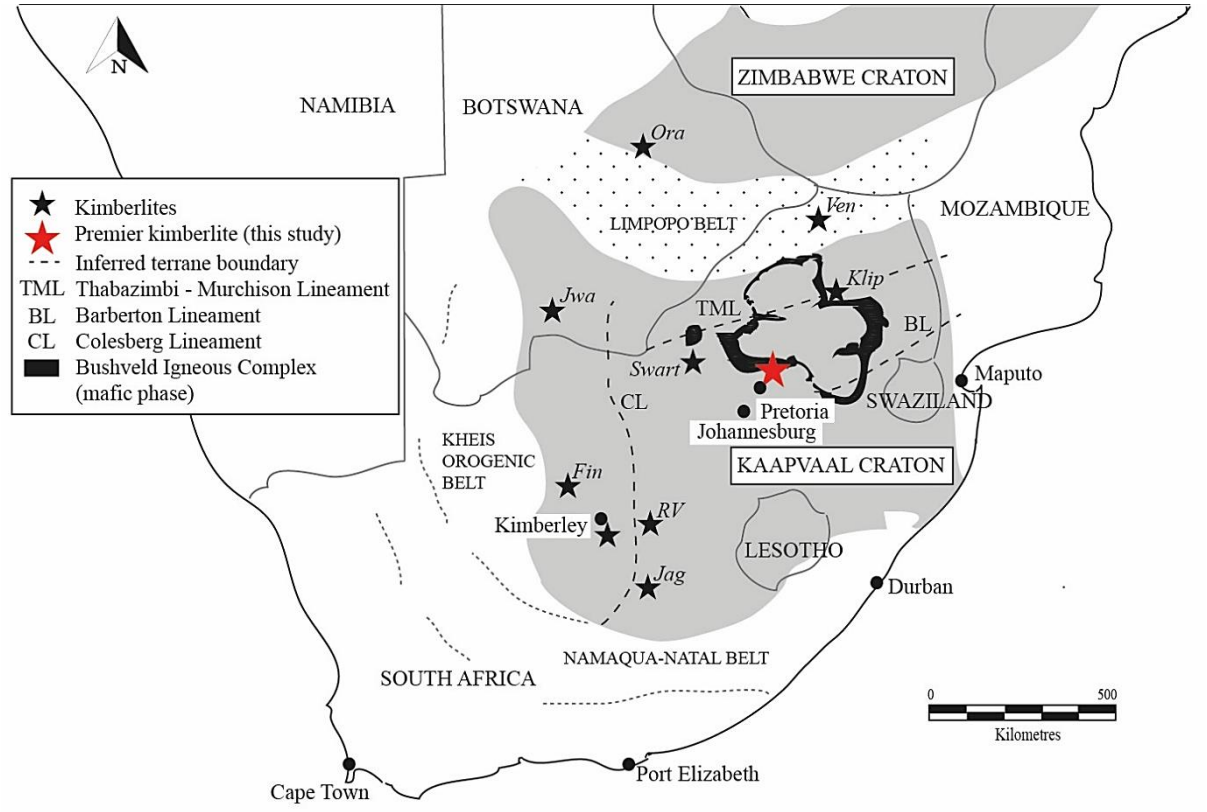

Fig. 4.1 *Schematic of the Kaapvaal craton modified after Friese et al. (2003). The Kaapvaal craton is subdivided into the Kimberley (western) and Witwatersrand (eastern) blocks along the Colesberg Lineament. Peridotite xenoliths are sampled from the Premier kimberlite, located in the north-central part of the craton near the western limb of the Bushveld complex.*

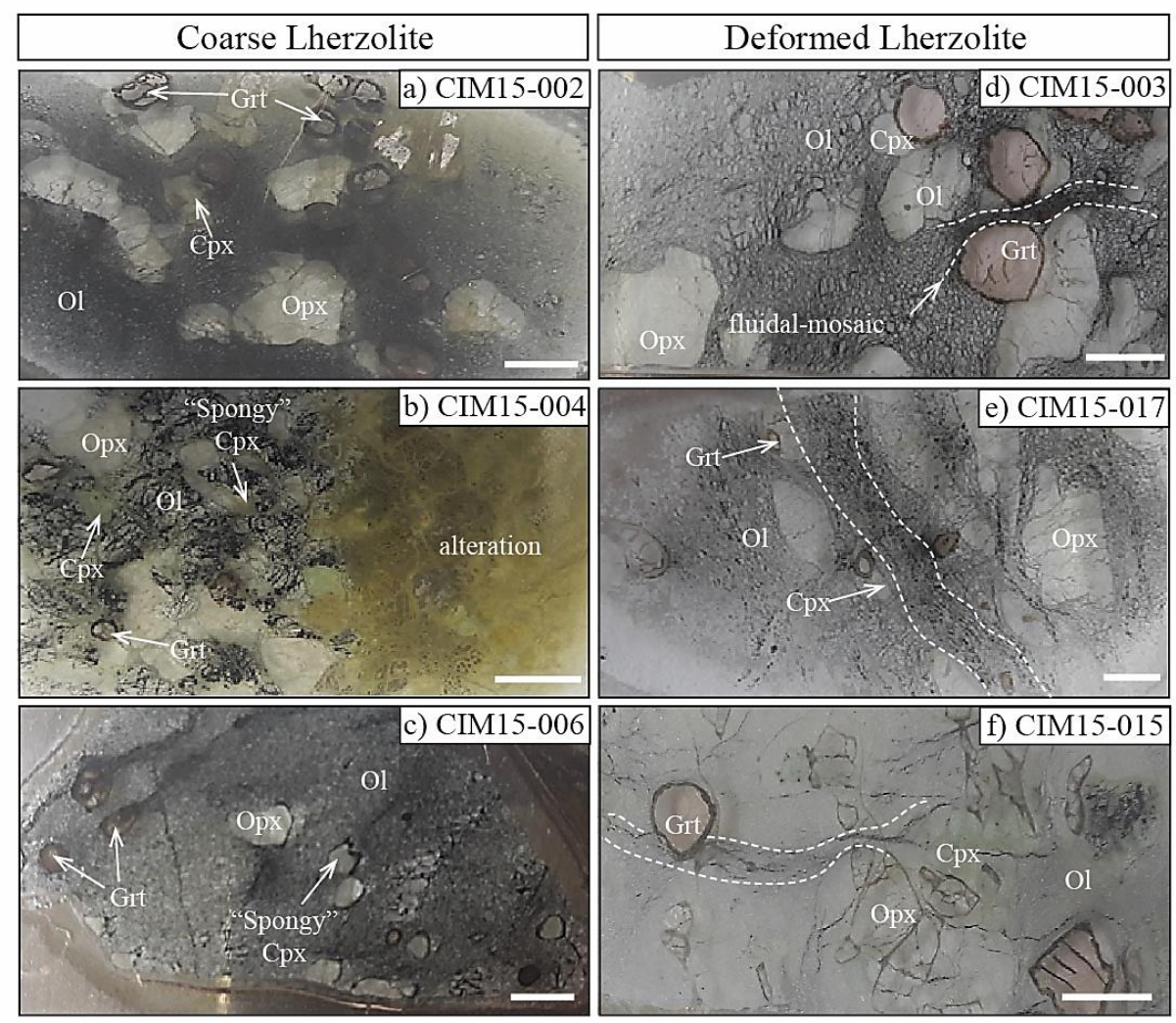

Fig. 4.2 *Select garnet-bearing lherzolite xenoliths from Premier kimberlite.* ***(a – c)*** *Coarse garnet-bearing lherzolites,* ***(d – f)*** *deformed garnet-bearing lherzolites. Scale bar = 5mm. Grt = garnet, Ol = olivine, Opx = orthopyroxene, Cpx = clinopyroxene. "Spongy" Cpx and fluidal-mosaic domains are described in* ***Section 4.3****.*

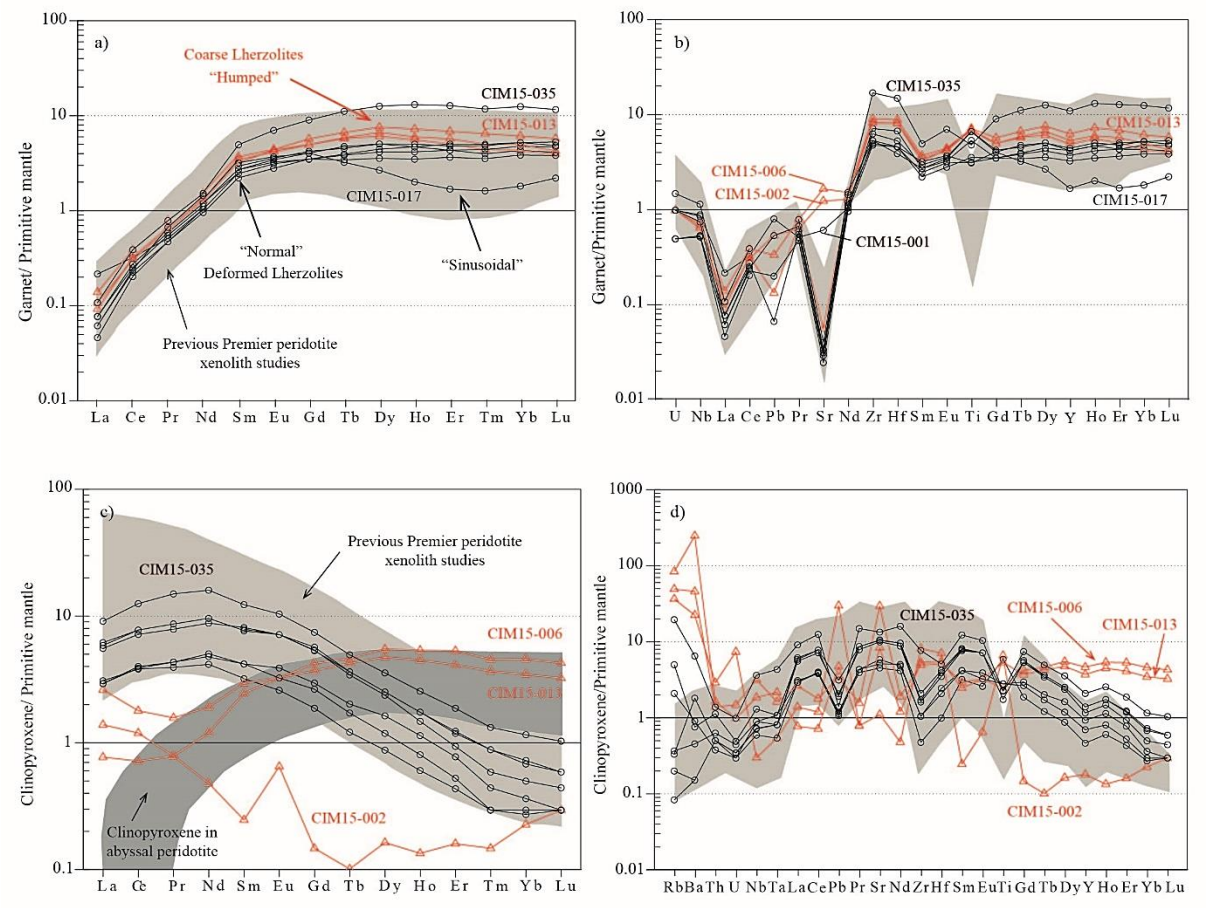

Fig. 4.3 *Primitive-mantle normalised REE and trace element patterns for garnet* ***(a - b)*** *and clinopyroxene* ***(c - d)*** *from the Premier garnet-bearing lherzolite xenoliths. Shown for comparison are Premier lherzolite garnet and clinopyroxene trace element patterns from previous studies (Light-grey field: Gregoire et al., 2003; Viljoen et al., 2009) as well as clinopyroxene from abyssal peridotite (Dark-grey field: Johnson et al., 1990; Rampone et al., 1996). Normalising values from McDonough and Sun (1995). The "humped", "normal" and "sinusoidal" REE patterns are described in* ***Section 4.5.1.2****.*

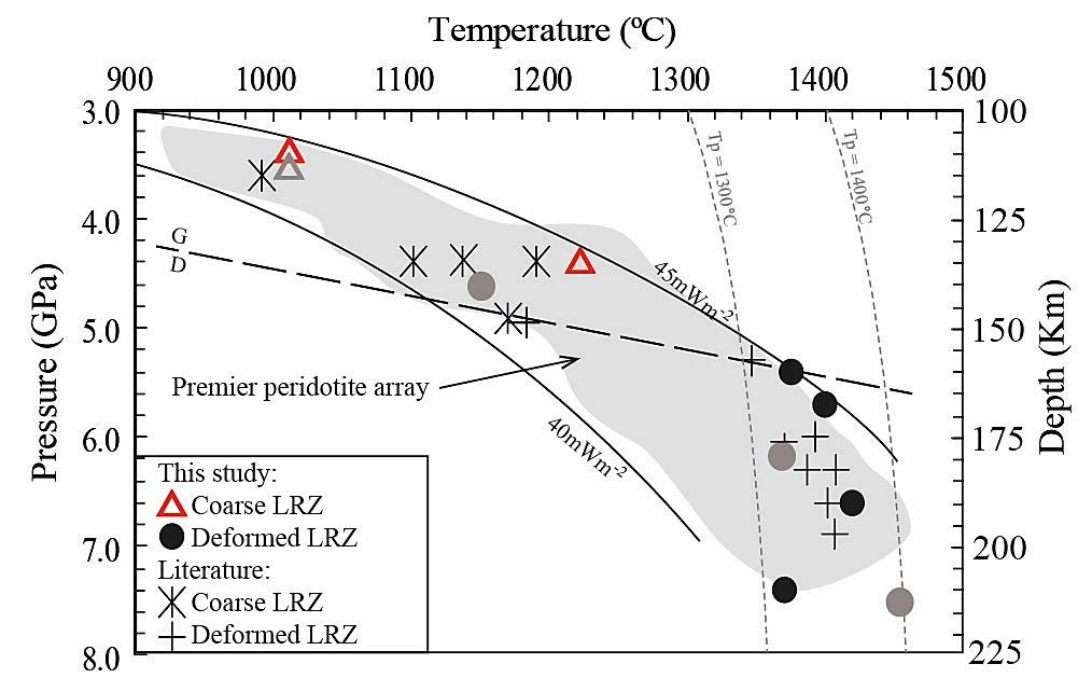

Fig. 4.4 *Premier garnet-bearing lherzolite P-T conditions were calculated iteratively using the four-phase geothermobarometer of Brey and Koëhler (1990). The equilibrium P-T$_{[BKN]}$ estimates yielded conditions from 3.4 to 7.4 GPa and 1011 to 1410 °C. The P-T$_{[BKN]}$ estimates for samples CIM15-013, -015, -016 and -035 are shown in grey due to minor Fe-Mg disequilibrium between their mineral phases (see* ***Section 4.5.2*** *and* ***4.6.1*** *for details), and P-T$_{[BKN]}$ estimates for sample CIM15-006 are not shown due to major Fe-Mg disequilibrium between the olivine, orthopyroxene and clinopyroxene mineral phases (see* ***Table 4.7****). Shown for comparison is the premier peridotite array (grey field) taken from Viljoen et al. (2009), as well as calculated P-T$_{[BKN]}$ estimates of select coarse and deformed-lherzolites taken from both Gregoire et al. (2003) and Viljoen et al. (2009). The graphite-diamond transition is from (Kennedy and Kennedy, 1976). Model conductive geotherms are from Pollack and Chapman (1977). The 1300 and 1400 °C mantle adiabats are from Kimura and Kawabata (2014).*

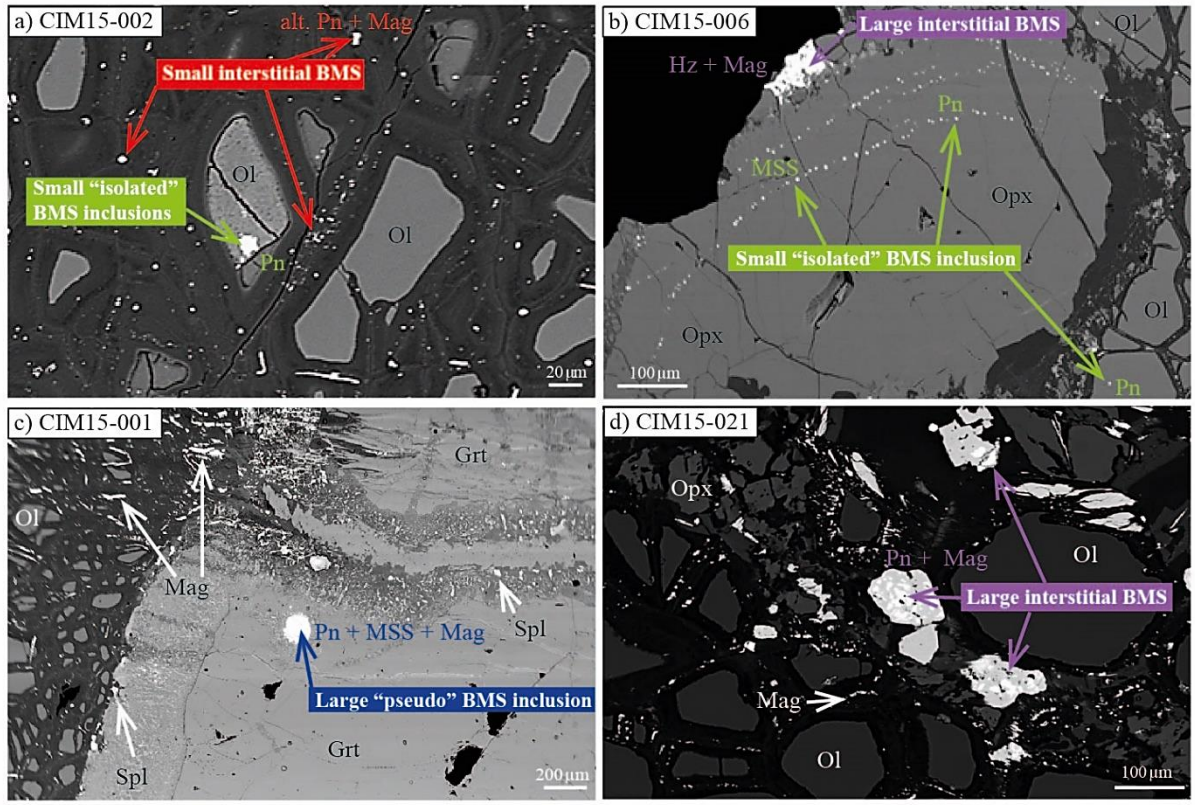

Fig. 4.5 *Select back-scattered electron images of BMS grains of different petrographic types (**see Section 4.5.3.2**) and assemblages from Premier garnet-bearing lherzolites.* ***(a)*** *Small "isolated" pentlandite (Pn) inclusion within olivine, and small interstitial Pn grain partially altered to magnetite (Mag) within the serpentinised olivine matrix.* ***(b)*** *Small "isolated" Pn and mono-sulphide solid solution (MSS) grains within olivine and along healed growth/fracture zones within orthopyroxene. Large interstitial BMS consisting of heazlewoodite (Hz) and ~40% Mag alteration located on the edge of the mount between an orthopyroxene porphyroclast and the olivine matrix.* ***(c)*** *Large BMS pseudo-inclusion consisting of remnant Pn and MSS with 10% Mag alteration located on a garnet crysal rim. Magnetite grains are diseminated throughout the serpentinised peridotite matrix and their elongate shape follows the direction of veining.* ***(d)*** *Large interstitial BMS grains that consist of Pn and >50% Mag alteration.*

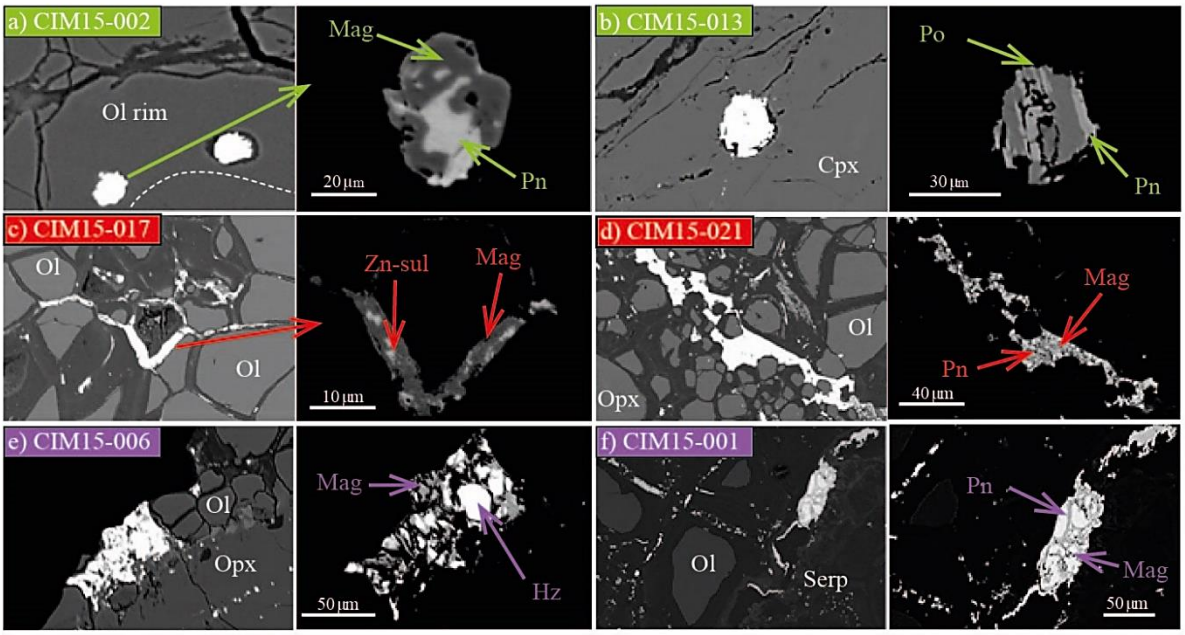

Fig. 4.6 *Detailed back-scattered electron images of BMS grains of different petrographic types and compositions from the Premier garnet lherzolite xenoliths.* ***(a)*** *Pentlandite inclusions with ~50% magnetite alteration located on the rim of an olivine crysal.* ***(b)*** *Small (<50 µm) isolated BMS inclusion within clinopyroxene consisting of a complex flame-like intergrowth of both pentlandite and pyrrhotite.* ***(c)*** *Small elongate BMS interstitials that follow the direction of veining.* ***(d)*** *Interstitial clusters of small pentlandite interstitials with ~40% magnetite alteration.* ***(e)*** *Large heazlewoodite interstitial with ~40% magnetite alteration.* ***(f)*** *Lagre interstitial sulphide consisting of pentlandite with 40% magnetite alteration, trails of minute interstitial sulphides radiate out from the large grain indicating decrepitation of the original sulphide.*

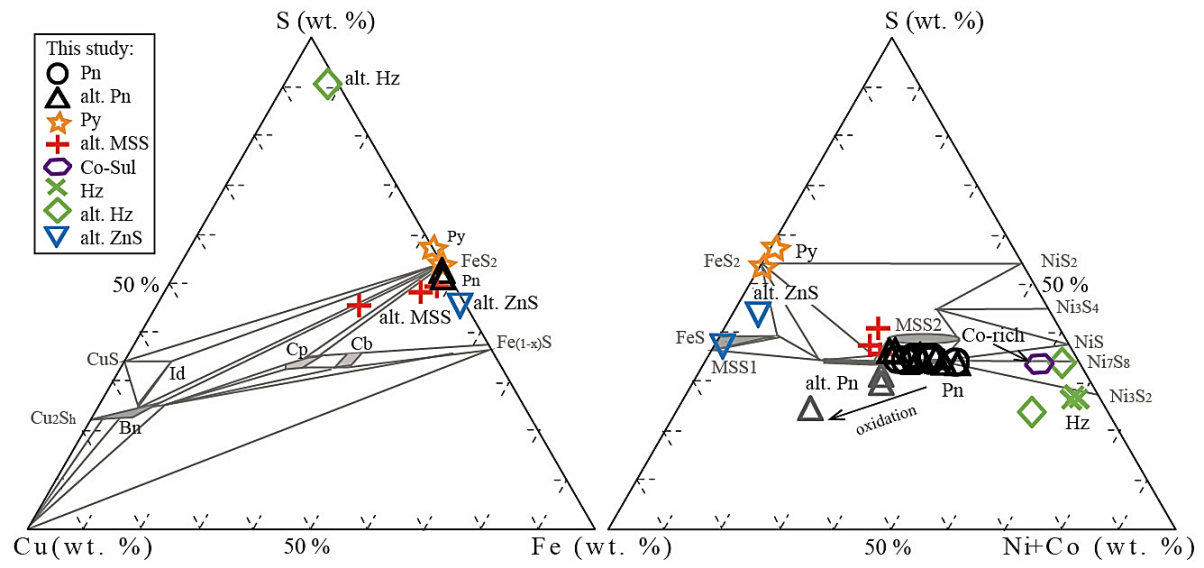

Fig. 4.7 *Premier BMS major element compositions in the Cu-Fe-Ni-S system at 300 ºC after Craig (1973) and Yund and Kullerud (1966). All sulphide major element compositions (see* ***Section 4.5.3.3****) are plotted on the ternary dagrams including the oxidised/altered (alt.) sulphide mineral phases. Notably, Pn, MSS, and Hz are prevalent thougout the sample suite. ZnS only occurs in deformed lherzolites CIM15-001 and -021, Py in coarse lherzolites CIM15-004 and -006, and Co-rich sulphide in coarse lherzolite CIM15-013. Pn = pentlandite, MSS = mono-sulphide solid solution, Co-Sul = cobalt-rich sulphide, Hz = heazlewoodite, ZnS = Zn-rich sulphide, Py = pyrite. Solid lines represent lie-lines between different sulphide compositions and grey fields are solid solutions of bornite (Bn), idanite (Id), chalcopyrite (Cp), cubanite (Cb), mono-sulphide solid solution (MSS) and pentlandite (Pn).*

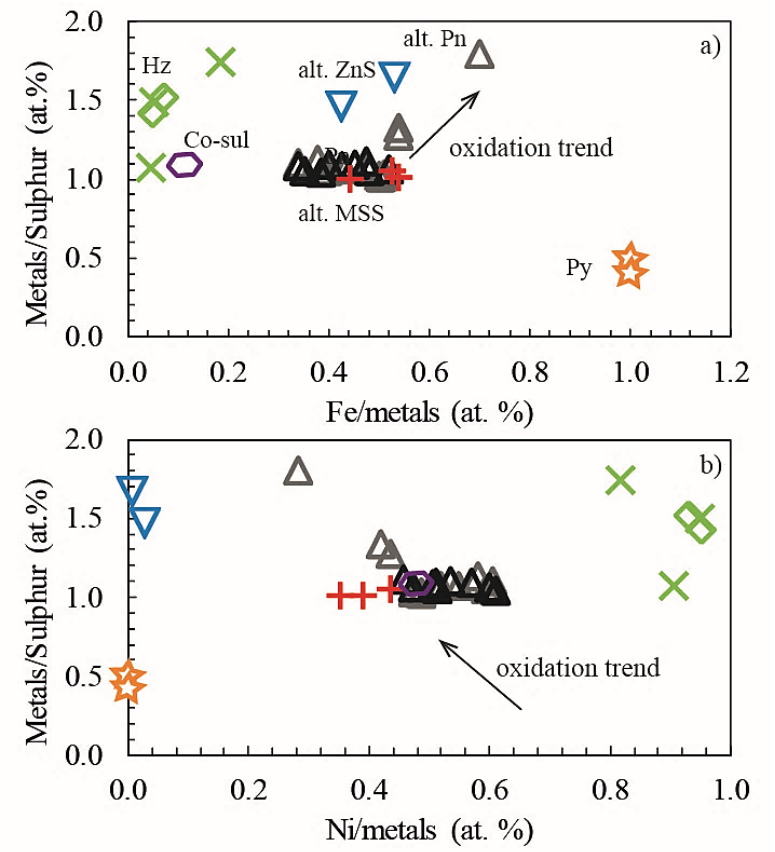

Fig. 4.8 *Premier sulphide major element compositions, including oxidised/altered sulphide mineral phases.* ***(a)*** *Fe/metals (Fe+Ni+Cu+Co±Zn) ratio vs. metals/sulphur ratio.* ***(b)*** *Ni/metals ratio vs. metals/sulphur ratio. Pn, MSS, and Hz are prevalent thougout the sample suite. ZnS only occurs in deformed lherzolites CIM15-001 and -021, Py in coarse lherzolites CIM15-004 and -006, and Co-rich sulphide in coarse lherzolite CIM15-013. Legend as in* ***Fig. 4.7****. Arrows and grey symbols represent increasing oxidation of the sulphide phases.*

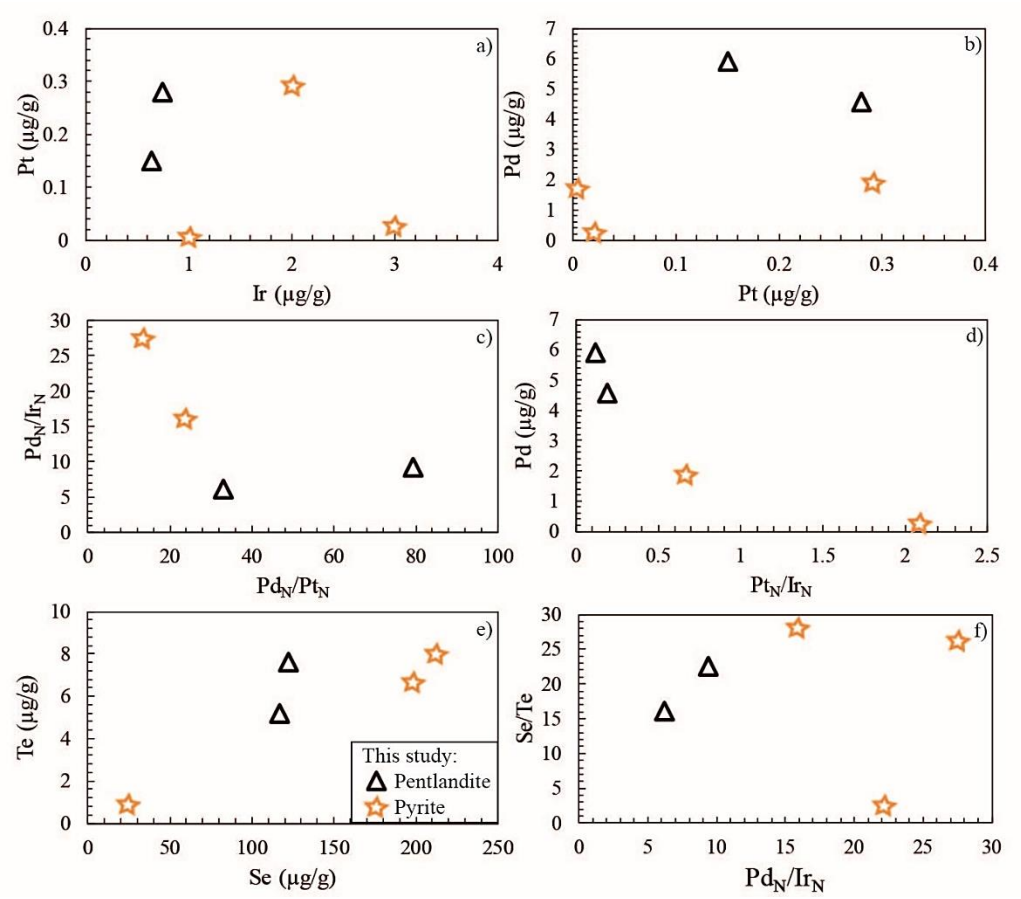

Fig. 4.9 *Binary variation plots of highly siderophile and chalcophile element concentrations and their inter-elemental ratios.* ***(a)*** *Ir vs. Pt.* ***(b)*** *Pt vs. Pd.* ***(c)*** *Pd_N/Pt_N vs. Pd_N/Ir_N.* ***(d)*** *Pt_N/Ir_N vs. Pd.* ***(e)*** *Te vs. Se.* ***(f)*** *Pd_N/Ir_N vs. Se/Te. Chondrite normalising values taken from Fischer-Gödde et al. (2010). The pentlandite and pyrite chondrite-normalised Pd/Pt, Pd/Ir, and Pt/Ir values fall within a large range displayed by metasomatised sulphides observed in abyssal peridotites (Alard et al.,* 2005*, 2011; Luguet and Pearson, 2019) as well as sulphides present in peridotite lithologies from the Bushveld Igneous Complex (Hutchinson and McDonald, 2008), see* ***Section 4.5.3.4*** *and* ***4.6.2*** *for details.*

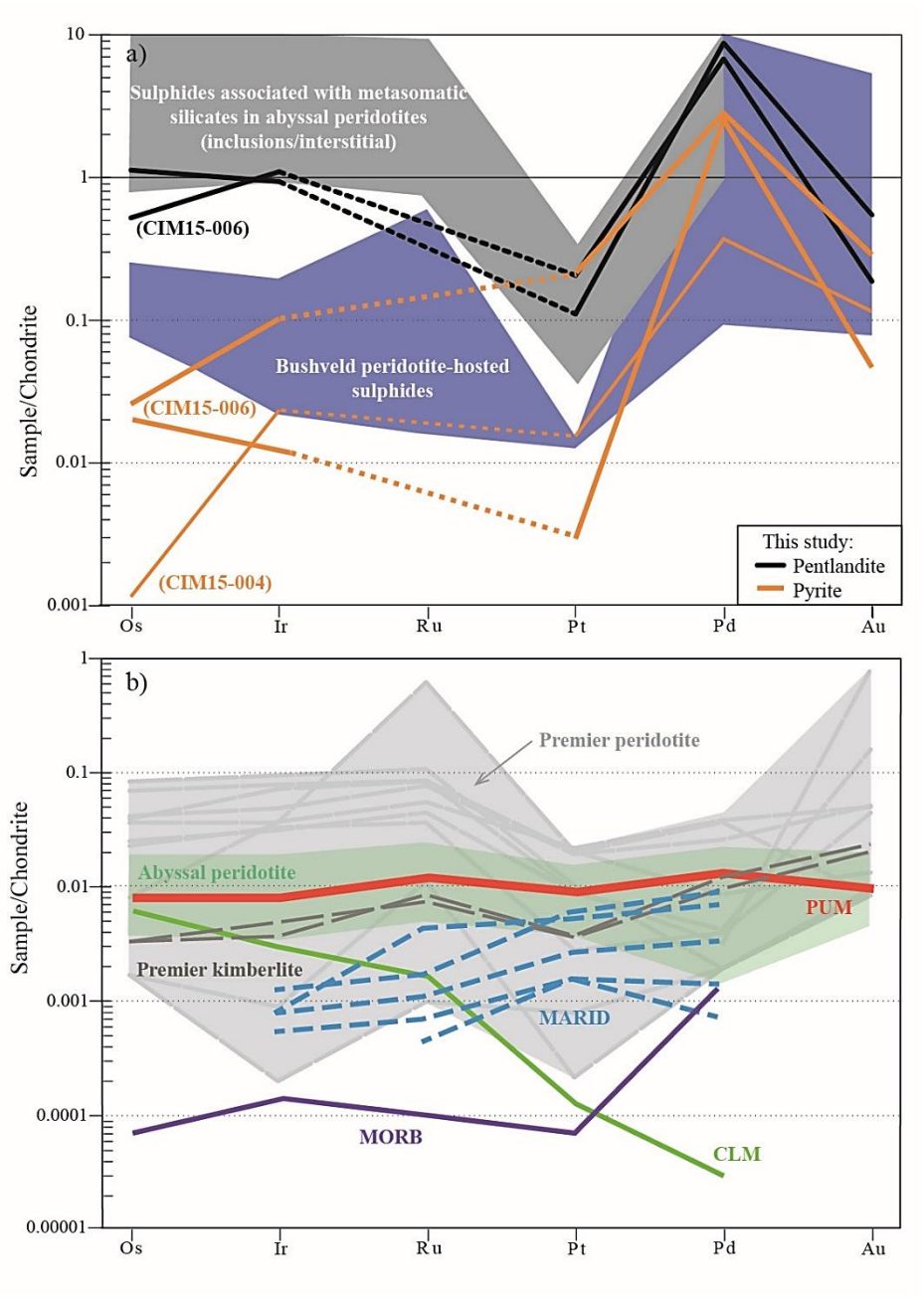

Fig. 4.10 (a) *In-situ chondrite-normalised HSE patterns for pentlandite and pyrite from Premier coarse-lherzolite xenoliths CIM15-006 and -004. The relatively Pd-enriched HSE patterns of these sulphides are comparable to abyssal peridotite-derived sulphides present either as inclusions within metasomatic silicates or as intergranular/interstitial grains associated with metasomatic silicates (grey filed; Alard et al., 2005, 2011), and to sulphides (pyrrhotite and pentlandite) present in peridotite lithologies from the Bushveld complex (dark blue field; Hutchinson and McDonald, 2008).* ***(b)*** *The in-situ HSE patterns for pentlandite and pyrite from Premier are enriched compared to whole-rock HSE abundances of both previously studied Premier xenoliths (Grey field with lines; Maier et al., 2005, 2012) and abyssal peridotites (Green field; Liu et al., 2008, 2009; Day et al., 2017), the primitive upper manlte (PUM = Red bold line; Becker et al., 2006), MORB (purple line; Day, 2013), and the cratonic lithospheric mantle (CLM = Green line; Day, 2013). Neither the Premier pentlandite nor pyrite HSE patterns bear strong resemblance to cratonic mantle MARID xenoliths (Blue dashed lines; Maier et al., 2012) or to the Premier kimberlite (Maier et al., 2005). Chondrite normalization values are from Fischer-Gödde et al. (2010).*

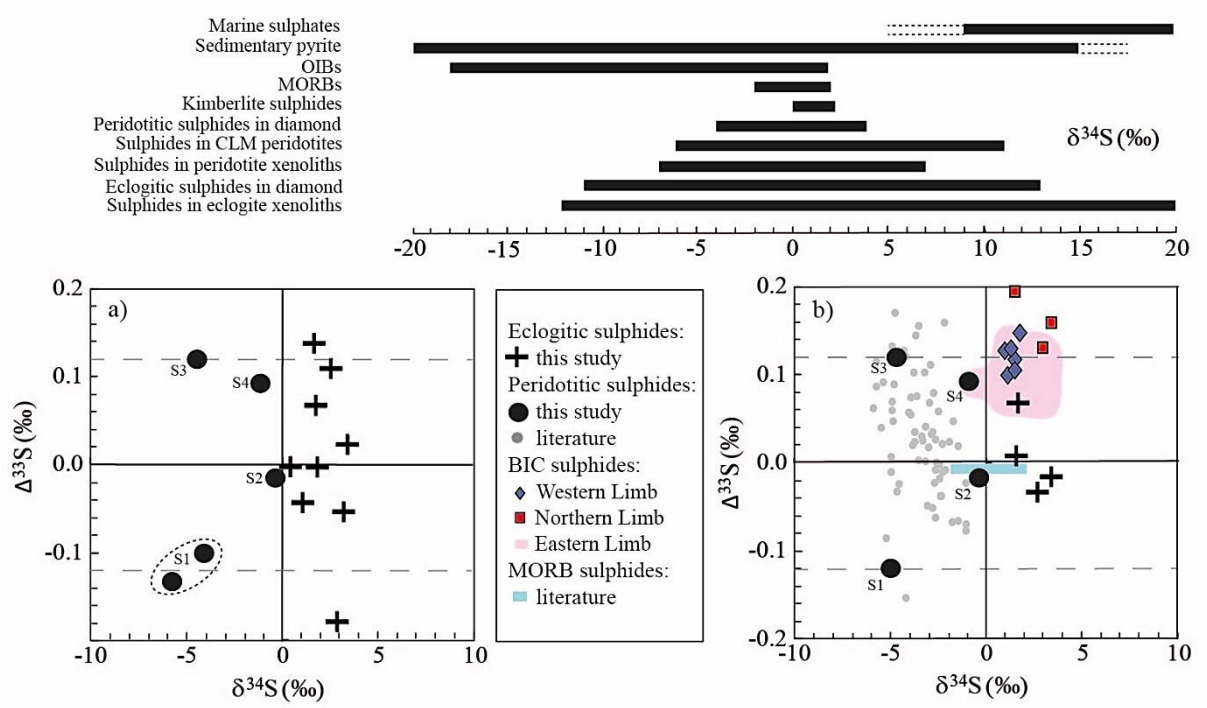

Fig. 4.11 *Plot of $\delta^{34}S$ (relative to CDT) vs $\Delta^{33}S$ for sulphides (Pn) from coarse lherzolite CIM15-006.* ***(a)*** *Individual measurements on each peridotite-derived sulphide grain (S1 to S4) plus sulphides from premier eclogite JJG-2717 (**Table 4.6**) are shown for comparison.* ***(b)*** *Average $\delta^{34}S$ vs. $\Delta^{33}S$ for each sulphide grain. The dashed field centered at $\Delta^{33}S = 0$ and extending from +0.12 to –0.12 ‰ represents the mass-dependent fractionation field (Farquhar et al. 2002). For comparison are peridotite-derived sulphides from the Bultfontein kimberlite (Giuliani et al., 2016), the Bushveld Igneous Complex (BIC; Penniston-Dorland et al., 2008, 2012; Magalhães et al., 2018), and from MORB (Labidi et al., 2012, 2013, 2014). Additionally, $\delta^{34}S$ (‰) values for marine sulphates, sedimentary pyrite, ocean island basalts (OIBs), magmatic sulphides in kimberlites, peridotitic and eclogitic sulphides in diamond, sulphides in CLM-derived peridotite and eclogite xenoliths brought to the surface by alkali-basalt and kimberlite magmatism, as well as sulphides in CLM peridotites are shown for comparison as total ranges (values from Giuliani et al. (2016), and references therein).*

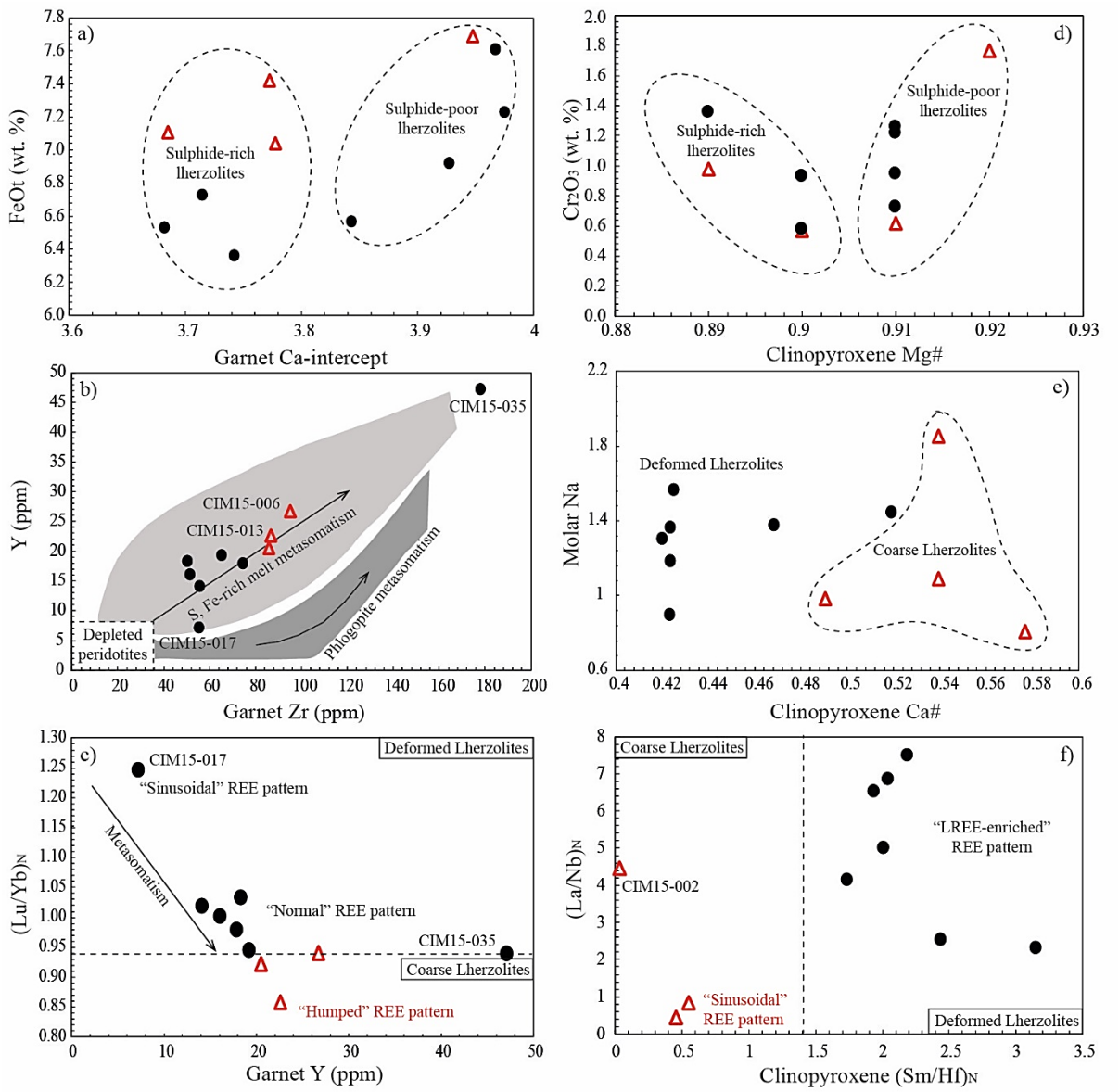

Fig. 4.12 (a) *Garnet Ca-intercept after Grutter et al. (2004) plotted as a function of total FeO (wt. %) content of the garnet-bearing lherzolite xenoliths from Premier.* ***(b)*** *Zr and Y abundances of garnet. Fields and metasomatic trends after Griffin et al. (1999) and Viljoen et al. (2009).* ***(c)*** *Garnet Y content plotted as a function of chondrite-normalised Lu/Yb ratio (McDonough and Sun, 1995). Garnet REE patterns as shown in* ***Figure 4.3****, and the arrow indicates progressive metasomatism of the peridotite xenoliths.* ***(d)*** *Clinopyroxene Mg# vs. Cr_2O_3 contents. The lherzolites are split into sulphide-rich and sulphide-poor samples (see* ***Table 4.2****).* ***(e)*** *Clinopyroxene Ca# plotted as a function of molar Na content. Coarse-lherzolites are increasingly more calcic than the deformed lherzolites.* ***(f)*** *Clinopyroxene chondrite-normalised Sm/Hf ratio vs. La/Nb ratio. Clinopyroxene REE patterns as shown in* ***Figure 4.3.***

CHAPTER 5

5. PRESENTATION OF THE RESEARCH PAPER

"THE MOBILITY OF SULPHUR IN THE UPPER MANTLE: CONSTRAINTS FROM S±C-BEARING ECLOGITE EXPERIMENTS"

This research paper has been submitted to Contributions to Mineralogy and Petrology for publication by the authors:

S. Burness, University of the Witwatersrand (primary author, conducted the research)

K.A. Smart, University of the Witwatersrand (supervisor, reviewed the manuscript)

G. Stevens, University of Stellenbosch (supervisor, advice on experimental technique and funding)

An experimental investigation was conducted on the behaviour of carbon- and sulphur- bearing eclogite at upper mantle conditions. The purpose of this study is to contribute to the knowledge of how volatiles (C, S) are cycled and stored within the mantle, especially relating to mantle metasomatism, diamond formation and contributions of recycled eclogite to OIB magmatism. Additionally, given the importance of sulphur to diamond formation (the preponderance of sulphide inclusions) as well as the possible mantle source of sulphide-hosted chalcophile elements for mantle-derived melts and crustal ore deposits, we have placed special emphasis on looking at the behaviour of sulphur in fertile eclogite. The study, conducted at conditions from 1050 to 1300 ºC and 2.0 to 3.5 GPa, reveals that sulphur, mobilized as either liquid sulphide or dissolved sulphur, requires transport within eclogite-derived silicate or carbonate-silicate melts, and not at all in purely carbonatitic type melts. This is due to the presence of non-bridging oxygen and higher Fe contents found in the more siliceous melts. Therefore, the formation of sulphide-bearing diamonds (although occurring at pressure above our investigated range) requires fluids or melts that contain a significant silicate component, additionally, if the sulphur content of OIB magmas is sourced from eclogite, again the mobilization requires semi-siliceous melts.

This manuscript contains new, original work that has not been previously published or submitted elsewhere. I performed all the experiments, data acquisitions and calculations independently under the guidance of Gary Stevens at Stellenbosch University. The original research idea was conceptualised by Gary Stevens and Kate Smart. I am the primary author of the manuscript and created all figures and tables independently. The manuscript benefitted from advice and revisions from both Katie Smart and Gary Stevens. Both co-authors agree to the use of this manuscript within this PhD thesis.

Contributions to Mineralogy and Petrology, Impact factor: 3.6

ABSTRACT

The melting and phase relations of S±C-bearing model eclogite has been investigated at upper mantle conditions, from 1050 to 1300 ºC and 2.0 to 3.5 GPa using a piston cylinder apparatus and graphite lined palladium-silver capsules. Experiments were performed on three different synthetic bulk compositions, SKG-1 (MORB-like glass "SKG" + 5 wt. % pentlandite), SKG-2 (SKG glass + 5 wt. % pentlandite + 4.7 wt.% CO_2 added as $CaCO_3$) and SKG-3 (SKG glass + 5 wt. % pentlandite + 11.8 wt.% CO_2 added as $CaCO_3$). Melts produced in the CO_2-free SKG-1 experiments have silicate-dominated, basaltic-andesite-type compositions (~57 wt.% SiO_2). Melts produced in the CO_2-bearing experiments range from silicate-dominated compositions (>50 wt. % SiO_2) through intermediate carbonate-silicate compositions (4.5 – 12.4 wt.% SiO_2 and 43 – 47 wt. % CO_2) to carbonate-dominated compositions (<2.4 wt.% SiO_2 and 42 – 53 wt.% CO_2). Liquid sulphide is only produced in experiments where silicic basaltic-andesite liquids are also formed, which correspond to higher degrees (>10%) of partial melting of both CO_2-free and CO_2-bearing eclogite. In contrast, dissolved sulphur is found in intermediate carbonate-silicate melts when the degree of partial melting of the CO_2-bearing eclogites exceeds 15%. In experiments conducted on CO_2-bearing eclogites where only carbonatitic melts are formed at relatively low degrees of melting (< 6%), sulphur remains as residual MSS. The experiments demonstrate that the mobilisation of sulphur (as liquid sulphide or dissolved sulphur) from upper mantle eclogite depends critically on the composition of the eclogite-derived melts, which in turn is controlled by both the degree of melting and volatile content of the system. The experiments of this study place constraints on the potential mechanisms for the metasomatic movement of sulphur within the upper mantle, with implications for diamond formation and sulphide-bearing mantle-derived magmatism.

KEYWORDS: Experimental petrology; deep carbon cycle; mantle redox; metasomatism; diamond inclusion; cratonic mantle lithosphere; ocean island basalt; sulphide; highly siderophile elements

5.1. INTRODUCTION

Volatile element concentrations control the temperature at which incipient mantle melting begins (Wyllie and Huang, 1976; Eggler, 1987; Yaxley and Green, 1994; Foley, 2010), with CO_2 and H_2O playing a significant role in both the position of upper-mantle peridotite and eclogite solidii (Mysen and Boettcher, 1975; Eggler, 1978; Dasgupta and Hirschmann, 2006; Foley et al., 2009), as well as determining the character of the resulting volatile-bearing, silica-undersaturated melts (e.g. Hammouda, 2003; Dasgupta et al., 2004, 2005; Yaxley and Brey, 2004; Litasov and Ohtani, 2010; Kiseeva et al., 2012). The occurrence of such melts in intraplate settings is suggested by the presence of alkali basalts and carbonatites in ocean island volcanism (Nelson et al., 1988; Mallik and Dasgupta, 2012; Schmidt and Weidendorfer ,2018) and is well documented by the occurrence of ultramafic alkaline volcanism, including kimberlites, carbonatites and lamprophyres in continental and cratonic settings (e.g. Tappe et al., 2008, 2018a; Foley, 2010). Previous experimental work has been dominated by CO_2±H_2O fluxed melting of upper mantle peridotite, pyroxenite and eclogite (Wallace and Green, 1988; Yaxley and Green, 1994; Hirose, 1997; Luth, 1999; Yaxley and Brey, 2004; Dasgupta and Hirschmann, 2006; Brey et al., 2008; Foley et al., 2009; Litasov and Ohtani, 2010; Kiseeva et al., 2012; Green, 2015; Hammouda and Keshav, 2015), with fewer studies focussing on the role and behaviour of sulphur (e.g. Metrich and Clocchiatti, 1996; Freda et al., 2005; Jugo et al., 2005; Jugo, 2009). Most investigations of sulphur in mantle magmatic systems have been centred around the partitioning of highly siderophile elements (HSE) between silicate and sulphide melts for application to magma ocean processes (e.g. Peach et al., 1990; Alard et al., 2000; Fonseca et al., 2011; Mungall and Brenan, 2014) and sulphur-silicate miscibility and ore petrogenesis (e.g. Mavrogenes and O'Neill, 1999; Holzheid and Grove, 2002; Bockrath et al., 2004; Mungall et al., 2006; Liu et al., 2007; Li and Ripley, 2009; Li and Audétat, 2012, 2013; Zajacz et al., 2013; Kiseeva and Wood, 2015; Liu and Brenan, 2015; Brenan et al., 2016). Few studies have placed emphasis on the importance of sulphur activity in petrogenetic processes that invoke volatile-driven mantle magmatism (e.g. Kullerud, 1963; Jégo and Dasgupta, 2014; Kiseeva et al., 2017).

It is well documented that subduction processes drive crust-mantle volatile recycling (Staudigel et al., 1996; Wallace, 2005; Poli et al., 2009; Métrich and Mandeville, 2010; Dasgupta, 2013), and subduction-related dehydration reactions contribute to increased concentrations of volatiles, including sulphur, within the upper mantle (Alt et al., 1993; Kelley and Cottrell, 2009; Evans et al., 2014; Evans and Powell, 2015). In contrast to the "accepted" primitive mantle $\delta^{34}S$ value of +0.5 ‰ (Chaussidon et al., 1989; Thomassot et al., 2009), recent studies of MORB (Labidi et al., 2012, 2014) and mantle-derived xenoliths suggest that the asthenospheric mantle contains subducted crustal heterogeneities. For example, the $\delta^{34}S$ values of sulphide inclusions in metasomatised mantle-derived peridotite xenoliths range between −6 and +7 ‰ (Tsai et al. 1979; Chaussidon et al., 1989; Giuliani et al., 2016), and it is proposed that the metasomatic agents that affected these rocks originated from sources containing subducted sediments with either positive (Farquhar et al., 2010) or negative (Canfield, 2004; Giuliani

et al., 2016) $\delta^{34}S$ values. Sulphide inclusions in diamonds show large ranges in $\delta^{34}S$ values (from -9 to +5.7 ‰) that further indicate the presence of recycled sedimentary/crustal material in the mantle (Eldridge et al., 1991; Farquhar et al., 2002; Cartigny et al., 2009; Thomassot et al., 2009). Additional evidence for the presence of recycled volatiles in the mantle is shown by eclogite-derived diamonds and with $\delta^{13}C$ isotope compositions that range outside the mantle average of -5‰ (Deines, 2002; Cartigny et al., 2014), to both extremely dep,leted (-40 ‰, Smart et al. 2011) and enriched (+1 ‰, Deines, 2002; Cartigny, 2005) values. Moreover, the relatively high sulphur contents (800 – 2400 µg/g S; (Perfit et al., 1983; Wallace and Carmichael, 1992; le Roux et al., 2006) of mafic arc magmas require sulphur concentrations in the mantle source to be in the range of 250 – 500 $\mu g.g^{-1}$ S (Métrich et al., 1999; De Hoog et al., 2001), higher than estimates for the depleted (MORB-source) mantle (70 – 200 ug/g; Saal et al., 2002; Lorand et al., 2003; Ding and Dasgupta, 2017).

Sulphur tends to be stored within redox-sensitive base-metal sulphides (Mitchell and Keays, 1981; Alard et al., 2000; Luguet et al., 2003, 2015; Lorand et al., 2013; Mungall and Brenan ,2014; Kiseeva et al., 2017a) and platinum group alloy minerals (e.g. PGM; Brenan and Andrews, 2001; Luguet et al., 2007) within the upper mantle. The mobility of sulphur requires that sulphide minerals breakdown in melt or fluid-forming reactions to allow for some sulphur abundance in a mobile phase. Volatile-driven redox melting (Foley, 2010; Hammouda and Keshav, 2015) within the upper mantle may be intrinsic to the movement of sulphur and associated metals in low degree partial melts that become effective metasomatic agents on segregation from their source rocks (Wallace and Carmichael, 1992; Rehkaemper et al., 1999; Alard et al., 2000; Arndt et al., 2005; Jugo, 2009; Wallace and Edmonds, 2011). While carbon-bearing metasomatism has been linked to various lithosphere enrichment processes including, diamond formation (Stachel and Harris, 2009; Shirey et al., 2013; Cartigny et al., 2014) and kimberlite magmatism as part of the deep carbon cycle (Tappe et al., 2017b), information on the behaviour of sulphur during metasomatism, and partial melting will provide additional constraints on sulphur-induced diamond nucleation (e.g. Bulanova, 1995; Palyanov et al., 2007; Thomassot et al., 2009; McDonald et al., 2017), metal transport (Barnes et al., 1988; Alard et al., 2000; Lorand and Luguet, 2016), as well as the deep sulphur cycle (e.g. Jugo, 2009; Ding and Dasgupta, 2017, 2018).

Here we present experimental results on the partial melting behaviour of a S±C-bearing model eclogite at 2.0 to 3.5 GPa and 1100 to 1300 ºC. Particular attention is placed on the relationship between sulphide-melt formation relative to carbonate-silicate melt formation under these upper mantle conditions. Our findings suggest that sulphur miscibility within carbonate-silicate partial melts of CO_2-bearing eclogite is largely governed by the composition of the melt and redox conditions of the eclogite. We will discuss the implications for the mobility of S-rich melts and associated HSEs within the mantle, including links to diamond formation and crustal ortho-magmatic ore genesis.

5.2. PREVIOUS WORK

A combination of petrology-based models and experiments have shown that partial melts of high-pressure basalt (up to ~30 GPa) cover a wide range of compositions due to the extreme bulk composition variability inherent to the mafic system (Hammouda and Keshav, 2015). In an approximately volatile-free system, these melts range from alkali to tholeiitic basalts, andesites and dacites (Sen and Dunn, 1994; Rapp and Watson, 1995; Pertermann and Hirschmann, 2003a). Excluding pressure and temperature, melt compositional variab,ility also depends upon the availability of volatiles (e.g. C, O, H; Foley, 2010; Luth, 2014), the degree of melting (e.g. Kogiso et al., 2004; Hammouda and Keshav, 2015) and the redox state of the system (Jayasuriya et al., 2004; Frost and McCammon, 2008; Stagno et al., 2013).

Volatiles such as CO_2 and H_2O affect mantle melting by depressing both peridotite and eclogite solidii (Wyllie, 1978; Taylor and Green, 1988; Foley et al., 2009; Luth, 2014: Thomson et al., 2016). Unlike the peridotite system, where two well-defined and-contrasting 'dry' and 'oxidised' (CO_2±H_2O) solidus curves can be outlined from experiments at 1 to 10 GPa and 1100 to 1800 °C (Falloon and Green, 1989; Dalton and Presnall, 1998; Hirschmann, 2000; Dasgupta and Hirschmann, 2006; Tappe et al., 2018b) (**Fig. 5.1a**), the CO_2±H_2O eclogite system is particularly complex because of the inherent compositional heterogeneity present in basalts. Two different solidus curves have been proposed for the CO_2-bearing eclogite system: a smooth curve (Yaxley and Brey, 2004) and a carbonate "ledge" similar to the ledge curve described for the CO_2-bearing peridotite system (Hammouda, 2003; Shirasaka and Takahashi, 2003; Dasgupta et al., 2004, 2005a; Kiseeva et al., 2012). The presence and shape of the carbonate "ledge" appears to be controlled by bulk compositional factors such as calcium content (Ca# = [100 x molar Ca/ (Ca +Mg + Fe_T)]), total alkali abundance (Na±K), alkali oxide/CO_2 ratios, and the presence of a H_2O component (Dasgupta et al., 2005a; Kiseeva et al., 2012). Importantly, silica-rich starting compositions tend to shift the carbonate ledge to higher pressures. For example, the carbonate ledge is reported at ~6.0 GPa by Hammouda (2003) using the relatively silica-rich starting composition OTBC (SiO_2 = 47.2 wt.%), whereas Dasgupta et al. (2004) reported the carbonate ledge at 3.0 GPa using a more silica-poor composition SLEC1 (SiO_2 = 41.2 wt.%) (**Table 5.1; Appendix A**). In addition, a high bulk Na_2O/CO_2 ratio tends to lower solidus temperatures due to the fluxing nature of alkalis (e.g. Dasgupta et al. 2004; Yaxley and Brey 2004). Therefore, while the lack of carbonate ledge in the experiments of Yaxley and Brey (2004) may be explained by a combination of systematic bulk composition effects, the most notable is the low molar Na_2O/CO_2 ratio of EC1 (0.04) that results in its increased solidus temperature relative to SLEC1 (0.23) of Dasgupta et al. (2004) (**Table 5.1; Fig. 5.1a**). Despite the solidus variability introduced by starting bulk composition, melts of CO_2-bearing eclogite can range from silicate-dominated melts through calcic-carbonatites (e.g. Hammouda, 2003; Kiseeva et al., 2012) to more magnesian dolomitic carbonatite compositions (Dasgupta et al., 2004, 2005a; Yaxley and Brey, 2004). Bulk composition effects aside, a common feature of the CO_2-bearing eclogite

system shows that an increase in pressure results in a shift to more magnesian melt compositions (Keshav and Gudfinnsson, 2010; Litasov and Ohtani, 2010; Kiseeva et al., 2013).

Solidus temperatures of approximately volatile-free eclogite and garnet pyroxenite range from ~1100 to 1150 °C at 2.0 GPa (Yasuda et al., 1994; Yaxley and Green, 1998; Hirose and Fei, 2002; Litasov and Ohtani, 2010), and are slightly below the melting temperatures of 1150 to 1200 °C for Fe-Ni-Cu sulphides at the same pressure (Bockrath et al., 2004; Li and Audétat, 2013). Sulphur solubility in silicate melts is expressed as sulphur concentration at sulphide saturation (i.e. SCSS; Mavrogenes and O'Neill, 1999) and is a complex function of both temperature and pressure (e.g. Wendlandt, 1982; Mavrogenes and O'Neill, 1999), oxygen fugacity and sulphur speciation (Scaillet and Pichavant, 2005; Jugo, 2009; Li and Ripley, 2009), silicate melt composition (specifically the FeO content; Holzheid and Grove, 2002; Liu et al., 2007; Li and Audétat, 2015), and the composition of the sulphide component (e.g. Smythe et al., 2017). Overall, a wide range of silicate melt compositions exhibit positive dependencies of SCSS on temperature (i.e. SCSS increases with increasing temperature; Jégo and Dasgupta, 2013; Ding and Dasgupta, 2018), and strong exponentially negative dependencies of SCSS on pressure (i.e. SCSS increases as pressure decreases; Holzheid and Grove, 2002). At equivalent pressure and temperature, mafic melts have higher SCSS than more siliceous melts due to their higher abundance of non-bridging oxygens, which allows sulphur to substitute for free oxygens, thereby allowing larger proportions of sulphur to dissolve in the melt (Fortin et al. 2015). For example; natural MORB has miscible sulphur contents of ~800 to 2500 µg/g (Wallace and Carmichael, 1992) and sulphur contents can reach up to ~1728 µg/g in OIB glasses (Labidi et al., 2015; Ding and Dasgupta, 2018) compared to maximum sulphur contents of ~300 µg/g in granitoid melts (Wedepohl, 1995). Additionally, oceanic basaltic magmas often contain small immiscible sulphide glob,ules (Mathez 1976; Peach et al., 1990), possibly ,indicating sulphur saturation on ascent and decompression of the magma (Parat et al., 2011).

Base-metal sulphides and metal alloys (e.g. platinum group minerals, PGM; Luguet et al., 2007) contain the upper mantle HSE inventory and occur in trace modal abundances (Mitchell and Keays, 1981; Alard et al., 2000). These elements have economic value as precious metals (e.g. Au, Ag, and PGE), as well as scientific value as geochemical tracers of mantle petrogenetic processes (Lorand et al., 2008; Luguet et al., 2015). Sulphide-silicate liquid trace element partitioning experiments show that HSE elements are preferentially sequestered into the sulphur-rich component (i.e. $D_{\text{sulphide phase/silicate phase}}$ >>100) in mafic silicate systems (e.g. Fleet et al., 1996; Bell et al., 2009; Li and Audétat, 2012, 2013; Kiseeva and Wood, 2013; Zajacz et al., 2013). Specifically, experiments in ultra-mafic and mafic systems show that sulphides probably melt incongruently to form Fe, Ni, Cu-bearing sulphide melt that concentrates P-PGE (Pt, Pd and Rh), and a refractory monosulphide solid solution (MSS) that concentrates I-PGE (Os, Ir and Ru) (c.f. Barnes et al., 1997; Alard et al., 2000; Bockrath et al., 2004; Mungall and Brenan, 2014). Additionally, Os, Ir, Ru and Pt-rich PGM crystals found in the highly

depleted harzburgites of the Lherz massif (France), are interpreted to have formed in response to the complete dissolution of base-metal sulphides by high-degree partial melting (>20 wt. %; Luguet et al., 2007). Therefore, the metasomatic mass transfer of sulphur and associated metals in the upper mantle is intrinsically linked to the melting systematics of sulphides and PGM in peridotite and eclogite lithologies, and consequently, by experimentally constraining the behaviour of sulphur during the melting systematics of CO_2-bearing eclogite, we are able to address the involvement of sulphur in mantle petrogenetic processes.

5.3. EXPERIMENTAL APPROACH

5.3.1. Starting materials

Three starting materials SKG-1, SKG-2 and SKG-3 (**Table 5.2**), were prepared for the experiments of this study. The starting materials comprise a basic MORB-like glass "SKG" (50.87 wt.% SiO_2, 7.92 wt. % MgO, 3.24 wt. % Na_2O+K_2O) that is similar in composition to G2 from Pertermann and Hirschmann, (2003) (**Table 5.1**). The synthetic glass was manufactured from analytical grade oxide (SiO_2, TiO_2, Al_2O_3, MgO, FeO, MnO) and carbonate ($CaCO_3$, Na_2CO_3 and K_2CO_3) powders. Trace elements were added from certified multi-element aqueous solutions in 2% HNO_3, and 5 ml of the trace element solution was added to the starting composition powder, introducing concentrations of ~50 to 1000 µg/g of each element to the final glass product. The mixture was homogenised under acetone in an automated agate ball mill and then dried at 100 °C for 24 hours. Once dried, the synthetic powder was lightly pressed into a pellet and fired in a zirconium crucible in a vertical, 1-atm CO-CO_2 gas mixing furnace at 1300 °C with an oxygen fugacity ($\Delta \log f O_2$) of -10.7 (i.e. ~FMQ-3) for 20 minutes. This enabled reduction of ferric to ferrous iron and decarbonation of the starting material. Details of the vertical 1-atm gas mixing furnace configuration, thermal profile and oxygen fugacity calibration are provided in **Appendix B**. The resultant SKG glass was optically homogenous, showing no evidence for the coexistence of immiscibility liquids at 1300 °C or exsolution of an immiscible liquid or formation of quench crystals on quenching. The glass major and minor element compositions (**Table 5.2**) were determined by ED and WD spectrometry on a ZEISS EVO scanning electron microscope (SEM) (**Section 5.4.1**), and trace element abundances were determined by LA ICP MS at the University of Stellenbosch (**Appendix C**).

A synthetic pentlandite (35.4 wt.% S, 2.03 wt.% Cu, 9.91 wt% Ni, 52.1 wt.% Fe + 100 µg/g Pt) was synthesized from mixtures of pure metals and sulphur powder in evacuated silica tubes at 1200 °C. The synthetic sulphide composition was tested for bulk chemical composition and chemical homogeneity by XRF and SEM analysis, respectively **(Table 5.2)**. The specific pentlandite major element composition was chosen as it is representative of eclogitic sulphide inclusions found in diamonds (e.g. Richardson et al., 2001) that were brought to the surface by Kaapvaal craton kimberlites. Five wt.% synthetic pentlandite (adding 1.8 wt.% S to the starting sample) was added to all the starting

compositions to ensure that there was sufficient sulphur in the system to produce sulphide phases large enough to be analysed by scanning electron microscopy (SEM) methods.

Starting composition "SKG-1" comprises the MORB-like glass "SKG" + 5 wt. % pentlandite. "SKG-2" comprises SKG glass + 5 wt. % pentlandite + 4.7 wt.% CO_2 (added as $CaCO_3$). In order for SKG-2 to retain a similar CaO content to the original SKG glass (i.e., 10 vs. 11.6 wt. % CaO), a new glass was created with less CaO so that sufficient $CaCO_3$ could be added to achieve a CO_2 content of 4.7 wt. % without significantly increasing the bulk CaO content.. "SKG-3" comprises SKG glass + 5 wt. % pentlandite + 11.8 wt.% CO_2 (added as $CaCO_3$), where the addition of $CaCO_3$ increased the CaO content of SKG-3 to 16.8 wt. %.

Previous experimental studies show that in order to foster detectable melt formation, more CO_2 is required than is observed in natural altered MORB compositions (e.g. Hammouda, 2003; Dasgupta et al., 2005; Kiseeva et al., 2012), where MORB generally contains ~3 wt.%, but can have up to 6 wt.% CO_2 (Staudigel et al., 1996; Alt and Teagle, 1999). Addition of CO_2 as $CaCO_3$ may have an effect on the position of the CO_2-bearing eclogite solidus and the compositions of the melts produced due to the excess of Ca (c.f. Dasgupta et al., 2005). Addition of a complex carbonate (e.g. a Ca-Mg-Fe-Na-K-bearing carbonate) or a P-T controlled ideal carbonate liquid would be ideal for replicating compositions of altered oceanic crust found in nature (c.f. Dasgupta et al., 2005). However, the Ca# [molar Ca/(Ca+Mg+Fe)] of the SKG-2 and SKG-3 starting compositions are 33 and 48 with Na_2O contents of 2.7 and 2.2 wt.%, respectively, falling within the range of altered oceanic crust compositions (see Figure 2 of Dasgupta et al., 2005), and the range of previous experimental starting compositions (**Table 5.1**).

5.3.2. Experimental methods

All SKG starting materials were loaded into graphite lined palladium-silver capsules (**Appendix B2**). The loaded capsules were flushed with argon gas before being arc welded shut. Two PdAg alloys were employed: $Pd_{30}Ag_{70}$ alloy was used for experiments conducted at temperatures below 1200 °C, and $Pd_{60}Ag_{40}$ was used for higher temperature experiments. PdAg alloys are more resistant to reaction with sulphur than platinum but are not completely inert, and additionally, PdAg alloy capsules may also leach Fe from Fe-bearing compositions, but not as severely as platinum does. Consequently, graphite sleeves were fashioned from high-grade (reduced permeability) graphite rods to prevent chemical interaction between the experimental charge and the capsule metals. Sealed capsules with a diameter equivalent to the internal diameter of the graphite furnace were placed into the experimental cell assembly, separated from the thermocouple only by the capsule wall and a 0.5mm thick alumina disk. All experiments used a salt sleeve to ensure hydrostatic pressure and a Pyrex liner between the salt sleeve and the graphite furnace, to insulate the furnace contents. The experimental cell assembly (**Appendix B3**) was loaded into a 10mm internal diameter Holloway design, non-end-loaded piston-cylinder apparatus. Temperature was controlled using a "Depths of the Earth" controller with type-K

(at 1100-1200°C) and type-R (at 1300°C) thermocouples. Based on temperature calibration experiments using the melting point of pure gold, the uncertainty between the measured temperature and the actual temperature over the area of the capsule was confirmed to be within 5 °C of the recorded temperature (**Appendix B4**). On starting each experiment, pressure was increased to 10% above the intended pressure at room temperature. Temperature was increased at 80 °C per minute until the intended temperature was attained. Pressure was measured using a Heisse gauge and the pressure for each run was set using the hot piston out technique. In this configuration, the pressure uncertainty is < 0.5 kbar (Johannes et al., 1971). The piston-cylinder apparatus creates a naturally reducing environment around the experimental capsule due to the graphite furnace (Médard et al., 2008), and the diffusive loss of hydrogen through the capsule wall was not considered a significant problem. However, precautions were taken to limit any possible hydrogen diffusion by using an alloy of higher proportion palladium for experiments at elevated temperatures (Holleck, 1970), and all capsules were placed into plugs of boron-nitride, which is virtually impermeable to hydrogen (Truckenbrodt et al., 1997; Truckenbrodt and Johannes, 1999). Experiments were conducted at pressures from 2.0 to 3.5 GPa and over the temperature range 1050 to 1350 ºC. The experiments remained at the set pressure-temperature conditions for a total run duration of 48 hours before being quenched isobarically to room temperature within a minute of terminating the experiment. Successful capsules were weighed immediately then pierced and dried in a furnace at 100°C for 24 hours and then weighed again. Any loss in mass indicated the presence of excess volatiles (e.g. CO_2-gas).

5.4. ANALYTICAL TECHNIQUES

5.4.1. Scanning electron microscopy

Successful experimental charges were sectioned to expose the run product, mounted in epoxy and placed under vacuum to fill any pore spaces with epoxy before being placed in a drying cupboard to cure. Run products were polished using diamond paste and due to the potentially water-soluble nature of the quenched carbonate-rich melts, water was avoided during all stages of sample preparation. The experimental charges were gold coated (~0.005 thickness) to allow for the analysis of elemental carbon in the carbonate-bearing phases. Major and minor element compositions of mineral and melt phases were determined using a Zeiss EVO MA15VP Scanning Electron Microscope (SEM) equipped with a link ISIS energy dispersive spectrometry (EDS) system containing an Oxford X-max silicon drift detector at the Central Analytical Facility (CAF) at Stellenbosch University, South Africa. Quantitative (EDS) sulphide and silicate mineral analysis was performed using an accelerating voltage of 20kV, a 10 s counting time and a beam current range of 19 to 21.5 nA. A working distance of 8.5 mm was used. Sulphur was measured for the sulphide phases and oxygen was calculated by stoichiometry for the silicates. Generally, the reported analyses represent averages of 2 to 10 replicates, depending on the volume of material available. All mineral and melt spectra produced were processed by ZAF corrections

and quantified using natural mineral and pure metal standards. The uncertainties associated with individual major and minor element EDS analysis spots is in the range of ±0.1 wt.%.

For the analysis of carbonate minerals and quenched melts, a Gatan cryogenic stage was fitted to the SEM and used to cool the samples to approximately -180 ºC using liquid nitrogen (Preston et al., 2003). This counteracts migration-related counting losses on light elements (e.g. Na, H, K, C). Quantitative (EDS) analysis was performed using an an accelerating voltage of 20kV, a 15 s counting time (30 s background) and a working distance of 8.5 mm. A rastered or defocussed beam was used ranging from 2 to 50 µm in diameter and the reported analyses of the carbonate-bearing phases are averages of 2 to 5 replicates, depending on the grain size or the dimensions of the interstitial melt pool. The compositions of the carbonate-bearing phases were analysed as wt.% of the elements, and carbon was quantified using a calcite mineral standard (see **Appendix D** for standard data reproducibility). CO_2 was then calculated from the measured carbon content and uncertainties associated with individual CO_2 values are in the range of ±0.2 wt.% **(Appendix D).**

5.5. EXPERIMENTAL RESULTS

A summary of the experimental run conditions and corresponding phase assemblages for the SKG-1, SKG-2 and SKG-3 starting compositions is depicted in **Figure 5.1b**. For all experiments, the silicate mineral assemblage is eclogitic, composed of various proportions garnet and omphacite ± coesite. The compositions of carbonate and sulphide phases depend on the starting composition, pressure, temperature and redox conditions of each experimental run. **Table 5.3** lists the details of the starting compositions, experimental conditions as well as the modal proportions calculated by mass balance of the phases produced as well as point counting methods. The garnet, clinopyroxene and coesite crystals are typically < 20 µm in diameter and are euhedral to rounded in shape. In a few experiments, garnet grains were very small (<10 µm) and contained abundant coesite and minor clinopyroxene inclusions (**Table 5.4**). Backscattered electron images as depicted in **Figure 2** were used to establish the textural characteristics of each experimental run and the extent of partial melting.

5.5.1. Approach to equilibrium

The experiments show evidence for a reasonable approach to equilibrium, with only minor compositional heterogeneity in the silicate phases. Application of the Ellis and Green (1979) and Krogh Ravna (2000) garnet-clinopyroxene Fe-Mg exchange thermometers to experiments SKG-1.1, SKG-2.1, and SKG-3.1, which do not show any silicate mineral compositional heterogeneity, yield temperatures within 48 ºC and 45 ºC, respectively, of the measured run temperature. Mass-balance calculations of phase proportions for all experiments are presented in **Table 5.3** and the resulting sum of squared residuals (Σr^2) range from 0.8 to 2.9. The modal proportion (in wt.%) of individual phases were calculated by an iterative sum of squared residuals minimization routine that considered the major

element compositions (in wt.%) of all phases and the bulk composition of the system. Relatively high Σr^2 may result from uncertainty in the measurement of carbon in the carbonate-silicate melts and calcio-dolomitic solid solution phase ($L_{Carb\text{-}Sil}$, L_{Carb} and CC-Dol_{ss}; **Table 5.4**). CO_2 is calculated from measured elemental carbon in the carbonate-silicate melts (see **Section 5.4.1**), which do not quench to glass but instead a mass of intergrown quench crystals **(Fig. 5.2d, e),** or by stoichiometry for the carbonate minerals. However, when mass-balance calculations include a CO_2-gas phase inferred to be present because of intergranular voids within run products, smaller Σr^2 values of up to 1.9 are calculated (see **Table 5.3**; with CO_2 values in parentheses). The sum of squared residual values of this study lie within the range of values calculated for previous CO_2-bearing eclogite experimental studies. For example, Dasgupta et al. (2005) report a range of Σr^2 (including CO_2) of 1.26 to 3.1 for their experiments using starting materials SLEC1, SLEC3 and SLEC4, and Yaxley and Brey (2004) report a Σr^2 range of 0.1 to 9.1 from experiments using EC1. Both studies ascribe their relatively high Σr^2 values to difficulties in the analysis of CO_2 and other light elements (e.g. Na_2O) in carbonate melts. In this study, the latter was greatly minimised by using a freezing stage during analysis.

5.5.2. Oxygen fugacity and sulphur speciation

The redox state of each experiment was controlled by the presence of the graphite inner capsule. Reaction of the graphite liner with any excess oxygen present in the starting materials as minor amounts of air not purged from the porous materials during gas flushing of the capsule, or as minor proportions of Fe_2O_3 resulting from the oxidation of FeO during milling and drying of the silicate starting powder, would have reacted with graphite to yielded oxygen fugacities at or below the CCO ($2CO + O_2 = 2CO_2$) buffer (Dasgupta et al., 2005a) at pressures of 2.0 – 3.0 GPa and temperatures of 1050 – 1300 ºC. Where possible, the oxybarometer of Stagno et al. (2015) was used to place some constraints on the oxygen fugacity of certain individual experiments using calculated (Droop, 1987) ferric iron contents ($Fe^{3+}/\Sigma Fe_{tot}$) of garnet (**Appendix E**). The uncertainty associated with the calculated oxygen fugacity value is conservatively ±1 log unit when the uncertainties of both the Droop, (1987) and Stagno et al. (2015) calculations are considered. The calculated oxygen fugacity ($\Delta \log fO_2$) of SKG-1.2 is FMQ-4.7 log units at 2.0 GPa and 1200 ºC (**Table 5.3**). This is close to the iron-wüstite (IW = $2(1\text{-}x)\ Fe + O_2 = 2\ Fe_{1-x}O$) buffer where metals, specifically Fe and Ni, can potentially form alloys (see **Section 5.5.4.3**). Experiments conducted using the CO_2-bearing eclogite bulk compositions (SKG-2 and SKG-3) are more oxidised than the carbonate-free model eclogite system (SKG-1). The calculated oxygen fugacity ($\Delta \log fO_2$) of SKG-2.1 is FMQ-1.9 log units at 2.0 GPa and 1200 ºC, and the $\Delta \log fO_2$ of SKG-3.3 is FMQ-2.9 log units at 2.5 GPa and 1300 ºC (**Table 5.3**). The higher oxygen fugacity in these experiments is attributed to the partial breakdown of $CaCO_3$ on melting, resulting in the presence of a CO_2-rich fluid in the equilibrium assemblage of the CO_2-bearing eclogite bulk compositions.

Sulphur speciation is largely governed by oxygen fugacity (e.g. Jugo et al., 2005b; Wallace, 2005; Jugo, 2009; Wallace and Edmonds, 2011; Zajacz, 2015), with the S^{2-} (sulphide) species dominating >95 % of sulphur speciation at $\Delta\log fO_2 \leq$ FMQ. With increased oxygen fugacity, i.e. between ~ 0.75 < FMQ < 1.9 $\Delta\log fO_2$ (e.g. Jugo, 2009), S^{2-} becomes increasingly unstable and S^{6+} (sulphate) species increase. Therefore, from our calculated experimental oxygen fugacities, we predict that S^{2-} will be the overwhelmingly dominant sulphur species in the run products from these experiments.

5.5.3. Phase assemblages, textural relationships, and modal proportions

5.5.3.1. SKG-1 (SKG glass + *5 wt.% Pn)*

The SKG-1 experiments contain 5 wt.% pentlandite (corresponding to 1.8 wt.% S; **Table 5.2**) and importantly do not contain any added carbonate. Experiments SKG-1.1 (2.0 GPa; 1100 ºC) and SKG-1.2 (2.0 GPa; 1200 ºC) crystallised garnet (16 – 30 wt.%) and clinopyroxene (36 – 30 wt.%), and SKG-1.2 also crystallised plagioclase (17 wt.%) and coesite (8 wt.%; **Table 5.3; Fig. 5.2a**). Both experiments produced relatively large garnet grains (>20 μm) separated by a groundmass of smaller (<15 μm) clinopyroxene grains. Large silicate-dominated (i.e. 57 wt.% SiO_2) melt pools, which quenched to easily identifiable glass products, formed towards the rims of the SKG-1.1 capsule (**Table 5.3**). At slightly higher temperatures, SKG-1.2 produced smaller and less abundant (10 wt.%) pools of silicate-dominated melt (56 wt.% SiO_2) at garnet and clinopyroxene triple-point junctions (**Fig. 5.2a**). The significant difference in melt volume produced by SKG-1.1 (43 wt.%) and SKG-1.2 (10 wt.%) can be explained by the crystallisation of both plagioclase (17 wt.%) and coesite (8 wt.%) in SKG-1.2. Discrete globules of sulphide melt (L_S) (**Table 5.5**) were observed between the silicate mineral phases and within the silica-rich melt of SKG-1.2 (**Fig. 5.2a**). In contrast, only rounded crystalline mono-sulphide solid solution (MSS) was observed in SKG-1.1. Note that at low pressure (2.0 GPa) both sulphide melt (L_S) and crystalline MSS have rounded shapes, so texture alone cannot distinguish between the two and geochemical criteria are required (discussed in **Section 5.5.4.3**).

5.5.3.2. SKG-2 (SKG glass + 5 wt.% Pn + 4.7 % CO_2)

The SKG-2 starting composition has a CO_2 content of 4.7 wt.% that is broadly comparable to average altered MORB compositions (~2–3 wt.% CO_2; Staudigel, 2003). Experiments conducted using SKG-2 produced variable proportions of silicate mineral phases including garnet (20 – 52 wt.%), clinopyroxene (14 – 46 wt.%) and coesite (0 – 11 wt.%), and the melts produced range from silicate-dominated (>50 wt.% SiO_2) to carbonate-dominated (i.e. <2.4 wt.% SiO_2 and 42 – 53 wt.% CO_2) compositions (**Table 5.4**) (**Section 5.5.4.2**). At 2.0 GPa and 1200 ºC, SKG-2.1 produced ~60 wt.% of silicate-dominated (54 wt. % SiO_2) melt (L_{Sil}) with minor dissolved CO_2 (4.1 wt.%), a small amount of $CaCO_3$ (< 0.02 wt.% by mass balance), and rounded globules of immiscible sulphide melt (L_S). The L_S occurs within the highly polymerised silicate-dominated melt (**Fig. 5.2b**) and at high dihedral angles >60 º to garnet and clinopyroxene mineral phases. The major sulphide component for all SKG-2

experiments conducted above 3.0 GPa (SKG-2.3, -2.4, -2.5) is rounded to sub-angular crystalline MSS (**Fig. 5.2c**). In experiments SKG-2.3, 2.4 and 2.5, the presence of a CO_2-rich gas phase was indicated by intergranular porosity in the capsule. Significant intergranular porosity was observed in the CO_2-bearing experiments that produced silicate-dominated melts (e.g. SKG-2.3; **Fig. 5.2c**), indicating that an equilibrium (supercritical) CO_2-fluid phase was present before quenching. This contrasts with experiments that produced lower volume carbonate-dominated melts (e.g. SKG-2.4 and SKG-2.5), where only a few pore spaces were observed, and the CO_2-fluid was interpreted to result from quenching of the carbonate-dominated melt.

5.5.3.3. SKG-3 (SKG glass + 5 wt.% Pn + 11.8 % CO_2)

The SKG-3 starting composition has a CO_2 content of 11.8 wt.% and this higher content is comparable to other CO_2-bearing eclogite experimental studies that contain between ~2.2 – 15 wt.% CO_2 (**Table 5.1 and Appendix A**). Experiments conducted using SKG-3 produced the phase assemblages shown in **Table 5.3** and **Figure 5.1b**. The major silicate minerals produced from SKG-3 include garnet (20 – 35 wt.%) and clinopyroxene (43 – 63 wt.%), and minor coesite (<2 wt.%) was found in SKG-3.2. The melts produced by SKG-3 range from intermediate carbonate-silicate melts (with 4.5 – 12.4 wt.% SiO_2 and 43 – 47 wt. % CO_2) in experiments SKG-3.1, -3.2 and -3.4 (<1150 ºC and 2.5 – 3.0 GPa) to carbonate-dominated melt (<2.4 wt.% SiO_2 and 42.4 wt. % CO_2) in experiment SKG-3.3 (1300 ºC and 2.5 Gpa). The intermediate carbonate-silicate and carbonate-dominated melts occur at low angles <60 º to the predominantly clinopyroxene groundmass, and both quench to fine-grained crystalline masses (**Fig. 5.2d, e**). Intergranular porosity observed in all SKG-3 experiments is evidence for the presence of a CO_2-rich gas phase in the capsule that probably results from quenching of the carbonate-silicate and carbonate-dominated melt phases (**Table 5.3**). Rounded to sub-angular crystalline MSS is the stable sulphide phase in all SKG-3 experiments at conditions between 2.5 to 3.0 GPa and 1050 to 1300 ºC (**Fig. 5.2d, e**).

5.5.4. Solidus location and phase chemistry

Phase compositions of the experimental run products are given in **Tables 5.4** and **5.5. Figure 5.1b** shows the observed phase assemblages as well as some inferred phase boundaries. In all cases where the presence of melt was indicated by interpretation of the SEM back-scattered electron images, mass-balance calculations confirmed the presence of melt by the low sum of squared residual (Σr^2) values, which would be markedly higher if melt was assumed to be absent (**Table 5.3**).

The solidus for the SKG-1 S-bearing (1.8 wt.% S; CO_2-free) eclogite system is comparable to the CO_2-free solidus located above 2.0 GPa and 1150 ºC for the G2 starting composition of Pertermann and Hirschmann (2003), after which the SKG glass composition was modelled (**Fig. 5.1b**). However, no sub-solidus SKG-1 experiment was conducted to bracket the solidus. At 2.0 GPa, the inferred sulphide solidus and liquidus in this carbonate-free system lie between 1150 and 1200 ºC (**Fig. 5.1b**).

The inferred solidus for the SKG-2 (1.8 wt. % S and 4.7 wt.% CO_2) CO_2-bearing eclogite system is above 3 GPa and 1150 ºC (**Fig. 5.1b**) and appears comparable to the SLEC3 (4.7 wt.% CO_2) solidus of Dasgupta et al. (2005) located above 3 GPa and between 1175 and 1200 ºC (**Fig. 5.1a**). The SKG-2 solidus falls at lower temperatures at 3.5 GPa (i.e. the solidus has a positive slope; **Fig. 5.1b**). The SKG-2 and SLEC3 starting compositions have similar SiO_2 contents (48.2 – 41.7 wt.%), virtually equal proportions of CO_2 (4.7 – 4.4 wt.%; added as $CaCO_3$), as well as high molar Na_2O/CO_2 ratios (0.4 – 0.23) relative to the other experiments. The high molar Na_2O/CO_2 ratio of these starting compositions tends to drive alkali (Na_2O and K_2O) fluxed melting over CO_2 fluxed melting (c.f. Dasgupta et al. 2004) which, in turn, lowers the solidus temperature of SKG-2 relative to SKG-1. The presence of L_S (sulphide liquid) in experiment SKG-2.1 at 2.0 GPa and 1200 ºC, suggests that this experiment is above the sulphide liquidus (**Fig. 5.1b**). At higher pressure and temperature conditions all SKG-2 experiments are below the sulphide solidus (**Fig. 5.1b**).

The SKG-3 CO_2-bearing eclogite solidus is inferred above 3 GPa to be between 1000 ºC and 1050 ºC (**Fig. 1b**) based on the occurrence of both CC-Dol and $L_{carb\text{-}sil}$ in experiment SKG-3.1. The carbonate-rich nature of the SKG-3 starting composition results in a low Na_2O/CO_2 ratio of 0.13 (i.e. Na_2O content is diluted by the increased CO_2 content of the bulk composition) and this promotes CO_2-fluxed melting. The solidus temperature of SKG-3 is assumed comparable to the inferred solidus temperature of the SLEC2 (1100 ºC; **Fig. 5.1a**) starting composition of Dasgupta et al. (2005) because this starting composition has a comparably low Na_2O/CO_2 ratio of 0.12. The run products of the SKG-3 experiments all contain MSS, and thus appear to be conducted at conditions below the sulphide solidus.

5.5.4.1. Silicate mineral assemblage

Garnet – The modal proportions of garnet tend to increase with increasing pressure, with 16 – 30 wt.% at pressures < 2.5 GPa and 33 – 52 wt.% at pressures > 3 GPa. Generally, the garnet compositions produced by this experimental study are slightly richer in iron than those found in natural eclogite xenoliths and in other experimental studies (**Fig. 5.3a**) because of the addition of 5 wt.% Pn (iron-rich sulphide) to the starting bulk composition. The garnet compositions recorded in the run products are solid solutions of pyrope, almandine and grossular with Mg# [molar Mg/ (Mg + Fe)] that range from 27 to 60, see **Appendix F**. Garnets produced from SKG-1 have higher proportions of pyrope (~43 mol. %) and almandine (~34 mol. %) components than grossular (~ 20 – 22 mol.%.) and classify as Group B **(Fig. 5.3a)** following the chemical classification of Coleman et al. (1965). Garnets from SKG-2 and SKG-3 generally have higher Fe contents (Group B and C; **Fig. 5.3a**) with almandine components that range from 35 – 67 mol. % (vs. 24 – 43 mol. % pyrope and 7 – 39 mol. % grossular), excluding experiment SKG-2.1 that has a garnet composition (51 mol.% Py, 33 mol.% Alm, 16 mol.% Gro) similar to the garnets produced by SKG-1. For SKG-2, the garnet almandine component ranges from 33 – 46 mol.% and decreases with increased degrees of partial melting (i.e. SKG-2.5 = 4 wt.% melt and

41 mol.% Grt_{alm} vs. SKG-2.2 = 0 wt.% melt and 46 mol.% Grt_{alm}). The garnet pyrope contents broadly increase with increasing temperature, and grossular contents generally increase with pressure (**Fig. 5.3a; Appendix F**). For example, at 2.0 GPa, garnets produced from SKG-2 have 16 mol.% grossular compared to 3 – 3.5 GPa where the grossular contents range from 18 – 30 mol.%. The high grossular contents are may result from the addition of $CaCO_3$ to SKG-2 and SKG-3.

Clinopyroxene – Clinopyroxenes are solid solutions of diopside, hedenbergite, aegirine and jadeite and classify as Group A or B using the MgO vs. Na_2O scheme of Taylor and Neal (1989) (**Fig. 5.3b**). The predominantly omphacitic clinopyroxene (7 – 18.4 wt.% Al_2O_3 and 1.5 – 6.6 Na_2O; **Table 5.4**) have a dominant diopside component 50 – 86 mol.%, a smaller jadeite component 14 – 50 mol. % and some contain aegirine (~2 – 17 mol.%). The ratio of Ca-Tschermak's to jadeite component is expressed as the ratio $Al^{[6]}/Al^{[4]}$ (Aoki and Shiba, 1973) are highest (> 2) for clinopyroxene stabilised at pressures > 3.0 GPa. Pyroxenes produced by the most CO_2-rich bulk composition SKG-3 are the most calcic because of bulk composition effects, with a wollastonite component [X_{Wo} = molar Ca/ (Ca+ Mg + Fet)] of 45 – 50 compared to clinopyroxene produced from both SKG-2 (36 – 44) and SKG-1 (44 – 45). The sodium content of the clinopyroxene is pressure-, temperature- and bulk-composition dependent. Specifically, Na content in clinopyroxene exhibits strong positive correlations with pressure at constant temperature, for example, the SKG-2.4 experiment at 1300 ºC and 3.0 GPa produced clinopyroxene with 5 wt% Na_2O, and SKG-2.5 at 1300 ºC and 3.5 GPa produced clinopyroxene with 6.5 wt.% Na_2O. In addition, Na_2O content in clinopyroxene is shown to decrease with increasing temperature, i.e. at a constant pressure of 3.0 GPa, SKG-3.1 produced clinopyroxene with 4.9 wt.% Na_2O and SKG-3.2 produced clinopyroxene with 4.0 wt.% Na_2O at temperatures of 1050 and 1150 ºC, respectively. Clinopyroxenes produced by either SKG-1 or SKG-2 in equilibrium with a silica-rich melt (L_{Sil}) are generally less sodic (1.5 – 2.6 wt.% Na_2O) than the pyroxenes (5 – 6.5 wt.% Na_2O) in equilibrium with calcio-dolomitic carbonatitic-type melts (L_{Carb}). Modal proportions of clinopyroxene tend to decrease with increased proportions of partial melting (**Table 5.3**), and the wide range of clinopyroxene compositions produced here compare well with natural eclogite and pyroxenite clinopyroxene (**Fig. 5.3b**).

Minor and trace silicate phases – Coesite is present in experiments that have relatively low melt proportions (<10 wt.%; SKG-2 bulk composition experiments). The coesite is 99.8 mol. % SiO_2, with minor Al_2O_3 and FeO contents. The plagioclase present in SKG-2.1 is anorthitic ($CaAl_2Si_2O_8$) with 51.6 mol. % An contents. Trace amounts of zircon (<0.5 wt.%) were noted in the SKG-2 and SKG-3 experiments and result from elevated concentrations of zirconium in the SKG glass composition because of firing the SKG powder in a zirconium crucible (see **Section 5.3.1**).

5.5.4.2. Quenched melt products

Silicate-dominated melt (L_{Sil}) – Silicate-dominated melts, identified here as melts with >50 wt.% SiO_2, are produced by the CO_2-free experiments of SKG-1 (**Fig. 5.2a**) and by two of the CO_2-bearing eclogite SKG-2 experiments (SKG.2-1 and SKG-2.3) (**Table 5.3, 5.4; Fig. 5.4a–d)**. The large difference in the molar proportion of silicate melt produced by SKG-1.1 (43 wt.%) and SKG-1.2 (10 wt.%) has been explained by the crystallisation of significant coesite (8 wt.%) and plagioclase (17 wt.%) in SKG-1.2 (**Fig. 5.1b**). The silicate-dominated melt compositions produced by SKG-1 are classified as trachy-andesite (SKG-1.1) and basaltic-andesite (SKG-1.2) according to the TAS classification scheme of le Bas et al. (1986) (**Fig. 5.4a**). At a constant pressure of 2.0 GPa, the trachy-andesitic melt of SKG-1.1 at 1100 ºC (molar Ca/[Ca+Mg] = 0.54; **Fig. 5.5a**) becomes less potassic and more magnesian and calcic (**Fig. 5.4b**) at 1200 ºC in SKG-1.2 (molar Ca/[Ca+Mg]) = 0.58; **Fig. 5.5a**). The silicate-dominated melt compositions produced by SKG-2 are classified as basaltic andesite (SKG-2.1) and "rhyolite" (SKG-2.3) (**Fig. 5.4a**; **Table 5.3**). However, the extremely small (2 – 5 µm) melt pools produced by SKG-2.3 (**Fig. 5.2c**) contain significant coesite crystals and due to size constraints, we were only able to obtain a mixed melt plus coesite crystal composition. It is inferred that the "rhyolite" melt is made up of a calculated 71 wt.% "basaltic-andesite" melt (with ~ 57 wt.% SiO_2; noted by the grey filled triangle in **Fig 5.4a**) and 29 wt.% coesite crystals (estimated from point counting the proportion of coesite in these areas). Compared to the basaltic-andesite melts produced by SKG-1, the melt produced by SKG-2.1 has a similar molar Ca/(Ca + Mg) value of 0.57 **(Fig. 5.5a)** but is more iron rich (8.4 vs. 2.9 – 5.2 wt.% FeO) (**Fig. 5.4c**). Importantly, the silicate-dominated melts produced by this study do not contain any appreciable (>0.1 wt.%) dissolved sulphur. The silicate-dominated (basaltic-andesite) melts produced here compare well compositionally with silicate-dominated melts produced by other volatile-free eclogite (Pertermann and Hirschmann, 2003a; Spandler et al., 2007) and CO_2-bearing eclogite experiments (Hammouda, 2003; Kiseeva et al., 2012), as well as natural MORB (Jenner and O'Neill, 2012) (**Fig. 5.4a–d**), except for FeO content (**Fig. 5.4c**), because the experiments of this study stabilise either sulphide liquid or residual MSS which contain large proportions of Fe.

Carbonate-silicate melt ($L_{Carb-Sil}$) – Intermediate carbonate-silicate melts (4.5 – 12.4 wt.% SiO_2, 30 – 46 wt.% CaO and 43 – 47 wt. % CO_2) are produced by SKG-3 experiments at low temperature between 1050 and 1150 ºC (**Fig. 5.5a–c**; **Table 5.3, 5.4**). At 3.0 GPa and 1050 ºC, experiment SKG-3.1 is located closest to the SKG-3 CO_2-bearing eclogite solidus (**Fig. 5.1b**) and contains both carbonate-silicate melt (15 wt.%) and crystals of calcio-dolomitic solid solution (1 wt.%). The calcio-dolomitic crystals and carbonate silicate melts have comparable FeO (4.2 vs. 4.5 wt.%) and MgO (3.9 vs. 4.2 wt.%) contents. The co-existing calcite-dolomite crystalline carbonate does not contain either sodium or sulphur like the carbonate melts. In addition, the carbonate-silicate melt has a lower molar Ca/(Ca + Mg) of 0.84 and Ca/Mg of 5.1 compared to the coexisting crystalline carbonate (0.89 and 8.1, respectively). The lower calcium content of the near solidus carbonate-silicate melt (CaO = 30 wt.%)

compared to the carbonate solid solution crystals (CaO = 44 wt.%) suggests that melting is probably controlled by the calcium carbonate solid solution (CC-Dol_{SS}) liquid melting loop previously described by Dasgupta et al. (2005) and modelled on the simple $CaCO_3$-$MgCO_3$ binary solvus of Irving and Wyllie (1975).

At 3.0 GPa, SKG-3.1 and SKG-3.2 produce 13 – 17 wt.% carbonate-silicate melts with 11.6 – 12.4 wt.% SiO_2, 2.9 – 3.2 wt.% Al_2O_3, 0.5 – 0.6 wt.% Na_2O and 2.8 – 4.5 wt.% FeO contents, and low molar Ca/(Ca + Mg) ratios of 0.84 to 0.89 (**Fig. 5.5a**). Comparatively, at lower pressures of 2.5 GPa, SKG-3.4 produces 17 wt.% carbonate-silicate melt with 4.5 wt % SiO_2, 2.4 wt.% Al_2O_3 and 3.2 wt.% FeO contents, and a high molar Ca/(Ca + Mg) ratio of 0.94 (**Fig. 5.5c**). Importantly, all these carbonate-silicate melts contain appreciable dissolved sulphur with 0.1 – 0.3 wt.% S.

Carbonate-dominated melt (L_{Carb}) – Carbonate-dominated melts (<2.4 wt.% SiO_2, 39 – 50 wt.% CaO and 42 – 53 wt.% CO_2) are produced by both the SKG-2 and SKG-3 CO_2-bearing eclogite compositions at 1300 ºC (**Fig. 5.5a–d**; **Table 5.3, 5.4**). These melts are small volume (4 – 6 wt.%) and contain low abundances of FeO (2.1 – 4.2 wt %), Al_2O_3 (0.4 – 0.9 wt.%), MgO (2.0 – 3.9 wt.%) and Na_2O (bdl – 0.2 wt.%). The carbonate-dominated melts produced by SKG-2 have lower molar Ca/(Ca + Mg) values of ~0.89 compared to the melt produced by SKG-3 (Ca/(Ca + Mg = 0.95; **Fig. 5.5c**) because SKG-3 has a greater amount of added $CaCO_3$. Importantly, the carbonate-dominated melts contain no appreciable (>0.1 wt.%) dissolved sulphur.

Partial melting of the CO_2-bearing eclogite bulk compositions appear to show that sulphur preferentially dissolves into intermediate carbonate-silicate melts with appreciable SiO_2, Al_2O_3 and FeO contents (e.g. SKG-3.1, SKG-3.2 and SKG-3.4) over melts that are almost purely carbonatitic (< 2.4 wt.% SiO_2, e.g. SKG-3.3). The compositions of both the carbonate-dominated and intermediate carbonate-silicate melts of this study compare favourably with carbonate-bearing melts produced by other CO_2-bearing eclogite experimental studies (**Fig. 5.6**) (Hammouda, 2003; Dasgupta et al., 2004, 2005a; Yaxley and Brey, 2004; Kiseeva et al., 2012) as well as natural oceanic calcitic carbonatites (Kogarko, 1993; Hoernle et al., 2002). However, the exaggerated calcium content of the carbonate-bearing melts produced here, results in less of a compositional overlap with continental carbonatites (Tappe et al., 2006) and Low-Mg carbonatitic-type diamond fluid inclusions (HDF's; Klein-BenDavid et al., 2009; Weiss et al., 2009; Zedgenizov et al., 2009) (**Fig. 5.6**).

5.5.4.3. Sulphur-rich phases

Both sulphide melt (L_S) and mono-sulphide solid solution (MSS) are produced in this experimental study, and these sulphur-rich phases make up a maximum of 6 wt.% of the experimental run products. We can distinguish between the two phases because MSS quenches to homogeneous, crystalline Fe-Ni-

Cu-(Co) solid solutions whereas sulphide melt (L_S) quenches or crystallizes to an intergrown assemblage of Fe, Ni-rich and Cu-rich sulphide minerals or Fe-Ni-(Cu) metal alloys (**Table 5.5**).

Sulphide melt (L_S) – Sulphide melt only formed in two (SKG-2.1 and SKG-1.2) out of the eleven experiments performed. The sulphide melt is only produced by the SKG-1 and SKG-2 starting compositions above 2.0 GPa and 1200 ºC (**Fig. 5.2a, b** and **5.7a**). The sulphide melt (L_S) produced by experiment SKG-2.1 quenches to an intergrowth of Fe, Ni-rich sulphide and a Cu-rich sulphide phases (**Table 5.5; Fig. 5.2b**). The Cu-rich sulphide contains 34.6 wt.% S, 53.8 wt.% Fe, 9.5 wt.% Cu, 0.7 wt.% Ni, and has an atomic metal (Fe + Cu + Ni)/sulphur ratio of 1.04 and a Cu/metals ratio of 0.13 (**Table 5.5**). The Fe, Ni-rich sulphide contains 38.1 wt.% S, 54 wt.% Fe, 5.7 wt.% Ni, 0.5 wt.% Cu, 0.6 wt.% Co, and has an atomic metal (Fe + Cu + Ni)/sulphur ratio of 0.91 and a Cu/metals ratio of 0.01.

The sulphide melt (L_S) produced by SKG-1.2 quenches to a Fe, Ni-rich sulphide and a Ni-Fe-(Cu) metal alloy (**Table 5.5; Fig. 5.2a** and **5.7a**). The Fe, Ni-rich sulphide comprises 37.3 wt.% S, 54.7 wt.% Fe, 5.2 wt.% Ni, 0.5 wt.% Cu, 0.7 wt.% Co, and has an atomic metal (Fe + Cu + Ni)/sulphur ratio of 0.94 and a Cu/metals ratio of 0.01. This Fe, Ni-rich sulphide is almost identical in composition to the Fe, Ni-rich sulphide quenched from the SKG-2.1 sulphide melt under the same pressure and temperature conditions. The second phase that quenched from the sulphide melt is a Fe-Ni-(Cu) metal alloy consisting of 3.5 wt.% S, 42.4 wt.% Fe, 1.0 wt.% Cu, 49.8 wt.% Ni, 2.3 wt.% Co. This metal alloy has an atomic metal (Fe + Cu + Ni)/sulphur ratio of 15.22 and a Cu/metals ratio of 0.01. The calculated oxygen fugacity of FMQ-4.7 log units for experiment SKG-1.2 (**Table 5.3**) is extremely close to the iron-wüstite (IW = $2(1\text{-}x)\ Fe + O_2 = 2\ Fe_{1-x}O$) buffer, where metal alloys are expected to form (Jacob et al., 2004). In addition, appreciable amounts of sulphur (3.5 wt.%) within the liquid alloy enhances the siderophile nature of Cu and Co (c.f. Li and Agee, 2001), allowing for significant enrichment of these metals in the Fe, Ni-alloy.

Mono-sulphide solid solution (MSS) – At pressures above 2.0 GPa rounded to sub-angular crystalline MSS is produced by all the experiments **(Fig. 5.3c – e** and **5.7 b,c**). These homogeneous Fe-Ni-Cu-(Co) solid solutions comprise 35.7 – 42.2 wt.% S, 39.1 – 54.6 wt.% Fe, 6.5 – 14.1 wt.% Ni, 1.3 – 5.2 wt.% Cu, and below detection limit to 0.4 wt.% Co (**Table 5. 5**). The atomic metal (Fe + Cu + Ni)/sulphur ratios of the crystalline MSS range between 0.75 and 1.03, and the Cu/metal ratios between 0.02 – 0.08 (**Fig. 5.7c**). The crystalline MSS have fairly constant Ni/ (Ni + Fe) ratios of ~0.2. In general, with increasing pressure the Fe content of MSS decreases for each bulk composition (**Fig. 5.7b**) and at constant pressure and increased temperature the MSS becomes slightly more Fe-rich. Moreover, MSS produced by SKG-3 is the most Fe-depleted compared to the MSS produced by the other starting compositions (**Table 5.5**; **Fig. 5.7b**). The MSS produced by both the SKG-2 and SKG-3 experiments define a trend of increasing oxidation (**Fig. 5.7b,c**) compared to the MSS produced by experiment SKG-1.1 (the carbonate-free SKG-1 starting composition). It is inferred that the MSS produced by the CO_2-

bearing eclogite experiments has undergone sulphidisation reactions (c.f. Delpech et al., 2012; Hughes et al., 2017) from interaction with the carbonate-bearing melts produced during partial melting (**Fig. 5.7c**). The MSS produced by this study is plotted on **Figure 5.7c** and is compared to the experimentally produced FeO-bearing sulphides from Liu et al. (2007) and Kiseeva and Wood (2013, 2015), MSS from both eclogite and pyroxenite xenoliths (Aulbach et al., 2009a) as well as diamond sulphide inclusions (Aulbach et al., 2012).

5.6. DISCUSSION

5.6.1. The role of sulphur in the melting of (CO_2-bearing) eclogite at upper mantle conditions

5.6.1.1. Sulphide anatexis in the silicate eclogite system

The inferred sulphide solidus and liquidus in the carbonate-free SKG-1 system lie between 1100 and 1200 ºC at 2.0 GPa (**Fig. 5.1b**). Sulphide melting at upper mantle conditions is largely dependent on the composition of the initial sulphide, and especially the nickel content (Bockrath et al., 2004; Li and Audétat, 2013). Therefore, the sulphide solidus and liquidus curves on **Figure 5.1b** are inferred to be at a similar position to those previously published by Li and Audétat (2013), who used an initial sulphide with comparable Ni content (e.g. 7 – 8 wt.% vs. 10 wt.% in SKG-1) (**Fig. 5.1a**). Above the liquidus, SKG-1.2 produced discrete globules of sulphide melt at >60º dihedral angles to the garnet and clinopyroxene matrix (**Fig. 5.2a**). The sulphide melt quenched to a Fe, Ni-rich sulphide and an Fe-Ni-(Cu) metal alloy. The metal alloy was stabilised on quenching because the experiments were conducted under relatively reducing conditions ($\Delta \log fO_2$ = FMQ-4.7 log units), close to the iron-wüstite buffer. The sulphide melt pools range from 1 to 20 µm in size and there is no evidence to suggest sulphide melt pools coalesce (e.g. no sulphide mineral network "trails" connecting individual melt pools; **Fig 5.2a**) irrespective of the volume of molten sulphide produced (up to 5 wt.%) or distance (<1 – 100 µm) between the different globules. This is a function of the high dihedral angles between the sulphide melt and the silicate crystals. Additionally, the basaltic-andesite melt produced by SKG-1.2 contains no detectable dissolved sulphur (EDS detection limit of 0.1 wt.% S). The globular texture and immiscible nature of the sulphide melt produced by the carbonate-free eclogite system (SKG-1) indicates that sulphide melt mobility within the upper mantle may be limited. This corresponds well with the experiments produced by Gaetani and Grove (1999) and Rose and Brenan (2001) that show non-wetting properties of iron sulphide liquids against silicate minerals under reducing conditions. Additional evidence for a lack of mobility of sulphide melt within natural basaltic systems at upper mantle conditions is shown by the 'nugget effect' of sulphides in eclogite xenoliths (e.g. **Fig. 5.8a,b**; Aulbach et al., 2009; Smart et al., 2009; Gréau et al., 2013; Luguet et al., 2015; Kiseeva et al., 2017a).

The absence of detectable dissolved sulphur in the basaltic-andesite melt produced by SKG-1.2 can be partially explained by the relatively high SiO_2 (56.4 wt.%; **Fig. 5.5a**) and low FeO (2.9 wt.%; **Fig.**

5.4c) content of the basaltic-andesite melt, the coexistence of iron-rich garnet and clinopyroxene mineral phases (**Fig. 5.3a, b**) and the relatively low pressure (2.0 GPa) and temperature (1200 ºC) conditions of the experiment. This corresponds well with other experimental studies which show that FeO content has a strong effect on sulphur solubility in silicate-dominated melts at mantle conditions (e.g. O'Neill and Mavrogenes, 2002; Liu et al., 2007; Wykes et al., 2015). Importantly, O'Neill and Mavrogenes (2002) and Wykes et al. (2015) demonstrate that the S^{2+} solubility is nonlinear when the silicate melt FeO content is low, passing through a minimum at ~4 wt.% FeO. Additionally, Liu et al. (2007) demonstrate that only small proportions of sulphur (0.12 – 0.18 wt.%) can dissolve in MORB-like melt with 4.4 to 9.9 wt.% FeO contents whereas, larger proportions (0.15 0.30 wt.% S) can dissolve in high-FeO (10 – 16.5 wt.%) Etna-type basalts at 1 GPa and 1250 to 1450°C.

The calculated oxygen fugacity of experiment SKG-1.2 is $\Delta\log fO_2$ = FMQ-4.7 log units and is buffered by the presence of the graphite capsule. Under such relatively reducing conditions the availability of non-bridging oxygens within mafic silicate melt is limited (Fortin et al. 2015), therefore lowering the potential for sulphur to substitute for non-bridging oxygens and dissolve any significant proportion of sulphur in the basaltic-andesite melt (**Table 5.5**). Therefore, immiscibility exists between the sulphide and mafic-silicate systems resulting in the stabilisation of a FeO-poor basaltic-andesite melt in equilibrium with sulphide liquid. In contrast, the experiments of Jugo et al. (2005a, b) show that at more oxidising conditions (i.e. a higher fO_2 of FMQ to FMQ +2), the solubility of sulphur may dramatically increase (up to 1.5 ± 0.3 wt.% S) in basaltic melts saturated with sulphate liquids at 1.0 to 1.6 GPa and 1300 to 1355 °C, only when sulphur speciation is dominated by S^{6+}.

In general, basaltic melts with low (<60º) dihedral angles and low interfacial energies (Minarik, 1998) are expected to form interconnected melt pathways between mantle minerals even at low melt fractions, therefore increasing their potential effectiveness as metasomatic agents within upper mantle lithologies (Harte et al., 1993). Given that immiscible sulphide melt and basaltic-andesite melt can be produced together at the PT conditions investigated (**Fig. 5.1b**), immiscible sulphide saturated basaltic-andesite melts may instead present an effective mechanism to mobilise sulphur within the upper mantle. This coupled movement of sulphur and silicate liquid will be further discussed in **Section 5.6.2**.

5.6.1.2. Sulphide anatexis in the CO_2-bearing eclogite system

Based on previous sulphide experiments (Bockrath et al., 2004; Li and Audétat, 2012) and this study, the sulphide solidus curve falls at lower temperature (at least 100 ºC) for a given pressure than the sulphide liquidus curve (see **Fig 5.1a,b**). For the CO_2-bearing eclogite system investigated here, immiscible sulphide melt is only present in CO_2-bearing experiment SKG-2.1, at 2.0 GPa and 1200 ºC (**Fig. 5.2b**). The remaining experiments conducted between 1050 and 1300 ºC and 2.5 and 3.5 GPa on the SKG-2 and SKG-3 S-bearing CO_2-bearing eclogite compositions were all below the sulphide solidus and instead lie within the MSS stability field (**Fig 5.1b; 5.2c-e**). The CO_2-bearing eclogite experiment

SKG-2.1 produced sulphide melt that quenched to Ni, Fe-rich sulphide and Cu-rich sulphide phases at a calculated oxygen fugacity of $\Delta\log fO_2$ = FMQ-1.9 log units. In comparison, experiment SKG-1.2 (noting this experiment was conducted on a carbonate-free bulk composition) produced sulphide melt that quenched to Ni, Fe-rich sulphide and Fe-Ni-(Cu)-rich metal alloy phases at a calculated $\Delta\log fO_2$ of FMQ-4.7 log units (i.e. close to the iron-wüstite buffer). Compositionally, the Ni, Fe-rich sulphide melt phases are almost identical for both experiments (**Fig. 5.7a**) and the Cu-rich sulphide phases and Fe-Ni-(Cu)-rich metal alloy make up less than 10 wt.% of the immiscible sulphide melt pools. Interestingly, the presence of up to 11.8 wt. % CO_2 (SKG-3) does not affect sulphide melting systematics at fO_2 < FMQ, between 1050 and 1300 ºC and 2.0 and 3.5 GPa. The addition of $CaCO_3$ to SKG-2 and SKG-3 instead seems only to constrain carbonate±silicate melting at the pressure and temperature conditions investigated.

5.6.1.3. Anatexis in the CO_2-bearing eclogite system with implications for the mobility of sulphur

The presence of sulphide (1.8 wt.% S) in the SKG-2 and SKG-3 starting compositions does not seem to have any effect on CO_2-bearing eclogite melting systematics at the temperature and pressure conditions investigated. Instead, both the proportion of $CaCO_3$ added to the SKG-2 and SKG-3 experiments and the behaviour of $CaCO_3$ on melting is important in determining the wide range of equilibrium melt compositions produced (**Figs. 5.4 and 5.5**), as well as the potential mechanisms for which sulphide may be mobilised together with these melts at upper mantle conditions.

For example, the lesser amount of $CaCO_3$ added to SKG-2 (4.7 wt.% CO_2) results in a higher bulk Na_2O/ CO_2 ratio of 0.4, which tends to drive alkali fluxed melting (c.f. Dasgupta et al. 2005) at lower temperatures (1150 – 1200 ºC). The melts produced by SKG-2 between 1150 and 1200 ºC are silicate-dominated (**Fig. 5.5a–d**), and we infer that the breakdown of $CaCO_3$ on melting results in a CO_2-rich gas phase (indicated by significant intergranular porosity) and the preferential sequestering of CaO into the silicate-dominated melt (**Fig. 5.4b**) and clinopyroxene phases (**Fig. 5.5d**). It is not uncommon to produce silicate-dominated melts from CO_2-bearing eclogite compositions with low CO_2 contents and relatively high Na_2O contents at upper mantle conditions. For example, Kiseeva et al. (2012) produced silicate-dominated (57 – 62 wt.% SiO_2) melts from starting composition GA1+10% $CaCO_3$ with a molar Ca/(Ca + Mg) ratio of 0.59 and a Na_2O/CO_2 ratio of 0.5 (**Fig. 5.4b – d**) at pressures between 3.5 and 5.0 GPa and temperatures of 1100 to 1400 ºC. In addition, Hammouda (2003) produced silicate-dominated (45 – 64 wt. % SiO_2) melts from starting composition OTBC with a molar Ca/(Ca + Mg) ratio of 0.23 and a Na_2O/CO_2 ratio of 0.65 (**Fig. 5.4b – d**) at pressures between 5.0 and 6.0 GPa and temperatures of 1150 to 1250 ºC.

The basaltic-andesite melt produced by SKG-2.1 is compositionally similar to the melts produced by the SKG-1 experiments (**Fig. 5.4 a–d**). Given that experiment SKG-2.1 produced ~60 wt.% basaltic-

andesite melt together with immiscible sulphide melt (**Section 5.6.1.2**), we suggest that the coupled movement of sulphide and silicate liquid described as a potential mechanism for sulphur mobility in the silicate eclogite system (**Section 5.6.1.1**) may also be applicable to the SKG-2 CO_2-bearing eclogite system at 1200 and 2.0 GPa. In contrast, experiment SKG-2.3 at 1150 ºC and 3.5 GPa, produced relatively low proportions (6 wt. %) of "Rhyolite" melt (basaltic-andesite melt plus coesite crystals) that is devoid of any appreciable (>0.1 wt.% S) dissolved sulphur. It is therefore expected that MSS will remain residual within the eclogite mineral residue until the degree of partial melting exceeds ~15% (e.g. Luguet et al., 2003; Bockrath et al., 2004; Peregoedova et al., 2004).

The most CO_2-rich starting composition, SKG-3, produced intermediate carbonate-silicate melts with 4.5 – 12 wt.% SiO_2, 2.4 – 3.2 wt.% Al_2O_3 and 2.8 – 4.5 wt.% FeO contents as well as significant sulphur contents (0.1 to 0.3 wt.% S; **Table 5.3**) at temperatures between 1050 and 1150 ºC. These carbonate-silicate melt compositions indicate that the dissolution of sulphur within carbonate-bearing melts may require the presence of a significant silicate and iron component for bridging within the carbonate-silicate melt structure, and that sulphur may reduce the solubility of carbon within carbonate-silicate melts. The solubility of sulphur in carbonate-silicate melts remains unconstrained partially due to a dearth of knowledge on the molecular structure of transitional carbonate-silicate melts. Recent developments in Raman and NMR spectroscopy, however, allow for the identification of different volatile species within carbonate-silicate melts and, consequently, some interpretations can be made on their ionic structure. For example, previous experimental studies show that CO_2 (up to several tens of wt.%) predominantly dissolves as the carbonate ion (CO_3^{2-}) in carbonate-silicate melts that are transitional between pure carbonatite and silicate liquids (~10 to ~40 wt% SiO_2; e.g. Mysen and Boettcher, 1975; Brey and Green, 1976; Fine and Stolper, 1985; Blank and Brooker, 1994; Brooker et al., 2001; Mysen, 2012; Moussallam et al., 2015, 2016). Transitional carbonate-silicate melts are likely composed of both carbonate and silicate sub-networks (Moussallam et al., 2016), where certain cations such as Mg^{2+} perform "network forming" roles and compete effectively for oxygen atoms with the Si and Al tetrahedra of the silicate sub-network, whereas other cations such as Ca^{2+} are considered "network modifiers" and tend to bond with the carbonate species (Mysen and Boettcher, 1975; Brooker et al., 2001), forming the carbonate sub-network. Interestingly, Brooker et al. (2001) show that Fe^{2+} seems to play a "network-forming role" within carbonate-silicate melts, and thus, any non-bridging oxygens associated with the Fe^{2+} could potentially serve as entry points for the dissolved sulphur observed within carbonate-silicate melts of this study.

Most recently, Woodland et al. (2019) used both experiments and solubility models to demonstrate the solubility of sulphur in carbonate-silicate melts at a range of mantle pressure (5 10.5 GPa) and temperature (1400 1600 °C) conditions. Their results indicate that sulphur solubility in Ca–Mg–Fe carbonate–silicate melt coexisting with sulphide melt, olivine, orthopyroxene and graphite (i.e. under reducing conditions) is mainly controlled by the FeO content of the melt and is far less dependent on

pressure and temperature constrains. Importantly, Woodland et al. (2019) show that 0.02 – 0.10 wt.% sulphur may dissolve in carbonate–silicate melts containing 1 10 wt. % FeO. These results compare favourably with the experiments of this study, which show that 0.1 0.3 wt.% sulphur may dissolve in carboante-silicate melts with similarly low FeO (2.8 4.8 wt. %) contents. As such, sulphide dissolved within carbonate-silicate melts may present an additional mechanism for the mobility of sulphur within the upper mantle.

Both SKG-2 and SKG-3 starting compositions produce carbonate-dominated melts (**Fig. 5.5a – d**) at 1300 ºC, and this switch from carbonate-silicate melts is attributed to increased dissolution of $CaCO_3$ into the melt phase at higher temperatures, with less physical evidence of $CaCO_3$ decomposition on melting from fewer intergranular CO_2-gas voids. Experiments SKG-2.4, SKG-2.5 and SKG-3.3 produce carbonate-dominated melts (**Fig. 5.5a–d; Section 5.5.4.2**), and the SKG-3.3 melt is more calcic in composition (**Fig. 5.5c**) due to bulk composition effects (i.e. higher amount of added $CaCO_3$). The carbonate-dominated melts do not contain any appreciable (>0.1 wt.% S) dissolved sulphur and the stability of MSS does not seem to be affected by the low proportion (4 – 6 wt.%) carbonate-dominated melts. Therefore, it is suggested that these calcic carbonatite-type melts contain insufficient non-bridging oxygens associated with Fe^{2+} in the predominantly carbonate network to allow for any significant sulphur dissolution. However, the carbonatitic melts produced here fall towards potentially unrealistically high Ca contents (see Section 5.4.2), and, if the eclogite-derived carbonatite melts were compositionally more similar to oceanic and cratonic carbonatites observed in nature (**Fig. 5.6**), we might expect greater proportions of sulphur to dissolve within carbonatitic melts.

Thus, the interplay between eclogite bulk composition, which may critically involve the presence of CO_2 or carbonate, and the composition of any resulting melts will have an influence on the mobility of sulphur in the mantle. Within the CO_2-bearing eclogite system, for example, sulphur could be mobilised as immiscible sulphide melt within silicate-dominated (basaltic-andesite type) melts at elevated temperatures, as was observed in the CO_2-free system (**Section 5.6.1.1**). Secondly, intermediate carbonate-silicate melts, which occur at melt fractions of >15% (**Table 5.3**), transport miscible sulphur. Finally, the carbonate-dominated (calcitic carbonatite-type) melts, which only occur at lower melt fractions, do not transport detectable sulphur and therefore the MSS remains in the eclogite residue. However, immiscible sulphide could potentially be transported if the carbonate-dominated melts were more Fe or Mg-enriched, due the network-forming nature of these cations in the melt structure.

5.6.2. Sulphur transport within eclogite-derived melts in the upper mantle

The experiments from this study demonstrate that the mobility of sulphur within the upper mantle relies upon either transport as immiscible sulphide-liquid within basaltic-andesite melts or, as dissolved sulphide within intermediate carbonate-silicate melts. Depending on the Si, Fe and CO_2 contents of

these melts, which impact melt viscosity and polymerization (Mysen, 2012; Moussallam et al., 2016), the S-bearing melts could be highly mobile, but potentially reactive within the upper mantle, and create new fertile lithologies (Hammouda and Laporte, 2000; Mallik and Dasgupta, 2012). Since sulphur must be present during mantle melting due to the presence of miscible sulphur and immiscible sulphide globules in MORB glasses (Perfit et al., 1983; le Roux et al., 2006) and other alkaline basalt, kimberlite and carbonatite-type magmas (e.g. Chaussidon et al., 1989), it is suggested that sulphur-bearing eclogites represent a potentially important melt source for creating the compositional variability seen in some of these silica-undersaturated mantle-derived magmas (Dasgupta et al., 2005b; Kogiso and Hirschmann, 2006; Ding and Dasgupta, 2018).

5.6.2.1. Creation of fertile sulphide-bearing mantle lithologies

Estimates for the sulphur content of the depleted MORB-source mantle are in the range of 70 to 200 µg/g (Lorand et al., 2003; Ding and Dasgupta, 2017). Effective metasomatic mass transfer of sulphide and associated trace elements can result in local enrichments within the mantle, and these enriched lithologies (e.g. 250 – 500 µg/g S; Métrich et al., 1999; De Hoog et al., 2001) may provide ideal source regions for mafic arc magmas that have relatively high sulphur contents (800 – 2400 µg/g S; Perfit et al., 1983; Wallace and Carmichael, 1992; le Roux et al., 2006). Our experimental results compare favourably with plentiful mantle xenolith evidence for local scale metasomatic enrichments of mantle peridotite and eclogite by sulphide-bearing, silicate-dominated melts. For example, the modal metasomatic addition of orthopyroxene, clinopyroxene, phlogopite plus sulphide to both cratonic mantle derived peridotite (e.g. Yaxley et al., 1991; Sweeney, 1994; Boyd et al., 1997; Kelemen et al., 1998; Rapp et al., 1999; Prouteau et al., 2001; Griffin et al., 2004; Bell et al., 2005; Ionov et al., 2018) and eclogite xenoliths (e.g. Appleyard, 2000; Schmickler et al., 2004; Gréau et al., 2013; Smart et al., 2009; Kiseeva et al., 2017; Wainwright et al., 2015; **Fig. 5.8**) is well documented and provides strong evidence for metasomatic components that contain both a silicate-rich melt and an immiscible sulphide-liquid. Evidence for metasomatic sulphur enrichment is also observed in non-cratonic mantle lithosphere, for example, extreme sulphur enrichment is shown by some sub-arc mantle-derived xenoliths where sulphur content can be as high as 1190 µg/g (McInnes et al., 2001). In addition, peridotite xenoliths recovered from oceanic island basalts also can show metasomatic addition of sulphide minerals, with bulk xenolith sulphur contents up to 270 µg/g (Lorand et al., 2004). As globular sulphide melts are shown to be relatively immobile (e.g. Lorand, 1991; Gréau et al., 2013), further mobility of sulphur within or out of the mantle may then require transport by silicate-dominated melts (e.g. basaltic melts; Mavrogenes and O'Neill, 1999) as dissolved or immiscible sulphide liquids, as we have demonstrated in our study.

5.6.2.2. Base metal sulphide mobility in the upper mantle

During partial melting of sulphide-bearing eclogite, the melting systematics of the silicate system largely determines the partitioning of lithophile trace elements (Irving, 1978; Klemme et al., 2002), while sulphur will dominantly control the movement of highly siderophile and chalcophile elements (Peach et al., 1990; Fleet et al., 1996; Mungall and Brenan, 2014). While MSS is stable over a wide range of pressure (2.0 to 3.5 GPa) and temperature (1050 to 1300 ºC) conditions that correspond to thermal conditions of thick continental lithospheric mantle (**Fig. 5.1b**), sulphide melt is only present at temperatures above 1200 ºC at 2.0 GPa, corresponding to thermal conditions more similar to the convecting upper mantle beneath ocean basins (**Fig. 5.1b**). These findings are consistent with those of Jenner et al. (2010) and Li and Audétat (2012) who demonstrate that MSS is the principal sulphide phase in the reduced upper mantle.

While the depleted upper mantle contains relatively little sulphur (~200 µg/g; Palme and O'Neill, 2003), saturation or removal of sulphide phases (i.e. MSS or sulphide liquids) during partial melting dictates the behaviour of both chalcophile and highly siderophile elements. Previous base metal sulphide studies have shown that sulphide melts incongruently to form Cu-Ni-rich sulphide melt, which concentrates Pt, Pd and Re (P-PGE), and refractory MSS, which concentrates Os, Ir and Ru (I-PGE) (Bockrath et al., 2004; Lorand et al., 2013; Mungall and Brenan, 2014). Additionally, experiments from this (e.g. SKG-1.2 and SKG-2.1) and other studies (e.g. Wendlandt, 1982; Peach et al., 1990; Fleet et al., 1996; Mavrogenes and O'Neill, 1999) show that sulphide melt will largely be extracted with basaltic melts during partial melting, while crystalline MSS tends to remain residual. This process may fractionate the P-PGE and I-PGE elements if the basaltic melt is sulphide saturated and MSS is still present within the mantle residue. Various mantle xenolith studies also indicate that mantle residues may be stripped of all base metal sulphides if the degree of partial melting exceeds ~15% (this study; Luguet et al., 2003, 2007). However, despite the consumption of all base metal sulphide, some I-PGE and Pt elements may remain within platinum group minerals, olivine and Cr-spinel mineral phases in mantle rocks (Luguet et al., 2007). While some authors suggest that the continental lithospheric mantle may be a significant source for magmatic crustal ore deposits (Griffin et al., 2013), our study, as well as previous work, demonstrates that sulphide (and its precious metal load) is not always effectively mobilized during partial melting events in the lithospheric mantle. Additionally, the importance of eclogite-hosted metals in the ore forming process may be limited (e.g. Arndt, 2013), due to the relative paucity of eclogite in the continental mantle relative to peridotite (Schulze, 1989), as well as the higher degrees of melting required for effective sulphide mobilisation (this study; Luguet et al., 2003, 2007).

5.6.2.3. Implications for diamond formation and mantle magmatism

The melts produced in our experiments share compositional similarities with some diamond-forming high-density fluids (HDFs; e.g. Schrauder and Navon, 1994) found trapped within diamonds

derived from the cratonic mantle. Specifically, the carbonate-silicate and carbonate-dominated (carbonatitic) liquids show some similarities to low-Mg carbonatitic HDF's (**Fig. 5.5d**; e.g. Klein-BenDavid et al., 2009; Weiss et al., 2009; Zedgenizov et al., 2009). In addition, all the produced basaltic-andesite silicate experimental liquids are similarities to silicic HDFs (**Fig. 5.6**). Our experiments clearly show that some carbonate-silicate liquids produced from upper mantle eclogites can bring along a sulphur or sulphide component, which may be significant for the petrogenesis of some suites of diamond that are dominated by sulphide mineral inclusions (Stachel and Harris, 2009). From the overabundance of sulphide-bearing diamonds found in some kimberlites it has been proposed that sulphide-bearing diamonds constitute a separate diamond paragenesis (S-type) and mechanism of diamond formation (Cartigny, 2005; Thomassot et al., 2009; Smart et al., 2017), which is supported by the close occurrence of sulphide and diamond found in some diamondiferous xenoliths (e.g. **Fig. 5.8b**; Taylor et al., 2000; Smart et al., 2009). This is further supported by multi-anvil experiments where diamond is formed by reduction of carbonate in the presence of sulphide or metal (Gunn and Luth, 2006; Palyanov et al., 2007, 2009). Together with the above lines of evidence, our results offer further support the suggestion that primary sulphur or sulphide is a catalyst to diamond growth (e.g. Haggerty, 1986; Palyanov et al., 2007, 2009), although our experiments were conducted outside the diamond stability field.

The participation of recycled crustal material (eclogite or pyroxenite) in mantle-derived magmatism has been long suggested (Hofmann and White, 1982), and more recently demonstratively shown by both the major element (Dasgupta et al., 2005a) and radiogenic isotope compositions of oceanic island basalts (e.g. Stracke, 2012). The lower solidus of eclogite (or pyroxenite) compared to peridotite (**Figure 5.1**; e.g. Pertermann and Hirschman, 2003b) ensures that during partial melting of a mixed mantle package, eclogite will contribute a disproportionately larger melt component (e.g. Sobolev et al., 2007; but see Rosenthal et al. 2018 for the effects of eclogite bulk composition). Additionally, it has been shown that melts from CO_2-bearing eclogite may account for certain major element characteristics of OIB (e.g. high TiO_2 and FeO) that cannot be explained by melt contributions from peridotite-eclogite or CO_2-bearing peridotite alone (Dasgupta et al., 2005b; Mallik and Dasgupta, 2012). Following on the potential melt contribution from eclogite to oceanic island volcanism, it has recently been shown that the sulphur content in many OIBs may rely upon a significant contribution from S-bearing recycled crustal material (now eclogite or pyroxenite). For example, Ding and Dasgupta (2018) show that the sulphur and chalcophile element contents of OIB require a source mantle that has higher sulphur contents than expected for MORB source mantle. Ding and Dasgupta (2018) further suggest that a possible source for OIB sulphur may be partially derived from melts of sulphur-enriched recycled crust or sedimentary material (now eclogite).

5.7. CONCLUSIONS

We have investigated the partial melting behaviour and phase relations of a S±C-bearing MORB-like eclogite (SKG) at temperatures of 1050 to 1300 ºC and pressures of 2.0 to 3.5 GPa. The experiments were conducted to assess the mobility of sulphur in eclogite-derived, potentially C-bearing partial melts at upper mantle conditions that may be applied to the convecting asthenospheric mantle beneath ocean basins, and the thick mantle lithosphere underlying continents. The experiments demonstrate that the character of the melt produced, be it a siliceous, carbonatitic, or a mixed silicate-carbonatite melt, governs whether sulphur or sulphide is mobilised at upper mantle conditions. At higher degrees of eclogite partial melting, the resulting siliceous and intermediate carbonate-silicate melts both appear to mobilise sulphur. Siliceous basaltic-andesite melts, generated during high-degree (up to 60%) alkali-fluxed partial melting of both the CO_2-free SKG-1 and CO_2-bearing SKG-2 bulk compositions, notably mobilise sulphur as an immiscible sulphide liquid within the silicate-dominated partial melts. At slightly lower degrees of melting (~15 %), intermediate carbonate-silicate melts have dissolved sulphur contents of up to 0.3 wt.%. In contrast, the low-degree carbonate-dominated (calcitic carbonatite-type) melts, do not contain measurable dissolved sulphur, and as well, the eclogite residues from these experiments contain stable MSS. This suggests that low-degree (<6 %) partial melts of CO_2-bearing eclogite do not present the most effective mechanism for the mobilisation of sulphur within the upper mantle. However, when partial melting increases to the point where intermediate silicate-carbonate melts begin to form, sulphide may be effectively mobilised as a miscible sulphur component.

Therefore, the critical factors concerning the mobility of sulphur in the upper mantle are the degree of melting of the S-bearing eclogite and the composition of the resulting melts. The CO_2-free basaltic-andesite melts and the intermediate carbonate-silicate melts are the best carriers of sulphur due the presence of prominent network-forming cations (e.g. Si and Fe). Whereas, purely (Fe-poor) carbonatitic melts, generated at lower degrees of partial melting, do not effectively move sulphur due to the absence of a Fe-bearing silicate cation network. Thus, effective transport of sulphur within the upper mantle and resulting mantle metasomatism plus diamond formation, as well as contribution to mantle-derived magmas, appears to require assistance from mixed carbonate±silicate melts.

REFERENCES

Alard, O., Griffin, W. L., Lorand, J. P., Jackson, S. E. and O'Reilly, S. Y. (2000). Non-chondritic distribution of the highly siderophile elements in mantle sulphides. Nature **407**(6806), 891.

Alt, J. C., Shanks III, W. C. and Jackson, M. C. (1993). Cycling of sulfur in subduction zones: The geochemistry of sulfur in the Mariana Island Arc and back-arc trough. Earth and Planetary Science Letters **119**(4), 477-494.

Alt, J. C. and Teagle, D. A. (1999). The uptake of carbon during alteration of ocean crust. Geochimica et Cosmochimica Acta **63**(10), 1527-1535.

Aoki, K. I. and Shiba, I. (1973). Pyroxenes from lherzolite inclusions of Itinome-gata, Japan. Lithos **6**(1), 41-51.

Appleyard, C. M. (2000). The geochemistry of a suite of eclogite xenoliths from the Rietfontein Kimberlite, South Africa (Unpublished doctoral dissertation, University of Cape Town).

Arndt, N. (2013). The lithospheric mantle plays no active role in the formation of orthomagmatic ore deposits. Economic Geology **108**(8), 1953-1970.

Arndt, N., Lesher, C. M. and Czamanske, G. K. (2005). Mantle-derived magmas and magmatic Ni-Cu-(PGE) deposits. Economic Geology, 100th Aniversary volume, ffhal-00016864f, 5-24.

Aulbach, S., Creaser, R. A., Pearson, N. J., Simonetti, S. S., Heaman, L. M., Griffin, W. L. and Stachel, T. (2009). Sulfide and whole rock Re–Os systematics of eclogite and pyroxenite xenoliths from the Slave Craton, Canada. Earth and Planetary Science Letters **283**(1-4), 48-58.

Aulbach, S., Stachel, T., Seitz, H. M. and Brey, G. P. (2012). Chalcophile and siderophile elements in sulphide inclusions in eclogitic diamonds and metal cycling in a Paleoproterozoic subduction zone. Geochimica et Cosmochimica Acta **93**, 278-299.

Baker, D. R. and Moretti, R. (2011). Modeling the solubility of sulfur in magmas: a 50-year old geochemical challenge. Reviews in Mineralogy and Geochemistry **73**(1), 167-213.

Barnes, S. J., Boyd, R., Korneliussen, A., Nilsson, L. P., Often, M., Pedersen, R. B. and Robins, B. (1988). The use of mantle normalization and metal ratios in discriminating between the effects of partial melting, crystal fractionation and sulphide segregation on platinum-group elements, gold, nickel and copper: examples from Norway. In Geo-platinum **87** (pp. 113-143). Springer, Dordrecht.

Barnes, S. J., Makovicky, E., Makovicky, M., Rose-Hansen, J. and Karup-Moller, S. (1997). Partition coefficients for Ni, Cu, Pd, Pt, Rh, and Ir between monosulfide solid solution and sulfide liquid and the formation of compositionally zoned Ni–Cu sulfide bodies by fractional crystallization of

sulfide liquid. Canadian Journal of Earth Sciences **34**(4), 366-374.

Bell, A. S., Simon, A. and Guillong, M. (2009). Experimental constraints on Pt, Pd and Au partitioning and fractionation in silicate melt–sulfide–oxide–aqueous fluid systems at 800 C, 150 MPa and variable sulfur fugacity. Geochimica et Cosmochimica Acta **73**(19), 5778-5792.

Blank, J. G. (1994). Experimental studies of carbon dioxide in silicate melts: solubility, speciation and stable isotope behavior. Reviews in Mineralogy and Geochemistry **30**, 157-186.

Bockrath, C., Ballhaus, C.and Holzheid, A. (2004). Fractionation of the platinum-group elements during mantle melting. Science **305**(5692), 1951-1953.

Boyd, F. R., Pokhilenko, N. P., Pearson, D. G., Mertzman, S. A., Sobolev, N. V. and Finger, L. W. (1997). Composition of the Siberian cratonic mantle: evidence from Udachnaya peridotite xenoliths. Contributions to Mineralogy and Petrology **128**(2-3), 228-246.

Brenan, J. M. and Andrews, D. (2001). High-temperature stability of laurite and Ru–Os–Ir alloy and their role in PGE fractionation in mafic magmas. The Canadian Mineralogist **39**(2), 341-360.

Brenan, J. M., Bennett, N. R, and Zajacz, Z. (2016). Experimental results on fractionation of the highly siderophile elements (HSE) at variable pressures and temperatures during planetary and magmatic differentiation. Reviews in Mineralogy and Geochemistry **81**(1), 1-87.

Brey, G. P., Bulatov, V. K., Girnis, A. V. and Lahaye, Y. (2008). Experimental melting of carbonated peridotite at 6–10 GPa. Journal of Petrology **49**(4), 797-821.

Brey, G. P. and Green, D. H. (1976). Solubility of CO_2 in olivine melilitite at high pressures and role of CO 2 in the Earth's upper mantle. Contributions to Mineralogy and Petrology **55**(2), 217-230.

Brooker, R. A., Kohn, S. C., Holloway, J. R. and McMillan, P. F. (2001). Structural controls on the solubility of CO_2 in silicate melts: part I: bulk solubility data. Chemical Geology **174**(1-3), 225-239.

Bulanova, G. P. (1995). The formation of diamond. Journal of Geochemical Exploration **53**(1-3), 1-23.

Canfield, D. E. (2004). The evolution of the Earth surface sulfur reservoir. American Journal of Science **304**(10), 839-861.

Cartigny, P. (2005). Stable isotopes and the origin of diamond. Elements **1**(2), 79-84.

Cartigny, P., Farquhar, J., Thomassot, E., Harris, J.W., Wing, B., Masterson, A., McKeegan, K. and Stachel, T. (2009). A mantle origin for Paleoarchean peridotitic diamonds from the Panda kimberlite, Slave Craton: evidence from 13C-, 15N-and 33, 34S-stable isotope systematics. Lithos **112**, 852-864.

Cartigny, P., Palot, M., Thomassot, E. and Harris, J. W. (2014). Diamond formation: a stable isotope perspective. Annual Review of Earth and Planetary Sciences **42**, 699-732.

Chaussidon, M., Albarède, F., & Sheppard, S. M. (1989). Sulphur isotope variations in the mantle from ion microprobe analyses of micro-sulphide inclusions. Earth and Planetary Science Letters **92**(2), 144-156.

Coleman, R. G., Lee, D. E., Beatty, L. B. and Brannock, W. W. (1965). Eclogites and eclogites: their differences and similarities. Geological Society of America Bulletin **76**(5), 483-508.

Dalton, J. A. and Presnall, D. C. (1998). Carbonatitic melts along the solidus of model lherzolite in the system CaO-MgO-Al 2 O 3-SiO 2-CO 2 from 3 to 7 GPa. Contributions to Mineralogy and Petrology **131**(2-3), 123-135.

Dasgupta, R. (2013). Ingassing, storage, and outgassing of terrestrial carbon through geologic time. Reviews in Mineralogy and Geochemistry **75**(1), 183-229.

Dasgupta, R. and Hirschmann, M. M. (2006). Melting in the Earth's deep upper mantle caused by carbon dioxide. Nature **440**(7084), 659.

Dasgupta, R., Hirschmann, M. M. and Dellas, N. (2005a). The effect of bulk composition on the solidus of carbonated eclogite from partial melting experiments at 3 GPa. Contributions to Mineralogy and Petrology **149**(3), 288-305.

Dasgupta, R., Hirschmann, M. M. and Stalker, K. (2005b). Immiscible transition from carbonate-rich to silicate-rich melts in the 3 GPa melting interval of eclogite+ CO2 and genesis of silica-undersaturated ocean island lavas. Journal of Petrology **47**(4), 647-671.

Dasgupta, R., Hirschmann, M. M. and Withers, A. C. (2004). Deep global cycling of carbon constrained by the solidus of anhydrous, carbonated eclogite under upper mantle conditions. Earth and Planetary Science Letters **227**(1-2), 73-85.

De Hoog, J. C. M., Taylor, B. E. and Van Bergen, M. J. (2001). Sulfur isotope systematics of basaltic lavas from Indonesia: implications for the sulfur cycle in subduction zones. Earth and Planetary Science Letters **189**(3-4), 237-252.

Deines, P. (2002). The carbon isotope geochemistry of mantle xenoliths. Earth-Science Reviews **58**(3-4), 247-278.

Delpech, G., Lorand, J. P., Grégoire, M., Cottin, J. Y. and O'Reilly, S. Y. (2012). In-situ geochemistry of sulfides in highly metasomatized mantle xenoliths from Kerguelen, southern Indian Ocean. Lithos **154**, 296-314.

Ding, S. and Dasgupta, R. (2017). The fate of sulfide during decompression melting of peridotite–

implications for sulfur inventory of the MORB-source depleted upper mantle. Earth and Planetary Science Letters **459**, 183-195.

Ding, S. and Dasgupta, R. (2018). Sulfur inventory of ocean island basalt source regions constrained by modeling the fate of sulfide during decompression melting of a heterogeneous mantle. Journal of Petrology **59**(7), 1281-1308.

Droop, G. T. R. (1987). A general equation for estimating Fe 3+ concentrations in ferromagnesian silicates and oxides from microprobe analyses, using stoichiometric criteria. Mineralogical magazine **51**(361), 431-435.

Eggler, D. H. (1987). Discussion of recent papers on carbonated peridotite, bearing on mantle metasomatism and magmatism: an alternative. Earth and planetary science letters **82**(3-4), 398-400.

Eggler, D. H. (1978). The effect of CO< 2) upon partial melting of peridotite in the system Na< 2) O-CaO-Al< 2) O< 3)-MgO-SiO< 2)-CO< 2) to 35 kb, with an analysis of melting in a peridotite-H< 2) O-CO< 2) system. American Journal of Science **278**(3), 305-343.

Eldridge, C. S., Compston, W., Williams, I. S., Harris, J. W. and Bristow, J. W. (1991). Isotope evidence for the involvement of recycled sediments in diamond formation. Nature **353**(6345), 649.

Ellis, D. J. and Green, D. H. (1979). An experimental study of the effect of Ca upon garnet-clinopyroxene Fe-Mg exchange equilibria. Contributions to Mineralogy and Petrology **71**(1), 13-22.

Evans, K. A. and Powell, R. (2015). The effect of subduction on the sulphur, carbon and redox budget of lithospheric mantle. Journal of Metamorphic Geology **33**(6), 649-670.

Evans, K. A., Tomkins, A. G., Cliff, J. and Fiorentini, M. L. (2014). Insights into subduction zone sulfur recycling from isotopic analysis of eclogite-hosted sulfides. Chemical Geology **365**, 1-19.

Falloon, T. J. and Green, D. H. (1989). The solidus of carbonated, fertile peridotite. Earth and Planetary Science Letters **94**(3-4), 364-370.

Farquhar, J., Wing, B. A., McKeegan, K. D., Harris, J. W., Cartigny, P. and Thiemens, M. H. (2002). Mass-independent sulfur of inclusions in diamond and sulfur recycling on early Earth. Science **298**(5602), 2369-2372.

Farquhar, J., Wu, N., Canfield, D. E. and Oduro, H. (2010). Connections between sulfur cycle evolution, sulfur isotopes, sediments, and base metal sulfide deposits. Economic Geology **105**(3), 509-533.

Fine, G. and Stolper, E. (1985). The speciation of carbon dioxide in sodium aluminosilicate glasses. Contributions to Mineralogy and Petrology **91**(2), 105-121.

Fleet, M. E., Crocket, J. H. and Stone, W. E. (1996). Partitioning of platinum-group elements (Os, Ir, Ru, Pt, Pd) and gold between sulfide liquid and basalt melt. Geochimica et Cosmochimica Acta **60**(13), 2397-2412.

Foley, S. F. (2010). A reappraisal of redox melting in the Earth's mantle as a function of tectonic setting and time. Journal of Petrology **52**(7-8), 1363-1391.

Foley, S. F., Yaxley, G. M., Rosenthal, A., Buhre, S., Kiseeva, E. S., Rapp, R. P. and Jacob, D. E. (2009). The composition of near-solidus melts of peridotite in the presence of CO_2 and H_2O between 40 and 60 kbar. Lithos **112**, 274-283.

Fonseca, R. O., Mallmann, G., O'Neill, H. S. C., Campbell, I. H. and Laurenz, V. (2011). Solubility of Os and Ir in sulfide melt: Implications for Re/Os fractionation during mantle melting. Earth and Planetary Science Letters **311**(3-4), 339-350.

Fortin, M. A., Riddle, J., Desjardins-Langlais, Y. and Baker, D. R. (2015). The effect of water on the sulfur concentration at sulfide saturation (SCSS) in natural melts. Geochimica et Cosmochimica Acta **160**, 100-116.

Freda, C., Baker, D. R. and Scarlato, P. (2005). Sulfur diffusion in basaltic melts. Geochimica et Cosmochimica Acta **69**(21), 5061-5069.

Frost, D. J. and McCammon, C. A. (2008). The redox state of Earth's mantle. Annu. Rev. Earth Planet. Sci. **36**, 389-420.

Giuliani, A., Fiorentini, M. L., Martin, L. A., Farquhar, J., Phillips, D., Griffin, W. L. and LaFlamme, C. (2016). Sulfur isotope composition of metasomatised mantle xenoliths from the Bultfontein kimberlite (Kimberley, South Africa): Contribution from subducted sediments and the effect of sulfide alteration on S isotope systematics. Earth and Planetary Science Letters **445**, 114-124.

Gréau, Y., Alard, O., Griffin, W. L., Huang, J. X. and O'Reilly, S. Y. (2013). Sulfides and chalcophile elements in Roberts Victor eclogites: unravelling a sulfide-rich metasomatic event. Chemical Geology **354**, 73-92.

Green, D. H. (2015). Experimental petrology of peridotites, including effects of water and carbon on melting in the Earth's upper mantle. Physics and Chemistry of Minerals **42**(2), 95-122.

Griffin, W. L., Begg, G. C. and O'Reilly, S. Y. (2013). Continental-root control on the genesis of magmatic ore deposits. Nature Geoscienc **6**(11), 905.

Griffin, W. L., Graham, S., O'Reilly, S. Y. and Pearson, N. J. (2004). Lithosphere evolution beneath the Kaapvaal Craton: Re–Os systematics of sulfides in mantle-derived peridotites. Chemical Geology **208**(1-4), 89-118.

Gunn, S. C. and Luth, R. W. (2006). Carbonate reduction by Fe-SO melts at high pressure and high temperature. American Mineralogist **91**, 1110-1116.

Haggerty, S. E. (1986). Diamond genesis in a multiply-constrained model. Nature **320**(6057), 34.

Hammouda, T. (2003). High-pressure melting of carbonated eclogite and experimental constraints on carbon recycling and storage in the mantle. Earth and Planetary Science Letters **214**(1-2), 357-368.

Hammouda, T. and Keshav, S. (2015). Melting in the mantle in the presence of carbon: Review of experiments and discussion on the origin of carbonatites. Chemical Geology **418**, 171-188.

Hammouda, T. and Laporte, D. (2000). Ultrafast mantle impregnation by carbonatite melts. Geology **28**(3), 283-285.

Harte, B., Hunter, R. H. and Kinny, P. D. (1993). Melt geometry, movement and crystallization, in relation to mantle dykes, veins and metasomatism. Philosophical Transactions of the Royal Society of London. Series A: Physical and Engineering Sciences **342**(1663), 1-21.

Hirose, K. (1997). Partial melt compositions of carbonated peridotite at 3 GPa and role of CO_2 in alkali-basalt magma generation. Geophysical Research Letters **24**(22), 2837-2840.

Hirose, K. and Fei, Y. (2002). Subsolidus and melting phase relations of basaltic composition in the uppermostlower mantle. Geochimica et Cosmochimica Acta **66**(12), 2099-2108.

Hirschmann, M. M. (2000). Mantle solidus: Experimental constraints and the effects of peridotite composition. Geochemistry, Geophysics, Geosystems **1**(10).

Hoernle, K., Tilton, G., Le Bas, M. J., Duggen, S. and Garbe-Schönberg, D. (2002). Geochemistry of oceanic carbonatites compared with continental carbonatites: mantle recycling of oceanic crustal carbonate. Contributions to Mineralogy and Petrology **142**(5), 520-542.

Hofmann, A. W. and White, W. M. (1982). Mantle plumes from ancient oceanic crust. Earth and Planetary Science Letters **57**(2), 421-436.

Holleck, G. L. (1970). Diffusion and solubility of hydrogen in palladium and palladium--silver alloys. The Journal of Physical Chemistry **74**(3), 503-511.

Holzheid, A. and Grove, T. L. (2002). Sulfur saturation limits in silicate melts and their implications for core formation scenarios for terrestrial planets. American Mineralogist **87**(2-3), 227-237.

Hughes, H. S., McDonald, I., Loocke, M., Butler, I. B., Upton, B. G. and Faithfull, J. W. (2017). Paradoxical co-existing base metal sulphides in the mantle: the multi-event record preserved in Loch Roag peridotite xenoliths, North Atlantic Craton. Lithos **276**, 103-121.

Irving, A. J. (1978). A review of experimental studies of crystal/liquid trace element partitioning. Geochimica et Cosmochimica Acta **42**(6), 743-770.

Irving, A. J. and Wyllie, P. J. (1975). Subsolidus and melting relationships for calcite, magnesite and the join $CaCO_3$-$MgCO_3$ 36 kb. Geochimica et Cosmochimica Acta **39**(1), 35-53.

Jacob, D. E., Kronz, A. and Viljoen, K. S. (2004). Cohenite, native iron and troilite inclusions in garnets from polycrystalline diamond aggregates. Contributions to Mineralogy and Petrology **146**(5), 566-576.

Jayasuriya, K. D., O'Neill, H. S. C., Berry, A. J. and Campbell, S. J. (2004). A Mossbauer study of the oxidation state of Fe in silicate melts. American Mineralogist **89**(11-12), 1597-1609.

Jégo, S. and Dasgupta, R. (2014). The fate of sulfur during fluid-present melting of subducting basaltic crust at variable oxygen fugacity. Journal of Petrology **55**(6), 1019-1050.

Jégo, S. and Dasgupta, R. (2013). Fluid-present melting of sulfide-bearing ocean-crust: Experimental constraints on the transport of sulfur from subducting slab to mantle wedge. Geochimica et Cosmochimica Acta **110**, 106-134.

Jenner, F. E. and O'Neill, H. S. C. (2012). Analysis of 60 elements in 616 ocean floor basaltic glasses. Geochemistry, Geophysics, Geosystems **13**(2).

Jenner, F. E., O'Neill, H. S. C., Arculus, R. J. and Mavrogenes, J. A. (2010). The magnetite crisis in the evolution of arc-related magmas and the initial concentration of Au, Ag and Cu. Journal of Petrology **51**(12), 2445-2464.

Johannes, W., Bell, P.M., Mao, H.K., Boettcher, A.L., Chipman, D.W., Hays, J.F., Newton, R.C. and Seifert, F. (1971). An interlaboratory comparison of piston-cylinder pressure calibration using the albite-breakdown reaction. Contributions to Mineralogy and Petrology **32**(1), pp.24-38.

Jugo, P. J. (2009). Sulfur content at sulfide saturation in oxidized magmas. Geology **37**(5), 415-418.

Jugo, P. J., Luth, R. W. and Richards, J. P. (2005a). An experimental study of the sulfur content in basaltic melts saturated with immiscible sulfide or sulfate liquids at 1300° C and 1· 0 GPa. Journal of Petrology **46**(4), 783-798.

Jugo, P. J., Luth, R. W. and Richards, J. P. (2005b). Experimental data on the speciation of sulfur as a function of oxygen fugacity in basaltic melts. Geochimica et Cosmochimica Acta **69**(2), 497-503.

Kelemen, P. B., Hart, S. R. and Bernstein, S. (1998). Silica enrichment in the continental upper mantle via melt/rock reaction. Earth and Planetary Science Letters **164**(1-2), 387-406.

Kelley, K. A. and Cottrell, E. (2009). Water and the oxidation state of subduction zone magmas. Science

325(5940), 605-607.

Keshav, S. and Gudfinnsson, G. H. (2010). Experimentally dictated stability of carbonated oceanic crust to moderately great depths in the Earth: Results from the solidus determination in the system CaO-MgO-Al_2O_3-SiO_2-CO_2. Journal of Geophysical Research: Solid Earth, **115**(B5).

Kiseeva, E. S., Fonseca, R. O. and Smythe, D. J. (2017). Chalcophile elements and sulfides in the upper mantle. Elements **13**(2), 111-116.

Kiseeva, E. S., Kamenetsky, V. S., Yaxley, G. M. and Shee, S. R. (2017). Mantle melting versus mantle metasomatism–"The chicken or the egg" dilemma. Chemical Geology **455**, 120-130.

Kiseeva, E. S., Litasov, K. D., Yaxley, G. M., Ohtani, E. and Kamenetsky, V. S. (2013). Melting and phase relations of carbonated eclogite at 9–21 GPa and the petrogenesis of alkali-rich melts in the deep mantle. Journal of Petrology **54**(8), 1555-1583.

Kiseeva, E. S. and Wood, B. J. (2015). The effects of composition and temperature on chalcophile and lithophile element partitioning into magmatic sulphides. Earth and Planetary Science Letters **424**, 280-294.

Kiseeva, E. S. and Wood, B. J. (2013). A simple model for chalcophile element partitioning between sulphide and silicate liquids with geochemical applications. Earth and Planetary Science Letters **383**, 68-81.

Kiseeva, E. S., Yaxley, G. M., Hermann, J., Litasov, K. D., Rosenthal, A. and Kamenetsky, V. S. (2012). An experimental study of carbonated eclogite at 3· 5–5· 5 GPa—implications for silicate and carbonate metasomatism in the cratonic mantle. Journal of Petrology **53**(4), 727-759.

Klein-BenDavid, O., Logvinova, A.M., Schrauder, M., Spetius, Z.V., Weiss, Y., Hauri, E.H., Kaminsky, F.V., Sobolev, N.V. and Navon, O. (2009). High-Mg carbonatitic microinclusions in some Yakutian diamonds—a new type of diamond-forming fluid. Lithos **112**, pp.648-659.

Klemme, S., Blundy, J. D. and Wood, B. J. (2002). Experimental constraints on major and trace element partitioning during partial melting of eclogite. Geochimica et Cosmochimica Acta **66**(17), 3109-3123.

Kogarko, L. N. (1993). Geochemical characteristics of oceanic carbonatites from the Cape Verde Islands. South African Journal of Geology **96**(3), 119-125.

Kogiso, T. and Hirschmann, M. M. (2006). Partial melting experiments of bimineralic eclogite and the role of recycled mafic oceanic crust in the genesis of ocean island basalts. Earth and Planetary Science Letters **249**(3-4), 188-199.

Kogiso, T., Hirschmann, M. M. and Pertermann, M. (2004). High-pressure partial melting of mafic

lithologies in the mantle. Journal of Petrology **45**(12), 2407-2422.

Krogh Ravna (2000). The garnet–clinopyroxene Fe^{2+}–Mg geothermometer: an updated calibration. Journal of metamorphic Geology **18**(2), 211-219.

Kullerud, G. (1963). The Fe-Ni-S system. Carnegie Institution Washington Year Book **62**, 175-189.

Labidi, J., Cartigny, P., Birck, J. L., Assayag, N. and Bourrand, J. J. (2012). Determination of multiple sulfur isotopes in glasses: A reappraisal of the MORB $\delta^{34}S$. Chemical Geology **334**, 189-198.

Labidi, J., Cartigny, P., Hamelin, C., Moreira, M. and Dosso, L. (2014). Sulfur isotope budget (^{32}S, 33S, ^{34}S and ^{36}S) in Pacific–Antarctic ridge basalts: A record of mantle source heterogeneity and hydrothermal sulfide assimilation. Geochimica et Cosmochimica Acta **133**, 47-67.

Labidi, J., Cartigny, P. and Jackson, M. G. (2015). Multiple sulfur isotope composition of oxidized Samoan melts and the implications of a sulfur isotope 'mantle array'in chemical geodynamics. Earth and Planetary Science Letters **417**, 28-39.

le Roux, P. J., Shirey, S. B., Hauri, E. H., Perfit, M. R. and Bender, J. F. (2006). The effects of variable sources, processes and contaminants on the composition of northern EPR MORB (8–10 N and 12–14 N): Evidence from volatiles (H_2O, CO_2, S) and halogens (F, Cl). Earth and Planetary Science Letters **251**(3-4), 209-231.

Li, C. and Ripley, E. M. (2009). Sulfur contents at sulfide-liquid or anhydrite saturation in silicate melts: empirical equations and example applications. Economic Geology **104**(3), 405-412.

Li, J. and Agee, C. B. (2001). The effect of pressure, temperature, oxygen fugacity and composition on partitioning of nickel and cobalt between liquid Fe-Ni-S alloy and liquid silicate: Implications for the Earth's core formation. Geochimica et Cosmochimica Acta **65**(11), 1821-1832.

Li, Y. and Audétat, A. (2012). Partitioning of V, Mn, Co, Ni, Cu, Zn, As, Mo, Ag, Sn, Sb, W, Au, Pb, and Bi between sulfide phases and hydrous basanite melt at upper mantle conditions. Earth and Planetary Science Letters **355**, 327-340.

Li, Y. and Audétat, A. (2013). Gold solubility and partitioning between sulfide liquid, monosulfide solid solution and hydrous mantle melts: Implications for the formation of Au-rich magmas and crust–mantle differentiation. Geochimica et Cosmochimica Acta **118**, 247-262.

Li, Y. and Audétat, A. (2015). Effects of temperature, silicate melt composition, and oxygen fugacity on the partitioning of V, Mn, Co, Ni, Cu, Zn, As, Mo, Ag, Sn, Sb, W, Au, Pb, and Bi between sulfide phases and silicate melt. Geochimica et Cosmochimica Acta **162**, 25-45.

Litasov, K. and Ohtani, E. (2010). The solidus of carbonated eclogite in the system $CaO–Al_2O_3–MgO–SiO_2–Na_2O–CO_2$ to 32 GPa and carbonatite liquid in the deep mantle. Earth and Planetary Science

Letters **295**(1-2), 115-126.

Liu, Y. and Brenan, J. (2015). Partitioning of platinum-group elements (PGE) and chalcogens (Se, Te, As, Sb, Bi) between monosulfide-solid solution (MSS), intermediate solid solution (ISS) and sulfide liquid at controlled fO_2–fS_2 conditions. Geochimica et Cosmochimica Acta **159**, 139-161.

Liu, Y., Samaha, N. T. and Baker, D. R. (2007). Sulfur concentration at sulfide saturation (SCSS) in magmatic silicate melts. Geochimica et Cosmochimica Acta **71**(7), 1783-1799.

Lorand, J. P. (1991). Sulphide petrology and sulphur geochemistry of orogenic lherzolites: a comparative study of the Pyrenean bodies (France) and the Lanzo Massif (Italy). Journal of Petrology **2**, 77-95.

Lorand, J. P., Alard, O., Luguet, A. and Keays, R. R. (2003). Sulfur and selenium systematics of the subcontinental lithospheric mantle: inferences from the Massif Central xenolith suite (France). Geochimica et Cosmochimica Acta **67**(21), 4137-4151.

Lorand, J. P., Delpech, G., Grégoire, M., Moine, B., O'Reilly, S. Y. and Cottin, J. Y. (2004). Platinum-group elements and the multistage metasomatic history of Kerguelen lithospheric mantle (South Indian Ocean). Chemical Geology **208**(1-4), 195-215.

Lorand, J. P. and Luguet, A. (2016). Chalcophile and siderophile elements in mantle rocks: Trace elements controlled by trace minerals. Reviews in Mineralogy and Geochemistry **81**(1), 441-488.

Lorand, J. P., Luguet, A. and Alard, O. (2013). Platinum-group element systematics and petrogenetic processing of the continental upper mantle: A review. Lithos **164**, 2-21.

Lorand, J. P., Luguet, A. and Alard, O. (2008). Platinum-group elements: a new set of key tracers for the Earth's interior. Elements **4**(4), 247-252.

Luguet, A., Behrens, M., Pearson, D. G., König, S. and Herwartz, D. (2015). Significance of the whole rock Re–Os ages in cryptically and modally metasomatised cratonic peridotites: Constraints from HSE–Se–Te systematics. Geochimica et Cosmochimica Acta **164**, 441-463.

Luguet, A., Lorand, J. P. and Seyler, M. (2003). Sulfide petrology and highly siderophile element geochemistry of abyssal peridotites: A coupled study of samples from the Kane Fracture Zone (45 W 23 20N, MARK area, Atlantic Ocean). Geochimica et Cosmochimica Acta **67**(8), 1553-1570.

Luguet, A., Shirey, S. B., Lorand, J. P., Horan, M. F. and Carlson, R. W. (2007). Residual platinum-group minerals from highly depleted harzburgites of the Lherz massif (France) and their role in HSE fractionation of the mantle. Geochimica et Cosmochimica Acta **71**(12), 3082-3097.

Luth, R. (2014). Volatiles in Earth's Mantle. In: Treatise on Geochemistry **3**(2), Holland H.D., Turekian K.K., (eds.). Elsevier, Oxford, 355–379.

Luth, R.W. (1999). Carbon and carbonates in the mantle. In: Mantle Petrology: Field Observations and High Pressure Experimentation: A Tribute to Francis R. (Joe) Boyd **6**. Fei Y, Bertka, C. M., Mysen, B. O. (ed). The Geochemical Society, 297-316.

Mallik, A and Dasgupta, R. (2012). Reaction between MORB-eclogite derived melts and fertile peridotite and generation of ocean island basalts. Earth and Planetary Science Letters **329**, 97-108.

Mandeville, C. W. (2010). Sulfur: A ubiquitous and useful tracer in Earth and planetary sciences. Elements **6**(2), 75-80.

Mathez, E. A. (1976). Sulfur solubility and magmatic sulfides in submarine basalt glass. Journal of Geophysical Research **81**(23), 4269-4276.

Mavrogenes, J. A. and O'Neill, H. S. C. (1999). The relative effects of pressure, temperature and oxygen fugacity on the solubility of sulfide in mafic magmas. Geochimica et Cosmochimica Acta **63**(7-8), 1173-1180.

McDonald, I., Hughes, H. S., Butler, I. B., Harris, J. W. and Muir, D. (2017). Homogenisation of sulphide inclusions within diamonds: A new approach to diamond inclusion geochemistry. Geochimica et Cosmochimica Acta **216**, 335-357.

McInnes, B. I., Gregoire, M., Binns, R. A., Herzig, P. M. and Hannington, M. D. (2001). Hydrous metasomatism of oceanic sub-arc mantle, Lihir, Papua New Guinea: petrology and geochemistry of fluid-metasomatised mantle wedge xenoliths. Earth and Planetary Science Letters **188**(1-2), 169-183.

Médard, E., McCammon, C. A., Barr, J. A. and Grove, T. L. (2008). Oxygen fugacity, temperature reproducibility, and H2O contents of nominally anhydrous piston-cylinder experiments using graphite capsules. American Mineralogist **93**(11-12), 1838-1844.

Metrich, N. and Clocchiatti, R. (1996). Sulfur abundance and its speciation in oxidized alkaline melts. Geochimica et Cosmochimica Acta **60**(21), 4151-4160.

Métrich, N., Schiano, P., Clocchiatti, R. and Maury, R. C. (1999). Transfer of sulfur in subduction settings: an example from Batan Island (Luzon volcanic arc, Philippines). Earth and Planetary Science Letters **167**(1-2), 1-14.

Minarik, W. G. (1998). Complications to carbonate melt mobility due to the presence of an immiscible silicate melt. Journal of Petrology **39**(11-12), 1965-1973.

Mitchell, R. H. and Keays, R. R. (1981). Abundance and distribution of gold, palladium and iridium in some spinel and garnet lherzolites: implications for the nature and origin of precious metal-rich intergranular components in the upper mantle. Geochimica et Cosmochimica Acta **45**(12), 2425-

2442.

Moussallam, Y., Florian, P., Corradini, D., Morizet, Y., Sator, N., Vuilleumier, R., Guillot, B., Iacono-Marziano, G., Schmidt, B.C. and Gaillard, F. (2016). The molecular structure of melts along the carbonatite–kimberlite–basalt compositional joint: CO_2 and polymerisation. Earth and Planetary Science Letters **434**, pp.129-140.

Moussallam, Y., Morizet, Y., Massuyeau, M., Laumonier, M. and Gaillard, F. (2015). CO2 solubility in kimberlite melts. Chemical Geology **418**, 198-205.

Mungall, J. E. and Brenan, J. M. (2014). Partitioning of platinum-group elements and Au between sulfide liquid and basalt and the origins of mantle-crust fractionation of the chalcophile elements. Geochimica et Cosmochimica Acta **125**, 265-289.

Mungall, J. E., Hanley, J. J., Arndt, N. T. and Debecdelievre, A. (2006). Evidence from meimechites and other low-degree mantle melts for redox controls on mantle-crust fractionation of platinum-group elements. Proceedings of the National Academy of Sciences **103**(34), 12695-12700.

Mysen, B. O. (2012). Silicate-COH melt and fluid structure, their physicochemical properties, and partitioning of nominally refractory oxides between melts and fluids. Lithos **148**, 228-246.

Mysen, B. O. and Boettcher, A. L. (1975). Melting of a hydrous mantle: I. Phase relations of natural peridotite at high pressures and temperatures with controlled activities of water, carbon dioxide, and hydrogen. Journal of Petrology **16**(1), 520-548.

Nelson, D. R., Chivas, A. R., Chappell, B. W. and McCulloch, M. T. (1988). Geochemical and isotopic systematics in carbonatites and implications for the evolution of ocean-island sources. Geochimica et Cosmochimica Acta **52**(1), 1-17.

Palme, H. and O'Neill, H. S. C. (2003). Cosmochemical estimates of mantle composition. Treatise on geochemistry **2**, 568.

Palyanov, Y. N., Borzdov, Y. M., Bataleva, Y. V., Sokol, A. G., Palyanova, G. A. and Kupriyanov, I. N. (2007). Reducing role of sulfides and diamond formation in the Earth's mantle. Earth and Planetary Science Letters **260**(1-2), 242-256.

Palyanov, Y. N., Kupriyanov, I. N., Borzdov, Y. M., Sokol, A. G., & Khokhryakov, A. F. (2009). Diamond crystallization from a sulfur− carbon system at HPHT conditions. Crystal Growth and Design **9**(6), 2922-2926.

Parat, F., Holtz, F. and Streck, M. J. (2011). Sulfur-bearing magmatic accessory minerals. Reviews in Mineralogy and Geochemistry **73**(1), 285-314.

Peach, C. L., Mathez, E. A. and Keays, R. R. (1990). Sulfide melt-silicate melt distribution coefficients

for noble metals and other chalcophile elements as deduced from MORB: Implications for partial melting. Geochimica et Cosmochimica Acta **54**(12), 3379-3389.

Peregoedova, A., Barnes, S. J. and Baker, D. R. (2004). The formation of Pt–Ir alloys and Cu–Pd-rich sulfide melts by partial desulfurization of Fe–Ni–Cu sulfides: results of experiments and implications for natural systems. Chemical Geology **208**(1-4), 247-264.

Perfit, M. R., Fornari, D. J., Malahoff, A. and Embley, R. W. (1983). Geochemical studies of abyssal lavas recovered by DSRV Alvin from Eastern Galapagos Rift, Inca Transform, and Ecuador Rift: 3. Trace element abundances and petrogenesis. Journal of Geophysical Research: Solid Earth **88**(B12), 10551-10572.

Pertermann, M., and Hirschmann, M. M. (2003a). Anhydrous partial melting experiments on MORB-like eclogite: phase relations, phase compositions and mineral–melt partitioning of major elements at 2–3 GPa. Journal of Petrology **44**(12), 2173-2201.

Pertermann, M., & Hirschmann, M. M. (2003b). Partial melting experiments on a MORB-like pyroxenite between 2 and 3 GPa: Constraints on the presence of pyroxenite in basalt source regions from solidus location and melting rate. Journal of Geophysical Research: Solid Earth, **108**(B2), 2125.

Poli, S., Franzolin, E., Fumagalli, P. and Crottini, A. (2009). The transport of carbon and hydrogen in subducted oceanic crust: An experimental study to 5 GPa. Earth and Planetary Science Letters **278**(3-4), 350-360.

Preston, R. F., Stevens, G. and McCarthy, T. S. (2003). Fluid compositions in equilibrium with silica-undersaturated magmas in the system Na_2O–Al_2O_3–SiO_2–H_2O: clues to the composition of fenitizing fluids. Contributions to Mineralogy and Petrology **144**(5), 559-569.

Prouteau, G., Scaillet, B., Pichavant, M. and Maury, R. (2001). Evidence for mantle metasomatism by hydrous silicic melts derived from subducted oceanic crust. Nature **410**(6825), 197.

Rapp, R. P., Shimizu, N., Norman, M. D. and Applegate, G. S. (1999). Reaction between slab-derived melts and peridotite in the mantle wedge: experimental constraints at 3.8 GPa. Chemical Geology **160**(4), 335-356.

Rapp, R. P. and Watson, E. B. (1995). Dehydration melting of metabasalt at 8–32 kbar: implications for continental growth and crust-mantle recycling. Journal of Petrology **36**(4), 891-931.

Rehkaemper, M., Halliday, A. N., Fitton, J. G., Lee, D. C., Wieneke, M. and Arndt, N. T. (1999). Ir, Ru, Pt, and Pd in basalts and komatiites: new constraints for the geochemical behavior of the platinum-group elements in the mantle. Geochimica et Cosmochimica Acta **63**(22), 3915-3934.

Rose, L. A. and Brenan, J. M. (2001). Wetting properties of Fe-Ni-Co-Cu-OS melts against olivine: Implications for sulfide melt mobility. Economic Geology **96**(1), 145-157.

Rosenthal, A., Yaxley, G.M., Crichton, W.A., Kovács, I.J., Spandler, C., Hermann, J., Sándorné, J.K., Rose-Koga, E. and Pelleter, A.A. (2018). Phase relations and melting of nominally 'dry'residual eclogites with variable CaO/Na2O from 3 to 5 GPa and 1250 to 1500° C; implications for refertilisation of upwelling heterogeneous mantle. Lithos **314**, 506-519.

Saal, A. E., Hauri, E. H., Langmuir, C. H. and Perfit, M. R. (2002). Vapour undersaturation in primitive mid-ocean-ridge basalt and the volatile content of Earth's upper mantle. Nature **419**(6906), 451.

Scaillet, B. and Pichavant, M. (2005). A model of sulphur solubility for hydrous mafic melts: application to the determination of magmatic fluid compositions of Italian volcanoes. Annals of Geophysics **48**, 671-698.

Schmickler, B., Jacob, D. E. and Foley, S. F. (2004). Eclogite xenoliths from the Kuruman kimberlites, South Africa: geochemical fingerprinting of deep subduction and cumulate processes. Lithos **75**(1-2), 173-207.

Schmidt, M. W. and Weidendorfer, D. (2018). Carbonatites in oceanic hotspots. Geology **46**(5), 435-438.

Schrauder, M. and Navon, O. (1994). Hydrous and carbonatitic mantle fluids in fibrous diamonds from Jwaneng, Botswana. Geochimica et Cosmochimica Acta **58**(2), 761-771.

Schulze, D. J. (1989). Constraints on the abundance of eclogite in the upper mantle. Journal of Geophysical Research: Solid Earth **94**(B4), 4205-4212.

Sen, C. and Dunn, T. (1994). Dehydration melting of a basaltic composition amphibolite at 1.5 and 2.0 GPa: implications for the origin of adakites. Contributions to Mineralogy and Petrology **117**(4), 394-409.

Shirasaka, M. and Takahashi, E. (2003). A genesis of carbonatitic melt within subducting oceanic crusts: high-pressure experiments in the system MORB-$CaCO_3$. In: International Kimberlite Conference: Extended Abstracts **8**, Victoria, Canada, 1-5.

Shirey, S.B., Cartigny, P., Frost, D.J., Keshav, S., Nestola, F., Nimis, P., Pearson, D.G., Sobolev, N.V. and Walter, M.J. (2013). Diamonds and the geology of mantle carbon. Reviews in Mineralogy and Geochemistry **75**(1), 355-421.

Smart, K. A., Cartigny, P., Tappe, S., O'Brien, H. and Klemme, S. (2017). Lithospheric diamond formation as a consequence of methane-rich volatile flooding: An example from diamondiferous eclogite xenoliths of the Karelian craton (Finland). Geochimica et Cosmochimica Acta **206**, 312-

342.

Smart, K. A., Chacko, T., Stachel, T., Muehlenbachs, K., Stern, R. A. and Heaman, L. M. (2011). Diamond growth from oxidized carbon sources beneath the Northern Slave Craton, Canada: a $\delta^{13}C$–N study of eclogite-hosted diamonds from the Jericho kimberlite. Geochimica et Cosmochimica Acta **75**(20), 6027-6047.

Smart, K. A., Heaman, L. M., Chacko, T., Simonetti, A., Kopylova, M., Mah, D. and Daniels, D. (2009). The origin of high-MgO diamond eclogites from the Jericho Kimberlite, Canada. Earth and Planetary Science Letters **284**(3-4), 527-537.

Smythe, D. J., Wood, B. J. and Kiseeva, E. S. (2017). The S content of silicate melts at sulfide saturation: new experiments and a model incorporating the effects of sulfide composition. American Mineralogist **102**(4), 795-803.

Sobolev, A.V., Hofmann, A.W., Kuzmin, D.V., Yaxley, G.M., Arndt, N.T., Chung, S.L., Danyushevsky, L.V., Elliott, T., Frey, F.A., Garcia, M.O. and Gurenko, A.A. (2007). The amount of recycled crust in sources of mantle-derived melts. Science **316**(5823), 412-417.

Spandler, C., Yaxley, G., Green, D. H. and Rosenthal, A. (2007). Phase relations and melting of anhydrous K-bearing eclogite from 1200 to 1600 C and 3 to 5 GPa. Journal of Petrology **49**(4), 771-795.

Stachel, T. and Harris, J. W. (2009). Formation of diamond in the Earth's mantle. Journal of Physics: Condensed Matter **21**(36), 364206.

Stagno, V., Frost, D. J., McCammon, C. A., Mohseni, H. and Fei, Y. (2015). The oxygen fugacity at which graphite or diamond forms from carbonate-bearing melts in eclogitic rocks. Contributions to Mineralogy and Petrology **169**(2), 16.

Stagno, V., Ojwang, D. O., McCammon, C. A. and Frost, D. J. (2013). The oxidation state of the mantle and the extraction of carbon from Earth's interior. Nature **493**(7430), 84.

Staudigel, H. (2003). Hydrothermal alteration processes in the oceanic crust. Treatise on geochemistry **3**, 659.

Staudigel, H., Plank, T., White, B. and Schmincke, H. U. (1996). Geochemical fluxes during seafloor alteration of the basaltic upper oceanic crust: DSDP Sites 417 and 418. Subduction: top to bottom, **96**, 19-38.

Stracke, A. (2012). Earth's heterogeneous mantle: a product of convection-driven interaction between crust and mantle. Chemical geology **330**, 274-299.

Tappe, S., Foley, S.F., Jenner, G.A., Heaman, L.M., Kjarsgaard, B.A., Romer, R.L., Stracke, A., Joyce,

N. and Hoefs, J. (2006). Genesis of ultramafic lamprophyres and carbonatites at Aillik Bay, Labrador: a consequence of incipient lithospheric thinning beneath the North Atlantic craton. Journal of Petrology **47**(7), 1261-1315.

Tappe, S., Foley, S. F., Kjarsgaard, B. A., Romer, R. L., Heaman, L. M., Stracke, A. and Jenner, G. A. (2008). Between carbonatite and lamproite—diamondiferous Torngat ultramafic lamprophyres formed by carbonate-fluxed melting of cratonic MARID-type metasomes. Geochimica et Cosmochimica Acta **72**(13), 3258-3286.

Tappe, S., Romer, R. L., Stracke, A., Steenfelt, A., Smart, K. A., Muehlenbachs, K. and Torsvik, T. H. (2017). Sources and mobility of carbonate melts beneath cratons, with implications for deep carbon cycling, metasomatism and rift initiation. Earth and Planetary Science Letters **466**, 152-167.

Tappe, S., Smart, K., Torsvik, T., Massuyeau, M. and de Wit, M. (2018a). Geodynamics of kimberlites on a cooling Earth: Clues to plate tectonic evolution and deep volatile cycles. Earth and Planetary Science Letters **484**, 1-14.

Tappe, S., Dongre, A., Liu, C. Z. and Wu, F. Y. (2018b). 'Premier'evidence for prolonged kimberlite pipe formation and its influence on diamond transport from deep Earth. Geology **46**(10), 843-846.

Taylor, L.A., Keller, R.A., Snyder, G.A., Wang, W., Carlson, W.D., Hauri, E.H., Mccandless, T., Kim, K.R., Sobolev, N.V. and Bezborodov, S.M. (2000). Diamonds and their mineral inclusions, and what they tell us: A detailed "pull-apart" of a diamondiferous eclogite. International Geology Review **42**(11), pp.959-983.

Taylor, L. A. and Neal, C. R. (1989). Eclogites with oceanic crustal and mantle signatures from the Bellsbank kimberlite, South Africa, Part I: mineralogy, petrography, and whole rock chemistry. The Journal of Geology **97**(5), 551-567.

Taylor, W. R., and Green, D. H. (1988). Measurement of reduced peridotite-COH solidus and implications for redox melting of the mantle. Nature **332**(6162), 349.

Thomassot, E., Cartigny, P., Harris, J. W., Lorand, J. P., Rollion-Bard, C. and Chaussidon, M. (2009). Metasomatic diamond growth: A multi-isotope study (13C, 15N, 33S, 34S) of sulphide inclusions and their host diamonds from Jwaneng (Botswana). Earth and Planetary Science Letters **282**(1-4), 79-90.

Thomson, A. R., Walter, M. J., Kohn, S. C. and Brooker, R. A. (2016). Slab melting as a barrier to deep carbon subduction. Nature **529**(7584), 76.

Truckenbrodt, J. and Johannes, W. (1999). H2O loss during piston-cylinder experiments. American

Mineralogist **84**(9), 1333-1335.

Truckenbrodt, J., Ziegenbein, D. and Johannes, W. (1997). Redox conditions in piston-cylinder apparatus: The different behavior of boron nitride and unfired pyrophyllite assemblies. American Mineralogist **82**(3-4), 337-344.

Tsai, H. M., Shieh, Y. N. and Meyer, H. O. (1979). Mineralogy and $^{34}S/^{32}S$ ratios of sulfides associated with kimberlite, xenoliths, and diamonds. In: The Mantle Sample. Boyd, F. R., and Meyer, H.O.A. (Eds.), American Geophysical Union, Washington, D.C., 87-103.

Wainwright, A. N., Luguet, A., Fonseca, R. O. C. and Pearson, D. G. (2015). Investigating metasomatic effects on the 187Os isotopic signature: a case study on micrometric base metal sulphides in metasomatised peridotite from the Letlhakane kimberlite (Botswana). Lithos **232**, 35-48.

Wallace, M. E. and Green, D. H. (1988). An experimental determination of primary carbonatite magma composition. Nature **335**(6188), 343.

Wallace, P. and Carmichael, I. S. (1992). Sulfur in basaltic magmas. Geochimica et Cosmochimica Acta **56**(5), 1863-1874.

Wallace, P. J. (2005). Volatiles in subduction zone magmas: concentrations and fluxes based on melt inclusion and volcanic gas data. Journal of volcanology and Geothermal Research **140**(1-3), 217-240.

Wallace, P. J., & Edmonds, M. (2011). The sulfur budget in magmas: evidence from melt inclusions, submarine glasses, and volcanic gas emissions. Reviews in Mineralogy and Geochemistry **73**(1), 215-246.

Wedepohl, K. H. (1995). The composition of the continental crust. Geochimica et cosmochimica Acta **59**(7), 1217-1232.

Weiss, Y., Kessel, R., Griffin, W.L., Kiflawi, I., Klein-BenDavid, O., Bell, D.R., Harris, J.W. and Navon, O. (2009). A new model for the evolution of diamond-forming fluids: Evidence from microinclusion-bearing diamonds from Kankan, Guinea. Lithos **112**, 660-674.

Wendlandt, R. F. (1982). Sulfide saturation of basalt and andesite melts at high pressures and temperatures. American Mineralogist **67**(9-10), 877-885.

Woodland, A. B., Girnis, A. V., Bulatov, V. K., Brey, G. P. and Höfer, H. E. (2019). Experimental study of sulfur solubility in silicate–carbonate melts at 5–10.5 GPa. Chemical Geology **505**, 12-22.

Wykes, J. L., O'Neill, H. S. C. and Mavrogenes, J. A. (2015). The effect of FeO on the sulfur content at sulfide saturation (SCSS) and the selenium content at selenide saturation of silicate melts.

Journal of Petrology **56**(7), 1407-1424.

Wyllie, P. J. (1978). Mantle fluid compositions buffered in peridotite-CO_2-H_2O by carbonates, amphibole, and phlogopite. The Journal of Geology **86**(6), 687-713.

Wyllie, P. J. and Huang, W. L. (1976). Carbonation and melting reactions in the system CaO–MgO–SiO_2–CO_2 at mantle pressures with geophysical and petrological applications. Contributions to Mineralogy and Petrology **54**(2), 79-107.

Yasuda, A., Fujii, T. and Kurita, K. (1994). Melting phase relations of an anhydrous mid-ocean ridge basalt from 3 to 20 GPa: Implications for the behavior of subducted oceanic crust in the mantle. Journal of Geophysical Research: Solid Earth **99**(B5), 9401-9414.

Yaxley, G. M. and Brey, G. P. (2004). Phase relations of carbonate-bearing eclogite assemblages from 2.5 to 5.5 GPa: implications for petrogenesis of carbonatites. Contributions to Mineralogy and Petrology **146**(5), 606-619.

Yaxley, G. M. and Green, D. H. (1994). Experimental demonstration of refractory carbonate-bearing eclogite and siliceous melt in the subduction regime. Earth and Planetary Science Letters **128**(3-4), 313-325.

Yaxley, G. M. and Green, D. H. (1998). Reactions between eclogite and peridotite: mantle refertilisation by subduction of oceanic crust. Schweiz. Mineral. Petrogr. Mitt **78**(2), 243-255.

Zajacz, Z. (2015). The effect of melt composition on the partitioning of oxidized sulfur between silicate melts and magmatic volatiles. Geochimica et Cosmochimica Acta **158**, 223-244.

Zajacz, Z., Candela, P. A., Piccoli, P. M., Sanchez-Valle, C. and Wälle, M. (2013). Solubility and partitioning behavior of Au, Cu, Ag and reduced S in magmas. Geochimica et Cosmochimica Acta **112**, 288-304.

Zedgenizov, D. A., Ragozin, A. L., Shatsky, V. S., Araujo, D., Griffin, W. L. and Kagi, H. (2009). Mg and Fe-rich carbonate–silicate high-density fluids in cuboid diamonds from the Internationalnaya kimberlite pipe (Yakutia). Lithos **112**, 638-647.

CHAPTER 5: TABLES

Table 5.1. Model mafic starting compositions used in previous experimental studies on mantle melting of eclogite or pyroxenite

	CO_2±H_2O-bearing MORB compositions							CO_2-free MORB compositions				
	EC1	SLEC1	SLEC2	SLEC3	SLEC4	OTBC	GA1cc	GA1	GA2	LW	G2	G2K
SiO_2	30.11	41.21	30.29	41.69	44.01	47.23	45.32	50.35	49.68	45.91	50.05	50.81
TiO_2	-	2.16	1.58	2.18	2.31	-	1.34	1.49	1.82	0.94	1.97	1.9
Al_2O_3	11.74	10.89	7.95	11.02	11.63	15.53	14.88	16.53	16.94	17.19	15.76	15.22
Cr_2O_3	-	0.09	0.05	0.09	0.09	-	-	-	0.08	-	-	-
FeOt	10.05	12.83	13.87	11.03	11.65	8.93	8.85	9.83	9.71	7.67	9.35	9.03
MnO	-	0.12	0.23	0.12	0.13	-	0.15	0.17	0.09	0.22	0.17	0.16
MgO	12.44	12.87	14.28	11.07	11.68	6.24	7.15	7.94	8.08	7.48	7.9	7.91
CaO	19.41	13.09	14.88	16.89	14.7	14.77	14.24	9.6	9.28	13.54	11.74	11.68
Na_2O	0.87	1.63	1.75	1.4	1.48	2.91	3.14	3.49	3.34	1.63	3.04	3.02
K_2O	-	0.11	0.1	0.1	0.1	0.02	0.40	0.44	0.37	0.14	0.03	0.26
P_2O_5	-	-	-	-	-	-	0.14	0.16	0.23	0.04	-	-
CO_2	15.38	5	14.99	4.42	2.21	4.43	4.4	-	-	-	-	-
H_2O	-	-	-	-	-	0.12	-	-	-	3.04	-	-
Total	100.00	100.00	99.97	100.01	99.99	99.88	100.00	100.00	99.63	97.09	100.01	99.99
Mg#	68.8	64.1	64.7	64.1	64.1	55.5	59.0	59.0	59.7	63.5	60.1	61.0
CaO/MgO	1.6	1.0	1.0	1.5	1.3	2.4	2.0	1.2	1.1	1.8	1.5	1.5
Na_2O/ CO_2	0.06	0.33	0.12	0.32	0.67	0.66	0.71	-	-	-	-	-
Ca#	48	35	35	44	39	50	48	36	35	48	41	41

EC1 = Yaxley and Brey (2004) ; SLEC1 = Dasgupta et al., 2004; SLEC2, SLEC3, SLEC4 = Dasgupta et al., 2005; OTBC = Hammouda (2003); GA1cc = Kiseeva et al., 2012
GA1 = Yaxley and Green (1994); GA2 = Spandler et al. (2008); LW = Lambert and Wyllie (1972); G2, G2K = Petermann and Hirschmann (2003); Ca# = [Ca/(Ca+Mg+Fe)]

Table 5.2. Composition of the "SKG" starting materials

	SKG glass	Calc. bulk	SKG-1	SKG-2	SKG-3	Trace elem.	(ppm)	cont.	(ppm)
SiO_2	50.87 (0.34)	SiO_2	50.8	48.2	40.4	Sc	680	Ba	734
TiO_2	1.41 (0.05)	TiO_2	1.4	1.5	1.2	V	703	La	775
Al_2O_3	15.79 (0.2)	Al_2O_3	15.8	15.2	12.8	Cr	777	Ce	736
Cr_2O_3	-	Cr_2O_3	-	-	-	Mn	880	Pr	716
FeOt	9.32 (0.29)	FeOt	12.7	13.4	11.8	Co	88.2	Nd	741
MgO	7.92 (0.12)	MnO	0.2	0.1	0.1	Ni	16.1	Sm	724
MnO	0.19 (0.01)	MgO	7.9	7.3	6.1	Cu	2.0	Eu	759
CaO	11.57 (0.1)	CaO	11.6	10.0	16.8	Zn	4.3	Gd	714
Na_2O	3.07 (0.06)	Na_2O	3.1	2.7	2.2	Ga	20.2	Tb	699
K_2O	0.17 (0.01)	K_2O	0.2	0.1	0.1	Ge	17.9	Dy	706
P_2O_5	-	CO_2	0.0	4.7	11.8	As	43.1	Ho	719
NiO	-	S (wt.%)	1.8	1.8	1.8	Se	80.5	Er	683
Total (wt. %)	100.31	Ni (wt.%)	0.5	0.5	0.5	Rb	185	Tm	664
-	-	Cu	0.1	0.1	0.1	Sr	795	Yb	703
	Pentlandite					Y	722	Lu	708
S	35.4 (0.2)	Mg#	53	49	48	Zr	801	Ta	795
Fe	52.1 (1.1)	Ca#	36	33	48	Nb	765	Re	76.2
Ni	9.9 (0.93)	CaO/MgO	1.5	1.4	2.8	Mo	405	Pt	65.4
Cu	2.1 (0.47)	Na_2O/ CO_2	-	0.40	0.13	Sb	37.8	Th	729
Total (wt. %)	99.4	-	-	-	-	Cs	96	U	749

Bulk compsositions normalised to 100%: SKG-1 = SKG glass + 5% Pn; SKG-2 = SKG glass + 5% Pn + 4.7% CO_2; SKG-3: SKG glass + 5% Pn + CO_2 was added as $CaCO_3$

Mg# = calculated from molar proportions; Ca# = molar [Ca/(Ca+Mg+Fe)]

Table 5.3. Partial melting experiments of "SKG" starting compositions

Experiment	Starting composition	Duration (hr)	Capsule material	Temperature (°C)	Pressure (GPa)	$\Delta \log fO_2$ (FMQ) (log units)	Phase assemblages	Equilibrium phases and modes											
								Grt	Cpx	Coe	Plg	MSS	L_S	L_{Sil}	L_{Carb}	$L_{Carb\text{-}Sil}$	CC-Dol_{SS}	$*CO_2$	Σr^2
SKG-1.1	SKG-1	48	$Pd_{30}Ag_{70}$ + graphite	1100	2	-	Grt + Cpx + MSS + L_{Sil}	0.16	0.36	-	-	0.05		0.43	-	-	-	-	2.5
SKG-1.2	SKG-1	48	$Pd_{30}Ag_{70}$ + graphite	1200	2	-4.7 ±1	Grt + Cpx + Coe + Plg + L_S + L_{Sil}	0.3	0.3	0.08	0.17	0.05	0.01	0.1	-	-	-	-	2.1
SKG-2.1	SKG-2	48	$Pd_{30}Ag_{70}$ + graphite	1200	2	-1.9±1	Grt + Cpx + L_S + L_{sil} + $*(CC_{SS})$	0.20 (0.15)	0.14 (0.15)	-	-	0.06 (0.02)	(0.04)	0.60 (0.63)	-	-	*(0.02)	-	1.5 (1.1)
SKG-2.2	SKG-2	48	$Pd_{60}Ag_{40}$ + graphite	1150	3	-	Grt + Cpx + Coe + MSS + $*(CO_2)$	0.52 (0.48)	0.43 (0.43)	0.01 (0.03)	-	0.04 (0.04)	-	-	-	-	-	*(0.02)	1.9 (1.1)
SKG-2.4	SKG-2	48	$Pd_{60}Ag_{40}$ + graphite	1300	3	-	Grt + Cpx + Coe + MSS + L_{Carb} + $*(CO_2)$	0.33 (0.35)	0.46 (0.44)	0.11 (0.1)	-	0.05 (0.05)	-	-	0.06 (0.05)	-	-	*(0.01)	2 (1.9)
SKG-2.3	SKG-2	48	$Pd_{30}Ag_{70}$ + graphite	1150	3.5	-	Grt + Cpx + Coe + MSS + L_{Sil} + $*(CO_2)$	(0.41)	(0.46)	(0.01)	-	(0.04)	-	(0.06)	-	-	-	*(0.03)	(2.6)
SKG-2.5	SKG-2	48	$Pd_{60}Ag_{40}$ + graphite	1300	3.5	-	Grt + Cpx + Coe + MSS + L_{Carb} + *(CO2)	0.51	0.33	0.08	-	0.04	-	-	0.04	-	-	-	0.8
SKG-3.4	SKG-3	48	$Pd_{30}Ag_{70}$ + graphite	1150	2.5	-	Grt + Cpx + MSS + $L_{Carb\text{-}Sil}$ + $*(CO_2)$	0.20 (0.18)	0.58 (0.60)	-	-	0.03 (0.03)	-	-	-	0.17 (0.15)	-	*(0.04)	2.9 (1.6)
SKG-3.3	SKG-3	48	$Pd_{60}Ag_{40}$ + graphite	1300	2.5	-2.9±1	Grt + Cpx + MSS + L_{Carb} + $*(CO_2)$	(0.22)	(0.63)	-	-	(0.04)	-	-	(0.04)	-	-	*(0.07)	1.8
SKG-3.1	SKG-3	48	$Pd_{60}Ag_{40}$ + graphite	1050	3	-	Grt + Cpx + MSS + $L_{Carb\text{-}Sil}$ + CC-Dol_{SS} +	0.35 (0.36)	0.43 (0.42)	-	-	0.05 (0.04)	-	-	-	0.17 (0.15)	0.01(0.01)	*(0.02)	1.2 (0.8)
SKG-3.2	SKG-3	48	$Pd_{60}Ag_{40}$ + graphite	1150	3	-	Grt + Cpx + Coe + MSS + $L_{Carb\text{-}Sil}$ + $*(CO_2)$	0.35 (0.33)	0.43 (0.45)	0.02 (0.02)	-	0.04 (0.04)	-	-	-	0.16 (0.13)	-	*(0.03)	2.1 (0.97)

SKG-1 = SKG glass + 5% Pn; SKG-2 = SKG glass + 5% Pn + 4.7% CO_2; SKG-3 = SKG glass + 5% Pn + 11.8% CO_2.

Grt = garnet; Cpx = clinopyroxene; Coe = Coesite; Plg = Plagioclase; MSS = mono-sulpide solid solution; L_S = sulphide liquid/melt; L_{Sil} = silicate liquid/melt; $L_{C\text{-}Sil}$ = Carbonate silicate liquid/melt; CC-Dol_{SS} = calcio-dolomitic solid solution; CC_{SS} = calcium carbonate

CO_2 = carbon dioxide; $\Delta \log fO_2$ = calculated oxgen fugacity relative to the FMQ buffer (calculation method described in **Section 5.2**).

* CO_2 gas was not directly measured but assumed present because of the presence of voids/bubbles found within the experimental run product, as well as a measured mass loss during capsule piercing and sample preparation

Phase assemblage modes were calculated by mass-balance equations using a multiple linear regression technique. Modes were calculated by wt. % of the elements analysed in each phase. When CO_2 is included in the mass-balance calculations, new mass-balance values

Σr^2 is the sum of squared residuals calculated using the modes obtained through mass-balance calculations and point counting of phases within the experimental run product. Inclusion of CO_2 in mass balance calculations lowers Σr^2 values.

Table 5.4. Experimental run-product mineral and quenched liquid compositons

Experiment	Phases	n	SiO_2	TiO_2	Al_2O_3	FeO	MgO	MnO	CaO	Na_2O	K_2O	CO_2	S	Total
SKG-1.1	Grt	16	39.6	1.9	21.4	16.9	11.8	bdl	8.4	bdl	bdl	bdl	bdl	99.9
	Cpx	14	51.9	0.9	7.0	6.5	13.2	bdl	18.9	1.6	bdl	bdl	bdl	100.0
	L_{Sil}	10	57.0	1.3	19.8	5.2	3.9	bdl	6.4	5.5	0.8	bdl	bdl	100.0
SKG-1.2	Grt	20	40.1	1.1	22.5	17.4	12.1	0.6	7.8	bdl	bdl	bdl	bdl	101.6
	Cpx	12	49.1	0.8	10.3	6.7	12.7	bdl	17.8	2.6	bdl	bdl	bdl	100.0
	Coe	5	99.7	0.2	0.2	bdl	bdl	bdl	bdl	bdl	bdl	bdl	bdl	100.0
	Plg	8	55.6	0.0	28.0	0.2	bdl	bdl	10.8	5.6	0.1	bdl	bdl	100.3
	L_{Sil}	30	56.4	2.0	17.4	2.9	6.1	bdl	11.9	2.9	0.2	bdl	bdl	99.8
SKG-2.1	Grt	6	39.6	0.7	22.0	16.3	14.1	0.3	6.2	bdl	bdl	bdl	bdl	99.2
	Cpx	8	50.1	0.6	8.2	8.3	14.6	bdl	17.2	1.5	bdl	bdl	bdl	100.5
	L_{Sil}	15	54.2	1.9	16.2	8.4	4.5	bdl	8.2	2.5	0.2	4.1	bdl	100.2
	*CC	-	bdl	bdl	bdl	bdl	bdl	bdl	56.0	bdl	bdl	44.0	bdl	100.0
SKG-2.2	Grt	7	42.2	1.5	19.2	19.9	5.8	0.2	10.3	0.3	bdl	bdl	bdl	99.3
	Cpx	8	55.3	1.2	14.1	5.5	9.4	bdl	9.8	5.2	0.5	bdl	bdl	101.1
	Coe	3	99.6	bdl	bdl	0.4	bdl	bdl	bdl	bdl	bdl	bdl	bdl	100.0
SKG-2.4	Grt	5	42.7	0.6	21.8	17.4	11.2	bdl	6.8	bdl	bdl	bdl	bdl	100.6
	Cpx	6	53.4	1.0	12.5	6.4	9.6	bdl	13.2	5.0	bdl	bdl	bdl	101.1
	Coe	2	99.6	0.5	0.6	0.3	bdl	bdl	bdl	bdl	bdl	bdl	bdl	100.9
	L_{Carb}	3	1.1	bdl	0.7	4.2	3.9	bdl	43.7	bdl	bdl	46.5	bdl	100.0
SKG-2.3	Grt	3	41.5	0.6	20.8	20.0	10.5	bdl	6.5	0.4	bdl	bdl	bdl	100.3
	Cpx	7	55.0	0.4	12.8	5.0	8.6	bdl	12.3	6.6	bdl	bdl	bdl	100.7
	Coe	1	99.5	bdl	bdl	0.5	bdl	bdl	bdl	bdl	bdl	bdl	bdl	100.0
"Rhyolite"	$L_{Sil+Coe}$	2	79.9	5.3	3.6	2.3	2.0	bdl	4.4	1.3	bdl	2.0	bdl	100.8
(-20% Coe)	$L_{Sil-Coe}$	calc.	56.8	5.3	3.6	2.3	2.0	bdl	4.4	1.3	bdl	3.0	bdl	(78)
SKG-2.5	Grt	3	43.0	0.9	19.4	18.7	9.0	0.2	8.0	0.9	bdl	bdl	bdl	100.0
	Cpx	3	54.7	1.2	13.1	5.0	8.0	bdl	11.7	6.5	bdl	bdl	bdl	100.1
	Coe	4	99.5	bdl	0.2	0.4	bdl	bdl	bdl	bdl	bdl	bdl	bdl	100.1
	L_{Carb}	2	0.4	0.0	0.4	3.3	3.7	bdl	39.4	0.0	bdl	52.8	bdl	100.0
SKG-3.4	Grt	7	44.0	1.2	20.4	26.7	5.7	bdl	2.2	bdl	bdl	bdl	bdl	100.1
	Cpx	10	51.1	0.8	12.6	7.7	9.7	bdl	15.6	3.6	bdl	bdl	bdl	101.1
	$L_{Carb-Sil}$	5	4.5	bdl	2.4	3.2	2.1	bdl	45.9	bdl	bdl	43.1	0.10	101.3
SKG-3.3	Grt	4	39.6	0.7	20.9	17.3	10.0	0.3	10.9	0.3	bdl	bdl	bdl	100.0
	Cpx	2	48.6	1.1	11.6	8.4	9.7	bdl	19.2	2.4	bdl	bdl	bdl	100.9
	L_{Carb}	5	2.4	bdl	0.9	2.1	2.0	bdl	49.6	0.2	bdl	42.4	bdl	99.7
SKG-3.1	Grt	3	41.4	0.8	19.5	17.5	6.2	bdl	14.2	0.8	bdl	bdl	bdl	100.3
	Cpx	4	53.5	0.5	12.5	5.6	8.8	bdl	14.6	4.9	bdl	bdl	bdl	100.4
	$CC\text{-}Dol_{SS}$	2	1.1	0.0	0.7	4.2	3.9	bdl	43.7	0.0	bdl	46.5	bdl	100.0
	$L_{Carb-Sil}$	2	12.4	1.6	3.2	4.5	4.2	bdl	29.9	0.5	bdl	43.7	0.29	100.0
SKG-3.2	Grt	3	40.7	1.0	20.9	20.0	7.8	0.2	9.4	bdl	bdl	bdl	bdl	100.0
	Cpx	4	51.9	0.4	10.2	6.4	9.3	0.0	17.8	4.0	bdl	bdl	bdl	100.0
	Coe	2	92.1	0.8	2.6	2.8	0.9	bdl	1.1	bdl	bdl	bdl	bdl	100.4
	$L_{Carb-Sil}$	1	11.6	0.0	2.9	2.8	2.7	bdl	32.4	0.6	bdl	46.9	0.27	100.0

Phase abbreviations as in **Table 3**. All values in wt. %. (*) = assumed present from mass balance calculations. bdl = below detection limit

Table 5.5. Experimental run-product sulphide melt (L_S) and mono-sulphide solid solution (MSS) compositions

Experiment	Sulphur-rich phases	Quench products		S (wt.%)	Fe (wt.%)	Cu (wt.%)	Ni (wt.%)	Co (wt.%)	Total	Metal/S (at.%)	Ni/(Ni +Fe) (at.%)	Cu/Metals (at.%)
	Synthetic pentlandite		20	35.4	52.1	2	9.9	bdl	99.4	1.03	0.15	0.03
SKG-1.1	MSS	MSS	10	35.7	54.6	1.3	8.8	0.0	100.4	1.03	0.13	0.02
SKG-1.2	L_S	Fe, Ni-rich sulphide	8	37.3	54.7	0.5	5.2	0.7	98.4	0.94	0.08	0.01
		Ni-Fe-(Cu) metal alloy	5	3.5	42.4	1.0	49.8	2.3	98.9	15.22	0.53	0.01
SKG-2.1	L_S	Fe, Ni-rich sulphide	6	38.1	54.0	0.5	5.7	0.6	98.8	0.91	0.09	0.01
		Cu-rich sulphide	5	34.6	53.8	9.5	0.7	0.0	98.6	1.04	0.01	0.13
SKG-2.2	MSS	MSS	5	42.2	40.6	4.0	11.3	0.4	98.4	0.75	0.21	0.06
SKG-2.4	MSS	MSS	3	39.5	45.6	2.6	12.3	0.3	100.3	0.87	0.20	0.04
SKG-2.3	MSS	MSS	3	37.8	44.6	3.6	12.0	0.4	98.4	0.90	0.20	0.05
	MSS	MSS	2	39.4	42.5	3.4	12.5	0.0	97.7	0.83	0.22	0.05
SKG-2.5	MSS	MSS	2	38.7	42.6	4.8	13.1	0.3	99.5	0.88	0.23	0.07
SKG-3.4	MSS	MSS	5	36.9	42.5	4.5	13.4	0.4	97.6	0.93	0.23	0.07
SKG-3.3	MSS	MSS	4	38.7	42.6	4.8	13.1	0.2	99.4	0.88	0.23	0.07
SKG-3.1	MSS	MSS	6	38.5	39.1	4.0	14.1	0.4	96.0	0.84	0.26	0.06
SKG-3.2	MSS	MSS	3	38.7	40.5	5.2	13.8	0.0	98.2	0.86	0.24	0.08

Metal/S = [(Fe+Cu+Ni+Co}/S]

CHAPTER 5: FIGURES

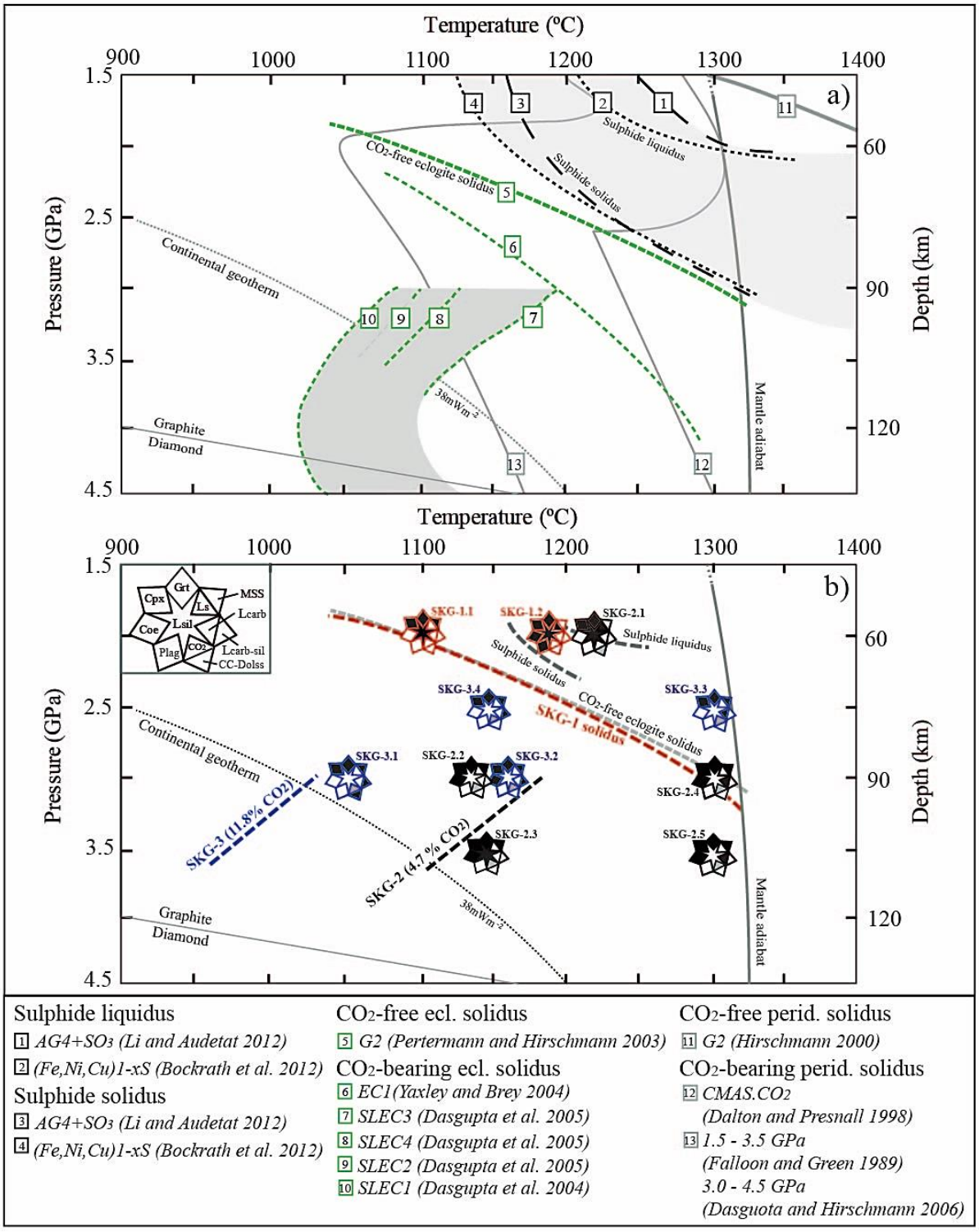

Fig. 5.1(a) *A summary of published sulphide, CO_2-bearing eclogite and peridotite melting curves. The 38mWm^{-2} continental geotherm is taken from Pollack and Chapman (1977), the 1300 ºC mantle adiabat is taken from Kimura and Kawabata (2014), and the and graphite-diamond stability field is taken from Kennedy and Kennedy (1976).* ***(b)*** *P-T diagram showing the experimental phase assemblages of the different SKG bulk compositons, plus the inferred location of the SKG-1, SKG-2 and SKG-3 S±C-bearing eclogite solidi as well as the inferred sulphide liquidus and solidus curves.*

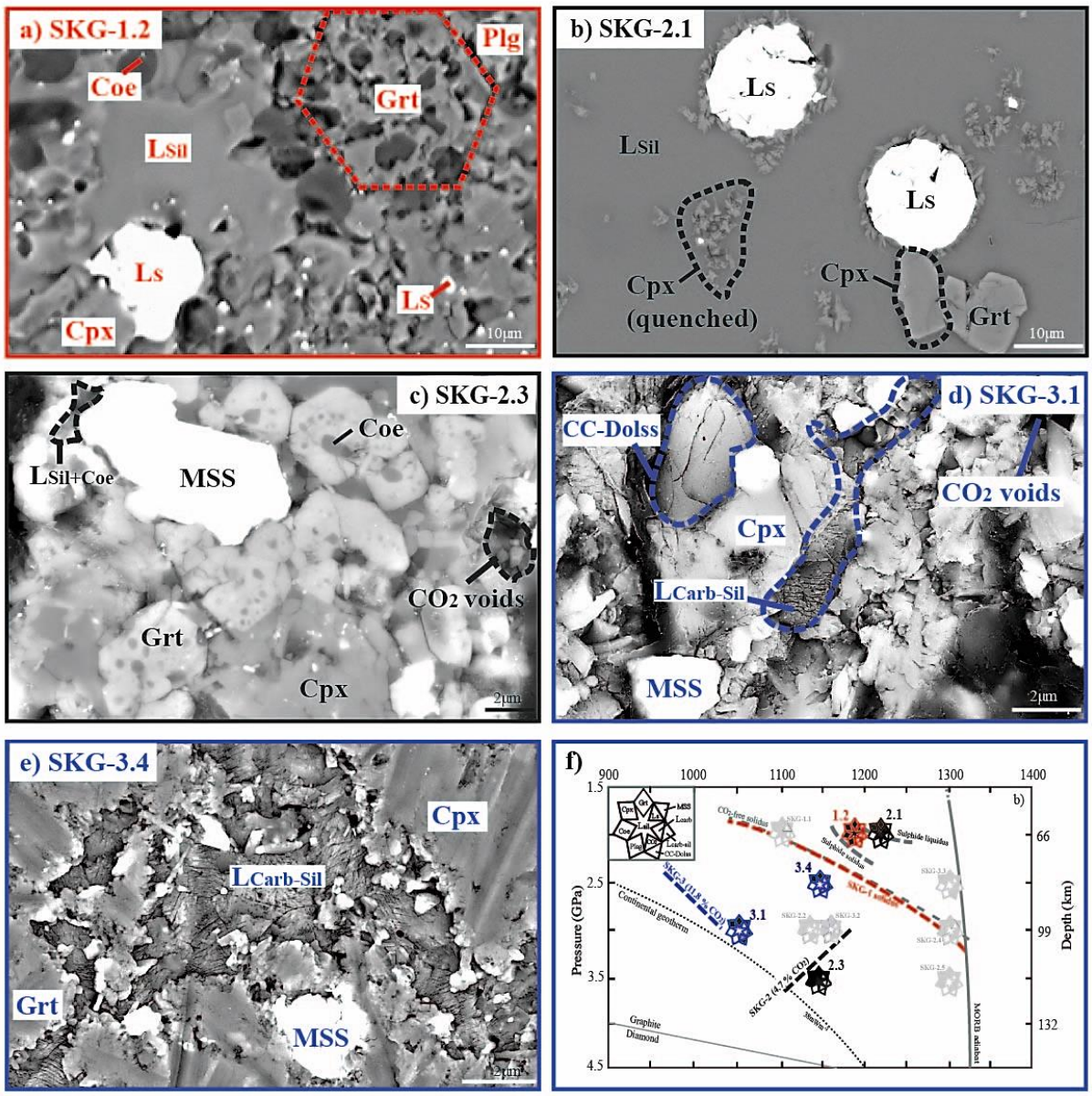

Fig. 5.2 *BSE images of select experimental runs.* ***(a)*** *SKG-1.2; 2.0 GPa and 1200 ºC. Small pockets of silicate-dominated melt (L_{Sil}) in contact with immiscible sulphide melt (L_S).* ***(b)*** *SKG-2.1; 2.0 GPa and 1200 ºC., Rounded globules L_S surrounded by some quenched clinopyroxene crystals within highly polymerised silicate-dominated melt.* ***(c)*** *SKG-2.3; 3.5 GPa and 1150 ºC. Large (>8 µm) crystalline MSS and small patchy $L_{Sil+Coe}$ and CO_2-voids.* ***(d)*** *SKG-3.1; 2.5 GPa and 1050 ºC. Both CC-DOl$_{SS}$ and $L_{Carb-Sil}$ phases and small (<2 µm) crystalline MSS.* ***(e)*** *SKG-3.4; 2.5 GPa and 1150 ºC. Crystalline MSS and intermediate carboante-silicate melt.* ***(f)*** *Phase assemblages of the selected experiments as shown in* ***Figure 5.1b****. Phase abbreviations as in* ***Table 5.3****.*

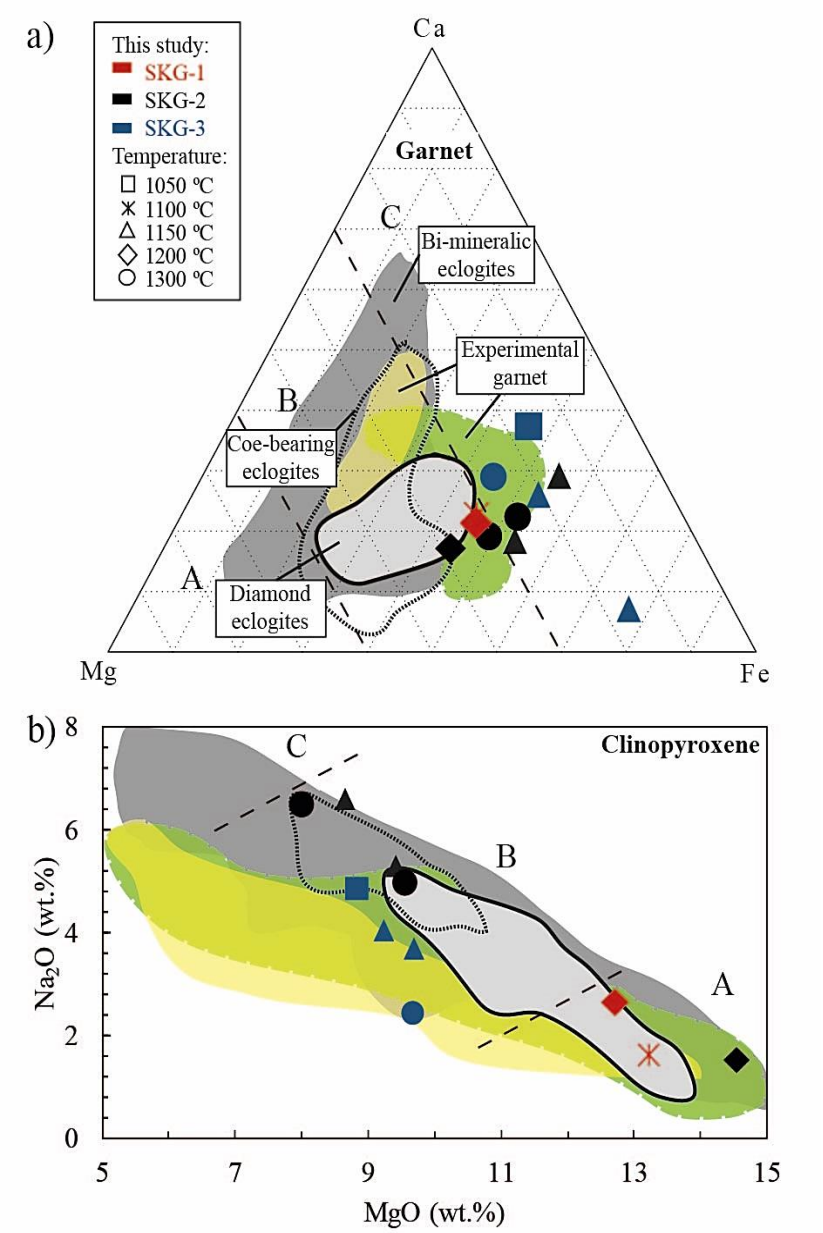

Fig. 5.3 (a) *Molar Mg-Ca-Fe diagram depicting the compositions of the experimental garnets. Dashed lines represent 10 % and the A-B-C classification scheme is from Coleman et al. (1965). Yellow field: garnets produced from volatile-free eclogite melting experiments (Pertermann and Hirschmann, 2003; Spandler et al., 2008). Green field: garnets produced from CO_2-bearing eclogite melting experiments (Dasgupta et al., 2004, 2005; Yaxley and Brey, 2004; Kiseeva et al., 2012). Dark-grey field: bi-mineralic eclogites from Kaapvaal craton kimberlites (Harte and Kirkley, 1997; Pyle and Haggert, 1998; Schulze et al., 2000; Jacob, 2004). Light grey field: diamond-bearing eclogites from Kaapvaal craton kimberlites (MacGregor and Manton, 1986; McCandless and Gurney, 1989; Jacob, 2004; Gréau et al., 2011; Riches et al., 2016). Dashed field: Coesite-bearing eclogites from Kaapvaal craton kimberlites (Schulze et al., 2000; Jacob et al., 2003).* ***(b)*** *Na_2O vs. MgO (wt. %) contents of clinopyroxene. A-B-C classification is from Taylor and Neal (1989).*

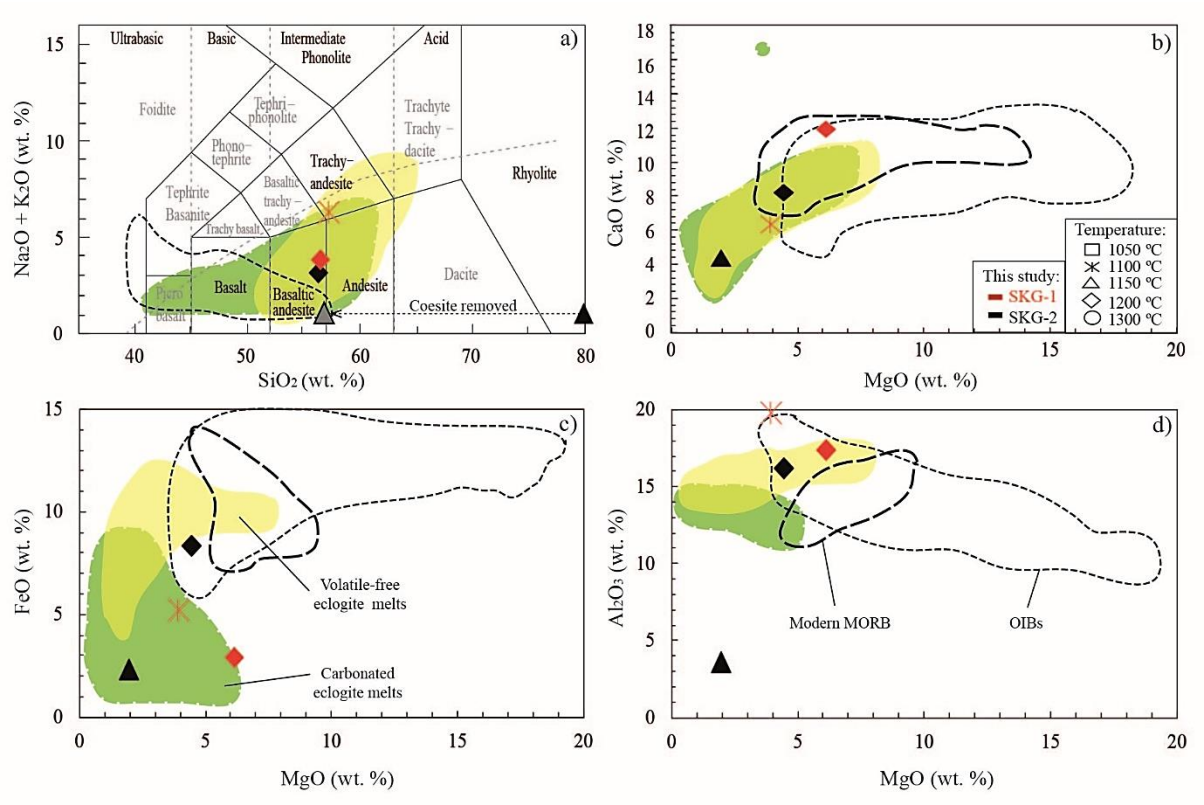

Fig. 5.4 *Multi-element variation diagrams showing the liquid silicate-dominated melt compositions produced by the SKG-1 and SKG-2 experiments.* ***(a)*** *SiO_2 vs. Na_2O+K_2O. TAS classification scheme from le Bas et al. (1986). Grey-filled triangle: calculated melt composition of SKG-2.3 after removal of 29 wt. % coesite.* ***(b)*** *MgO vs. CaO.* ***(c)*** *MgO vs. FeO.* ***(d)*** *MgO vs. Al_2O_3. Shown for comparison: modern MORB from Jenner and O'Neill, (2012), OIBs from the GEOROC database. Volatile-free eclogite-derived melts from Pertermann and Hirschmann, (2003) and Spandler et al. (2008). Carbonated eclogite-derived silicate-dominated melts from Kiseeva et al. (2012) and Hammouda (2003).*

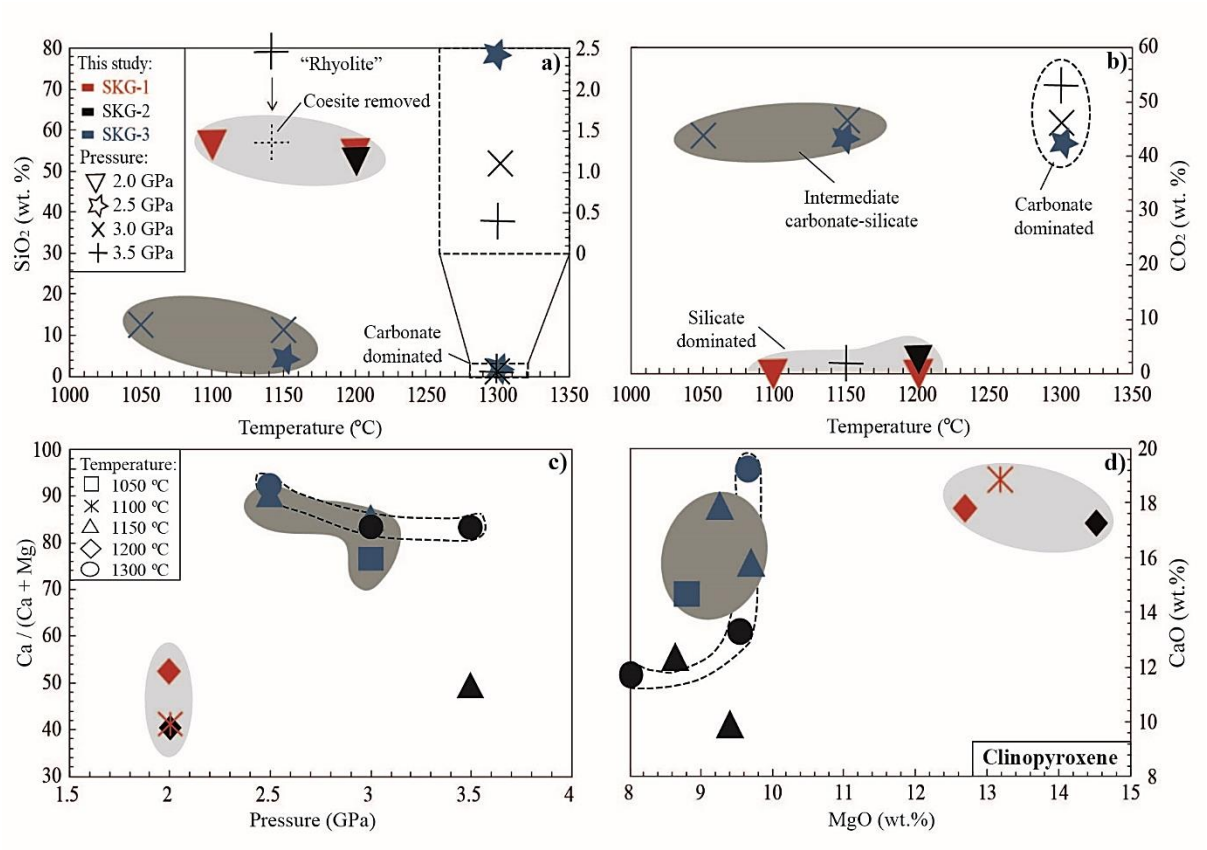

Fig. 5.5 *Temperature (°C) vs.* ***(a)*** *SiO_2 (wt. %) and* ***(b)*** *CO_2 (wt. %) of the SKG experimental melts.* ***(c)*** *Pressure (GPa) vs. molar Ca /(Ca + Mg) of the SKG experimental melts.* ***(d)*** *MgO (wt. %) vs. CaO (wt.%) of the SKG experimental clinopyroxenes. Dark-grey field: intermediate carbonate-silicate melts; light-grey field: silicate-dominated (basaltic-andesite) melts; black stippled line: carbonate-dominated melts from this study.*

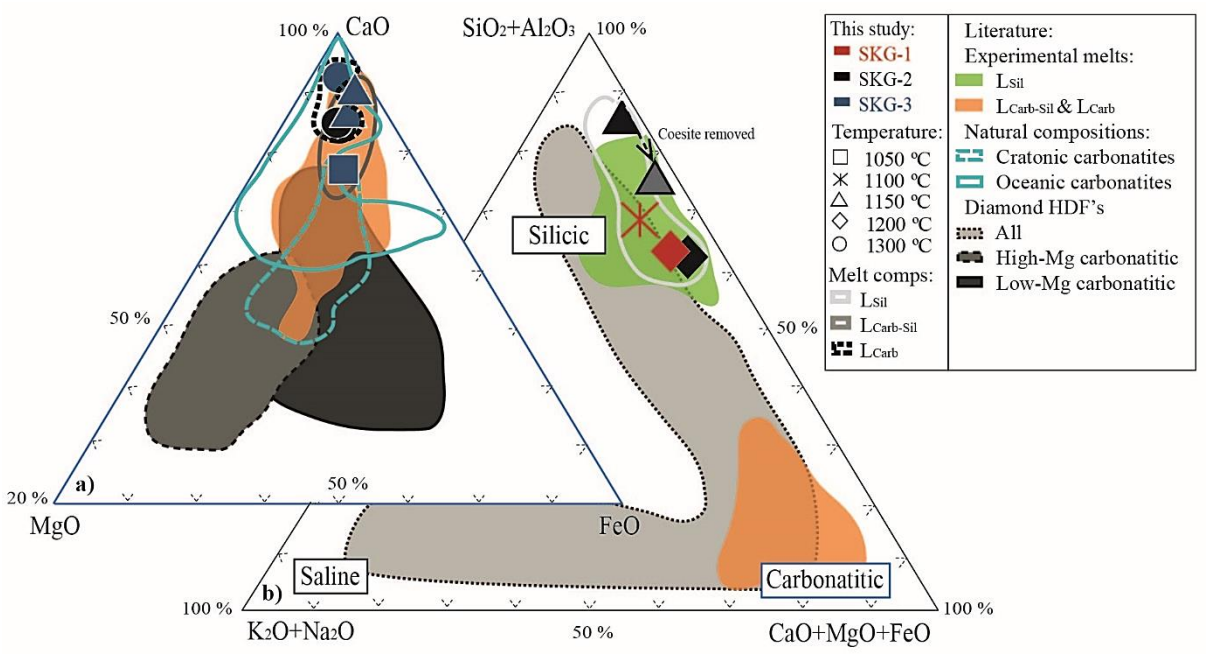

Fig. 5.6 *Ternary diagrams* ***(a)*** *and* ***(b)*** *showing the SKG experimental melt compositions in wt.%. Dashed arrows represent 10 % increments. For comparison on* ***(a)****: Orange field: intermediate carbonate-silicate and carbonate-dominated melts from CO_2-bearing eclogite experiments (Hammouda, 2003; Dasgupta et al., 2004, 2005; Yaxley and Brey, 2004; Kiseeva et al., 2012). Natural oceanic carbonatites from Hoernle et al. (2002) and Kogarko (1993). Natural cratonic carbonatites from Tappe et al. (2006). High-Mg carbonatitic-type HDF's from Klein-BenDavid et al. (2009); Low-Mg carbonatitic-type HDF's from Zedgenizov et al. (2009) and Weiss et al. (2009). For comparison on* ***(b)****:Orange field: intermediate carbonate-silicate and carbonate-dominated melts from CO_2-bearing eclogite experiments (Hammouda, 2003; Dasgupta et al., 2004, 2005; Yaxley and Brey, 2004; Kiseeva et al., 2012). Green field: silicate-dominated melts from CO_2-bearing eclogite experiments (Hammouda, 2003; Kiseeva et al., 2012). Diamond HDF compilation from Weiss et al. (2015).*

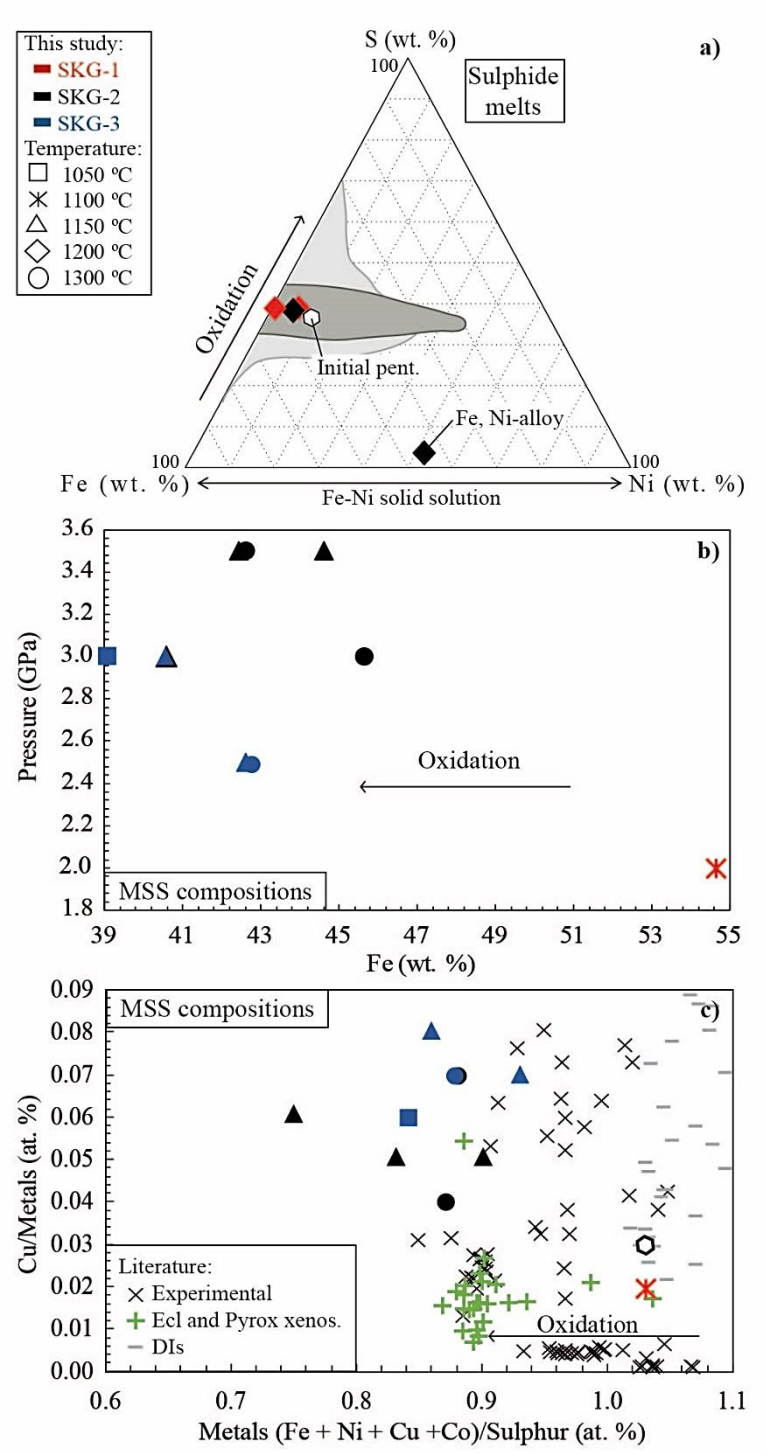

Fig. 5.7 (a) *Fe-Ni-S (wt. %) ternary diagram showing the experimentally produced sulphide melt compositions at 2.0 GPa and 1200 ºC. Also shown is the Fe, Ni, (Cu)-S alloy produced in exeriment SKG-1.2. Dark-grey field:Diamond sulphide inclusions from Alard et al. (2000) and Deines and Harris (1995). Light-grey field: mantle derived sulphides from eclogite and pyroxenite xenoliths (Aulbach et al., 2009; Gréau et al., 2013; Burness et al. in review), MORB (Roy-Barman et al., 1998; Patten et al., 2013) and OIB (Bennet et al., 2000) sources.* ***(b)*** *Experimentally produced MSS Fe (wt. %) composition vs. experimental pressure (GPa).* ***(c)*** *Metals (Fe+Ni+Cu+Co)/Sulphur (at. %) vs. Cu/Metals (at. %) of experimentally produced MSS. Shown for comparison: Experimentally produced MSS from Kiseeva and Wood (2013, 2015) and Liu et al. (2007), sulphide in eclogite and pyroxenite xenoliths from Aulbach et al. (2009), sulphide diamond inclusions from Aulbach et al. (2012). Arrows indicate the oxidation trend of the experimentally produced sulphide melts* ***(a)*** *and MSS* ***(b, c)***

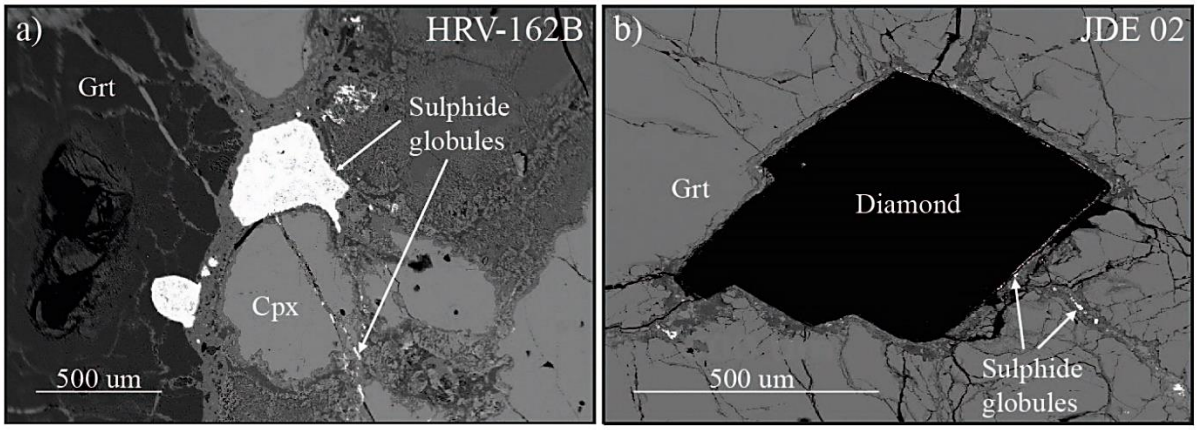

Fig. 5.8 (a) *Backscattered electron microprobe image of globular sulphides along spongy clinopyroxene grain boundaries as well as sulphide partially included within garnet of eclogite HRV-162B from Roberts Victor Kimberlite, South Africa.* ***(b)*** *Backscattered electron microprobe image of globular sulphide trails around a diamond inclusion within garnet of eclogite JDE 02 from Jericho Kimberlite, Canada (Smart et al., 2009).*

CHAPTER 6

6. CONCLUSIONS AND IMPLICATIONS

6.1. MAJOR FINDINGS

This study investigated the behaviour of sulphur and associated highly siderophile and chalcophile elements during mantle petrogenetic processes. Experiments conducted from 2 to 3.5 GPa and 1050 to 1300 ºC show that the critical factors concerning the mobility of sulphur in upper mantle eclogite are the degree of melting of the sulphur±carbon-bearing eclogite and the composition of the resulting melts. The sulphide solidus and liquidus curves lie between 1150 and 1200 ºC at 2 GPa within the CO_2-free SKG eclogite system, and the addition of up to 11.8 wt.% CO_2 to SKG does not seem to affect the melting systematics of sulphide at $\log fO_2$ < FMQ. Instead, the addition of CO_2 seems only to constrain carbonate±silicate melting at the pressure and temperature conditions investigated. Sulphur is best mobilised as immiscible sulphide liquid melt pools together with CO_2-free basaltic-andesite melts, and additionally, as dissolved elemental sulphur within intermediate carbonate-silicate melts at > 15 % partial melting of the sulphur±carbon-bearing eclogite compositions. These experimental results compare favourably with plentiful mantle xenolith evidence for local scale metasomatic enrichments of mantle eclogite by sulphur-bearing silicate-dominated melts as well as sulphur-bearing silica-undersaturated melts (e.g. Appleyard, 2000; Schmickler et al., 2004; Aulbach et al., 2009; Gréau et al., 2013), where sulphides are precipitated together with seconodary silicate minerals (e.g. clinopyroxene) or even carbonates (e.g. Ionov et al., 1992, 1996; Ionov, 1998).

Complementary investigations of Kaapvaal cratonic mantle-derived peridotite and eclogite xenoliths support these experimental findings by demonstrating that secondary sulphide precipitation is intimately linked to metasomatism of the host eclogite or peridotite silicate assemblage. The investigation of mantle xenoliths demonstrated that sulphide stability and geochemistry, especially PGE content, is largely dependent on the redox and chemical composition of the metasomatic melt/fluid. In Kaapvaal eclogite xenoliths, it was observed that two distinct types of metasomatism affected the shallower versus the deeper eclogites. The deeper eclogites were metasomatised by a relatively oxidising silica-undersaturated (perhaps proto-kimberlitic) fluid that precipitated minimal secondary clinopyroxene and associated sulphide. These sulphides display large fractionations between P-PGE and I-PGE and significant Pt depletions. The shallower eclogites were metasomatised by a basaltic-type melt that precipitated large proportions of secondary clinopyroxene and associated sulphide. In contrast to the deeper eclogite-derived sulphides, the shallower eclogite-derived sulphides display relatively "flat" chondrite normalised HSE patterns and sometimes Pd-enrichments. In Premier peridotite xenoliths, it was observed that a single pervasive Fe- and S-rich metasomatic agent affected both the shallower, low-temperature coarse lherzolites and the deeper, higher-temperature deformed lherzolites. The sulphides derived from Premier coarse lherzolites display similar HSE systematics to the "mid-

lithospheric" eclogite xenoliths, with large fractionations between P-PGE and I-PGE and significant Pd enrichments. This evidence suggests that mixed volatile (sulphur+carbon) melts can result in contrasting styles of metasomatism on interaction with upper mantle lithologies. Moreover, the precipitation of secondary silicate minerals plus sulphide to the metasomatised mantle lithology increases its fertility, and subsequent partial melting of these fertile lithologies may contribute to the S- and HSE-enrichment seen in some mantle derived magmas (Metrich and Clocchiatti, 1996; De Hoog et al., 2004; Jugo, 2009; Métrich and Mandeville, 2010).

6.1.1. Kaapvaal cratonic mantle eclogite petrogenesis with emphasis on the effects of S-bearing metasomatism

In Chapter 3, I investigated the geochemical, stable isotopic and petrologic characteristics of S-bearing mantle-derived eclogite and pyroxenite xenoliths from Kimberley (Kamfersdam), Roberts Victor, Jagersfontein, Swartruggens and Premier kimberlite occurrences on the Kaapvaal craton. The eclogite xenoliths have large compositional ranges that correspond to basaltic, picritic and gabbroic protolith compositions. They exhibit a wide range of garnet-clinopyroxene Fe-Mg exchange temperature (930 to 1251 °C) and pressure conditions (2.2 to 7.9 GPa) that correspond to a depth range of ~70 – 260 km. Most of the xenoliths display oxygen isotope compositions (see **Section 3.5.6**) from 5.6 to 10.4 ‰, which is higher than the mantle average (5.5 ± 0.4 ‰; Mattey et al., 1994). This combined with high Cs contents (up to 59 ppm), the occurrence of coesite and/or kyanite as well as positive Eu and Sr anomalies, suggests that many of the eclogites had low-pressure sea-water altered oceanic crustal protoliths (MacGregor and Manton, 1986; Pernet-Fisher et al., 2014; Riches et al., 2016), which were subsequently subducted and transported into the cratonic mantle lithosphere. The eclogite xenoliths show some depth correlations with silicate and sulphide mineral composition, as well as redox composition, prompting separation of the xenoliths into two distinct groups.

The first group is characterised by eclogites with lower "mid-lithospheric" equilibration conditions (<170 km) and calculated redox compositions equivalent to ambient peridotitic mantle (e.g. overlapping $\Delta \log f O_2$ with Kaapvaal peridotite xenoliths, see **Section 3.5.5**). This group of eclogites display notable evidence for both cryptic and modal metasomatism. The metasomatism resulted in the modal addition of significant secondary clinopyroxene and sulphide mineral phases as well as lesser phlogopite, and additionally, the eclogite whole-rock compositions show marked enrichments in both MgO and LREE. The sulphides display positively sloping chondrite-normalised HSE patterns and sometimes Pd-enrichments (**Section 3.5.7.5**). It is suggested that these "mid-lithospheric" eclogites were metasomatised by a S-rich metasomatic melt with a redox composition close to that of ambient mantle, such as melts produced during relatively large degrees of mantle melting, which would be relatively volatile-poor and likely basaltic to picritic in nature (Wood et al., 1990; Presnall et al., 2002). Such large-degree silicate melts are well established to have relatively "flat" HSE patterns (Alard et al., 2005;

Ireland et al., 2009; Fonseca et al., 2011; Day et al., 2013). Specific enrichment of basaltic/picritic components to the mid-lithospheric eclogites derived from kimberlites in the Kimberley area. suggested a possible link between the metasomatic fluids/melts affecting these eclogites and the geographically closely associated Karoo LIP magmas. Additionally, the eclogite xenolith sulphides and the Karoo mafic magmas have HSE affinities, with comparatively relatively "flat" chondrite normalised HSE patterns and similar I-PGE/P-PGE fractionations (Jourdan et al., 2007; Zhang et al., 2008). Therefore, it is suggested that there exists a petrogenetic link between the S-rich (and "basaltic") metasomatism of these mid-lithospheric eclogites and the Karoo LIP magmatism.

The second group of Kaapvaal eclogites is characterised by deeper equilibration conditions (>150 km) and relatively oxidised (e.g. 0.5 to 2 log units above ambient mantle conditions at equivalent depths; **Section 3.5.5**) redox compositions. These eclogites show marked whole-rock LREE depletions and contain far fewer sulphides than the mid-lithospheric eclogites. Importantly, the sulphides that are found in these depeer eclogites have relatively I-PGE-poor compositions, featuring high P-PGE/I-PGE fractionations and large Pt depletions (**Section 3.5.7.5**). It is suggested that metasomatism of the deepest eclogites involved a relatively oxidizing agent, possibly kimberlite-related, which added sulphides to the eclogites without imparting considerable incompatible-element enrichments to the silicate assemblage or the addition of significant secondary clinopyroxene or phlogopite. The sulphide HSE systematics (i.e. lower overall concentrations in PGE) support interaction with a oxidising agent probably generated by low degrees of partial melting (c.f. Delpech et al., 2012; Luguet et al., 2015; Luguet and Pearson, 2019), which are known to have relatively highly fractionated P-PGE/I-PGE contents (Maier et al., 2005; Tappe et al., 2017a).

The results from the eclogite silicate and sulphide investigations suggest that the Kaapvaal lithospheric mantle underwent a minimum of two distinct pulses of metasomatism. Importantly, the Fe- and S-rich basaltic melt metasomatism of the eclogites in the shallower parts of the cratonic mantle displayed similarities to the Karoo LIP magmas. Therefore, it is suggested that the metasomatism may be linked to large scale, location-specific magmatism, which has previously been shown to affect both the craton and the cratonic mantle lithosphere (Rehfeldt et al., 2008; Jacob et al., 2009; Giuliani et al., 2014). In contrast, metasomatism of the deeper equilibrated eclogites suggests interaction from percolating S-bearing silica-undersaturated melts, which are probably not linked to any specific large-scale magmatic event that affected both the lithospheric mantle and the craton.

6.1.2. Premier peridotite petrogenesis with emphasis on the effects of S-bearing metasomatism

In Chapter 4, I investigated the geochemical, stable isotopic and petrologic characteristics of sulphide-bearing peridotite xenoliths from the Premier kimberlite. The Premier garnet-bearing peridotites can be divided into low-temperature coarse lherzolite and high-temperature deformed

lherzolite varieties. The coarse lherzolites display a "cooler/shallower" narrow range in temperature (1010 – 1221 ºC) and pressure (3.4 – 4.4 GPa) conditions and the deformed lherzolites display a much larger and "warmer/deeper" range of temperatures (1144 – 1459 °C) and pressures (4.6 – 7.5 GPa). The low-temperature, coarse lherzolites show evidence of depletion and subsequent re-enrichment events. Initial depletion of the shallow coarse lherzolites is shown by minor depletions in Y and HREE in garnet, which probably resulted from the large scale melt extraction during craton formation that is well documented in Kaapvaal cratonic mantle peridoties (Walter, 1998; Carlson et al., 2005). Depleted geochemical signatures are also observed from some coarse-lherzolite clinopyroxene REE patterns that closely resemble depleted abyssal peridotite clinopyroxene (see **Section 4.5.1.2**; Johnson et al., 1990; Rampone et al., 1996). Subsequent re-fertilisation of the Premier coarse lherzolites is evidenced by the modal addition of secondary "spongy" clinopyroxene and sulphide (and associated magnetite) mineral phases, as well as the cryptic enrichment of garnet in basaltic components (e.g. Fe, Ca, Al) as well as Zr, Ti, and Sr and clinopyroxene in LREE. The high-temperature, deformed lherzolites do not show as clear evidence for a primary depletion event. Garnet in these peridotites exhibit flat HREE patterns and clinopyroxene show "normal" relatively LREE-enriched convex up patterns. The deeper lherzolites show less evidence for secondary clinopyroxene addition (coupled to secondary sulphide±magnetite), in addition to relatively high Fe contents that may have resulted from secondary "Fe-bearing" metasomatism. It is suggested that both the shallower-coarse and deeper-deformed lherzolites underwent metasomatism by a Fe-rich basaltic-type melt, perhaps related to mantle plume upwelling and the emplacement of the Bushveld Igneous Complex, a conclusion that has been made previously for Premier xenoliths and diamond inclusions (Danchin, 1979; Richardson and Shirey, 2008; Jacob et al., 2009).

Further investigation of the Premier peridotite base metal sulphides revealed a large range of compositions from both lherzolite groups. Unfortunately, due to the friability of most recovered sulphides, only pentlandite and pyrite grains from two coarse-lherzolites were measured for HSE (**Section 4.5.3.4**). The sulphide chondrite-normalised HSE patterns are positively sloped with fractionated P-PGE/I-PGE and significant Pd-enrichments, which overlap with the HSE patterns of evolved Cu-Ni-rich sulphides found as inclusions within metasomatic silicates or as intergranular blebs within other mantle peridotites (e.g. Alard et al., 2005; Luguet and Pearson, 2019). Moreover, both the HSE abundances and patterns of the Premier lherzolite-derived sulphides overlap with sulphides present in peridotite lithologies of the Bushveld Igneous Complex (Hutchinson and McDonald, 2008), the 2 Ga LIP through which the Premier kimberlite erupted. The similarity in Premier peridotite and ultramaifc Bushveld lithology sulphide HSE patterns may suggest a genetic link between S-bearing metasomatism of the north-central Kaapvaal cratonic mantle and the Bushveld magmatic event (e.g. Maier et al., 2005, 2012). Limited analyses of four sulphides from a single Premier coarse lherzolite show $\Delta^{33}S$ = -0.14 – +0.12 ‰ and $\delta^{34}S$ = -5.73 – -0.48 ± 0.08 ‰, which, albeit limited results, hint at the presence of a

recycled sulphur component (Farquhar et al., 2010; Penniston-Dorland et al., 2012; Giuliani et al., 2016). Comparison of the coarse-lherzolite multiple sulphur isotope compositions (i.e. non-zero $\Delta^{33}S$ and negative $\delta^{34}S$ values) with those of Bushveld peridotite-derived sulphides (i.e. non-zero $\Delta^{33}S$ and variable $\delta^{34}S$; Penniston-Dorland et al., 2012; Magalhães et al., 2018) could tentatively suggest that the source of the Bushveld sulphides may have been inherited from the cratonic mantle, but further peridotite sulphide analyses is necessary.

6.1.3. Sulphur±carbon-bearing eclogite experiments with emphasis on the mobility of sulphur/sulphide in the upper mantle

In Chapter 5, I investigated the partial melting behaviour and phase relations of a S±C-bearing MORB-like eclogite (SKG) at upper mantle pressures (2.0 – 3.5 GPa) and temperatures (1050 – 1300 ºC). All experiments formed variable proportions of garnet, clinopryxoene plus or minus coesite and sulphide as mono-sulphide solid solution. The experimental results show that silicate-dominated basaltic-andesite melts, generated during high-degree (up to 60%) alkali-fluxed partial melting of both the CO_2-free and CO_2-bearing MORB-like eclogite, mobilise sulphur as an immiscible sulphide liquid within the "siliceous" partial melts. The silicate-dominated melts importantly contain >50 wt. % SiO_2 and 2.9 – 8.4 wt. % FeO, and have dihedral angles <60º, while the sulphide liquid formed rounded, globular, isolated pools. The intermediate carbonate±silicate melts (with dihedral angles of 30 to 60º) are produced at ~15 % partial melting of the CO_2-bearing MORB-like eclogite. Importantly, these melts contain 4.5 – 12.4 wt.% SiO_2, 2.8 – 4.5 wt.% FeO and 43 – 47 wt. % CO_2 as well as up to 0.3 wt.% dissolved elemental sulphur. At much lower degrees of partial melting (<6 %) carbonate-dominated (calcic carbonatite-type) melts do not contain measurable sulphide liquid or dissolved elemental sulphur, and instead MSS is stable within the eclogite silicate residuum. Moreover, these carbonate-dominated melts contain <2.4 wt.% SiO_2, 2.1 – 4.2 wt.% FeO and 42 – 53 wt.% CO_2 and have very low dihedral angles (<30 º).

Therefore, these experiments demonstrate that the carbonatitic melts are S-free but, as recognized in previous work (e.g Harte et al., 1993), would readily form an interconnected metasomatic network within the upper mantle. In contrast, the more silciate-dominated compositions (basaltic-andesite and intermediate carbonate-silicate), although they can carry a sulphur load, may be relatively less mobile within the upper mantle due to their larger (30 – 60º) dihedral angles. The degree of partial melting in the sulphur±carbon-bearing eclogite system largely governs the character of the partial melt produced, which then further affects the potential mobility of sulphur or sulphide at upper mantle pressure and temperature conditions. Specifically, sulphur is best mobilised by the basaltic-andesite and intermediate carbonate-silicate melts because of the presence Si and importantly Fe, which are prominent network-forming cations (Moussallam et al., 2016). That is, these cations are present in critical quantalities that can therefore ensure enough open sites to which sulphur can bond. Thus, transport of sulphur within

the upper mantle seems to critically involve support from mixed carbonate±silicate melts during moderate degrees of partial melting of basaltic lithologies.

6.2. SUMMARY AND FUTURE DIRECTIONS

We can demonstrate from both the mantle xenolith and experimental research presented here that sulphur is a key volatile in tracing mantle petrogenetic processes. The nature of metasomatism of the cratonic lithospheric mantle, with links to the cratonic crusts evolutionary history, has long been investigated (e.g. Davis et al., 2003; Griffin et al., 2003; Schmitz et al., 2004; Rollinson, 2010). But, sulphur with its affinity for the non-silicate minerals and HSE elements can provide further constrains on evaluating the evolution of the CLM (e.g. Alard et al., 2000, 2005; Lorand and Grégoire, 2006; Lorand et al., 2013; Luguet and Pearson, 2019). Importantly, the cratonic lithospheric mantle with its sulphur budget and HSE load has been implicated as a potential source of mantle-derived magmas that eventually supply crustal ortho-magmatic deposits through the deep sulphur cycle (Alt et al., 2012; Ding and Dasgupta, 2017, 2018).

The experiments of this study specifically highlight that pure sulphide melt is largely immobile within the MORB-eclogite system at the temperatures and pressures investigated unless aided by more fluid-mobile carbonate±silicate melts. This lack of mobility of sulphide melt is supported by the 'nugget effect' of sulphides in CLM-derived eclogite xenoliths (Aulbach et al., 2009a; Smart et al., 2009; Gréau et al., 2013).The restriction of sulphur mobility to silicate-dominated or intermediate carbonate-silicate melts, correlates with investigations of cratonic mantle-derived peridotite and eclogite xenoliths that demonstrate that the metasomatic addition of sulphide is closely linked to metasomatism of the silicate assemblage. Moreover, these types of melts are often cited as potential metasomatic agents of the CLM and can be linked to several important lithosphere enrichment processes. For example, enrichment of the CLM in sulphur and HSEs provides a fertile source for S±C-rich mantle magmatism (e.g. sulphur-rich OIB/MORB; De Hoog et al., 2004; Jugo, 2009) or even the transport of sulphur and highly siderophile elements (i.e. economic metals; Fleet et al., 1996; Li and Audétat, 2012; Griffin et al., 2013) to the surface during mantle-derived magmatic ore generation processes. In this study, chemical similarities were found between the metasomatic signatures of the Premier peridotites including their sulphides and Bushveld magmas. Attempts to use sulphur isotopes to further trace links between the metasomatic agent and Bushveld magmas was not entirely successful due to analytical challenges. However, there was some overlap in non-zero $\Delta^{33}S$ and $\delta^{34}S$ values between the coarse-lherzolite sulphides and sulphides from the Bushveld. Still, the sulphur isotopic characteristics of the coarse Premier peridotite sulphides demonstrated that there may be a recycled crustal sulphur component in the CLM-derived metasomatic fluids (Farquhar et al., 2002, 2010; Giuliani et al., 2016). Yet, the paucity of data largely restricts further interpretations of this process.

Sulphur-induced diamond formation may also stem from sulphide acting as a reducing agent for CO_2-rich fluids at upper mantle conditions within the diamond stability field (e.g. Palyanov et al., 2007, 2009). The exaggerated abundance of sulphide-bearing diamonds at some kimberlite localities have prompted them to be considered a separate diamond petrogenetic group (S-type), and many diamond fluid inclusion studies suggest that these diamonds probably precipitated from S-bearing carbonatitic-type fluids (e.g. Cartigny et al., 2009; Thomassot et al., 2009; Weiss et al., 2009). Conversely, our experimental studies show that more silicic "intermediate" melts/fluids are needed to move sulphur within a MORB-eclogite system and therefore, additional experiments within the diamond stability field are needed to remedy this ambiguity.

Our investigations as well as other studies (e.g. Jugo et al., 2005; Luguet et al., 2007; Alard et al., 2011; Luguet and Pearson, 2019) demonstrate that sulphide is extremely redox sensitive. Given that the peridotite dominated upper mantle becomes increasingly more reduced with depth (Woodland and Koch, 2003), it would be pertinent to conduct S±C-bearing peridotite and eclogite experiments under more reducing conditions in order to assess the potential effectiveness of this melting on sulphur mobility. Additionally, the experiments of this study also show that sulphur dissolution within various intermediate eclogite-derived melt compositions relies heavily on the presence of Si and Fe as "network-forming" cations. Therefore, it is suggested that similar mixed volatile experiments be conducted on peridotitic bulk rock compositions because they will most probably present larger quantities of these cations to bond with sulphur, as shown by peridotite-derived Mg, Fe-rich carbonatites that are better represented in nature than the calcic carbonatites produced in this study. Peridotite is also the dominant mantle source rock of the most abundant mantle-derived magmatism on Earth (e.g. MORB and OIB; Green et al., 1987; Hirschmann et al., 2003). Therefore, the mixed (carbon+sulphur) volatile-bearing peridotite experiments will be imperative to a better understanding of the contribution that sulphur and carbon-bearing petrogenetic processes play in the chemical evolution of the mantle.

REFERENCES

Alard, O., Griffin, W. L., Lorand, J. P., Jackson, S. E. and O'Reilly, S. Y. (2000). Non-chondritic distribution of the highly siderophile elements in mantle sulphides. Nature **407**(6806), 891.

Alard, O., Lorand, J. P., Reisberg, L., Bodinier, J. L., Dautria, J. M. and O'Reilly, S. Y. (2011). Volatile-rich metasomatism in Montferrier xenoliths (Southern France): Implications for the abundances of chalcophile and highly siderophile elements in the subcontinental mantle. Journal of Petrology **52**(10), 2009-2045.

Alard, O., Luguet, A., Pearson, N.J., Griffin, W.L., Lorand, J.P., Gannoun, A., Burton, K.W. and O'Reilly, S.Y. (2005.) In situ Os isotopes in abyssal peridotites bridge the isotopic gap between MORBs and their source mantle. Nature **436**(7053), 1005.

Alt, J.C., Garrido, C.J., Shanks III, W.C., Turchyn, A., Padrón-Navarta, J.A., Sánchez-Vizcaíno, V.L., Pugnaire, M.T.G. and Marchesi, C. (2012). Recycling of water, carbon, and sulfur during subduction of serpentinites: A stable isotope study of Cerro del Almirez, Spain. Earth and Planetary Science Letters **327**, 50-60.

Appleyard, C. M. (2000). The geochemistry of a suite of eclogite xenoliths from the Rietfontein Kimberlite, South Africa (unpublished doctoral dissertation, University of Cape Town).

Aulbach, S., Creaser, R. A., Pearson, N. J., Simonetti, S. S., Heaman, L. M., Griffin, W. L. and Stachel, T. (2009). Sulfide and whole rock Re–Os systematics of eclogite and pyroxenite xenoliths from the Slave Craton, Canada. Earth and Planetary Science Letters **283**(1-4), 48-58.

Carlson, R. W., Pearson, D. G. and James, D. E. (2005). Physical, chemical, and chronological characteristics of continental mantle. Reviews of Geophysics **43**(1).

Cartigny, P., Farquhar, J., Thomassot, E., Harris, J.W., Wing, B., Masterson, A., McKeegan, K. and Stachel, T. (2009). A mantle origin for Paleoarchean peridotitic diamonds from the Panda kimberlite, Slave Craton: evidence from ^{13}C-, ^{15}N-and $^{33, 34}S$-stable isotope systematics. Lithos **112**, pp.852-864.

Danchin, R. V. (1979). Mineral and bulk chemistry of garnet lherzolite and garnet harzburgite xenoliths from the Premier Mine, South Africa. The Mantle Sample: Inclusion in Kimberlites and Other Volcanics **16**, 104-126.

Davis, W. J., Jones, A. G., Bleeker, W. and Grütter, H. (2003). Lithosphere development in the Slave craton: a linked crustal and mantle perspective. Lithos **71**(2-4), 575-589.

Day, J. M., Pearson, D. G. and Hulbert, L. J. (2013). Highly siderophile element behaviour during flood basalt genesis and evidence for melts from intrusive chromitite formation in the

Mackenzie large igneous province. Lithos **182**, 242-258.

De Hoog, J. C. M., Hattori, K. H. and Hoblitt, R. P. (2004). Oxidized sulfur-rich mafic magma at Mount Pinatubo, Philippines. Contributions to Mineralogy and Petrology **146**(6), 750-761.

Delpech, G., Lorand, J. P., Grégoire, M., Cottin, J. Y. and O'Reilly, S. Y. (2012). In-situ geochemistry of sulfides in highly metasomatized mantle xenoliths from Kerguelen, southern Indian Ocean. Lithos **154**, 296-314.

Ding, S. and Dasgupta, R. (2017). The fate of sulfide during decompression melting of peridotite–implications for sulfur inventory of the MORB-source depleted upper mantle. Earth and Planetary Science Letters **459**, 183-195.

Ding, S. and Dasgupta, R. (2018). Sulfur inventory of ocean island basalt source regions constrained by modeling the fate of sulfide during decompression melting of a heterogeneous mantle. Journal of Petrology **59**(7), 1281-1308.

Farquhar, J., Wing, B. A., McKeegan, K. D., Harris, J. W., Cartigny, P. and Thiemens, M. H. (2002). Mass-independent sulfur of inclusions in diamond and sulfur recycling on early Earth. Science **298**(5602), 2369-2372.

Farquhar, J., Wu, N., Canfield, D. E. and Oduro, H. (2010). Connections between sulfur cycle evolution, sulfur isotopes, sediments, and base metal sulfide deposits. Economic Geology **105**(3), 509-533.

Fleet, M. E., Crocket, J. H. and Stone, W. E. (1996). Partitioning of platinum-group elements (Os, Ir, Ru, Pt, Pd) and gold between sulfide liquid and basalt melt. Geochimica et Cosmochimica Acta **60**(13), 2397-2412.

Fonseca, R. O., Mallmann, G., O'Neill, H. S. C., Campbell, I. H. and Laurenz, V. (2011). Solubility of Os and Ir in sulfide melt: Implications for Re/Os fractionation during mantle melting. Earth and Planetary Science Letters **311**(3-4), 339-350.

Gaetani, G. A. and Grove, T. L. (1999). Wetting of mantle olivine by sulfide melt: implications for Re/Os ratios in mantle peridotite and late-stage core formation. Earth and Planetary Science Letters **169**(1-2), 147-163.

Giuliani, A., Fiorentini, M. L., Martin, L. A., Farquhar, J., Phillips, D., Griffin, W. L. and LaFlamme, C. (2016). Sulfur isotope composition of metasomatised mantle xenoliths from the Bultfontein kimberlite (Kimberley, South Africa): Contribution from subducted sediments and the effect of sulfide alteration on S isotope systematics. Earth and Planetary Science Letters **445**, 114-124.

Giuliani, A., Phillips, D., Maas, R., Woodhead, J.D., Kendrick, M.A., Greig, A., Armstrong, R.A.,

Chew, D., Kamenetsky, V.S. and Fiorentini, M.L. (2014). LIMA U–Pb ages link lithospheric mantle metasomatism to Karoo magmatism beneath the Kimberley region, South Africa. Earth and Planetary Science Letters **401**, 132-147.

Gréau, Y., Alard, O., Griffin, W. L., Huang, J. X. and O'Reilly, S. Y. (2013). Sulfides and chalcophile elements in Roberts Victor eclogites: unravelling a sulfide-rich metasomatic event. Chemical Geology **354**, 73-92.

Green, D. H., Falloon, T. J. and Taylor, W. R. (1987). Mantle-derived magmas-roles of variable source peridotite and variable CHO fluid compositions. In: Magmatic Processes: Physicochemical Principles, Mysen, B.O., (ed.). Geochemical Society, Specical Publication **1**, London, 139–63.

Griffin, W. L., Begg, G. C. and O'reilly, S. Y. (2013). Continental-root control on the genesis of magmatic ore deposits. Nature Geoscience **6**(11), 905.

Griffin, W. L., O'Reilly, S. Y., Natapov, L. M. and Ryan, C. G. (2003). The evolution of lithospheric mantle beneath the Kalahari Craton and its margins. Lithos **71**(2-4), 215-241.

Harte, B., Hunter, R. H. and Kinny, P. D. (1993). Melt geometry, movement and crystallization, in relation to mantle dykes, veins and metasomatism. Philosophical Transactions of the Royal Society of London. Series A: Physical and Engineering Sciences **342**(1663), 1-21.

Hirschmann, M. M., Kogiso, T., Baker, M. B. and Stolper, E. M. (2003). Alkalic magmas generated by partial melting of garnet pyroxenite. Geology **31**(6), 481-484.

Hutchinson, D. and McDonald, I. (2008). Laser ablation ICP-MS study of platinum-group elements in sulphides from the Platreef at Turfspruit, northern limb of the Bushveld Complex, South Africa. Mineralium Deposita **43**(6), 695.

Ionov, D. (1998). Trace element composition of mantle-derived carbonates and coexisting phasesin peridotite xenoliths from alkali basalts. Journal of Petrology **39**(11-12), 1931-1941.

Ionov, D. A., Hoefs, J., Wedepohl, K. H. and Wiechert, U. (1992). Content and isotopic composition of sulphur in ultramafic xenoliths from central Asia. Earth and Planetary Science Letters **111**(2-4), 269-286.

Ionov, D. A., O'Reilly, S. Y., Genshaft, Y. S. and Kopylova, M. G. (1996). Carbonate-bearing mantle peridotite xenoliths from Spitsbergen: phase relationships, mineral compositions and trace-element residence. Contributions to Mineralogy and Petrology **125**(4), 375-392.

Ireland, T. J., Walker, R. J. and Garcia, M. O. (2009). Highly siderophile element and ^{187}Os isotope systematics of Hawaiian picrites: implications for parental melt composition and source

heterogeneity. Chemical Geology **260**(1-2), 112-128.

Jacob, D. E., Viljoen, K. S. and Grassineau, N. V. (2009). Eclogite xenoliths from Kimberley, South Africa: a case study of mantle metasomatism in eclogites. Lithos **112**, 1002-1013.

Johnson, K. T., Dick, H. J. and Shimizu, N. (1990). Melting in the oceanic upper mantle: an ion microprobe study of diopsides in abyssal peridotites. Journal of Geophysical Research: Solid Earth **95**(B3), 2661-2678.

Jourdan, F., Féraud, G., Bertrand, H., Watkeys, M. K. and Renne, P. R. (2007). Distinct brief major events in the Karoo large igneous province clarified by new 40Ar/39Ar ages on the Lesotho basalts. Lithos **98**(1-4), 195-209.

Jugo, P. J. (2009). Sulfur content at sulfide saturation in oxidized magmas. Geology **37**(5), 415-418.

Jugo, P. J., Luth, R. W. and Richards, J. P. (2005). Experimental data on the speciation of sulfur as a function of oxygen fugacity in basaltic melts. Geochimica et Cosmochimica Acta **69**(2), 497-503.

Lee, C. T. A. (2006). Geochemical/petrologic constraints on the origin of cratonic mantle. Geophysical monograph **164**, 89-114.

Li, Y. and Audétat, A. (2012). Partitioning of V, Mn, Co, Ni, Cu, Zn, As, Mo, Ag, Sn, Sb, W, Au, Pb, and Bi between sulfide phases and hydrous basanite melt at upper mantle conditions. Earth and Planetary Science Letters **355**, 327-340.

Lorand, J. P.and Gregoire, M. (2006). Petrogenesis of base metal sulphide assemblages of some peridotites from the Kaapvaal craton (South Africa). Contributions to Mineralogy and Petrology **151**(5), 521.

Lorand, J. P., Luguet, A. and Alard, O. (2013). Platinum-group element systematics and petrogenetic processing of the continental upper mantle: A review. Lithos **164**, 2-21.

Luguet, A., Behrens, M., Pearson, D. G., König, S. and Herwartz, D. (2015). Significance of the whole rock Re–Os ages in cryptically and modally metasomatised cratonic peridotites: Constraints from HSE–Se–Te systematics. Geochimica et Cosmochimica Acta **164**, 441-463.

Luguet, A., and Pearson, G. (2019). Dating mantle peridotites using Re-Os isotopes: The complex message from whole rocks, base metal sulfides, and platinum group minerals. American Mineralogist: Journal of Earth and Planetary Materials **104**(2), 165-189.

Luguet, A., Shirey, S. B., Lorand, J. P., Horan, M. F. and Carlson, R. W. (2007). Residual platinum-group minerals from highly depleted harzburgites of the Lherz massif (France) and their role in HSE fractionation of the mantle. Geochimica et Cosmochimica Acta **71**(12), 3082-3097.

MacGregor, I. D. and Manton, W. I. (1986). Roberts Victor eclogites: ancient oceanic crust. Journal of Geophysical Research: Solid Earth **91**(B14), 14063-14079.

Magalhães, N., Penniston-Dorland, S., Farquhar, J. and Mathez, E. A. (2018). Variable sulfur isotope composition of sulfides provide evidence for multiple sources of contamination in the Rustenburg Layered Suite, Bushveld Complex. Earth and Planetary Science Letters **492**, 163-173.

Maier, W. D., Peltonen, P., Juvonen, R. and Pienaar, C. (2005). Platinum-group elements in peridotite xenoliths and kimberlite from the Premier kimberlite pipe, South Africa. South African Journal of Geology **108**(3), 413-428.

Maier, W. D., Peltonen, P., McDonald, I., Barnes, S. J., Barnes, S. J., Hatton, C. and Viljoen, F. (2012). The concentration of platinum-group elements and gold in southern African and Karelian kimberlite-hosted mantle xenoliths: implications for the noble metal content of the Earth's mantle. Chemical Geology **302**, 119-135.

Mandeville, C. W. (2010). Sulfur: A ubiquitous and useful tracer in Earth and planetary sciences. Elements 6(2), 75-80.

Mattey, D., Lowry, D. and Macpherson, C. (1994). Oxygen isotope composition of mantle peridotite. Earth and Planetary Science Letters **128**(3-4), 231-241.

Metrich, N. and Clocchiatti, R. (1996). Sulfur abundance and its speciation in oxidized alkaline melts. Geochimica et Cosmochimica Acta **60**(21), 4151-4160.

Moussallam, Y., Florian, P., Corradini, D., Morizet, Y., Sator, N., Vuilleumier, R., Guillot, B., Iacono-Marziano, G., Schmidt, B.C. and Gaillard, F. (2016). The molecular structure of melts along the carbonatite–kimberlite–basalt compositional joint: CO_2 and polymerisation. Earth and Planetary Science Letters **434**, 129-140.

Palyanov, Y. N., Borzdov, Y. M., Bataleva, Y. V., Sokol, A. G., Palyanova, G. A. and Kupriyanov, I. N. (2007). Reducing role of sulfides and diamond formation in the Earth's mantle. Earth and Planetary Science Letters **260**(1-2), 242-256.

Palyanov, Y. N., Kupriyanov, I. N., Borzdov, Y. M., Sokol, A. G. and Khokhryakov, A. F. (2009). Diamond crystallization from a sulfur− carbon system at HPHT conditions. Crystal Growth and Design **9**(6), 2922-2926.

Penniston-Dorland, S. C., Mathez, E. A., Wing, B. A., Farquhar, J. and Kinnaird, J. A. (2012). Multiple sulfur isotope evidence for surface-derived sulfur in the Bushveld Complex. Earth and Planetary Science Letters **337**, 236-242.

Pernet-Fisher, J.F., Howarth, G.H., Liu, Y., Barry, P.H., Carmody, L., Valley, J.W., Bodnar, R.J., Spetsius, Z.V. and Taylor, L.A. (2014). Komsomolskaya diamondiferous eclogites: evidence for oceanic crustal protoliths. Contributions to Mineralogy and Petrology **167**(3), p.981.

Presnall, D. C., Gudfinnsson, G. H. and Walter, M. J. (2002). Generation of mid-ocean ridge basalts at pressures from 1 to 7 GPa. Geochimica et Cosmochimica Acta **66**(12), 2073-2090.

Rampone, E., Hofmann, A. W., Piccardo, G. B., Vannucci, R., Bottazzi, P. and Ottolini, L. (1996). Trace element and isotope geochemistry of depleted peridotites from an N-MORB type ophiolite (Internal Liguride, N. Italy). Contributions to Mineralogy and Petrology **123**(1), 61-76.

Rehfeldt, T., Foley, S. F., Jacob, D. E., Carlson, R. W. and Lowry, D. (2008). Contrasting types of metasomatism in dunite, wehrlite and websterite xenoliths from Kimberley, South Africa. Geochimica et Cosmochimica Acta **72**(23), 5722-5756.

Richardson, S. H. and Shirey, S. B. (2008). Continental mantle signature of Bushveld magmas and coeval diamonds. Nature **453**(7197), 910.

Riches, A.J.V., Ickert, R.B., Pearson, D.G., Stern, R.A., Jackson, S.E., Ishikawa, A., Kjarsgaard, B.A. and Gurney, J.J. (2016). In situ oxygen-isotope, major-, and trace-element constraints on the metasomatic modification and crustal origin of a diamondiferous eclogite from Roberts Victor, Kaapvaal Craton. Geochimica et Cosmochimica Acta **174**, pp.345-359.

Rollinson, H. (2010). Coupled evolution of Archean continental crust and subcontinental lithospheric mantle. Geology **38**(12), 1083-1086.

Schmickler, B., Jacob, D. E. and Foley, S. F. (2004). Eclogite xenoliths from the Kuruman kimberlites, South Africa: geochemical fingerprinting of deep subduction and cumulate processes. Lithos **75**(1-2), 173-207.

Schmitz, M. D., Bowring, S. A., de Wit, M. J. and Gartz, V. (2004). Subduction and terrane collision stabilize the western Kaapvaal craton tectosphere 2.9 billion years ago. Earth and Planetary Science Letters **222**(2), 363-376.

Smart, K. A., Cartigny, P., Tappe, S., O'Brien, H. and Klemme, S. (2017). Lithospheric diamond formation as a consequence of methane-rich volatile flooding: An example from diamondiferous eclogite xenoliths of the Karelian craton (Finland). Geochimica et Cosmochimica Acta **206**, 312-342.

Smart, K. A., Heaman, L. M., Chacko, T., Simonetti, A., Kopylova, M., Mah, D. and Daniels, D. (2009). The origin of high-MgO diamond eclogites from the Jericho Kimberlite, Canada. Earth and Planetary Science Letters **284**(3-4), 527-537.

Tappe, S., Brand, N.B., Stracke, A., van Acken, D., Liu, C.Z., Strauss, H., Wu, F.Y., Luguet, A. and Mitchell, R.H. (2017). Plates or plumes in the origin of kimberlites: U/Pb perovskite and Sr-Nd-Hf-Os-CO isotope constraints from the Superior craton (Canada). Chemical Geology **455**, pp.57-83.

Thomassot, E., Cartigny, P., Harris, J. W., Lorand, J. P., Rollion-Bard, C. and Chaussidon, M. (2009). Metasomatic diamond growth: A multi-isotope study (^{13}C, ^{15}N, ^{33}S, ^{34}S) of sulphide inclusions and their host diamonds from Jwaneng (Botswana). Earth and Planetary Science Letters **282**(1-4), 79-90.

Walter, M. J. (1998). Melting of garnet peridotite and the origin of komatiite and depleted lithosphere. Journal of Petrology **39**(1), 29-60.

Weiss, Y., Kessel, R., Griffin, W.L., Kiflawi, I., Klein-BenDavid, O., Bell, D.R., Harris, J.W. and Navon, O. (2009). A new model for the evolution of diamond-forming fluids: Evidence from microinclusion-bearing diamonds from Kankan, Guinea. Lithos **112**, pp.660-674.

Wilson, A. H., Shirey, S. B. and Carlson, R. W. (2003). Archaean ultra-depleted komatiites formed by hydrous melting of cratonic mantle. Nature **423**(6942), 858.

Wood, B. J., Bryndzia, L. T. and Johnson, K. E. (1990). Mantle oxidation state and its relationship to tectonic environment and fluid speciation. Science **248**(4953), 337-345.

Woodland, A. B. and Koch, M. (2003). Variation in oxygen fugacity with depth in the upper mantle beneath the Kaapvaal craton, Southern Africa. Earth and Planetary Science Letters **214(**1-2), 295-310.

Zhang, M., O'Reilly, S. Y., Wang, K. L., Hronsky, J. and Griffin, W. L. (2008). Flood basalts and metallogeny: the lithospheric mantle connection. Earth-Science Reviews **86**(1-4), 145-174.

APPENDICES

ADDITIONAL DATA: MULTIPLE SULPHUR ISOTOPES

MULTIPLE SULPHUR ISOTOPE COMPOSITIONS OF KAAPVAAL XENOLITH-HOSTED SULPHIDES

Multiple sulphur isotopes are effective tools to trace the presence of recycled sedimentary material in the mantle. Due to the differences in "mantle" vs. "crustal" S isotope signatures, the presence of sedimentary material can be evaluated in mantle-derived magmas (e.g. OIB; Labidi et al., 2014) and diamond formation fluids (e.g. Cartigny et al., 2009; Thomassot et al., 2009). Importantly, a combination of measured $\delta^{32}S$, $\delta^{33}S$, $\delta^{34}S$ and $\delta^{36}S$ can in particular be used to trace the presence of Archean sedimentary material in mantle-derived materials, due to the mass-independent sulphur isotope fractionation (S-MIF) of surficial material that occurred during the Archean in response to the activity of UV radiation in the absence of a modern atmosphere (Thomassot et al., 2015). Thus, non-zero $\Delta^{33}S$ values ($\Delta^{33}S \sim 0$ for all mass-dependent S isotope fractionation) can be used to clearly indicate the presence of recycled Archean sedimentary sulphur in the geologic rock record.

Twenty-one (21) sulphide grains were investigated from eight eclogite xenoliths and one peridotite xenolith from the Roberts Victor, Jagersfontein and Premier kimberlites located on the Kaapvaal craton, South Africa. Sulphides were extracted from the xenoliths and analyzed for major element composition (S, Fe, Cu, Ni, Co, O; **Fig. 1**), including element mapping, using a Zeiss EVO MA15VP scanning electron microprobe at the Central Analytical Facility (CAF) of Stellenbosch University, South Africa. Only sulphides that demonstrated low levels of oxidation and alteration were included in this study. The sulphides analyzed in this study include penlandite, chalcopyrite and pyrite. Samples were then mounted in indium rings and coated with gold for the multiple sulphur isotope determinations (^{32}S, ^{33}S, ^{34}S, ^{36}S) using the Cameca IMS 1270 ion microprobe at CNRS (Nancy) in August 2018.

The resulting $\delta^{34}S$ values for the Kaapvaal eclogites range from -5.7 to +29 ‰ (**Table 1; Fig. 2**). Most sulphides from the eclogites have values that cluster between 0 to +3.5‰, but sulphides from the Jagersfontein eclogite JJG-2929 have isotopically more depleted S isotope compositions of -2.6 to -3.9 ±0.08‰. Importantly, sulphides from Roberts Victor eclogite MBK have extremely enriched ^{34}S isotope compositions with $\delta^{34}S$ values from +13 to +29 ±0.006 ‰. The $\Delta^{33}S$ values for all eclogite samples vary between -0.3 and +0.2‰. Sulphides from the Premier peridotite xenolith have $\delta^{34}S$ values between -5.7 and -0.5 ±0.08‰, with $\Delta^{33}S$ values between -0.1 and +0.1‰.

Preliminary interpretations of this data suggest that most eclogite-hosted sulphide from the previously studied (see **Chapter 3**) Kaapvaal eclogites show some slight depletion (Roberts Victor HRV-174A; -5.7 ‰; Jagersfontein JJG-2919 -2.6 to -3.9‰) and enrichment (most samples; up to +3.5) compared to the accepted ^{34}S isotope composition of the mantle (~0.5‰; Chaudisson et al., 1989). This

variation observed in the eclogite samples may be ascribed to input from recycled crustal material, however, the variation also falls close to the range shown by MORB (~-2 to +1 ‰; Labidi et al., 2012; 2014), such that some of the eclogite sulphide $\delta^{34}S$ variation may simply reflect the natural sulphur isotope variation present in the depleted mantle. However, of note, sulphides from Roberts Victor eclogite MBK show extremely enriched sulphur isotope compositions with $\delta^{34}S$ values between +13 to +29‰, which clearly must involve a recycled (sedimentary) component.

Previous studies on Kaapvaal-Zimbabwe sulphide diamond inclusions reveal an Archean sedimentary component due to non-zero $\Delta^{33}S$ values (e.g. Thomassot et al., 2009; Farquar et al., 2002). In this study we find no evidence of a mass-independent sulphur isotope signature that would indicate Archean sedimentary sulphur. The $\Delta^{33}S$ values from all measured sulphides fall between -0.29 and +0.2‰, which is essentially within uncertainty of the expected sulphur mass-dependent fractionation ($\Delta^{33}S$~0 ‰; **Figure. 2**). Thus, while a recycled sulphur component is clearly necessary in the formation of some Kaapvaal eclogitic sulphides, this component does not necessarily need to be Archean and may relate to the metasomatic mobilization of younger (post-Archean) sedimentary materials.

REFERENCES

Cartigny, P., Farquhar, J., Thomassot, E., Harris, J.W., Wing, B., Masterson, A., McKeegan, K. and Stachel, T. (2009). A mantle origin for Paleoarchean peridotitic diamonds from the Panda kimberlite, Slave Craton: evidence from 13C-, 15N-and 33, 34S-stable isotope systematics. Lithos **112**, 852-864.

Chaussidon, M., Albarède, F. and Sheppard, S. M. (1989). Sulphur isotope variations in the mantle from ion microprobe analyses of micro-sulphide inclusions. Earth and Planetary Science Letters **92**(2), 144-156.

Farquhar, J., Wing, B. A., McKeegan, K. D., Harris, J. W., Cartigny, P. and Thiemens, M. H. (2002). Mass-independent sulfur of inclusions in diamond and sulfur recycling on early Earth. Science **298**(5602), 2369-2372.

Labidi, J., Cartigny, P., Birck, J. L., Assayag, N. and Bourrand, J. J. (2012). Determination of multiple sulfur isotopes in glasses: A reappraisal of the MORB $\delta^{34}S$. Chemical Geology **334**, 189-198.

Labidi, J., Cartigny, P., Hamelin, C., Moreira, M. and Dosso, L. (2014). Sulfur isotope budget (^{32}S, ^{33}S, ^{34}S and ^{36}S) in Pacific–Antarctic ridge basalts: A record of mantle source heterogeneity and hydrothermal sulfide assimilation. Geochimica et Cosmochimica Acta **133**, 47-67.

Thomassot, E., Cartigny, P., Harris, J. W., Lorand, J. P., Rollion-Bard, C. and Chaussidon, M. (2009). Metasomatic diamond growth: A multi-isotope study (^{13}C, ^{15}N, ^{33}S, ^{34}S) of sulphide inclusions and their host diamonds from Jwaneng (Botswana). Earth and Planetary Science Letters **282**(1-4), 79-90.

Thomassot, E., O'Neil, J., Francis, D., Cartigny, P. and Wing, B. A. (2015). Atmospheric record in the Hadean Eon from multiple sulfur isotope measurements in Nuvvuagittuq Greenstone Belt (Nunavik, Quebec). Proceedings of the National Academy of Sciences **112**(3), 707-712.

Table 1. Sulphur isotope measurements of xenolith-derived sulphides from Kaapvaal xenoliths

Run number	Sample name	Location	Rock type	**d34S vs CDT**	Err	**Δ33S**
Sample8-S1@1	HRV-172A	Roberts Victor	eclogite	-1.130	0.061	0.04
Sample2-S2@2	HRV-174A	Roberts Victor	Eclogite	-3.384	0.061	-0.08
Sample2-S2@3				-2.801	0.061	0.06
Sample2-grain1@2				-3.504	0.061	0.09
Sample2-grain1@1				-3.885	0.061	0.07
Sample2-grain3@1				-5.724	1.314	-0.02
Sample10-grain1@1	MBK	Roberts Victor	Eclogite	13.298	0.061	0.18
Sample10-grain1@2				13.650	0.061	0.05
Sample10-grain2@1				29.034	0.061	0.00
Sample10-grain3@1				25.467	0.061	-0.01
Sample10-grain3@2				26.317	0.061	-0.03
Sample10-grain4@1				20.001	0.061	-0.05
Sample10-grain4@2				19.626	0.061	-0.08
Sample10-grain5@1				24.595	0.061	0.02
Sample10-grain5@2				24.786	0.061	-0.04
Sample12-grain1@1	HRV-172B	Roberts Victor	Eclogite	2.452	0.061	-0.05
Sample12-grain1@2				1.758	0.061	-0.12
Sample4-grain1@1	HRV-161B	Roberts Victor	Eclogite	2.973	0.110	0.20
Sample4-grain1@2				3.264	0.110	-0.07
Sample4-grain1@3				2.418	0.110	-0.03
Sample4-grain1@4				3.194	0.110	0.01
Sample1-grain1@1	HRV-161A	Roberts Victor	Eclogite	1.660	0.110	-0.09
Sample1-grain1@2				2.264	0.110	-0.04
Sample1-grain1@3				1.923	0.110	-0.06
Sample1-grain4@1				1.658	0.110	0.10
Sample1-grain4@2				1.808	0.110	-0.08
Sample1-grain4@3				1.581	0.110	-0.21
Sample1-grain4@4				1.783	0.110	-0.13
Sample15-grain1@1	JJG-2717	Premier	Eclogite	2.519	0.110	0.11
Sample15-grain1@2				2.808	0.110	-0.18
Sample15-grain2@1				1.718	0.110	0.06
Sample15-grain2@2				1.828	0.110	0.00
Sample15-grain2@3				1.031	0.110	-0.04
Sample15-grain3@1				3.457	0.110	0.02
Sample15-grain3@2				3.167	0.110	-0.05
Sample15-grain4@1				0.445	0.110	0.00
Sample15-grain4@2				1.701	0.110	0.14
Sample9-grain1@1	JJG-2919	Jagersfonein	Eclogite	-3.980	0.078	0.18
Sample9-grain1@2				-2.801	0.079	0.06
Sample9-grain1@3				-2.937	0.078	-0.08
Sample9-grain1@4				-2.596	0.078	-0.29
Sample14-grain2@1	CIM15-006	Premier	Peridotite (DEF LRZ)	-4.238	0.078	-0.10
Sample14-grain2@2				-5.732	0.079	-0.14±0.02
Sample14-grain3@1				-0.477	0.079	-0.02
Sample14-grain4@1				-4.556	0.079	0.12
Sample14-grain5@1				-1.0992	0.0793	0.09

Δ33S = δ33S measured - δ33S predicted (c.f. Thomassot et al. 2009).

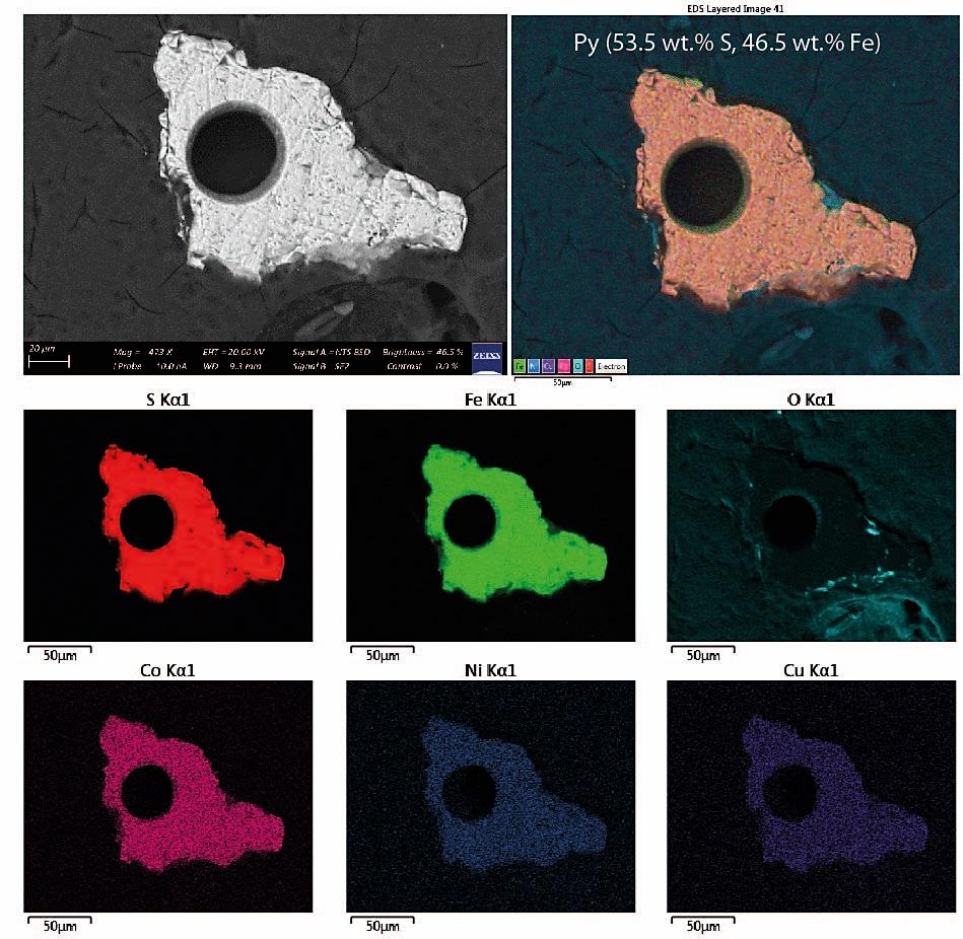

Fig. 1. *Multi-element compositional map of pyrite extracted from an eclogite xenolith from Roberts Victor kimberlite, South Africa.*

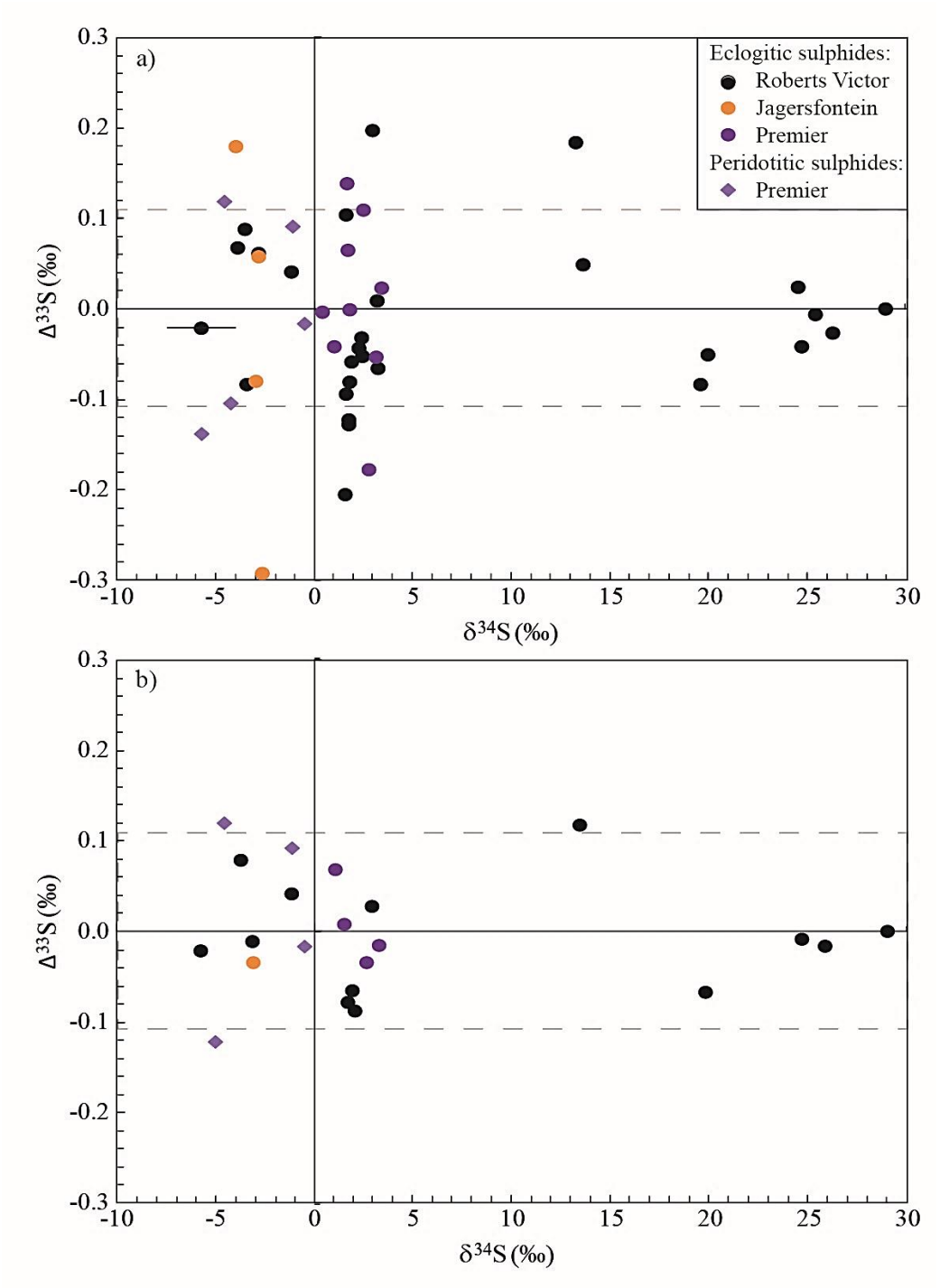

Fig. 2. *Plot of $\delta^{34}S$ vs MIF ($\Delta^{33}S$) for mantle-derived eclogite and peridotite sulphides from the Kaapvaal craton. (a) Individual measurements. (b) Average value measured for each sulphide grain. The stippled box centered at $\Delta^{33}S = 0$ and extending from +0.12 to –0.12 ‰ is assumed to represent the mass-dependent field (Farquhar et al., 2002).*

CHAPTER 3: APPENDICES

"SULPHUR-RICH MANTLE METASOMATISM OF KAAPVAAL CRATON ECLOGITES AND ITS ROLE IN REDOX-CONTROLLED PLATINUM GROUP ELEMENT MOBILITY"

APPENDIX A:

EXAMPLES OF POINT COUNRING METHODS

Appendix A. Examples of point counting methods using the ©jmicrovision 1.2.7 software

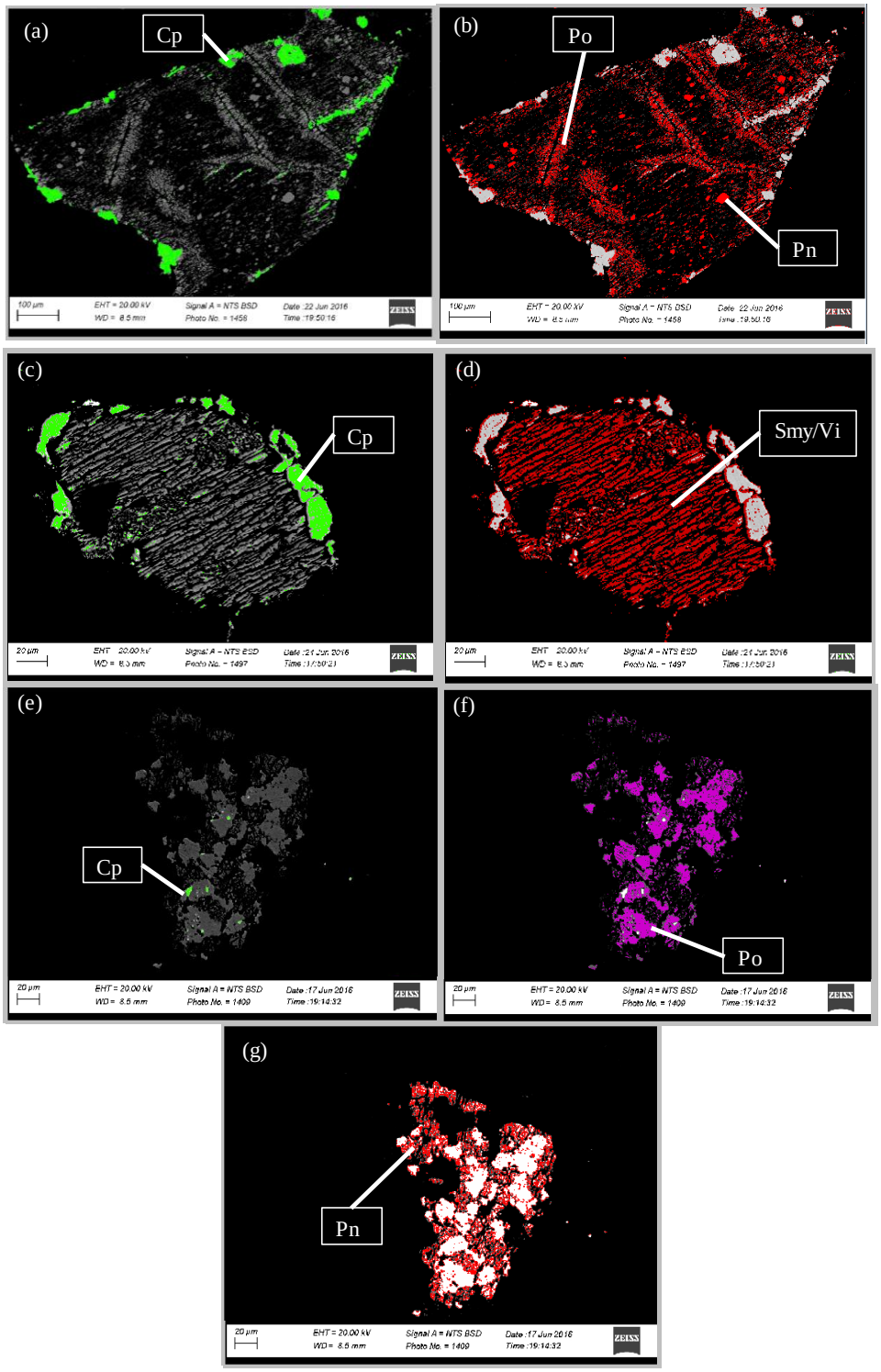

APPENDIX B:

ASIMEX STANDARDS USED IN SEM ROUTINE

Appendix B. SEM major and minor element analyses of NiS5b, marcasite, pentlandite, pyrope, Cr diopside and biotite standards

Mineral Standard:	NiS5b			NiS5b (published)	
Spot size:	30µm			30µm	
Spot number:	19			20	
Element (wt. %)	*Avg.*	*1-σ*	*mdl*	*Avg.*	*1-σ*
Ni	68.28	1.42	0.1	67.37	1.78
Fe	3.16	0.82	0.1	3.26	0.80
Cu	0.98	0.25	0.1	1.18	0.24
S	27.15	0.27	0.2	27.87	0.37
Total	99.57	2.76		99.68	3.20

Mineral Standard:	Marcasite			(ASTIMEX)	
Spot size:	30µm			30µm	
Spot number:	5			20	
Element (wt. %)	*Avg.*	*1-σ*	*mdl*	*Avg.*	*1-σ*
S	53.28	0.51	0.2	53.46	0.36
Fe	46.72	0.38	0.1	46.54	0.27
Total	100.00	0.89		100.00	0.63

Mineral Standard:	Pentlandite			(ASTIMEX)	
Spot size:	30µm			30µm	
Spot number:	5			20	
Element (wt. %)	*Avg.*	*1-σ*	*mdl*	*Avg.*	*1-σ*
S	32.76	0.13	0.2	33.01	0.27
Fe	31.23	0.23	0.1	30.77	0.17
Co	0.15	0.03	0.06	0.10	0.07
Ni	36.47	0.18	0.1	36.12	0.31
Total	100.61	0.57		100.00	0.82

Mineral Standard:	Pyrope			(ASTIMEX)	
Spot size:	30µm				
Spot number:	5				
Compound (wt. %)	*Avg.*	*1-σ*	*mdl*	*Avg.*	*1-σ*
SiO_2	41.83	0.19	0.1	41.45	1.02
TiO_2	1.21	0.03	0.015	1.16	0.70
Al_2O_3	21.47	0.07	0.2	21.32	0.60
Cr_2O_3	0.70	0.06	0.017	0.58	0.40
FeO	11.37	0.11	0.1	11.15	0.02
MnO	0.13	0.07	0.063	0.27	0.30
MgO	18.74	0.30	0.1	19.33	0.06
CaO	4.17	0.24	0.1	4.65	0.01
Total (wt. %)	99.62	1.07		99.91	3.11

Mineral Standard:	Cr Diopside			(ASTIMEX)	
Spot size:	30µm				
Spot number:	5				
Compound (wt. %)	*Avg.*	*1-σ*	*mdl*	*Avg.*	*1-σ*
SiO_2	54.82	1.10	0.1	54.59	1.30
TiO_2	0.15	0.30	0.012	0.10	0.40
Cr_2O_3	0.47	0.20	0.038	0.50	0.30
FeO	1.42	0.20	0.01	1.39	0.17
MgO	17.44	0.15	0.1	17.14	0.20
CaO	24.80	0.35	0.1	25.50	0.20
Na_2O	0.51	0.40	0.04	0.44	0.30
Total (wt. %)	99.61	2.70		99.66	2.87

Mineral Standard:	Biotite			(ASTIMEX)	
Spot size:	30µm				
Spot number:	5				
Compound (wt. %)	*Avg.*	*1-σ*	*mdl*	*Avg.*	*1-σ*
SiO_2	39.80	0.54	0.1	38.72	1.04
TiO_2	1.65	0.06	0.01	1.77	0.08
Al_2O_3	15.58	0.23	0.2	15.13	0.58
FeO	10.41	0.16	0.1	10.72	0.15
MnO	0.10	0.03	0.041	0.04	0.03
MgO	19.87	0.18	0.1	19.52	0.33
CaO	0.07	0.02	0.028	0.10	0.02
K_2O	9.81	0.05	0.1	9.91	0.11
H_2O	3.37	0.37	n/a	4.11	n/a
Total (wt. %)	100.66	1.64		100.02	2.34

Average abundances determined by scanning electron microprobe (SEM) analysis, CAF - Stellenbosch University
1- σ = within-run precition, mdl = mean detection limits
ASTIMEX = published mineral composition (Astimex Scienific Limited, MINM25-53 #03-0400)
NiS5b (published) = taken from Mungall and Brenan, (2014) and Brenan (2015).

APPENDIX C:

STANDARDS USED DURING LA-ICP-MS ANALYSIS

Appendix C. Standard analyses and associated errors for LA-ICPMS trace element analyses.

	NIST 612	Iolite		BCR	Iolite		BHVO	Iolite			$NiS5_b$	Iolite	
	Avg. (ppm)	2 - σ	mdl	Avg. (ppm)	2 - σ	mdl	Avg. (ppm)	2 - σ	mdl		Avg. (ppm)	2 - σ	mdl
Sc	39.9	1.2	0.1	32.9	2.1	0.3	30.7	1.2	0.2	^{99}Ru	57.39	5.7	0.02
V	38.8	1.5	0.05	423	24	0.13	317	16	0.1	^{101}Ru	58.47	6.4	0.02
Co	35.5	1.3	1.01	37.1	0.9	1.8	44.3	0.3	1.4	^{103}Rh	151.71	13.7	0.10
Ni	38.8	1.8	1.5	11.8	1.3	0.5	119.3	2.4	0.1	^{105}Pd	155.23	14.3	0.005
Cu	37.8	1.5	1.1	16.7	4.3	0.18	123.7	3.3	0.1	^{106}Pd	152.29	13.5	0.029
Zn	39.2	3.6	1.1	153	28	0.16	120	18	0.1	^{108}Pd	154.39	13.6	0.005
Rb	31.4	1.2	0.01	45.2	1.9	0.03	8.8	2.4	0.01	^{185}Re	35.53	3.1	0.07
Sr	78.4	2.4	0.01	327	13	0.02	377	19	0.01	^{187}Re	35.31	3.2	0.05
Y	38.3	0.9	0.006	32.3	4.7	0.02	22.8	3.2	0.01	^{188}Os	81.44	7.5	0.005
Zr	37.9	0.7	0.01	170	14	0.03	153	17	0.02	^{189}Os	81.47	7.4	0.013
Nb	38.9	0.9	0.01	12	0.6	0.16	17	1.3	0.2	^{193}Ir	80.14	8.2	0.005
Cs	52.7	1.3	0.013	1.13	0.03	0.02	0.1	0.01	0.01	^{195}Pt	93.29	10.4	0.07
Ba	39.3	2.2	0.04	655	28	0.06	124	7	0.07	^{197}Au	8.38	0.8	0.01
La	36.1	0.9	0.002	25	0.3	0.007	15	0.2	0.01	^{75}As	52.25	5.3	1.50
Ce	38.5	1	0.003	51	2.3	0.007	36	1.6	0.01	^{82}Se	101.14	18.4	1.1
Pr	37.9	0.8	0.002	6.5	0.2	0.01	4.9	0.5	0.01	^{125}Te	109.66	12.2	0.1
Nd	35.5	1.4	0.01	28	0.9	0.04	23	1.5	0.03	^{208}Pb	62.20	6.1	0.1
Sm	37.7	1.1	0.02	6.4	0.2	0.03	5.8	0.3	0.02	^{107}Ag	2.20	0.3	0.05
Eu	35.6	0.9	0.005	1.9	0.07	0.009	2	0.2	0.009	^{209}Bi	97.79	7.3	0.09
Gd	37.2	1.2	0.016	6.4	0.3	0.03	5.7	0.5	0.04				
Tb	37.6	0.8	0.004	1	0.07	0.004	0.9	0.02	0.006				
Dy	35.5	1.1	0.012	6.1	0.4	0.17	4.9	0.4	0.12				
Ho	38.3	0.9	0.003	1.3	0.2	0.004	0.9	0.03	0.01				
Er	37.9	0.8	0.007	3.5	0.2	0.012	2.3	0.3	0.01				
Tm	36.8	0.9	0.002	0.5	0.1	0.004	0.3	0.04	0.005				
Yb	39.2	1	0.012	3.4	0.3	0.02	1.9	0.1	0.01				
Lu	37	0.9	0.002	0.5	0.04	0.004	0.4	0.01	0.03				
Hf	36.7	0.9	0.008	4.8	0.3	0.02	4.1	0.22	0.2				
Ta	37.6	0.9	0.001	0.7	0.08	0.004	1.1	0.05	0.002				
Pb	38.7	1.6	0.012	10	1	0.01	1.8	0.1	0.01				
Th	37.8	0.6	0.004	5.6	0.3	0.005	1.1	0.12	0.003				
U	37.4	1.1	0.002	1.7	0.1	0.004	0.5	0.12	0.005				
K	66.4	2.1	2.3	14903	180	5.7	4233.9	87	3.1				
Cr	36.4	2.5	0.2	17.2	2.6	0.9	294	4.3	1.1				
Mn	38.7	0.9	1.1	1550	35	2.3	1347	38	2.6				
Mo	37.4	4.2	0.002	273	3.8	0.01	3.8	0.4	0.02				
W	38	4.4	0.01	0.5	0.1	0.01	0.23	0.1	0.02				

Average abundances determined by LA ICP MS, CAF - Stellenbosch University

Sil. Glass = NIST silicate glass standard, Iolite = Iolite ©2017 software package, 2 - σ = within run precision, mdl = mean detection limit

APPENDIX D:

MINIMUM DETECTION LIMITS AND ASSOCIATED UNCERTAINTIES FOR LA-ICPMS TRACE ELEMENT ANALYSES.

Appendix D. Minimum detection limits and associated uncertainties for LA-ICPMS trace element analyses.

Sample	ROVIC-MBK			MBK			JJG-4492			HRV-174A			HRV-174B		
ME Class	Ky-gabbroic			Picritic			Ky-grospydite			Picritic			Basaltic		
TE Class	LREE-depleted	2 - σ	mdl	LREE-enriched	2 - σ	mdl	LREE-depleted	2 - σ	mdl	LREE-depleted	2 - σ	mdl	Sinusoidal	2 - σ	mdl
mineral:	*Gt*			*Gt*			*Gt*			*Gt*			*Gt*		
Sc	42	0.43	0.228	83	1.7	10.538	21	0.81	2.750	54	0.98	0.037	80	0.58	0.083
V	111	5.3	0.142	99	1.8	11.138	33	1.0	4.400	63	1.8	0.033	211	0.65	0.083
Co	88	2.6	0.058	55	1.5	5.088	44	1.3	4.767	59	0.97	0.017	71	0.66	0.058
Ni	104	18.1	0.874	31	2.9	2.188	30	2.1	3.500	14.8	1.3	0.144	20.7	1.5	0.126
Cu	1.4	0.47	0.143	0.3	0.15	0.181	0.6	0.17	0.223	0.1	0.111	0.039	3.2	0.038	0.186
Zn	108	9.8	0.664	14	2.0	1.763	93	5.0	7.800	29	2.3	0.096	85	1.3	0.278
Rb	0.58	5.8	0.049	0.09	0.065	0.048	0.03	0.010	0.054	0.0	0.16	0.016	0.2	0.007	0.021
Sr	3.4	4.8	0.023	0.8	0.20	0.105	7.5	0.53	1.100	0.7	0.36	0.041	0.5	0.055	0.056
Y	18	0.17	0.013	23	0.48	3.175	5	0.23	0.817	30	0.29	0.003	53	0.30	0.100
Zr	33	1.2	0.027	58	1.3	8.225	28	0.84	4.433	35	0.35	0.006	3	0.37	0.079
Nb	0.14	0.70	0.014	0.18	0.054	0.038	0.08	0.032	0.028	0.16	0.031	0.002	0.00	0.017	0.002
Cs	0.02	0.23	0.021	0.06	0.030	0.018	bdl	bdl	0.022	0.0	0.010	0.005	0.0	0.001	0.009
Ba	8.9	9.6	0.590	5.8	2.0	0.203	bdl	bdl	0.430	0.5	1.3	0.030	0.6	0.089	0.023
La	0.3	1.8	0.026	0.5	0.21	0.027	0.1	0.044	0.029	0.0	0.066	0.002	0.0	0.007	0.002
Ce	0.9	3.1	0.009	0.3	0.14	0.044	1.1	0.097	0.180	0.3	0.11	0.003	0.0	0.020	0.003
Pr	0.2	0.32	0.007	0.1	0.027	0.020	0.4	0.051	0.063	0.1	0.019	0.002	0.0	0.010	0.001
Nd	1.9	1.1	0.002	0.8	0.19	0.198	2.9	0.37	0.597	1.4	0.14	0.014	0.3	0.083	0.009
Sm	1.4	0.69	0.099	1.1	0.22	0.265	1.9	0.33	0.392	1.6	0.092	0.009	0.6	0.081	0.010
Eu	0.7	0.089	0.001	0.6	0.099	0.138	1.1	0.12	0.178	0.8	0.037	0.003	0.4	0.036	0.004
Gd	2.5	0.067	0.087	3.0	0.34	0.611	1.9	0.29	0.460	2.8	0.12	0.011	2.6	0.13	0.012
Tb	0.5	0.051	0.007	0.6	0.062	0.111	0.2	0.043	0.047	0.6	0.018	0.002	0.7	0.022	0.002
Dy	3.3	0.099	0.054	4.2	0.35	0.780	1.0	0.198	0.215	4.5	0.14	0.008	7.3	0.11	0.011
Ho	0.7	0.018	0.014	0.8	0.077	0.122	0.2	0.035	0.043	1.1	0.029	0.002	1.9	0.030	0.004
Er	1.9	0.051	0.040	2.4	0.24	0.386	0.4	0.092	0.118	3.9	0.086	0.005	6.9	0.10	0.010
Tm	0.26	0.012	0.024	0.34	0.045	0.066	0.05	0.019	0.017	0.6	0.024	0.002	1.1	0.018	0.002
Yb	1.6	0.075	0.030	2.5	0.26	0.416	0.5	0.14	0.109	4.56	0.163	0.014	8.31	0.13	0.015
Lu	0.24	0.008	0.005	0.40	0.052	0.074	0.07	0.022	0.021	0.7	0.029	0.003	1.4	0.019	0.002
Hf	0.7	0.13	0.035	0.5	0.093	0.084	0.4	0.096	0.091	0.30	0.048	0.007	0.11	0.03	0.005
Ta	0.01	0.084	0.009	0.02	0.010	0.011	0.01	0.008	0.008	0.0	0.002	0.001	0.0	0.002	0.002
Pb	0.1	0.27	0.108	0.3	0.10	0.191	bdl	bdl	0.157	0.02	0.094	0.010	0.48	0.008	0.019
Th	0.04	0.38	0.014	0.13	0.048	0.008	bdl	bdl	0.011	0.02	0.013	0.003	0.00	0.004	0.001
U	0.01	0.067	0.007	0.01	0.010	0.008	bdl	bdl	0.011	0	0.004	0.002	0	0.003	0.001

Appendix D. Minimum detection limits and associated uncertainties for LA-ICPMS trace element analyses (continued)

HRV-162A Gabbroic LREE-depleted	2 - σ	mdl	HRV-162B Gabbroic LREE-depleted	2 - σ	mdl	HRV-161A Picritic/ Phl-ecl. LREE-enriched	2 - σ	mdl	HRV-161B Picritic/ Phl-ecl. LREE-enriched	2 - σ	mdl	HRV-172A Basaltic LREE-enriched	2 - σ	mdl	HRV-172B Ky-grospydite LREE-depleted	2 - σ	mdl	EJB-86 Gabbroic LREE-depleted	2 - σ	mdl
Gt			*Gt*			*Gt*			*Gt*			*Gt*			*Gt*			*Gt*		
35	0.57	0.040	35	0.50	0.035	28	1.6	10.538	29	1.4	10.538	21	0.27	0.041	25	0.42	0.043	33	1.7	0.083
45	0.64	0.033	42	0.64	0.027	38	1.9	11.138	39	1.8	11.138	61	0.89	0.041	51	0.70	0.031	122	1.6	0.083
68	0.92	0.013	68	0.88	0.015	48	1.6	5.088	47	1.7	5.088	79	0.92	0.033	46	0.61	0.016	59	0.59	0.070
43.2	1.1	0.143	44.6	1.3	0.117	16.2	3.2	2.188	16.4	2.7	2.188	122.5	2.0	0.098	33.7	1.0	0.141	78.3	1.6	0.126
0.7	0.10	0.037	0.7	0.11	0.024	0.1	0.26	0.181	0.1	0.15	0.181	1.6	0.12	0.042	0.6	0.091	0.031	1.0	0.0	0.186
131	3.2	0.097	131	3.0	0.118	56	1.78	1.763	54	1.4	1.763	129	3.3	0.102	139	3.2	0.116	114	1.27	0.278
0.8	0.091	0.013	0.6	0.071	0.008	0.1	0.01	0.048	0.2	0.05	0.048	0.1	0.02	0.011	1.0	0.12	0.014	bdl	0.006	0.021
2.0	0.103	0.006	3.8	0.30	0.008	0.7	0.31	0.105	0.7	0.21	0.105	0.9	0.073	0.007	38.4	3.6	0.005	3.5	0.061	0.060
11	0.14	0.002	11	0.19	0.003	10	0.52	3.175	10	0.72	3.175	22	0.28	0.010	16	0.23	0.002	20	0.41	0.100
17	0.27	0.005	17	0.31	0.005	6	1.4	8.225	6	1.4	8.225	44	0.46	0.020	51	0.65	0.004	73	1.1	0.010
0.03	0.005	0.003	0.06	0.014	0.003	0.02	0.007	0.002	0.01	0.012	0.003	0.02	0.007	0.002	0.11	0.016	0.003	bdl	0.017	0.002
0.0	0.009	0.005	1.5	0.008	0.004	0.003	0.027	0.003	0.02	0.034	0.003	0.05	0.023	0.003	0.8	0.041	0.004	bdl	0.001	0.009
4.5	0.34	0.035	1.2	1.2	0.049	bdl	0.098	0.016	7.0	0.085	0.017	0.3	0.095	0.017	7.0	2.19	0.032	bdl	0.023	0.002
0.1	0.010	0.003	0.3	0.026	0.003	0.03	0.010	0.002	0.1	0.015	0.002	0.1	0.010	0.002	0.3	0.030	0.001	0.1	0.007	0.002
0.3	0.028	0.002	0.8	0.046	0.003	0.3	0.031	0.003	0.3	0.023	0.002	0.3	0.022	0.002	1.5	0.089	0.002	0.8	0.020	0.003
0.1	0.014	0.002	0.2	0.017	0.002	0.1	0.019	0.001	0.1	0.014	0.001	0.1	0.013	0.001	0.5	0.027	0.003	0.3	0.010	0.001
1.4	0.11	0.012	1.5	0.11	0.014	1.2	0.11	0.009	1.2	0.11	0.009	2.1	0.11	0.009	4.3	0.18	0.008	3.2	0.011	0.009
1.2	0.11	0.018	1.1	0.099	0.022	0.9	0.16	0.010	0.9	0.18	0.010	2.3	0.15	0.010	2.4	0.15	0.013	2.7	0.095	0.010
0.8	0.05	0.004	0.8	0.048	0.003	0.5	0.053	0.002	0.4	0.060	0.003	1.1	0.053	0.003	1.2	0.054	0.004	1.2	0.061	0.004
1.7	0.123	0.014	1.7	0.13	0.016	1.7	0.20	0.011	1.7	0.18	0.011	4.3	0.19	0.011	3.2	0.18	0.010	3.7	0.21	0.015
0.3	0.019	0.002	0.3	0.019	0.002	0.3	0.041	0.003	0.3	0.030	0.003	0.7	0.028	0.003	0.5	0.027	0.002	0.6	0.025	0.002
1.8	0.11	0.007	1.9	0.094	0.005	1.9	0.213	0.010	1.8	0.18	0.009	4.5	0.17	0.009	3.1	0.130	0.009	3.9	0.12	0.012
0.4	0.023	0.002	0.4	0.026	0.002	0.4	0.041	0.002	0.3	0.039	0.002	0.8	0.032	0.002	0.6	0.028	0.002	0.8	0.040	0.004
1.2	0.075	0.007	1.3	0.070	0.006	0.9	0.064	0.005	0.9	0.096	0.005	2.0	0.085	0.005	1.7	0.096	0.006	2.1	0.12	0.010
0.2	0.017	0.002	0.2	0.014	0.002	0.1	0.017	0.001	0.1	0.013	0.001	0.2	0.015	0.001	0.2	0.016	0.002	0.3	0.020	0.002
1.40	0.096	0.008	1.37	0.091	0.005	0.82	0.081	0.006	0.84	0.053	0.006	1.57	0.077	0.006	1.69	0.096	0.012	2.14	0.135	0.015
0.2	0.016	0.002	0.2	0.017	0.002	0.1	0.014	0.001	0.1	0.032	0.001	0.2	0.014	0.001	0.3	0.018	0.002	0.3	0.023	0.002
0.29	0.034	0.007	0.29	0.033	0.006	0.07	0.087	0.003	0.06	0.051	0.004	0.66	0.047	0.004	0.99	0.063	0.004	1.22	0.038	0.005
0.0	0.001	0.002	0.0	0.002	0.002	0.0	0.002	0.001	0.0	0.001	0.001	0.0	0.002	0.001	0.0	0.002	0.001	bdl	0.002	0.002
0.03	0.011	0.009	0.07	0.023	0.012	0.00	0.027	0.008	bdl	0.022	0.009	0.09	0.022	0.009	0.08	0.018	0.010	bdl	0.007	0.019
0.03	0.007	0.003	0.05	0.011	0.002	0.01	0.002	0.001	0.02	0.002	0.001	0.01	0.002	0.001	0.02	0.005	0.002	0.00	0.002	0.001
0	0.002	0.003	0	0.003	0.002	0	0.002	0.002	0	0.002	0.002	0	0.002	0.002	0	0.003	0.003	0	0.002	0.001

Appendix D. Minimum detection limits and associated uncertainties for LA-ICPMS trace element analyses (continued)

JJG-2914 Picritic Sinusoidal	2 - σ	mdl	JJG-2919 Basaltic Sinusoidal	2 - σ	mdl	JJG-2920 Picritic LREE-enriched	2 - σ	mdl	CIM15-101 Gab/bas LREE-enriched	2 - σ	mdl	CIM15-102 Picritic LREE-enriched	2 - σ	mdl	ST16-H-04 Pyroxenite Sinusoidal	2 - σ	mdl	JJG-2717 Basaltic LREE-depleted	2 - σ	mdl
Gt			*Gt*			*Gt*			*Gt*			*Gt*			*Gt*			*Gt*		
52	1.9	8.780	68	0.802	0.046	46	1.3	7.817	44	0.600	4.836	55	0.700	3.600	60	0.64	0.102	47	0.54	0.035
60	2.0	8.900	208	1.9	0.093	74	2.4	14.667	71	0.900	6.184	102	1.2	4.712	158	1.5	0.155	88	0.80	0.028
58	2.0	7.420	76	0.873	0.030	54	1.5	6.017	63	0.900	2.712	39	0.700	2.300	46	0.54	0.045	75	0.95	0.006
12.9	1.6	2.040	22.1	0.725	0.092	12.1	1.600	2.233	17.7	0.900	1.152	12.8	0.700	1.250	20.7	0.63	0.118	45.1	0.91	0.074
bdl	bdl	0.26	2.9	0.170	0.034	bdl	0.1	0.332	0.1	0.050	0.132	0.1	0.050	0.050	0.3	0.08	0.048	1.0	0.10	0.035
29	3.7	3.660	87	2.3	0.108	159	6.2	8.983	111	2.9	2.140	10	0.850	0.200	47	1.8	0.428	54	1.6	0.113
bdl	0.033	0.048	0.02	0.010	0.009	bdl	bdl	0.090	bdl	0.009	0.036	0.1	0.040	0.006	0.1	0.03	0.174	38.6	0.88	0.006
0.3	0.21	0.42	0.1	0.020	0.003	1.0	0.148	0.166	0.9	0.870	0.066	3.0	0.430	0.066	2.7	0.19	0.018	11.6	1.04	0.005
27	0.97	5.300	54	0.498	0.037	24	0.537	4.017	20	0.240	1.736	31	0.300	1.736	45	0.48	0.066	26	0.29	0.001
35	1.1	6.340	2	0.065	0.006	8	0.848	6.017	6	0.180	3.750	20	0.330	3.750	66	0.78	0.304	71	0.67	0.003
0.08	0.056	0.050	bdl	0.002	0.002	bdl	0.030	0.011	0.05	0.050	0.010	0.13	0.130	0.010	0.28	0.10	0.016	0.54	0.03	0.002
bdl	bdl	0.017	bdl	bdl	0.002	bdl	bdl	0.090	bdl	0.007	0.020	0.6	0.060	0.020	0.3	0.07	0.005	0.5	0.03	0.003
bdl	1.10	0.61	bdl	0.031	0.024	bdl	bdl	0.248	bdl	0.030	0.093	2.2	0.400	0.093	13.3	2.6	0.070	64.6	3.7	0.020
0.0	0.077	0.11	bdl	0.002	0.002	bdl	0.019	0.014	0.01	0.007	0.008	0.3	0.060	0.008	0.2	0.02	0.002	0.2	0.02	0.001
0.2	0.075	0.11	0.0	0.003	0.002	0.3	0.050	0.057	0.3	0.030	0.018	0.8	0.100	0.018	0.7	0.06	0.006	0.6	0.04	0.001
0.1	0.041	0.055	0.0	0.003	0.001	0.1	0.027	0.037	0.2	0.020	0.010	0.1	0.020	0.010	0.2	0.02	0.002	0.2	0.01	0.001
0.8	0.27	0.31	0.3	0.040	0.008	1.6	0.248	0.255	2.1	0.180	0.082	1.4	0.160	0.082	2.2	0.11	0.009	2.9	0.14	0.006
1.1	0.40	0.38	0.7	0.065	0.008	1.1	0.243	0.252	2.1	0.190	0.095	0.8	0.100	0.095	1.4	0.10	0.008	4.5	0.16	0.005
0.8	0.14	0.17	0.5	0.028	0.002	1.0	0.098	0.148	1.0	0.060	0.049	0.4	0.040	0.049	0.6	0.05	0.003	2.2	0.06	0.002
2.6	0.42	0.61	2.7	0.111	0.008	2.8	0.327	0.582	3.4	0.210	0.206	1.5	0.160	0.206	2.8	0.13	0.015	8.4	0.22	0.008
0.6	0.093	0.13	0.8	0.029	0.002	0.5	0.063	0.122	0.6	0.030	0.040	0.4	0.025	0.040	0.7	0.02	0.002	1.2	0.03	0.001
3.7	0.38	0.96	7.3	0.162	0.010	3.7	0.353	0.722	3.8	3.780	0.256	4.0	4.050	0.256	6.4	0.16	0.016	6.2	0.16	0.005
1.0	0.096	0.22	2.0	0.051	0.007	0.9	0.097	0.182	0.8	0.040	0.053	1.1	0.040	0.053	1.7	0.05	0.005	1.0	0.03	0.001
3.4	0.40	0.76	6.9	0.117	0.022	2.7	0.258	0.595	2.2	0.126	0.170	3.9	0.140	0.170	5.6	0.10	0.012	2.2	0.07	0.003
0.5	0.085	0.14	1.1	0.032	0.003	0.4	0.061	0.080	0.3	0.026	0.026	0.6	0.030	0.026	0.8	0.03	0.003	0.2	0.01	0.001
4.29	0.54	0.99	8.50	0.172	0.023	3.04	0.320	0.623	2.29	0.150	0.180	4.45	0.210	0.180	6.12	0.19	0.014	1.48	0.07	0.005
0.5	0.072	0.16	1.3	0.037	0.004	0.5	0.059	0.104	0.3	0.030	0.031	0.7	0.040	0.031	1.0	0.03	0.003	0.2	0.01	0.001
0.25	0.083	0.10	0.08	0.015	0.003	0.10	0.110	0.141	0.06	0.017	0.040	0.20	0.030	0.040	1.37	0.08	0.006	0.81	0.04	0.003
0.0	0.013	0.011	bdl	0.001	0.001	bdl	0.006	0.009	0.0	0.001	0.004	0.0	0.003	0.004	0.0	0.00	0.001	0.0	0.01	0.001
0.00	bdl	0.23	0.01	0.007	0.007	bdl	bdl	0.360	0.01	0.010	0.098	0.09	0.026	0.098	0.02	0.02	0.073	0.07	0.01	0.005
0.00	0.020	0.033	bdl	bdl	0.002	bdl	bdl	0.081	bdl	0.002	0.016	0.05	0.160	0.016	0.02	0.00	0.002	0.02	0.00	0.001
bdl	0.013	0.014	bdl	bdl	0.001	0	0.010	0.016	0	0.004	0.005	0	0.005	0.005	0	0.01	0.003	0	0.00	0.002

Appendix D. Minimum detection limits and associated uncertainties for LA-ICPMS trace element analyses.

Samp.	ROVIC-MBK			MBK			JJG-4492			HRV-174A			HRV-174B			HRV-162A		
mineral:	Cpx	2 - σ	mdl	Cpx	2 - σ	mdl	Cpx	2 - σ	mdl	Cpx	2 - σ	mdl	Cpx	2 - σ	mdl	Cpx	2 - σ	mdl
Sc	5	0.71	0.054	36	0.38	0.025	6	0.15	0.038	19	0.35	0.0275	25	0.25	0.023	9	0.20	0.028
V	1	1.4	0.049	329	2.1	0.017	57	0.76	0.028	417	3.6	0.0195	513	2.9	0.016	179	1.5	0.022
Co	0	1.4	0.017	24	0.30	0.008	17	0.34	0.008	30	0.50	0.007	38	0.23	0.004	21	0.31	0.008
Ni	1	2.4	0.194	282	2.1	0.090	158	2.3	0.117	277	3.1	0.095	300	1.0	0.046	234	2.6	0.115
Cu	2	0.44	0.057	1	0.064	0.020	6	0.87	0.025	9	0.30	0.020	7	0.22	0.017	8	0.36	0.021
Zn	5	3.1	0.154	13	0.51	0.048	51	1.6	0.090	56	1.8	0.073	77	0.82	0.061	69	1.6	0.084
Rb	32	0.11	0.012	bdl	0.003	0.006	1.97	0.11	0.009	0.03	0.015	0.007	0.22	0.029	0.005	1.3	0.085	0.007
Sr	27	0.27	0.012	304	2.3	0.004	170	2.2	0.010	282	3.3	0.004	18	2.8	0.002	179	2.8	0.006
Y	1.0	0.27	0.005	4.1	0.062	0.002	0.0	0.009	0.003	2.0	0.048	0.001	1.2	0.053	0.001	0.6	0.025	0.001
Zr	74	0.47	0.008	91	0.67	0.002	9	0.16	0.004	27	0.335	0.003	4	1.7	0.002	12	0.17	0.002
Nb	0.88	0.023	0.004	1.07	0.030	0.001	0.06	0.011	0.002	0.03	0.007	0.001	0.00	0.13	0.001	0.06	0.008	0.002
Cs	0.81	0.007	0.004	bdl	0.001	0.003	0.26	0.032	0.004	0.60	0.12	0.003	0.18	0.011	0.002	12	1.1	0.002
Ba	591	2.2	0.067	0	0.088	0.019	2712	98.0	0.039	1	0.13	0.018	1	0.45	0.009	197	13.4	0.030
La	1.3	0.032	0.003	6.7	0.080	0.002	0.3	0.018	0.003	1.3	0.049	0.001	0.0	0.099	0.001	0.7	0.032	0.002
Ce	2	0.061	0.004	25	0.19	0.002	1	0.032	0.001	6	0.091	0.002	0.1	0.25	0.001	3	0.062	0.002
Pr	0.2	0.020	0.005	4.3	0.054	0.001	0.1	0.011	0.003	1.1	0.037	0.001	0.0	0.064	0.001	0.5	0.021	0.002
Nd	1.0	0.10	0.009	23.6	0.15	0.017	0.5	0.30	0.010	5.9	1.5	0.017	0.4	0.30	0.006	2.5	0.12	0.008
Sm	0.1	0.13	0.018	6.4	0.17	0.005	0.1	0.035	0.012	1.3	0.11	0.007	0.3	0.12	0.006	0.6	0.057	0.011
Eu	0.1	0.048	0.005	1.8	0.045	0.002	0.2	0.012	0.002	0.4	0.028	0.002	0.1	0.029	0.002	0.2	0.020	0.003
Gd	0.1	0.17	0.017	4.4	0.14	0.006	0.1	0.017	0.014	0.9	0.080	0.010	0.4	0.076	0.004	0.4	0.048	0.006
Tb	0.0	0.031	0.002	0.4	0.015	0.001	0.0	0.002	0.002	0.1	0.011	0.002	0.1	0.010	0.001	0.0	0.006	0.001
Dy	0.1	0.17	0.010	1.5	0.059	0.008	0.0	0.007	0.010	0.5	0.040	0.003	0.3	0.040	0.002	0.2	0.024	0.004
Ho	0.03	0.035	0.003	0.18	0.010	0.001	bdl	0.001	0.002	0.09	0.008	0.001	0.05	0.006	0.001	0.02	0.004	0.001
Er	0.1	0.021	0.002	0.3	0.022	0.003	bdl	0.003	0.007	0.2	0.025	0.003	0.1	0.019	0.003	0.05	0.010	0.004
Tm	0.01	0.021	0.002	0.03	0.004	0.001	bdl	bdl	bdl	0.02	0.004	0.001	0.01	0.003	0.001	0.004	0.002	0.002
Yb	0.1	0.12	0.011	0.1	0.017	0.007	bdl	0.003	0.009	0.1	0.029	0.007	0.1	0.015	0.002	0.0	0.010	0.006
Lu	0.02	0.019	0.003	0.01	0.003	0.001	bdl	bdl	0.002	0.01	0.004	0.001	0.01	0.003	0.001	0.004	0.002	0.001
Hf	1.8	0.061	0.006	2.3	0.067	0.004	0.4	0.040	0.005	1.7	0.072	0.004	0.4	0.073	0.002	0.6	0.042	0.007
Ta	0.06	0.003	0.002	0.14	0.008	0.001	0.03	0.005	0.001	0.00	0.001	0.001	bdl	0.011	0.001	0.004	0.002	0.001
Pb	4.0	0.022	0.014	0.5	0.036	0.006	0.3	0.029	0.008	0.6	0.046	0.008	0.1	0.038	0.003	0.3	0.029	0.007
Th	0.30	0.009	0.003	0.14	0.010	0.001	0.01	0.001	0.003	0.004	0.002	0.002	bdl	0.010	0.001	0.03	0.004	0.002
U	0.19	0.005	0.003	0.03	0.004	0.001	0.01	0.006	0.003	bdl	0.001	0.002	bdl	0.004	0.001	bdl	0.002	0.002

Appendix D. Minimum detection limits and associated uncertainties for LA-ICPMS trace element analyses.

HRV-162B			HRV-161A			HRV-161B			HRV-172A			HRV-172B			EJB-86			JJG-2914		
Cpx	2 - σ	mdl	Cpx	2 - σ	mdl	Cpx	2 - σ	mdl	Cpx	2 - σ	mdl	Cpx	2 - σ	mdl	Cpx	2 - σ	mdl	Cpx	2 - σ	mdl
8	0.168	0.025	9	0.21	0.020	10	0.13	0.020	11	0.16	0.022	5	0.19	0.033	8	1.1	0.065	22	0.74	0.057
128	0.96	0.024	167	1.7	0.680	168	24.0	0.740	206	1.7	0.017	127	1.7	0.025	339	23.1	0.104	368	14.8	0.045
19	0.32	0.008	18	0.61	0.010	18	0.6	0.010	37	0.49	0.004	15	0.34	0.008	23	1.4	0.077	21	0.75	0.016
200	1.9	0.122	170	1.8	0.200	165	1.50	0.164	744	9.5	0.043	198	3.3	0.133	470	5.1	1.979	114	3.6	0.207
12	0.35	0.026	2	0.19	0.034	2	0.27	0.040	12	1.5	0.020	3	0.17	0.023	9	1.1	0.516	1	0.30	0.033
67	1.8	0.091	45	3.1	0.096	43	2.7	0.084	78	2.0	0.056	64	2.3	0.104	68	3.1	1.163	21	1.9	0.139
0.01	0.006	0.008	0.1	0.12	0.005	0.06	0.030	0.006	5.26	0.33	0.005	5.01	0.23	0.006	5.52	0.91	0.556	0.02	0.32	0.013
132	1.3	0.007	828	10.0	0.020	843	8.9	0.020	244	7.7	0.002	215	3.3	0.005	269	1.8	0.430	294	9.2	0.008
0.4	0.024	0.002	1.5	0.23	0.039	1.6	0.18	0.033	3.3	0.06	0.001	0.2	0.019	0.002	0.5	0.47	0.020	3.2	0.18	0.003
9	0.14	0.004	14	0.70	0.068	13	0.97	0.035	64	1.0	0.002	15	0.32	0.002	44	1.123	0.131	79	1.9	0.005
0.01	0.005	0.002	0.02	0.070	0.001	0.02	0.070	0.001	3.86	0.15	0.001	0.19	0.018	0.001	0.16	0.41	0.007	0.80	0.072	0.003
bdl	0.002	0.002	0.01	0.020	0.001	0.06	0.020	0.002	117	3.8	0.002	17	0.40	0.003	6	0.21	0.013	bdl	0.010	0.004
48	0.668	0.022	2	0.088	0.019	2	0.090	0.019	380	66.4	0.017	1053	23.3	0.045	532	31.8	7.300	bdl	1.7	0.510
0.3	0.020	0.002	12.3	0.38	0.002	12.8	0.42	0.002	14.5	0.39	0.001	0.6	0.033	0.002	1.1	0.032	0.003	3.1	0.17	0.007
2	0.044	0.002	39	4.1	0.002	40	3.1	0.002	30	0.45	0.001	2	0.065	0.002	4	0.068	0.004	14	0.47	0.003
0.3	0.017	0.001	5.9	0.054	0.001	6.0	0.071	0.001	3.6	0.05	0.001	0.3	0.018	0.001	0.6	0.020	0.005	3.0	0.13	0.001
1.8	0.097	0.008	26.2	0.15	0.026	26.9	0.19	0.030	14.8	0.20	0.004	1.5	0.205	0.005	3.1	0.15	0.009	17.4	0.25	0.007
0.4	0.055	0.009	4.0	0.18	0.005	4.1	0.21	0.005	2.7	0.10	0.005	0.2	0.043	0.008	0.7	0.12	0.018	3.9	0.36	0.015
0.2	0.019	0.004	0.9	0.045	0.002	0.9	0.021	0.002	0.8	0.02	0.002	0.1	0.016	0.003	0.2	0.052	0.005	1.0	0.14	0.005
0.3	0.037	0.009	2.0	0.12	0.006	2.0	0.080	0.006	1.9	0.07	0.005	0.1	0.031	0.012	0.4	0.17	0.017	2.5	0.16	0.018
0.0	0.006	0.001	0.2	0.015	0.001	0.2	0.030	0.001	0.2	0.01	0.001	0.0	0.004	0.001	0.04	0.056	0.001	0.2	0.042	0.002
0.1	0.023	0.006	0.6	0.049	0.007	0.6	0.054	0.006	0.9	0.04	0.004	0.1	0.014	0.007	0.2	0.17	0.010	1.0	0.210	0.006
0.02	0.004	0.002	0.07	0.010	0.001	0.07	0.010	0.001	0.13	0.01	0.001	0.01	0.003	0.002	0.02	0.035	0.003	0.13	0.028	0.002
0.03	0.011	0.002	0.1	0.010	0.002	0.1	0.030	0.002	0.3	0.02	0.003	0.02	0.007	0.004	0.04	0.021	0.002	0.3	0.062	0.009
0.003	0.002	0.001	0.01	0.004	0.001	0.01	0.004	0.001	0.03	0.00	0.001	0.002	0.001	0.002	0.005	0.021	0.002	0.03	0.010	0.002
0.0	0.009	0.006	0.0	0.017	0.007	0.0	0.017	0.007	0.2	0.01	0.004	0.005	0.005	0.008	0.02	0.083	0.008	0.2	0.039	0.010
0.002	0.001	0.001	0.004	0.003	0.001	0.004	0.003	0.001	0.02	0.00	0.001	bdl	0.001	0.001	0.003	0.016	0.001	0.02	0.009	0.003
0.4	0.037	0.004	0.3	0.067	0.004	0.3	0.067	0.004	2.6	0.06	0.003	1.0	0.053	0.006	2.2	0.058	0.008	2.3	0.16	0.006
0.002	0.001	0.001	0.004	0.008	0.001	0.003	0.008	0.001	0.20	0.01	0.000	0.01	0.003	0.001	0.01	0.025	0.001	0.17	0.029	0.002
0.2	0.020	0.010	7.5	0.36	0.014	7.5	0.012	0.006	1.1	0.31	0.004	0.2	0.026	0.010	1.1	0.075	0.060	0.4	0.17	0.015
0.00	0.001	0.001	0.33	0.010	0.001	0.31	0.010	0.001	1.33	0.05	0.001	0.04	0.006	0.002	0.02	0.023	0.001	0.03	0.016	0.004
bdl	0.001	0.002	0.03	0.002	0.001	0.03	0.003	0.001	0.35	0.02	0.001	0.01	0.003	0.001	0.01	0.012	0.001	0.02	0.009	0.003

Appendix D. Minimum detection limits and associated uncertainties for LA-ICPMS trace element analyses.

JJG-2919			JJG-2920			CIM15-101			CIM15-102			ST16-H-04			JJG-2717		
Cpx	2 - σ	mdl	Cpx	2 - σ	mdl	Cpx	2 - σ	mdl	Cpx	2 - σ	mdl	Cpx	2 - σ	mdl	Cpx	2 - σ	mdl
25	0.35	0.057	18	1.4	0.048	19	0.30	0.075	29	0.40	2.100	23	0.19	0.021	55	1.1	0.065
515	4.8	0.740	770	40.1	0.039	368	2.6	0.810	459	3.1	12.600	240	1.6	0.014	191	2.4	0.104
38	0.52	0.062	22	1.5	0.014	25	0.35	1.200	16	0.20	0.080	29	0.25	0.004	84	1.4	0.077
302	2.0	0.561	152	9.2	0.143	168	1.9	4.200	176	1.7	0.561	202	1.3	0.054	175	5.1	1.979
7	1.0	0.277	5	0.59	0.035	2	0.12	0.027	0.2	0.040	0.007	2	0.07	0.017	7	0.85	0.516
76	2.1	0.161	62	4.9	0.176	86	2.1	0.190	9	0.48	0.161	57	0.85	0.053	81	2.1	1.163
bdl	0.017	0.010	35	2.5	0.011	bdl	0.003	0.003	0.13	0.020	0.005	0.01	0.005	0.005	667	9.0	0.556
17	0.28	0.058	1460	121.9	0.007	514	4.9	6.500	806	7.2	0.120	391	3.1	0.003	469	14.5	0.430
1.2	0.042	0.006	4.3	0.71	0.003	1.6	0.050	0.180	5.7	0.080	0.010	3.6	0.05	0.001	30.2	0.47	0.020
4	0.11	0.018	47	11.8	0.006	15	0.21	0.020	66	0.54	0.018	24	0.20	0.002	87	1.2	0.131
bdl	0.002	0.005	1.46	2.9	0.002	0.29	0.29	0.005	1.12	1.1	0.006	0.18	0.01	0.001	10	0.23	0.007
bdl	0.008	0.002	1	0.12	0.004	bdl	0.003	0.004	0.21	0.040	0.002	bdl	0.001	0.002	9	0.19	0.013
bdl	0.092	0.040	159	742.7	0.056	0	0.040	0.060	15	2.1	0.040	1	0.11	0.009	3308	96.7	8.280
bdl	0.003	0.001	2.8	0.83	0.003	3.1	0.060	0.002	12.6	0.19	0.001	3.1	0.04	0.001	6.9	0.35	0.004
0.09	0.012	0.003	7	2.14	0.003	14	0.14	0.005	56	0.47	0.003	16	0.11	0.001	9	0.45	0.005
0.0	0.006	0.001	1.0	0.28	0.002	2.8	0.040	0.001	9.8	0.11	0.001	3.1	0.03	0.001	1.0	0.053	0.002
0.4	0.040	0.006	4.6	1.04	0.013	15.7	0.34	0.006	45.9	0.52	0.006	14.6	0.18	0.004	4.4	0.22	0.013
0.3	0.041	0.009	0.9	0.34	0.001	3.3	0.16	0.020	6.2	0.18	0.009	2.1	0.07	0.004	2.7	0.15	0.011
0.1	0.012	0.002	0.3	0.12	0.001	0.9	0.040	0.002	1.3	0.050	0.002	0.5	0.02	0.001	1.8	0.062	0.005
0.3	0.038	0.005	0.9	0.34	0.014	1.8	0.10	0.005	3.0	0.12	0.005	1.5	0.06	0.004	6.9	0.25	0.017
0.1	0.007	0.001	0.1	0.052	0.002	0.1	0.11	0.001	0.3	0.014	0.001	0.2	0.01	0.001	1.2	0.036	0.002
0.3	0.026	0.007	0.8	0.25	0.010	0.5	0.54	0.007	1.6	1.6	0.010	0.9	0.03	0.003	6.8	0.18	0.014
0.05	0.006	0.003	0.15	0.046	0.002	0.06	0.007	0.003	0.24	0.013	0.003	0.15	0.01	0.001	1.1	0.032	0.003
0.1	0.016	0.004	0.4	0.12	0.004	0.1	0.020	0.004	0.5	0.030	0.004	0.3	0.02	0.002	2.7	0.084	0.008
0.01	0.003	0.001	0.06	0.023	0.002	0.01	0.003	0.007	0.05	0.006	0.001	0.03	0.003	0.001	0.31	0.017	0.002
0.1	0.014	0.005	0.4	0.114	0.010	0.1	0.016	0.005	0.3	0.030	0.005	0.2	0.01	0.003	1.9	0.083	0.008
0.01	0.003	0.001	0.06	0.022	0.002	0.01	0.002	0.001	0.03	0.004	0.001	0.02	0.002	0.000	0.25	0.016	0.002
0.3	0.025	0.005	1.3	0.41	0.007	0.5	0.040	0.005	2.8	0.070	0.005	1.4	0.04	0.002	1.3	0.058	0.008
bdl	bdl	0.034	0.09	0.16	0.003	0.02	0.004	0.034	0.04	0.005	0.002	0.02	0.002	0.001	0.38	0.025	0.001
bdl	0.004	0.019	3.1	0.34	0.014	0.3	0.027	0.020	2.7	0.081	0.020	1.0	0.03	0.003	1.1	0.075	0.126
bdl	bdl	0.001	0.37	0.11	0.004	0.02	0.005	0.001	0.85	0.030	0.003	0.02	0.003	0.001	0.30	0.023	0.002
bdl	bdl	0.001	0.27	0.066	0.003	0.01	0.003	0.001	0.05	0.007	0.002	0.01	0.002	0.001	0.12	0.012	0.002

APPENDIX D.1:

MINIMUM DETECTION LIMITS AND ASSOCIATED UNCERTAINTIES FOR LA-ICP-MS TRACE ELEMENT SULPHIDE ANALYSES

Appendix D.1 Minimum detection limits and associated uncertainties for LA-ICPMS trace element sulphide analyses

Sample HRV-161B						
Mss	Avg. (ppm)	2 - σ	mdl	Avg. (ppm)	2 - σ	mdl
^{75}As	120	11.0	0.5	3520	120	0.2
^{77}Se	68.8	6.30	0.7	119	8.6	0.9
^{101}Ru	0.61	0.06	0.007	1.53	0.1	0.006
^{106}Pd	4.48	0.20	0.01	0.102	0.08	0.007
^{107}Ag	5.28	0.10	0.08	35.5	0.7	0.01
^{125}Te	14.2	1.90	0.1	24.1	3.9	0.09
^{185}Re	0.39	0.03	0.003	0.47	0.02	0.004
^{189}Os	0.09	0.0	0.008	0.40	0.10	0.08
^{193}Ir	0.138	0.02	0.003	0.358	0.070	0.001
^{195}Pt	2.490	0.2	0.04	1.340	0.100	0.030
^{197}Au	bdl	0.003	0.006	0.11	0.08	0.006
^{208}Pb	37	0.3	0.06	66	2.30	0.007
^{209}Bi	0.41	0.3	0.02	1.28	0.04	0.01
^{39}K	603	6.4	2	721	6.1	1.7
^{51}V	53.1	5.5	0.1	32.7	0.6	0.02
^{52}Cr	161	10	0.6	98.1	7.9	0.1
^{55}Mn	359	5.6	0.6	620	10	1.6
^{59}Co	9590	540	0.09	7100	715	0.1
^{64}Zn	24.7	3.7	0.3	240	12	0.7
^{95}Mo	512	5.5	0.1	580	6.7	0.1
^{180}W	0.17	0.05	0.009	1.29	0.40	0.01

*Note two representative samples were chosen to show the minimum and maximum compositional heterogeneity

APPENDIX E:

SELECT MAJOR AND MINOR ELEMENT COMPOSITIONS OF SECONDARY CLINOPYROXENE, AS WELL AS PHLOGOPITE AND KYANITE FROM THE KAAPVAAL CRATON ECLOGITE XENOLITHS

Appendix E. Select major and minor element compositions of secondary clinopyroxene, as well as phlogopite and kyanite from the Kaapvaal eclogite xenoliths

Sample	ROVIC-MBK	HRV-174A	HRV-162A	HRV-162B	HRV-161A	HRV-161B	HRV-172A	JJG-2919	CIM15-101	ST16-H-04
mineral:	*Cpx*	*Cpx*	*Cpx*	*Cpx*	*Cpx*	*Cpx*	*Cpx*	*Cpx*	*Cpx*	*Cpx*
SiO_2	53.6	53.4	53.5	54.0	55.2	55.5	54.0	54.6	53.9	50.6
TiO_2	0.5	0.5	0.5	0.5	0.1	0.2	0.5	0.5	0.5	0.4
Al_2O_3	9.9	6.1	4.0	2.9	4.1	7.2	6.9	5.3	5.4	7.2
Cr_2O_3	0.22	0.16	0.08	0.00	0.33	0.32	bdl	bdl	bdl	bdl
FeO	3.6	5.9	5.2	5.8	3.5	3.1	4.9	5.2	3.8	8.2
MnO	bdl	0.30	0.05	bdl	bdl	bdl	bdl	bdl	0.00	0.85
MgO	11.7	13.8	15.3	15.7	15.8	12.6	13.2	13.5	16.5	16.4
CaO	16.1	17.1	19.0	20.0	18.6	15.3	18.4	18.0	16.2	15.1
Na_2O	4.4	2.7	1.6	1.9	2.3	4.7	2.9	3.1	2.2	0.7
K_2O	bdl	bdl	0.1	bdl	bdl	0.1	bdl	bdl	bdl	bdl
Total (wt. %)	100.0	100.0	99.3	100.7	100.0	99.1	100.7	100.2	98.5	99.4
Mg#	85	81	84	83	89	88	83	82	88	78
Cpx Class	B	B	A	A	A	A	B	B	A	A

Sample	ROVIC-MBK	MBK	HRV-161A	HRV-161B	CIM15-102	ST16-H-04
mineral:	*Phl*	*Phl*	*Phl*	*Phl*	*Phl*	*Phl*
SiO_2	38.01	41.66	38.56	40.11	41.08	40.69
TiO_2	2.44	0.80	1.50	1.52	0.63	1.88
Al_2O_3	17.79	12.69	17.00	15.19	13.54	14.62
Cr_2O_3	0.13	0.49	0.27	0.20	bdl	0.19
FeO	9.04	4.11	6.72	6.12	3.39	7.20
MgO	17.65	24.20	20.46	21.30	24.43	20.84
NiO	bdl	0.18	bdl	bdl	bdl	bdl
K2O	9.68	9.86	9.56	9.78	9.54	9.15
Na2O	0.19	0.48	0.43	0.33	0.71	0.31
Cl	bdl	bdl	bdl	bdl	bdl	bdl
F	0.31	0.20	0.21	0.18	bdl	0.38
Total (wt. %)	95.24	94.67	94.71	94.74	93.31	95.26
Mg#	72	91	81	84	94	81

Sample	ROVIC-MBK	JJG-4492	HRV-172B
mineral:	*Ky*	*Ky*	*Ky*
SiO_2	37.04	36.79	37.47
TiO_2	0.17	bdl	bdl
Al_2O_3	61.66	62.09	63.22
Cr_2O_3	0.25	bdl	bdl
FeO	0.25	0.19	0.29
MgO	0.1	0.1	bdl
Total (wt. %)	99.47	99.17	100.98

Average abundances determined by scanning electron microprobe (SEM) analysis, CAF - Stellenbosch University
See Appendix B for element precision and mdl.

CHAPTER 4: APPENDICES

"PERVASIVE FE- AND S-RICH METASOMATISM OF THE CRATONIC LITHOSPHERIC MANTLE BELOW PREMIER KIMBERLITE, SOUTH AFRICA"

APPENDIX A:

ASIMEX STANDARDS USED IN SEM ROUTINE

Appendix A. SEM major and minor element analyses of NiS5b and other ASTIMEX standards

Mineral Standard:	NiS5b			NiS5b (published)	
Spot size:	30µm			30µm	
Spot number:	19			20	
Element (wt. %)	*Avg.*	*1-σ*	*mdl*	*Avg.*	*1-σ*
Ni	68.28	1.42	0.1	67.37	1.78
Fe	3.16	0.82	0.1	3.26	0.80
Cu	0.98	0.25	0.1	1.18	0.24
S	27.15	0.27	0.2	27.87	0.37
Total	99.57			99.68	
Mineral Standard:	Marcasite			(ASTIMEX)	
Spot size:	30µm			30µm	
Spot number:	5			20	
Element (wt. %)	*Avg.*	*1-σ*	*mdl*	*Avg.*	*1-σ*
S	53.28	0.51	0.2	53.46	0.36
Fe	46.72	0.38	0.1	46.54	0.27
Total	100.00			100.00	
Mineral Standard:	Pentlandite			(ASTIMEX)	
Spot size:	30µm			30µm	
Spot number:	5			20	
Element (wt. %)	*Avg.*	*1-σ*	*mdl*	*Avg.*	*1-σ*
S	32.76	0.13	0.2	33.01	0.27
Fe	31.23	0.23	0.1	30.77	0.17
Co	0.15	0.03	0.06	0.10	0.07
Ni	36.47	0.18	0.1	36.12	0.31
Total	100.61			100.00	
Mineral Standard:	Magnetite			(ASTIMEX)	
Spot size:	30µm				
Spot number:	5				
Compound (wt. %)	*Avg.*	*1-σ*	*mdl*	*Avg.*	*1-σ*
Cr_2O_3	0.1	0.20	0.1	0.20	0.20
FeO	31.0	0.05	0.1	31.03	0.42
Fe_2O_3	68.9	0.15	0.1	68.76	0.70
Total (wt. %)	100.00			99.99	

Average abundances determined by scanning electron microprobe (SEM) analysis, CAF - Stellenbosch University

1- σ = within-run precition, mdl = mean detection limits

ASTIMEX = published mineral composition (Astimex Scienific Limited, MINM25-53 #03-0400)

NiS5b (published) = taken from Mungall and Brenan, (2014).

Appendix A. SEM major and minor element analyses of NiS5b and other ASTIMEX standards (continued)

Mineral Standard:	Pyrope			(ASTIMEX)	
Spot size:	30µm				
Spot number:	5				
Compound (wt. %)	*Avg.*	*1-σ*	*mdl*	*Avg.*	*1-σ*
SiO_2	41.83	0.19	0.1	41.45	1.02
TiO_2	1.21	0.03	0.015	1.16	0.70
Al_2O_3	21.47	0.07	0.2	21.32	0.60
Cr_2O_3	0.70	0.06	0.017	0.58	0.40
FeO	11.37	0.11	0.1	11.15	0.02
MnO	0.13	0.07	0.063	0.27	0.30
MgO	18.74	0.30	0.1	19.33	0.06
CaO	4.17	0.24	0.1	4.65	0.01
Total (wt. %)	99.62			99.91	
Mineral Standard:	Cr Diopside			(ASTIMEX)	
Spot size:	30µm				
Spot number:	5				
Compound (wt. %)	*Avg.*	*1-σ*	*mdl*	*Avg.*	*1-σ*
SiO_2	54.82	1.10	0.1	54.59	1.30
TiO_2	0.15	0.30	0.012	0.10	0.40
Cr_2O_3	0.47	0.20	0.038	0.50	0.30
FeO	1.42	0.20	0.01	1.39	0.17
MgO	17.44	0.15	0.1	17.14	0.20
CaO	24.80	0.35	0.1	25.50	0.20
Na_2O	0.51	0.40	0.04	0.44	0.30
Total (wt. %)	99.61			99.66	
Mineral Standard:	Diopside			(ASTIMEX)	
Spot size:	30µm				
Spot number:	5				
Compound (wt. %)	*Avg.*	*1-σ*	*mdl*	*Avg.*	*1-σ*
SiO_2	55.40	0.50	0.1	55.37	0.50
TiO_2	0.07	0.04	0.010	0.08	0.03
Al_2O_3	0.10	0.06	0.020	0.09	0.05
FeO	0.05	0.07	0.01	0.05	0.06
MgO	18.63	0.05	0.1	18.62	0.30
CaO	25.75	0.35	0.1	25.73	0.10
Total (wt. %)	100.00			99.94	
Mineral Standard:	Olivine			(ASTIMEX)	
Spot size:	30µm				
Spot number:	5				
Compound (wt. %)	*Avg.*	*1-σ*	*mdl*	*Avg.*	*1-σ*
SiO_2	41.6	0.20	0.1	41.58	0.5
MgO	50.4	0.10	0.10	50.43	0.3
MnO	0.1	0.10	0.01	0.10	0.1
FeO	7.5	0.30	0.1	7.51	0.2
NiO	0.4	0.30	0.01	0.38	0.2
Total (wt. %)	100.03			100.00	

Average abundances determined by scanning electron microprobe (SEM) analysis, CAF - Stellenbosch University

1- σ = within-run precition, mdl = mean detection limits

ASTIMEX = published mineral composition (Astimex Scienific Limited, MINM25-53 #03-0400)

NiS5b (published) = taken from Mungall and Brenan, (2014).

APPENDIX B:

GARNET, CLINOPYROXENE, OLIVINE AND ORTHOPYROXENE TRACE ELEMENT CONCENTRATIONS AND ASSOCIATED UNCERTAINTIES FOR LA-ICP-MS ANALYSES.

Appendix B. Select garnet and clinopyroxene trace element compositions and associated undcertainties for LA-ICP-MS trace element abundances

Sample	CIM15-001		CIM15-002		CIM15-003		CIM15-006		CIM15-013		CIM15-015		CIM15-016		CIM15-017		CIM15-021		CIM15-035	
Texture	Def LRZ		Crs LRZ		Def LRZ		Crs LRZ		Crs LRZ		Def LRZ		Def LRZ		Def LRZ		Def LRZ		Def LRZ	
TE class	Normal		Humped		Normal		Humped		Humped		Normal		Normal		Sinusoidal		Normal		Normal	
mineral:	*Grt*	*2 - σ*	*Grt*	*2 - σ*	*Grt*	*2 - σ*	*Grt*	*2 - σ*	*Grt*	*2 - σ*	*Grt*	*2 - σ*	*Grt*	*2 - σ*	*Grt*	*2 - σ*	*Grt*	*2 - σ*	*Grt*	*2 - σ*
Sc	85	1.3	103	1.1	88	1.0	99	1	95	1.1	87	0.9	74	0.7	109	1.3	74	1	223	3
V	253	3.3	318	2.4	245	3.6	323	2.7	304	4	221	2.1	244	1.7	284	3.0	235	2	518	8
Mn	1933	17.4	2038	13.1	1858	12.9	2157	13	1924	14	1932	12	1863	11	1924	11.9	1876	12	5664	72
Co	44	0.74	45	0.83	43	0.69	43	0.7	44	0.8	43	0.7	46	0.6	43	0.8	45	0.7	87	1
Ni	130	2.4	135	2.5	117	2.1	136	2.9	140	3	122	1.9	137	2	132	2.8	120	1.9	155	2.4
Cu	0.96	0.25	0.99	0.12	0.36	0.07	0.82	0.096	0.63	0.12	0.61	0.097	0.60	0.08	0.41	0.09	0.50	0.08	0.65	0.06
Zn	14	0.8	15	0.9	13	0.7	15	0.9	16	0.99	14	0.9	19	0.9	15	1	17	0.9	31	0.9
Rb	4.7	0.19	3.7	0.17	0.3	0.09	5.0	0.2	0.2	0.08	bdl	bdl	bdl	bdl	0.03	0.04	bdl	0.006	0.01	0.008
Sr	12.1	2.2	24.6	1.6	0.67	0.07	32.9	0.5	1.1	0.12	0.58	0.069	0.62	0.06	0.80	0.09	0.49	0.06	0.67	0.05
Y	18	0.3	21	0.3	16	0.3	27	0.3	23	0.3	14	0.2	19	0.2	7.2	0.2	18	0.3	47	0.7
Zr	75	1.1	86	0.9	52	0.6	95	0.9	87	1.0	56	0.6	66	0.7	56	0.6	50	0.5	178	2.7
Nb	0.58	0.04	0.42	0.04	0.56	0.03	0.48	0.03	0.45	0.038	0.34	0.03	0.35	0.03	0.75	0.052	0.35	0.03	0.49	0.03
Ba	521	34	301	6	5.8	0.5	94	3.9	9.5	3.2	0.1	0.06	bdl	bdl	bdl	bdl	bdl	bdl	bdl	bdl
La	0.14	0.02	0.07	0.01	0.05	0.01	0.09	0.02	0.06	0.012	0.04	0.010	0.05	0.009	0.07	0.01	0.03	0.010	0.04	0.007
Ce	0.54	0.04	0.51	0.04	0.46	0.03	0.65	0.04	0.54	0.04	0.38	0.03	0.42	0.029	0.65	0.05	0.34	0.04	0.40	0.02
Pr	0.13	0.02	0.16	0.02	0.15	0.02	0.20	0.02	0.17	0.02	0.12	0.02	0.14	0.01	0.20	0.02	0.12	0.02	0.17	0.01
Nd	1.3	0.11	1.6	0.12	1.5	0.11	1.9	0.16	1.7	0.22	1.3	0.1	1.4	0.12	1.9	0.16	1.2	0.1	1.8	0.10
Sm	1.1	0.12	1.4	0.12	1.0	0.11	1.5	0.15	1.3	0.18	1.1	0.1	1.2	0.12	1.3	0.15	0.90	0.11	2.01	0.13
Eu	0.53	0.03	0.64	0.04	0.48	0.03	0.68	0.05	0.67	0.067	0.50	0.05	0.55	0.04	0.57	0.06	0.43	0.05	1.08	0.05
Gd	2.2	0.14	2.7	0.16	1.9	0.14	3.1	0.17	2.7	0.18	1.9	0.2	2.3	0.15	2.2	0.2	1.9	0.2	4.9	0.2
Tb	0.47	0.03	0.57	0.03	0.38	0.02	0.66	0.03	0.58	0.034	0.34	0.03	0.45	0.03	0.32	0.02	0.39	0.03	1.10	0.04
Dy	3.4	0.17	4.1	0.15	2.8	0.12	5.1	0.2	4.5	0.2	2.4	0.13	3.4	0.14	1.8	0.1	3.0	0.2	8.5	0.2
Ho	0.70	0.03	0.83	0.03	0.62	0.03	1.08	0.04	0.89	0.043	0.52	0.03	0.75	0.04	0.30	0.02	0.70	0.04	1.95	0.06
Er	1.9	0.09	2.2	0.09	1.9	0.09	3.0	0.1	2.5	0.15	1.6	0.09	2.1	0.09	0.74	0.06	2.2	0.1	5.6	0.17
Tm	0.27	0.02	0.30	0.02	0.30	0.02	0.44	0.03	0.34	0.03	0.24	0.02	0.33	0.016	0.11	0.01	0.34	0.03	0.80	0.03
Yb	1.9	0.12	0.1	0.12	2.1	0.10	2.7	0.16	2.2	0.17	1.7	0.1	2.3	0.13	0.8	0.09	2.3	0.1	5.5	0.2
Lu	0.28	0.02	0.27	0.02	0.32	0.02	0.39	0.03	0.29	0.025	0.26	0.02	0.33	0.02	0.15	0.02	0.36	0.03	0.79	0.03
Hf	1.9	0.1	2.3	0.1	1.3	0.09	2.5	0.1	2.3	0.15	1.1	0.08	1.5	0.07	1.3	0.08	1.3	0.09	4.2	0.16
Ta	0.05	0.008	0.04	0.008	0.06	0.008	0.05	0.009	0.04	0.010	0.04	0.008	0.03	0.005	0.08	0.010	0.04	0.009	0.04	0.006
Pb	0.12	0.03	0.08	0.02	0.01	0.01	0.05	0.015	0.02	0.01	0.03	0.01	bdl	bdl	bdl	bdl	bdl	bdl	0.08	0.02
Th	0.02	0.005	0.02	0.005	0.02	0.004	0.02	0.006	0.01	0.005	0.01	0.005	0.02	0.007	0.03	0.008	0.01	0.006	0.01	0.004
U	0.02	0.005	0.02	0.006	0.02	0.005	0.02	0.007	0.02	0.007	0.01	0.005	0.01	0.005	0.03	0.008	0.01	0.006	0.02	0.006

Appendix B. Select garnet and clinopyroxene trace element compositions and associated undcertainties for LA-ICP-MS trace element abundances (continued)

mineral:	*Cpx*	*2 - σ*	*Cpx*	*2 - σ*	*Cpx*	*2 - σ*	*Cpx*	*2 - σ*	*Cpx*	*2 - σ*	*Cpx*	*2 - σ*	*Cpx*	*2 - σ*	*Cpx*	*2 - σ*	*Cpx*	*2 - σ*	*Cpx*	
Sc	19	0.3	1.9	0.11	14	0.3	74	0.6	73	1	18	0.2	30	0.4	33	0.6	34	0	31	0.5
V	224	2	1.1	0.07	171	2	307	3	295	3	184	2	392	4	464	3	379	4	341	3.4
Mn	898	4.6	28	0.9	841	4.2	1865	11	2176	28	901	4	2159	20	2015	23	2029	17	804	7.8
Co	32	0.4	1.6	0.4	31	0.5	65	1	79	1	32	0.4	71	0.7	65	1.0	64	1	30	1.2
Ni	559	4.8	28	4.1	543	6.1	553	7	1084	17	538	4	1239	11	1194	15	1140	12	387	5.8
Cu	4.44	0.16	1.4	0.09	2.40	0.36	16.90	1.6	1.49	0.2	3.91	0.15	7.28	0.2	8.37	1.2	8.27	0.24	1.7	0.4
Zn	16	0.8	4.6	0.3	15	0.7	27	1	54	2.5	18	0.7	43	0.8	36	1.8	33	1	14	1.1
Rb	0.2	0.1	21.9	0.5	3.0	0.6	29.6	1.2	50.4	2.1	1.3	0.09	0.12	0.06	0.05	0.06	0.22	0.07	12	1.05
Sr	116	1.3	22	0.4	90	1.1	588	10	166	6.3	102	1	199	2	208	2	210	2	267	3.9
Y	4	0.05	0.8	0.03	2	0.01	20	0.2	16	0.2	3	0.06	6	0.1	6	0.1	5	0	8.6	0.25
Zr	11	0.2	86	0.8	5	0.2	52	0.6	56	0.8	11	0.2	17	0.3	18	0.3	22	0	81	1.4
Nb	0.47	0.04	0.20	0.02	0.86	0.16	2.09	0.07	1.22	0.07	0.39	0.03	0.48	0.03	0.59	0.03	0.59	0.03	2.4	0.08
Cs	0.01	0.01	0.54	0.08	0.24	0.06	0.27	0.03	6.59	0.3	0.15	0.01	bdl	0.004	0.003	0.001	0.01	0.01	0.2	0.03
Ba	12	0.5	148	2.3	5	1.3	303	9.3	1633	133	6	0.4	1	0.2	1	0.1	3	0	43	2.5
La	1.9	0.04	0.9	0.04	2.0	0.08	1.7	0.06	0.5	0.04	1.9	0.04	3.6	0.1	4.0	0.0	3.8	0.1	5.9	0.2
Ce	6.5	0.10	1.6	0.06	6.4	0.09	3.0	0.08	1.2	0.08	6.7	0.1	12	0.2	13	0.2	13	0	21	0.2
Pr	1.1	0.04	0.2	0.02	1.0	0.03	0.4	0.02	0.2	0.02	1.1	0.04	2.0	0.04	2.2	0.03	2.2	0.0	3.8	0.1
Nd	6.0	0.19	0.6	0.06	5.2	0.15	2.4	0.2	1.5	0.13	6.3	0.2	11	0.2	12	0.9	12	0	20	0.6
Sm	1.7	0.08	0.09	0.04	1.3	0.10	1.2	0.1	1.0	0.10	1.7	0.1	3.1	0.1	3.2	0.0	3.3	0.1	5.0	0.2
Eu	0.6	0.04	0.09	0.02	0.4	0.02	0.5	0.03	0.5	0.04	0.5	0.03	1.1	0.03	1.1	0.03	1.1	0.0	1.6	0.1
Gd	1.61	0.1	0.08	0.02	1.02	0.06	2.30	0.1	2.02	0.15	1.44	0.1	2.90	0.12	3.09	0.02	2.93	0.09	4.05	0.2
Tb	0.20	0.01	0.01	0.005	0.12	0.009	0.46	0.03	0.42	0.03	0.17	0.01	0.36	0.02	0.36	0.02	0.34	0.02	0.49	0.03
Dy	1.1	0.06	0.11	0.02	0.59	0.04	3.7	0.15	3.2	0.14	0.8	0.06	1.7	0.1	1.7	0.1	1.6	0.1	2.4	0.2
Ho	0.17	0.009	0.02	0.006	0.091	0.01	0.80	0.03	0.67	0.03	0.12	0.01	0.26	0.01	0.26	0.01	0.22	0.01	0.4	0.03
Er	0.34	0.03	0.07	0.01	0.19	0.02	2.33	0.1	1.8	0.09	0.23	0.02	0.54	0.03	0.52	0.03	0.41	0.03	0.8	0.07
Tm	0.03	0.005	0.01	0.007	0.022	0.00	0.31	0.02	0.25	0.01	0.02	0.005	0.06	0.01	0.06	0.01	0.04	0.01	0.09	0.01
Yb	0.16	0.02	0.10	0.02	0.12	0.02	2.02	0.09	1.53	0.1	0.13	0.02	0.32	0.03	0.30	0.02	0.22	0.03	0.5	0.06
Lu	0.02	0.004	0.02	0.005	0.016	0.00	0.29	0.01	0.22	0.01	0.02	0.004	0.04	0.005	0.04	0.004	0.03	0.00	0.07	0.02
Hf	0.69	0.04	2.00	0.11	0.28	0.02	1.46	0.06	1.57	0.08	0.59	0.05	0.99	0.05	1.11	0.03	1.19	0.06	1.4	0.1
Ta	0.03	0.005	0.02	0.005	0.043	0.01	0.06	0.007	0.08	0.01	0.02	0.003	0.03	0.004	0.03	0.002	0.04	0.01	0.2	0.01
Pb	0.16	0.02	4.48	0.09	0.17	0.02	0.51	0.04	0.71	0.4	0.18	0.02	0.31	0.03	0.29	0.03	0.47	0.07	0.2	0.05
Th	0.04	0.007	0.23	0.02	0.09	0.03	0.11	0.02	0.13	0.09	0.03	0.01	0.04	0.01	0.04	0.01	0.05	0.01	0.1	0.02
U	0.007	0.002	0.15	0.01	0.01	0.00	0.03	0.006	0.02	0.007	0.006	0.003	0.007	0.003	0.006	0.002	0.009	0.003	0.02	0.005

Appendix B. Select olivine and orthopyrxene and trace element compositions and associated uncertainties for LA-ICP-MS trace element abundances (continued)

Sample	CIM15-001		CIM15-002		CIM15-003		CIM15-006		CIM15-013		CIM15-015		CIM15-016		CIM15-017		CIM15-021		CIM15-035	
Texture	Def LRZ		Crs LRZ		Def LRZ		Crs LRZ		Crs LRZ		Def LRZ		Def LRZ		Def LRZ		Def LRZ		Def LRZ	
mineral:	*Ol*	*2 - σ*	*Ol*	*2 - σ*	*Ol*	*2 - σ*	*Ol*	*2 - σ*	*Ol*	*2 - σ*	*Ol*	*2 - σ*	*Ol*	*2 - σ*	*Ol*	*2 - σ*	*Ol*	*2 - σ*	*Ol*	*2 - σ*
Sc	3.7	0.28	3.1	0.18	2.6	0.13	4.7	0.12	4.2	0.12	4.8	0.1	4.4	0.1	5.3	0.12	4.8	0.1	3.3	0.22
V	11.4	1.7	11.2	0.28	9.4	0.3	13.2	0.20	12.8	0.19	10.2	0.2	11.6	0.2	10.9	0.39	11.0	0.2	1.8	0.13
Cr	191	51	448	4.4	326	3.4	549	2.1	480	3.8	314	2.4	294	2.1	513	11	196	1.8	61	1.5
Mn	872	120	819	9.8	800	4.0	933	4.6	882	4.7	863	4.3	872	4.0	888	8	873	5	1113	8.8
Co	151	20	138	4.6	136	1.9	140	1.5	146	1.2	142	1.5	148	1.2	139	3	150	2	141	2
Ni	3018	450	2973	58	2975	31	2683	18	3055	18	2806	21	3059	16	2949	25	2794	15	2689	30
Cu	4.8	0.97	6.3	0.29	7.0	0.24	8.0	0.20	5.6	0.29	6.4	0.2	6.0	0.2	5.2	0.3	5.0	0.2	1.4	0.15
Zn	78	8.1	58	2	58	2.6	65	1.6	67	1.3	62	1.3	79	1.4	61	2.0	76	1.9	71	4.6
Rb	bdl	2.4	0.05	0.05	0.01	0.009	bdl	0.01	bdl	0.06	0.02	0.01	bdl	0.01	0.02	0.06	0.04	0.01	0.08	0.01
Sr	0.01	2.6	0.48	0.20	0.07	0.43	0.01	0.05	0.02	0.03	0.18	0.06	0.01	0.01	0.01	0.03	0.08	0.02	0.70	0.01
Y	0.02	0.09	0.02	0.01	0.01	0.02	0.02	bdl	0.02	0.01	0.02	0.01	0.02	0.01	0.00	0.01	0.01	0.01	0.03	0.01
Zr	0.10	9.9	0.72	0.03	0.09	0.02	0.13	0.02	0.11	0.02	0.15	0.02	0.12	0.01	0.06	0.02	0.10	0.02	0.47	0.04
Nb	0.01	0.03	0.03	0.02	0.02	0.01	0.01	0.01	0.02	0.01	0.07	0.01	0.02	0.01	0.02	0.01	0.01	0.01	0.44	0.05
mineral:	*Opx*	*2 - σ*	*Opx*	*2 - σ*	*Opx*	*2 - σ*	*Opx*	*2 - σ*	*Opx*	*2 - σ*	*Opx*	*2 - σ*	*Opx*	*2 - σ*	*Opx*	*2 - σ*	*Opx*	*2 - σ*	*Opx*	*2 - σ*
Sc	5.9	0.18	5.8	0.17	4.7	0.14	7.6	0.13	6.9	0.14	7.1	0.14	6.9	0.1	8.1	0.1	6.0	0.1	5.3	0.14
V	58	0.9	57	0.62	47	0.51	63	0.55	59	0.65	48	0.52	54	0.6	49	0.6	55	0.5	45	0.55
Cr	2207	30	2831	27	2104	15	3229	21	2770	22	1819	11	1685	14	2788	25	1154	9	1753	15
Mn	891	5	924	4.8	886	5.5	966	5.7	911	6	867	4.2	894	5.3	918	6	899	5	874	6.7
Co	59	1.0	60	0.63	60	0.58	59	0.41	62	0.7	57	0.51	63	0.6	60	0.8	64	0.7	59	0.85
Ni	972	9	972	5.9	979	7.3	843	4.9	970	5.8	832	3.7	966	4.7	940	6.0	947	5	797	5.7
Cu	4.6	0.21	4.0	0.22	2.9	0.3	4.8	0.17	3.5	0.15	3.4	0.13	3.7	0.1	3.0	0.13	2.9	0.1	1.4	0.09
Zn	35	1.8	34	1.2	35	0.92	36	0.96	38	1.0	34	0.86	44	0.9	35	0.97	44	1	44	2.1
Rb	0.34	0.1	1.44	0.06	0.88	0.15	0.38	0.006	0.21	0.05	0.06	0.02	0.57	0.07	0.71	0.06	0.48	0.05	3.99	0.05
Sr	3.40	0.4	4.93	0.2	3.10	0.39	3.21	0.08	2.32	0.1	1.80	0.07	2.21	0.1	2.66	0.1	1.79	0.1	15.03	0.1
Y	0.24	0.02	0.20	0.01	0.13	0.01	0.26	0.02	0.21	0.02	0.17	0.01	0.22	0.02	0.05	0.01	0.19	0.01	0.14	0.02
Zr	0.94	1	0.85	0.03	0.36	0.04	0.63	0.04	0.55	0.03	0.59	0.03	0.56	0.03	0.22	0.02	0.52	0.03	0.93	0.04
Nb	0.09	0.02	0.12	0.01	0.20	0.09	0.06	0.01	0.06	0.01	0.06	0.01	0.06	0.01	0.08	0.01	0.10	0.01	0.77	0.02
Cs	0.06	0.04	0.27	0.03	0.12	0.02	0.03	0.01	0.03	0.01	0.01	0.00	0.06	0.01	0.16	0.02	0.11	0.01	0.13	0.01
Ba	3.5	0.53	6.4	0.32	6.4	1.2	8.4	0.05	6.0	0.41	1.5	0.2	2.9	0.3	3.0	0.2	1.3	0.02	31.0	0.6
La	0.03	0.01	0.06	0.005	0.08	0.04	0.02	0.004	0.02	0.004	0.02	0.00	0.02	0.00	0.02	0.01	0.03	0.16	0.36	0.01
Ce	0.12	0.02	0.14	0.009	0.18	0.07	0.08	0.01	0.08	0.01	0.07	0.01	0.08	0.01	0.07	0.01	0.10	0.01	0.69	0.01
Pr	0.02	0.01	0.02	0.01	0.02	0.01	0.02	0.01	0.02	0.01	0.01	0.01	0.02	0.01	0.01	0.01	0.02	0.01	0.08	0.01
Nd	0.10	0.05	0.11	0.01	0.12	0.04	0.10	0.03	0.10	0.02	0.08	0.02	0.10	0.02	0.09	0.02	0.10	0.02	0.30	0.03
Sm	0.04	0.02	0.04	0.01	0.03	0.02	0.03	0.01	0.05	0.02	0.03	0.011	0.04	0.01	0.03	0.02	0.04	0.01	0.07	0.01
Eu	0.01	0.006	0.02	0.004	0.01	0.005	0.02	0.004	0.02	0.005	0.01	0.004	0.02	0.004	0.01	0.004	0.02	0.005	0.02	0.005
Gd	0.05	0.022	0.05	0.01	0.03	0.01	0.05	0.02	0.05	0.02	0.03	0.013	0.05	0.01	0.02	0.01	0.04	0.02	0.04	0.01
Tb	0.008	0.003	0.007	0.002	0.006	0.003	0.008	0.002	0.007	0.002	0.006	0.002	0.009	0.0024	0.003	0.001	0.008	0.002	0.005	0.001
Dy	0.05	0.02	0.05	0.01	0.03	0.01	0.05	0.011	0.05	0.01	0.04	0.012	0.05	0.01	0.01	0.007	0.04	0.01	0.03	0.01
Ho	0.009	0.003	0.008	0.003	0.005	0.002	0.009	0.003	0.009	0.003	0.004	0.002	0.008	0.002	0.002	0.001	0.007	0.002	0.005	0.002
Er	0.02	0.01	0.02	0.01	0.01	0.00	0.03	0.01	0.02	0.01	0.02	0.01	0.02	0.01	bdl	bdl	0.02	0.01	0.01	0.01
Tm	0.004	0.003	0.003	0.001	0.002	0.001	0.003	0.002	0.003	0.001	0.002	0.001	0.002	0.001	bdl	0.000	0.003	0.001	0.002	0.001
Yb	0.02	0.01	0.01	0.01	0.01	0.01	0.02	0.01	0.01	0.01	0.01	0.01	0.02	0.01	bdl	bdl	0.02	0.01	0.01	0.01
Lu	0.003	0.002	0.002	0.001	0.001	0.001	0.003	0.001	0.002	0.001	bdl	bdl	0.002	0.001	0.001	0.001	0.003	0.001	0.003	0.001
Hf	0.04	0.02	0.04	0.007	0.02	0.009	0.03	0.009	0.03	0.007	0.04	0.008	0.03	0.007	0.01	0.005	0.02	0.007	0.02	0.004
Ta	0.01	0.01	0.01	0.01	0.01	0.01	bdl	bdl	0.01	0.01	bdl	bdl	0.01	0.01	0.01	0.01	0.01	0.01	0.05	0.01
Pb	0.09	0.04	0.05	0.01	0.06	0.02	0.08	0.01	0.03	0.008	0.01	0.007	0.02	0.006	0.02	0.009	0.01	0.005	0.13	0.02
Th	0.009	0.007	0.007	0.001	0.02	0.009	0.001	0.001	0.001	0.001	bdl	bdl	0.001	0.001	0.001	0.001	0.005	0.002	0.06	0.003
U	0.003	0.003	0.008	0.001	0.002	0.001	bdl	bdl	0.001	0.001	bdl	bdl	bdl	0.001	0.001	0.001	0.004	0.002	0.012	0.003

APPENDIX C:

STANDARD ANALYSIS AND ASSOCIATED ERRORS FOR LA-ICPMS TRACE ELEMENT ANALYSIS

Appendix C. Standard analyses and associated errors for LA-ICPMS trace element analyses.

	NIST 612	Iolite		BCR	Iolite		BHVO	Iolite	
	Avg. (ppm)	2 - σ	mdl	Avg. (ppm)	2 - σ	mdl	Avg. (ppm)	2 - σ	mdl
Sc	39.9	1.2	0.1	32.9	2.1	0.3	30.7	1.2	0.2
V	38.8	1.5	0.05	423	24	0.13	317	16	0.1
Co	35.5	1.3	1.01	37.1	0.9	1.8	44.3	0.3	1.4
Ni	38.8	1.8	1.5	11.8	1.3	0.5	119.3	2.4	0.1
Cu	37.8	1.5	1.1	16.7	4.3	0.18	123.7	3.3	0.1
Zn	39.2	3.6	1.1	153	28	0.16	120	18	0.1
Rb	31.4	1.2	0.01	45.2	1.9	0.03	8.8	2.4	0.01
Sr	78.4	2.4	0.01	327	13	0.02	377	19	0.01
Y	38.3	0.9	0.006	32.3	4.7	0.02	22.8	3.2	0.01
Zr	37.9	0.7	0.01	170	14	0.03	153	17	0.02
Nb	38.9	0.9	0.01	12	0.6	0.16	17	1.3	0.2
Cs	52.7	1.3	0.013	1.13	0.03	0.02	0.1	0.01	0.01
Ba	39.3	2.2	0.04	655	28	0.06	124	7	0.07
La	36.1	0.9	0.002	25	0.3	0.007	15	0.2	0.01
Ce	38.5	1	0.003	51	2.3	0.007	36	1.6	0.01
Pr	37.9	0.8	0.002	6.5	0.2	0.01	4.9	0.5	0.01
Nd	35.5	1.4	0.01	28	0.9	0.04	23	1.5	0.03
Sm	37.7	1.1	0.02	6.4	0.2	0.03	5.8	0.3	0.02
Eu	35.6	0.9	0.005	1.9	0.07	0.009	2	0.2	0.009
Gd	37.2	1.2	0.016	6.4	0.3	0.03	5.7	0.5	0.04
Tb	37.6	0.8	0.004	1	0.07	0.004	0.9	0.02	0.006
Dy	35.5	1.1	0.012	6.1	0.4	0.17	4.9	0.4	0.12
Ho	38.3	0.9	0.003	1.3	0.2	0.004	0.9	0.03	0.01
Er	37.9	0.8	0.007	3.5	0.2	0.012	2.3	0.3	0.01
Tm	36.8	0.9	0.002	0.5	0.1	0.004	0.3	0.04	0.005
Yb	39.2	1	0.012	3.4	0.3	0.02	1.9	0.1	0.01
Lu	37	0.9	0.002	0.5	0.04	0.004	0.4	0.01	0.03
Hf	36.7	0.9	0.008	4.8	0.3	0.02	4.1	0.22	0.2
Ta	37.6	0.9	0.001	0.7	0.08	0.004	1.1	0.05	0.002
Pb	38.7	1.6	0.012	10	1	0.01	1.8	0.1	0.01
Th	37.8	0.6	0.004	5.6	0.3	0.005	1.1	0.12	0.003
U	37.4	1.1	0.002	1.7	0.1	0.004	0.5	0.12	0.005
K	66.4	2.1	2.3	14903	180	5.7	4233.9	87	3.1
Cr	36.4	2.5	0.2	17.2	2.6	0.9	294	4.3	1.1
Mn	38.7	0.9	1.1	1550	35	2.3	1347	38	2.6
Mo	37.4	4.2	0.002	273	3.8	0.01	3.8	0.4	0.02
W	38	4.4	0.01	0.5	0.1	0.01	0.23	0.1	0.02

Average abundances determined by LA ICP MS, CAF - Stellenbosch University

Sil. Glass = NIST silicate glass standard, Iolite = Iolite ©2017 software package, 2 - σ = within run precision, mdl = mean detection limit

CHAPTER 5: APPENDICES

"THE MOBILITY OF SULPHUR IN THE UPPER MANTLE: CONSTRAINTS FROM S±C-BEARING ECLOGITE EXPERIMENTS"

APPENDIX A:

MULTI-ELEMENT VARIATION DIAGRAMS

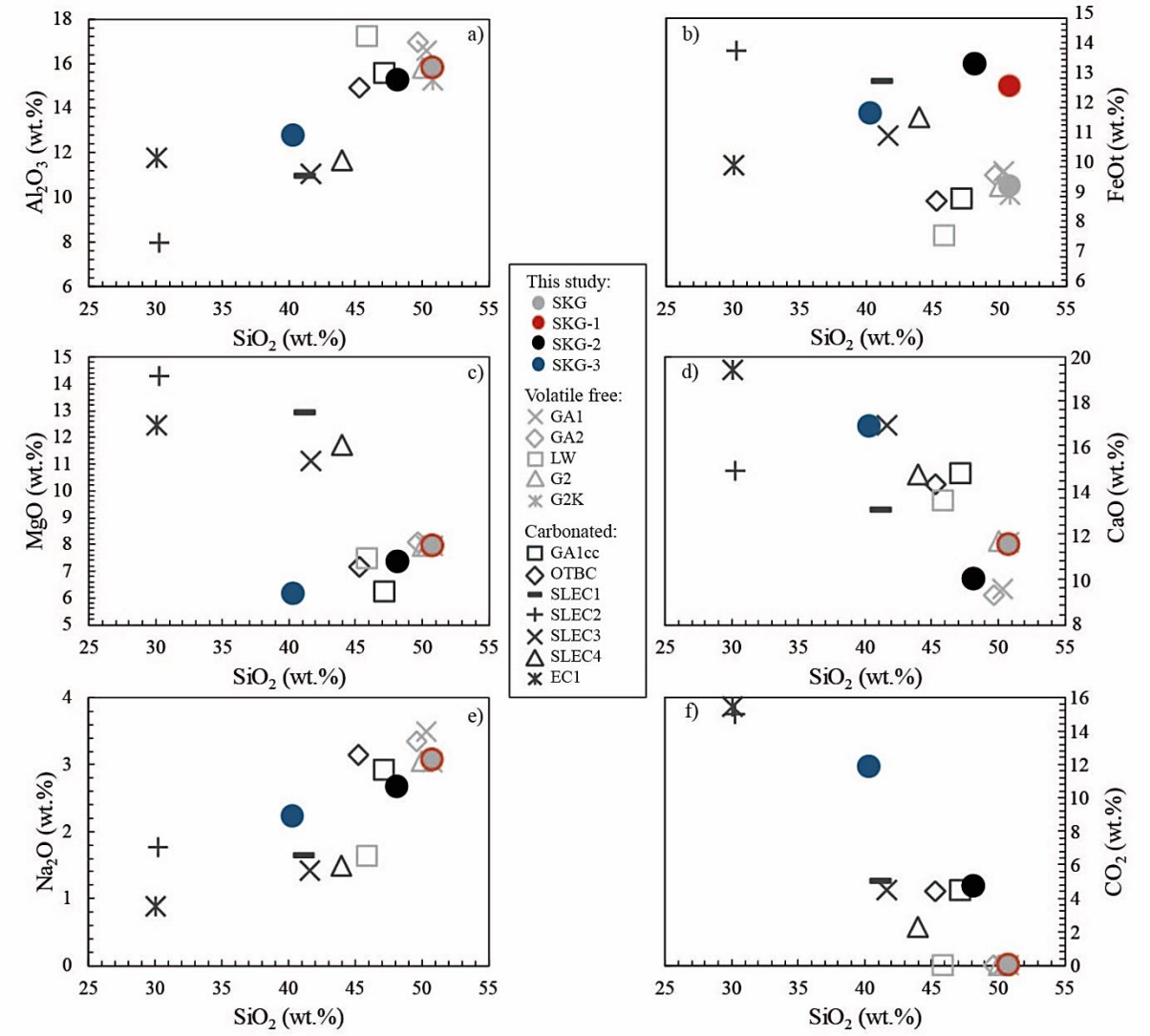

Multi-element variation diagrams showing the SKG starting compositions of this study and those of other volatile-free (GA1 = Yaxley and Green (1994); GA2 = Spandler et al. (2008); LW = Lambert and Wyllie (1972); G2, G2K = Pertermann and Hirschmann (2003)) and carbonated eclogite (EC1 = Yaxley and Brey (2004) ; SLEC1 = Dasgupta et al. 2004; SLEC2, SLEC3, SLEC4 = Dasgupta et al. 2005; OTBC = Hammouda (2003); GA1cc = Kiseeva et al. 2012) experimental studies. (a) SiO_2 vs. Al_2O_3; (b) vs. FeOt; (c) vs. MgO; (d) vs. CaO; (e) vs. Na_2O; (f) vs. CO_2

.

APPENDIX B:

VERTICAL 1-ATM GAS MIXING FURNACE CONFIGURATION

The SKG synthetic glass was fired at an oxygen fugacity of QFM-2 (log fO_2 = -9) in a top-loaded vertical gas mixing (CO + CO_2) furnace. The Carbolite furnace was modified with a bottom opening valve for sample quenching within a water bath. As shown in **Figure 1**, gas flows from the bottom of the ceramic work tube past the sample located in the furnace hot spot (±10cm length) to the top where it is extracted into the fume hood. A gas controller regulates the flow of both CO_2 and CO gas creating a reducing environment within the work tube. At temperatures above 1200°C the oxygen fugacity in the 1atm CO-CO_2 gas mixing furnace is expected to be equivalent to the actual CO-CO_2 mixture used and is expected to be homogeneous throughout the work tube (Huebner, 1975).

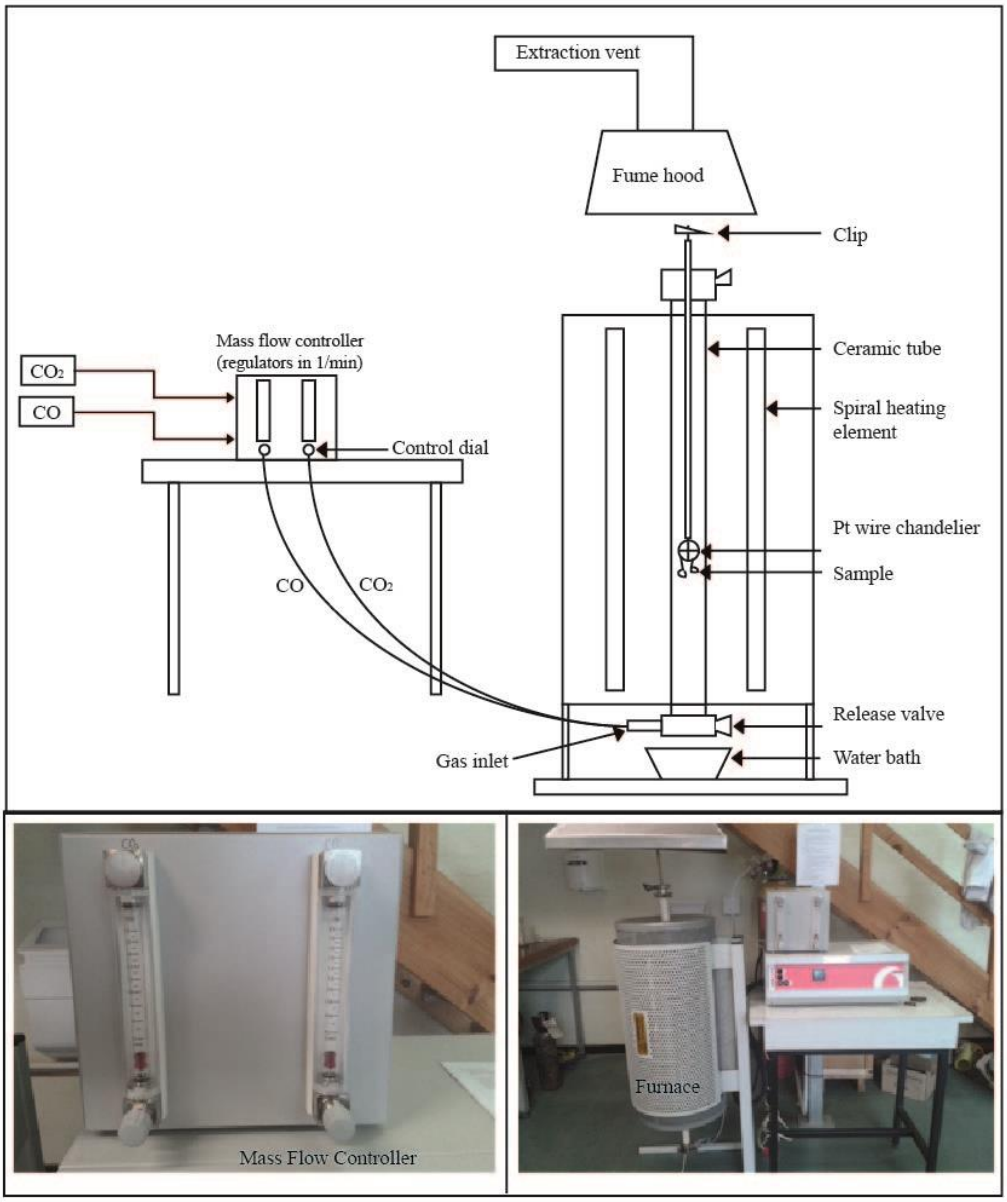

Figure 1. *Schematic of the vertical 1-atm gas mixing furnace components and the mass flow controller*

THERMAL PROFILE

The thermal profile of a furnace is dependent on the furnace design, temperature, gas composition and gas flow (c.f. Doyle, 2011). A thorough temperature calibration of the vertical 1atm, CO-CO_2 mixing furnace was conducted, capturing the thermal profile of the working tube and the exact position of the hotspot. The results of the calibration tests are presented below and compare well with the expected symmetrical temperature profile described by Huebner (1975) for a similar CO-CO_2 gas mixing furnace at temperatures close to 1400°C.

Method:

The furnace "hotspot", or area of peak temperature, was located by feeding (at 1cm increments) a type-R thermocouple into the work tube. At a working temperature of 1200°C and no gas flowing, the hotspot was located 3cm above the centre point of the furnace (46cm from the top) and extended downwards for 10cm. The offset between the hotspot temperature and the programmed temperature was never more than 2°C. The results of the thermal profile tests are shown in **Table 1** and **Figure 2** below. The introduction of the CO-CO_2 gas flow did not change the position or temperature of the furnace hotspot.

Table 1. Thermal profiles of the Carbolite CO-CO_2 gas mixing furnace

T_p 1200ºC (no gas flowing) – Thermal profile 1		T_p 1200ºC (no gas flowing) – Thermal profile 2	
	$Temp_h$ (ºC)	Distance into furnace (cm)	$Temp_h$ (ºC)
41	1190	41	1190
46	1198	46	1198
47	1199	47	1199
48	1200	48	1199
51	1200	51	1201
58	1201	58	1201
59	1198	59	1200

T_p = Programmed temperature; $Temp_h$ = Temperature of hotspot on handheld thermocouple

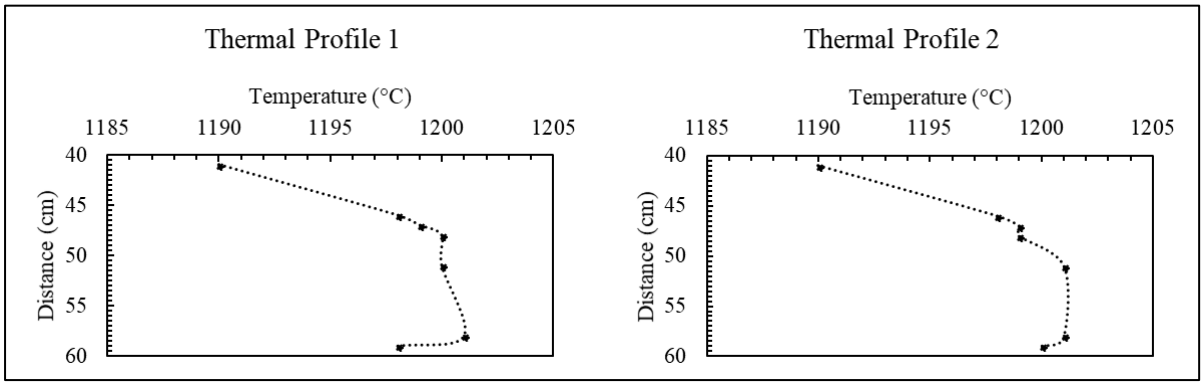

***Figure 2**. Thermals profiles 1 and 2 for the vertical 1-atm, CO-CO_2 gas mixing furnace*

OXYGEN FUGACITY CONFIGURATION OF THE FURNACE

The desired fO_2 composition within the furnace was achieved by mixing different proportions of CO and CO_2 gas, regulated by a manual mass flow controller (**Figure. 1**). Initially, the mass flow rates of the controller were verified using a simple gas flow timing exercise in conjunction with ***Equation 1***.

[***Equation1****:* Δf mass flow = $f$vol flow × $f$vol mass]

The gas flow timing exercise comprised various calculated proportions of CO_2 and CO gas to be funnelled into and disperse water from a 600 ml submerged beaker. For example; the 1 litre per minute controller was set at a 60% CO_2 gas flow with 0% CO, and it took 57 seconds to vet the beaker of water.

Oxygen fugacity calibration at the furnace hotspot:

The fO_2 (oxygen fugacity) of the hotspot was verified using the fO_2-dependant solubility of Fe in an anorthite ($CaAl_2Si_2O_8$) and diopside ($CaMgSi_2O_6$) eutectic melt composition (AD), previously defined by Holzheid et al. (1997). The synthetic AD powder was created using reagent grade oxide (50.33 wt.% subsequently mixed with hydrated polyethylene oxide to make a semi-solid "toothpaste-like" consistency. A portion of this starting composition mixture was then mounted onto Fe-wire loops made from thin (0.2cm) iron wire and suspended off a platinum wire chandelier (**Figure 3a, b**).

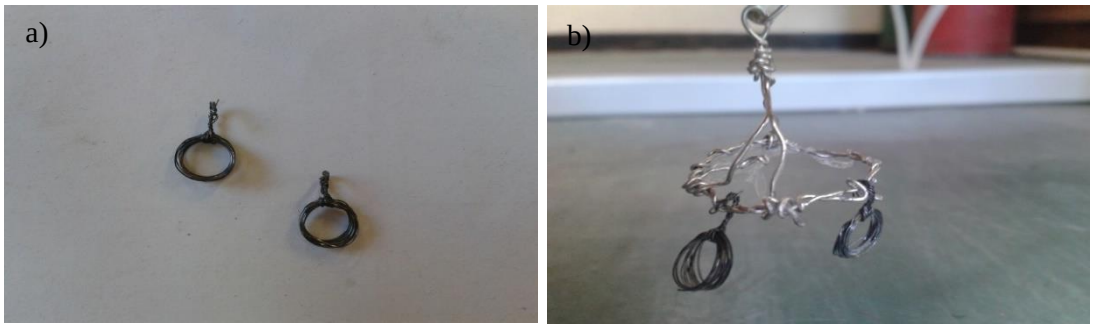

Figure 3. *a) Iron wire loops. b) Iron loops attached to Pt chandelier.*

Three different experiments were conducted at 1300 ºC with oxygen fugacities (fO_2) between QFM-2 and QFM-4. The experimental glass products were then analysed using the scanning electron microprobe (SEM) at the University of Stellenbosch and their compositions are shown in **Table 2**.

Table 2. Anorthite-Diopside glass compositions and calculated oxygen fugacity compositions

Run	CO-CO_2	Average wt% oxide of glass (n=10)[a]							Number of moles (calculated)							Calculated $\log X_{FeO}$	Calculated $\log fO_2$
	(l/min)	MgO	Al_2O_3	SiO_2	CaO	MnO	FeO	Total	MgO	Al_2O_3	SiO_2	CaO	MnO	FeO	Total		
Cal_50	0.5-0.5	2.3	5.8	20.8	9.4	0.0	61.8	100.0	0.0	0.0	0.1	0.1	0.0	0.7	1	-0.13	-10.65
Cal_70	0.3-0.7	1.9	6.6	28.2	12.1	0.2	51.0	100.0	0.0	0.0	0.2	0.1	0.0	0.6	1	-0.19	-10.76
Cal_70b	0.3-0.7	3.2	7.8	28.1	12.6	0.0	48.3	100.0	0.0	0.0	0.2	0.1	0.0	0.6	1	-0.21	-10.8
Cal_80	0.2-0.8	6.4	9.4	31.8	14.5	0.0	37.9	100.0	0.1	0.0	0.2	0.1	0.0	0.5	1	-0.29	-10.97

[a] The initial oxide mixture was prepared at the University of Cape Town under the guidance of Patricia Doyle.

The fO_2 of the hotspot was determined using ***Equation 2***, derived from Holzheid et al. (1997) and adapted for a CO_2-CO furnace by Doyle (2011). The results are tabulated in **Table 2** and depicted on **Figure 4**.

[***Equation 2***: $\log fO_2 = 2(\log \gamma_{FeO} + \log X_{FeO} - \log K^{Fe-FeO(I)})$]

Where:

fO_2 = oxygen fugacity at 1300°C (T_h)

γ_{FeO} = ~1.367 (from O'Neill and Eggins, 2002)

X_{FeO} = the mole fraction of FeO in the anorthite-diopside (AD) melt

$K^{Fe-FeO(I)}$ = the equilibrium co-efficient of the reaction: $Fe(s) + \frac{1}{2}O_2 = FeO(s) = FeO(I)$

$= e^{\Delta G/(-RT)}$

Where: $\Delta G = -244118 + 115.559T - 8.474T \times \ln T$

$R = 8.314472(15)\ JK^{-1}mol^{-1}$

$T = temperature\ (K)$

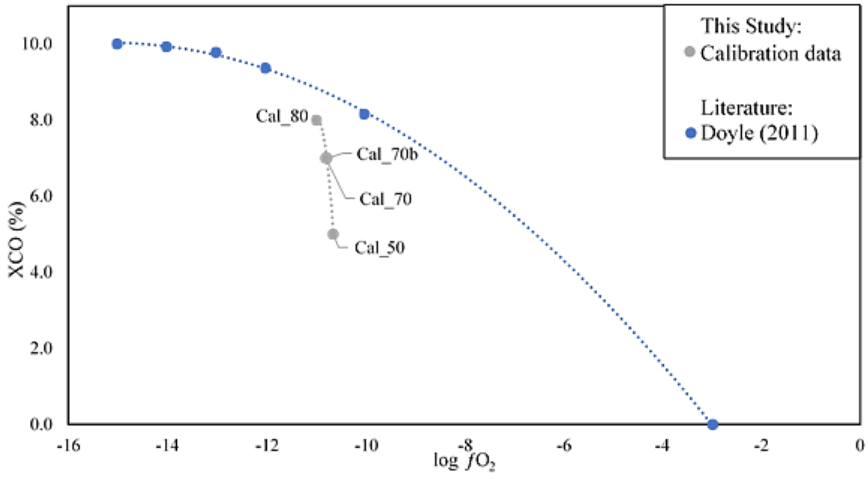

Figure 4. *Log fO_2 as a function of XCO.*

The experiments of this study show that for each CO-CO_2 mixing interval there is only a very small change in logfO_2 compared to the Doyle (2011) study. However, data published by Deines et al. (1974) also predicts a rather small change in logfO_2 for the same gas mixing interval at atmospheric pressure and thus, the results of this study are considered both accurate and reliable.

APPENDIX B2:

DETAILED CAPSULE CONFIGURATION

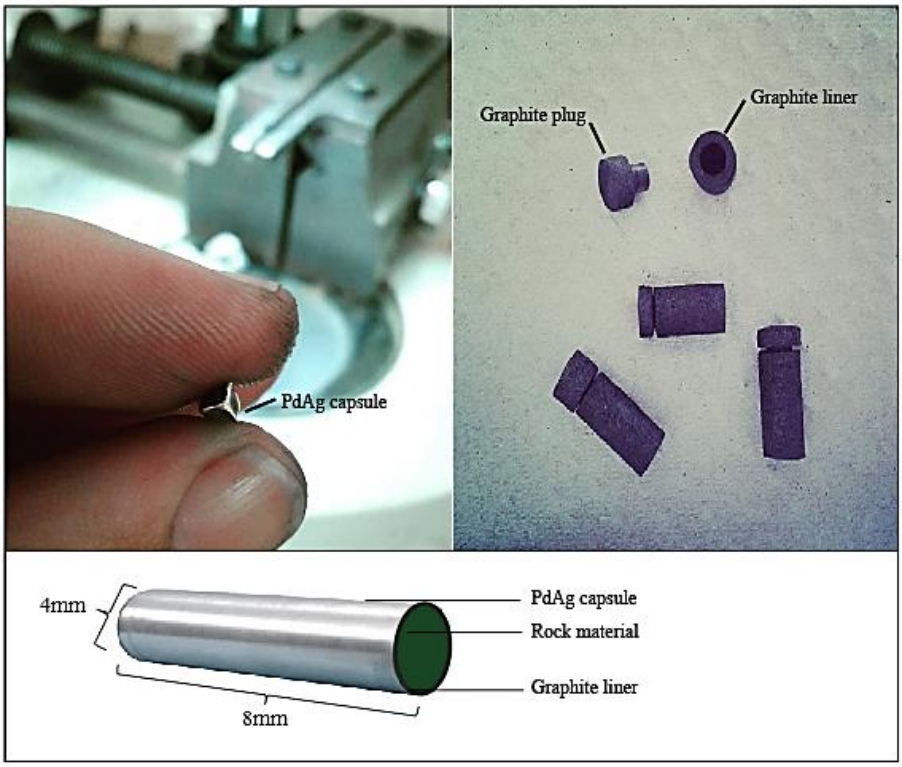

APPENDIX B3:

EXPERIMENTAL CELL ASSEMBLY

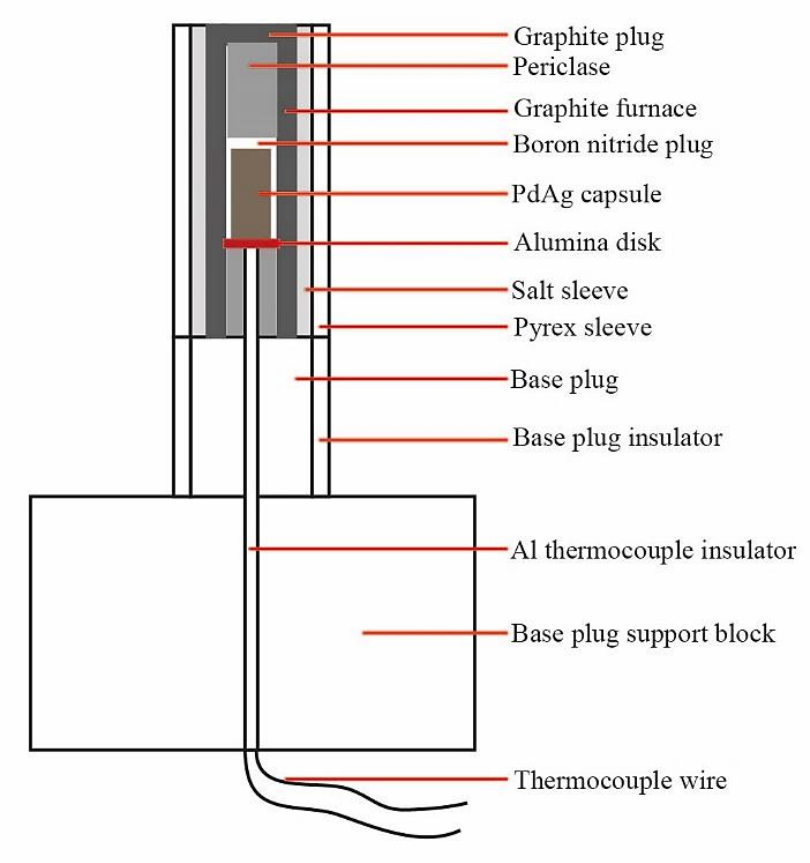

APPENDIX B4:

TEMPERATURE CALIBRATION EXPERIMENTS OF THE PISTON CYLINDER APPARATUS

Method:

Gold melting experiments were used to determine the accuracy between the actual and measured temperature of each experimental run. A gold sheet (5mm x 5mm x 0.1mm thickness) of 99% purity was placed vertically in the experimental cell assembly and secured by a periclase rod. Melting experiments were then conducted at a pressure of 1.0 GPa and temperatures of between 1064 °C and ~1115 °C ±4 °C (**Table 1**), the melting point of gold at 1. 0GPa (Cohen et al., 1966). Based on these experiments the error between the actual and measured temperature of each run is confirmed to be within 5 °C of the estimate.

Table 1. *Gold melting experiments for temperature calibration of the piston cylinder apparatus*

Run number	Metal (99.99% purity)	Duration (min)	Pressure (GPa)	Temperature (°C)	(Gold sheet)
Ca_01	Au	60	1.0	1111	deformed (potential melting)
Ca_02	Au	15	1.0	1064	no melting evident
Ca_03	Au	15	1.0	1084	no melting evident
Ca_04	Au	15	1.0	1105	no melting evident

In addition, a temperature gradient was mapped by measuring the change in temperature between the centre point of the furnace "Set" and a junction 5mm below this point (**Table 2**). A thermocouple was fashioned to have two junctions exactly 5mm apart (**Fig. 1**) and the resultant experiment shows a thermal gradient of ~20°C above and below the central junction.

Table 2. Thermal gradient calibration experiment

Run number	Time	[b]Temperature (°C) "Multical"	[a]Temperature (°C) "Set"	Pressure (Gpa)	Voltage (Volts)	Ampere (Amps)	% Power
Ca_05	10:13	1092	1101	1.00	120	9	39
Ca_05	10:18	1089	1101	0.97	119	9	39
Ca_05	10:23	1084	1101	0.95	119	9	39
Ca_05	10:40	1079	1099	1.00	119	9	39
Ca_05	10:50	1081	1102	1.00	119	9	39
Ca_05	11:10	1081	1100	0.98	119	9	39

Note: [a] Temperature measured by the "Depths of the Earth" temperature control unit at the centre (mid-point) of the graphite furnace. [b] Temperature measured by the hand-held unit with the thermocouple sitting 5mm below the midpoint.



Figure 1. Thermocouple for the temperature gradient experiment

Appendix C. Trace element composition of the SKG glass

Analytical conditions:

Laser:
Resonetics 193nm Excimer laser
Energy: 2.5J/cm2
Frequency: 10 Hz
Spot: 100µm per sample
Ablation gas: He @ 0.30L/min
Ablation time: 10sec background, 40sec ablation

ICP-MS:
Agilent 7700
Carrier gas: 1L/min Ar + 0.003L/min Nitrogen

Reference standard values: Jochum, K. P., Nohl, U., Herwig, K., Lammel, E., Stoll, B. and Hofmann, A. W. (2005), GeoReM: A New Geochemical Database for Reference Materials and Isotopic Standards. Geostandards and Geoanalytical Research, 29: 333–338. doi: 10.1111/j.1751-908X.2005.tb00904.x

Values in ppm		Sc	V	Cr	Mn	Co	Ni	Cu	Zn	Ga	Ge	As	Se	Rb	Sr	Y	Zr	Nb	Mo	Rh	Pd	Sn	Sb	Cs
LA QC std	Certified BCR glass	33.00	425	17	1550	38	13	21	125	23	1.5	0.65	0.072	47	342	35.00	184	12.5	270.00			2.6	0.35	1.16
	Average Analysed	**31.95**	**390.38**	**14.62**	1566.26	**36.48**	**11.99**	**16.88**	**146.15**	**21.83**	**2.03**	**0.87**	**0.59**	**47.46**	**319.96**	**31.37**	**173.38**	**10.52**	**240.26**			**1.82**	**0.33**	**1.10**
	Repl 1	32.09	392.27	15.11	1577.83	36.38	12.10	16.86	148.48	22.09	1.90	0.86	0.67	48.03	323.03	31.56	174.52	10.60	243.46	0.00	0.11	1.86	0.34	1.13
	Repl 2	31.80	388.49	14.13	1554.69	36.57	11.87	16.90	143.82	21.57	2.15	0.87	0.50	46.89	316.88	31.17	172.24	10.44	237.05	<0.0020	0.10	1.78	0.32	1.08
	% Deviation	*3.2*	*8.1*	*14.0*	*1.0*	*4.0*	*7.8*	*19.6*	*16.9*	*5.1*	*35.1*	*33.6*	*714.6*	*1.0*	*6.4*	*10.4*	*5.8*	*15.8*	*11.0*			*29.8*	*5.9*	*4.9*
Sara	SKG glass g1_1	679.87	702.85	783.04	980.35	102.78	20.51	2.29	4.79	24.46	20.26	47.62	83.58	223.66	790.19	731.82	805.10	761.58	574.51	78.03	800.13	0.72	45.29	123.09
	SKG glass g1_2	668.68	716.46	789.15	1020.14	119.77	25.13	2.41	6.19	27.08	20.20	46.01	82.76	240.24	786.17	712.87	794.65	764.53	602.94	76.83	703.88	0.63	42.38	126.01
	SKG glass g1_3	676.33	709.76	780.75	971.47	103.89	20.46	2.30	4.57	24.91	20.51	50.50	83.78	217.49	786.90	722.80	796.90	763.02	568.33	84.20	812.70	0.68	48.25	116.39
	SKG glass g2_1	683.93	690.79	772.80	583.94	34.75	5.36	1.42	1.55	13.34	16.67	46.58	79.26	107.92	802.47	721.70	799.26	752.42	133.18	98.72	531.35	0.38	38.69	51.69
	SKG glass g2_2	691.61	694.27	777.26	599.53	35.82	5.46	1.37	1.71	15.08	18.17	49.28	82.98	111.32	811.34	728.17	809.61	770.23	133.53	100.85	544.58	0.39	39.75	52.54
	SKG glass g2_3	680.14	699.65	766.74	604.13	42.45	5.16	1.45	1.88	17.11	19.71	45.01	81.61	109.16	810.30	720.76	796.36	778.95	141.27	92.45	535.15	0.57	37.92	52.90
	SKG glass g3_1	674.79	699.20	777.27	1063.57	121.09	22.17	2.31	6.41	20.77	16.09	39.71	77.25	232.02	788.12	721.21	798.54	757.23	503.31	58.45	723.85	0.39	35.30	125.04
	SKG glass g3_2	674.71	700.60	765.52	1047.13	119.78	20.49	2.04	5.69	20.32	13.84	25.77	75.42	218.16	784.01	713.03	798.03	761.90	448.97	38.40	410.22	0.24	20.59	107.71
	SKG glass g3_3	688.22	716.89	776.48	1048.47	113.50	20.31	2.44	5.47	18.67	15.52	37.04	77.92	206.54	791.01	727.38	807.91	770.96	535.00	58.49	736.23	0.36	32.29	111.82

Values in ppm		Ba	La	Ce	Pr	Nd	Sm	Eu	Gd	Tb	Dy	Ho	Er	Tm	Yb	Lu	Hf	Ta	Re	Pt	Au	Pb	Th	U
LA QC std	Certified BCR glass	683	24.7	53.3	6.7	28.9	6.59	1.97	6.71	1.02	6.44	1.27	3.7	0.51	3.39	0.503	4.84	0.78				11	5.9	1.69
	Average Analysed	**619.38**	**25.24**	**51.35**	**6.31**	**27.48**	**6.20**	**1.95**	**6.50**	**0.99**	**6.06**	**1.24**	**3.29**	**0.48**	**3.17**	**0.47**	**4.72**	**0.70**				**10.42**	**5.62**	**1.66**
	Repl 1	625.53	25.41	52.03	6.37	27.58	6.08	1.96	6.62	0.98	6.06	1.25	3.31	0.48	3.16	0.47	4.77	0.71	0.01	0.22	0.02	10.68	5.65	1.68
	Repl 2	613.23	25.06	50.67	6.24	27.37	6.31	1.93	6.37	1.00	6.06	1.23	3.27	0.48	3.18	0.47	4.67	0.70	0.01	0.22	0.02	10.16	5.58	1.64
	% Deviation	*9.3*	*2.2*	*3.7*	*5.9*	*4.9*	*6.0*	*1.2*	*3.2*	*3.0*	*5.9*	*2.5*	*11.1*	*6.5*	*6.5*	*7.5*	*2.5*	*9.9*				*5.3*	*4.8*	*2.0*
Sara	SKG glass g1_1	725.01	784.74	741.20	721.69	749.00	741.27	779.43	725.36	707.83	713.20	727.75	694.17	673.14	707.94	714.90	881.40	788.29	84.73	65.56	44.53	0.82	728.89	744.51
	SKG glass g1_2	716.57	769.64	736.82	712.14	737.61	720.09	762.56	704.31	692.41	696.48	712.36	674.33	656.08	694.63	698.79	867.56	783.41	81.69	65.08	45.02	0.85	717.11	744.47
	SKG glass g1_3	712.54	775.42	739.55	718.27	741.97	718.94	764.11	714.49	699.10	705.50	720.48	682.46	663.88	701.78	706.49	877.26	784.83	92.93	73.37	49.35	0.84	724.80	746.71
	SKG glass g2_1	761.51	774.64	733.58	714.65	739.71	736.64	761.91	716.63	699.47	705.78	718.47	687.95	666.36	702.19	710.11	882.75	784.48	82.84	82.58	51.07	0.22	731.78	745.83
	SKG glass g2_2	780.96	787.83	746.69	726.28	749.98	725.81	767.44	721.88	706.61	711.46	725.83	687.71	666.81	714.57	715.29	890.43	796.54	85.27	86.86	50.20	0.24	742.99	757.04
	SKG glass g2_3	767.11	781.12	743.44	722.26	751.36	719.84	754.53	712.24	704.52	715.54	720.07	678.15	661.67	704.48	710.00	882.82	793.12	78.85	86.42	45.69	0.29	728.74	775.45
	SKG glass g3_1	719.31	767.85	724.90	706.42	731.96	736.81	748.34	712.74	695.55	697.78	715.09	680.88	663.54	696.97	705.23	875.36	799.37	66.23	48.51	34.54	0.83	725.44	737.45
	SKG glass g3_2	712.90	760.85	722.03	703.12	727.91	708.73	739.13	700.81	686.29	692.85	707.61	673.70	653.58	694.64	698.81	877.48	805.92	45.42	31.16	21.26	0.68	724.10	743.58
	SKG glass g3_3	712.57	772.60	736.99	715.75	738.07	710.15	752.72	715.84	703.52	711.42	726.90	690.96	669.22	707.54	716.80	891.44	816.39	68.05	49.35	32.53	0.68	737.72	750.01

APPENDIX D:

ASIMEX CALCITE STANDARD USED IN SEM ROUTINE

Appendix D. Calcite standard compositional variability

ASTIMEX Standard	Calcite	Calcite	Calcite	Calcite	Calcite	Calcite	Calcite	Calcite	Calcite	Calcite	Calcite		Calcite
Spot no	1	2	3	4	5	6	7	8	9	10	Avg.	1 σ	Pub. Value
Element (%)													
C	12.07	12.03	12.11	12.06	11.95	11.97	11.99	12.06	12.03	12.05	12.03	0.047	12.02
Ca	39.91	39.94	40.02	40.01	39.86	39.93	39.97	40.04	39.99	40.01	39.97	0.054	39.98
Mg	0.01	0.01	bdl	0.01	bdl	bdl	bdl	0.01	0.01	0.01	0.01	0.005	0.01
Mn	bdl	0.01	bdl	bdl	bdl	bdl	bdl	bdl	0.01	0.01	0.01	0.005	0.01
Total:	51.99	51.99	52.13	52.08	51.81	51.90	51.96	52.11	52.04	52.08	52.01		52.02
Weight (%) of the compound													
CO_2	44.23	44.08	44.37	44.19	43.79	43.86	43.93	44.19	44.08	44.15	44.09	0.17	44.04
CaO	55.84	55.88	55.99	55.98	55.77	55.87	55.93	56.02	55.95	55.98	55.92	0.07	55.94
MgO	0.02	0.02	bdl	0.02	bdl	bdl	bdl	0.02	0.02	0.02	0.02	0.010	0.02
MnO	bdl	0.02	bdl	bdl	bdl	bdl	bdl	bdl	0.01	0.01	0.01	0.007	0.01
Total:	100.09	100	100.36	100.19	99.56	99.73	99.86	100.23	100.06	100.16	100.02		100.00

Element (%) analysed by the SEM. Weight (%) of the compound is calculated using ideal oxygen.

APPENDIX E:

CALCULATED OXYGEN FUGACITY OF INDIVIDUAL EXPERIMENTS

Appendix E. Calculated oxygen fugacity of individual experiments using calculated ferric iron contents ($Fe^{3+}/\Sigma Fe_{tot}$) of the experimentally produced garnet (Droop, 1987).

1			*1200*			*2*			*1200*			*3*			*1300*		
Pressure (GPa)		**2**	EG			**Pressure (GPa)**		**2**	EG			**Pressure (GPa)**		**2.5**	EG		
Temperature (°C)		**1200**			1060	**Temperature (°C)**		**1200**			1157	**Temperature (°C)**		**1300**			1341
Run:		***cpx***		***garnet***		Run:		***cpx***		***garnet***		Run:		***cpx***		***garnet***	
SKG-1.2						*SKG-2.1*						*SKG-3.3*					
wt%						wt%						wt%					
SiO2		**40.11**		**49.06**		***SiO2***		**39.60**		**50.10**		***SiO2***		**39.60**		**48.55**	
Al2O3		**22.52**		**10.30**		***Al2O3***		**22.02**		**8.24**		***Al2O3***		**20.91**		**11.61**	
CaO		**7.79**		**17.79**		***CaO***		**6.16**		**17.22**		***CaO***		**10.87**		**19.15**	
FeO		**17.43**		**6.67**		***FeO***		**16.52**		**8.25**		***FeO***		**17.46**		**8.42**	
MgO		**12.06**		**12.70**		***MgO***		**14.09**		**14.55**		***MgO***		**10.02**		**9.68**	
Na2O		**0.00**		**2.62**		***Na2O***		**0.00**		**1.54**		***Na2O***		**0.30**		**2.44**	
TiO2		**1.11**		**0.84**		***TiO2***		**0.65**		**0.64**		***TiO2***		**0.72**		**1.07**	
Total		**101.03**		**100**		***Total***		**99.04**		**100.55**		***Total***		**99.88**		**100.92**	
Fe3+grt				**0.03**		***Fe3+grt***				**0.11**		***Fe3+grt***				**0.08**	
logfo2andr		-11.91				***logfo2andr***		-9.06				***logfo2andr***		-8.74			
FMQ		-7.18				***FMQ***		-7.18				***FMQ***		-5.86			
Δlogfo2		**-4.74**				***Δlogfo2***		**-1.89**				***Δlogfo2***		**-2.88**			

APPENDIX F:

EXPERIMENTAL RUN-PRODUCT SILICATE MINERAL AND QUENCHED LIQUID COMPOSITIONS

Appendix F. Experimental run-product silicate and quenched liquid compositons, end-member calculations and molar Mg# numbers

Experiment	Phases	n	SiO_2	TiO_2	Al_2O_3	FeO	MgO	MnO	CaO	Na_2O	K_2O	CO_2	S	Total	Endmembers (mol. %)					Mg# [molar Mg/ (Mg + Fe)]
SKG-1.1	Grt	16	39.6	1.9	21.4	16.9	11.8	-	8.4	-	-	-	-	99.9	43.1 Py	34.6 Alm	22.2 Gro	0 Sp		
	Cpx	14	51.9	0.9	7.0	6.5	13.2	-	18.9	1.6	-	-	-	100.0	0 Aeg	13.5 Jad	86.5 Diop	44.6 Wo		
	L_{Sil}	10	57.0	1.3	19.8	5.2	3.9	-	6.4	5.5	0.8	-	-	100.0						0.57
SKG-1.2	Grt	20	40.1	1.1	22.5	17.4	12.1	0.6	7.8	-	-	-	-	101.6	43.5 Py	35.1 Alm	20.2 Gro	1.2 Sp		
	Cpx	12	49.1	0.8	10.3	6.7	12.7	-	17.8	2.6	-	-	-	100.0	16.8 Aeg	4.3 Jad	78.9 Diop	43.81 Wo		
	Coe	5	99.7	0.2	0.2	-	-	-	-	-	-	-	-	100.0						
	Fs	8	55.6	0.0	28.0	0.2	-	-	10.8	5.6	0.1	-	-	100.3						0.79
	L_{Sil}	30	56.4	2.0	17.4	2.9	6.1	-	11.9	2.9	0.2	-	-	99.8						
SKG-2.1	Grt	6	39.6	0.7	22.0	16.3	14.1	0.3	6.2	-	-	-	-	99.2	50.6 Py	32.9 Alm	15.9 Gro	0.7 Sp		
	Cpx	8	50.1	0.6	8.2	8.3	14.6	-	17.2	1.5	-	-	-	100.5	11.3 Aeg	2.6 Jad	86.1 Diop	39.3 Wo		
	L_{Sil}	15	54.2	1.9	16.2	8.4	4.5	-	8.2	2.5	0.2	4.1	-	100.2						0.49
SKG-2.2	Grt	7	42.2	1.5	19.2	19.9	5.8	0.2	10.3	0.3	-	-	-	99.3	23.8 Py	45.6 Alm	30.1 Gro	0.5 Sp		
	Cpx	8	55.3	1.2	14.1	5.5	9.4	-	9.8	5.2	0.5	-	-	101.1	0 Aeg	49.2 Jad	50.8 Diop	35.9 Wo		
	Coe	3	99.6	-	-	0.4	-	-	-	-	-	-	-	100.0						
SKG-2.3	Grt	3	41.5	0.6	20.8	20.0	10.5	-	6.5	0.4	-	-	-	100.3	39.7 Py	42.5 Alm	17.8 Gro	0 Sp		
	Cpx	7	55.0	0.4	12.8	5.0	8.6	-	12.3	6.6	-	-	-	100.7	1.5 Aeg	47.6 Jad	50.9 Diop	43.5 Wo		
	L_{Sil}	2	79.9	5.3	3.6	2.3	2.0	-	4.4	1.3	-	2.0	-	100.8						0.6
SKG-2.4	Grt	5	42.7	0.6	21.8	17.4	11.2	-	6.8	-	-	-	-	100.6	43.4 Py	37.7 Alm	18.9 Gro	0 Sp		
	Cpx	6	53.4	1.0	12.5	6.4	9.6	-	13.2	5.0	-	-	-	101.1	0 Aeg	40.6 Jad	59.4 Diop	41.9 Wo		
	Coe	2	99.6	0.5	0.6	0.3	-	-	-	-	-	-	-	100.9						
	$L_{C\text{-}Sil}$	3	1.1	-	0.7	4.2	3.9	-	43.7	-	-	46.5	-	100.0						0.62
SKG-2.5	Grt	3	43.0	0.9	19.4	18.7	9.0	0.2	8.0	0.9	-	-	-	100.0	35.4 Py	41.4 Alm	22.7 Gro	0.5 Sp		
	Cpx	3	54.7	1.2	13.1	5.0	8.0	-	11.7	6.5	-	-	-	100.1	0 Aeg	50.2 Jad	49.8 Diop	43.7 Wo		
	Coe	4	99.5		0.2	0.4	-	-	-	-	-	-	-	100.1						
	$L_{C\text{-}Sil}$	2	0.4	0.0	0.4	3.3	3.7	-	39.4	0.0	-	52.8	-	100.0						0.67
SKG-3.1	Grt	3	41.4	0.8	19.5	17.5	6.2	-	14.2	0.8	-	-	-	100.3	23.7 Py	37.4 Alm	38.9 Gro	0 Sp		
	Cpx	4	53.5	0.5	12.5	5.6	8.8	-	14.6	4.9	-	-	-	100.4	0 Aeg	37.7 Jad	62.3 Diop	46.8 Wo		
	CC-Dol_{SS}	2	1.1	0.0	0.7	4.2	3.9	-	43.7	0.0	-	46.5	-	100.0						
	$L_{C\text{-}Sil}$	2	12.4	1.6	3.2	4.5	4.2	-	29.9	0.5	-	43.7	0.29	100.0						0.62
SKG-3.2	Grt	3	40.7	1.0	20.9	20.0	7.8	0.2	9.4	-	-	-	-	100.0	30.2 Py	43.4 Alm	26 Gro	0.4 Sp		
	Cpx	4	51.9	0.4	10.2	6.4	9.3	0.0	17.8	4.0	-	-	-	100.0	5.9 Aeg	22.9 Jad	71.1 Diop	49.9 Wo		
	Coe	2	92.1	0.8	2.6	2.8	0.9	-	1.1	-	-	-	-	100.4						
	$L_{C\text{-}Sil}$	1	11.6	0.0	2.9	2.8	2.7	-	32.4	0.6	-	46.9	0.27	100.0						0.64
SKG-3.3	Grt	4	39.6	0.7	20.9	17.3	10.0	0.3	10.9	0.3	-	-	-	100.0	36.2 Py	35.1 Alm	28.2 Gro	0.5 Sp		
	Cpx	2	48.6	1.1	11.6	8.4	9.7	-	19.2	2.4	-	-	-	100.9	8.3 Aeg	10.4 Jad	81.3 Diop	48.9 Wo		
	$L_{C\text{-}Sil}$	5	2.4	-	0.9	2.1	2.0	-	49.6	0.2	-	42.4	-	99.7						0.53
SKG-3.4	Grt	7	44.0	1.2	20.4	26.7	5.7	-	2.2		-	-	-	100.1	25.5 Py	67.4 Alm	7.12 Gro	0 Sp		
	Cpx	10	51.1	0.8	12.6	7.7	9.7	-	15.6	3.6	-	-	-	101.1	0 Aeg	29.5 Jad	70.5 Diop	44.5 Wo		
	$L_{C\text{-}Sil}$	5	4.5	-	2.4	3.2	2.1	-	45.9	-	-	43.1	0.10	101.3						0.63

Phase abbreviations as in **Table 4.3 and 4.4**. All values in wt. %.